Publication No. U-3034

RE-ENTRY AND SPACE SYSTEMS PROGRAMS

FINAL REPORT

STUDY OF A HIGH RESOLUTION FACSIMILE SYSTEM EXPERIMENT ON THE SURFACE OF THE PLANET MARS

Prepared for: Jet Propulsion Laboratory
California Institute of Technology
Pasadena, California

Under Contract: JPL Contract No. 950996

Prepared by: Engineering

Approved by:

R. A. Mills
Program Engineer

W. A. Orum
Program Supervisor

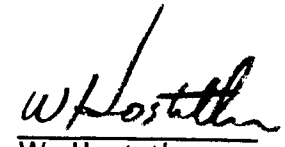

W. Hostetler
Program Manager

25 February 1965

AERONUTRONIC
DIVISION OF PHILCO CORPORATION
A SUBSIDIARY OF Ford Motor Company
FORD ROAD/NEWPORT BEACH, CALIFORNIA

ABSTRACT

13574

A six-month Study Program was performed under JPL Contract 950996 to determine the feasibility of conducting a high resolution facsimile camera experiment on the surface of the planet Mars. The mission considered would begin just prior to a 300 to 500 feet per second impact on the Martian surface and would last until the facsimile picture data were transmitted to earth. The total weight which was to be considered for the hard landing capsule was restricted to the range of 300 to 600 pounds. The salient capsule subsystems which were parametrically studied during the program are as follows:

Hard Landing Technology

High Resolution Facsimile System

Telecommunications

Transmitter and Antenna Configuration

Memory Systems

Thermal Control

Sterilization

Beneficial results were arrived at in several of the above areas with a significant advance having been made in the field of hard impact technology. A mathematical model was derived for the unidirectional balsa wood impact limiter which took into account both the dynamic and static impact characteristics of the limiter.

The study concluded with the conceptual design of a 450-pound capsule capable of surviving a 400 feet per second impact and subsequently scanning and transmitting back to Earth a 24 x 24 degree picture.

It was concluded that such a capsule is feasible for a 1969 to 1971 Mars mission.

Author

CONTENTS

CONTENTS (continued)

ILLUSTRATIONS

ILLUSTRATION (Continued)

ILLUSTRATION (Continued)

ILLUSTRATIONS (Continued)

ILLUSTRATIONS (Continued)

ILLUSTRATIONS (Continued)

ILLUSTRATIONS (Continued)

ILLUSTRATIONS (Continued)

SECTION 1

INTRODUCTION

This is the final report prepared by the Aeronutronic Division of the Philco Corporation for the Jet Propulsion Laboratory, California Institute of Technology, in accordance with the requirements of JPL Contract No. 950996. This contract was for a study to determine the feasibility and capabilities of a hard-landing capsule to perform a high resolution facsimile experiment for an early Mars mission.

The study was constrained in scope by certain mission requirements. These were: a capsule payload consisting of a high resolution facsimile camera with all subsystems required to transmit the picture to Earth, a mission sequence beginning just prior to surface impact, a total weight range of 300 to 600 lbs, a landing velocity of up to 500 ft/sec, omni-directional impact protection furnished by balsa wood, and a complete capsule capable of terminal heat sterilization.

The study started with a trade-off study phase to explore in parametric fashion all the capsule variables associated with the facsimile camera, hard-landing impact protection, capsule thermal control, data transmission, and electrical power source. These results are presented in the report as parametric curves, whenever possible, to show the effects of varying specific parameters. An important task during this phase was the capsule impact analysis. The analysis originally made for the Ranger capsule was extended to include dynamic effects, larger capsule sizes, curved landing surfaces, and much greater impact velocities.

An important task in the study was the preparation of the report, Capsule Impact Technology, Aeronutronic Publication No. U-3031. This report was

prepared at JPL request to better document Aeronutronic's knowledge in the field of hard-landing capsules. Essentially, the report summarizes the analytical, design, and test experience of Aeronutronic during its several lunar and planetary capsule programs.

The last portion of the study was concerned with establishing a complete conceptual design for a capsule in order to determine system feasibility. It was shown that it is feasible to design a 450 lb capsule which can land on Mars at 400 ft/sec, obtain a 24° by 24° high resolution facsimile picture, and transmit this data directly to Earth. This final report shows just what such a capsule can accomplish, how it performs these tasks, and how the variations in performance are related to the system mission.

The study defined the technical areas most needing additional effort, as listed below in order of importance:

(1) Sterilizable batteries.

(2) Test verification of impact model analysis.

(3) Development of an impactable 20 watt transmitter.

(4) Obtaining of more balsa test data.

(5) Better definition of picture requirements, (resolution, necessary grey levels, picture angular size).

(6) Sterilizable pyrotechnic devices.

(7) Impactable thermal insulation.

The problem of a sterilizable power supply was found to have several promising solutions -- but needing continued development. Both silver-zinc batteries with inorganic separators and high-temperature thermal batteries appear to offer practical solutions to the sterilizable power supply requirements. Solutions to the remaining problems on the list should yield in straightforward fashion to a normal development program.

It was concluded that a hard-landing Mars Facsimile Capsule is feasible, and that it can be planned for an early mission since the weight is low, no complicated landing system need be developed, the capsule performance is not sensitive to assumptions about the Mars surface or atmosphere, and the development ground-work was accomplished during the Ranger capsule program. The capsule is capable of returning pictorial data which has value in the diverse fields of biology, meteorology, geology, astronomy, physics, and engineering. With an early program go-ahead, the capsule could be available for launch in the 1969-1971 time period.

SECTION 2

TECHNICAL SUMMARY

This section summarizes the information presented in the subsequent parts of the report regarding the Capsule Conceptual Design and the trade-off Studies.

2.1 CAPSULE CONCEPTUAL DESIGN

Section 4 describes a specific capsule design which is capable of performing the hard-landing high-resolution-facsimile camera mission. This design is intended to demonstrate feasibility and acquaint the reader with all the subsystems comprising a capsule. The performance characteristics of the design represent one set of design points taken from the trade-off curves given in the later sections of this report. Table 2.1-I lists the important performance characteristics and Figure 1 illustrates the conceptual design.

The 115-pound inner payload is protected by 335 pounds of balsa during a 400 ft/sec impact against a hard surface. The balsa impact limiter is spherical, providing equal protection against impacts in any direction. After landing, the balsa is separated from the payload, the floated payload erects to the local vertical, porting of the flotation shells occurs, and the camera viewing tube is extended upward. On top of the viewing tube, a helical antenna is erected to permit direct communication with Earth.

The capsule payload consists of the facsimile camera, a silver-zinc battery, thermal insulation, water for thermal control, signal handling electronics, a magnetic core memory, and a triode-cavity transmitter.

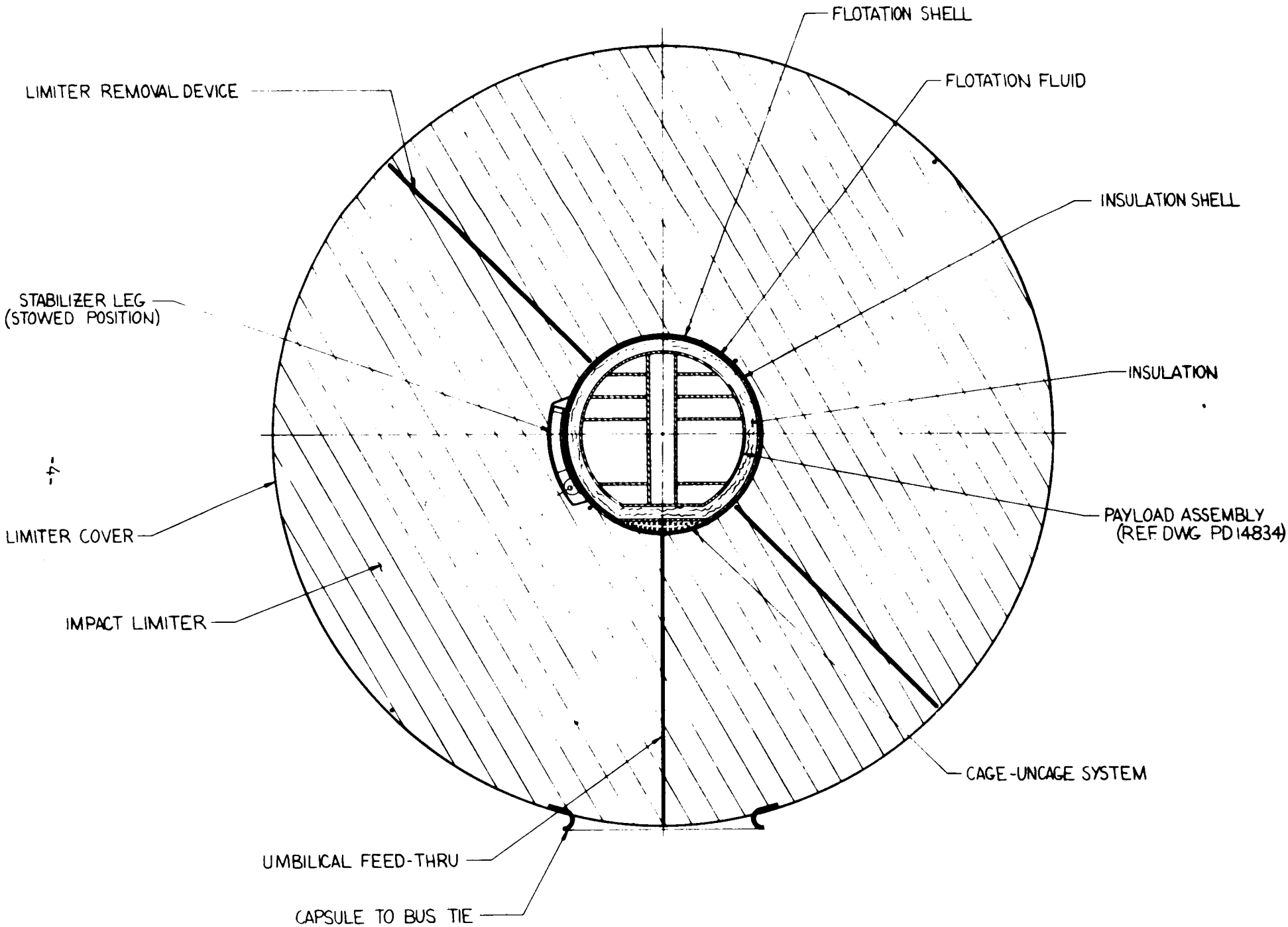

FIGURE 1. TYPICAL CAPSULE CONFIGURATION

TABLE 2.2-I

CAPSULE CHARACTERISTICS

Payload Weight	115 lbs.
Total Capsule Weight	450 lbs.
Maximum Impact Velocity	400 ft/sec
Picture Size	$24^{\circ} \times 24^{\circ}$
Resolution	0.1°
Scan Time	1 hour
Gray Levels	16
Total Data	2.5×10^{5} bits
Transmission Distance	1.2 AU
Transmission Data Rate	12 bits/second
Transmission Time per Day	2 hours
Antenna Gain	12 db
Transmitter Power	20 watts
Transmission Frequency	S-Band
Maximum Capsule Surface Life	4 days

The facsimile camera will obtain a 24^{o} x 24^{o} picture having a resolution of 0.1^{o} and 16 gray levels. The 2.5×10^{5} bits of picture data will be stored in a magnetic core memory until they are transmitted by the 20 watt transmitter. Transmission will occur for 2 hours per day at a rate of 12 bits/sec.

Electrical power for the capsule is furnished by a secondary silver-zinc battery with an energy density of 40 watts-hours/lb. The entire capsule, including the battery, will be sterilized before launch at a temperature of 135^{o}C for 24 hours. Thermal control of the payload on the surface is achieved entirely passively. Low-conductivity insulation surrounds the payload to balance the internal heat dissipation with the heat lost to the generally cold Martian environment. In addition, water is provided for boil-off to limit the maximum payload temperature to approximately 100^{o}F.

The vertically-oriented antenna of the capsule imposes some restrictions on possible landing sites. It is generally costly in capsule power and thermal control water to have a long surface operating life; therefore, a maximum amount of picture data must be transmitted to Earth each day. This requires a narrow-beam antenna for high gain. Such an antenna is usable only at the Martian latitudes where Earth passes near the zenith. The landing site is therefore restricted to somewhere within 26 degrees of the equator, the exact latitude depending upon the arrival date.

2.2 TRADE-OFF STUDIES

The major technical results of the study are included in Section 5, Trade-off Studies, and Section 6, Appendicies. The salient results of the trade-off studies are summarized below.

2.2.1 SYSTEM CONSIDERATIONS

Section 5.1 of the Trade-off Studies investigates certain aspects of the capsule which could not be included conveniently in the subsequent subsystem sections. The basic capabilities of the MFC are described and reasons are given why a facsimile camera is so well suited to a hard landing capsule. A brief explanation is given of what value a surface picture of Mars could have and what additional experiments could possibly be included within the same capsule.

The communication geometry for the landing period of 1968 to 1975 is also shown in Section 5.1. It is pointed out that equatorial landing sites are interesting from the scientific viewpoint and are also easiest to accommodate with a simple capsule antenna. An example is used to illustrate the relationship between the landing site and the probable sequence of capsule surface operations.

Sterilization considerations for the capsule are included within the system section but also throughout the subsystem discussions. The expected sterilization requirements involving post-assembly heating of the total capsule within a biological barrier are reviewed. The effects of this heat treatment are predicted on most components and subsystems.

2.2.2 IMPACT ANALYSIS

All of the analytical models considered during the study utilize balsa wood which has its grain oriented radially. It is assumed that the direction of impact is unknown; therefore, the limiter must absorb energy equally well in all directions.

The study analysis began with an examination of the crushing process in balsa. It was determined that the crushing front propagated through the limiter by means of a shock wave. The shock heating associated with the discontinuity across the shock wave is proportional to the square of the instantaneous velocity and becomes a significant factor for impact velocities in excess of 200 ft/sec. This effect represents an increase in the energy absorbing capability of balsa wood above the static mechanical crushing energy. Next, a general spherical impact limiter model was developed which accounts for the cross-grain compressive stress, the shock-heating effect, and the static mechanical crushing energy for impacts on curved landing surfaces. The derivation of this model results in an integral which must be numerically integrated. Figures 2 and 3 parametrically illustrate the capability of a balsa limiter based upon the dynamic model. These figures depict the total weight and radius which are necessary to provide impact protection for various payload weights at various impact velocities. Also shown are the impact decelerations which can be anticipated for each configuration.

The effect of landing on a curved hard surface was calculated for the case of the radius of curvature of the surface being twice that of the impact limiter. The maximum velocity capability for the particular configuration on a flat surface was 438 ft/sec with the concave surface increasing the capability to 515 ft/sec and the convex surface reducing the capability to 375 ft/sec.

The effect of varying the balsa density within the impact limiter was investigated to determine whether such a technique could improve the limiter velocity capability. It was determined that more dense balsa on the outer portion of the limiter would reduce the total decelerations associated with a particular configuration, but that the maximum impact velocity capability would not be increased. If the more dense material is placed inside (adjacent the payload), the maximum allowable impact velocity is decreased and the peak deceleration increased.

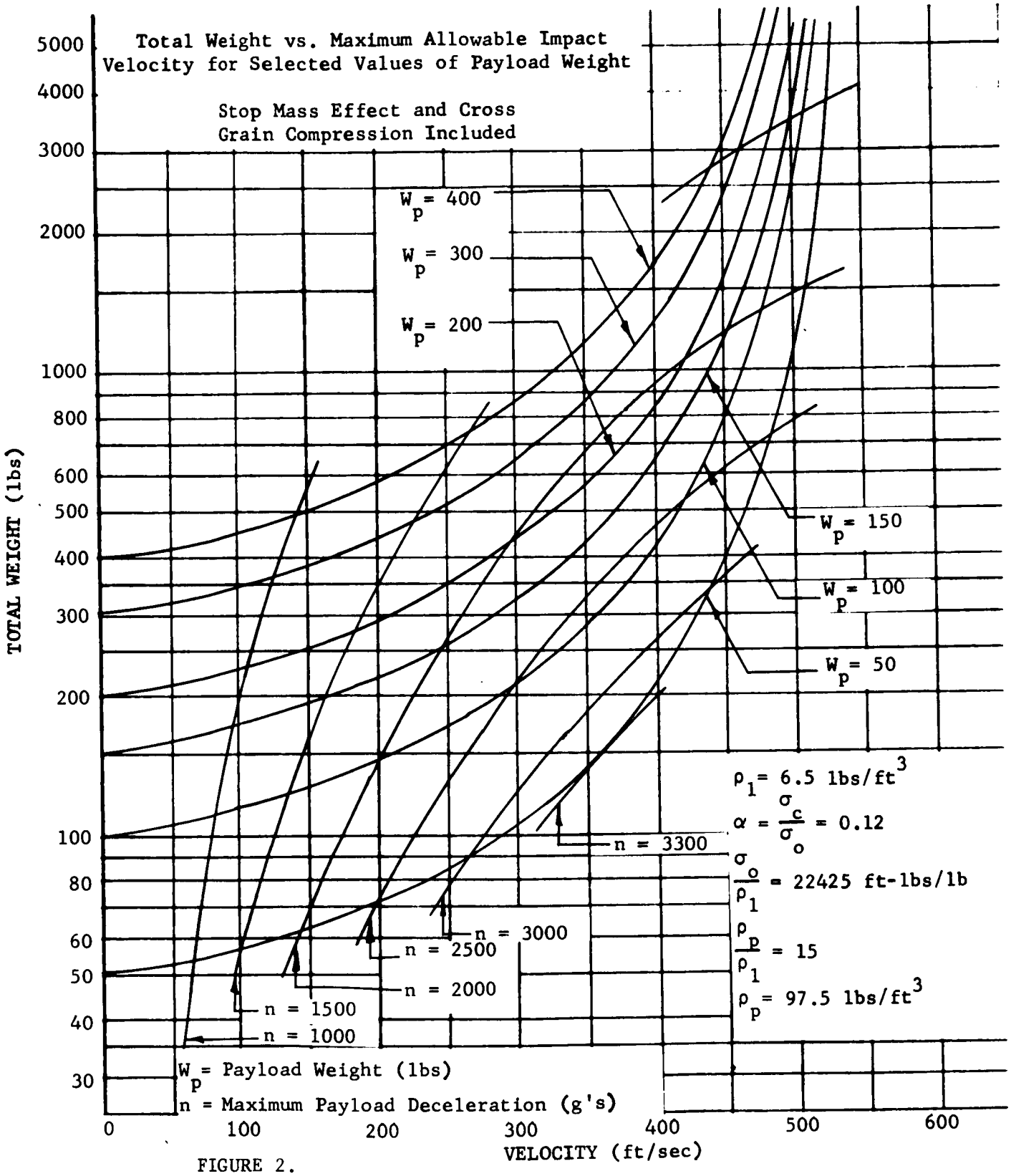
Total Weight vs. Maximum Allowable Impact Velocity for Selected Values of Payload Weight
Stop Mass Effect and Cross Grain Compression Included
TOTAL WEIGHT (lbs)
VELOCITY (ft/sec)
5000
4000
3000
2000
1000
800
600
500
400
300
200
100
80
60
50
40
30
0
100
200
300
400
500
600
W_p = 400
W_p = 300
W_p = 200
W_p = 150
W_p = 100
W_p = 50
n = 3300
n = 3000
n = 2500
n = 2000
n = 1500
n = 1000
ρ_1 = 6.5 lbs/ft^3
α = σ_c/σ_o = 0.12
σ_o/ρ_1 = 22425 ft-lbs/lb
ρ_p/ρ_1 = 15
ρ_p = 97.5 lbs/ft^3
W_p = Payload Weight (lbs)
n = Maximum Payload Deceleration (g's)

FIGURE 2.

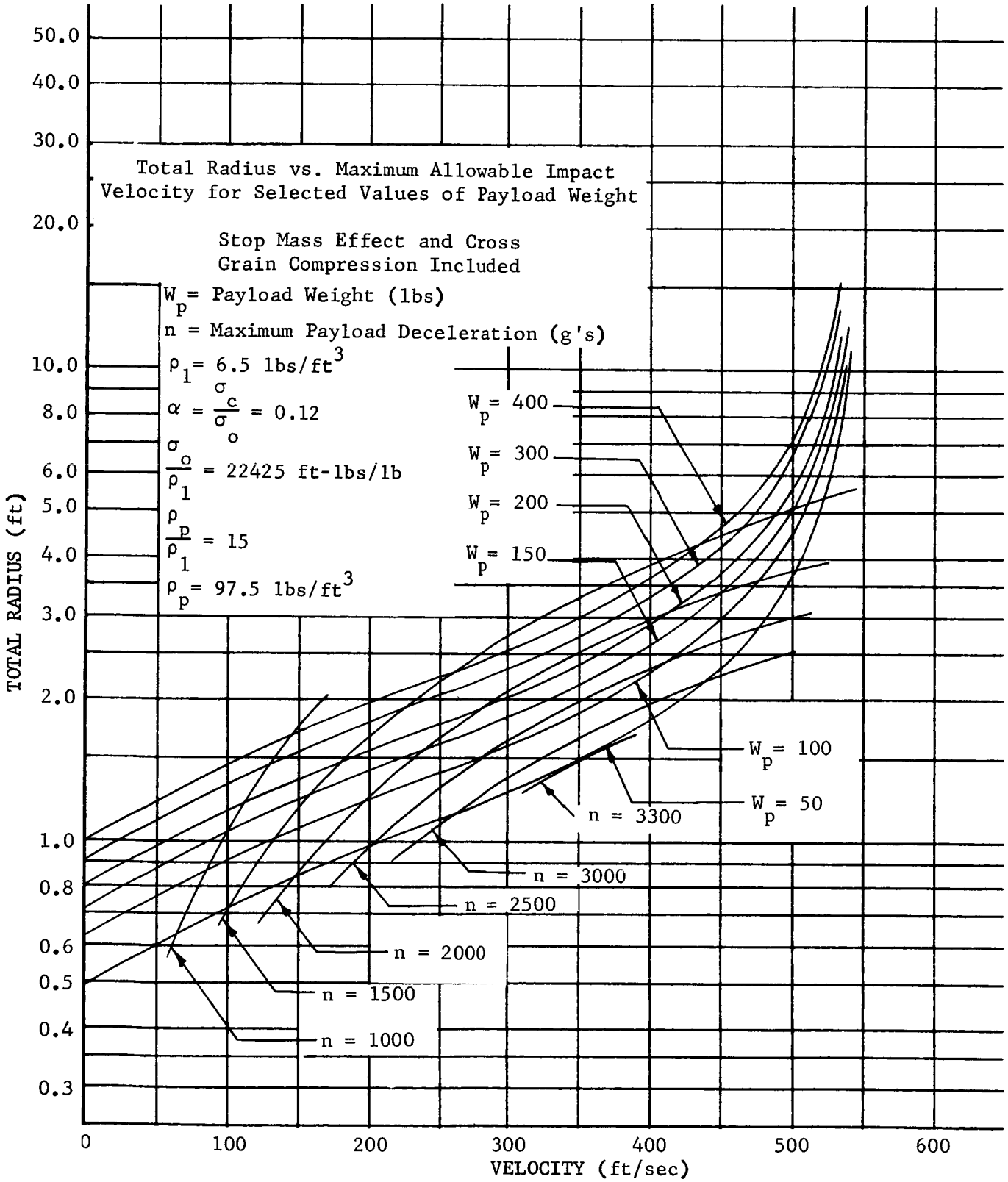
Total Radius vs. Maximum Allowable Impact Velocity for Selected Values of Payload Weight
Stop Mass Effect and Cross Grain Compression Included
W_p = Payload Weight (lbs)
n = Maximum Payload Deceleration (g's)
ρ_1 = 6.5 lbs/ft^3
$\alpha = \frac{\sigma_c}{\sigma_o}$ = 0.12
$\frac{\sigma_o}{\rho_1}$ = 22425 ft-lbs/lb
$\frac{\rho_p}{\rho_1}$ = 15
ρ_p = 97.5 lbs/ft^3
W_p = 400
W_p = 300
W_p = 200
W_p = 150
W_p = 100
W_p = 50
n = 3300
n = 3000
n = 2500
n = 2000
n = 1500
n = 1000
TOTAL RADIUS (ft)
VELOCITY (ft/sec)
50.0
40.0
30.0
20.0
10.0
8.0
6.0
5.0
4.0
3.0
2.0
1.0
0.8
0.6
0.5
0.4
0.3
0
100
200
300
400
500
600

FIGURE 3

There was also an investigation into the conditions under which payload movement within the impact limiter can occur. This analysis involves two fundamental considerations: (1) the payload-to-limiter density ratio; and (2) the balsa cross-grain stress. The first consideration determines whether the balsa below the payload can support the payload during impact without being stressed above its crushing stress. The second consideration determines whether the limiter can support its upper portion during impact; if it can not then an additional load is transmitted through the payload which adds to the stress on the balsa wood below the payload. Section 6.3 discusses this phenomenon more thoroughly and indicates the conditions under which payload movement will begin.

2.2.3 HRF CAMERA

Section 5.3 concerns the high resolution facsimile camera and its application to the MFC mission. The radiometry of the Mars surface was calculated using atmospheric transmission and surface reflectance properties furnished by JPL. The resulting irradiance for the camera sensor is shown to be strong in the infrared region of the Solar spectrum and well suited to a silicon photo sensor. Figure 4 indicates the irradiance vs. wavelength which can be expected on the surface of Mars; also shown is the relative response of a silicon detector which has been chosen for this application.

The photometry of the facsimile camera system was analyzed and trade-off curves derived which show the parameters which can be varied in establishing a camera design. Figure 5 relates the camera near field distance, angular resolution, pinhole diameter, lens-to-pinhole distance, and lens focal length.

It is concluded that the HRF camera is well suited to both stereo and multi-spectral adaptations. These areas are not deeply analyzed because of program limitations and the feeling that data transmission limitations will preclude their inclusion in an early mission.

2.2.4 TELECOMMUNICATIONS

The telecommunication analysis analyzed several methods by which the facsimile data could be transmitted from Mars to Earth. First, a direct link was considered using a typical Mariner PCM/PSK/PM modulation format at S-Band. Figure 6 illustrates the power levels required of the transmitter to result in useful data rates. Communication distances of 1 to 1.2 AU resulted from the missions considered and in order to operate in the linear (most efficient) region of the curves transmitter power of 10 to 20 watts was primarily considered. This results in data transmission rates of 8 to 17 bits/second. Lower power requirements can be obtained with a "multiple frequency shift" method, but it is not currently

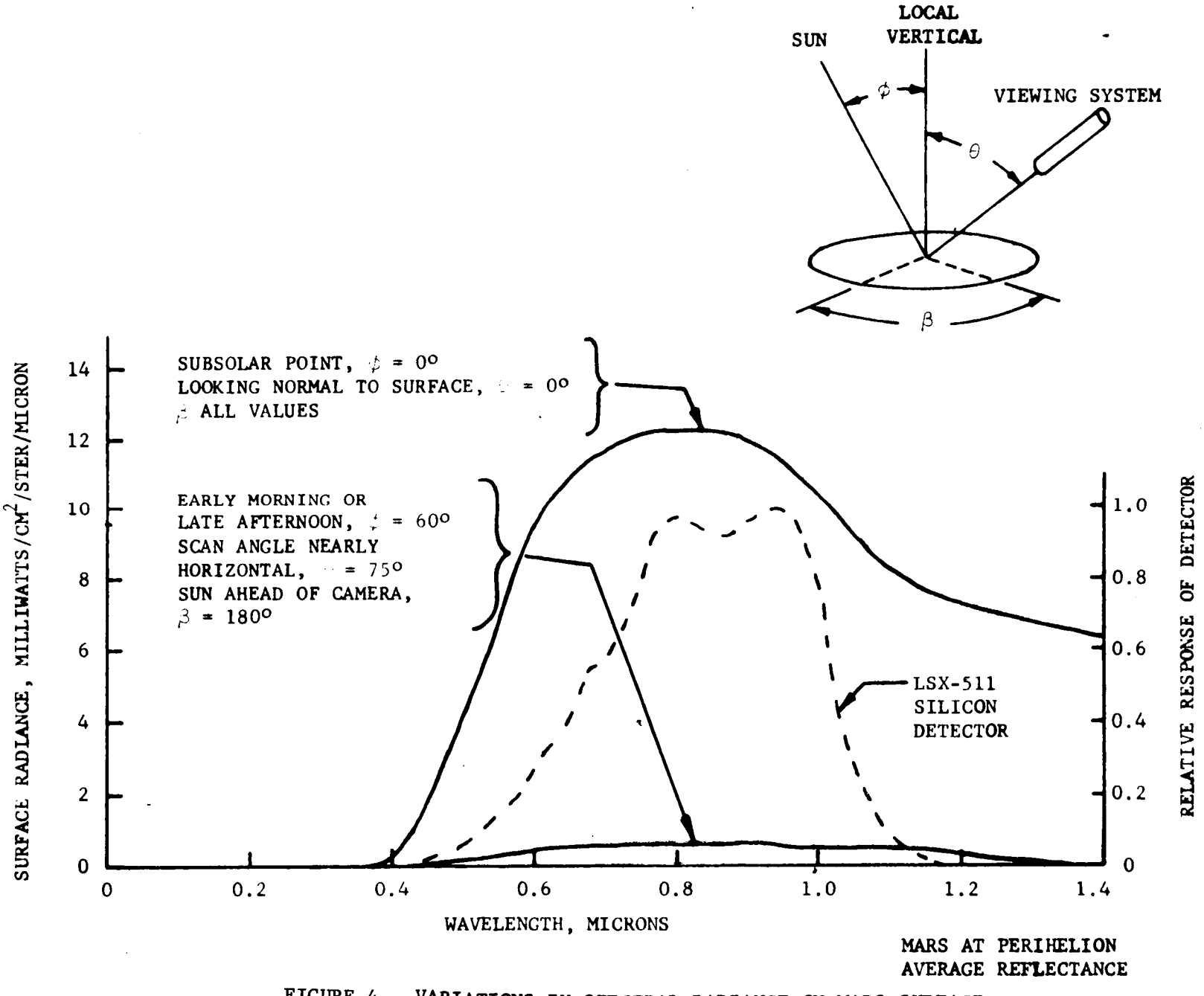

FIGURE 4. VARIATIONS IN SPECTRAL RADIANCE ON MARS SURFACE

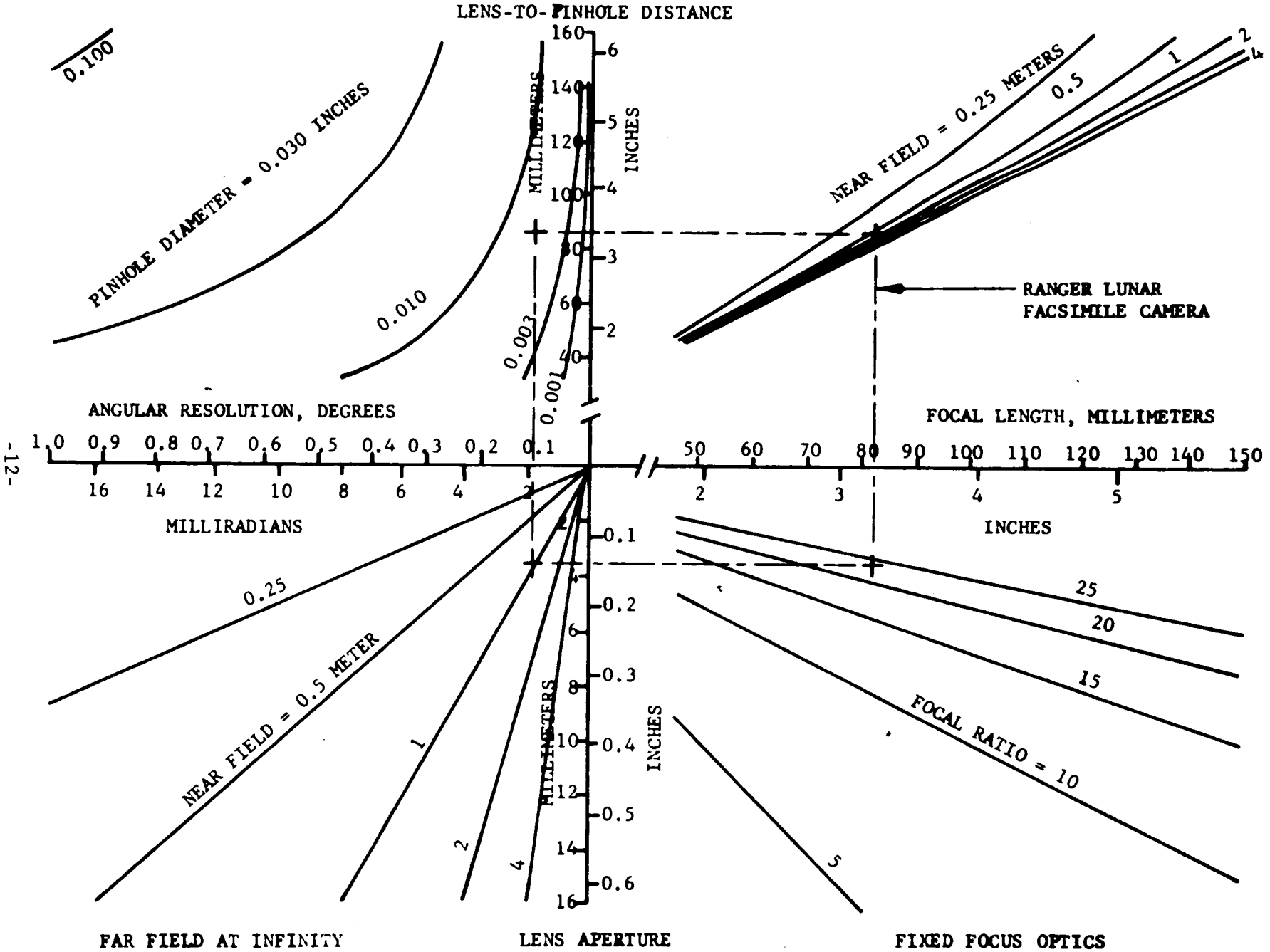
LENS-TO-PINHOLE DISTANCE
0.100
PINHOLE DIAMETER = 0.030 INCHES
0.010
0.003
0.001
MILLIMETERS
INCHES
NEAR FIELD = 0.25 METERS
0.5
1
2
4
RANGER LUNAR
FACSIMILE CAMERA
ANGULAR RESOLUTION, DEGREES
FOCAL LENGTH, MILLIMETERS
MILLIRADIANS
INCHES
0.25
NEAR FIELD = 0.5 METER
1
2
4
5
25
20
15
FOCAL RATIO = 10
FAR FIELD AT INFINITY
LENS APERTURE
FIXED FOCUS OPTICS

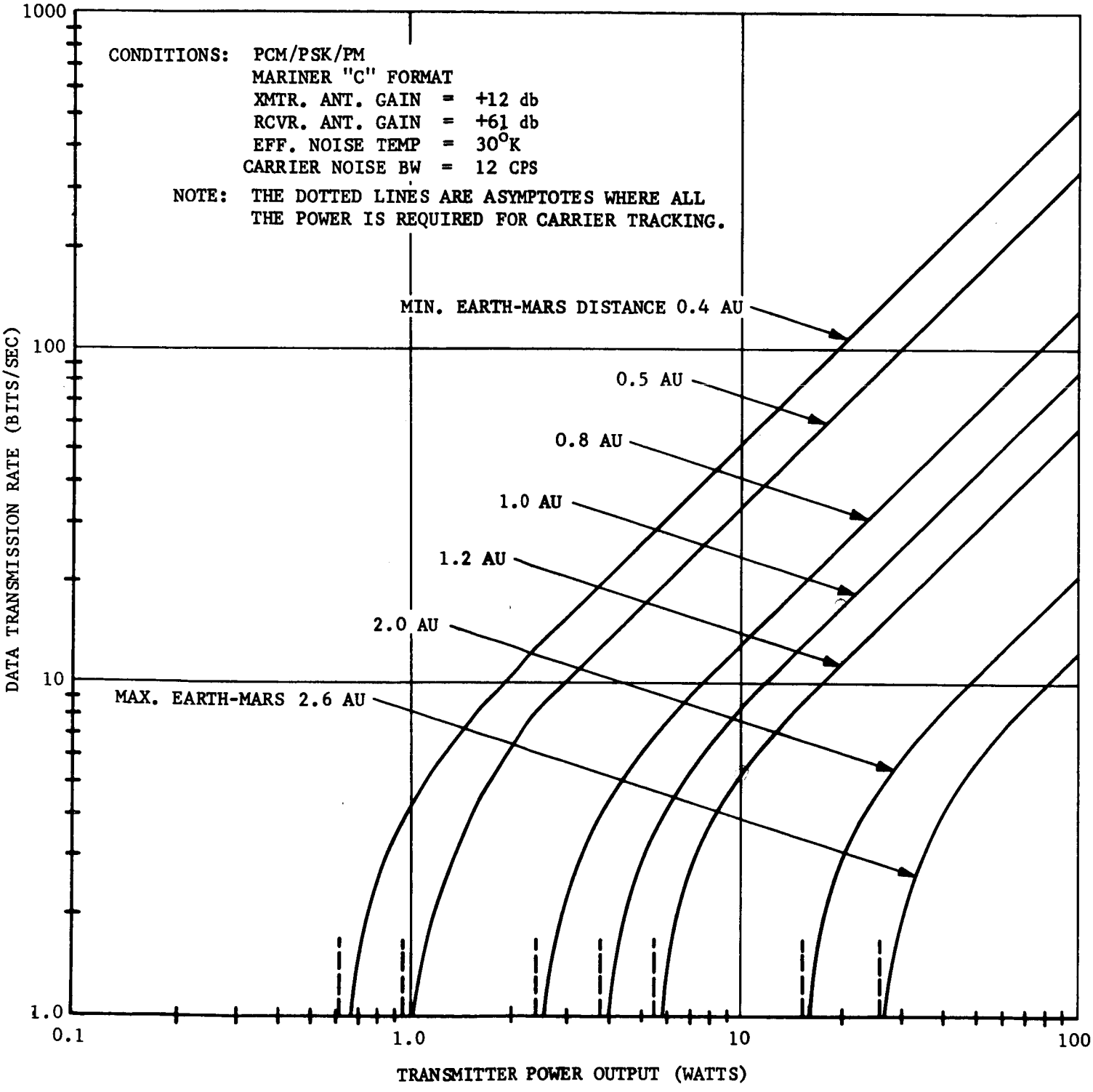

R11198

FIGURE 6 . TRANSMISSION CAPABILITY FROM MARS.

employed by the existing DSN stations; consequently, it was not incorporated in the MFC.

The use of the fly-by spacecraft as a data relay was also considered. This method was found to be feasible at a frequency of 230 mc; however, it would, of course, require additional interfaces with the spacecraft. The predicted reliability of this method of Mars-Earth communication is less than that for the direct link because of the increased serial data handling.

It was also determined that is is possible for the MFC to receive commands from Earth. The weight penalty of several pounds, however, did not seem to have any compensating benefits for the capsules considered.

2.2.5 TRANSMITTER

Several methods of implementing S-band transmitters were considered in the transmitter study. The output stages evaluated include vaccum triodes, varactor multipliers, amplitrons, and travelling wave tubes. The power output (10-20- watt) and shock requirements narrow the choice to the varactor multiplier and vacuum triode. The varactor multipliers result in an overall transmitter efficiency of only 7.5% but have good shock resistance. Vacuum tubes result in an overall transmitter efficiency of 18% but with less impact resistance. Section 5.5 includes several circuit diagrams of proposed transmitter configurations utilizing available components.

2.2.6 ANTENNA

Several antenna configurations were considered for use on the MFC; however, the requirements that the antenna present a low cross-sectional area to the Martian winds and be easily deployable from within the capsule narrowed the selection to an end-fire helix. Figure 7 illustrates the method of determining the optimum gain and beamwidth characteristics for a passive, vertically-oriented antenna with assumed landing and pointing errors. The conclusion is reached that a 42^{o} beamwidth, 12 db antenna is a desirable solution under certain distance, landing site, and transmitter power conditions.

The problem of antenna breakdown in the Martian atmosphere was reviewed, and it was concluded that there will be no difficulty at the probable MFC power level of less than 30 watts.

2.2.7 CAPSULE ELECTRONICS

Section 5.7 looks at the problems of data handling and sequencing for the capsule. The requirement for analog-to-digital conversion is easily

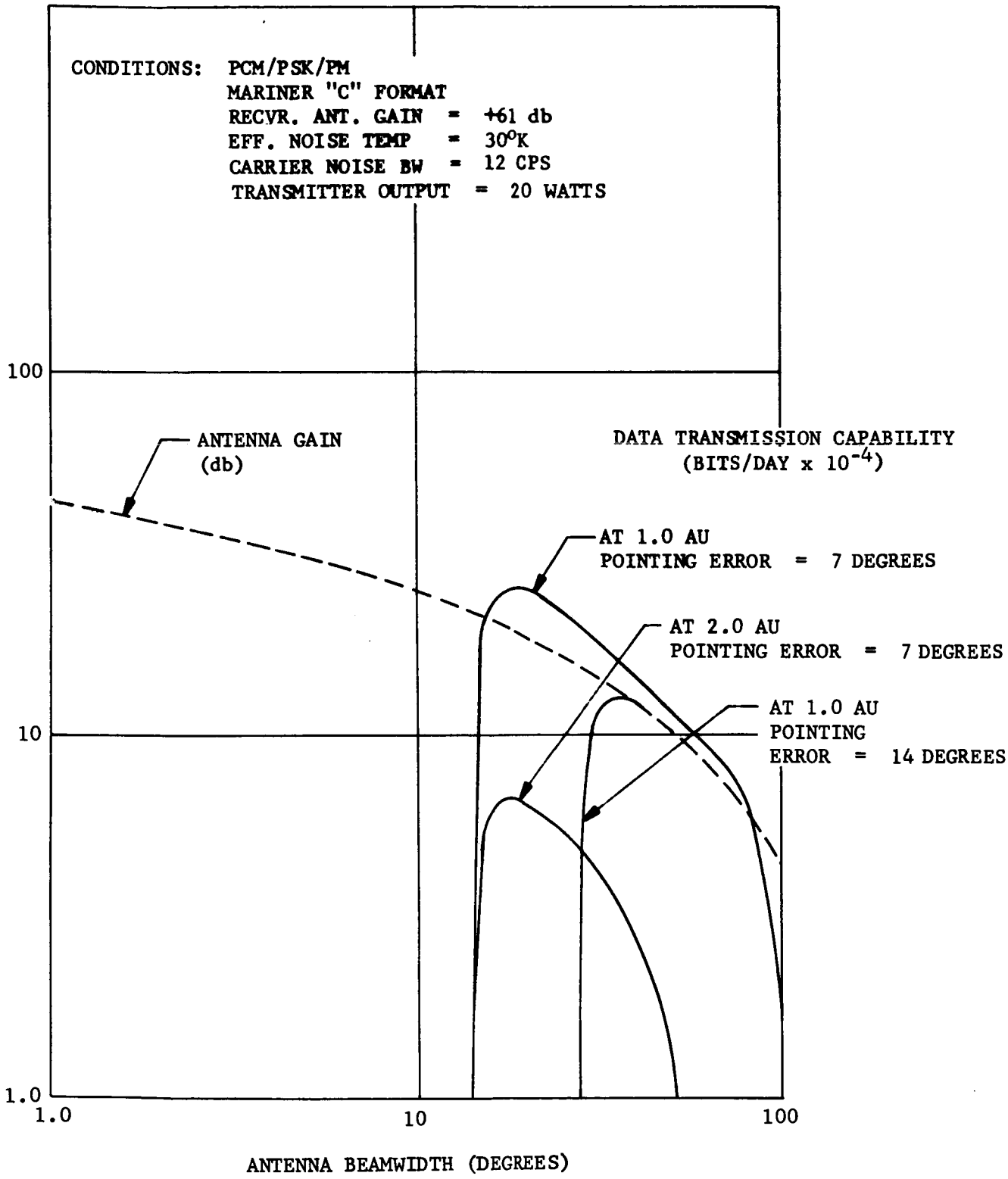

FIGURE 7. TOTAL BITS TRANSMITTED vs. ANTENNA BEAM WIDTH

R11204

satisfied with available hardware. A tape recorder is necessary for storing the picture data if the total number of bits exceeds 10^6. Shock resistant tape recorders have been developed, but there are still sterilization problems with the magnetic tape.

For storing fewer than 10^6 bits, magnetic core memories appear attractive for the MFC. Aeronutronic has previously operated one such unit during an impact acceleration without loss of data.

The sequencing requirements for the capsule do not present any problems because most of the time intervals are not critical. It is proposed that the data transmission period be timed either from some initial event or from a Sun position.

A considerable number of electronic components have been qualified for high-shock use during the Range Lunar Capsule and other programs. It is concluded reliable impact designs are possible with an adequate development program.

2.2.8 POWER SOURCES

Potential power sources for the capsule were reviewed in the power supply task. The characteristics of chemical batteries, fuel cells, radioisotope batteries, and solar cells were examined. The sterilization, shock, and weight requirements of the MFC are found to limit the power choice to chemical batteries. Two alternate electrical power sources are proposed.

One is a secondary silver-zinc battery with an inorganic separator currently under development by Astropower. An actual performance curve of a single cell operating at 135°C is shown in Figure 8. It is estimated that energy densities of 70 watt-hours per pound should be obtainable from a battery composed of similar cells.

The other power source which appears promising is a thermal battery which operates at a temperature of 450°C. At temperatures below its operating temperature, the thermal battery is an inert piece of electrical equipment. For this reason, it inherently lends itself to the sterilization and impact requirements of the MFC. A conceptual design of a thermal battery which will operate for several days and yield energy densities of 70 watt-hours per pound is described in Section 6.4.

It is concluded that additional battery development effort is required to overcome the sterilization problems, but it is reasonable to expect a performance of 40 watt-hours/lb from a battery meeting the MFC requirements.

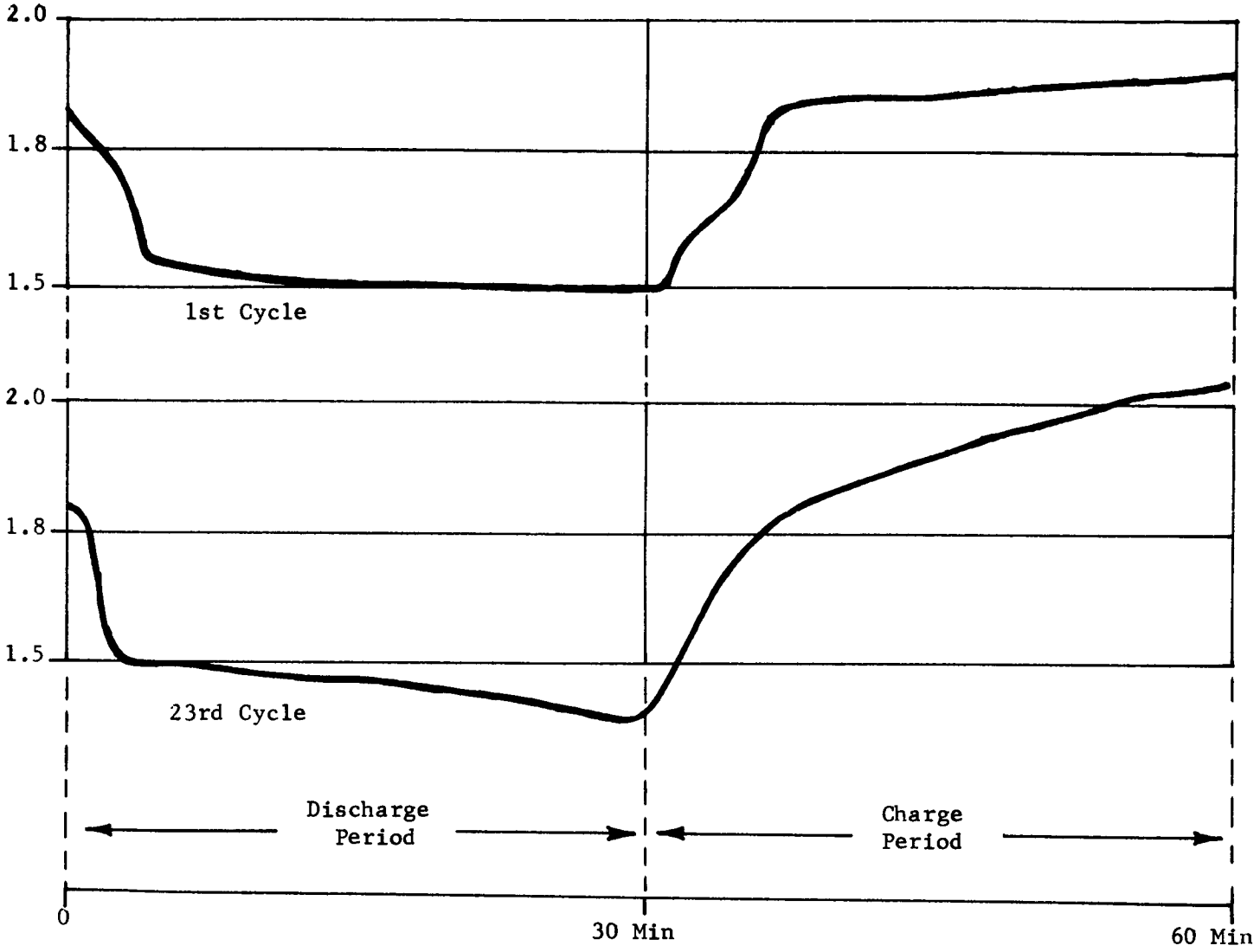

Astro-Power Silver Zinc Battery No. 127-052
30% depth of discharge
30 Minute discharge @ 10 ma/cm^2
30 Minute charge @ 15 ma/cm^2
Temperature = 135°C

FIGURE 8. CYCLE TEST OF SILVER-ZINC BATTERY AT 135°C

2.2.9 THERMAL CONTROL

The primary thermal control requirements are to protect the capsule power supply and electronic equipment from the low temperature of the Mars environment. Estimates were made of the heat losses from the sphere due to radiation, convection, and conduction. Heat gains to the sphere were calculated for solar radiation, surface radiation, and internal power dissipation.

A number of possible thermal control systems, both active and passive, were examined for possible use in the MFC. It is concluded that the optimum system is a passive one employing thermal insulation to balance the capsule heat losses to the heat gains. The system also employs a water boil-off/freeze system to limit the payload temperatures to between the range of 32 and 100°F. Typical temperature histories for a capsule are shown in Figures 2-9 and 2-10.

2.2.10 CAPSULE DESIGN

Trade-offs were conducted to determine the complete capsule configurations which were necessary to meet varying impact requirements. The capsule stability on a 5° slope in the Martian wind is found to necessitate the removal of the impact limiter from the payload and the deployment of stabilizing legs.

Equations were derived based upon previous development programs which permit the calculation of the weights and volumes of the various mechanical components within the capsule for various impact conditions and capsule configurations.

The starting point is the performance requirement for taking a 24° x 24° high resolution facsimile picture. Then performance parameters are chosen for all of the capsule subsystems - camera, data storage, battery, antenna, transmitter, and thermal controls. After these parameters are picked the total battery weight required to perform the mission can be determined. Once the battery weight is found and an impact velocity chosen, then in an iterative analysis of the mechanical subsystems, the total capsule weight can be determined. Figure 11 illustrates the results of the capsule design task with a plot of the total capsule weight versus the maximum allowable impact velocity for various values of battery weights.

2.3 CONCLUSIONS

A number of general conclusions concerning the Mars Facsimile Capsule were reached during the study. These conclusions deserve special emphasis and for this reason are listed below.

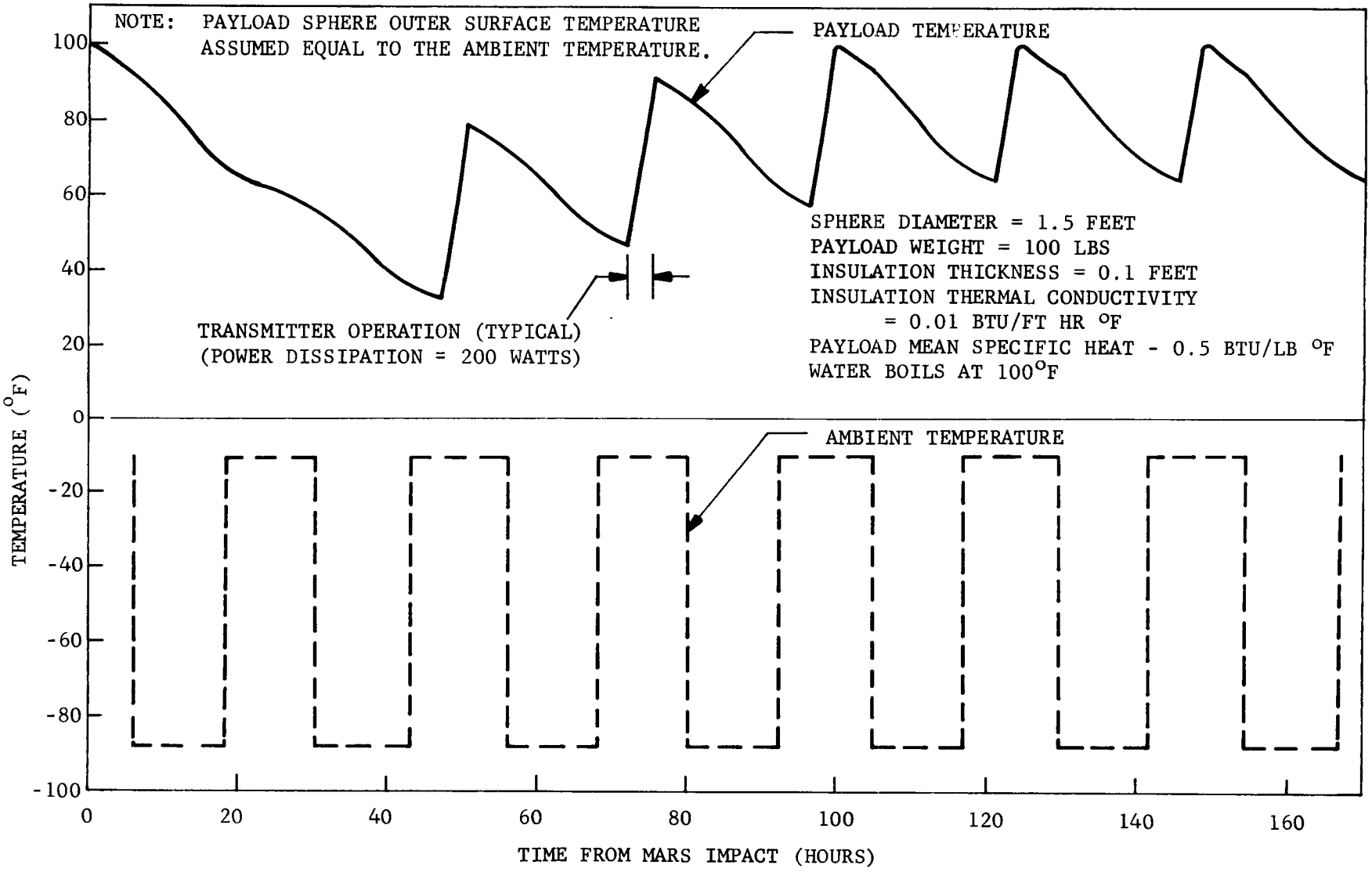

FIGURE 9. TYPICAL PAYLOAD TEMPERATURE HISTORY FOR A MARS MINIMUM TEMPERATURE ENVIRONMENT.

R11179

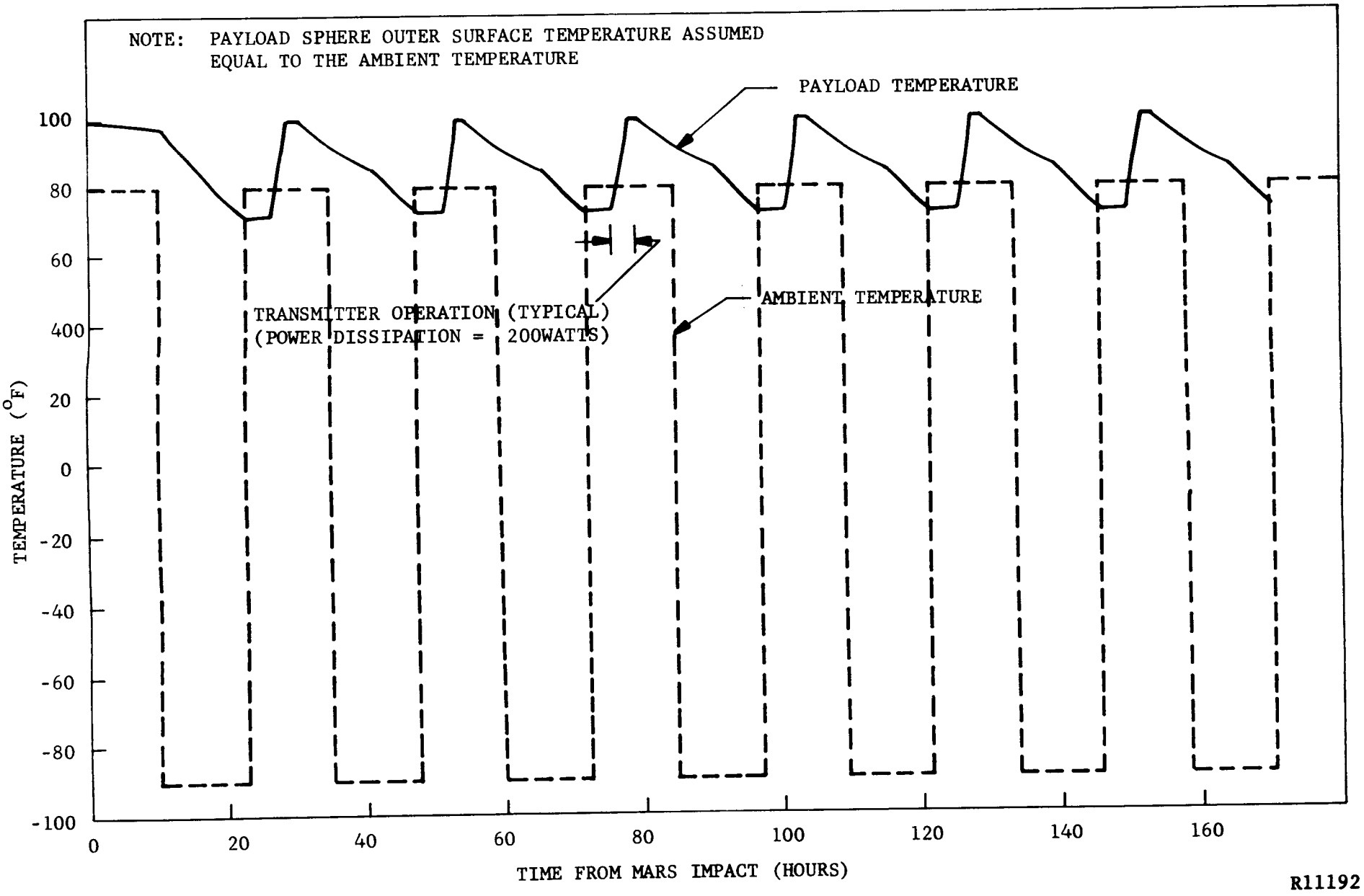
NOTE: PAYLOAD SPHERE OUTER SURFACE TEMPERATURE ASSUMED EQUAL TO THE AMBIENT TEMPERATURE
PAYLOAD TEMPERATURE
AMBIENT TEMPERATURE
TRANSMITTER OPERATION (TYPICAL)
(POWER DISSIPATION = 200WATTS)
TEMPERATURE (°F)
100
80
60
400
20
0
-20
-40
-60
-80
-100
0
20
40
60
80
100
120
140
160
TIME FROM MARS IMPACT (HOURS)
R11192

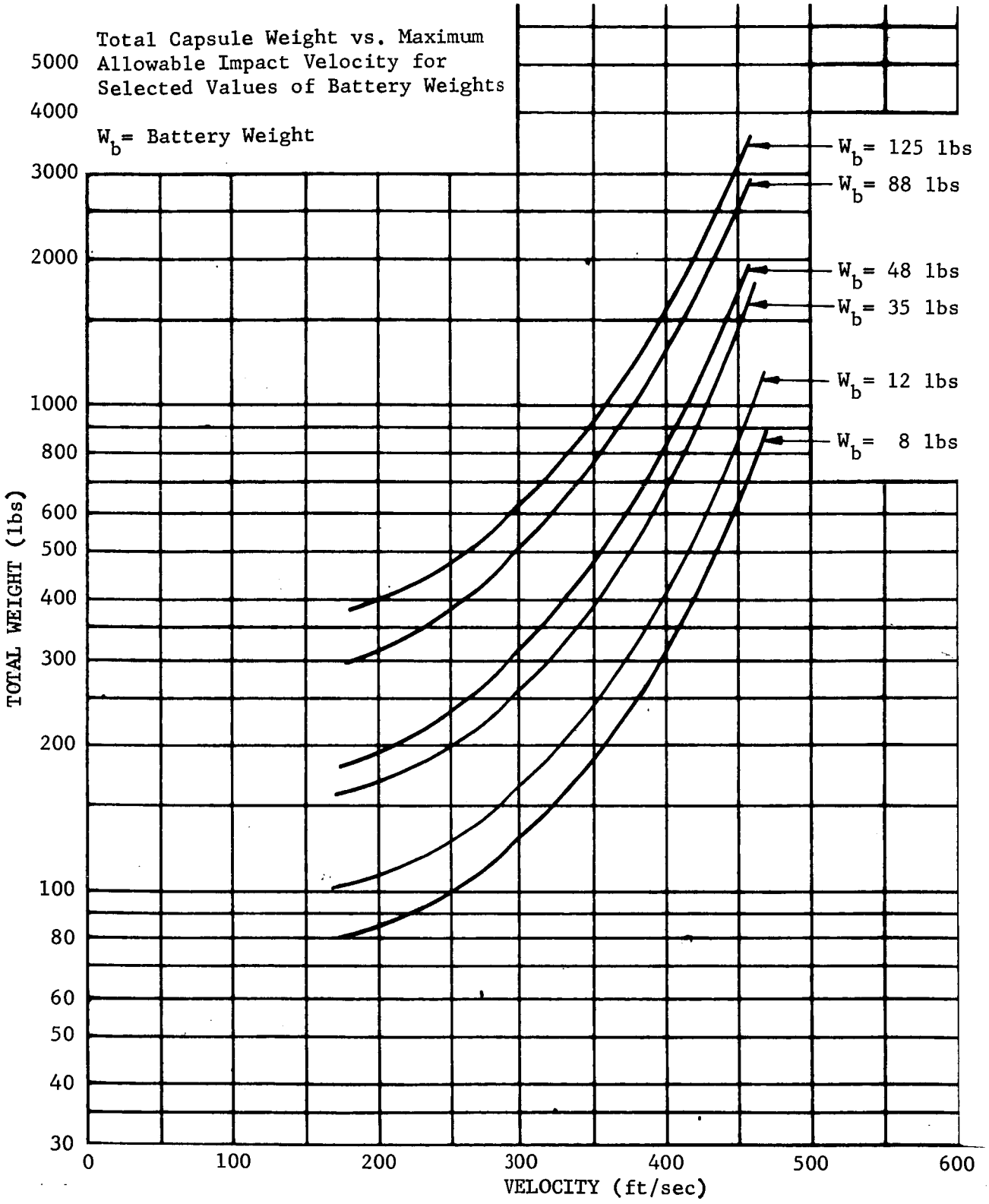
Total Capsule Weight vs. Maximum Allowable Impact Velocity for Selected Values of Battery Weights
W_b= Battery Weight
W_b= 125 lbs
W_b= 88 lbs
W_b= 48 lbs
W_b= 35 lbs
W_b= 12 lbs
W_b= 8 lbs
TOTAL WEIGHT (lbs)
5000
4000
3000
2000
1000
800
600
500
400
300
200
100
80
60
50
40
30
0
100
200
300
400
500
600
VELOCITY (ft/sec)

FIGURE 11.

a. At velocities in the 300 - 500 ft/sec range, the major portion of the total capsule weight is devoted to the impact limiting balsa. For this reason there can be large performance payoffs in picture taking capability by altering the impact requirements. One possible method might be the use of an auxiliary parachute to provide a directional control on the capsule during entry through the Martian atmosphere. This would permit the shaping of the impact limiter such that less protection is provided in the directions where only secondary impacts are expected. It is estimated that as much as a 25 percent improvement in overall capability would result from the introduction of such a feature.

b. There has been no experimental verification of the analytical model used in the impact analysis. Tests have been made at 200 ft/sec but some of the predicted effects are not detectable at this low velocity.

c. The static tests conducted on balsa specimens during the Lunar programs yielded specific energy capabilities of 12,000 to 27,000 ft-lbs/lb. Since the Ranger missions could be successfully accomplished with a configuration which utilized the average capability (18,000 ft-lbs/lb) of balsa wood there was no attempt to improve the limiter performance through balsa selection. It is felt that by examining the characteristics of balsa wood, particular specimens which exhibit higher crush energies can be chosen for use in the limiter with a resultant increase in limiter capability. For the conceptual design configuration a 5 percent increase in the specific energy absorption capability of the limiter could in effect double the battery weight.

d. There is need for a further definition of pictorial requirements. A picture contains a great deal of significant information but also a corresponding large amount of data to transmit. Therefore, it is important to optimize the picture requirements in terms of field of view, angular resolution, gray levels, and spectral response.

e. There appear to be solutions for all the sterilization problems of the capsule with the exception of the battery. Recently there has been significant progress made in both silver-zinc and thermal batteries, and with an extensive development program it is felt that a useful and feasible design can be found for the capsule mission. The feasibility of the entire MFC concept is strongly related to how much energy density can be obtained from a sterilizable power source. Less than 10 watt-hours/pound makes a capsule mission almost impossible; however, over 25 watt-hours/pound assures mission feasibility. It now seems reasonable to predict an achievable battery performance of 40 watt-hours/pound for 1969-1971 missions.

f. A transmitter output power of 5 - 20 watts is almost a necessity to transmit a meaningful picture from a landed MFC. There are several ways in which 20 watt impactable transmitters can be designed. A solid-

state 20 watt transmitter can be designed using state-of-the-art components and with a development program it is felt a 20 watt triode cavity transmitter can be designed to withstand the high g impact.

h. A Mars Facsimile Capsule mission is feasible for the 1969-1971 time period. There are a number of areas requiring concerted development effort but not any areas which raise serious doubts about feasibility. There is, of course, some degree of uncertainty in what the exact performance characteristics of such a capsule will be.

SECTION 3

STUDY OBJECTIVES AND CONSTRAINTS

3.1 OBJECTIVES

An understanding of the study objectives and constraints is necessary to properly evaluate the technical material in the remainder of the report. The study contract called for an investigation into the optimum functional characteristics of a High Resolution Facsimile experiment to be landed on the surface of Mars. In order to limit the scope of the study to reasonable size and to assure useful results, JPL placed further constraints on the investigation. The purpose of the study became one of determining if a hard-landing HRF capsule were feasible for an early Mars mission and, if so, what performance characteristics were available for trade-off purposes.

The reason for the emphasis on feasibility determination was that it was not evident that a Mars facsimile experiment could even be accomplished within allowable weight limits. The largest obstacles to such a mission were though to be the high impact velocity, the great communication distance, and the necessity for heat sterilization.

The exact work statement for the contract is given in Section 3.2. However, the work statement doesn't include essential mission information that formed important constraints for the study. These constraints were:

(a) The capsule landing study should not consider any terminal descent system. Study begins just prior to impact at a specified velocity.

(b) Capsule weight will be in the range of 300 to 600 pounds.

(c) The maximum expected impact velocity will be 500 ft/sec. The payload shock level should not exceed 5000 g's.

(d) The study should consider only balsa wood as an impact limiting material. Only omnidirectional protection should be considered.

(e) The study should consider mainly the 1969 and 1971 launch opportunities.

(f) The capsule communications study should not consider an orbital spacecraft relay link.

The task for Aeronutronic, then, was that of starting with the knowledge gained in the Ranger Lunar capsule programs and extending it to the new Mars mission. The Lunar programs had included all of the essential areas of interest -- impact protection, facsimile camera, thermal control, data storage, data transmission, and sterilization. But the Mars mission had a completely new set of requirements. For example, the communication distance was 400 times greater, the impact velocity up to 2-1/2 times greater, and total capsule weight up to 6 times greater. The Martial environment, atmosphere, planetary rotation and solar radiation were all new effects to investigate. Additionally, the specified heat sterilization requirements introduced new complications in certain capsule subsystems, such as the electrical power source.

JPL and Aeronutronic agreed to certain changes in work statement interpretation during the contract in order to channel the study effort to subjects needing greater emphasis. The first such change was to have Aeronutronic produce a Capsule Impact Technology Report in exchange for reducing effort on Items (a) (2) vi, viii, and x of the Work Statement. This reduction minimized the study effort which was devoted to studying the effects of repetitive pictures, changing lighting angles, stereo pictures, and multispectral capability. The Capsule Impact Technology report, Aeronutronic Publication U-3031, is an accumulation of the previously unpublished capsule impact information. As a result of the Ranger programs, Aeronutronic has considerable knowledge and information relating to the analysis, design, fabrication and testing of hard-landing space capsules, but because much of this information was not readily accessible, JPL requested that Aeronutronic assemble and publish it as an important task during the study. The completed report contains summaries of six technical subjects as well as the unedited internal memos on these subjects over the five year period 1959 to 1965. The six technical subjects are:

(1) Impact Analysis

(2) Balsa Wood Characteristics

(3) Mechanical

(4) Capsule Control Techniques

(5) Electrical

(6) Impact Testing

Another work scope change occurred later when Work Statement Item (a)(3) was minimized and Item (a)(5)(ii)(B) eliminated in order to place more emphasis on a dynamic analysis of the capsule impact limiter. This change de-emphasized the conceptual design effort and eliminated all work on a Development Plan. However, the impact analysis was enlarged to include consideration of such things as variable density material and both concave and convex landing surfaces.

3.2 STATEMENT OF WORK

a. The Contractor shall conduct a study program to define the optimum functional characteristics of a High Resolution Facsimile (HRF) system and related subsystems for accomplishment of an experimental mission on the surface of the planet Mars. In the performance of this study the Contractor shall:

(1) Prepare summary performance analyses and trade-off studies, in parametric form, to determine the sensitivity of various trade-off factors and the effect of varying specific parameters.

(2) Consider the following performance characteristics with emphasis applied to items (iv) (vii) and (xi).

(i) Thermal characteristics, including passive and active control system.

(ii) Optical system characteristics, including lens sizes and system focal lengths.

(iii) Telecommunications data rates and corresponding power requirements.

(iv) The use of memory systems in conjunction with high-speed sensing and low data rate transmission.

(v) System requirements for varying scan rates, including sensing element characteristics, light level requirements, and resolution.

(vi) The effect of lighting angle change on pictorial data.

(vii) Effect on system characteristics of landing system transients based on reasonable hard landing parameters or soft landing requirements.

(viii) Evaluation of repetitive picture taking at separate intervals, and with varying view fields.

(ix) Evaluation of stereo in enhancing data value.

(x) Evaluation of multispectral capability in enhancing data value.

(xi) The effect of sterilization and associated requirements on system design and performance, including heat and sterile assembly.

(3) Prepare design layouts and sketches where necessary to define system parameters.

(4) Participate in two (2) technical review and planning meetings.

(5) Prepare and submit to JPL the following:

(i) One (1) vellum and six (6) copies of an informal monthly progress report.

(ii) One (1) vellum and twenty (20) copies of a final technical report which shall include, but not necessarily be limited to

(A) System description data developed during the study.

(B) A development plan, including schedule and budgeting costs, for the defined optimum system.

(C) Overall results of the study effort.

(D) An Appendix consisting of all data generated during the study.

(iii) One (1) vellum and six (6) copies of a Monthly Cost Report, on JPL Form 0330, July 1962.

b. JPL will:

(1) Define the environmental conditions under which the HRF system is expected to operate.

(2) Define the Mars Surface Model.

(3) Provide the geophysical characteristics of Mars.

(4) Provide the photometric characteristics of Mars and the Martian surface.

(5) Provide the Deep Space Instrumentation Facility interface characteristics during mission time period.

3.3 ENVIRONMENTAL MODEL

In accordance with the study contract, JPL furnished Aeronutronic with an Environmental Model to be used during the study. This model is included in the Appendix as Section 6.1 and is briefly summarized in Table 3.3-I.

It is interesting to note the special influence that this environmental model has on the Mars Facsimile Capsule, compared to the Moon's environment on the Lunar Facsimile Capsule. The high velocity winds increase the problems of capsule stability and antenna deployment. The presence of an atmosphere creates the possibility of heat dissipation through convection but makes it risky to utilize thermal super-insulation requiring a vacuum. The temperature extremes are smaller than on the Moon and generally make thermal control less difficult. The combination of high wind and dust makes the operation of the facsimile camera mechanism more difficult since the viewing window must be exposed to this hostile environment. Possible solutions to the dust problem are to extend the viewing tube a greater distance above the surface, to employ a window wiping device, and to keep the window covered when not in use.

The planet rotation has an adverse effect on the facsimile camera since the lighting angle and intensity vary rapidly during the day. The rotation also places undesired limitations on the possible communication time to Earth each day.

The surface topography of Mars is so uncertain that few conclusions can be made about its effect on the MFC. The prediction of fewer craters is an advantage since landing in a crater would restrict the viewing scene and ambient light. The suggested presence of jagged boulders and rocks is a great disadvantage since impact protection against them is difficult.

TABLE 3.3-I

ENVIRONMENT MODEL SUMMARY

Wind	Not greater than 60 meters/second; less than 30 meters/second, 80% of time.
Surface Pressure	40 ± 20 millibars
Atmospheric Composition	3 mb of CO_2
	2 mb of A
	35 mb of N_2
Ground Temperature	$310^{\circ}K$ maximum
	$200^{\circ}K$ minimum
Air Temperature	$250^{\circ}K$ maximum at 2 meters
	$205^{\circ}K$ minimum

Topography, geophysical parameters, and photometric characteristics are included in the complete model.

Prevailing gentle slopes (except for craters) are a definite advantage for capsule stability in the high winds.

Uncertainties in the surface pressure and atmospheric composition are of little importance to the MFC during surface operation. The surface pressure and atmospheric composition are important for antenna breakdown considerations but the MFC is generally power limited for other reasons. The atmospheric density will, of course, have great influence on the capsule impact velocity. However, if the capsule is designed for the highest predicted impact velocity, then the entire capsule concept is relatively independent of the atmospheric characteristics.

SECTION 4

CONCEPTUAL DESIGN FOR A MARS FACSIMILE CAPSULE

4.1 GENERAL DESCRIPTION

A preliminary design for a Mars Facsimile Capsule is presented here to illustrate what constitutes a hard landing capsule. The design approaches described in this section are further explained and justified in Section 5, Design Trade-Off Studies. The conceptual design is illustrated by the configuration drawings of Figures 12 and 13.

The capsule is a self-contained planetary experiment which provides its own impact protection, thermal control, electrical power, and data communications. The experiment device within the capsule is a high resolution facsimile camera for obtaining a visual picture from the surface of Mars. Capsule performance capability for the parameters chosen permits landing on the surface at a velocity of 400 ft/sec, taking a 24^{o} x 24^{o} high resolution picture, and transmitting the picture data directly to Earth.

Figure 12 shows the crushable impact limiter which houses the instrument sphere. The impact limiter is made of balsa wood with its grain in the radial direction. This limiter is removed following impact by means of a Mild Detonating Fuse which is placed along, and interconnecting, three orthogonal great circles located on the inner and outer limiter surfaces. These explosives are initiated by means of three independent time-delayed firing trains, which are encapsulated within the limiter, and inertia-activated during atmospheric entry. The limiter is removed in 8 spherical segments thereby allowing the passive deployment of 6 spring loaded stabilization legs located on 3 orthogonal axes. These legs form a firm tripod support for the subsequent porting and erection events.

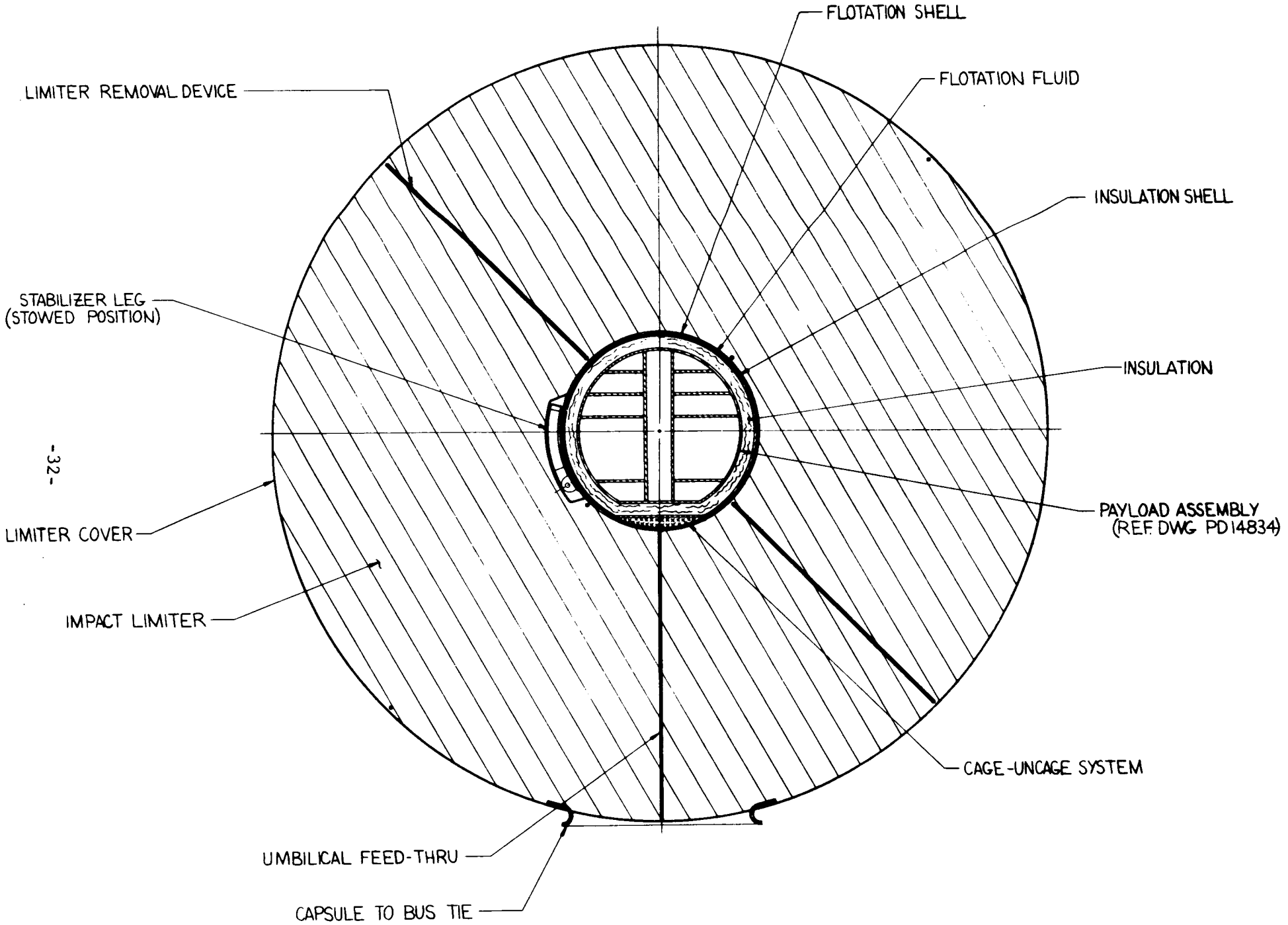

FIGURE 12. TYPICAL CAPSULE CONFIGURATION

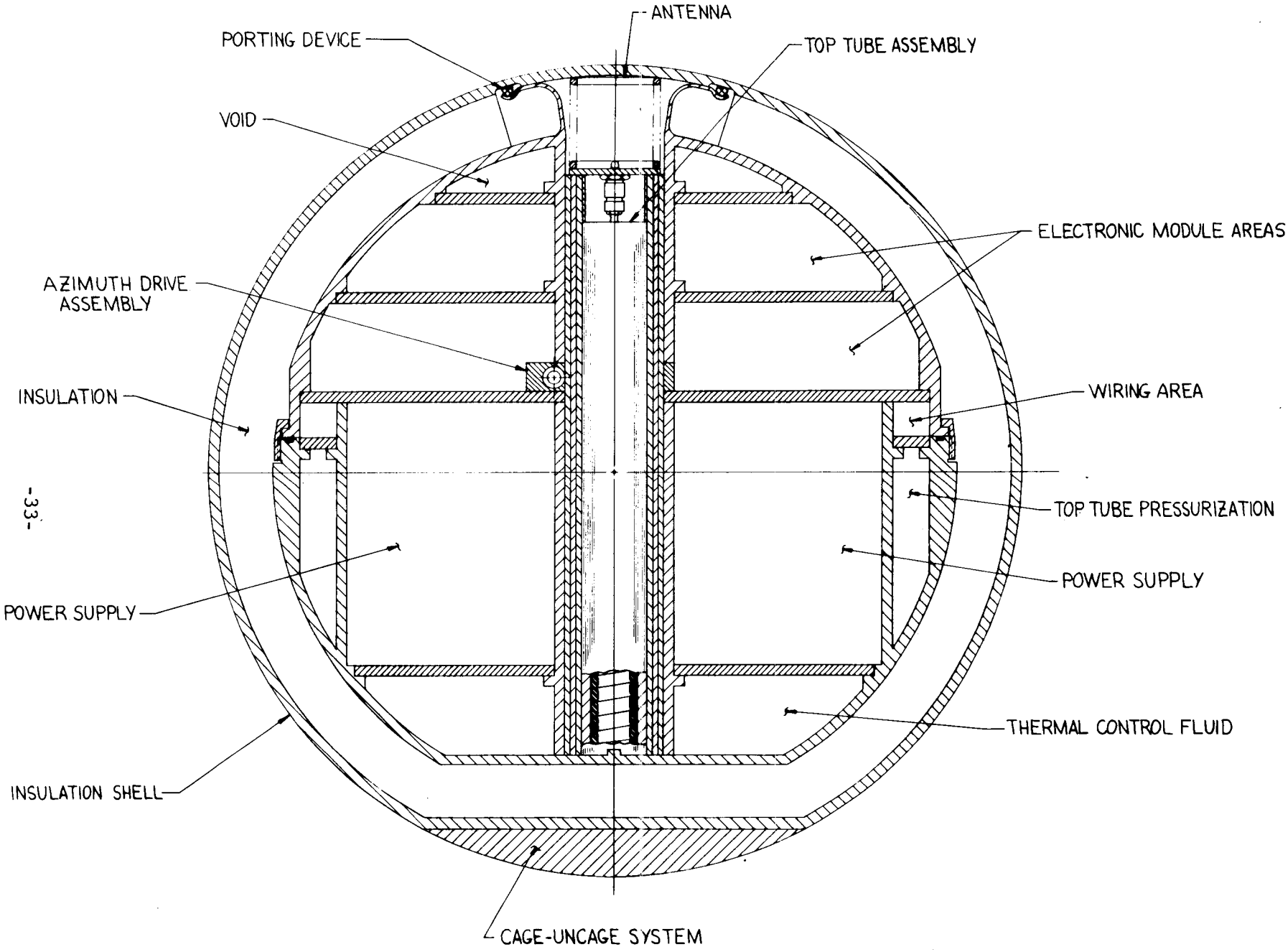

FIGURE 13. TYPICAL PAYLOAD CONFIGURATION

The floated instrument payload is shown in Figure 13. It consists of an electronics section, a power supply, a porting device, a thermal control system and a top tube assembly all housed within and supported by a pair of metal hemispherical structures joined at their equator by a threaded coupling nut. This structure is in turn surrounded by a layer of thermal insulation and retained within a fiberglass shell which is supported by the flotation fluid. The instrument payload is erected within its stabilized outer shell by means of flotation fluid. This is achieved by a displacement of the center of gravity of the neutrally buoyant floating payload from its center of buoyancy (geometrical center), allowing passive erection to local vertical prior to the top tube porting event. Following erection to local vertical, the payload is caged within this flotation fluid by a pyrotechnic actuated locking device located on the exterior of the floated fiberglass insulation shell.

A porting operation next occurs which permits a tube to be extended to several feet above the Mars surface. This tube contains the antenna and the scanning mechanism of the facsimile camera.

4.2 CHARACTERISTICS

The important performance characteristics of the capsule conceptual design are shown in Table 4.2-I. This specific capsule design is based on the capability of obtaining a 24^{o} x 24^{o} high resolution facsimile picture. This is a rather arbitrary choice for a picture size, based on a subjective evaluation of what a minimum picture should be. Obviously, the picture size can be increased by any of the following means:

(1) Decreasing the impact velocity.

(2) Increasing the total capsule weight.

(3) Using fewer grey levels.

(4) Using a larger picture resolution.

The resultant facsimile picture is not restricted to the square shape indicated. Any picture aspect ratio is possible without more than a slight change in the camera mechanism. For instance, the 24^{o} x 24^{o} picture is equivalent to either a 10^{o} x 58^{o} or a 58^{o} x 10^{o} picture.

The camera will obtain a picture, with a resolution of 0.1^{o}, which will show surface objects as close as 1 meter away. The picture also remains in focus for objects at infinity, such as clouds or the horizon. Capsule design is based on a picture with approximately 16 $\sqrt{2}$ grey levels (dynamic range of 40 db).

TABLE 4.2-I

CAPSULE CHARACTERISTICS

Payload Weight	115 lbs.
Total Capsule Weight	335 lbs.
Maximum Impact Velocity	400 ft/sec.
Picture Size	24^{o} x 24^{o}
Resolution	0.1^{o}
Scan Time	1 hour
Grey Levels	16
Total Data	2.5×10^{5} bits
Transmission Distance	1.2 AU
Transmission Data Rate	12 bits/second
Transmission Time per Day	2 hours
Antenna Gain	12 db
Transmitter Power	20 watts
Transmission Frequency	S-Band
Maximum Capsule Surface Life	4 days

Capsule impact velocity capability was chosen at 400 ft/sec to place it in the center of the 300 to 500 ft/sec range of interest. The impact capability is based on average balsa characteristics, a flat unyielding impact surface, and unidirectional impact protection. Changes from these conditions can either increase or decrease the impact capability. It is reasonable to expect that selection of balsa will result in some definite improvement in impact capability. If the capsule has any type of impact direction orientation, considerable improvement in impact protection can be obtained by altering the spherical shape of the limiter to favor the required directions. Analyses and tests have shown that the major portion of the capsule kinetic energy is dissipated during the first capsule impact, hence the protection against secondary impacts due to bouncing need not be as great.

The capsule will transmit the 230,000 bits of picture data to Earth with a triode-cavity 20 watt transmitter at the rate of 12 bits/sec. Transmission will be limited to 2 hours per day by the antenna beamwidth; therefore, it will take at least three days to transmit all the picture data.

The estimated weight breakdown for the capsule is given in Table 4.2-II. It can be seen that the largest portion of the weight is devoted to the balsa impact limiter. This is, of course, the reason for the emphasis during the entire study on obtaining the maximum efficiency from the impact limiter.

4.3 SEQUENCE OF EVENTS

A typical terminal event sequence for the Mars Facsimile Capsule is given in Table 4.3-I. The capsule timers will be initiated upon atmospheric entry by the activation of several inertia actuated "g" switches.

Three "g" switches together with independent timers and batteries will be encapsulated within the impact limiter for activation of the impact limiter removal device (Mild Detonating Fuse) following landing. Several such timers are provided to preclude the possibility of damage and possible malfunction following impact. Following limiter removal, the 6 spring loaded stabilization legs located within the confines of the separate limiter segments will be passively deployed and the payload allowed to erect within its flotation fluid. After a reasonable period of time to damp payload oscillation within its flotation fluid, the post impact caging foot will be engaged by an inertia activated internal timer, thereby locking the payload within its previously stabilized outer shell.

The capsule is ported by a Flexible Linear Shaped Charge located directly above the erectable top tube. Actuation of this charge by an internal timer cuts a hole in both the inner and outer fiberglass shells, thereby allowing the top tube and antenna to erect. Top tube erection is

TABLE 4.2-II

CAPSULE CHARACTERISTICS

WEIGHT ESTIMATE

Top Tube Assembly		1.2	
Azimuth Drive		0.6	
Transmitter		9.2	
Core Memory		6.0	
Signal Electronics		1.8	
Antenna		1.8	
Extension Mechanism		0.4	
Caging Mechanism		1.5	
Porting Mechanism		2.0	
Structure		10.7	
Thermal Control Fluid		1.3	
Battery		18.0	
Insulation		5.5	
Insulation Shell		8.5	
Flotation Fluid		3.5	
Flotation Shell		10.1	
Stabilizing Legs		3.0	
Limiter Removal Device		3.0	
Impact Limiter		33.5	
Impact Limiter Cover		2.7	
	Size Estimate	450	lbs.
Limiter Inner Radius		0.605	ft.
Limiter Outer Radius		2.35	ft.

TABLE 4.3-I

MFC SEQUENCE OF EVENTS

1. Removal of Biological Barrier
2. Bus Separation
3. MFC Deceleration
   a. Initiate Payload Timer (inertia switch)
   b. Initiate Limiter Timer (inertia switch)
   c. Uncage Payload
4. Impact
5. Limiter Removal (timed from 3.b.)
6. Stabilization (automatic)
7. Orientation (automatic)
8. Caging (Timed from 3.a.)
9. Porting (Timed from 3.a.)
10. Top Tube Erection (Automatic)
11. Antenna Deployment (Automatic)
12. Electronics Activation (Timed from 3.a.)
13. Image Scan and Storage (Timed from 3.a.)
14. Transmission (external sensor)

accomplished passively by gas pressure entrapped within the voids of the payload structure. The antenna is a spring-like device whose deployment is also passive.

Following top tube erection, the internal timer activates the electronics and scan mechanism, to begin the facsimile imaging operation. The picture data will be stored in digital form in a core memory unit.

Data transmission to Earth will occur in the mornings of the succeeding 3 days when Earth passes nearly overhead. The data transmission will be preprogrammed to occur only during the time the antenna is pointed towards Earth.

4.4 SUBSYSTEM DESCRIPTION

4.4.1 HRF CAMERA

The HRF camera for the MFC consists of the items shown in the functional diagram of Figure 14. The components within the top tube assembly are shown in the schematic of Figure 15.

The optical window transmits radiation from the scene to the scanning mirror. The primary function of the window is to provide a seal so that the camera housing may be kept clean.

The mirror assembly provides a highly reflecting flat surface which uniformly rotates through a vertical scan angle. The optical properties of the mirror are such that, as it continuously scans the vertical angular scene field, it directs the radiation within the instantaneous field of view onto the objective. The scanning mirror is caused to nod in the vertical direction by a cam and follower arrangement which is driven by a synchronous motor and gear box.

The camera contains a fixed focus optical veiwing assembly. The objective collects radiation from the scanning mirror and then transfers the radiation onto a detector. The objective is located vertically below the nodding mirror and will be an achromat lens coated and corrected for the scene spectral region of interest. The lens will be optimized for both diameter and focal length. A small diameter pinhole is placed close to the detector, at or near the image plane of the objective, to define an instantaneous field of view and the near field distance. The interior of the telescope will contain several graduated light baffles and many smaller baffles or threads on the inside of the tube to limit unwanted reflections. The tube will also be coated with a low reflectance optical black paint to reduce light scattering. A mechanical chopper is located between the objective and the pinhole but near the image plane to modulate the incident radiation to permit electronic signal amplification.

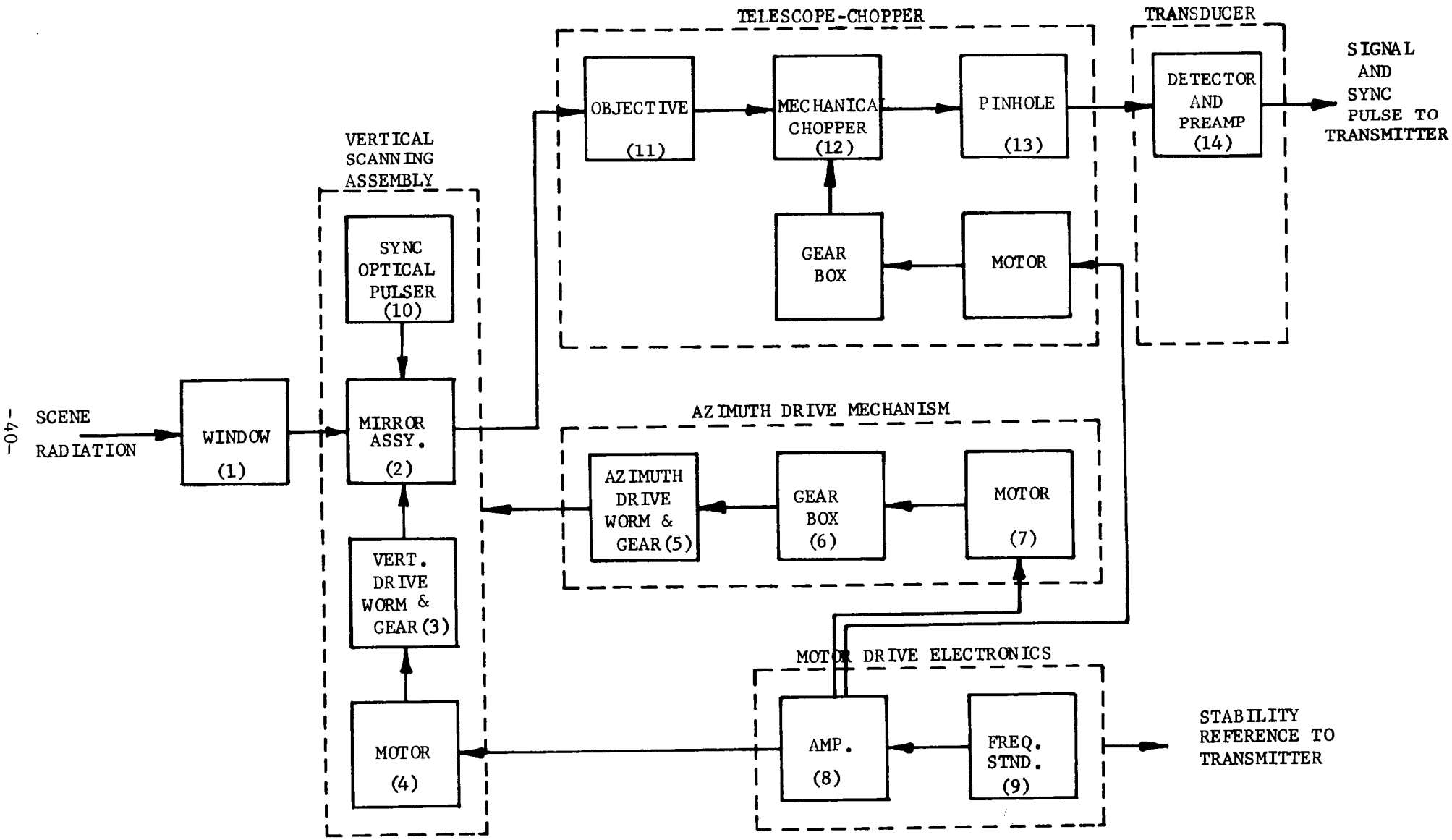

FIGURE 14. MARS FACSIMILE CAMERA FUNCTIONAL DIAGRAM

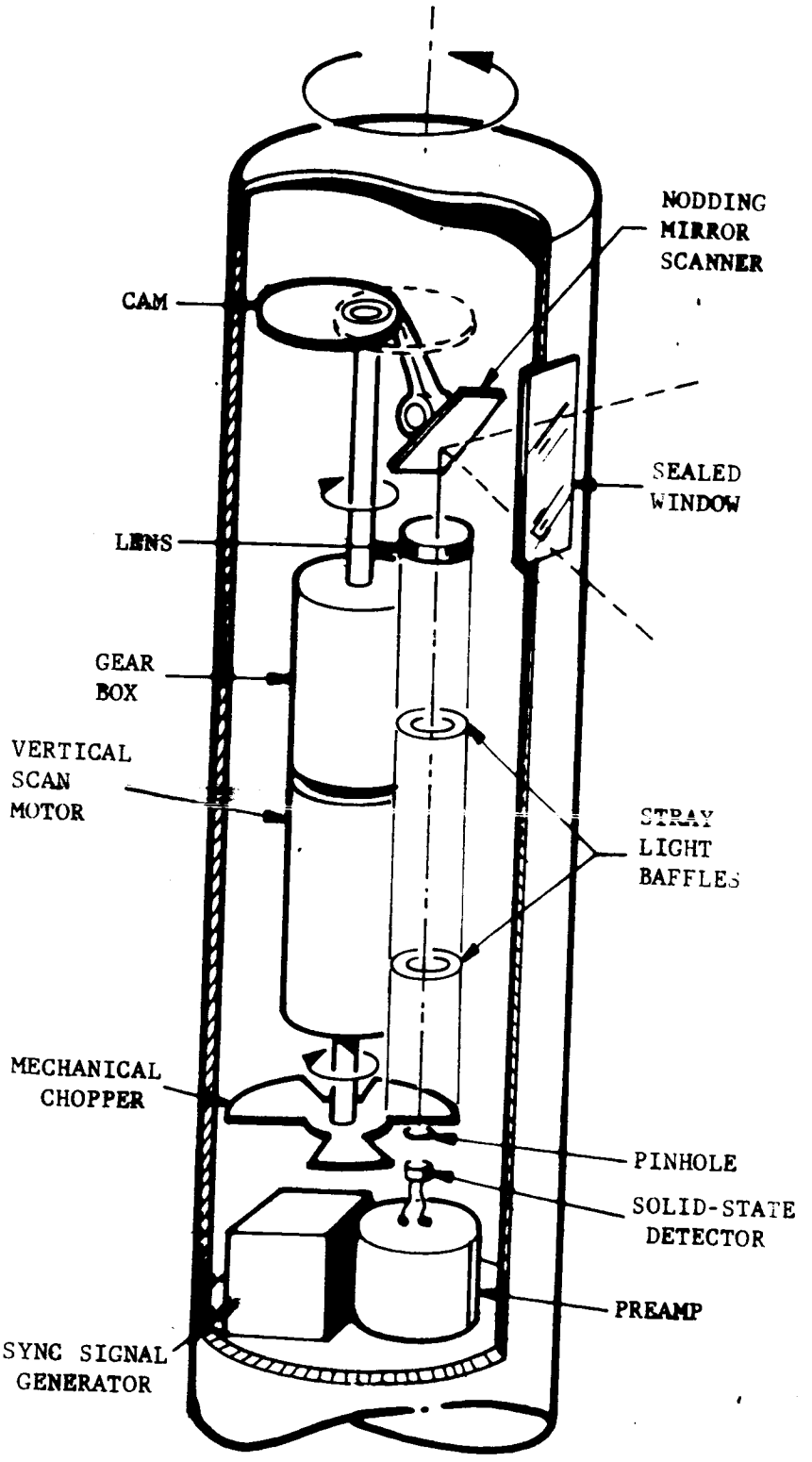

FIGURE 15. TOP TUBE SCHEMATIC

R11180

The azimuth drive worm is mounted to the base structure which does not revolve. The worm gear is hubbed into the azimuth tube and contains sufficient teeth to revolve the azimuth tube at the desired rpm compatible with the vertical scan. A gear box will be used to gear down the normally high-rpm motor to provide a smooth azimuth scan motion compatible with the vertical scanning mirror.

Vertical and azimuth drive hysteresis synchronous motors will be used to ensure reliable video and scanning synchronization. A frequency standard (tuning fork) is utilized to provide motor drive signals. The amplified frequency standard output is used to drive both the vertical and horizontal scanning motors.

The surface spectral radiometry of Mars dictates that a silicon detector be used as the camera transducer to achieve maximum spectral response. The silicon detector is also capable of withstanding the prolonged high temperature environment associated with sterilization of the capsule. The detector and preamplifier for the Mars Facsimile Camera are considered as an integral unit due to the fact that the preamp must be located as close as possible to the detector to minimize detector lead capacitance. The size of the detector will be kept small so that the inherent capacitance will not limit the detector response time or increase the noise signal. The detector will be positioned to receive all of the radiation transmitted through the pinhole aperture. The detector signal is amplified and then fed to the signal handling electronics for digital encoding and storage.

4.4.2 CAPSULE ELECTRONICS

The electronics subsystems for the conceptual design capsule are shown in block diagram form in Figure 16. In several cases, alternate modes of operation and means of mechanization are possible as discussed elsewhere in this report. The approach described here is considered to be a practical and useful one and utilizes a fixed pointing antenna and no command receiver whereby the mission can be accomplished more reliably.

The design is based upon a fixed, medium gain, conical pattern antenna (+ 12 db, 42^{o}, 1/2 power beamwidth) which is erected to the local vertical with the camera mechanism. Picture taking and subsequent data transmission are programmed for favorable periods and controlled by a Sun sensor which may be arranged to sense either Martian sunrise or a selected angle of the Sun from the zenith. Data transmission over a period of several days is assumed to allow transmission of 1/4 million bits of data with a 20-watt transmitter (2 to 20 bits/sec at distances between 0.8 to 2.0 AU).

If it were decided to scan the scene slowly as the information is transmitted, no storage would be required, however, such a scene would be taken under changing conditions of lighting and perhaps other environments such

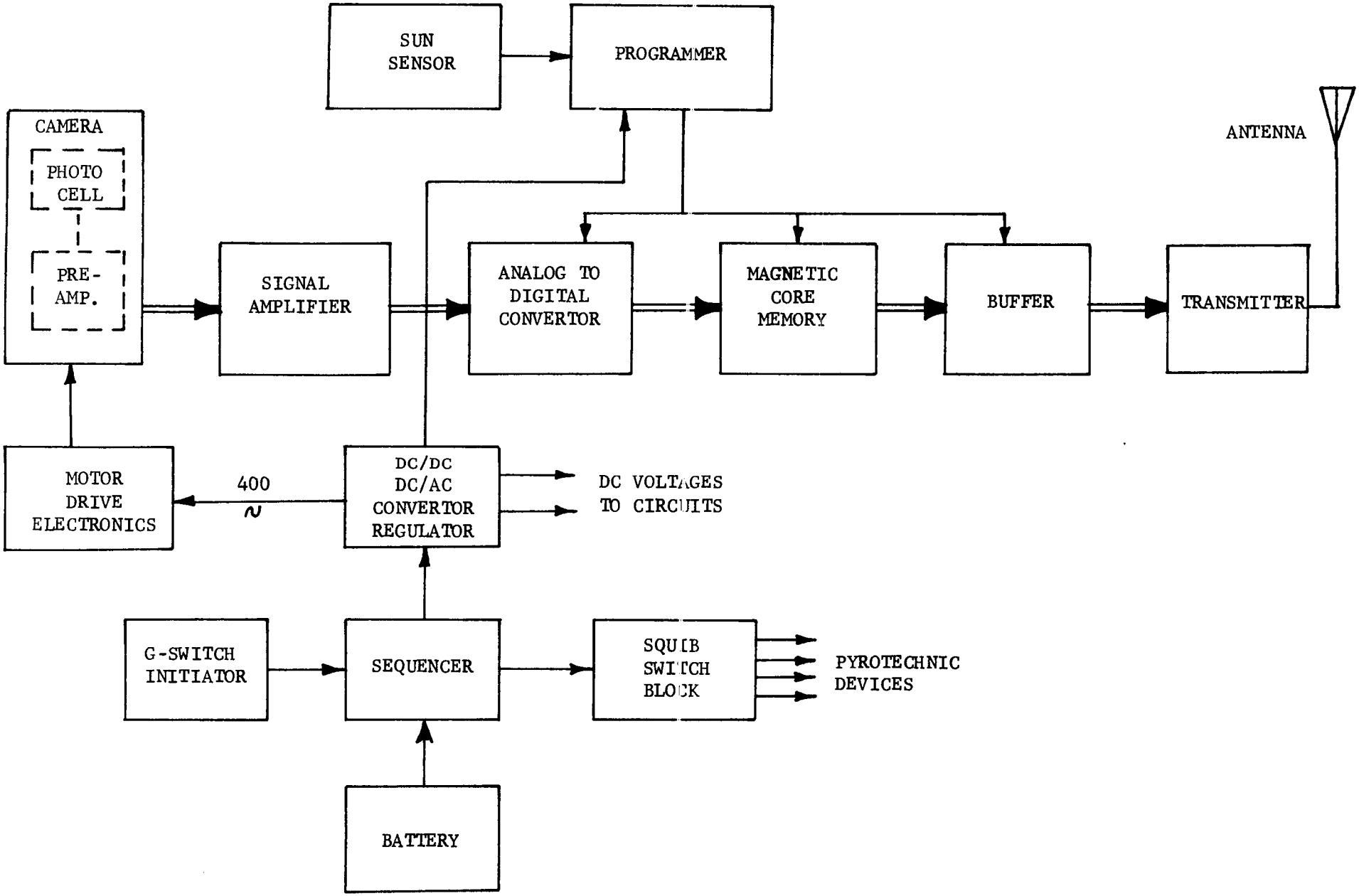

FIGURE 16. CAPSULE ELECTRONIC SUBSYSTEM

as wind and dust. This mode of operation has interesting effects upon the information content in a single transmitted scene and increases the likelihood of obtaining good picture detail if dust conditions are changing. A 1/4 million bit core storage memory is included in this design to permit a fast scan with delayed transmission. The weight and volume estimates are based on an existing 1 million bit memory. A tape recorder/reproducer would represent a lighter memory but at present it appears a special development will be required to achieve a sterilizable tape.

The camera's hysteresis-synchronous motors will be controlled by a stable electromechanical fork reference. A suitable fork reference was qualified to 3000 g, 3 msec impacts on the LFC program. The same 400 cps signal is supplied to the Programmer as a clock source so that A/D conversion and data framing can be made integrally related to the picture scan line. Then line sync can be flagged in the data frame word position. A possible format, similar to that of Mariner C is as follows:

	ONE DATA FRAME									
	"Word" No. 1							Data Words	Word No. n Frame Sync & Data Flag								
	X	X	X	X	X	X	X	0		1	1	1	1	1	1	X	X	1
VIDEO	ELEMENT				ELEMENT				Line Sync →	1	1	1	1	1	1	0	0	1
									Data →	1	1	1	1	1	1	1	1	1
MISC.	OTHER DATA									1	1	1	1	1	1	1	0	1

It is assumed that each picture element will be coded to 4 bits (16 levels). Therefore, a 9 bit "data" word is more efficient than the 7 bit word of Mariner C. The 9 bit "data" word is made up to 2 picture elements followed by a "0" bit which makes the frame sync word unique in each frame. One bit position in the frame word is upset periodically to denote line sync.

All capsule functions are initiated with the appropriate delays by the sequencer and timer which is initiated by a g-switch during atmospheric entry. The functions of timing, actuation, power conversion, etc., are already highly developed as the requirements are so close to those of the previously developed Ranger Seismometer and Facsimile Capsules.

4.4.3 POWER SOURCE

The capsule conceptual design is based on the use of a secondary silver-zinc chemical battery as the electrical power source. This battery employs inorganic separators and can be sterilized in the wet state. The battery will be charged during spacecraft flight to ensure full charge immediately before the landing sequence.

The battery provides 28 volts output to directly operate the triode-cavity transmitter. The expected energy density of the battery is 40 watt-hours per pound for the predicted drain rate and mission duration. Battery construction will be similar to that employed in the Ranger hard-landing capsules; tightly compressed bipolar cells will be encapsulated with epoxy-fiberglass.

Rather obviously, the described battery isn't readily available and will require considerable development effort. Elsewhere in this report, the reasons for expecting this performance are given.

4.4.4 TRANSMITTER

The MFC requires a phase-stable S-band transmitter with a power output capability in the range of 10 to 20 watts. Several design configurations to meet these requirements are possible; the configuration chosen for this design concept is a solid state signal source driving two triode-cavity amplifiers.

A 20-watt design utilizing two 10-watt ceramic triodes of design similar to the 5-watt GE 2835 or RCA A-21509 triode-cavities which were previously qualified by Aeronutronic on the Range programs for 3000g, 3 ms impacts is shown in Figure 17. Overall efficiency is 17.7% including a 1.2 db loss associated with the hybird power combiner. This design configuration includes a transistor crystal oscillator, a buffer, transistor power amplifiers, and varactor multipliers.

4.4.5 ANTENNA

The antenna for the MFC conceptual design is an erectable helix which is vertically oriented with the camera top tube assembly. The helix antenna is inherently adaptable to applications requiring erectable devices because it closely resembles a coil spring. Either mechanical erection or inflation may be used to deploy the helix, in fact, inflatable helices have been commercially available for several years.

The sketch in Figure 18 indicates the dimensions of the antenna envelope, which is a circular cylinder. The following table summarizes the electrical and mechanical characteristics of the 12 db gain helix. For higher gains, the only numbers that change are number of turns and length. These, however, increase rapidly with increasing gain.

Gain	12 db
Half Power Beamwidth	42 degrees
Number of Turns	10
Length (excluding ground plane)	11.5 inches
Ground Plane Diameter	4.2 inches
Helix Pitch Angle	13 degrees
Helix Diameter	1.7 inches

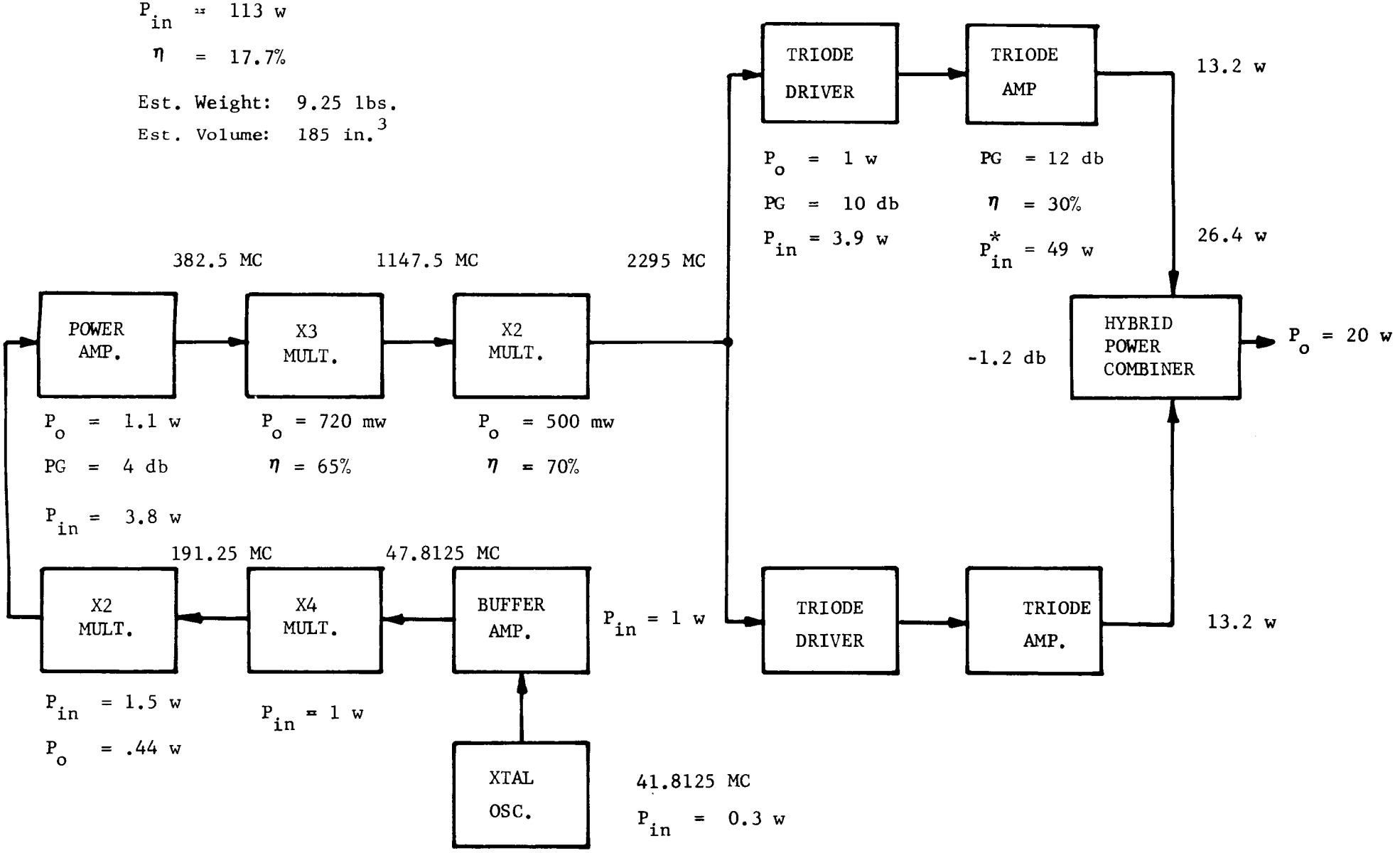

*Includes power supply η = 90%

FIGURE 17: S-BAND TRANSMITTER 10-WATT TRIODE CAVITY AMPLIFIERS

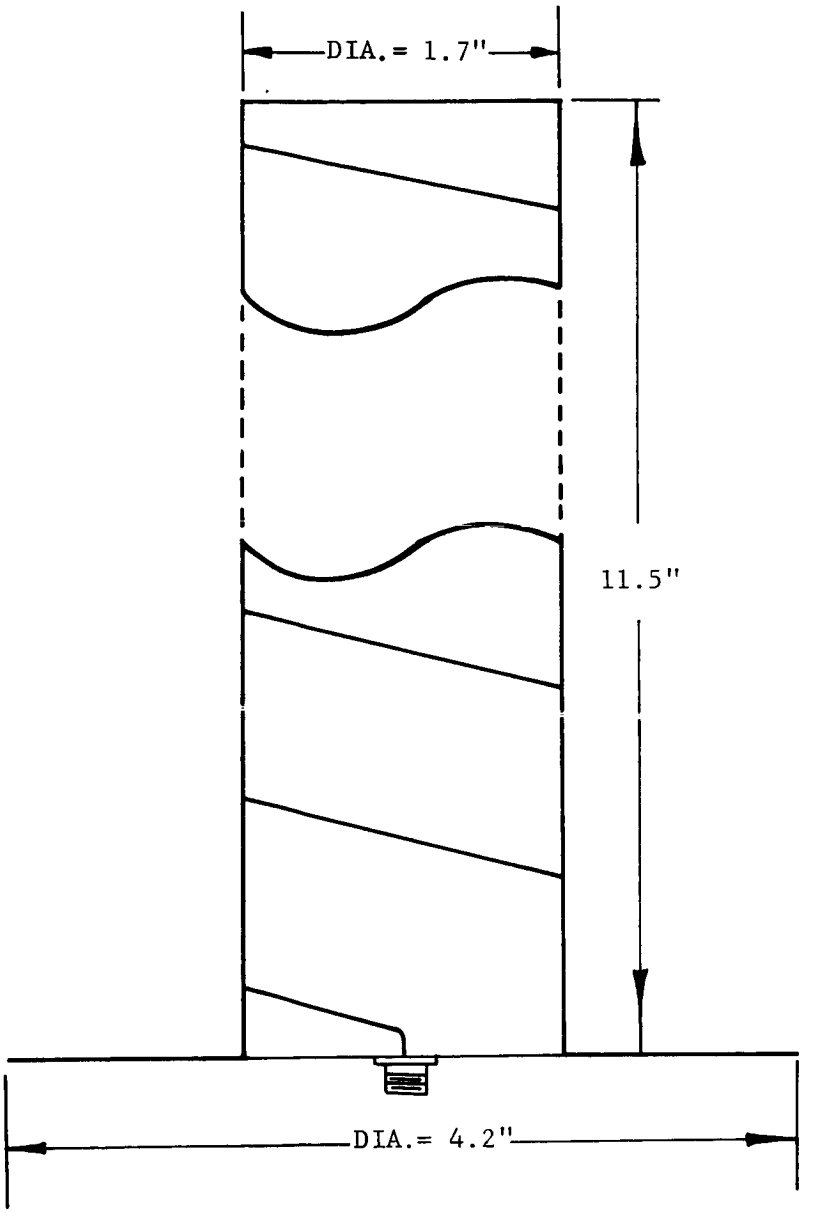

FIGURE 18. TEN-TURN HELIX ANTENNA

The choice of an erection technique must include consideration of sterilization temperature, wind loading, and degradation from wind-carried particles. An inflatable cylindrical sock to which the helix is mechanically erected must be made heavy enough to defy puncture by flying sand and other particles. For these reasons, mechanical erection is favored at this time.

A mechanical telescope, metal or dielectric, will be used in the center of the helix. The telescope projects a flat, circular dielectric disk the proper distance along the axis of the antenna, thus deploying the helical winding which is terminated at the disk. The winding itself will have high electrical conductivity and will deploy so that the pitch angle is constant along the helix.

4.4.6 LIMITER COVER

It is necessary that a cover be provided for the impact limiter to (a) prevent loss of moisture during sterilization and transit which results in a decrease in balsa wood yield strength and consequently energy absorption capabilities, (b) to increase limiter impact strength, (c) to prevent loss off limiter sections during primary impact which may be necessary to absorb secondary impacts, and (d) to provide abrasion resistance for "sliding" impacts.

A typical cover construction is that developed by Aeronutronic for the Lunar Seismometer Capsule. It consists of 2 layers of fiberglass fabric with an intermediary layer of Silicon Modified Rubber. The former provides strength for primary impact and abrasion resistance while the latter acts as a moisture barrier possessing sufficient elasticity to prevent loss of limiter sections necessary for secondary impact protection.

4.4.7 IMPACT LIMITER

The impact limiter is a laminated balsa wood sphere with a thin shell cover. This limiter surrounds and is bonded to the spherical fiberglass flotation shell.

The limiter is constructed of balsa wood blocks which are pre-selected and assembled into composite blocks of specified density and grain orientation. Then the final sphere lamination is performed in a manner which orients the balsa grain in a nominal radial direction about the capsule to provide maximum specific energy absorption. All bonding will be performed using high temperature, heat sterilizable resin. Assembly will be performed in precision metal fixtures using vacuum bags to hold the balsa parts in place. Upon final assembly, the inside hemispherical surfaces of the two limiter halves will be machined to the contour of the specific payload scheduled for that assembly, and the two halves bonded to the flotation shell and to each other. The cover will be fabricated in place by a sequential lay-up process.

4.4.8 FLOTATION SYSTEM

The flotation system consists of two concentric spherical shells of epoxy-fiberglass construction separated by a layer of neutrally buoyant flotation fluid. The outer, or flotation, shell is made of of two hemispheres with the impact limiter bonded to its outer surface. The inner or insulation shell is of similar construction but it is smaller in size. In one end, the insulation shell is depressed and the cage-uncage system is mounted. Diametrically opposed, the inner surface of the shell has a circular groove into which the flexible shaped charge for porting is set. This shell also acts to hold the insulation in place.

Erection of the payload is effected by an offset of the payload center of gravity with respect to its center of buoyancy (geometrical center).

4.4.9 UMBILICAL CABLE

An umbilical cable extends from the inner payload through the impact limiter to the exterior of the capsule. This cable passes through the flotation fluid via the cage-uncage system. Thus, it is disengaged and the payload is allowed to float free prior to impact.

This provides a checkout capability for the capsule and a means for activating the power supply prior to launch without interferring with capsule erection.

4.4.10 PAYLOAD STRUCTURE

The payload sphere structure contains and supports all subassemblies which make up the inner sphere of the capsule. It consists of an upper brazed hemisphere, a lower brazed hemisphere, an electronics plate, a battery plate, and a coupling unit.

The upper brazed hemisphere houses the electronics system modules along with the azimuth drive mechanism for the top tube. For ease of assembly, the electronics area is broken up into two levels separated by the electronics plate. A tubular section is provided at the center of the structure for support and extension of the top tube and antenna assemblies. The support shown for the flexible linear shaped charge porting charge will be flexible enough to survive impact (without imparting excessive loads into the structure), while sufficiently rigid to support the detonation forces of the shaped charge.

The lower brazed hemisphere houses the power supply, the thermal control fluid and a pressurization system for top tube extension along with a tubular section for supporting the top tube assembly. The battery plate rests between the battery and the lower electronics compartment and distributes the load between the two.

The upper and lower hemispheres will be machined from a brazable 6061-T6 aluminum billet while the plates will be made from a high strength 7075-T6 aluminum plate. The only steel part in the payload structure is the coupling nut which joins the two hemispheres. This nut satisfies the requirements of simplicity, interchangeability, ease of assembly, continuous clamping, high load capacity, and minimum diametrical allowance. The structure includes an "0" ring at the equator to seal off the inner payload.

4.4.11 TOP TUBE ASSEMBLY

The Top Tube Assembly consists of a housing which encloses a mirror scanner, a vertical scan mechanism, a mechanical chopper and a signal electronics which condition an image for recording and subsequent transmission. Mounted atop the top tube is the antenna system which also acts to cage the top tube axially during impact. Surrounding this tube are the extension tubes which serve to erect the top tube above the capsule following porting.

The Top Tube Assembly is extended through the use of a pressurization fluid stored in the lower hemisphere. As the lower portion of theTop Tube Assembly reaches the top of the inner extension tube, it is locked in place by a snap ring and sealed with an "0" ring. This process is repeated with the extension tubes until maximum extension has been achieved. The coaxial cable for antenna transmission and the wiring for the top tube electronics are passed down the top tube and extension tubes. In the stowed position, they are coiled under the Top Tube Assembly. As the tube extends, the cable is uncoiled.

The various components in the Top Tube Assembly are keyed to the housing which is keyed to the structure to prevent rotation in the stowed position. In addition, grooves are provided in the structure to permit wire routing and pressurization. The azimuth position is controlled by the azimuth drive assembly which rotates the tube after extension.

4.4.12 THERMAL CONTROLS

Payload temperature control on the Martian surface is achieved by a passive system utilizing a thermal insulation surrounding the inner payload and a water boil-off-freezing system within the payload. The thermal insulation provides the coarse temperature control and is sized to provide an approximate heat balance between heat gain from internal power dissipation and heat losses to the ambient surroundings. The water boil-off-freezing subsystem provides for fine temperature control maintaining the payload temperature between 32°F and 100°F.

The thermal insulation must also resist the crushing load of impact and provide a means for keeping the inner sphere concentric with the insulation shell, a necessary condition for the accurate erection of the floating inner sphere.

The thermal insulation shown in the conceptual design is assumed to have the low thermal conductivity of Min-K-503 and the mechanical properties necessary to survive impact. The MIN-K-503 insulation does not appear to have acceptable mechanical properties. Thus, an insulation development program may be required to obtain a low thermal conductivity material (at Martian ambient pressures) with acceptable mechanical properties. If such a material is not obtained, other insulating materials are available whose thickness would be approximately twice as great as that indicated in the conceptual design.

SECTION 5

TRADEOFF STUDIES

5.1 SYSTEM CONSIDERATIONS

This section reviews the overall system considerations involved in performing a Mars Facsimile Capsule (MFC) mission. The study constraints did not permit consideration of such subjects as the launch vehicle, spacecraft, trajectories or atmospheric entry. Rather, the system discussions are confined to the subjects of Capsule Value, Landing Sites, and Sterilization.

a. Capabilities. The MFC is a self-sufficient payload package which can be landed on the surface of Mars at velocities up to 500 ft/sec. This upper velocity corresponds to the terminal descent velocity of a low-ballistic-coefficient entry body into the assumed least dense Martian atmosphere. Therefore, the MFC does not require a sophisticated landing system involving retro motors, altimeters, parachutes, etc. The entire MFC hard landing concept is relatively independent of any assumptions on Martian environment (including atmospheric density and composition). The impact limiting method of the MFC provides complete omni-directional protection against an infinitely hard surface. Contained within the MFC are its own attitude orientation, thermal control, data storage, and facsimile viewing systems which are based on hardware previously designed and successfully tested. The capsule is capable of transmitting pictorial data directly to Earth without dependence upon an orbiter or flyby spacecraft as a relay station.

The primary task of the MFC is to obtain a visual image from the Martian surface. Depending upon the intent, the visual image can have varied and multiple scientific uses. Data from the capsule can include a picture which extends from a near-field of a few feet to a far-field showing clouds above the horizon. In its more advanced forms, the MFC can scan the area around the landing site and transmit to Earth only the picture data of greatest importance. Such selection can be internally programmed or based on received commands. The basic facsimile camera operation is adaptable to the functions of multispectral or colored viewing, stereo viewing, and obtaining sequential pictures. These added functions may not be possible on the earliest missions with the lowest capsule weights.

b. HRF Advantages. Because the high resolution facsimile (HRF) concept is not widely understood, it is useful to enumerate some of its inherent advantages over other imaging systems (such as ones utilizing vidicon tubes). The list below applies principally to a facsimile camera which is a part of the payload within a hard landing capsule.

(1) The sensing element can be located within a small, easily deployed tube. Only a small aperture is exposed to the environment.

(2) The camera mechanism is rugged and resistant to high level shock (over 4000 g's).

(3) The camera is compatible with heat sterilization.

(4) The reproduced image is linear without any edge or corner distortion.

(5) The picture aspect ratio can be whatever desired.

(6) Panoramic and wide-angle pictures are possible without mosaic reconstruction.

(7) There is an infinite depth of field with high resolution (fixed optics).

(8) HRF has both photometric and photogrammetric image point stability because a single lens and detector are used serially for an entire image.

(9) A large dynamic range of many gray scales is possible.

(10) The camera is operable over a wide temperature range.

(11) There is no data decay due to direct image storage.

(12) The camera requires low power and no warm-up time.

(13) HRF camera can be used at low scan rates to match a restricted data transmission rate.

(14) Easily adaptable to color and stereo viewing.

c. Utilization of Results. Many scientists and engineers have expressed a desire for a visual image of the Mars surface but their specific reasons are sometimes difficult to describe in quantitative terms. Primarily, it appears the desire arises from a need for a maximum amount of information from what is now a completely unknown area. The eye is the prime input sensor for the human mind and people are accustomed to accepting and evaluating new information in visual form.

Visual images contain information on sizes, shapes, textures, arrangements, contrasts, movement, locations, etc. -- things which are very difficult to instrument in any other manner. Furthermore, an image sensor can accomodate and report on a completely unexpected situation -- such as the

presence of paving blocks, trees, buildings, canals, or springs. An HRF camera picture contains information valuable to specialists in many fields. Some of the specific areas of interest are listed below:

(1)	Biology	Life detection (morphology), ecology.
(2)	Paleontology	Fossil detection
(3)	Meteorology	Cloud formations, dust storms, frost, electrical phenomena
(4)	Geology	Topography, surface material classification, erosion, meteoric craters, protuberances, particle sizes
(5)	Physics	Surface reflectance
(6)	Engineering	Manned landing site evaluations, surface characteristics
(7)	General	An understandable accomplishment of space exploration

d. Added Measurements. Rather obviously, an early Mars lander capsule might contain more than just an HRF camera system. It is expected that the HRF camera might constitute the largest amount of weight, generate the most data, and require the most electrical power. However, certain other valuable measurements could be included in the payload with little penalty. These are listed below without any explanation; however, they have all been evaluated with regard to their importance in the manned and exobiological exploration of Mars. (See Reference 1).

ADDED MEASUREMENTS

(1) Seismometer

(2) Air temperature

(3) Surface temperature

(4) Surface radioactivity

(5) Wind force

(6) Sky brightness

(7) Atmospheric composition

(8) Atmospheric pressure at surface

(9) Surface conductivity

(10) Humidity

(11) Dust concentration

(12) Solar spectrum and irradiance

(13) Ionizing radiation

(14) Magnetic field at surface

(15) Gravitational field at surface

e. Feasibility. The Ranger program involved extensive development of the hard-landing capsule concept. Aeronutronic, under JPL contract, developed, built, and tested the Lunar Seismometer Capsules. Three of these capsules were launched on Ranger spacecraft but the missions were aborted due to failures not connected with the capsules.

Additionally, also under JPL contract, the High Resolution Facsimile Camera mechanism and core memory storage unit were developed and tested for use in Lunar Capsules. All of this work forms a firm foundation in the areas of the MFC with which this report is concerned. The MFC represents a considerable extension over the Lunar Capsule hardware, but not a leap into a completely unknown area. The gross characteristics differences are illustrated below:

ITEM	LUNAR FACSIMILE CAPSULE	MARS FACSIMILE CAPSULE
Payload Weight (lbs)	50	50-150
Balsa Limiter Weight (lbs)	40	200-500
Total Capsule Weight (lbs)	90	300-600
Transmitter Power	5 W	20 W
Frequency	960 MC	2295 MC
Battery Weight (lbs)	8	18-40
Max. Impact Velocity	200 ft/sec	500 ft/sec
Payload Shock Environment	3000 g	3000 g

The study revealed several technical areas which need concentrated development effort before an MFC mission can occur. These are:

(1) Sterilizable battery

(2) 20-watt impactable S-band transmitter

(3) Low-conductivity impactable insulation

(4) Sterilizable pyrotechnic devices

(5) Verification testing of balsa wood performance in large spheres at high velocities

The sterilizable battery appears to be the greatest problem and, of course, is currently under concentrated investigation by NASA. Acceptable solutions to this problem appear to be in sight in both the silver-zinc and thermal battery concepts. The problems in developing an impactable 20-watt S-band transmitter are not at all overwhelming at this time. Impactable transmitters of several watts output at L-band have already been proved for use at high shock levels.

A dense, low-conductivity, impactable insulation is desirable for the MFC but there are alternate solutions if this material cannot readily be developed. The obvious solutions are to accept the payload penalty due to more insulation weight or more battery weight for a heater. The capsule requires sterilizable pyrotechnic devices but these appear to be available, although little test or reliability information currently exists.

Last, there is need for further analytical and experimental investigation of impacting large capsules at the new high velocities. Such investigations would be expected to reveal additional problems, but none without solutions.

On this basis, the conclusion is reached that it is technically feasible to develop an MFC with the stated performance for a 1969 or 1971 Mars Mission.

5.1.2 LANDING SITES

The study contract did not call for any investigation of landing sites, trajectories, or entry methods. However, questions of landing sites naturally become important whenever communications from Mars are involved. Therefore, several aspects of the communication geometry were investigates and are recorded here.

a. Geometry. Figures 19 and 20 show the communication distance from Mars to Earth as a function of calendar date for the time period of 1968-1975. These curves illustrate that the distance varies from

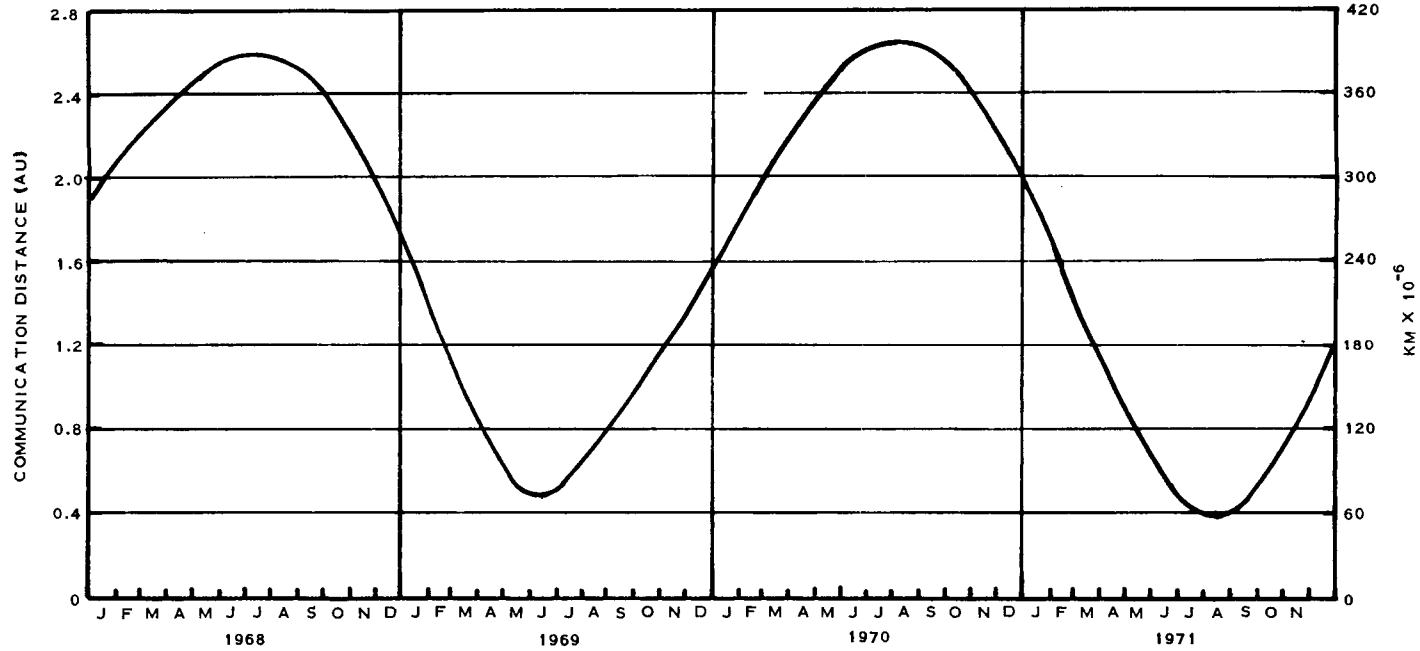

R11219

FIGURE 19 - MARS TO EARTH COMMUNICATION DISTANCE 1968 - 1971

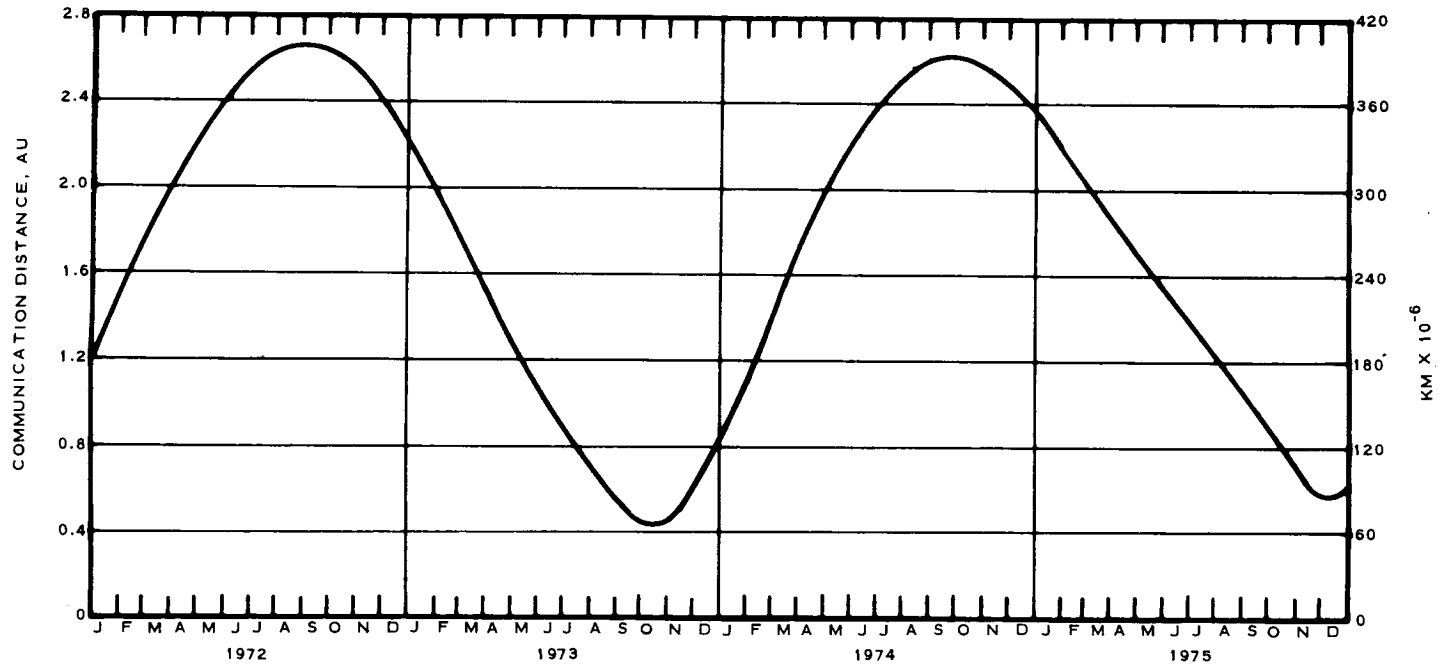

R11195

FIGURE 20 - MARS TO EARTH COMMUNICATION DISTANCE 1972 - 1975

approximately 0.4 to 2.6 astronautical units (AU). With a known Mars arrival date, one can easily find the communication distance. Figures 21 and 22 show the planetary communication angles for the same time period. Two important conclusions can be drawn from these curves. First, there are time periods when the Sun comes between Earth and Mars, making communications extremely difficult. Secondly, from Mars the Earth usually appears within 40 degrees of the Sun. This last factor may have significance in trying to devise a way for aiming an antenna from the surface of Mars at Earth.

Figure 23 is an ecliptic projection for a typical 1971 Type I Mars trajectory. The spacecraft, Earth and Mars are shown at launch, at arrival, and at 20 days before and after arrival. This figure serves only to give a perspective view of the communication geometry.

b. Locations. Figures 24, 25, 26, and 27 all show the effect of the MFC landing location on the possible communication time per day with Earth. Possible communication time is defined as the percent of the day that line-of-sight vision exists between the Martian surface and the center of Earth. For each of the curves, it is assumed that the Earth must be at least 10° above the Martian horizon before it is visible. The variable in the curves is the latitude of the MFC landing site. The curves show the polar regions fluctuate between having continuous and no communication capability. The equatorial area (zero latitude) has nearly a constant 50% communication capability. All of the curves imply that the MFC be capable of radiating energy to Earth regardless of where in the sky the Earth is located. In other words. to take advantage of the communication time shown in Figures 24 to 27 , the MFC would need wither an Earth-tracking antenna or an antenna with hemispherical coverage.

Near-equatorial landing sites appear attractive for an MFC mission for these reasons:

(1) Equatorial landing sites are generally easier to achieve from a spacecraft because the trajectory dispersions can be larger.

(2) The equatorial regions are interesting investigative areas. These regions are best observed from Earth and therefore any new data can be correlated with existing knowledge. Swan and Sagan in Reference 2 list the following recommended landing sites for obtaining exobiological information:

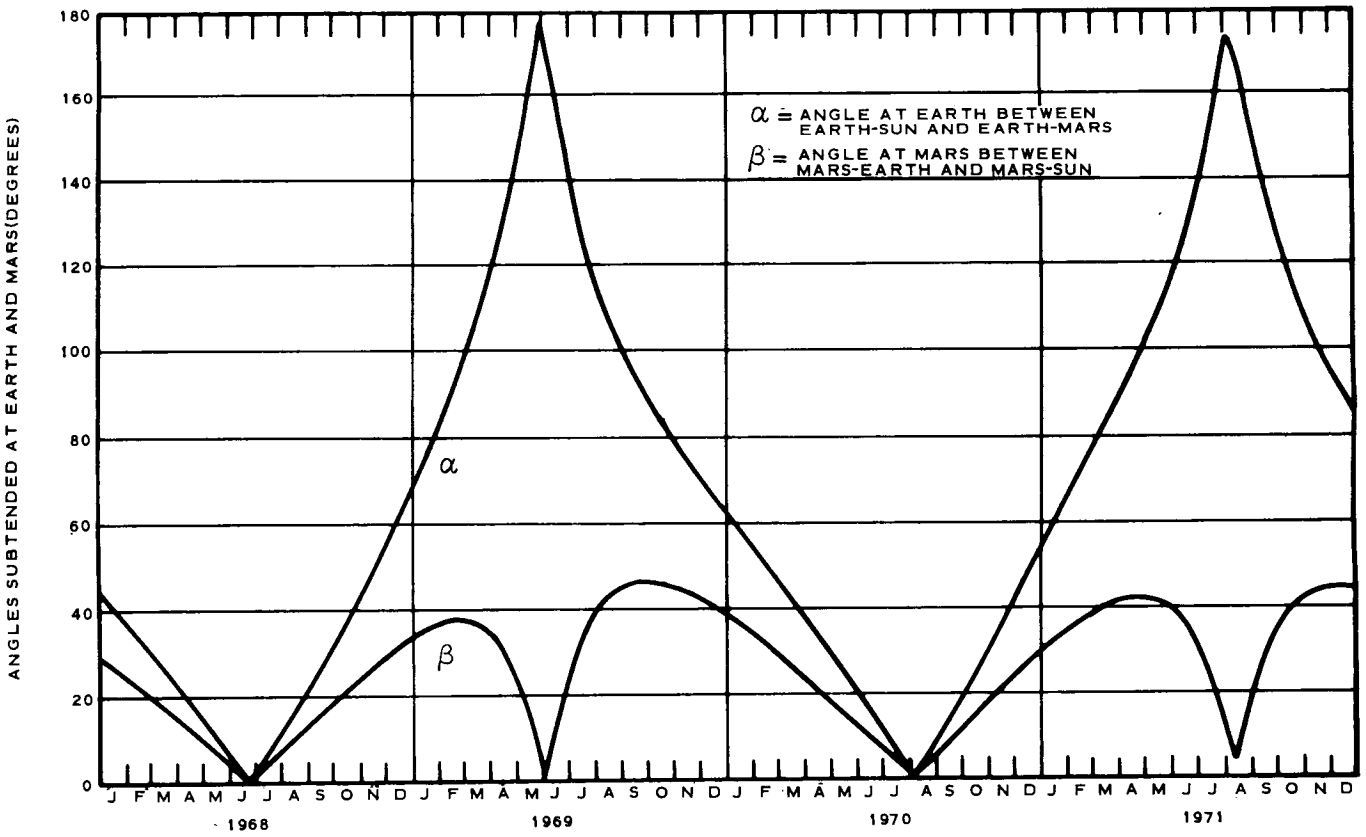

R11209

FIGURE 21 - ANGLES SUBTENDED AT EARTH AND MARS 1968 - 1971

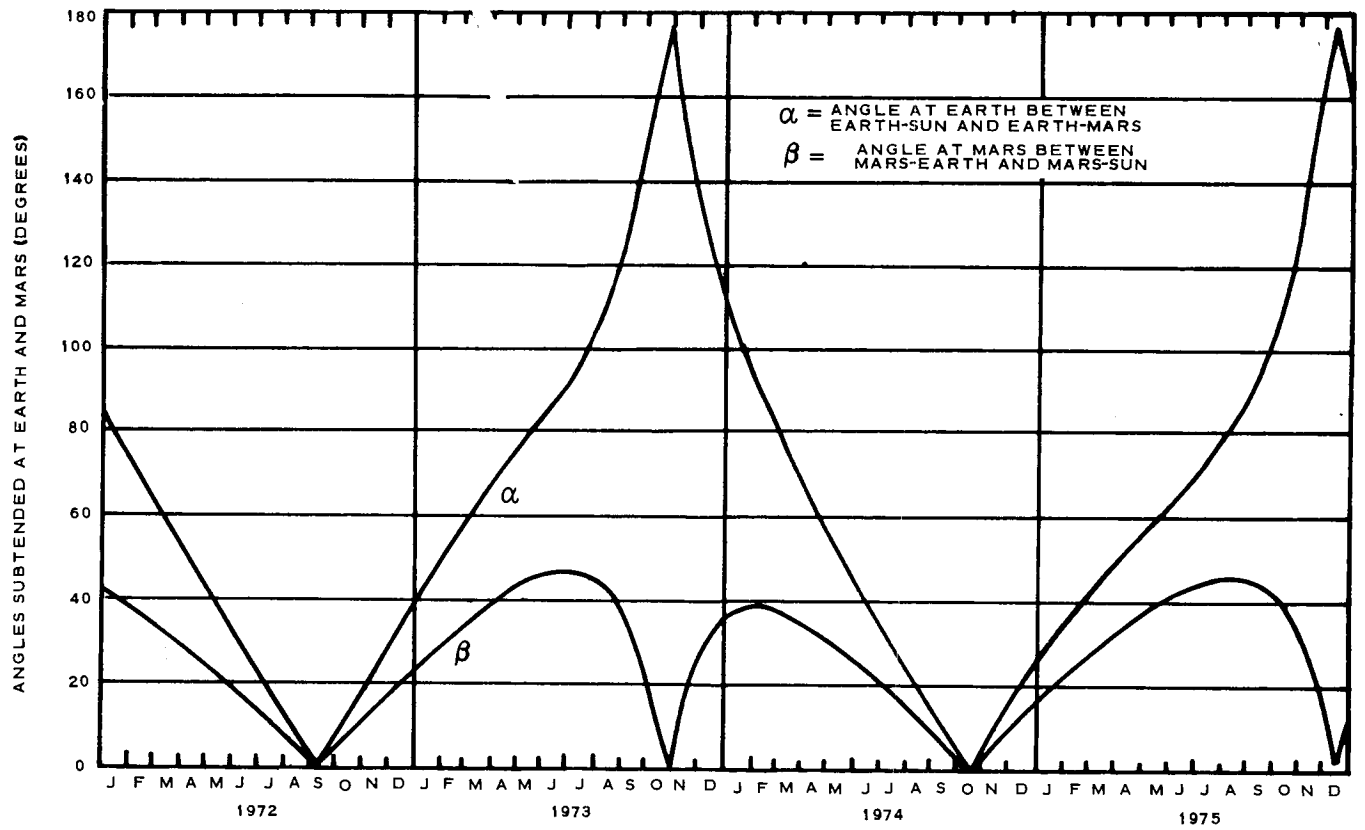

R11211

FIGURE 22 - ANGLES SUBTENDED AT EARTH AND MARS 1972 - 1975

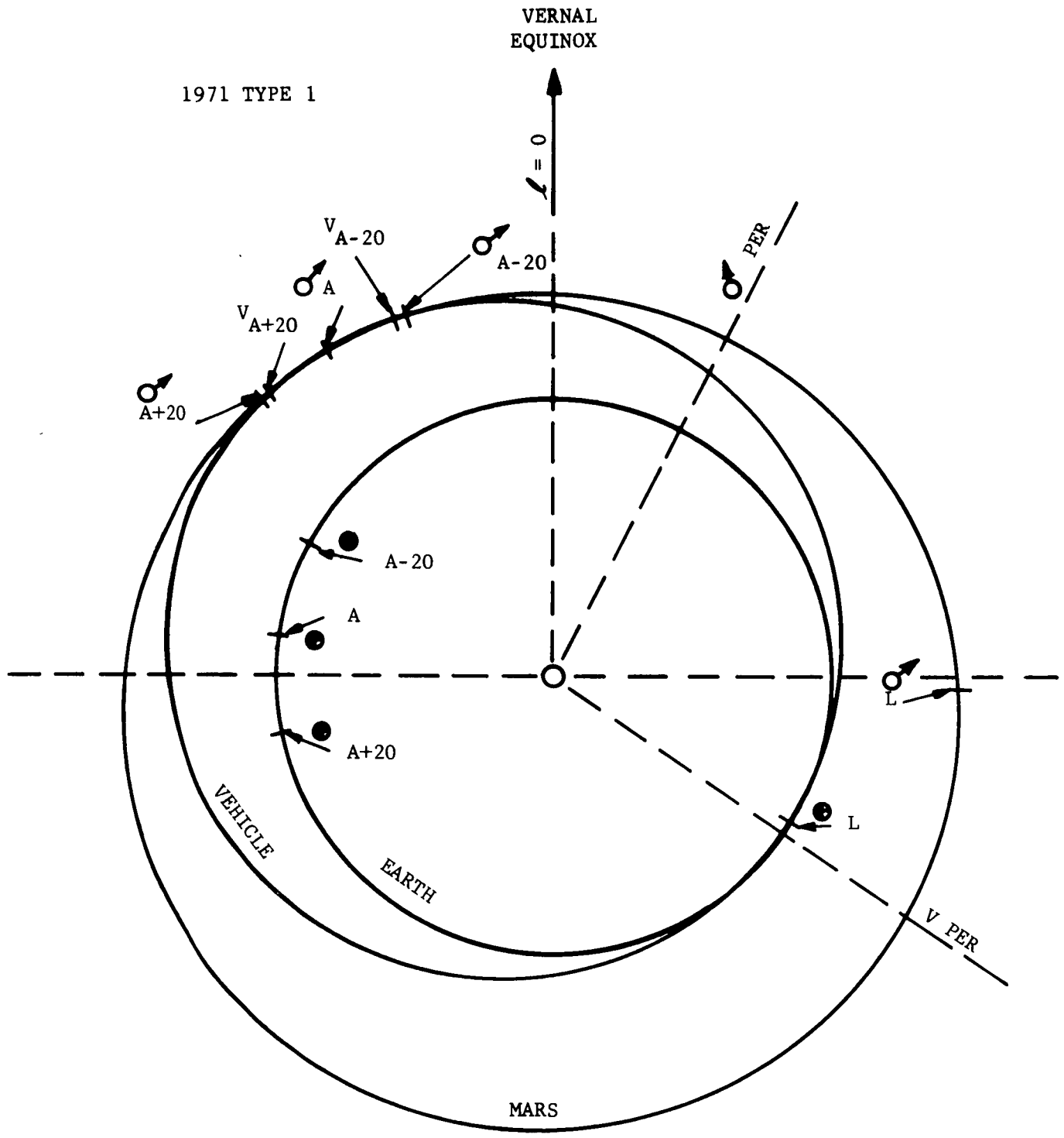

L DATE MAY 22, 1971
A DATE DEC 15, 1971
TRIP TIME 207 DAYS

L	LAUNCH
A	ARRIVAL
V	VEHICLE
●	EARTH
♂	MARS
PER	PERIHELION

FIGURE 23 - ECLIPTIC PROJECTION MARS TRAJECTORY

R11196

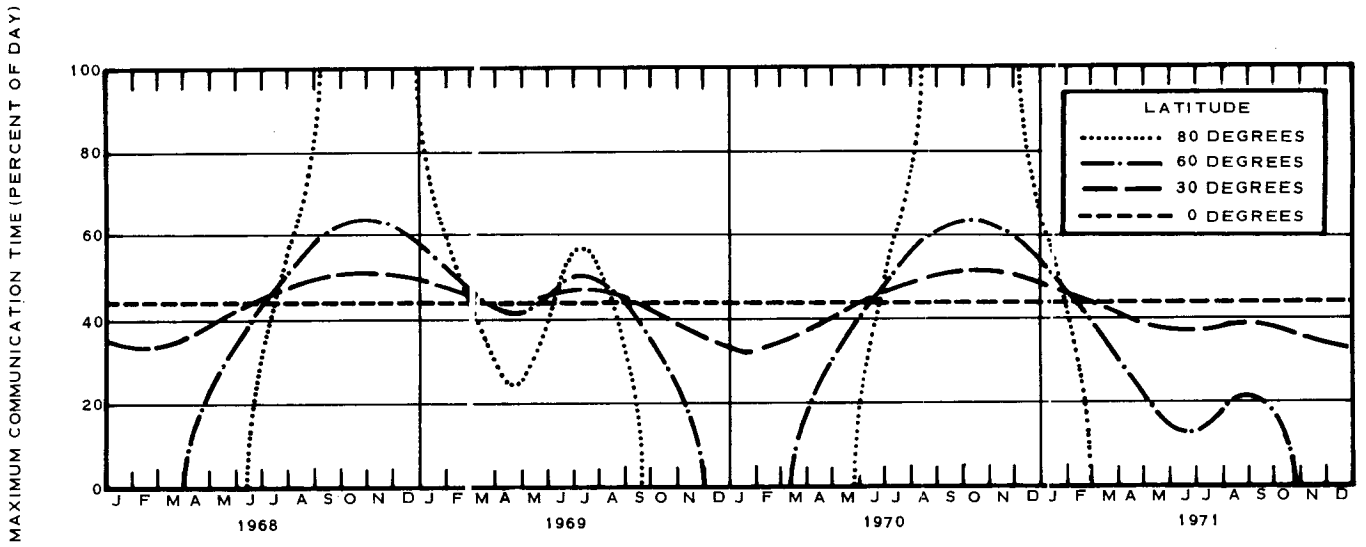

FIGURE 24 - EFFECT OF MFC LOCATION ON DIRECT COMMUNICATION WITH EARTH
1968 - 1971

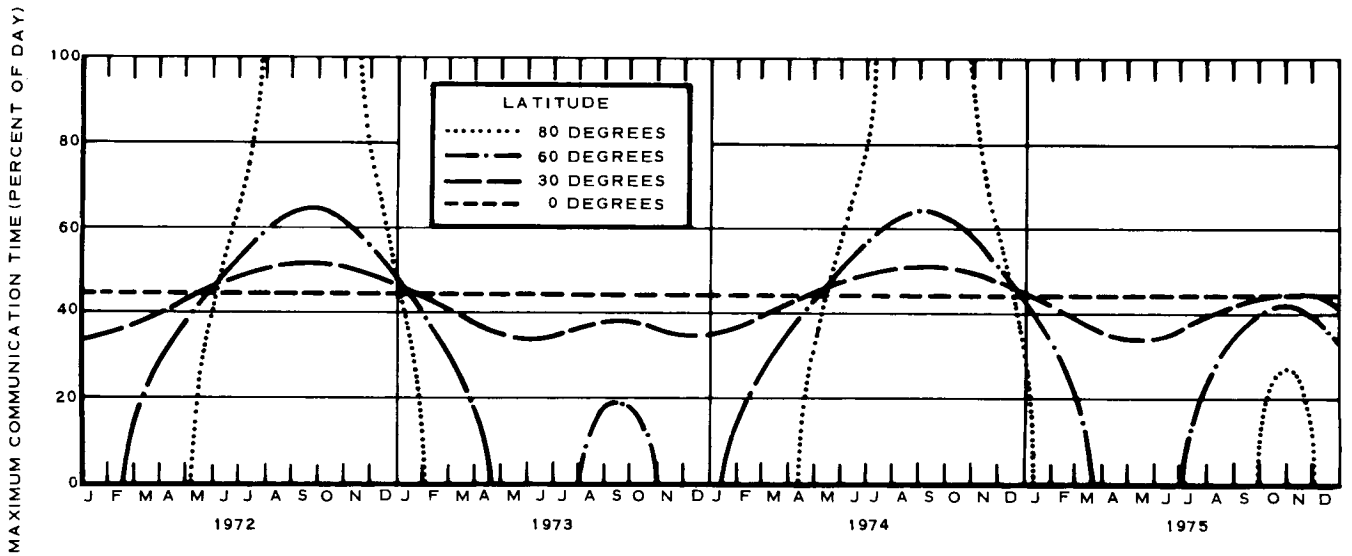

R11168

FIGURE 25 - EFFECT ON MFC LOCATION ON DIRECT COMMUNICATION WITH EARTH
1972 - 1975

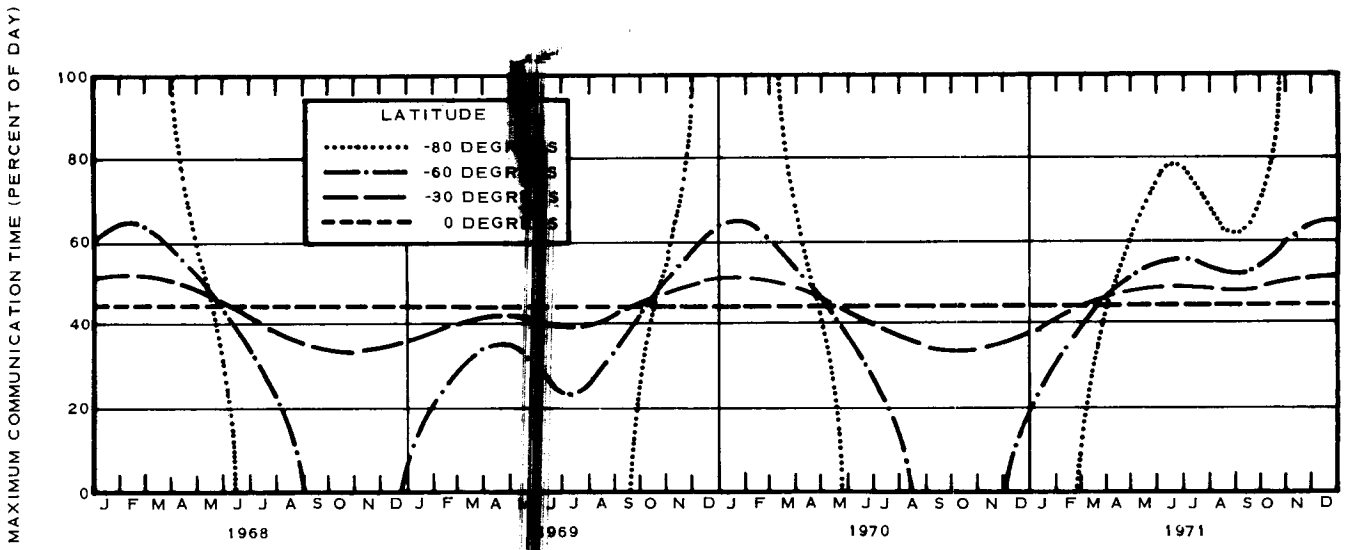

R11170

FIGURE 26 - EFFECT ON MFC LOCATION ON DIRECT COMMUNICATION WITH EARTH 1968 - 1971

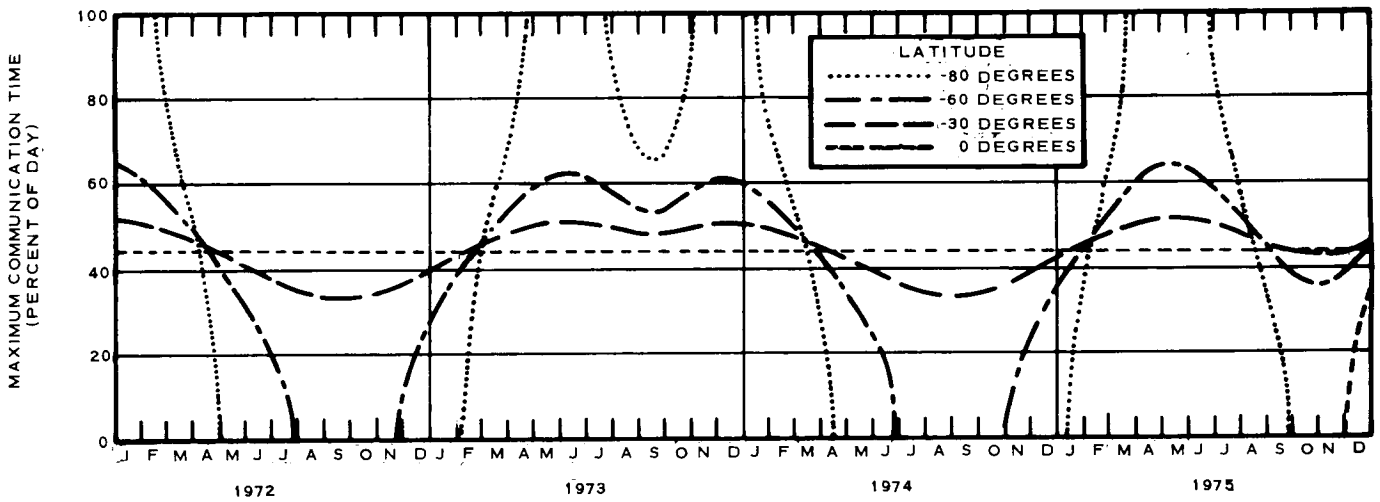

R11210

FIGURE 27 - EFFECT ON MFC LOCATION ON DIRECT COMMUNICATION WITH EARTH
1972 - 1975

1969	Longitude	Latitude
Solis Lacus	90	- 28
Syrtis Major	290	+ 10
Mare Sirenum	140	- 30
Lunae Paulus	65	+ 15
Trivicum Charontis	198	+ 20

1971	Longitude	Latitude
Polar Cap	40	- 82
Mare Cimmerium	235	- 18
Lunae Paulus	65	+ 15
Aurorae Sinus	50	- 15
Solis Lacus	90	- 28
Mare Serpentis	315	- 30

Many of these areas are close to the equator.

(3) The simplest antenna for the MFC is one which directs the transmitted signal vertically from the surface. This type of antenna requires only vertical erection -- no complicated pointing or continuous tracking. However, such an antenna is only useful at the Martian latitudes where the Earth passes nearly overhead.

above the Martian equator for the time period of 1968-1975. The elevation ranges from about -26 to +26 degrees. Therefore, the Earth will always come within 26° of passing overhead for a landing site chosen on the equator. Obviously, a landing site for a specific date can be chosen near the equator so that the Earth passes directly overhead.

(4) The solar radiation at the equator makes the obtaining of pictures easier because the lighting is more intense, more nearly constant throughout the year, and more predictable. These benefits are due to the smaller effects of the radiation transmission through the atmosphere. Therefore, the HFC camera has a better chance of obtaining a good quality picture of a dark environment if it is near the equator.

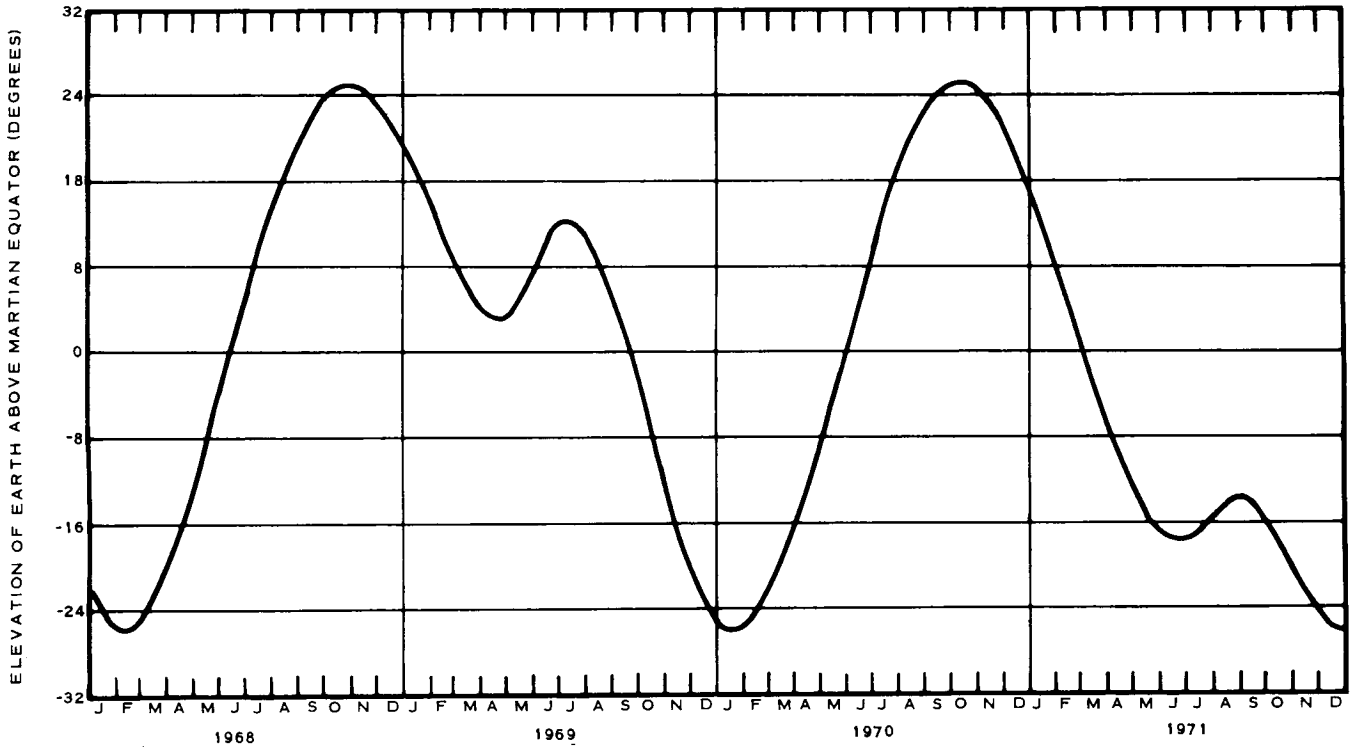

FIGURE 28 - ELEVATION OF EARTH ABOVE MARTIAN EQUATOR, 1968 - 1971

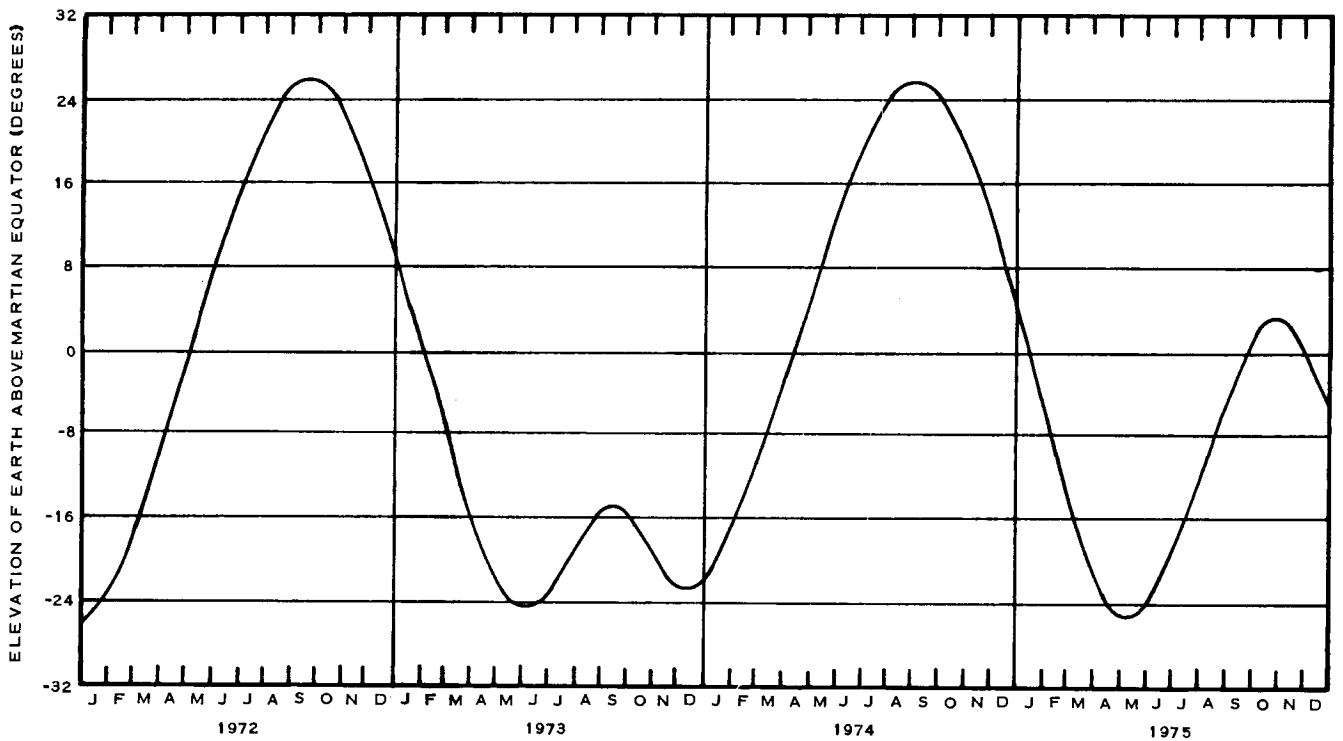

R11194

FIGURE 29 - ELEVATION OF EARTH ABOVE MARTIAN EQUATOR, 1972 - 1975

c. Sequence. Some general conclusions can be made about the relation of the landing site to the sequence of capsule operations. To do this, it is easiest to assume certain specific landing conditions since no particular landing trajectories were specified for this study. Equal or similar conclusions can be reached for other landing conditions. The assumed landing conditions are:

(1) A specific landing date of 15 December 1971.

(2) A landing site choice near the Martian equator.

(3) A nearly vertical atmospheric descent trajectory.

Figure 30 is a Solar referenced map of Mars for these particular conditions. To start, we will discuss just what this map shows.

Near the center of Figure 30 is the Solar-vector point through which passes the line between the centers of Mars and the Sun. The map is referenced to longitude to this point so the Sun can move only up and down in latitude with changing calendar time. The latitude for the map is based on the true equator of Mars. The plot therefore resembles a map of Mars, except the coordinate system does not rotate as the planet rotates about its axis, thereby leaving the actual aerographic longitude undefined.

The position of the Sun for the assumed landing date is 19 degrees below the equator, while the Earth is 24 degrees below the equator and 46 degrees west of the Sun. For the particular case, the arrival asymptote approaches Mars from a position 6 degrees below the equator and 97 degrees west of the Sun. The solid line represents the terminator, or boundary between the sunlit and dark zones of the surface. The line connecting the dots, enclosing the Earth's position, indicates the portion of the planet which is in line-of-sight view of the Earth. The dashed line in the right hand portion of the figure encloses the area which definitely cannot be reached by a ballistic entry trajectory.

Now to examine the map for conclusions about the capsule sequence. The assumption of a nearly vertical atmospheric descent means that the landing site will be somewhere within a small circle surrounding the arrival asymptote. The map shows that the landing site is in view of Earth but that landing will occur at about sunrise. The capsule will have to wait many hours until the best lighting occurs for obtaining a high resolution facsimile picture -- it will be six hours until noon. However, it will be only 3.4 hours until the Earth is directly overhead -- the best time for communicating with a vertically oriented antenna. Thus, it seems unlikely that a picture can be taken the first morning in time to communicate a significant portion of it to the Earth.

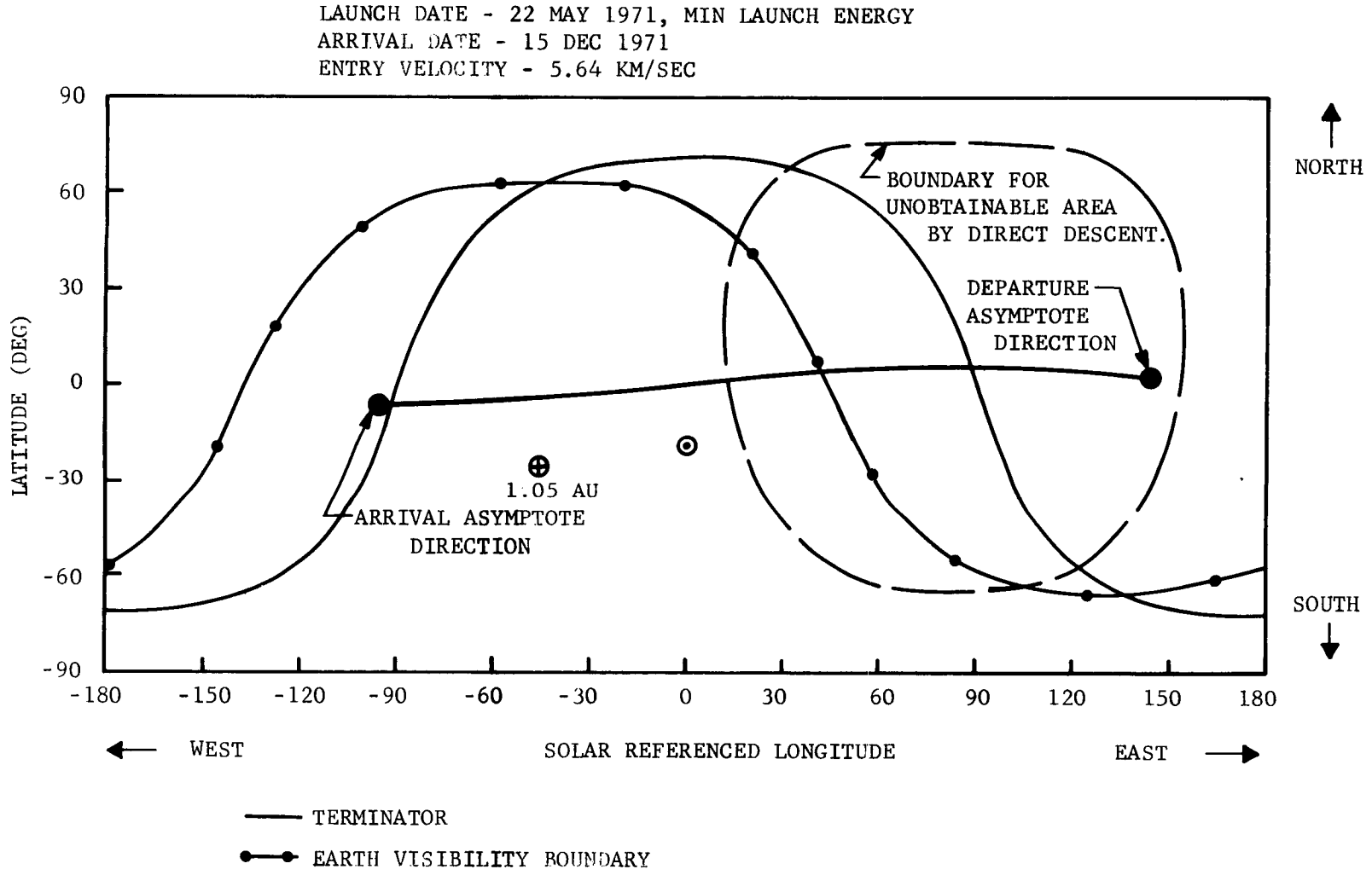

FIGURE 30 . SITE ATTAINMENT GEOMETRY, 1971 TYPE I

There are, however, significant advantages in taking an entire picture the first day and recording it for subsequent transmission. After landing there should be enough delay provided before taking a picture to ensure that the landing dust has settled. However, it is advantageous to operate the camera as soon as possible and to avoid subsequent sand storms, evening winds, and unpredicted diurnal temperature variations as the camera scanning window and the azimuth drive mechanisms are somewhat unavoidably exposed to the exterior environment.

Thus, it seems likely that the capsule will obtain a picture in late morning or early afternoon to maximize the ambient light but still have some shadows. Shadows appear necessary to provide contrast and aid in depth, size and direction perception. The picture will be stored internally by means of a tape recorder or magnetic core memory. The transmission of picture data will begin on the day after the landing. The time of transmission will be internally programmed from some measurable event such as spacecraft separation, surface impact, sunrise, or local noon. Data will be transmitted for several hours each day until it has all been transmitted at least once.

If the capsule capabilities permit, it would be valuable to perform the following variations of the basic HRF picture-taking function.

(1) Take stereo pictures by displacement of the HRF viewing window

(2) Obtain facsimile pictures using only specific filtered sections of the radiation spectrum; i.e., color pictures.

(3) Take pictures at different times or days to observe scenic changes

(4) Employ commands from Earth to concentrate the data capability on the most important areas of pictorial information.

5.1.3 STERILIZATION

One of the major tasks during the study was the consideration of the sterilization requirements for the MFC. First, the anticipated sterilization requirements were reviewed and it was concluded that a terminal heat soak was the probable and also most severe sterilization requirement. Therefore, throughout the trade-off studies and conceptual design effort only materials, components and processes were considered which were compatible with the heat sterilization criteria. More detailed consideration of sterilization effects can be found in other parts of this report, particularly in the sections on balsa, data memories, and power supplies.

a. Requirements. There were no specific sterilization requirements imposed on the MFC by JPL during the study contract. However, several preliminary NASA documents (References 3, 4, and 5) exist which indicate what the probable requirements will be. These are summarized below:

(1) Clean Room Assembly. The capsule shall be assembled in a standard clean room from parts and subassemblies which shall be individually sterile.

(2) Heat Cycle (Flight). The entire capsule shall be subjected to a temperature of 135°C for 24 hours. The most thermally isolated component shall meet this time requirement, meaning that some components may be held at this temperature for more than 24 hours.

(3) Heat Cycle (Type Approval). The entire capsule shall demonstrate flight qualification by being subjected to three separate cycles of 145°C for 36 hours. It shall subsequently demonstrate proper functional operation.

(4) Biological Barrier. The capsule shall be sterilized in a container which is a biological barrier. It shall remain in this container during flight until the spacecraft is a considerable distance away from Earth.

It is evident that the sterilization requirements resolve themselves to design problems of using the correct components and materials capable of withstanding the long term (108 hours minimum) heat soak at high temperature (145°C). There are also innumerable associated problems of assembly, test, and checkout but these were only lightly considered during the **ual design stage.**

b. Design Considerations. The following items discuss some of the design problems and solutions for obtaining a Mars Facsimile Capsule which can withstand the terminal heat sterilization.

(1) Structure. The structure will be constructed of aluminum alloy. In general, the properties of these materials are unaffected by a 300°F heat soak for periods on the order of 100 hours. An exception is the high strength 7075-T6 alloy whose tensile yield strength is reduced 10% by a 100 hour soak at 300°F; in the event this material is used, this expected degradation will be accounted for.

(2) Impact Limiter. Previous tests performed on heat sterilized balsa wood impact limiters have indicated that to prevent degradation of physical properties following sterilization it is necessary to prevent loss of moisture. Failure to heed this precaution results in the balsa wood becoming brittle, accompanied by a reduction in energy absorption reliability.

The MFC limiter will be fabricated using a high temperature resin system capable of tolerating the 293°F sterilization level temperatures. Then, prior to sterilization, the limiter will be sealed, thereby preventing any loss of moisture and hence degradation during soak at elevated temperatures.

(3) Motors. The small size #5 motors utilized in the MFC system are well suited to tolerate the 293°F sterilization temperature. The winding insulation is rated for 200°C (392°F), and all winding assemblies are routinely baked at 300°F during their manufacture.

(4) Gearheads and Bearings. All gears, bearings and gearhead assemblies are constructed of similar metals and hence expand uniformly during elevation to sterilization temperatures. No degradation is anticipated.

(5) Thermal Control Elements. The thermal control system consists of a passive high temperature capability insulation together with a water boil-off/freezing system. The water tankage and associated hardware will be designed with sufficient strength to retain the 60 psia vapor pressure of water at sterilization temperatures (293°F).

(6) Flotation System. The flotation system consists of Freon 113 and 114 mixed as required to obtain a density corresponding to that of thepayload. Considering as a worst case the condition of F114 at 145°C we can establish a peak pressure during sterilization of 470 psia in the flotation fluid. Since the corresponding stress imposed in the flotation shell is well below the levels for which the shell is stressed to survive impact, no difficulties are anticipated.

(7) Electrical Components. The electronic components to be utilized in the MFC system are all rated to be capable of surviving the 293°F sterilization temperature. The following specific elements will be utilized:

Tantalum Capacitors

Glass Capacitors

Carbon Resistors

Silicon Semi-conductors

An example of the temperature capabilities of silicon semi-conductors is found in the following environmental exposure given to 100% of specific Fairchild semi-conductors prior to delivery:

200°C (Min.) for 24 hours (Min.)

3 cycles - 60°C to 200°C

(8) Ordnance. Special effort will be directed towards the selection of ordnance items which are capable of tolerating long term soak at elevated temperature.

An item of particular interest is the temperature tolerance of the Mild Detonating Fuse (MDF) and the Flexible Linear Shaped Charge (FLSC) which are used for limiter removal and porting, respectively. In general, these standard items when fabricated of RDX and sealed with detonators are only rated for 230°F for 24 hours. However, it is possible to have this material fabricated of special high temperature compositions (e.g., Dupont"TACOT") which are rated for 550°F.

(9) Memory Systems. Because of the low storage requirement a miniaturized, solid state core memory is currently contemplated for use on the MFC and its performance is not degraded by temperatures of 293°F. Should larger storage requirements be encountered a tape recorder instrumentation would be required. On these instruments the operating temperature is restricted to the range -40°F to +185°F by the characteristics of the Mylar instrumentation tape. Additionally, at temperatures over +165°F and humidities of 95 percent, the oxide binder breaks down and attaches itself to the rollers, guides, and heads with the result that subsequent performance is greatly degraded. In view of these difficulties if a tape recorder were necessary it would appear desirable to use Vicalloy metal tape for the recorder. Although this results in a 10 to 1 increase in tape weight, this would not be large relative to the total weight of the recorder.

(10) Power Supply. Present system considerations indicate the silver-zinc battery to be an optimum choice for the MFC power supply. However, dry heat sterilization

of such a sealed silver-zinc battery assembly represents extreme difficulties in the light of present development status.

One problem of silver-zinc cells is that both electrode materials are soluble in the Potassium Hydroxide electrolyte. This phenomena exposes the separator material to metallic ions which results in their deterioration at the high sterilization temperatures. Although it appears that satisfactory separator materials will be developed in the near future, there are other additional problems. If the battery is sterilized in the charged state, the silver peroxide rapidly decomposes to silver oxide resulting in a significant loss in battery capacity.

A possible solution to the battery problem is to sterilize dry, uncharged cells. This approach, however, entails filling and charging the battery following terminal heat sterilization. This imposes severe mechanization difficulties and precludes the necessary re-sterilization in the case of a repair.

An alternate battery solution is to abandon the silver-zinc battery completely and utilize a thermal battery which inherently can withstand sterilization since it normally operates at a temperature above 145°C. This approach is further discussed elsewhere in the report.

(11) Miscellaneous. High temperature resins and sealants would be used throughout the capsule. In general, this would involve 300°F cure cycles during assembly. Lubricants would also be selected for high temperature capability. Silicone lubricants which have been used in the past for LFC bearing assemblies subject to operation in a hard vacuum would be entirely satisfactory for this purpose.

Micro-miniature electrical connectors constructed of a Diayllyl Pthalate compound capable of tolerating extreme temperature limits are available and have been previously demonstrated to properly perform during and following a 3000 g impact.

(12) Assembly. The landing assemblies shall be assembled in a standard clean room using parts each of which, after heat sterilization at Type Approval levels, shall be capable of meeting reliability requirements and be sterile.

Simple parts such as wire, resistors, capacitors, motors, lenses, fasteners, "O" rings, and other piece parts which are not capable of being disassembled shall be heat sterilized after manufacture and brought into the next higher assembly area in a sterile condition. Complex parts such as the top tube and associated electronic subassemblies shall be assembled in standard clean rooms using sterile parts.

All plastics, adhesives, potting compounds, lubricants, elastomers, sealants, solders, and other structural materials which are not inherently sporicidal will be sterilized before they are used in higher levels of assembly.

The completely assembled capsule will then be placed in a biological barrier (e.g., shroud or canister) and heated in an atmosphere of dry nitrogen until the most thermally isolated component has temperature stabilized at 135°C. Since the interior temperature of flight assemblies cannot be measured, the time required for the most thermally isolated component to reach equilibrium temperature will be established during development tests. The assembly will then be maintained at a 135°C equilibrium temperature for a period of 24 hours.

For the type approval unit the stabilization temperature shall be raised to 145°C and the time duration increased to 36 hours. Additionally, the unit shall be cycled three times to cover the possibility of a flight re-sterilization. After the third exposure, and stabilization at room conditions the assembly shall be energized and satisfactory operation will be demonstrated. The biological barrier in which the capsule has been heat sterilized will not be opened until the vehicle has passed beyond the Earth's atmosphere, after launch. In the event a capsule develops a malfunction after final sterilization, it shall be opened and repaired only in a standard clean room. It shall then be replaced in its biological barrier and again heat sterilized. The container serving as a biological barrier will also function to maintain the correct humidity in the impact limiting balsa wood.

c. Conclusions. It is concluded that the Mars Facsimile Capsule has no special sterilization problems that do not exist for all other planetary capsules. The main area of concern is the problem of obtaining a heat-sterilizable battery. However, this problem is somewhat tempered because of the following special battery requirements:

(1) The operating life is only several days.

(2) The battery can possibly be charged immediately before use.

(3) The battery can possibly be activated immediately before use.

Additional problem areas of lesser concern are the performance characteristics of pyrotechnic devices and balsa after heat sterilization. Present indications are that adequate pyrotechnic devices have or shortly will be developed. Previous tests (Reference 6) showed that balsa performance should be adequate, but more verification is needed.

It is believed that compatibility with ethylene oxide will pose no problem, should this become a requirement. Previous tests (Reference 6) showed no problem with the materials commonly used in a hard-landing capsule.

REFERENCES

1. "Study of a Manned Mars Excursion Module, Final Report", Aeronutronic Publication No. C-2379, 20 December 1963.

2. P. Swan and C. Sagan, "Martian Landing Sites for the Voyager Mission", Journal of Spacecraft and Rockets, Vol. 2, No. 1, January-February 1965, p. 18.

3. "Environmental Test Specification Compatibility Test for Planetary Dry Heat Sterilization Requirements", NASA.

4. "Recommended Procedures for Sterilizing Spacecraft Hardware", Office of Space Science and Applications, NASA, Uncoordinated Draft.

5. Bruch, C. W., "Memorandum to all Bioscience Program Office Contractors Concerned with the Science of Experiments and the Development of Appropriate Instrumentation for the Detection of Extraterrestrial Life",NASA.

6. MacDonald, A. G., "Lunar Seismometer Capsule Sterilization Final Report", Aeronutronic Report LC(b)-411, 29 October 1962.

5.2 IMPACT ANALYSIS

5.2.1 ANALYTICAL MODELS

a. Studies of Basic Problems in the Dynamics of Crushup. In Appendix 6.2, analytical studies are performed in order to arrive at a fundamental understanding of some of the essential features of dynamic crushup phenomena. Mathematical complexities tend to obscure some of the basic aspects of the physical processes under consideration. In order to distill out the essence of the physical problem, the approach adopted here is to utilize mathematical representations based on idealizations and simplifications which retain the important characteristics of the physical situation being modeled. The studies in Appendix 6.2 are concerned with the treatment of "one dimensional problems" which illustrate some important characteristics of shock wave phenomena in the propagation of crushing deformation.

The essential features of the dynamic mechanical behavior of crushable materials such as balsa wood are represented by a model in which crushing deformation under "quasi-static" conditions takes place at a constant stress level σ_y until the crushing strain (crushing deformation divided by original uncrushed length) attains a certain ultimate value ϵ_c (where, of course, $\epsilon_c < 1.0$) after which the material is regarded as essentially rigid. The model assumes that under dynamic conditions crushing cannot take place until the stress reaches the level σ_y. In Appendix 6.2, it is shown that the dynamic propagation of crushing deformation takes place by means of a "shock process." A shock wave of "crushing front" advances into the uncrushed material. Behind the shock front, the material is crushed up to the ultimate crushing strain ϵ_c. The stress level in the uncrushed material immediately ahead of the crushing front is σ_y, and in the crushed material immediately behind the front the stress is σ_c. The stress discontinuity, $\sigma_c - \sigma_y$, across the shock, in the case where the material on one side of the front has velocity V and the material on the other side has no velocity, is shown to be given by

$$\sigma_c - \sigma_y = \frac{\rho_o V^2}{\epsilon_c}$$

where ρ_o is the mass density of the uncrushed material. It is seen that finite velocities V always imply a finite shock strength; that is, a finite stress discontinuity $\sigma_c - \sigma_y$, with the shock strength being proportional to the square of the velocity V.

It is also demonstrated in Appendix 6.2 that in addition to the energy absorbed in crushing deformation, energy is dissipated across the shock

front. The energy per unit mass dissipated across the shock is

$$(1/2)\ \bar{V}^2\ \epsilon_c^2$$

where $\bar{V}$ is the velocity of the uncrushed material relative to the shock front. In the case where the crushed material behind the shock front has zero velocity, the energy per unit mass dissipated across the shock is $1/2\ V^2$, where V is the absolute velocity of the uncrushed material.

It is demonstrated in Appendix 6.2 that the energy which can be absorbed in the dynamic deformation of a crushable material is the mechanical energy of crushing deformation plus the energy dissipated across the shock front during the crushing process. For the case of an impact on a rigid plane of a cylindrical impact limiter of crushable material protecting a rigid mass, it is shown that the ratio of the energy dissipated across the shock front to the energy absorbed in mechanical crushing formation during the impact process is

$$\frac{\beta}{1 - e^{-\beta}} - 1$$

where

$$\beta = \frac{\rho_o V_o^2}{2\epsilon_c \sigma_y}$$

and V_o is the initial impact velocity.

b. Studies of Spherical Impact Limiter Dynamics

(1) Curved Impact Surfaces. In Appendix 6.3, the symmetrical impact of a spherical limiter of crushable material against a curved surface is considered. Concave and convex hemispherical surfaces are treated, and the results are indicated for the limiting case of a flat surface (infinite radius of curvature). Expressions are developed for the forces acting and the energy absorbed in mechanical crushing deformation.

Shock phenomena involving consideration of the finite depth of crushed material above the impact surface and the energy dissipated in the shock wave (crushing front) propagation are not treated. Numerical calculations are based on analyses presented in Appendix 6.2 indicate that the neglect of finite depth on shock dissipation energy of impact velocity absorbing

capability is on the order of 5 percent at around 450 fps impact velocity. The neglect of such effects seems justified in an analysis which is aimed at providing an initial assessment of the importance of impact surface curvature effects.

The situation under consideration is depicted in Figure 31 and in more detail in Figure 32 for a convex impact surface. Figure 32 is a radial section through the limiter and curved impact surface delineating the essential features of the geometry of the situation. The radian crushing strength of the limiter material is denoted by σ and the cross grain strength ratio by α. The differential vertical force of dF_V acting on an elemential ring (see Figure 31) of the curved impact surface is

$$dF_V = 2 \pi \sigma \left[\cos \phi + \alpha \tan (\alpha \pm \Psi) \sin \phi\right] r^2 \sin \phi \, d\phi \qquad (1)$$

In the above equation the plus sign (of the $\pm$ sign) applies to the case of a convex surface and the minus sign to a concave surface. For the case of a homogeneous limiter; that is, the crushing strength σ is a constant (independent of radius), this equation is integrated over the contact surface and a closed form result is obtained in Appendix 6.3.1. The mechanical energy of crushing deformation; that is, the integral of the force F_V over the impact stroke ($\int F_V \, ds$), is also obtained in closed form for the case of constant crushing strength σ. The expressions for force and energy for the limiting case of a flat impact surface are given.

For the more general case of a nonhomogeneous limiter in which the crushing strength σ is an arbitrary function of radius, the force and energy integrals were programmed for calculation by a high speed digital computer.

(2) Laminated Spherical Impact Limiter. Appendix 6.3.2 essentially extends the analysis of the preceding section, Appendix 6.3.1, to obtain closed form expressions for the force and energy integrals for a particular class of non-homogeneous spherical limiters in the case of impact on a flat surface. Limiters with discrete laminations are considered. The limiter is constructed of a number of layers of crushable material, each having radially oriented grain. The properties of each lamination are constant throughout that layer and each layer can have mechanical properties and thickness different from the others. The results of this analysis indicates that the shape of the acceleration versus time curve for the payload can be altered using this laminated technique but that it is doubtful if the overall limiter capabilities can be increased.

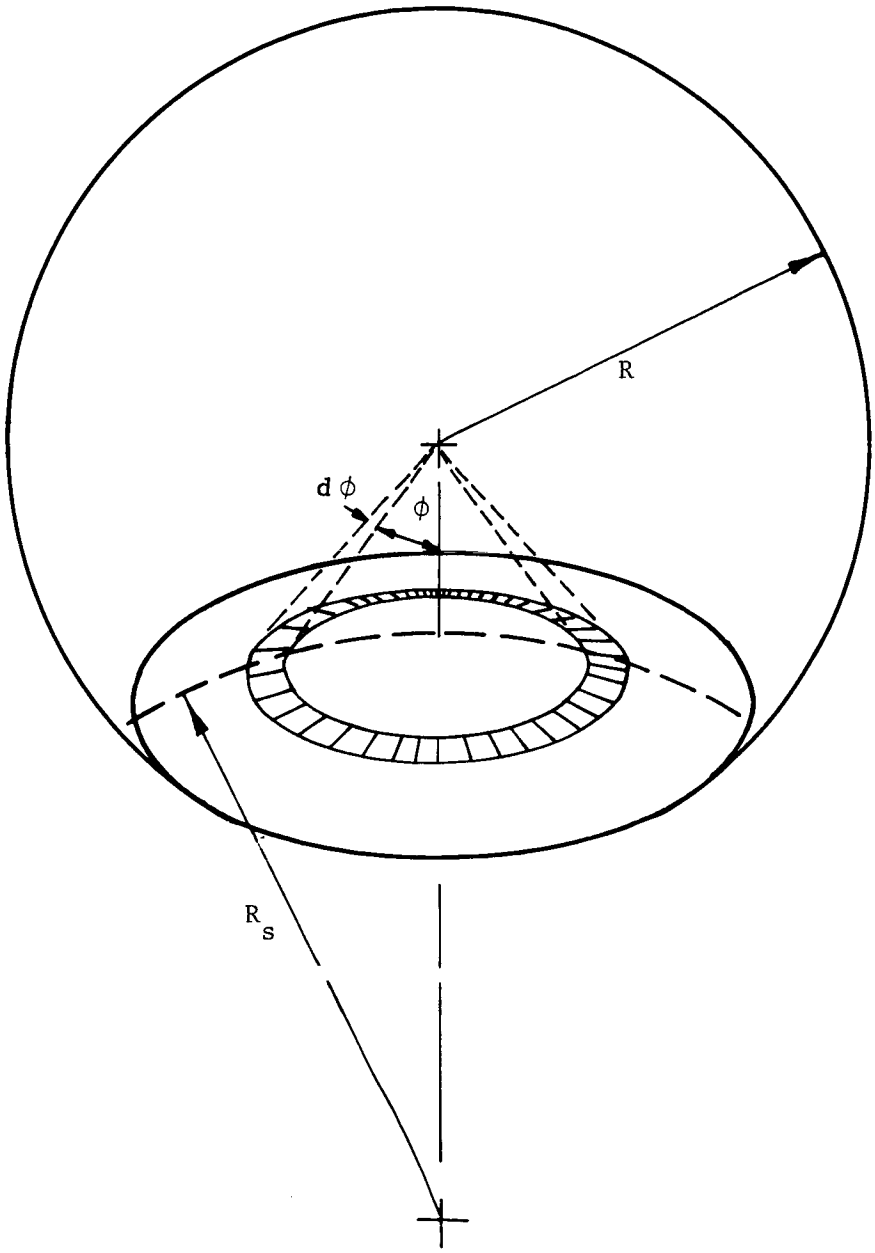

IMPACT ON A CONVEX CURVED SURFACE

FIGURE 31

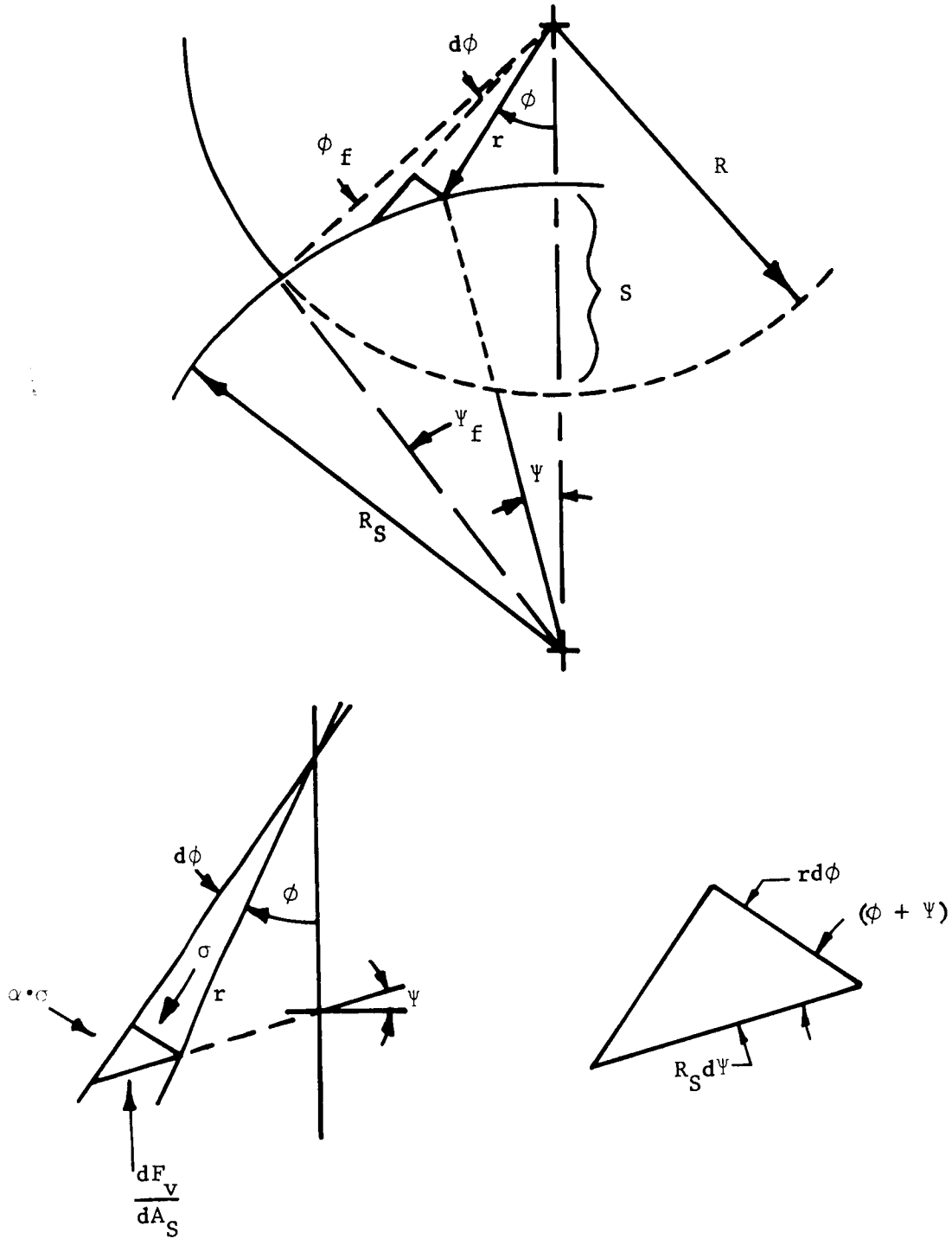

CONVEX IMPACT SURFACE

FIGURE 32

(3) Effect of Stopped, Crushed Mass. Appendix 6.3.3 presents a rather general analysis (*) accounting for shock phenomena in the impact of a mass of crushable material against a rigid surface. It is shown that

$$\frac{dV}{dt} = \frac{-F_y}{M_T - M_c} \qquad (2)$$

where

V is the velocity of the moving mass in the system at any time.

t is time.

F_y is the vertical force acting on a surface immediately ahead of the crushing front.

M_T is the total mass of the system.

M_c is the mass of the stopped, crushed material at the instant under consideration (i.e., when the velocity is V).

The impact velocity absorbing capability over a crushing stroke S_p is shown to be given by

$$\frac{V_o^2}{2} = \int_o^{S_f} \frac{F_Y \, ds}{M_T - M_c} \qquad (3)$$

where V_o is the initial impact velocity.

Typical results of an approximate solution are presented for a spherical

(4) Payload Breakaway ("Cannon Ball Effect"). At sufficiently high impact acceleration levels, it is possible for the inertia loading of the payload to give rise to crushing of the limiter material immediately adjacent to the payload. This payload breakaway phenomenon ("or cannon ball effect") is investigated in Appendix 6.3.4. A minimum value of the ratio of limiter radius to payload radius is calculated below which the "cannon ball effect" cannot occur. This minimum radius ratio is calculated

(*) The analysis is based on the model of crushable material mechanical behavior utilized in Appendix 6.2.

as a function of cross grain crushing strength ratio. The ratio of limiter density to payload density above which there can be no payload breakaway is also computed. This density ratio is computed as a function of the limiter to payload radius ratio.

It is demonstrated that for a sufficiently high limiter to payload radius ratio, the cross grain strength of the limiter material at the sides of the payload is not adequate to sustain the inertia loads from the limiter material above the payload. These inertia loads must then be carried via a loadpath through the payload and this can result in the occurrence of the "cannon ball effect" at lower accelerations than otherwise expected.

5.2.2 CAPABILITY TRADE-OFFS

a. Impact Limiter Requirements. Hard landing of the capsule on the Martian surface requires the use of some form of impact limiter in order to reduce the peak deceleration to a level which can be survived. It is felt that this limiting function can be best performed with the least complexity by a limiter with omni-directional capability. The requirement for omni-directional impact limiting capability with little or no rebound is satisfied by adoption of a spherical impact limiter consisting of an inelastic crushable material.

Balsa wood was chosen as the limiter material due to its outstanding energy absorption capacity per pound of material. The balsa wood limiter was developed for application on the Ranger Seismometer Capsule, and extensive testing has demonstrated it to be readily producible and reliable. The wood used is especially selected and processed.

b. Impact Limiter Material Properties. Figure 33 is representative of the simplified model used to simulate the crushable balsa limiter in the analysis of limiter impact dynamics. In this model, the balsa grain is radially oriented where R_p is the total radius of limiter material and payload, and V is the velocity at impact. The compression of the balsa parallel and perpendicular to the grain has been included in the representation of the vertical force during the crushing stroke from $r = R_t$ to $r = r_{final}$.

The load deflection curve typical of that for balsa is given in Figure 34. Crushing deformation takes place at nearly a constant stress level σ_o until a compressive strain of magnitude $(1 - \epsilon)\, d$ is reached. Thereafter, compressibility is negligible relative to the magnitude of $(1 - \epsilon)\, d$ and the stress increases at nearly constant strain. At stresses smaller than σ_o, compressibility is negligible compared to the magnitude of $(1 - \epsilon)\, d$. Strain rate effects have not been included.

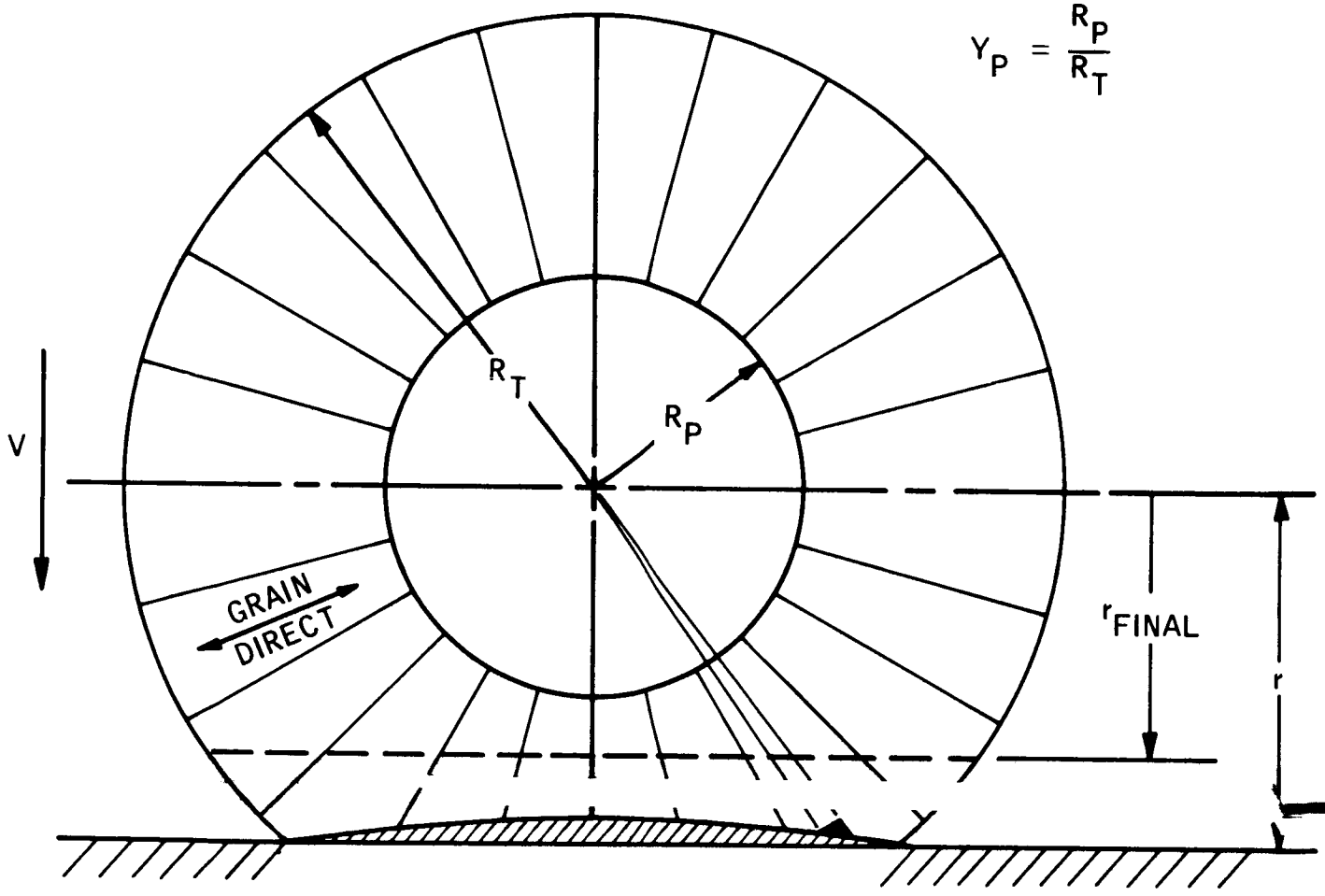

FIGURE 33

TYPICAL BALSA ELEMENT UNDER LOAD

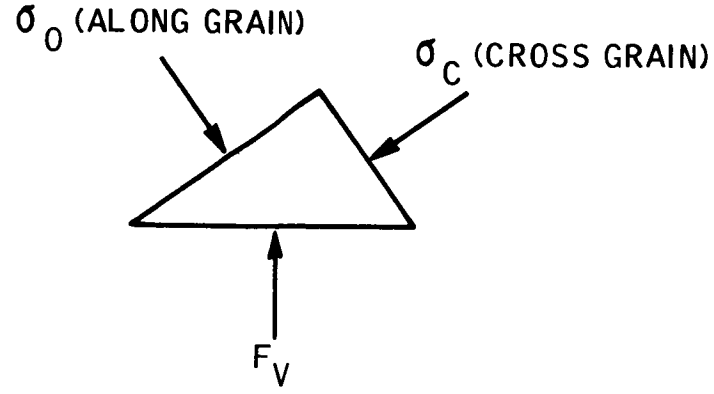

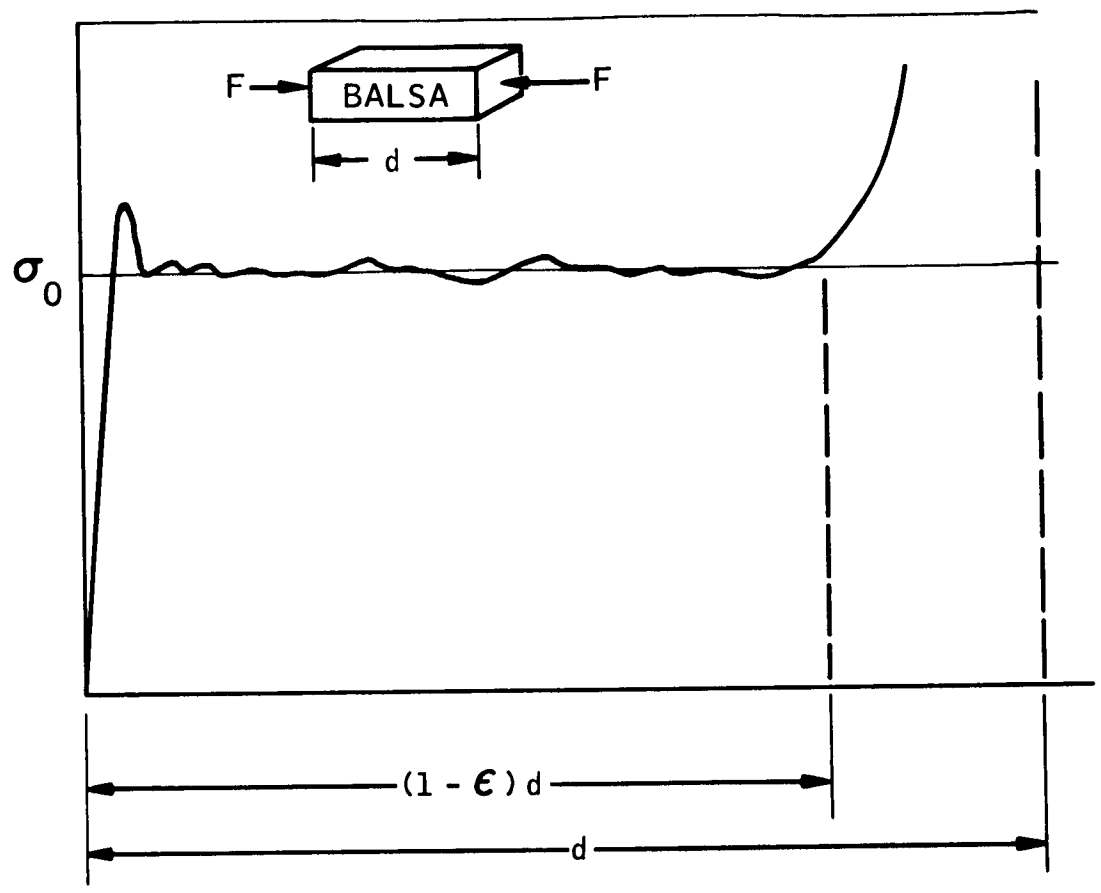

MATERIAL EFFICIENCY:

$$\eta = \frac{\text{ENERGY ABSORBING CAPABILITY}}{\text{WEIGHT}}$$

$$= \frac{\sigma_0 \times A \times (1 - \epsilon) d}{\rho_\ell \times A \times d}$$

$$\eta = \frac{\sigma_0}{\rho_\ell} (1 - \epsilon)$$

WHERE ρ_ℓ = DENSITY OF LIMITER MATERIAL

FIGURE 34

The material efficiency η is defined as the ratio of energy absorbing capability to weight. This is shown to be related to the yield stress and density of the limiter material by the relation

$$\eta = \frac{\sigma_o}{\rho_1} (1 - \epsilon)$$

Tests of numerous balsa samples indicate a value of ϵ of 0.2.

The curve of efficiency η of balsa vs. density of the balsa limiter used in the impact limiter analysis is presented in Figure 35 . This curve is based on an analysis of static test data on energy absorption of balsa. The slope of this curve was fairly well established by the analysis, however, considerable variation in level was encountered due to variation in moisture content and balsa quality.

A variety of metal, plastic, honeycomb and wood materials have been compared by Kornhauser (Reference 1), on the basis of their energy absorbing capacities. Balsa wood is best as shown in Table 5.2-I with an efficiency factor η of 17,800 ft-lbs/lb. There is some evidence that much higher efficiency factors are achieved under actual dynamic conditions but the quantity of data is limited. Hence, this analysis is based on the more conservative values.

The impact limiter trade-off analysis considers the energy absorption due to mechanical crushing in the direction parallel to the grain of the balsa as well as in the cross grain direction. This corresponds to forces in the radial tangential directions in the spherical limiter. The variation of σ_c/σ_o with balsa density is presented in Figure 36 where σ_c is the cross grain yield stress and σ_o is the yield stress parallel to the grain. This curve is based on an analysis of test data and represents an average of values for σ_c parallel and perpendicular to the radial growth rings.

c. Impact Limiter Design Trade-off Charts. A rigorous derivation of the force and energy equations for impact of a crushable spherical impact limiter on a hard surface is presented in Section 5.2.1 and Appendicies 6.2 and 6.3 together with a discussion of the dynamic process which takes place during crushing of the limiter. Initial trade-off analyses were begun with the assumption that all the impact energy is absorbed in purely mechanical crushing of the impact limiter. With this assumption a closed form solution for the energy absorbed by the limiter could be obtained. By equating kinetic energy at impact to the energy capable of being absorbed by the limiter a trade-off equation was derived which relates impact limiter properties, weight of limiter and payload, and impact velocity. This equation is

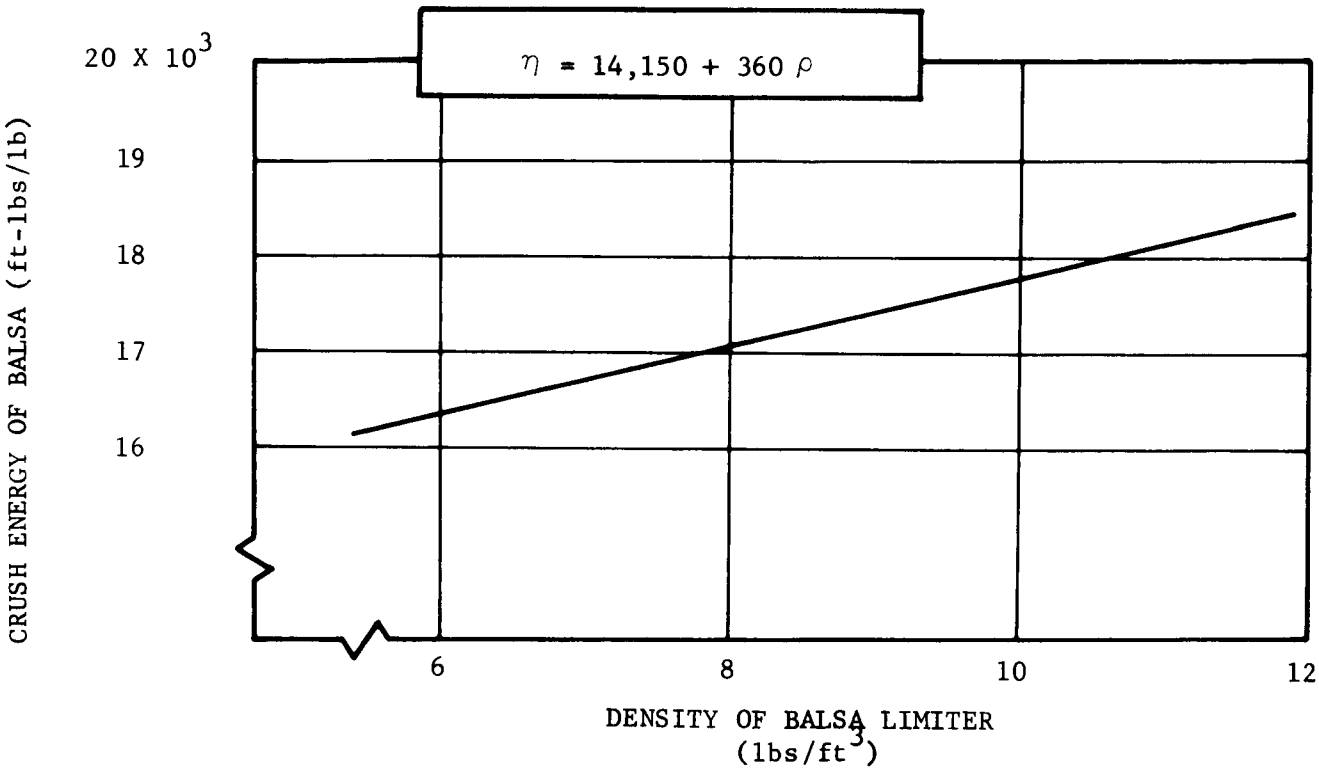

RESULTS OF STATISTICAL ANALYSIS OF STATIC TEST DATA
ON ENERGY ABSORPTION OF BALSA

FIGURE 35

TABLE 5.2-I

ENERGY ABSORBING MATERIALS

MATERIAL	YIELD STRESS PSI	DENSITY LB/FT^3	ENERGY ABSORPTION FT-LB/LB
1025 STEEL	36,00	489	2,940
4130 STEEL	70,000	489	5,410
4340 STEEL	103,00	489	7,700
24S ALUMINUM	40,000	173	5,100
MAGNESIUM	15,000	111	3,680
TITANIUM	50,000	284	6,150
T-22 STYROFOAM		1.5	3,840
HD-1 STYROFOAM		3.0	2,500
HD-2 STYROFOAM		4.5	4,000
ECCOFOAM S		10.0	2,120
HONEYCOMB, ALUMINUM		4.5	9,900
HONEYCOMB, S. STL.		8.9	3,360
BALSA		8.1	17,800
SUGAR PINE		22.4	13,800

REF. M. KORNHAUSER, "STRUCTURAL EFFECTS OF IMPACT," SPARTAN BOOKS, BALTIMORE, 1964

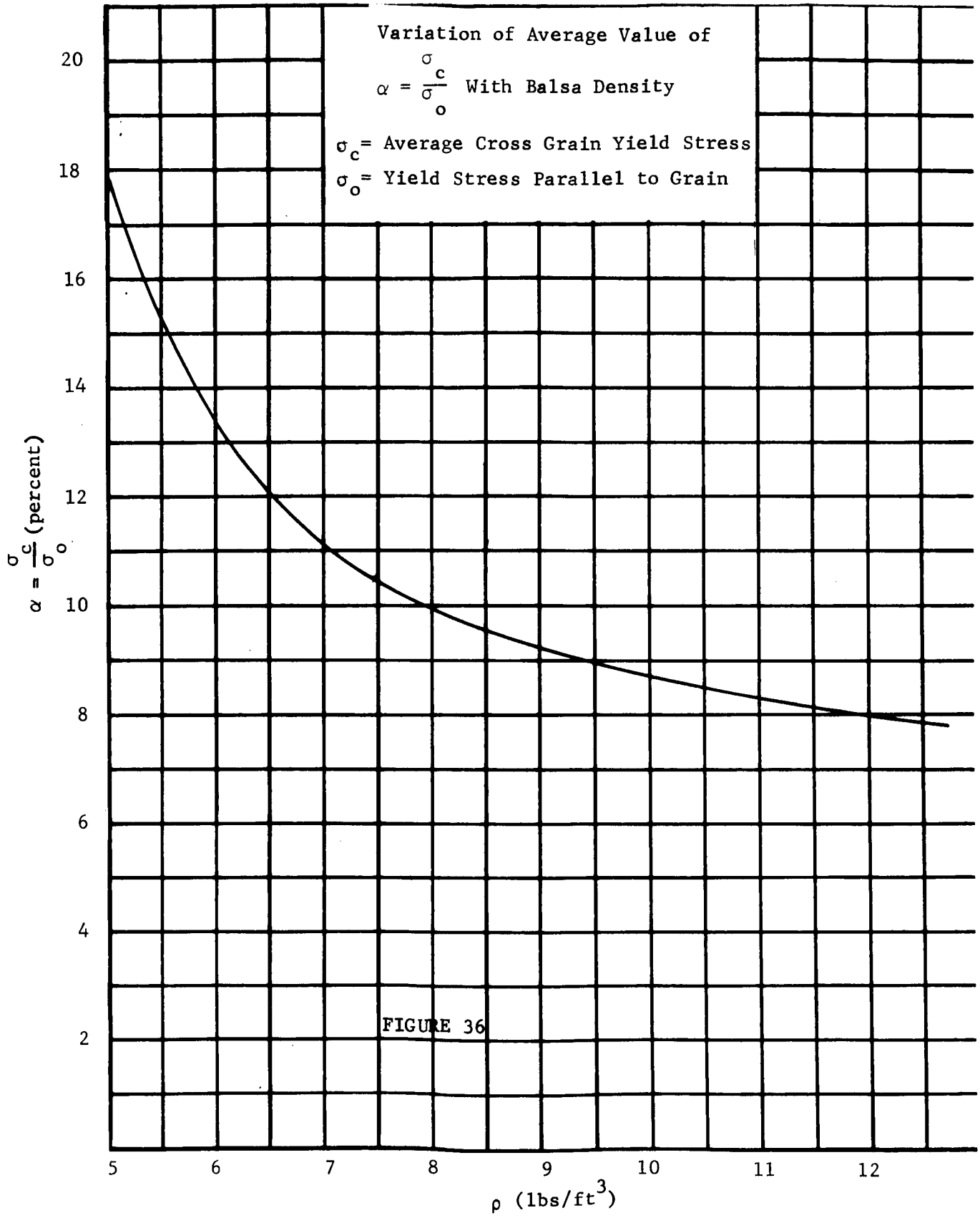
Variation of Average Value of
$\alpha = \frac{\sigma_c}{\sigma_o}$ With Balsa Density
σ_c = Average Cross Grain Yield Stress
σ_o = Yield Stress Parallel to Grain
$\alpha = \frac{\sigma_c}{\sigma_o}$ (percent)
20
18
16
14
12
10
8
6
4
2
5
6
7
8
9
10
11
12
ρ (lbs/ft^3)

FIGURE 36

$$\frac{1}{v^2}\frac{\sigma_o}{\rho_1} = \frac{3\left[1 - y_p^{\,3}\left(1 - \frac{\rho_p}{\rho_1}\right)\right]}{g\left\{(1-\alpha)\left[1 - y_o^{\,3}\left(1 - 3\ln y_o\right) + \frac{3}{2}\alpha\left(2 - 3y_o + y_o^{\,3}\right)\right]\right\}} \quad (4)$$

where

R_p is the radius of the payload capsule.

R_t is the total radius of the limiter and payload capsule

r is the distance from the sphere center to the impact plane

σ_o is the yield stress parallel to the balsa grain

σ_c is the yield stress cross grain

r_o is the final value of r

ρ_p is the weight density of the payload

ρ_1 is the weight density of the limiter

V is the maximum allowable impact velocity

and

$$y = \frac{r}{R_r} \; ; \quad y_o = \frac{r_o}{R_t} \; ; \quad y_p = \frac{R_p}{R_t} \; ; \quad \alpha = \frac{\sigma_c}{\sigma_o}$$

In addition y_o is related to y_p by

$y_o = y_p\,(1 - \epsilon) + \epsilon$ where $\epsilon = 0.2$ for balsa.

A second trade-off equation can be obtained which relates load factor , η, to limiter material and size when the total weight, W_T, of the limiter and payload is considered constant during the compression stroke. This expression is

$$R_p\, n\left(\frac{\rho_1}{\sigma_o}\right) = \frac{3}{4} y_p \left\{\frac{\left[2\,(1-\alpha)\,y^2 \ln\frac{1}{y} + \alpha\,(1 - y^2)\right]}{1 - y_p^{\,3}\left(1 - \frac{\rho_p}{\rho_1}\right)}\right\} \quad (5)$$

A series of trade-off curves for use in limiter design may be generated from the above equations. Data from use of the first equation have been used to generate the trade-off chart presented in Figure 37. In this chart, curves for the nondimensional parameter $Y_p = R_p/R_t$ have been plotted as a function of the parameter $1/v^2 \ \sigma_o/\rho_1$ for four values of the density ratio ρ_p/ρ_1. The curves have been computed for a value of $\alpha = \sigma$ cross grain/ σ parallel grain = 0.12. It can be seen that there is an impact velocity limit, corresponding to $Y_p = 0$, where for a spherical impact limiter the useful payload radius and weight must be equal to zero. At this velocity the limiter is capable of stopping only its own mass. This impact velocity limit is independent of payload weight and of impact deceleration but is a function of limiter compressive stress and density and will vary somewhat for the range of balsa densities considered practical for impact limiter construction.

The second of the two general trade-off charts is obtained by use of the second of the above two equations and is presented in Figure 38. Curves of the non-dimensional parameter Y_o are plotted as a function of the parameter $R_p n \ \rho_1/\sigma_o$ again for $\alpha = 0.12$ and for the four values of ρ_p/ρ_1 used in Figure 37. These curves may be used to obtain the maximum load factor reached during the compressive stroke of the limiter as a function of limiter material properties and limiter and payload size and weight. The maximum load factor is of interest since the size and weight of the payload structure required is a function of load factor.

Since the weight for a given limiter design was considered constant in this simplified analysis the maximum load factor, and maximum value of Equation (5) during the stroke, will occur at

$$y_{f_{max}} = e^{\frac{1}{-2\ (1\ -\ \alpha)}}$$

In generating the curves in Figure 38, then, the value of y in Equation (5) must be $y = y_o$ for values of $y_o > Y_{f_{max}}$, and $y = y_{f_{max}}$ for values of $y_o \leqq y_{f_{max}}$.

It should be noted, again, that Equations (4) and (5) and the data in Figures 37 and 38 account for only energy absorbed in mechanical crushing of the balsa limiter. Below an impact velocity of approximately 200 ft/ sec, the errors introduced by the assumptions are less than 3 percent on load factor and are negligible on total size and weight of limiter required for a given payload. Therefore, these curves may be used to obtain reasonably good results for limiter design in the low impact velocity region. Above 200 ft/sec, the errors in energy absorption capability and load factor indicated by the simplified analysis become much more significant. Because the weight of structure and flotation shell are a function of load

Tradeoff Chart for
Spherical Impact Limiter Design

Cross Grain Compression Included

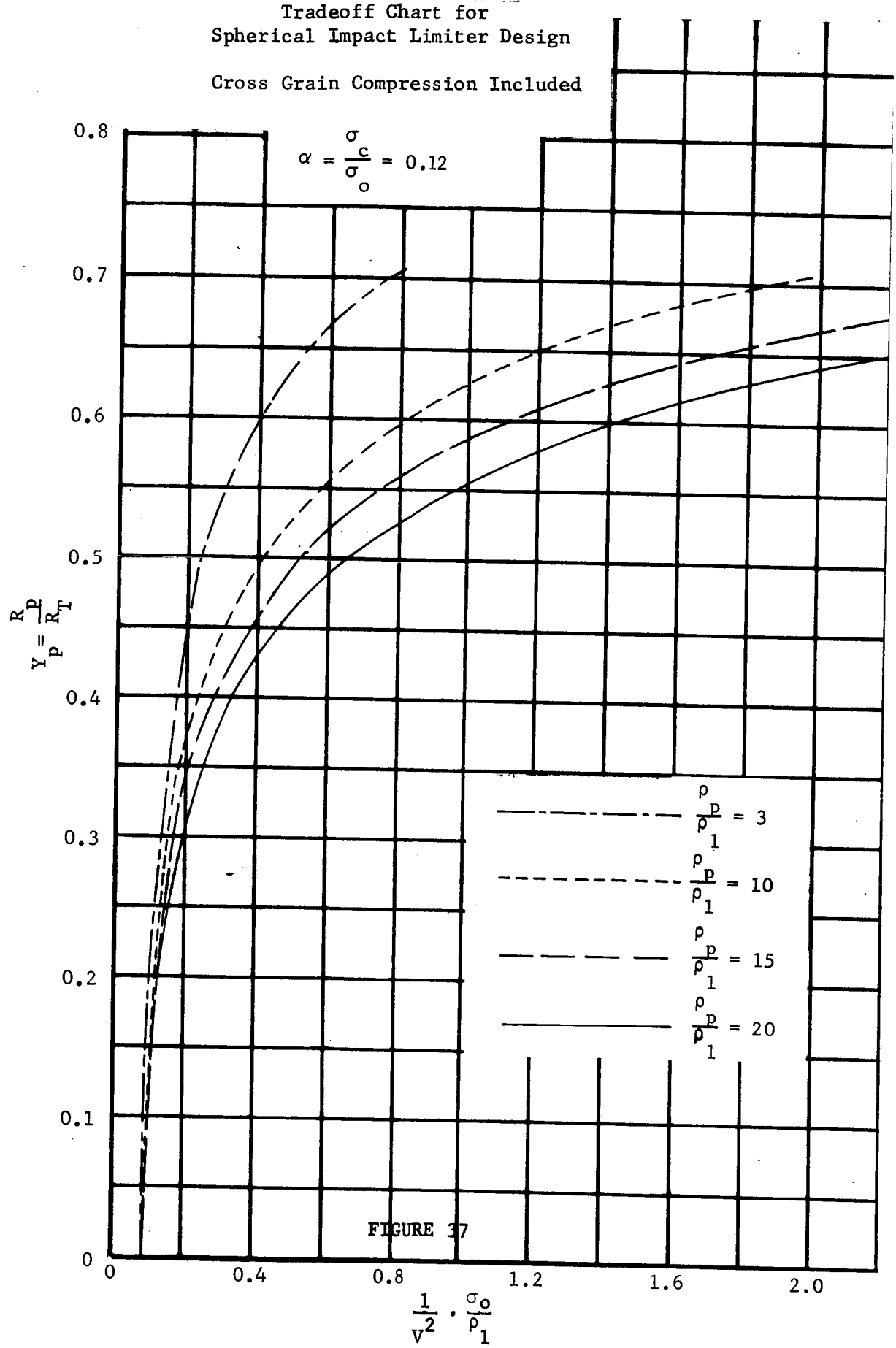

FIGURE 37

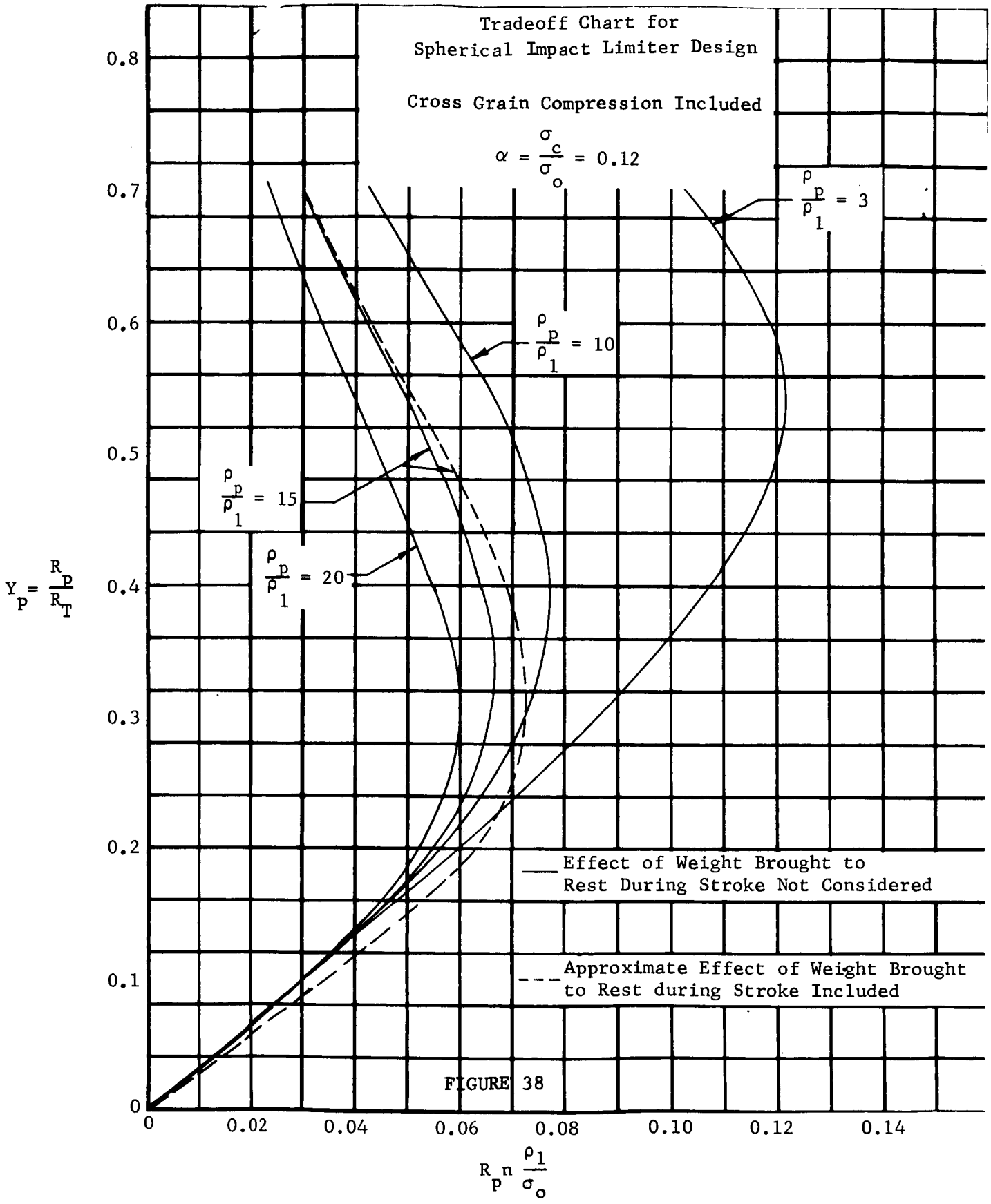
Tradeoff Chart for
Spherical Impact Limiter Design
Cross Grain Compression Included
$\alpha = \frac{\sigma_c}{\sigma_o} = 0.12$
$\frac{\rho_p}{\rho_1} = 3$
$\frac{\rho_p}{\rho_1} = 10$
$\frac{\rho_p}{\rho_1} = 15$
$\frac{\rho_p}{\rho_1} = 20$
Effect of Weight Brought to Rest During Stroke Not Considered
Approximate Effect of Weight Brought to Rest during Stroke Included
$Y_p = \frac{R_p}{R_T}$
$R_p n \frac{\rho_1}{\sigma_o}$
0
0.1
0.2
0.3
0.4
0.5
0.6
0.7
0.8
0.02
0.04
0.06
0.08
0.10
0.12
0.14

FIGURE 38

factor, the total weight and size of the capsule indicated by the simplified analysis may vary appreciably from that indicated by an analysis based on a more detailed representation of the crushing process.

A more sophisticated examination of the dynamic crushing process is given in Appendix 6.2 where it is shown that the instantaneous crushing zone is propagated through the limiter as a shock wave and is analogous to a shock wave in a fluid medium. The energy dissipated across this shock wave as shock heating is shown in Appendix 6.2.4 to be identical to the change in kinetic energy obtained by a reduction in total mass as some of the material is brought to rest during the crushing stroke. Since the additional energy dissipated can be determined from the mass of crushed material brought to rest, this effect will be called the stop mass effect in further discussion of the impact limiter analysis.

The additional energy absorbtion capability due to the stop mass effect has been included in the derivation of the spherical impact limiter trade-off equations. When the total mass of limiter and sphere is considered constant during the stroke, the relationship between energy absorbed and the initial kinetic energy is given by

$$\frac{1}{2} V^2 = \frac{\int_{y_o}^{1} F_v(y)\, dy}{M_T}$$

Inclusion of the stop mass effect alters the form of the right hand side so that

$$\frac{1}{2} V^2 = \int_{y_o}^{1} \frac{F_v(y)\, dy}{M_T - \frac{\pi}{3} \rho_o R_T^3 (2 - 3y + y^3)}$$

The mass term in the denominator is now a function of y and must be included under the integral sign. This expression cannot be integrated over the stroke in closed form and numerical integration techniques must be employed. A computer program to evaluate the integral has been written. The maximum load factor, which is the maximum value of the terms under the integral sign, and the point in the stroke at which the maximum value occurs is also obtained by the computer program.

Data obtained from the program have been used to generate the trade-off charts given in Figures 39 and 40. These charts are analogous to Figures 37 and 38 where stop mass effects were not included and are given

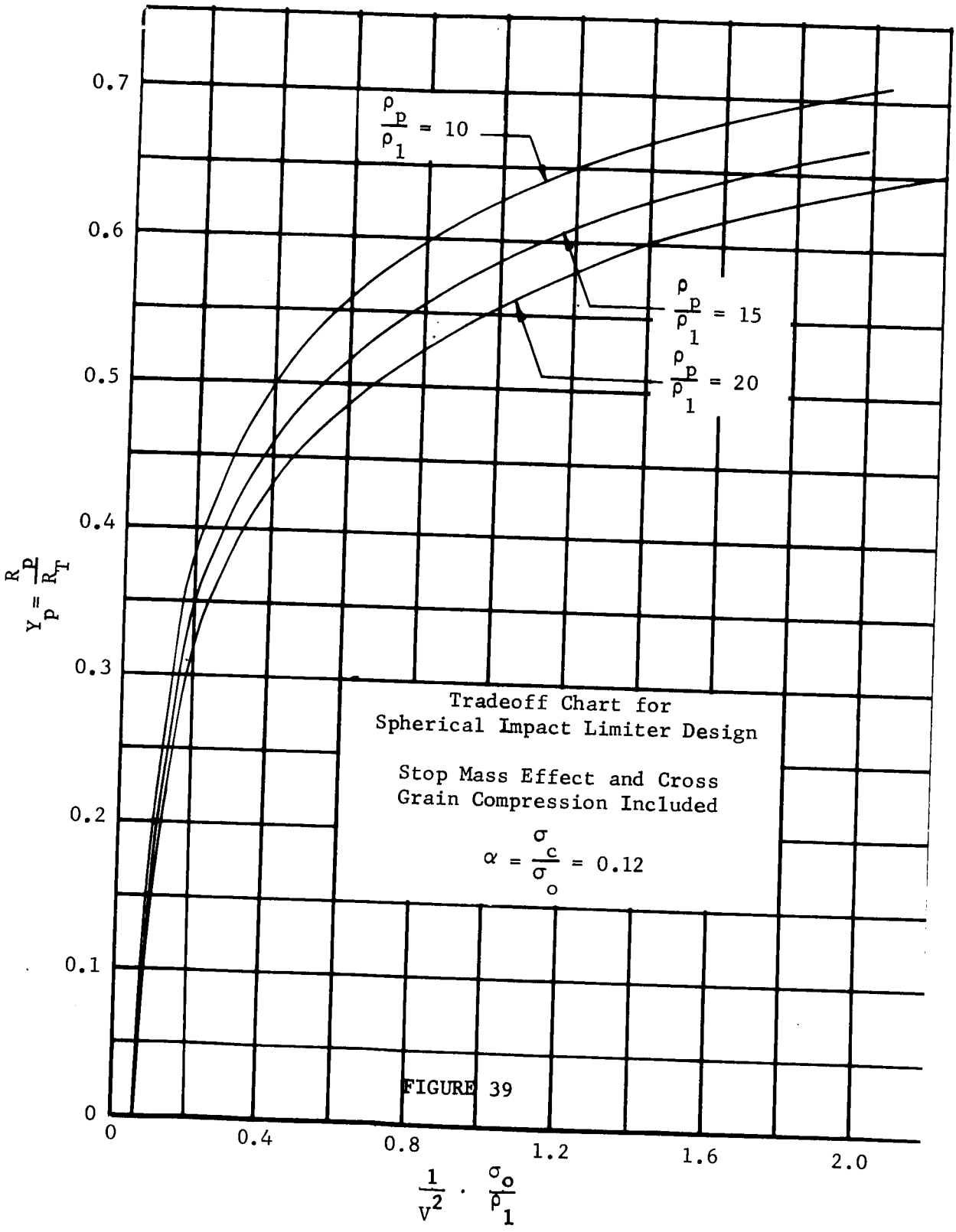
0.7
0.6
0.5
0.4
0.3
0.2
0.1
0
0
0.4
0.8
1.2
1.6
2.0
$\frac{\rho_p}{\rho_1} = 10$
$\frac{\rho_p}{\rho_1} = 15$
$\frac{\rho_p}{\rho_1} = 20$
$Y = \frac{R_p}{R_T}$
$\frac{1}{V^2} \cdot \frac{\sigma_o}{\rho_1}$
Tradeoff Chart for
Spherical Impact Limiter Design
Stop Mass Effect and Cross
Grain Compression Included
$\alpha = \frac{\sigma_c}{\sigma_o} = 0.12$

FIGURE 39

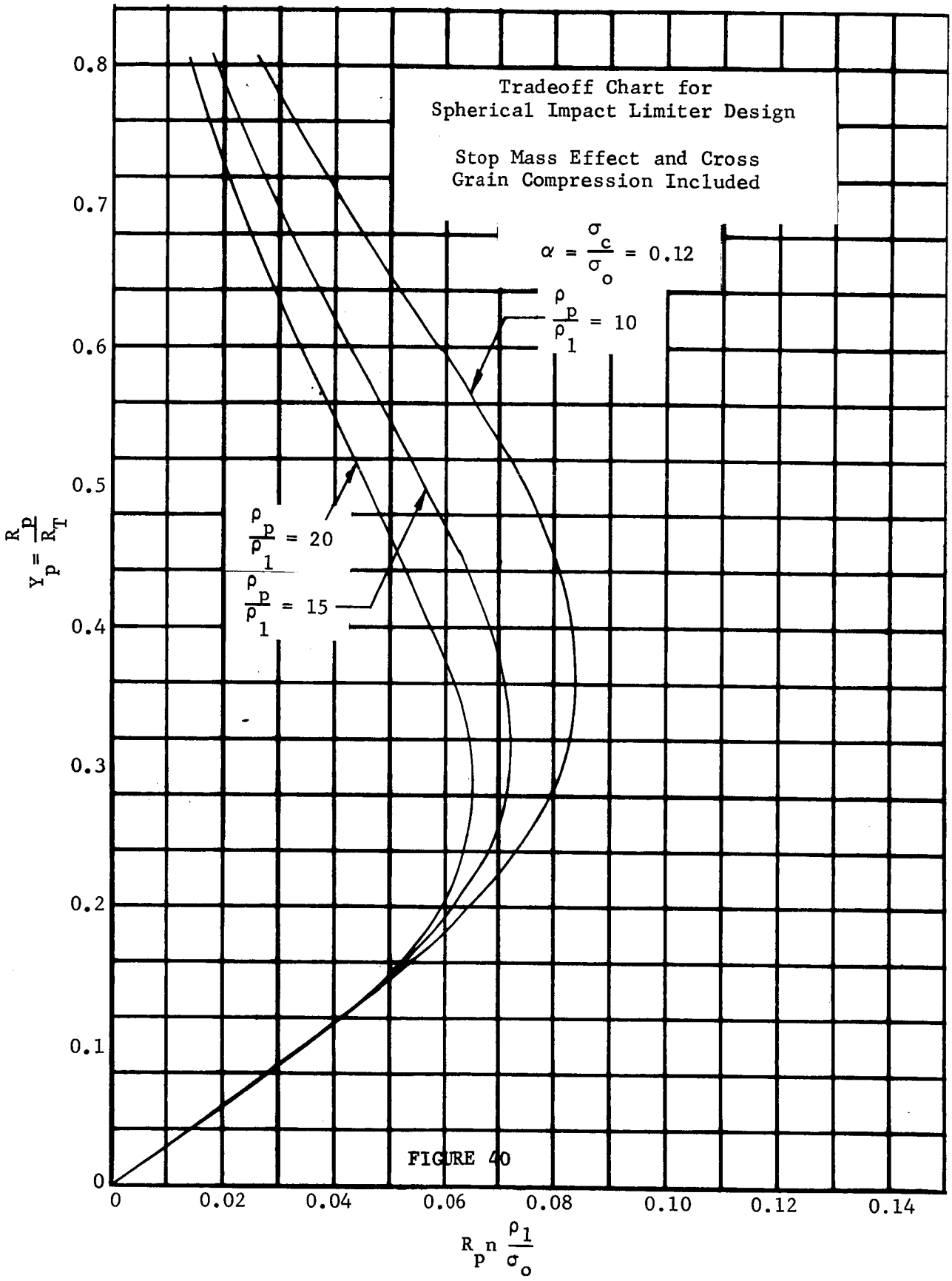
Tradeoff Chart for
Spherical Impact Limiter Design
Stop Mass Effect and Cross
Grain Compression Included
$\alpha = \frac{\sigma_c}{\sigma_o} = 0.12$
$\frac{\rho_p}{\rho_1} = 10$
$\frac{\rho_p}{\rho_1} = 20$
$\frac{\rho_p}{\rho_1} = 15$
$Y_p = \frac{R_p}{R_T}$
$R_p n \frac{\rho_1}{\sigma_o}$
0
0.1
0.2
0.3
0.4
0.5
0.6
0.7
0.8
0.02
0.04
0.06
0.08
0.10
0.12
0.14

FIGURE 40

for $\alpha = 0.12$ and $\rho_p/\rho_1 = 10$, 15 and 20 as before. An additional set of charts for $\alpha = 0.08$ are given in Appendix 6.6 as Figures 146 and 147. The value of $\alpha = 0.12$ corresponds to a value of $\rho_1 = 6.5$ lbs/ft^3 and $\alpha = 0.08$ corresponds to $\rho_1 = 12$ lb/ft^3, as can be seen in Figure 36. The two values of ρ_1 represent the lower and upper bounds of the range of balsa densities considered practical for impact limiter construction. For this range of balsa densities, the density ratios $\rho_p/\rho_1 = 10$, 15 and 20 cover the payload density range considered obtainable.

Comparison of the curves in Figure 37 with those in Figure 39 where the stop mass effect has not been included shows that the curves in Figure 39 have shifted slightly to the left. For a given limiter size and total weight, this shift corresponds to an increase in maximum allowable impact velocity, or, for a given impact velocity and payload size, the shift corresponds to a reduction in required limiter size. The inclusion of the stop mass effect will also result in increased load factors. For ease of comparison, the curve for $\rho_p/\rho_1 = 15$ from Figure 40 is plotted in Figure 38. It can be seen that there can be an increase in load factor by as much as 13 percent for values of Y_p near the knee of the curves. Impact velocities below 200 ft/sec will yield values of Y_p generally above 0.5 where it can be seen that consideration of the stop mass effect has only a small effect on load factor.

It should be pointed out that the equations on which the trade-off charts have been based are fairly general. These basic equations may be used to design spherical impact limiters constructed of other crushable materials in addition to balsa with the proper substitution of values for the parameters α, ρ_1, and σ_o.

Two additional charts are given in Figures 148 and 149 of Appendix 6.6. These are alternate presentations of Figures 39 and 40 . These two charts will be useful to determine values of Y_p for impact velocities approaching the limiting impact velocity. The use of the design trade-off charts will be illustrated in the following section.

d. Computation Procedure Using Design Trade-off Chart. The general trade-off curves given in Figures 39 and 40 may be used to determine spherical impact limiter requirements for a fairly wide range of parameters. The use of these curves is best illustrated through the following example and step-by-step procedure.

(1) Given a payload weight $W_p = 85$ pounds and a payload radius $R_p = .542$ feet, the density of the payload ρ_p is found to be $\rho_p = 127.5$ lbs/ft^3.

(2) Select a value of limiter density, for the example $\rho_1 = 8.5$ lbs/ft^3, and therefore, $\rho_p/\rho_1 = 15$.

(3) The efficiency factor for a balsa limiter of $\rho_1 = 8.5$ lbs/ft^3 can be obtained from Figure 35 where $\eta = 14{,}150 + 360\ \rho_1$. Then $\eta = 17{,}210$ ft-lbs/lb.

(4) The value of σ_o/ρ_1 is obtained from $\sigma_o/\rho_1 = \eta/1 - \epsilon$ when $\epsilon = 0.2$ for balsa. Then $\sigma_o/\rho_1 = 17{,}210/1\text{-}0.2 = 21{,}500$ ft-lb/lb.

(5) For $\rho_1 = 8.5$ lbs/ft^3 the value of $\alpha = \sigma$ cross grain/σ parallel grain = 0.095 from Figure 36. For values of $\alpha > 0.10$ use the trade-off charts for $\alpha = 0.12$ while for values of $\alpha < 0.10$ use charts for $\alpha = 0.08$. Then, for $\rho_1 = 8.5$ lbs/ft^3 use the charts corresponding to $\alpha = 0.08$.

(6) With the value of σ_o/ρ_1 and the desired impact velocity determine $1/v^2 \cdot \sigma_o/\rho_1$. For this example let V = 200 ft/sec, then $1/v^2\ \sigma_o/\rho_1 = .538$.

(7) Entering Figure 146 corresponding to $\alpha = 0.08$ with the value of $1/V^2\ \sigma_o/\rho_1 = .538$ and for the curve corresponding to $\rho_p/\rho_1 = 15$, Y_p is found to be $Y_p = .500$.

(8) The total radius of the limiter plus payload is obtained from $R_t = R_p/Y_p = 0.542/0.504 = 1.08$ ft.

(9) The total weight of limiter plus payload can be computed from $W_t = 4/3\ \pi\ \rho_1\ (R_t^3 - R_p^3) + W_p$. For the values of the various parameters determined previously, $W_t = 124$ lbs.

(10) The maximum load factor to be encountered during the compression stroke can be determined through use of the curves given in Figures 147 and 40. For $\alpha = 0.08$ and with the value of $Y_p = .500$, Figure 147 is used to obtain the value of the parameter $R_p n\ \rho_1/\sigma_o$. From the appropriate curve for $\rho_p/\rho_1 = 15$, the value of $R_p n\ \rho_1/\sigma_o = 0.055$.

(11) The load factor is computed from $n = (R_p n \cdot \rho_1/\sigma_o) \times \sigma_o/\rho_1 \cdot 1/R_p$, or $n = 2180$.

It should be pointed out that this example represents only one way in which the Design Charts can be used. The procedure may be reversed, for example, and the maximum allowable impact velocity can be determined for a given load factor and limiter size and weight.

e. Specific Design Curves from Trade-Off Charts. A more specific set of design curves may be obtained from the general trade-off charts through use of the procedure outlined in Section 5.2.2.d. Curves of total weight of limiter and payload, total radius of limiter and payload, and load factor as functions of maximum allowable impact velocity have been generated in this manner for selected values of payload weight. These curves are presented in Figures 41 and 45, for a balsa density of $\rho_1 = 6.5$ lbs/ft^3 and a density ratio of $\rho_p/\rho_1 = 15$, corresponding to a payload density of 97.5 lbs/ft^3. The density values used are typical of densities from previous capsule and limiter designs.

The curves of Figures 41 and 42 are based on the general trade-off charts given in Figures 37 and 38 and do not include the stop mass effect. They are included here only for comparison with the sets of curves presented in Figures 43 and 44 which include the stop mass effect. Comparison of Figure 41 with Figure 43, and Figure 42 with Figure 44, will indicate the error introduced in impact velocity for a given size and weight when the stop mass is not included. This error is particularly apparent as the limiting impact velocity is approached.

A study of Figure 43 for total weight of limiter and payload vs. impact velocity, and of Figure 44 for total radius of limiter and payload vs. impact velocity, reveals several points of interest. At a velocity of $V = 0$ ft/sec the total weight and total radius are equal to the weight of the payload capsule and to the radius of the capsule since no limiter is required. For impact velocities approaching the limiting velocity, the total weight and total radius approach infinity for a given payload size and weight. The reason for this can be seen in Figure 39 where the value of $Y_p = R_p/R_t$ approaches zero as the impact velocity limit is approached. To satisfy the condition that $Y_p = 0$, either R_p must go to zero for a given limiter size, or as in the case here, R_t must approach infinity for a given size payload. Since the total radius R_t must go to infinity, then the weight of the limiter also must go to infinity.

Lines of constant load factor are also shown in Figures 43 and 44. These lines will converge at $W_t = 0$ and $R_t = 0$ for zero impact velocity. It can be seen that the maximum load factor for a given payload weight is reached at about 375 ft/sec. For impact velocities greater than this value, the load factor decreases while the rate of change in payload weight and size

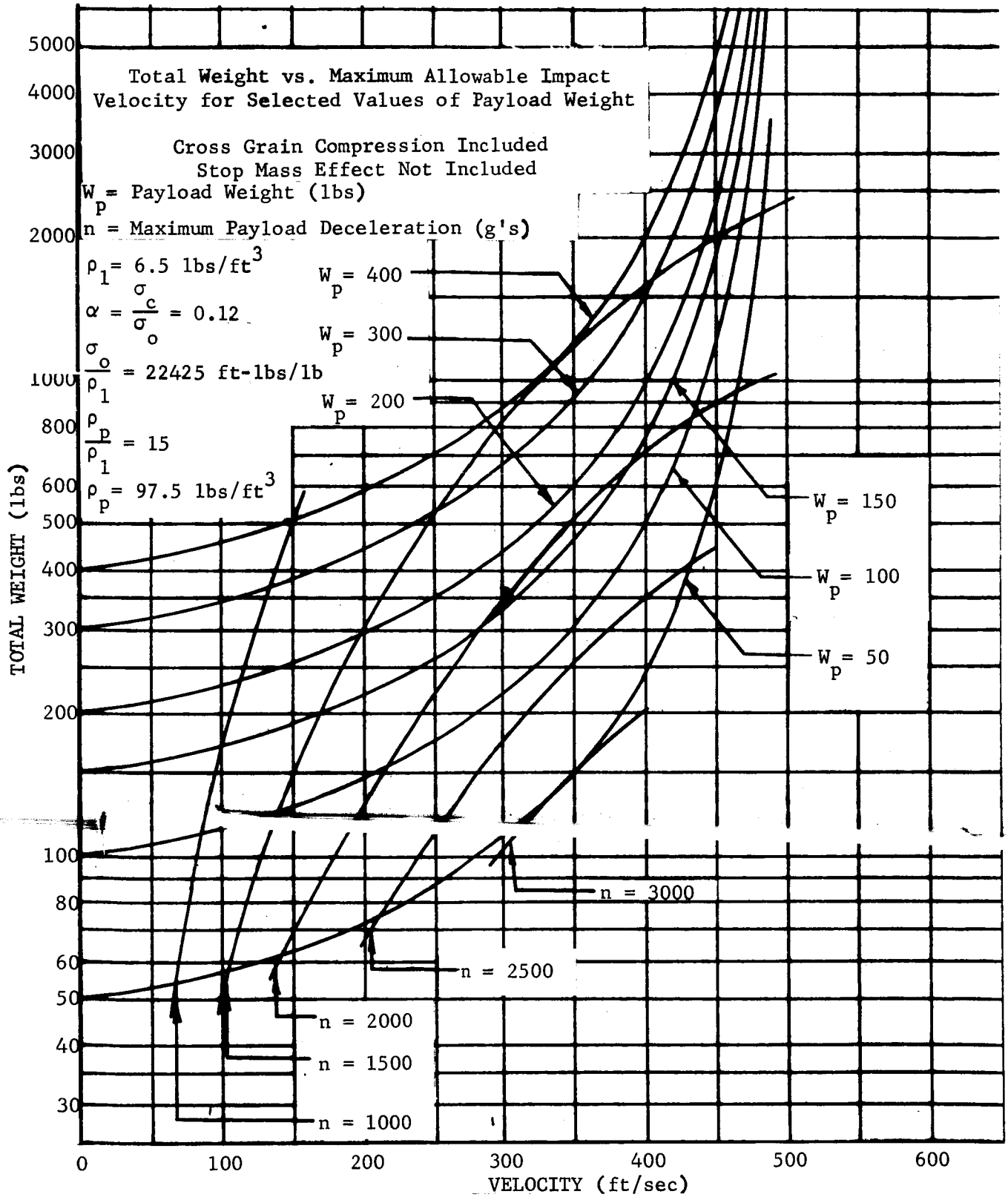
Total Weight vs. Maximum Allowable Impact Velocity for Selected Values of Payload Weight
Cross Grain Compression Included
Stop Mass Effect Not Included
W_p = Payload Weight (lbs)
n = Maximum Payload Deceleration (g's)
ρ_1 = 6.5 lbs/ft^3
$\alpha = \frac{\sigma_c}{\sigma_o}$ = 0.12
$\frac{\sigma_o}{\rho_1}$ = 22425 ft-lbs/lb
$\frac{\rho_p}{\rho_1}$ = 15
ρ_p = 97.5 lbs/ft^3
W_p = 400
W_p = 300
W_p = 200
W_p = 150
W_p = 100
W_p = 50
n = 3000
n = 2500
n = 2000
n = 1500
n = 1000
TOTAL WEIGHT (lbs)
VELOCITY (ft/sec)
5000
4000
3000
2000
1000
800
600
500
400
300
200
100
80
60
50
40
30
0
100
200
300
400
500
600

FIGURE 41

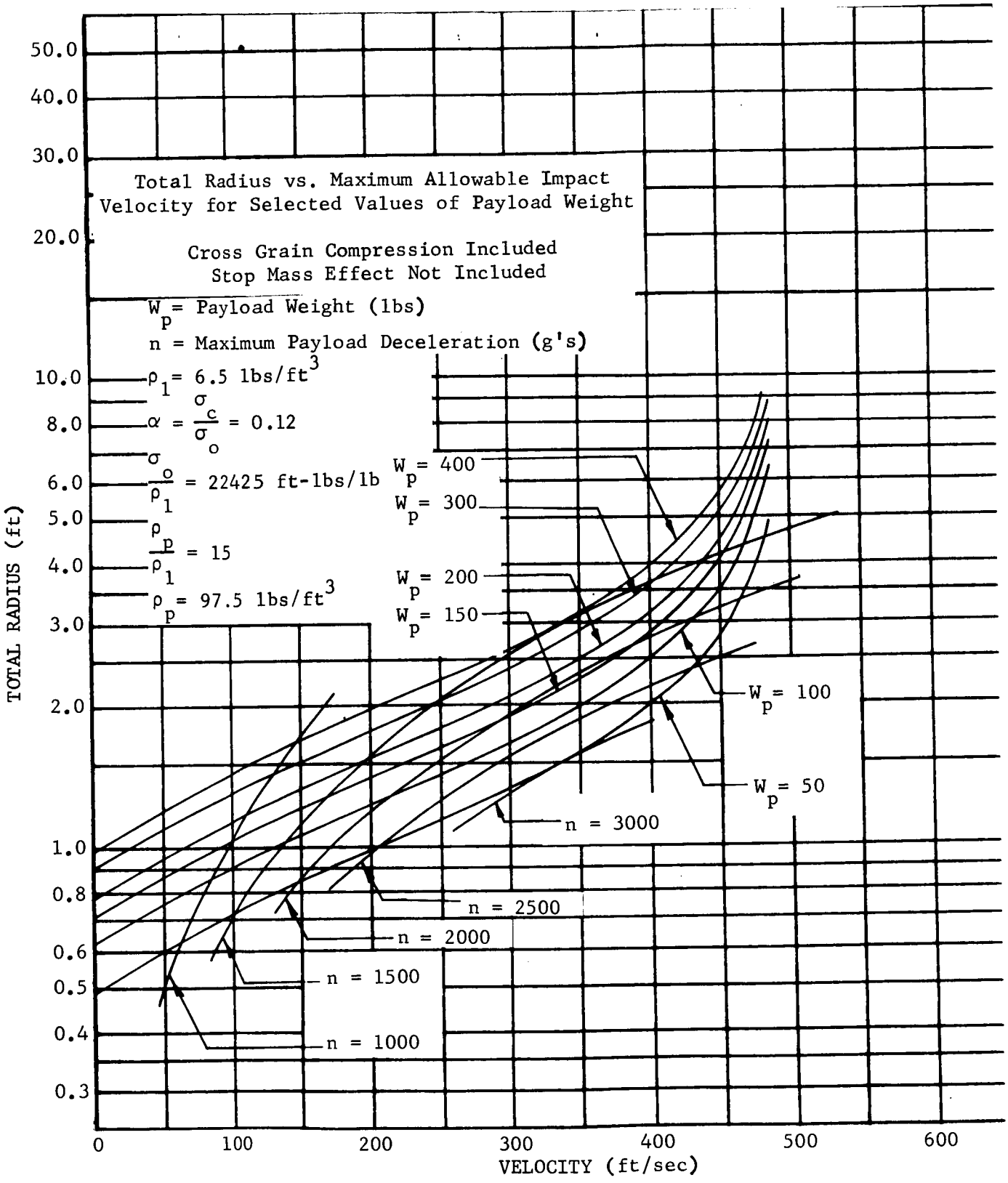
Total Radius vs. Maximum Allowable Impact Velocity for Selected Values of Payload Weight
Cross Grain Compression Included
Stop Mass Effect Not Included
W_p = Payload Weight (lbs)
n = Maximum Payload Deceleration (g's)
ρ_1 = 6.5 lbs/ft^3
$\alpha = \frac{\sigma_c}{\sigma_o}$ = 0.12
$\frac{\sigma_o}{\rho_1}$ = 22425 ft-lbs/lb
$\frac{\rho_p}{\rho_1}$ = 15
ρ_p = 97.5 lbs/ft^3
W_p = 400
W_p = 300
W_p = 200
W_p = 150
W_p = 100
W_p = 50
n = 3000
n = 2500
n = 2000
n = 1500
n = 1000
TOTAL RADIUS (ft)
50.0
40.0
30.0
20.0
10.0
8.0
6.0
5.0
4.0
3.0
2.0
1.0
0.8
0.6
0.5
0.4
0.3
0
100
200
300
400
500
600
VELOCITY (ft/sec)

FIGURE 42

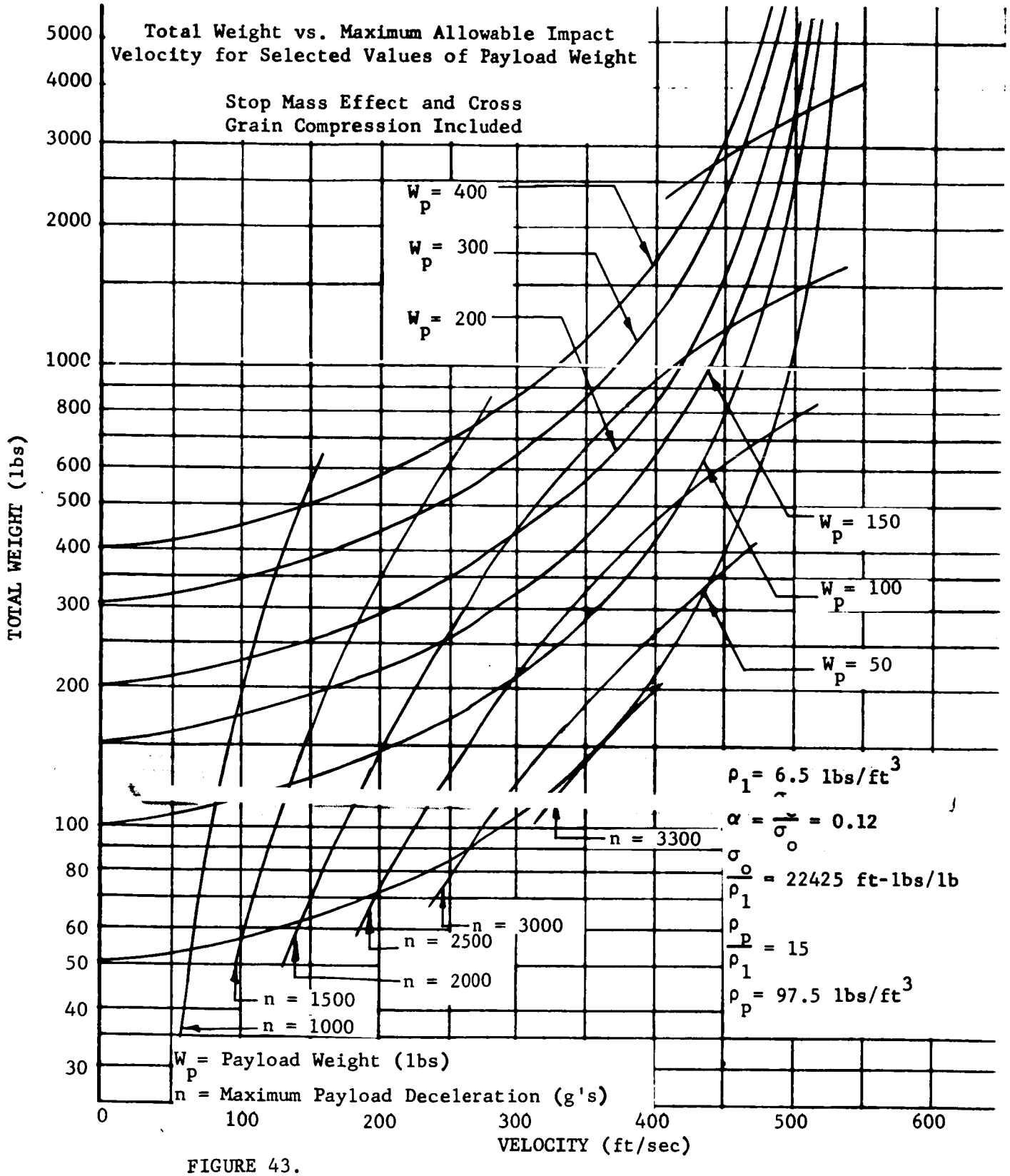
Total Weight vs. Maximum Allowable Impact Velocity for Selected Values of Payload Weight
Stop Mass Effect and Cross Grain Compression Included
TOTAL WEIGHT (lbs)
VELOCITY (ft/sec)
W_p = 400
W_p = 300
W_p = 200
W_p = 150
W_p = 100
W_p = 50
n = 3300
n = 3000
n = 2500
n = 2000
n = 1500
n = 1000
ρ_1 = 6.5 lbs/ft^3
$\alpha = \frac{\sigma}{\sigma_o} = 0.12$
$\frac{\sigma_o}{\rho_1}$ = 22425 ft-lbs/lb
$\frac{\rho_p}{\rho_1}$ = 15
ρ_p = 97.5 lbs/ft^3
W_p = Payload Weight (lbs)
n = Maximum Payload Deceleration (g's)

FIGURE 43.

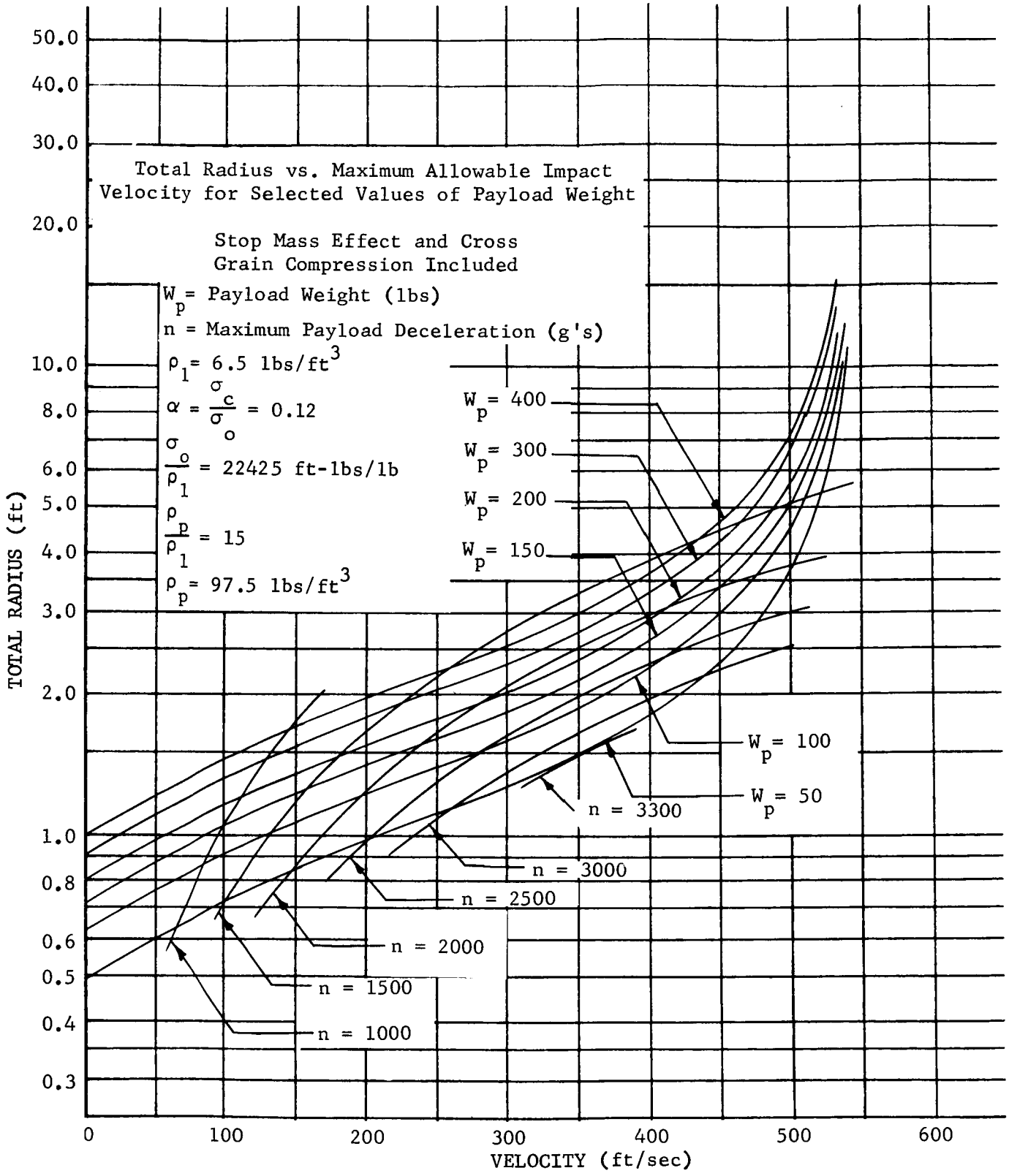
Total Radius vs. Maximum Allowable Impact Velocity for Selected Values of Payload Weight
Stop Mass Effect and Cross Grain Compression Included
W_p = Payload Weight (lbs)
n = Maximum Payload Deceleration (g's)
ρ_1 = 6.5 lbs/ft^3
$\alpha = \frac{\sigma_c}{\sigma_o} = 0.12$
$\frac{\sigma_o}{\rho_1}$ = 22425 ft-lbs/lb
$\frac{\rho_p}{\rho_1}$ = 15
ρ_p = 97.5 lbs/ft^3
W_p = 400
W_p = 300
W_p = 200
W_p = 150
W_p = 100
W_p = 50
n = 3300
n = 3000
n = 2500
n = 2000
n = 1500
n = 1000
TOTAL RADIUS (ft)
VELOCITY (ft/sec)
50.0
40.0
30.0
20.0
10.0
8.0
6.0
5.0
4.0
3.0
2.0
1.0
0.8
0.6
0.5
0.4
0.3
0
100
200
300
400
500
600

FIGURE 44.

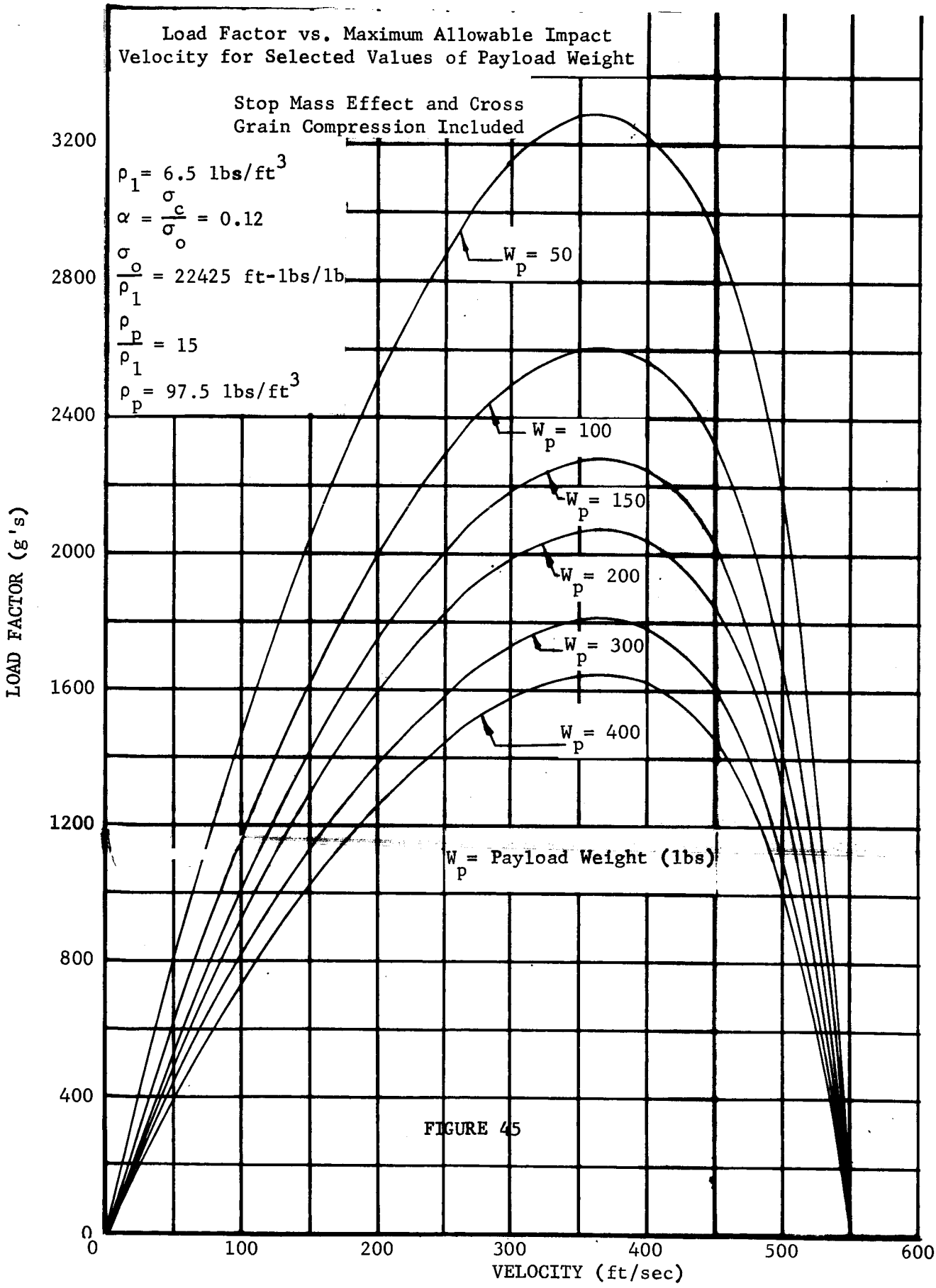
Load Factor vs. Maximum Allowable Impact Velocity for Selected Values of Payload Weight
Stop Mass Effect and Cross Grain Compression Included
$\rho_1 = 6.5$ lbs/ft^3
$\alpha = \frac{\sigma_c}{\sigma_o} = 0.12$
$\frac{\sigma_o}{\rho_1} = 22425$ ft-lbs/lb
$\frac{\rho_p}{\rho_1} = 15$
$\rho_p = 97.5$ lbs/ft^3
$W_p = 50$
$W_p = 100$
$W_p = 150$
$W_p = 200$
$W_p = 300$
$W_p = 400$
W_p = Payload Weight (lbs)
LOAD FACTOR (g's)
VELOCITY (ft/sec)
0
400
800
1200
1600
2000
2400
2800
3200
0
100
200
300
400
500
600

FIGURE 45

rapidly increases. This point in velocity for peak load factor, then, may be thought of as an optimum design point. Increasingly severe penalties are paid in terms of limiter weight and size for impact velocity capability above 400 ft/sec.

The variation in load factor with impact velocity for a given payload weight is shown in Figure 45. These curves were used to obtain the lines of constant load factor in Figures 43 and 44. It can be seen that load factor goes to zero as impact velocity goes to zero. This is due to the fact that the force developed must go to zero while the weight of limiter and payload remains finite. The reason the load factor also goes to zero at the limiting impact velocity may be easily explained. The load factor has been defined as force/weight. As the impact velocity limit is approached, it was shown in Figure 43 that the total weight approached infinity. Since the force now remains finite then the load factor must approach zero.

It can also be seen that the load factor is higher for low payload weights compared to that obtained with high payload weights. This is due to the larger limiter required to absorb the kinetic energy associated with the high payload weights. The larger limiter results in greater impact stroke capability. The force developed in the limiter during crushing is a function of contact area and available stroke. As the size of a spherical limiter is increased, then, the force developed will increase as a function of the square of the total radius while the mass will increase as the cube, and therefore, the maximum load factor will decrease with increasing payload weight.

Some additional curves showing the variation in total weight and total radius with impact velocity are given in Appendix 6.6 for other density values and density ratios. The data in Figures 150 and 151 of the Appendix are for a limiter density of 6.5 lbs/ft^3 and a payload density of 130 lbs/ft^3. Data in Figures 152 and 153 are for a limiter density of 12 lbs/ft^3 and a payload density of 120 lbs/ft^3.

The preceding discussion considered the variations in total weight, total radius, and load factor with impact velocity and payload weight for a fixed value of limiter density and payload to limiter density ratio. In Figure 46 the variations in load factor, total weight, and total radius with impact velocity are shown for a fixed payload weight and density for selected values of limiter density. The data are presented for a payload weight of 100 lbs and a payload density of 130 lbs/ft^3. The payload radius corresponding to these values is 0.5675 feet.

The same characteristics observed previously for variations in impact velocity can again be found. It can be seen, however, that there is at most a 4 percent difference in total weight below 450 ft/sec for balsa densities ranging from 6.5 lbs/ft^3 to 13 lbs/ft^3. At 500 ft/sec impact

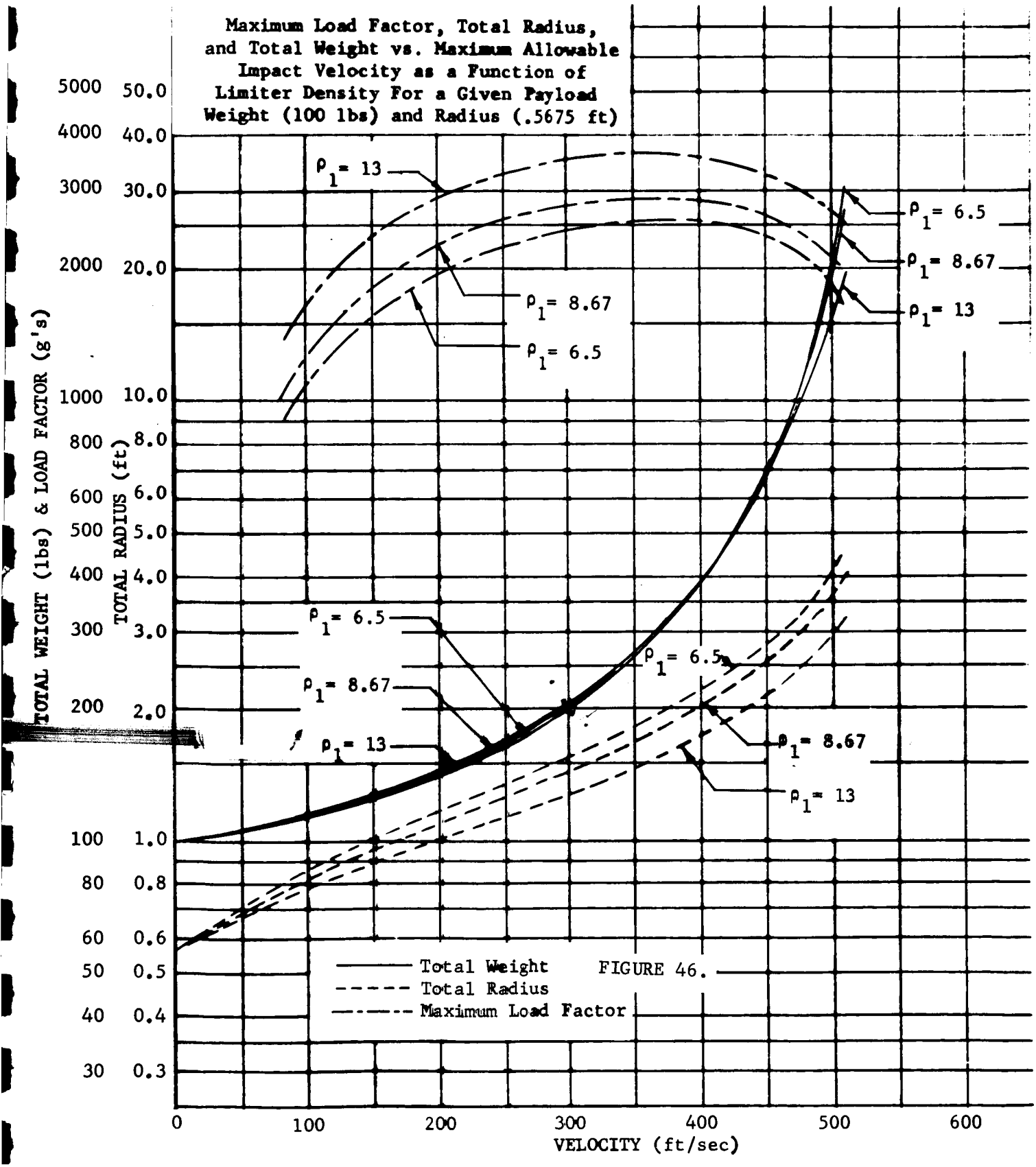
Maximum Load Factor, Total Radius, and Total Weight vs. Maximum Allowable Impact Velocity as a Function of Limiter Density For a Given Payload Weight (100 lbs) and Radius (.5675 ft)
TOTAL WEIGHT (lbs) & LOAD FACTOR (g's)
TOTAL RADIUS (ft)
VELOCITY (ft/sec)
5000
4000
3000
2000
1000
800
600
500
400
300
200
100
80
60
50
40
30
50.0
40.0
30.0
20.0
10.0
8.0
6.0
5.0
4.0
3.0
2.0
1.0
0.8
0.6
0.5
0.4
0.3
0
100
200
300
400
500
600
ρ_1= 13
ρ_1= 8.67
ρ_1= 6.5
ρ_1= 6.5
ρ_1= 8.67
ρ_1= 13
ρ_1= 6.5
ρ_1= 8.67
ρ_1= 13
ρ_1= 6.5
ρ_1= 8.67
ρ_1= 13
Total Weight
Total Radius
Maximum Load Factor

FIGURE 46.

velocity, the difference in total weight is more significant with the higher limiter density value appearing to be more favorable. The total radius, i.e., thickness of limiter, required will also be less for the higher limiter density values. The difference is on the order of one foot between $\rho_1 = 6.5$ lbs/ft^3 and $\rho_1 = 13$ lbs/ft^3 at an impact velocity of 500 ft/sec. If size must be considered, this difference can be significant if high impact velocity capability is required.

The use of high density balsa, however, will result in significantly higher values of maximum load factor. Where the trade-offs in limiter and payload size and weight are considered on the purely analytical basis as has been done above, the importance of the maximum load factor is not immediately apparent. The thickness of material and weight of the structure making up the payload is directly affected by the maximum load factor. Therefore, additional trade-offs related to the construction of the payload and limiter must be considered. A discussion of these problems is given in Section 5.10.

f. Additional Considerations. Some additional effects which can influence impact limiter design have been considered. The data presented up to this point have been based on impact against a flat surface, and in addition, the limiter has been assumed to homogeneous, i.e., of constant density. The limiter analysis has been extended to include the effects of impact against a curved surface and the use of a non-homogeneous limiter where the yield stress and balsa density are not constant through the limiter. The derivation of the force and energy equations are given in Sections 6.2 and 6.3 of the Appendix.

Integration of the general force equation for the energy absorbed in crushing of the limiter when these added effects are included cannot be obtained in closed form and numerical integration techniques are required. The general expressions for force and energy have been programmed for solution on a digital computer. The computer program will permit the trade-offs between the combined effects of impact on either flat, concave, or convex surfaces, variation in limiter density, impact velocity, limiter material, and payload size and weight to be readily determined.

(1) Impact on a Spherical Surface. Although the computer program is required in order to generate data for detailed trade-off studies, some general trends have been obtained. An integration of the energy expression for impact on a spherical surface can be obtained in closed form if the limiter is assumed to be made of constant density balsa and the stop mass effect is neglected. The equation for energy absorbed during crushing of the limiter is then

$$\frac{\int_o^{S_f} F_V \, ds}{\pi R_T^3 \sigma_o} = \pm \beta^3 \left\{ \frac{1}{2} \left(\frac{1 - \beta^3}{2} \right) \left[(1 + \alpha) \left(\frac{1 - \beta^2}{2} \right) - (1 - \alpha) \right] \left(\frac{1}{P_f} - \frac{1}{P_o} \right) \right.$$

$$+ \frac{1}{2} \left[(1 + \alpha) \left(\frac{1 + \beta^2}{2} \right) - (1 - \alpha) \left(\frac{2}{3} + \frac{\beta^2}{2} \right) \right] (P_f - P_o)$$

$$- \frac{2}{3} \left(\frac{1-\alpha}{2} \right) \left(\frac{P_f^2 - P_o^2}{2} \right) + \left(\frac{7-13\alpha}{24} \right) \left(\frac{P_f^3 - P_o^3}{3} \right) +$$

$$\left. \left(\frac{1 - \alpha}{2} \right) \left[\left(\frac{1}{P_f} - \frac{8}{3} + 2P_f - \frac{1}{3} P_f^3 \right) \ln \left| \frac{1 - P_f}{\beta} \right| \right] \right\}$$

where

$\beta = \frac{R_t}{R_s}$ = ratio of total radius of sphere R_t to radius of curvature of surface R_s

$\alpha = \frac{\sigma_c}{\sigma_o}$ = ratio of cross grain yield stress to yield stress parallel to grain

$P_o = 1 \pm \beta$

$$P_f = 1 \pm \left(\beta - \frac{S_f}{R_s} \right)$$

Where S_f is the stroke and $S_f = (R_t - R_p)(1 - \epsilon)$. The upper sign applies to convex impact surfaces and the lower sign to concave impact surfaces.

Comparisons of the energy absorbed on impact with flat, concave and convex surfaces have been made. In general, impact on a concave surface will increase the energy absorption capability of a given impact limiter over that obtained for impact on a flat surface. This is due to the fact

that more of the limiter is brought into contact with the surface and crushing takes place over a greater area. Conversely, impact on a convex surface will reduce the capability of a given limiter.

As an illustration of the magnitude of the increase or decrease in capability, assume that $\beta = 1/2$, or the radius of a curvature of the surface is twice the radius of the sphere. This may be considered as approaching the limiting value of β for which the equations hold while still retaining some physical significance. For a typical limiter, assume that $R_p = .496$ ft, $R_t = 2.48$ ft, $S_f = 1.5872$ ft, $\rho_1 = 6.5$ lbs/ft^3, and $\alpha = 0.12$. Then, for an impact on a concave surface the increase in energy absorbtion over that obtained for impact on a flat surface is about 38 percent. Impact on a convex surface of similar curvature, $\beta = 1/2$, will yield an energy absorption capability 73 percent of the flat surface impact capability. These values may be related to maximum allowable impact velocity by equating energy absorbed to the kinetic energy at impact. For the assumed sphere the maximum allowable impact velocities are

(1) Flat surface, $\beta = 0$; $V = 438$ ft/sec

(2) Concave surface, $\beta = 1/2$; $V = 515$ ft/sec

(3) Convex surface, $\beta = 1/2$; $V = 375$ ft/sec

Several geometric restrictions are necessary due to assumptions made in the derivation of the force equation. The radius of curvature of the spherical convex surface, or hill, and the height of the hill must be greater than

$$d = \frac{(2 R_T - S_f) S_f}{2 [R_s + (R_T - S_f)]}$$

where R_t is the total radius of the limiter, S_f is the total stroke and R_s is the radius of curvature of the surface. For the spherical concave surface, or hole, the radius of curvature must be greater than the total radius of limiter plus payload. The depth of the hole required to satisfy the assumptions must be greater than

$$d = \frac{(2 R_T - S_f) S_f}{2 [R_s - (R_T - S_f)]}$$

A detailed study of the trade-offs for the impact on curved surfaces for various limiter configurations requires a number of permutations of the design parameters affecting limiter size and weight. To properly accomplish this study the computer program is necessary. This program will be available for follow-on program studies and can be extended to cover curved surfaces other than spherical.

(2) Non-Homogeneous Limiter Construction Effects. Effects of non-homogeneous limiter construction, i.e., a limiter constructed of layers of balsa of different density and yield stress, can be investigated to a limited extent by simplification of the general force equation. A closed form integration of the force to obtain the energy absorbed in crushing has been performed for an impact limiter consisting of two layers of balsa of different density and yield stress when impacted on a flat surface. Two force equations are required, one for the force in the outer balsa layer and one for the force in the inner layer. For the two layer laminated limiter the following definitions are required. The total radius of the sphere is defined as R_t, the radius of the outer edge of the inner layer as R_1, the yield stress for the inner layer as σ_1, and for the outer layer as σ_2, and the ratio of cross grain yield stress to parallel grain yield stress for inner and outer layers as α_1, and α_2. In addition, if we define $R_1/R_t = Z_1$ and $(R_t - S)\ R_t = Z$ where S is the stroke then the force equations are

I. $Z_1 < Z$

$$F_V = 2\pi\ R_T^2\ \sigma_2 \left[Z^2\ (\alpha_2 - 1)\ \ln Z + \frac{\alpha_2}{2}\ (1 - Z^2)\right]$$

II. $Z_1 > Z$

$$F_V = 2\pi\ R_T^2 \left\{\sigma_1 \left[Z^2\ (\alpha_1 - 1)\ \ln \frac{Z}{Z_1} + \frac{\alpha_1}{2}\ (Z_1^2 - Z^2)\right]\right.$$

$$\left. + \sigma_2 \left[Z^2\ (\alpha_2 - 1)\ \ln Z_1 + \frac{\alpha_2}{2}\ (1 - Z_1^2)\right]\right\}$$

Integration of the force over the stroke from $Z = 1$ to $Z = Z_f$ yields the expression for energy absorbed in crushing

$$\frac{\int_1^{Z_f} F_V\ dZ}{2\pi\ R_T^3} = \frac{E_T}{2\pi\ R_T^3} = \sigma_2 \left\{\frac{(1 - \alpha_2)}{9}\ (3\ Z_f^3\ \ln Z_1 + 1 - Z_1^3)\right.$$

$$\left. + \frac{\alpha_2}{2} \left[1 - Z_f - \frac{1}{3}\ (1 - Z_1^3) - Z_1^2\ (Z_1 - Z_f)\right]\right\}$$

$$+\sigma_1 \left\{ \frac{(1-\alpha_1)}{9} \left[z_f^3 \left(3 \ln \frac{z_f}{z_1} - 1\right) + z_1^3 \right] + \frac{\alpha_1}{2} \left[z_1^2 (z_1 - z_f) - \frac{1}{3} (z_1^3 - z_f^3) \right] \right\}$$

These equations have been used to make some preliminary observations. For a given payload weight W_p and total weight of payload and limiter W_t, a reduction in load factor over a uniform density limiter can be obtained by use of high density balsa in the outer layer of the limiter with low density balsa around the payload capsule. This can be accomplished for little or no change in maximum impact velocity capability. The reason for this reduction in load factor is due to the fact that the dense material in the outer layer permits a quicker build-up of the force while the stroke remains the same as for the equivalent limiter made of constant density balsa. If the dense balsa is placed near the payload capsule with lighter balsa toward the outside of the limiter a significant reduction in impact capability for the layered limiter is encountered over that for the constant density limiter.

As an illustration, the following example may be considered. Assume a payload weight of 50 lbs and a total weight of 610 lbs corresponding to a payload radius of 0.463 ft and a total radius of 2.316 ft. If the limiter is divided into two layers of equal thickness, then for an outer layer of 12 lb/ft^3 balsa and an inner layer of 6.5 lbs/ft^3 balsa, neglecting the stop mass effect, a maximum impact velocity of 471 ft/sec is possible with a maximum load factor of 2009 g's. A limiter of constant density of the same weight as the layered limiter would be made of 10.84 lb/ft^3 balsa. The maximum allowable impact velocity would be 474 ft/sec and the maximum load factor would be 2860 g's.

A similiar example was worked out for the reverse situation of a 6.5 lb/ft^3 outer layer and an inner layer of 12 lb/ft^3 balsa. The total radius and payload weight were kept the same, hence the total weight dropped to 330 lbs due to the decrease in volume occupied by the more dense balsa. For this example the velocity capability was 425 ft/sec as compared to the equivalent capability of a 330 lb, constant density limiter of 442 ft/sec.

There are many possible configurations for the laminated limiter. In order to perform a detailed study of balsa density variation effects, a computer program is necessary. This program is available for investigating specific preliminary design configurations.

5.2.3 BALSA WOOD

a. Utilization of Balsa. The attempt to obtain better impact limiter performance on the Ranger programs ended when the tests on the assembled capsules indicated performance was sufficient such that the capsule configuration and weight was within the limits which would produce a successful mission. For this reason, many balsa characteristics were not investigated; and as a consequence, there exist many areas where the performance of balsa limiters could be improved. Relatively early in the study program it became quite apparent that the performance of the balsa impact limiter would play a significant role in the overall capability of the capsule. Because of this, the analytical model previously developed during the Ranger programs was re-evaluated and new parameters were introduced so that the model would more closely represent the real world.

One of the parameters introduced in the new model was the cross grain energy absorption capability of balsa wood. Direct measurements of this parameter have never been taken, however, a measure of the relative strengths of balsa wood parallel and perpendicular to the grain can be found by comparing the stress at the proportional limit in each case. Curves have been plotted by the Department of Agriculture (Reference 2) for stress at the proportional limit versus specific gravity parallel and perpendicular to the grain, and from these, inferences can be drawn concerning the relative crush energies of balsa wood.

Figure 47 illustrates the fact that there are two directions perpendicular to the grain which must be considered. There can be tangential or radial loading depending upon the orientation of the balsa wood's growth rings. Figure 48 is a plot of the perpendicular radial and tangential to the grain stress as a percentage of parallel to the grain loading for various balsa densities.

Although several areas yet remain to be fully investigated utilizing the new, more complete model, an area of investigation which will yield a significant increase in balsa limiter performance has been neglicted. During the Ranger programs, over 300 pieces of balsa wood were subjected to crush tests and the resultant crush energies recorded. The majority of these tests were conducted on a 160,000 pound Riehle testing machine with a constant deflection of two inches per minute with a 1.13 inch diameter (1 in^2 area) punch pressed into balsa specimen in the direction of the grain. The force-deflection curves were automatically recorded and then integrated from the beginning of the strokes to the point of sharp rise in the loading forces, indicating "bottoming" of the balsa specimen. Because of the nature of the current contract, there could be no experimental investigation of the performance characteristics of balsa wood. Hence, it was impossible to test small, individual balsa specimens and attempt to discover the reason different specimens exhibit different crush energies.

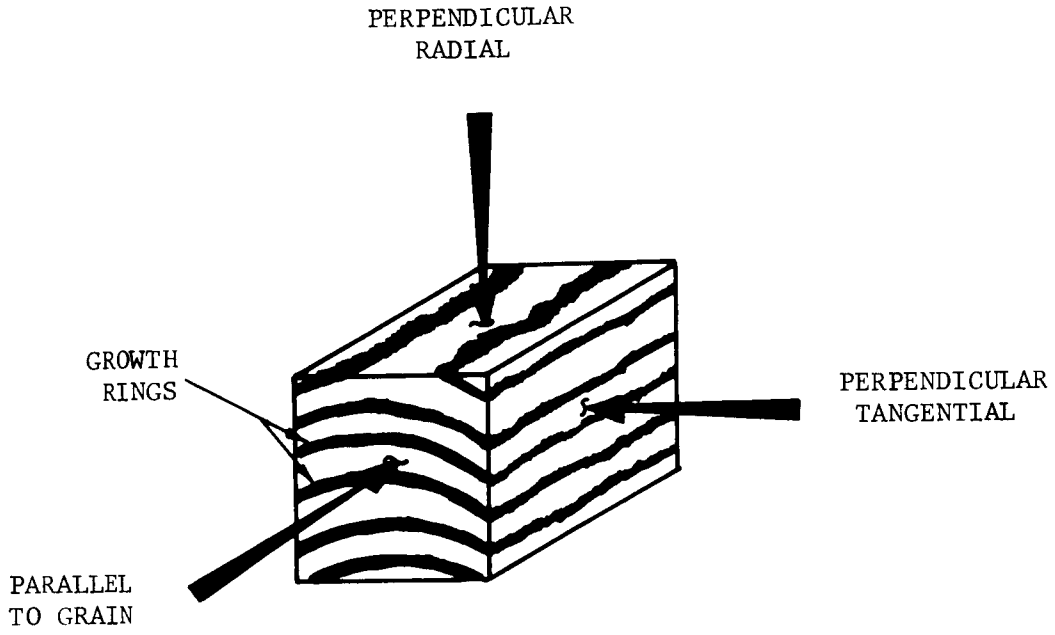

CROSS GRAIN TERMINOLOGY

FIGURE 47

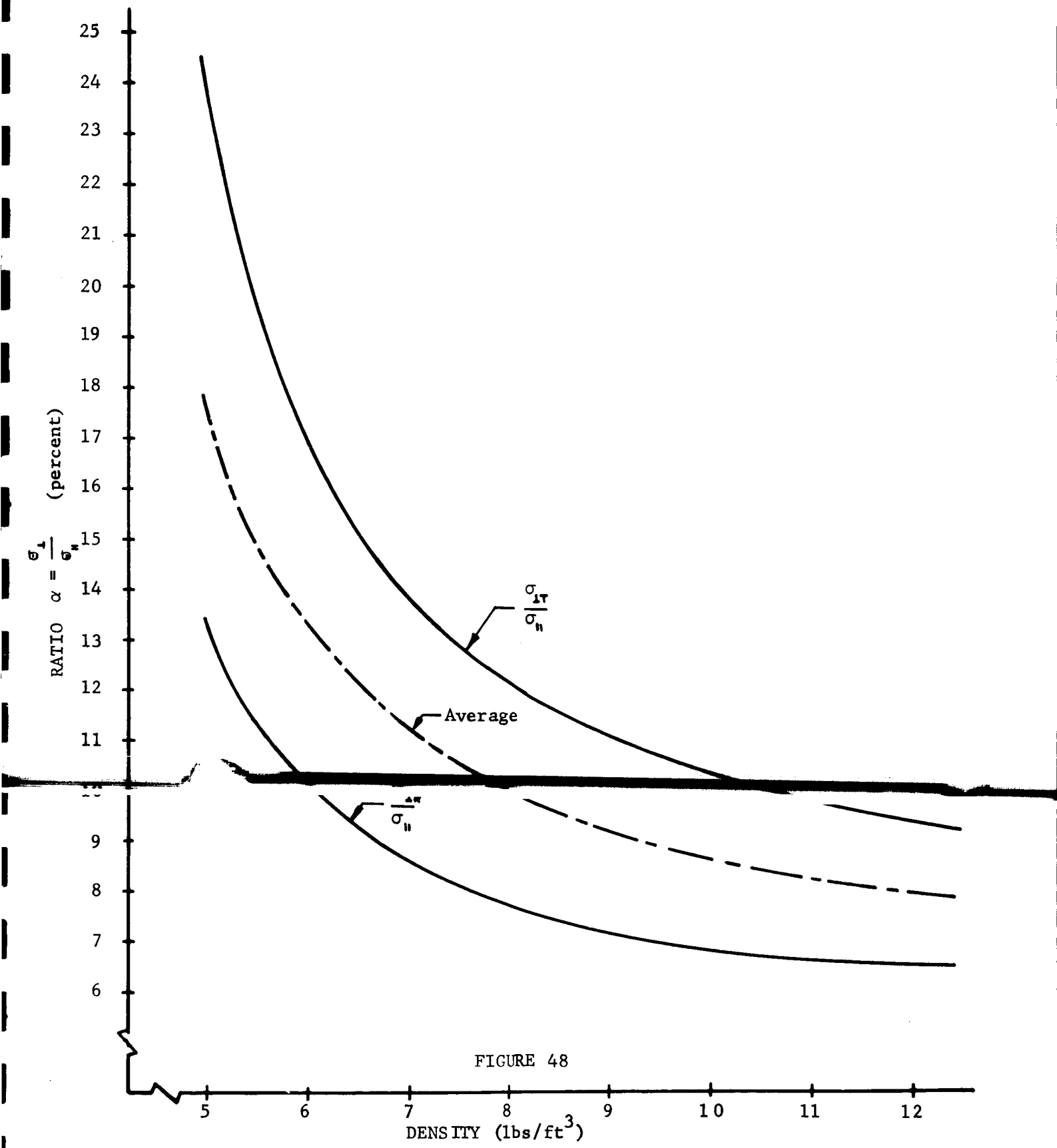
RATIO $\alpha = \frac{\sigma_\perp}{\sigma_\parallel}$ (percent)
25
24
23
22
21
20
19
18
17
16
15
14
13
12
11
9
8
7
6
$\frac{\sigma_{\perp T}}{\sigma_\parallel}$
Average
$\frac{\sigma_{\perp H}}{\sigma_\parallel}$
5
6
7
8
9
10
11
12
DENSITY (lbs/ft^3)

FIGURE 48

b. Analysis of Test Data. During the current program, the results of the many Ranger tests were accumulated and a statistical analysis conducted using the data. A correlation analysis of crush energy onto balsa density was performed on the data obtained from 172 tests conducted at room temperatures. The results of this analysis is as follows:

$\eta = 14{,}150 + 360\rho$

where

η = specific crush energy ft-lbs/lb

ρ = balsa density lbs/ft^3

and

$\bar{\eta}$ = 17,241 ft-lbs/lb (mean value)

$\bar{\rho}$ = 8.60 lbs/ft^3 (mean value)

η = 9,689 to 29,904 (range)

ρ = 5.173 to 17.56 (range)

σ_η = 3,482 ft-lbs/lb (standard deviation)

σ_ρ = 3.18 lbs/ft^3 (standard deviation)

Analysis of the regression coefficients reveals the following results:

σ_a = 254 (standard deviation of η intercept)

σ_b = 79 (standard deviation of slope)

r^2 = 5.32 percent (percentage of total variance explained by linear regression equation)

Probability < 0.0005 that η is independent of ρ.

The portion of the total variance in the parameter η which is explained by the regression equation is only 5.32 percent. This relatively small reduction in total variance is explained by the fact that the slope of the regression line is near zero, that the variance of ρ is small, and that the variance in η for each value of ρ is quite large. Thus to reduce the uncertainty in the estimation one or more of the above causes must be reduced. The slope of the regression line cannot be changed because

presumably it reflects the true characteristic of the balsa wood. A larger dispersion of specimen densities could be chosen, however, the practical limits of balsa densities seem to range between 5 and 15 lbs/ft^3 and deceleration considerations for most applications indicate the densities of primary concern are between 6 and 8 lbs/ft^3. Thus the best way to reduce the uncertainty is to reduce the variance in η; this can possibly be accomplished by increasing the number of test data; but, even more useful would be to discover the cause of the large variance and select only particular specimens. By analyzing and discovering the reasons why different specimens of similar densities exhibit different crushing characteristics, one not only reduces the uncertainty in the crush energy but particular pieces with higher or lower yields can be selected or rejected and thereby improve the overall design for which the balsa was being used.

For the application considered here, a relatively small improvement in balsa performance will result in a significant improvement in capsule performance. As can be seen in Figures 43 and 152, the percentage of total capsule weight devoted to the limiter ranges from 20 percent to 80 percent. Thus, a one percent increase in balsa performance will permit approximately a 3-4 percent increase in overall capsule performance. This, when coupled with the fact that there has never been an attempt to improve the limiter performance through balsa selection (other than restricted density), leads one to be optimistic about the improvement in capsule performance which could result from additional investigations of balsa characteristics.

c. Balsa Sterilization. The sterilization requirements will impose some design constraints upon the balsa wood impact limiter, although none severe enough to alter the overall limiter performance. During the Ranger programs several balsa specimens were subjected to 125°C for 24 hours and then tested as described earlier (Reference 3). These specimens became brittle and unreliable, although those specimens which did not split apart during testing exhibited about the same crush energy as unbaked balsa wood. Three specimens which were baked at 125°C for 24 hours and then remoisturized to 10 percent humidity did not exhibit any of the above characteristics and behaved similar to unbaked balsa wood. Additional experimentation is required in this area, however, it appears that if the outer limiter shell is constructed to prohibit any loss of vapor (this should also be done to prevent outgassing during transient), the performance of the balsa impact limiter will not be degraded by sterilization requirements.

REFERENCES

1. Kornhauser, M., "Structural Effects of Impact," Spartan Books, Baltimore, 1964.

2. "Strength and Related Properties of Balsa and Quipo Woods," Report No. 1511, United States Department of Agriculture, Forest Service, Forest Products Laboratory, Madison, Wisconsin, November 1955.

3. MacDonald, A. G., "Lunar Seismometer Capsule, Sterilization Final Report," Aeronutronic Report LC(b)-411, October 29, 1962.

5.3 FACSIMILE CAMERA

5.3.1 DESCRIPTION

The function of the High Resolution Facsimile (HRF) camera is to record a picture which is obtained by continuously scanning the surrounding scene with a telescope having a very narrow instantaneous field of view. The HRF camera senses brightness data and transduces radiant energy into electrical energy and establishes the format by which a scene is represented electrically. The HRF playback machine performs the reciprocal operation to present an accurate reproduction of the detected information.

The camera contains a fixed-focus optical viewing assembly, electromechanical driving and scanning mechanisms that provide motion through the view field, a photoelectric transducer and associated signal, and synchronization and motor drive electronics. (Figure 49). The synchronization electronics provides timing signals to insure accurate positioning of the data readout.

A facsimile camera has already been developed for space applications by Aeronutronic for use in the Ranger program. The camera scanned 50 degrees vertical by 360 degrees horizontal to give a panoramic picture in which the dynamic range of the data was 100:1 (40 db) and the resolution was better than 0.1 degree.

The optical viewing assembly of the HRF camera may consist merely of an objective lens that focuses the radiation through a pinhole onto a photosensitive detector. The following evaluation of performance assumes this to be a simple thin converging lens. The effects of chromatic and monochromatic aberrations will not be discussed, and only first order theory of geometric optics are presented. In practice, a thick rather than a thin lens is used; but within the precision of first order theory, the analysis and diagrams are interchangeable. It should be recalled that the first and second principal planes do not usually coincide in a thick lens.

In Figure 50a is shown a lens with entrance aperture D and a pinhole of diameter D_o a distance x_2' behind the lens, as well as the image in object space of the pinhole, a distance x_2 from the lens. It can be shown that this image pinhole is just as effective as a real pinhole in determining whether or not flux from a source in object space passes through the real pinhole; in what follows, therefore, only the image pinhole will be considered. Also shown in Figure 50a are the distances x_1, x_2, and x_3 corresponding to the "near field," "hyperfocal distance," and "far field." Figure 50b is similar to 50a except the pinhole has been positioned so

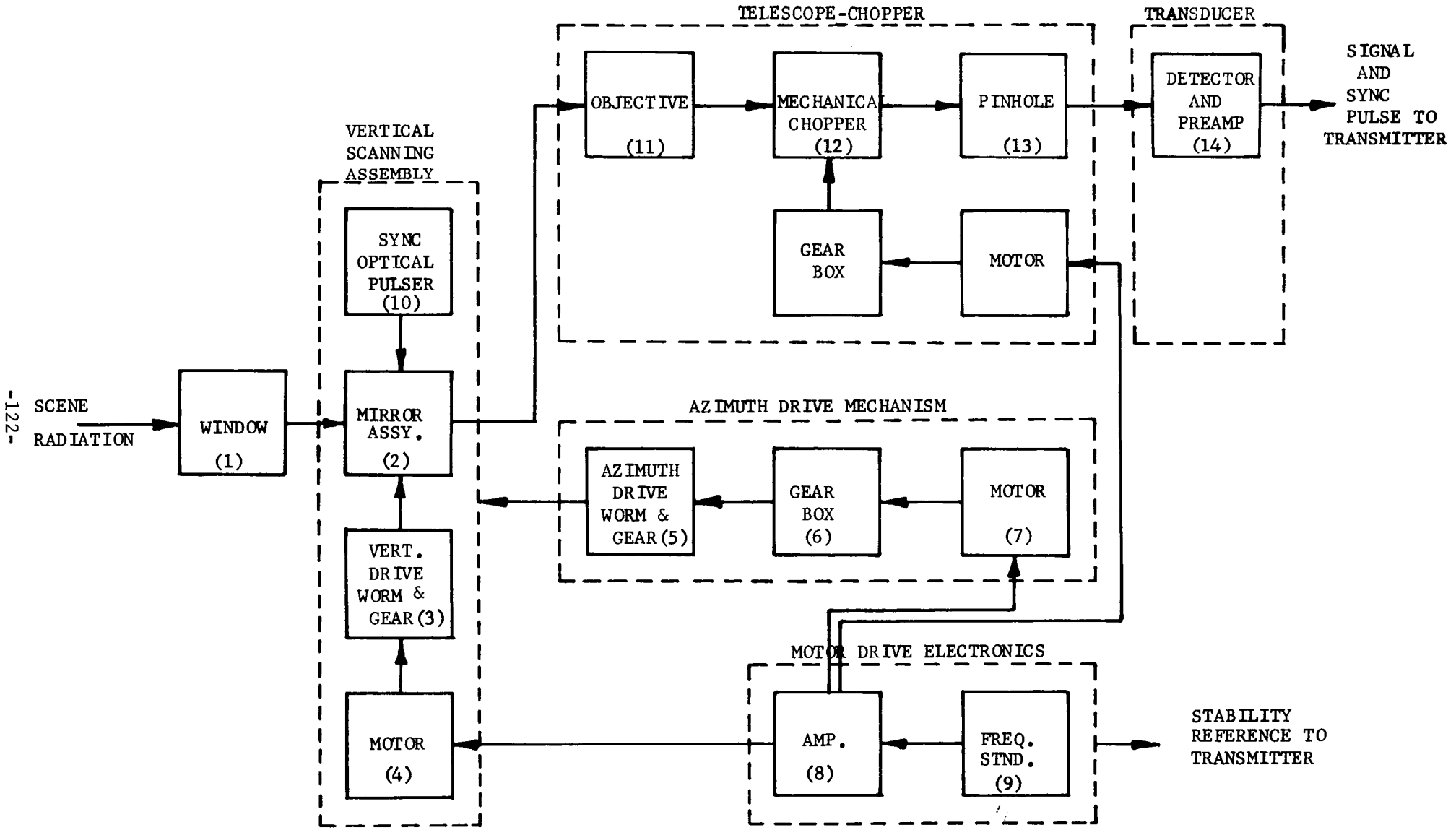

FIGURE 49 MARS FACSIMILE CAMERA FUNCTIONAL DIAGRAM

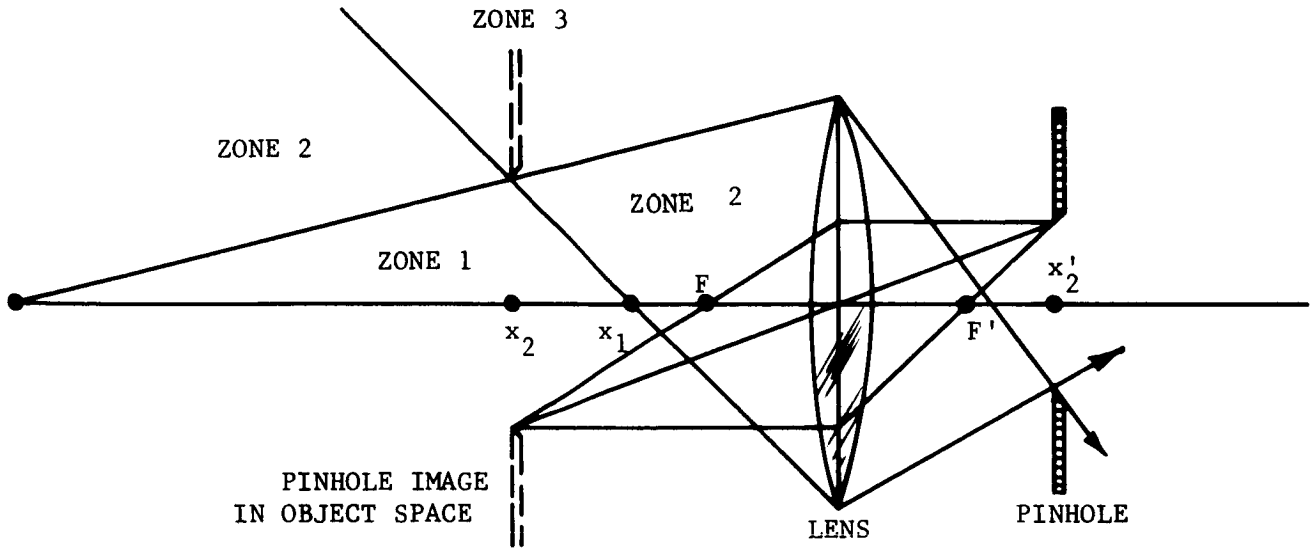

(A) GENERAL CASE

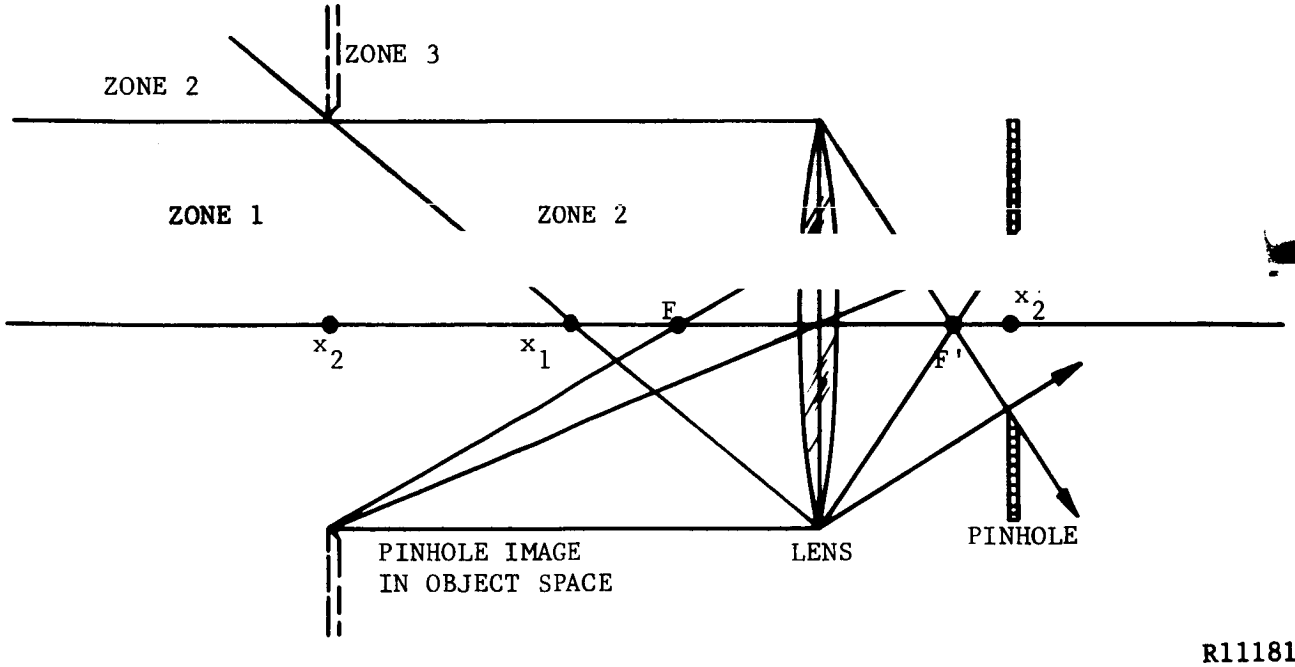

R11181

(B) $x_3 = \infty$

FIGURE 50. FIELD OF VIEW GEOMETRY

that $x_3 = \infty$; this is called the "matched condition." (Note: The nomenclature "hyperfocal distance" for the distance x_2 is incorrect in the case illustrated in Figure 50a, but for uniformity it will be so designated here.)

Inasmuch as the HRF camera is essentially a flux detector, as opposed to a visual instrument, the most important relationship is: which points in object space contribute to the flux "seen" by the sensor (photomultiplier, etc.) and to what extent. Accordingly, in Figure 50 "half" of object space is shown divided into three zones, which are defined as follows:

Zone 1 — Considering light sources in this zone, all flux which is intercepted by the lens also passes through the pinhole.

Zone 2 — Vignetting occurs to some extent; that is, some of the flux which passes through the lens does not pass through the pinhole.

Zone 3 — None of the flux which passes through the lens passes through the pinhole.

Notice the relationship between these zones and x_1, x_2, and x_3.

Figures 51, 52, 53, and 54 illustrate the method of determining in which zone a point lies and also indicates how the amount of flux intercepted by the system might be evaluated (vignetting diagram). The cone of flux intercepted by the lens (Ω_L) and the cone of flux intercepted by the pinhole (Ω_P) intersect in a "cone" whose cross section at the principal plane is indicated by the cross-hatched area (ΔA). This represents the flux which passes through both the lens and the pinhole. Figures 55a and 55b show (schematically) the variation of ΔA with position in the object field for the two different system configurations. The figures are interpreted as follows: (notice that again only "half" of object space is considered) consider a series of infinite, uniformly radiant planes perpendicular to the optical axis; then Figure 55 illustrates the degree to which flux from these planes is transmitted by the pinhole. That is, except for consideration of the diminution of irradiance by the square of the distance, the figures show the flux distribution "seen" by the pinhole.

The angular resolution of the HRF camera is defined as the plane angle subtended by a cone whose base is the pinhole (or its image) and whose apex is the center of the lens (Figure 56). Obviously at the hyperfocal distance, α sharply defines the field of view of the optical system. As

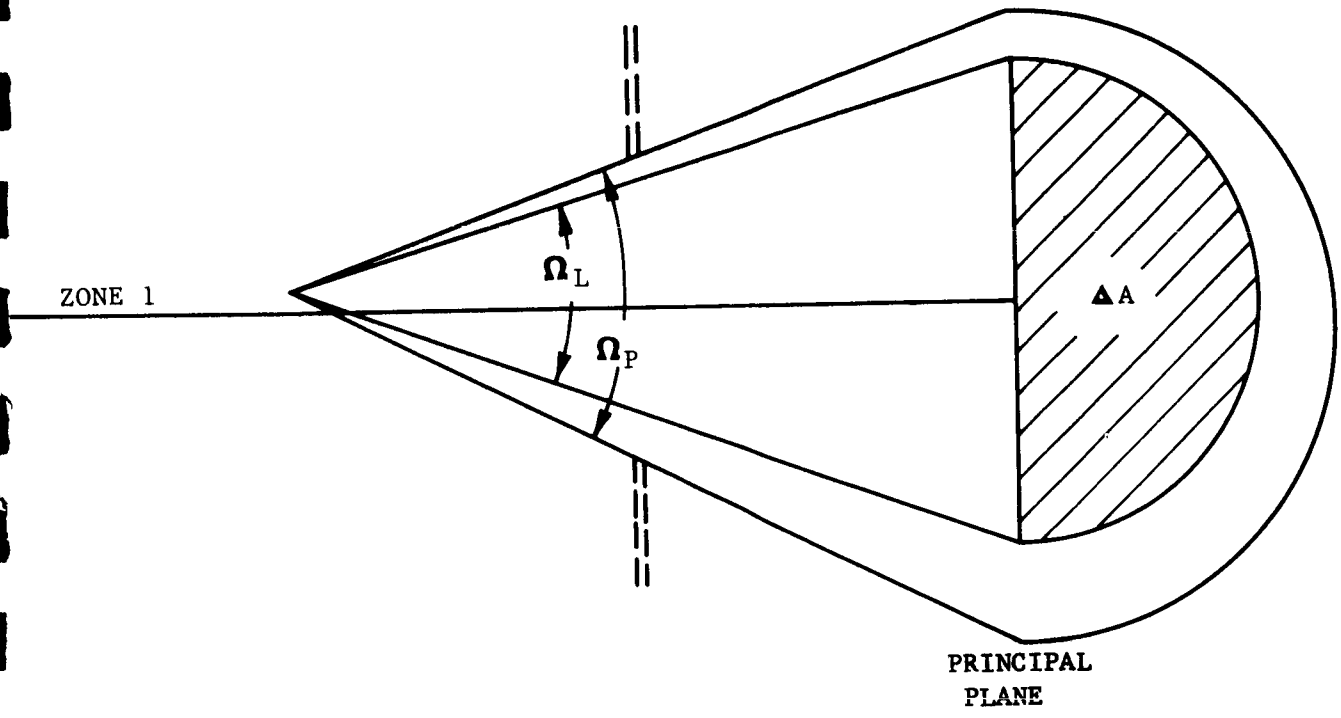

FIGURE 51. FLUX FROM A POINT IN ZONE 1 SEEN BY THE SYSTEM

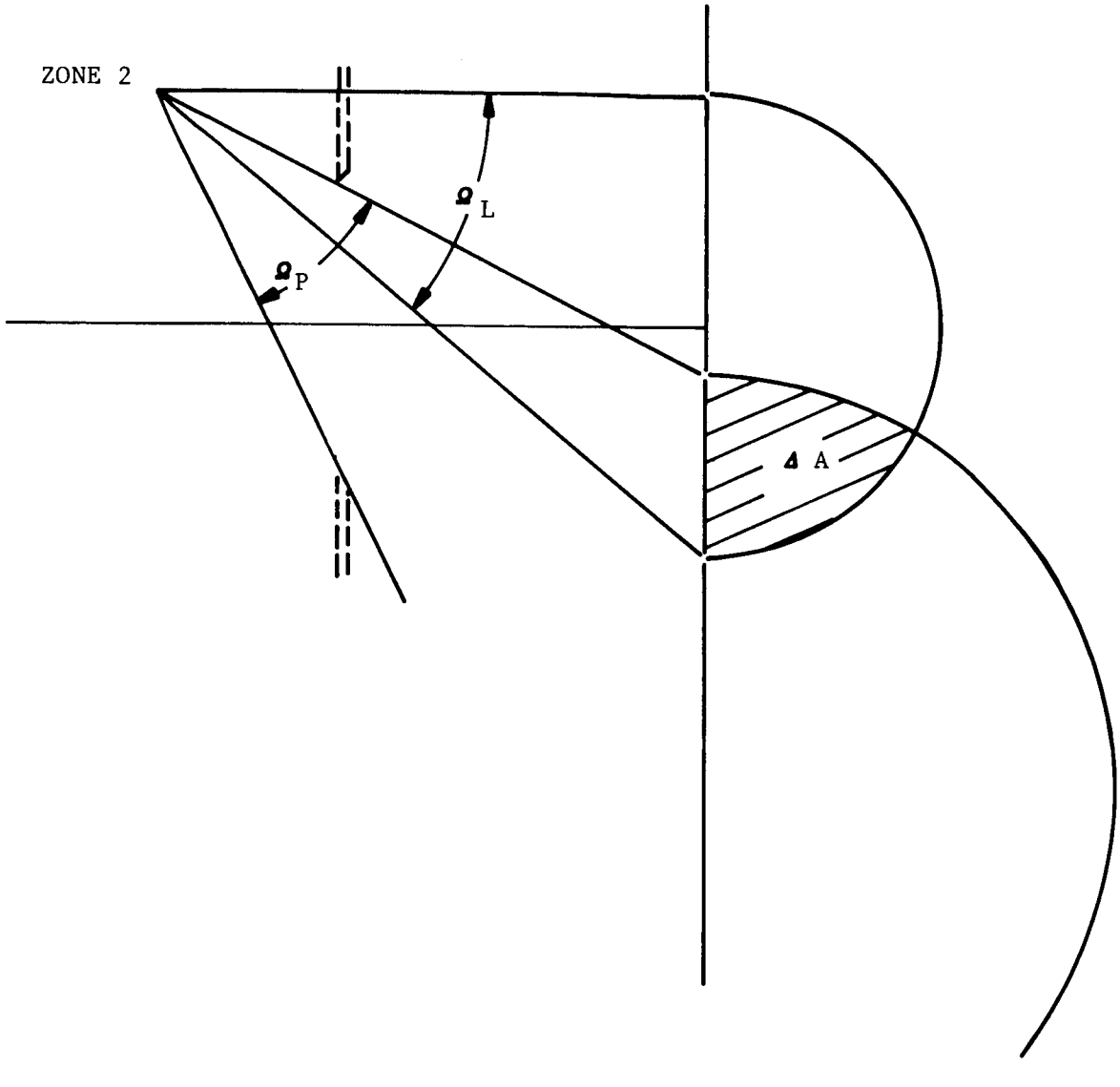

FIGURE 52. FLUX FROM A POINT IN ZONE 2 SEEN BY THE SYSTEM

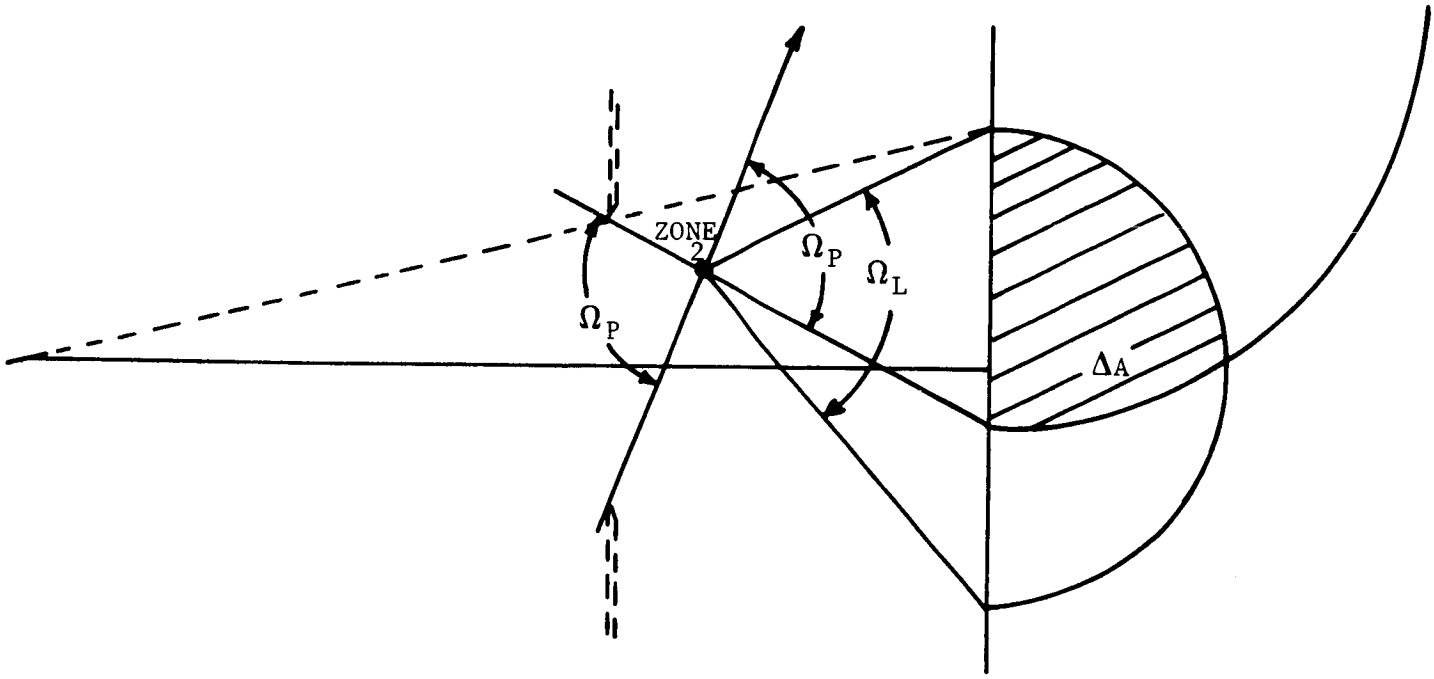

R11185

FIGURE 53. FLUX SEEN BY THE SYSTEM, POINT IN ZONE 2, NEARER THAN HYPERFOCAL DISTANCE

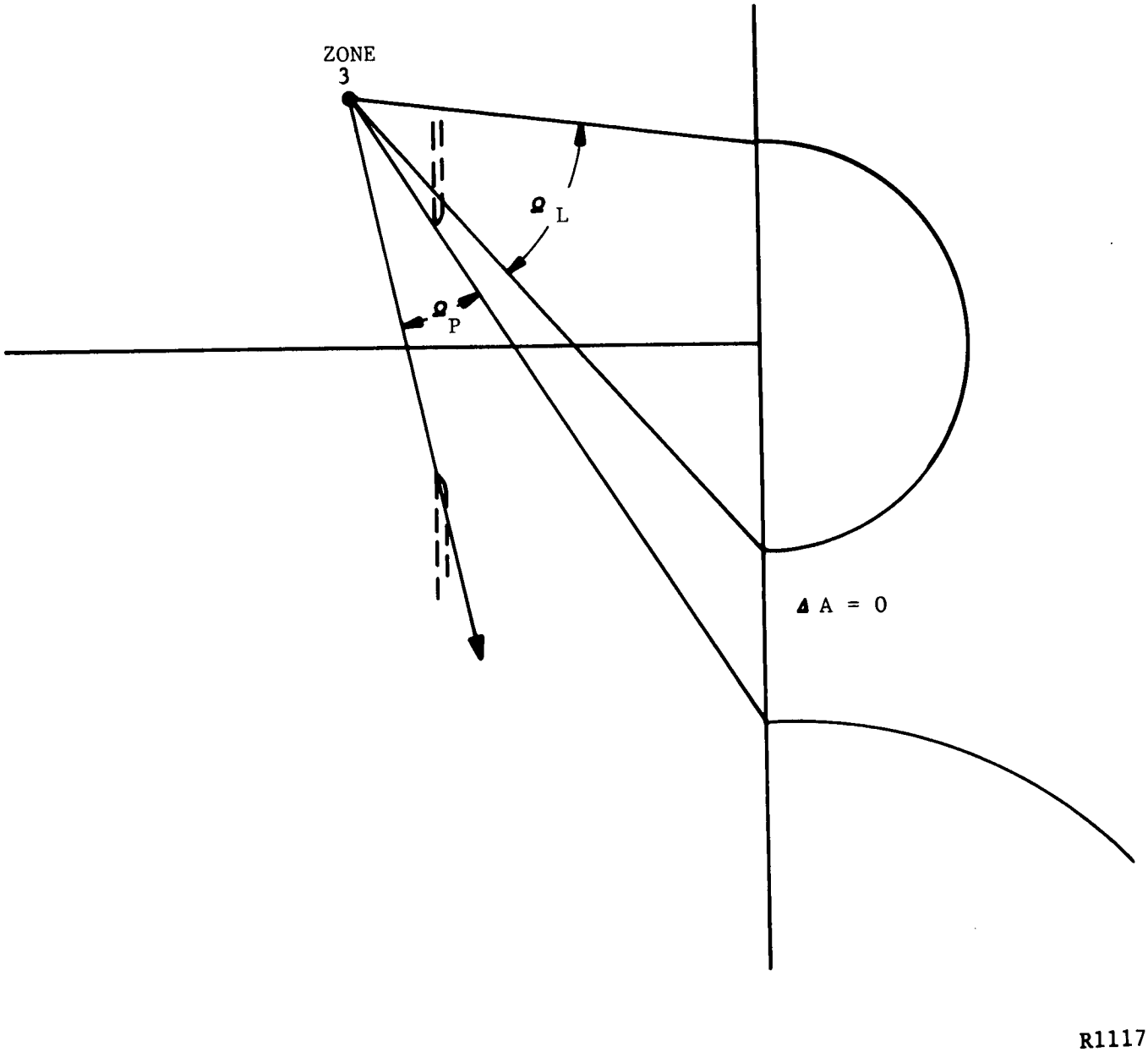

FIGURE 54. FLUX FROM A POINT IN ZONE 3 SEEN BY THE SYSTEM

R_L = LENS RADIUS

R'_P = PINHOLE IMAGE RADIUS

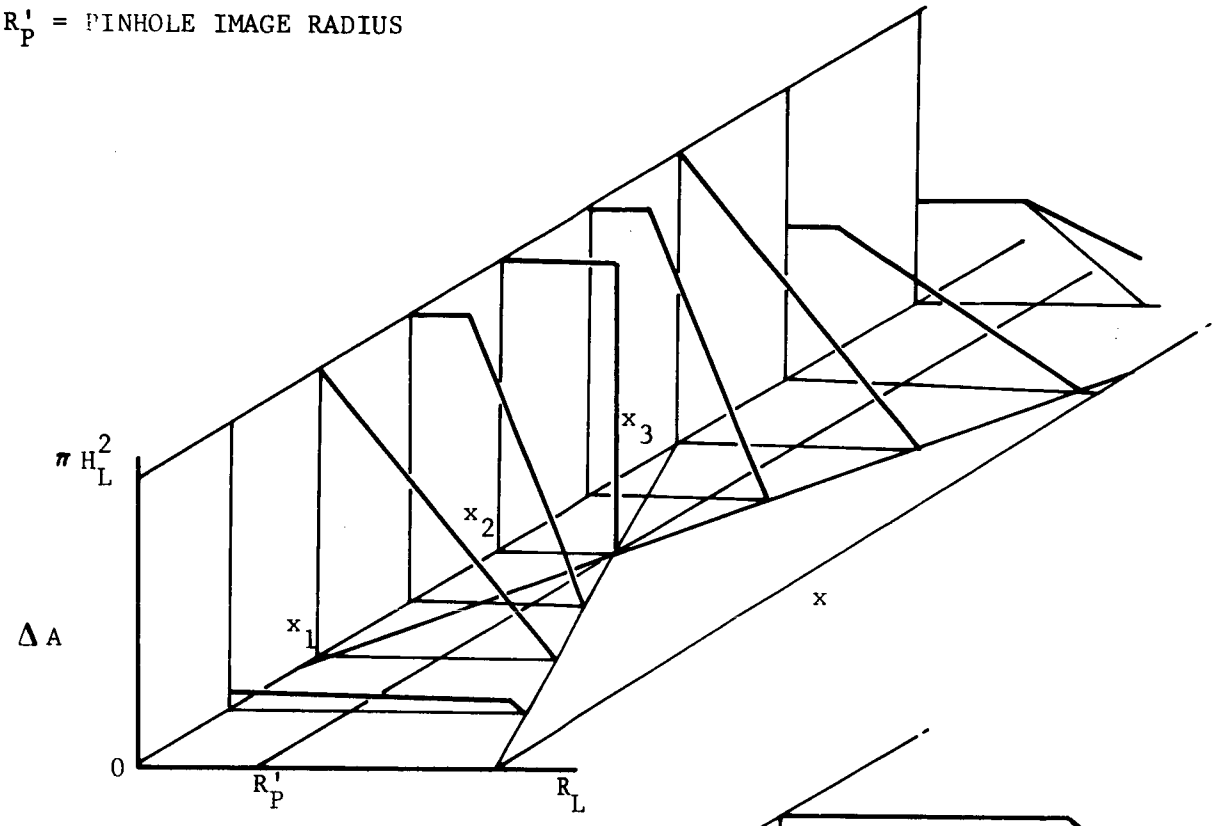

(a) GENERAL CASE.

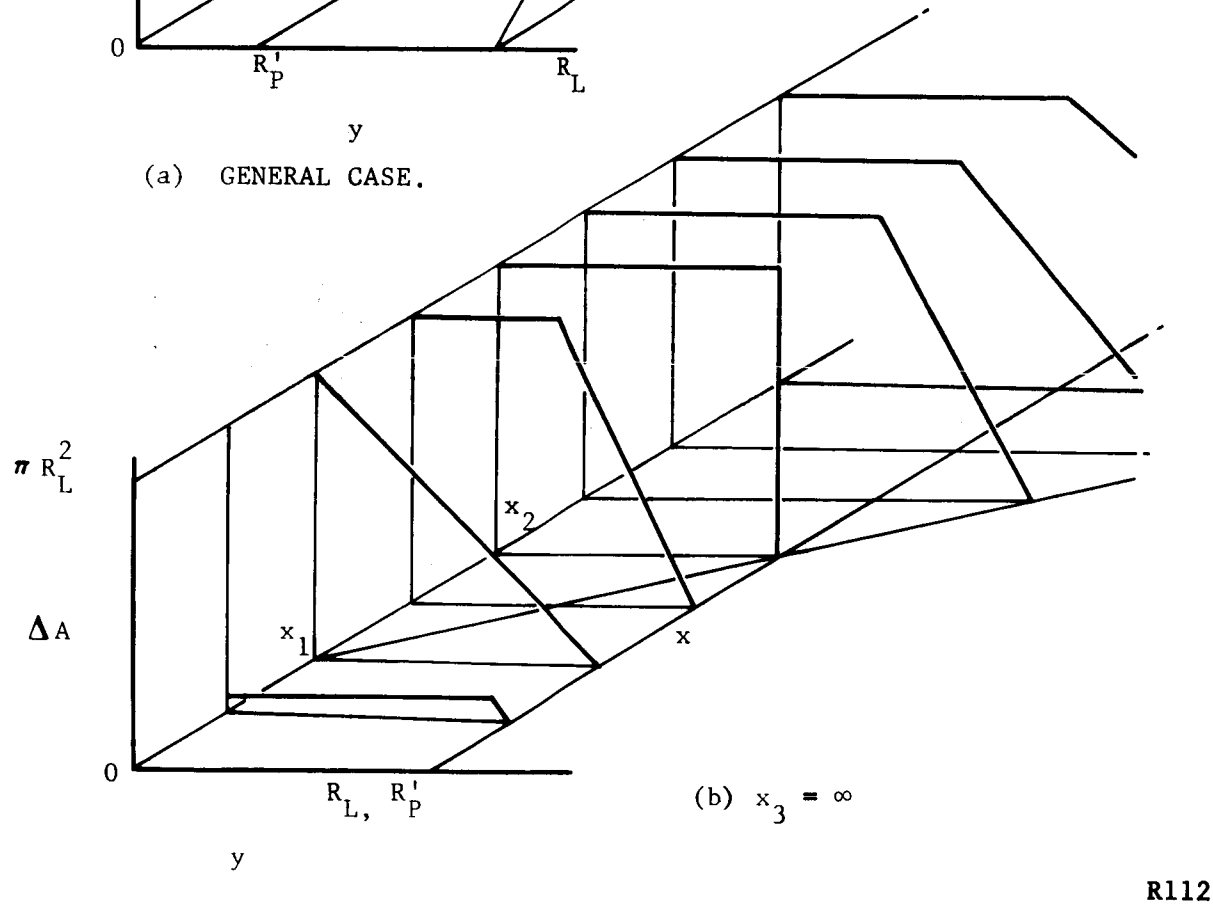

(b) $x_3 = \infty$

R11216

FIGURE 55. FLUX DISTRIBUTION

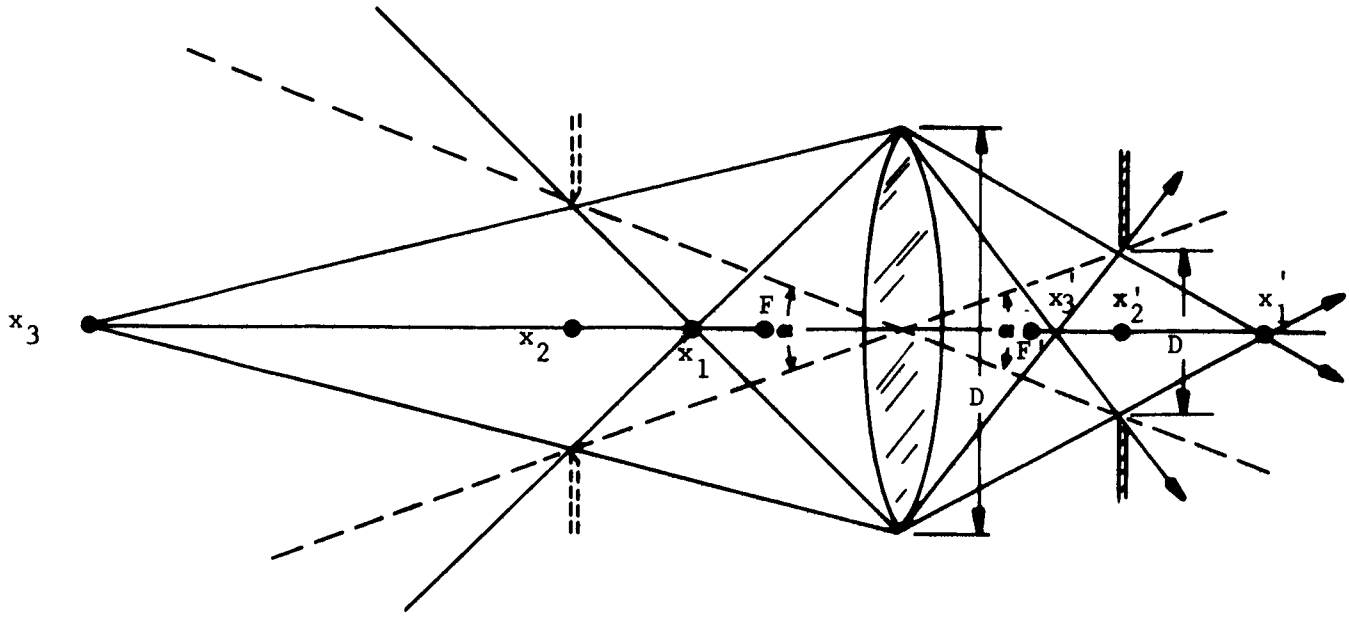

(a) GENERAL CASE

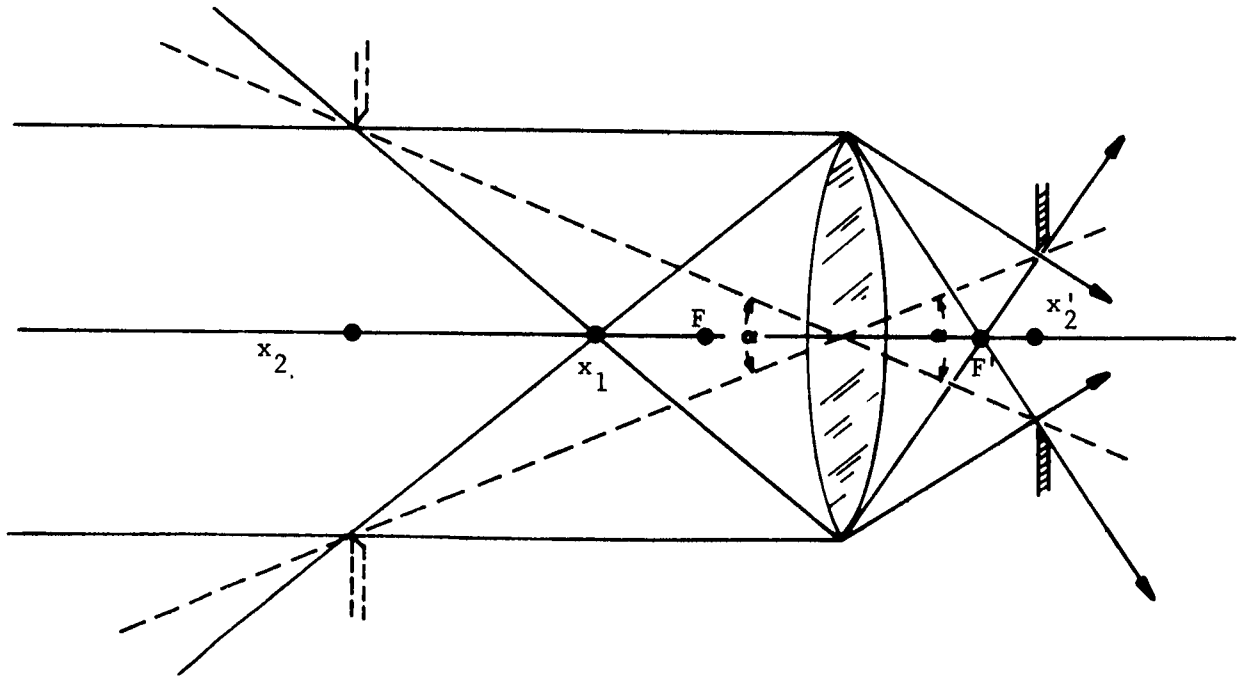

(b) $x_3 = \infty$

R11221

FIGURE 56. ANGULAR RESOLUTION

objects away from the hyperfocal distance are considered, however, the significance of α is no longer clear. Nevertheless, α can be qualitatively accepted as defining the field of view of the system inasmuch as a relatively small percent of the flux from the real field of view (where the real field of view = Zone 1 + Zone 2) comes from that portion of the field outside the cone α. The square-wave response of the resulting HRF image will be somewhat less, however, than what might be expected if there were a clear-cut angular resolution. That is, square-wave response in the facsimile photograph will be maximum for objects at the hyperfocal distance but will decrease as objects away from the hyperfocal point are considered.

Figure 57 illustrates the case where $x_2 = \infty$; i.e., the pinhole is located in the focal plane. In this case, there is no place in object space (except infinity) where α sharply defines the field of view. On the other hand, the flux distribution in the real field of view is more symmetrical with respect to the cone α than in the other two configurations.

Figure 58 compares (in object space) the real fields of view for the three system configurations, where all three have the same angular resolution. The shaded areas represent Zone(s) 1. Present Aeronutronic HRF systems use the matched configuration inasmuch as it affords the nearest near field as well as an infinite "depth of field" $(x_3 - x_1)$.

Referring to the geometry of Figure 56 : For flux from "near field" objects

$$\frac{D}{x_1'} = \frac{D_o}{x_1' - x_2'} \tag{1}$$

For flux from "far field" objects

$$\frac{D}{x_3} = \frac{D_o}{x_2' - x_3'} \tag{2}$$

For small angles

$$\alpha = \frac{D_o}{x_2'} \tag{3}$$

Combining equations (1) and (3) gives

$$\alpha = D \frac{x_1' - x_2'}{x_1' x_2'} \tag{4}$$

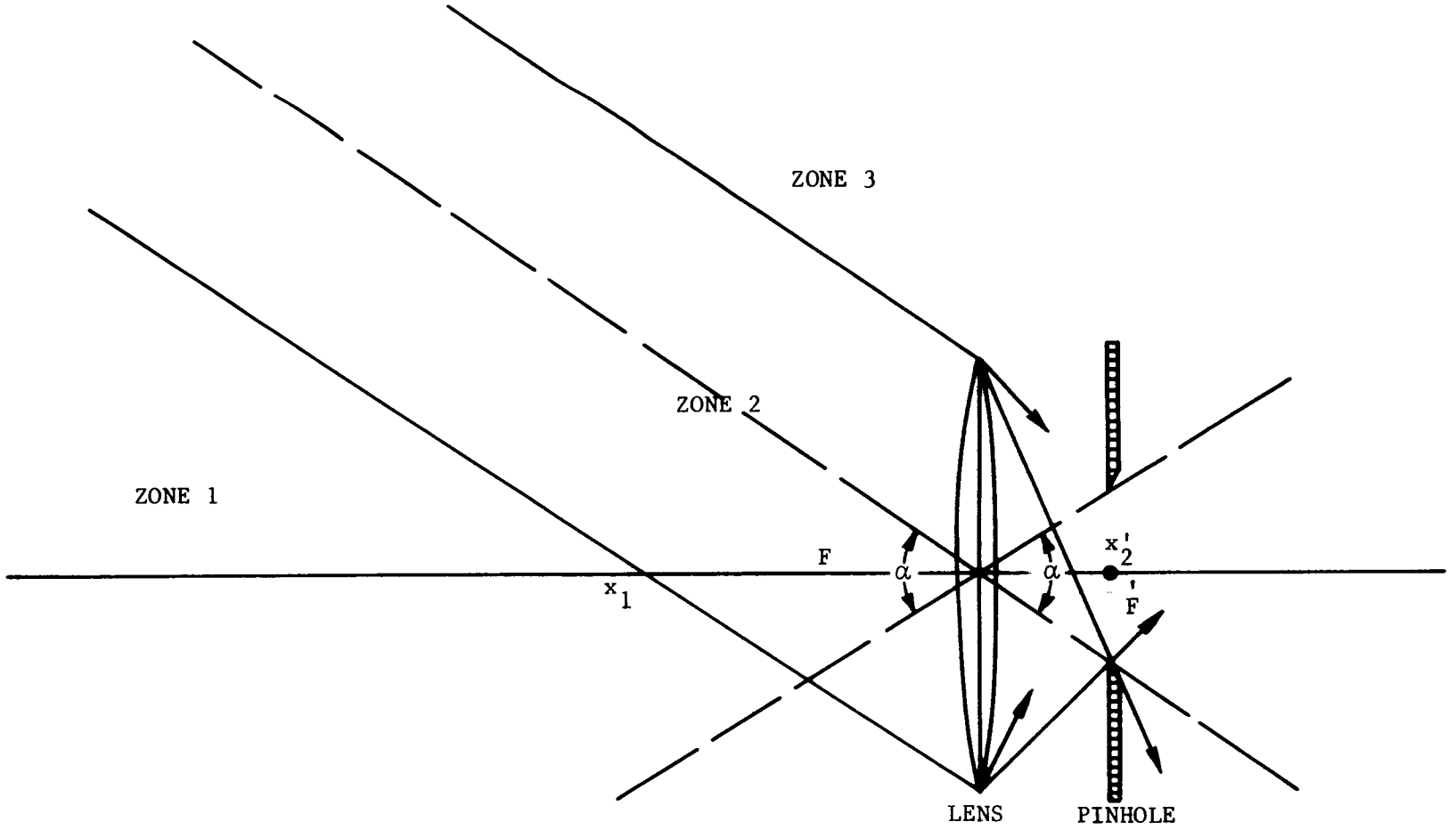

R11218

FIGURE 57. FIELD OF VIEW GEOMETRY, PINHOLE IN FOCAL PLANE, $X_2 = \infty$

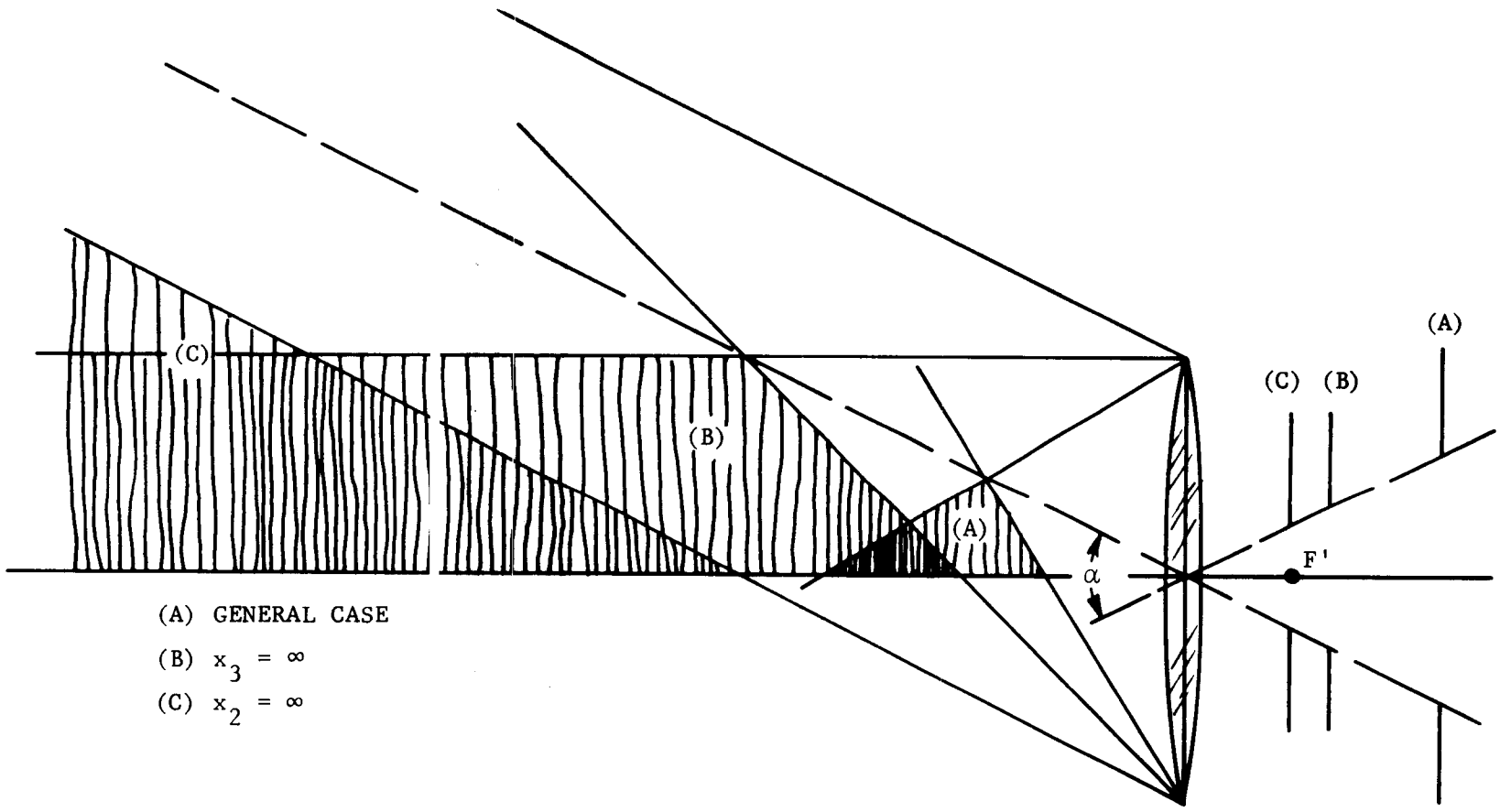

R11182

FIGURE 58. COMPARISON OF FIELDS OF VIEW FOR CONSTANT ANGULAR RESOLUTION

and combining equations (2) and (3) gives

$$\alpha = D \frac{x_2' - x_3'}{x_2' x_3'} \tag{5}$$

Gaussian lens equations for the points shown in Figure are

$$\frac{1}{f} = \frac{1}{x_1} + \frac{1}{x_1'} \tag{6}$$

$$\frac{1}{f} = \frac{1}{x_2} + \frac{1}{x_2'} \tag{7}$$

$$\frac{1}{f} = \frac{1}{x_3} + \frac{1}{x_3'} \tag{8}$$

Combining first Equations (6) and (7) gives

$$\frac{1}{x_1} - \frac{1}{x_2} = \frac{1}{x_2'} - \frac{1}{x_1'} = \frac{x_1' - x_2'}{x_1' x_2'} \tag{9}$$

and then Equations (7) and (8) gives

$$\frac{1}{x_2} - \frac{1}{x_3} = \frac{1}{x_3'} - \frac{1}{x_2'} = \frac{x_2' - x_3'}{x_2' x_3'} \tag{10}$$

Combining Equations (4) with Equation (9) and rearranging gives

$$x_1 = \frac{x_2 D}{D + x_2 \alpha} \tag{11}$$

Combining equation (5) with Equation (10) and rearranging gives

$$x_3 = \frac{x_2 D}{D - x_2 \alpha} \tag{12}$$

If the far field is at infinity, as in Figure 56b, then $x_3 = \infty$ and Equation (12) represents the matched condition.

$$\alpha = \frac{D}{x_2} \tag{13}$$

Inserting this into Equation (11) yields

$$x_2 = 2x_1 \tag{14}$$

x_2 is twice the distance of the near field and is called the hyperfocal distance. Also, when $x_3 = \infty$ then from Equation (8)

$$x_3' = f \tag{15}$$

If the lens is stopped down by an iris, then Equations (1) and (2) become inequalities.

$$\frac{D}{x_1'} < \frac{D_o}{x_1' - x_2'} \tag{16}$$

$$\frac{D}{x_3'} < \frac{D_o}{x_2' - x_3'} \tag{17}$$

Proceeding as before leads to

$$x_1 > \frac{x_2 D}{D + x_2 \alpha} \tag{18}$$

$$x_3 < \frac{x_2 D}{D - x_2 \alpha} \tag{19}$$

Letting $x_3 = \infty$ gives the inequality

$$\alpha > \frac{D}{x_2} \tag{20}$$

The relationship between x_1 and x_2 similar to Equation (14) is indeterminate.

For the case where the pinhole is placed in the focal plane, as in Figure 57.

$$x_2' = f \quad ; \quad x_2 = \infty \tag{21)(22}$$

Equation (3) then becomes

$$\alpha = \frac{D_o}{f} \tag{23}$$

Furthermore, combining Equations (4), (6), and (21)

$$\alpha = \frac{D}{x_1} \tag{24}$$

The focal ratio, f-stop, or f/number of lens is designated here as n_f and is the ratio of the focal length to the lens diameter.

$$n_f = \frac{f}{D} \tag{25}$$

The lateral magnification is m.

$$m = \frac{x_1'}{x_1} \tag{26}$$

Design trade-off parameters of basic concern are the diameter of the lens of the viewing optics (and correspondingly the dimensions of the scanning mechanism) and the responsivity and noise characteristics of available sensors. The parameters which are chosen must be such that at the low light level and with reasonably small optics, radiation sufficient to provide an adequate signal-to-noise ratio is received by the sensor at the necessary scanning rates.

5.3.3 PHOTOMETRY

The spectral radiant flux incident on a facsimile camera, positioned as in Figure 59 at a distance x from the surface of spectral radiance N_λ, is given by

$$P_{i_\lambda} = N_\lambda \, \Omega_D \, \Omega_S \, x^2 \tag{27}$$

where Ω_D is the solid angle subtended by the viewing optics at the surface and Ω_S is the solid angle subtended by the instantaneous field of view of the camera. Therefore, for a lens of diameter D and instantaneous field of view (i.e., angular resolution) α (defined by a circular pinhole of diameter D_o a distance x_2' behind lens)

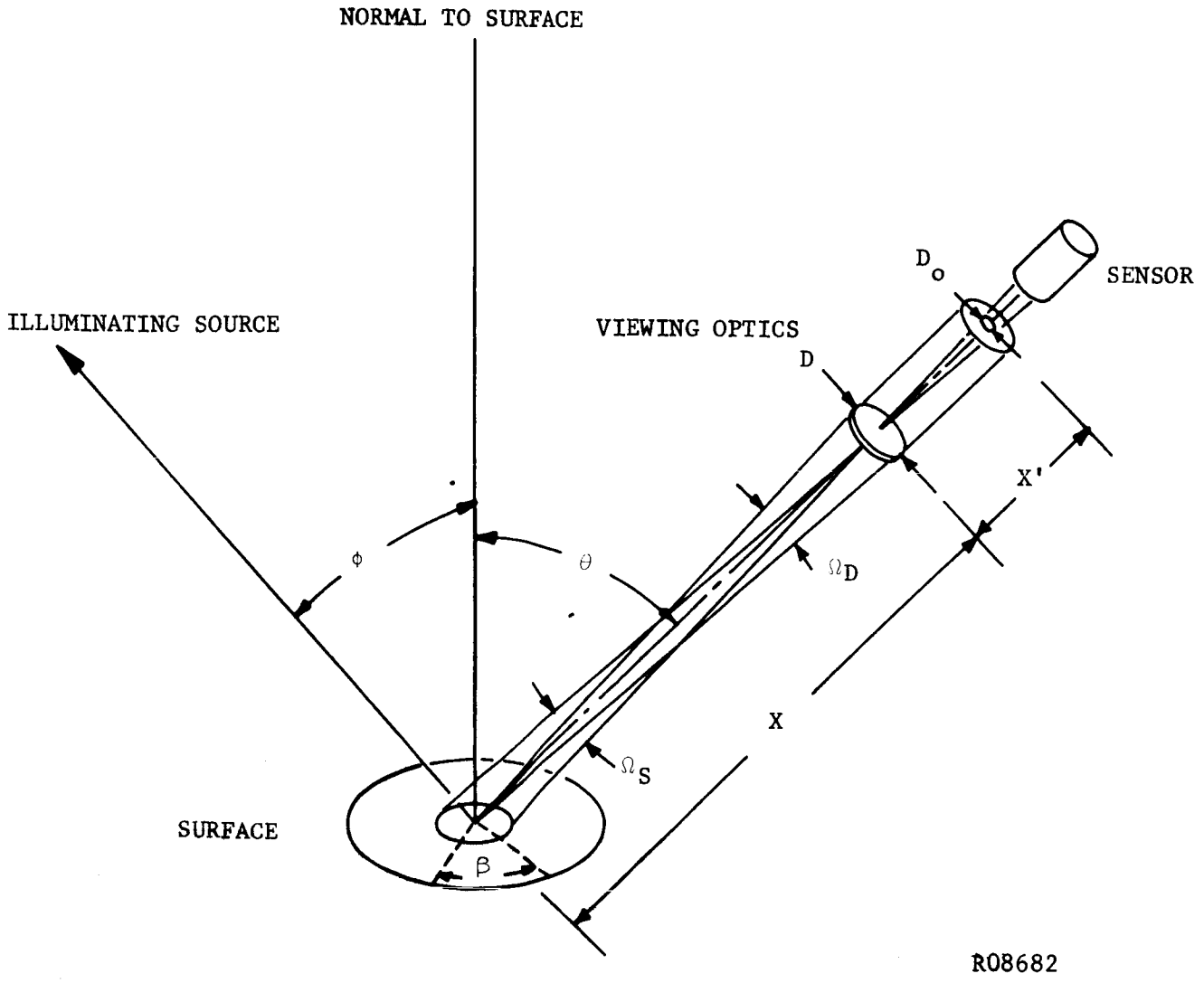

FIGURE 59. GEOMETRY OF IRRADIANCE OF HRF CAMERA

$$\Omega_D = (\frac{\pi}{4}) \frac{D^2}{x^2} \tag{28}$$

$$\Omega_S = \frac{\pi}{4} (\frac{D_o}{x_2'})^2 = \frac{\pi}{4} \alpha^2 \tag{29}$$

The spectral radiance N_λ of the surface is defined as the flux reflected (or emitted) per unit solid angle per unit area perpendicular to the viewing direction per unit wavelength. If the power spectral density of the illuminating flux in radiant flux per unit area per unit wavelength is denoted by S_λ, where it is assumed that the source of this flux is sufficiently far removed so that the rays from it may be considered parallel, then the radiance is given by

$$N_\lambda = \rho \, S_\lambda \, \xi \tag{30}$$

The reflectance of the surface, ρ, is the ratio of reflected to incident flux, and the goniometric characteristic, ξ, may be a function of the viewing angle θ, the azimuth angle β, and the lighting angle ϕ (Figure 59).

In the spectral regions considered here, both ρ and ξ are assumed to be independent of wavelength. For a Lambertian (diffuse) reflector

$$\xi = (\frac{1}{\pi}) \cos \phi \tag{31}$$

In other cases ξ may be more complex, such as the apparent scattering that has been observed on the moon and Mars when viewed from the Earth; it has been postulated to obey the photometric function Φ, shown graphically in Figure 60.

$$\xi = (\frac{1}{\pi}) \Phi \tag{32}$$

Combining Equations (27), (28), (29), and (30), therefore, and if the transmissibility of the optics is K, then the spectral radiant flux received by the sensor is

$$P_\lambda = (\frac{\pi}{4})^2 \, K \, D^2 \, \alpha^2 \, \rho \, \xi \, S_\lambda \text{ (watts/micron)} \tag{33}$$

The radiance can be expressed alternatively in terms of the luminance of the surface.

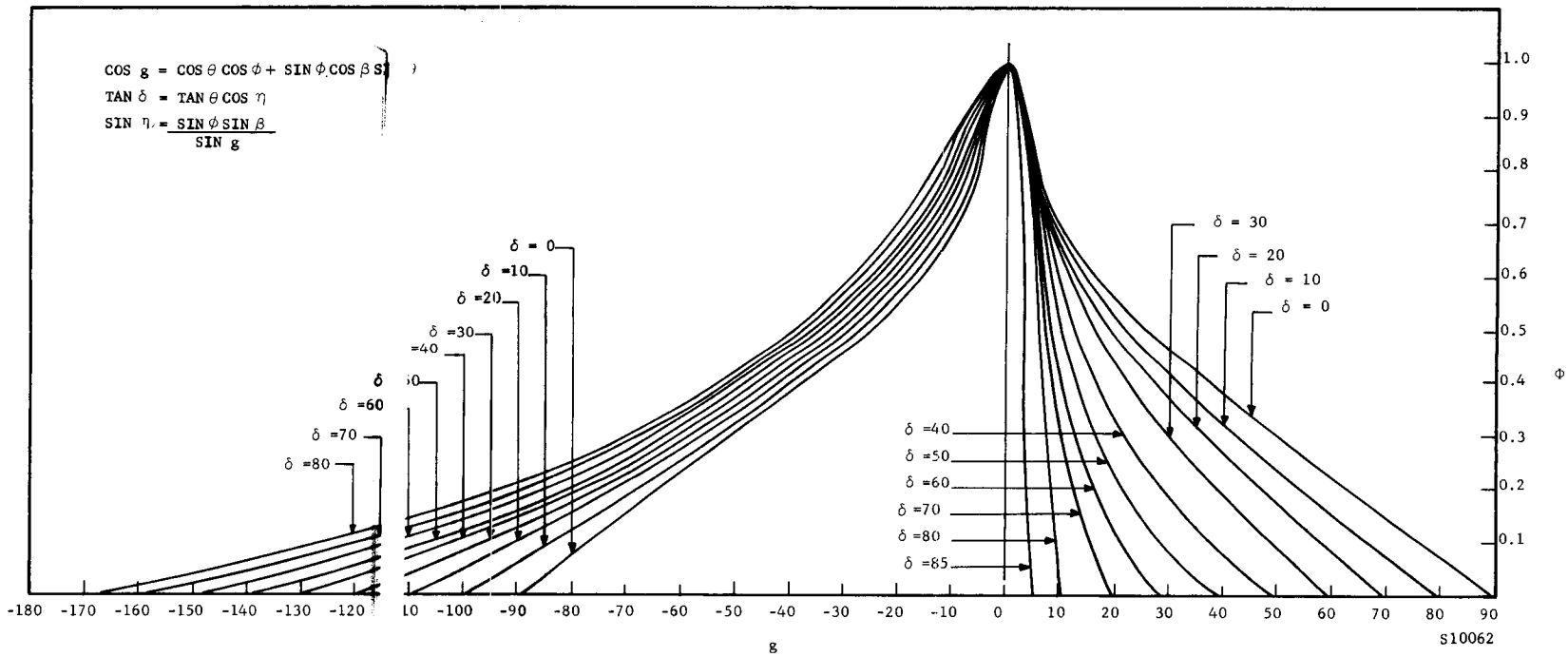

FIGURE 60. PHOTOMETRIC FUNCTION OF LUNAR SURFACE

FIGURE 60. PHOTOMETRIC FUNCTION OF LUNAR SURFACE

Luminance is defined as the radiance detectable by the human eye and is given by

$$B = 929\,\pi \int \rho\,\xi\,S_\lambda\,\epsilon_\lambda\,d\lambda \text{ foot-lamberts} \tag{34}$$

where ϵ_λ is the luminous efficiency of the "standard observer" in lumens/watt.

Inasmuch as $\rho\,\xi$ has been assumed independent of wavelength, Equation (34) can be solved for that product: for solar radiation outside the earth's atmosphere,

$$\rho\,\xi \approx \frac{8}{\pi} \times 10^{-5}\,B \tag{35}$$

whereas for solar radiation at sea level (at noon on a clear day)

$$\rho\,\xi \approx \frac{10}{\pi} \times 10^{-5}\,B \tag{36}$$

If the upper and lower luminance extremes in a scene are B_1 and B_2, the corresponding number of grey shades, S, is defined by

$$B_1/B_2 = 2^{S/2} \tag{37}$$

In most applications, the HRF camera must respond linearly over a dynamic range (B_1/B_2) of nearly 100:1

According to well-known laws of illumination, the spectral radiant solar flux outside of the Mars atmosphere is simply that outside of the Earth's atmosphere decreased by the square of the ratio of distances of the two planets from the Sun. In terms of irradiance,

$$(S_\lambda)_{Mars} = \left| \frac{x_{Earth}}{x_{Mars}} \right|^2 (S_\lambda)_{Earth} \text{ watts/cm}^2 \tag{38}$$

Figure 61 shows S_λ at both Earth (1 AU) and Mars (perihelion = 1.381431 AU, aphelion = 1.665951 AU, semi-major axis = 1.523691 AU).

The variation of the distance of Mars from the Sun is given in Figure 62 for the (Earth) years 1969 - 1973.

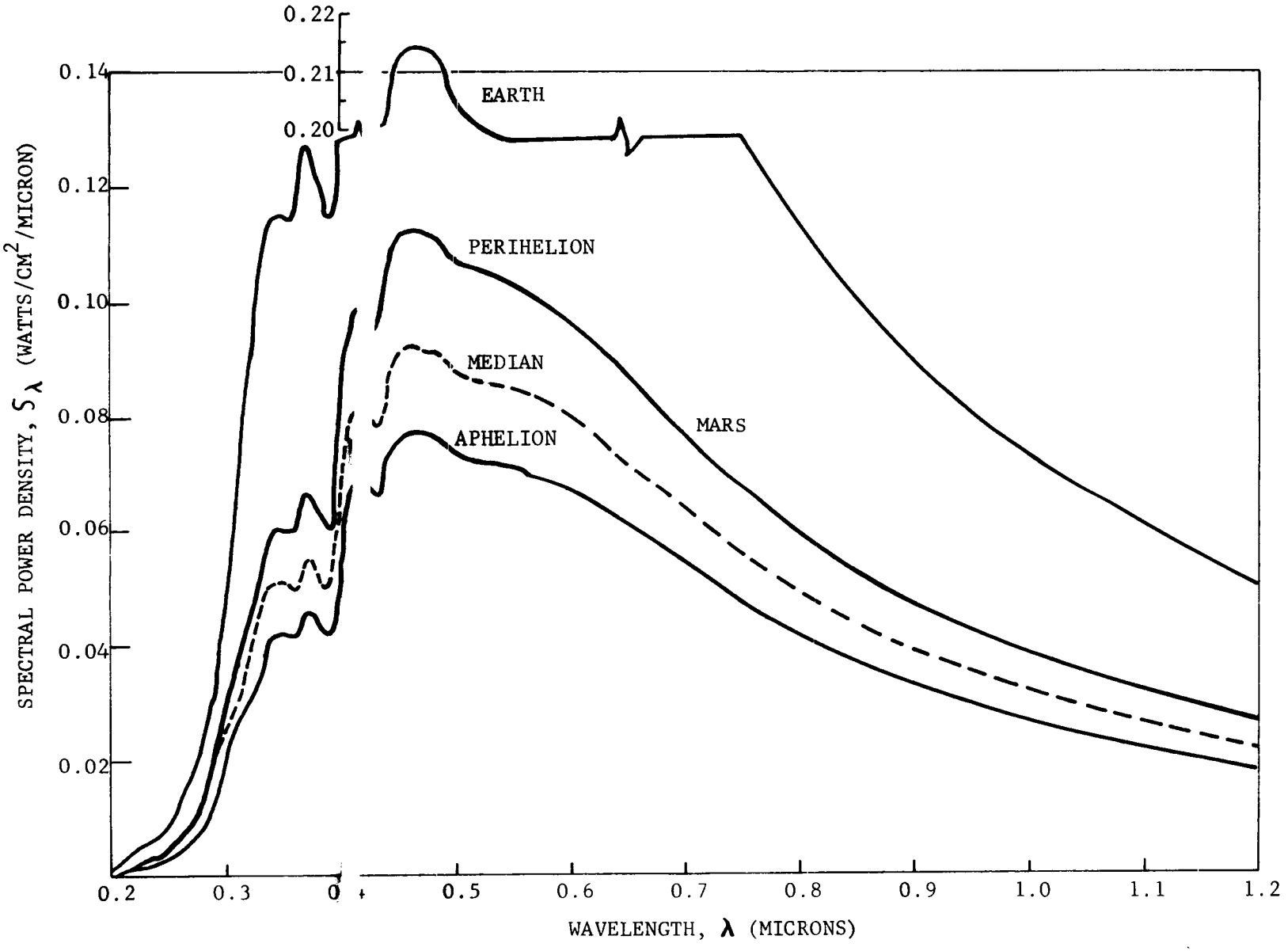

FIGURE 61. SOLAR IRRADIANCE AT EARTH AND MARS

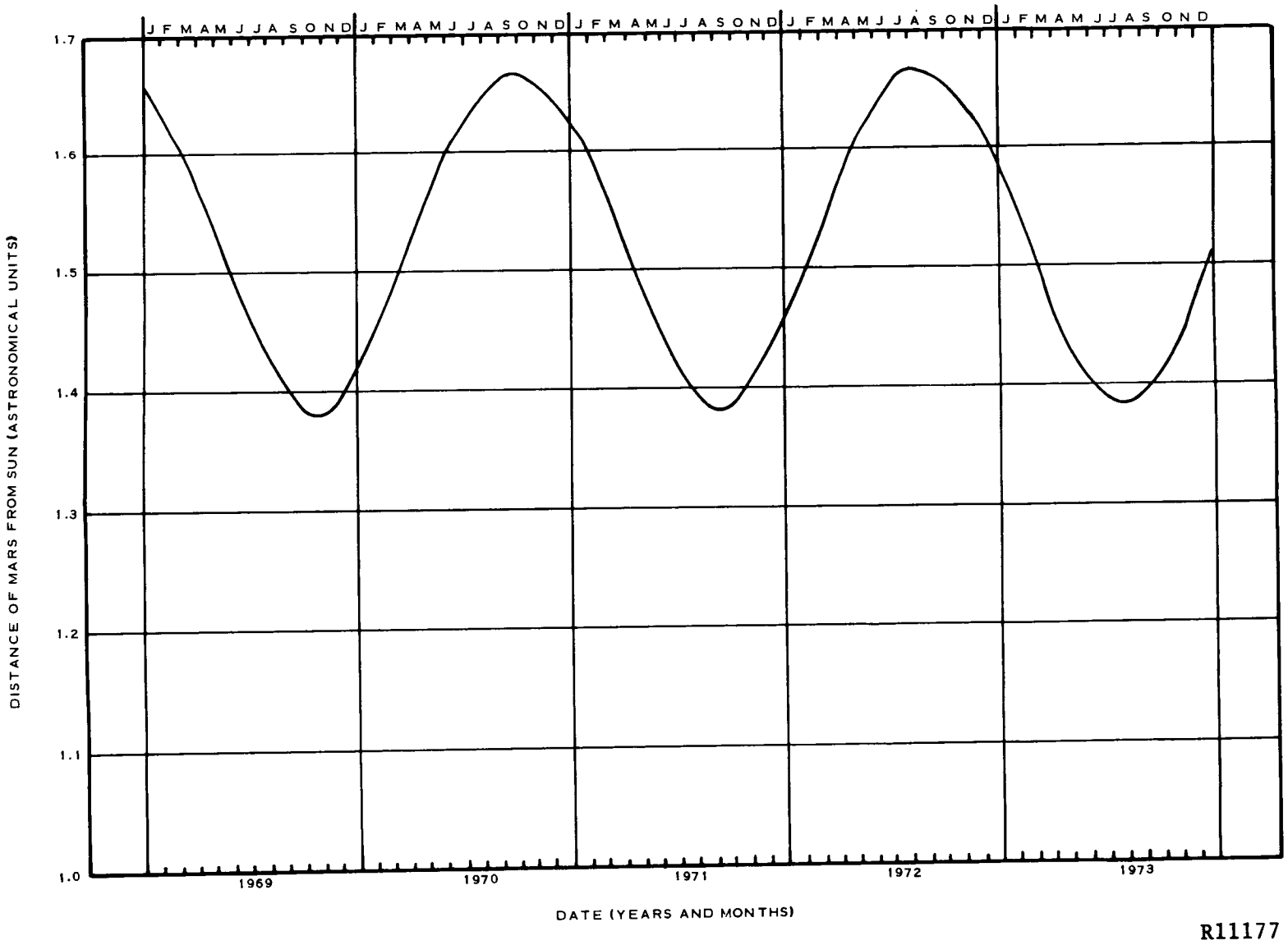

FIGURE 62. DISTANCE OF MARS FROM THE SUN, 1969 - 1973

The spectral radiance of the Martian surface as seen on the surface is given by

$$N_\lambda = \rho_\lambda \xi \sigma_\lambda S_\lambda \text{ watts/cm}^2\text{/steradian/micron} \quad (39)$$

This is derived from Reference (1). The scattering characteristic ξ of the Martian surface has been postulated to be the same as that for the lunar surface:

$$\xi = \frac{1}{\pi} \Phi \quad (40)$$

The photometric function Φ is shown in Figure 60. It is seen to be wavelength independent. The reflectivity ρ_λ is the ratio of reflected to incident flux. The transmission coefficient σ_λ of the Martian atmosphere is given by

$$\sigma_\lambda = P_\lambda^{\sec \phi} \quad (41)$$

where P_λ has been given in Reference (1) and ϕ is the lighting angle (angle to sun from local vertical). Values of ρ_λ and σ_λ are given in Table 5.3-I and Figure 63.

The radiance of the surface is N_λ:

$$N_\lambda = \rho_\lambda \xi \sigma_\lambda S_\lambda$$

The results in Figures 64 through 67 are for combinations of:

(1) Sun angle to vertical ϕ = 20 degrees, 40 degrees, and 60 degrees.

(2) Camera angle to vertical θ = 0 degree, 30 degrees, and 75 degrees.

(3) Angle between the sun and the camera φ = 0 degree, 90 degrees, and 180 degrees.

The shift towards the red is accounted for by the rise in reflectivity with wavelength. The greatest illumination levels result for the sun directly overhead. A dynamic range of 20:1 results for these combinations.

TABLE 5.3-I

MARTIAN RADIOMETRIC CHARACTERISTICS

λ	ρ_λ	σ_λ				
Microns		(p_λ) $\phi = 0^\circ$	20°	40°	60°	80°
< 0.3	0.240	0.000	0.000	0.000	0.000	0.000
0.350	0.240	0.025	0.020	0.008	0.001	0.000
0.405	0.240	0.051*	0.042	0.021	0.003	0.000
0.425	0.240	0.119*	0.104	0.062	0.014	0.000
0.455	0.242*	0.306*	0.284	0.213	0.094	0.001
0.460	0.246*	0.334*	0.311	0.239	0.112	0.002
0.495	0.272*	0.453*	0.430	0.356	0.205	0.015
0.520	0.289*	0.540*	0.519	0.447	0.292	0.029
0.543	0.335*	0.599*	0.579	0.512	0.359	0.055
0.580	0.405*	0.692*	0.676	0.618	0.478	0.120
0.598	0.442*	0.711*	0.695	0.641	0.505	0.140
0.640	0.528*	0.741*	0.727	0.676	0.549	0.178
0.700	0.640	0.780	0.768	0.723	0.608	0.239
0.800	0.840	0.790	0.778	0.735	0.624	0.257
> 0.9	1.000	0.800	0.788	0.747	0.640	0.276

*Reference (1)

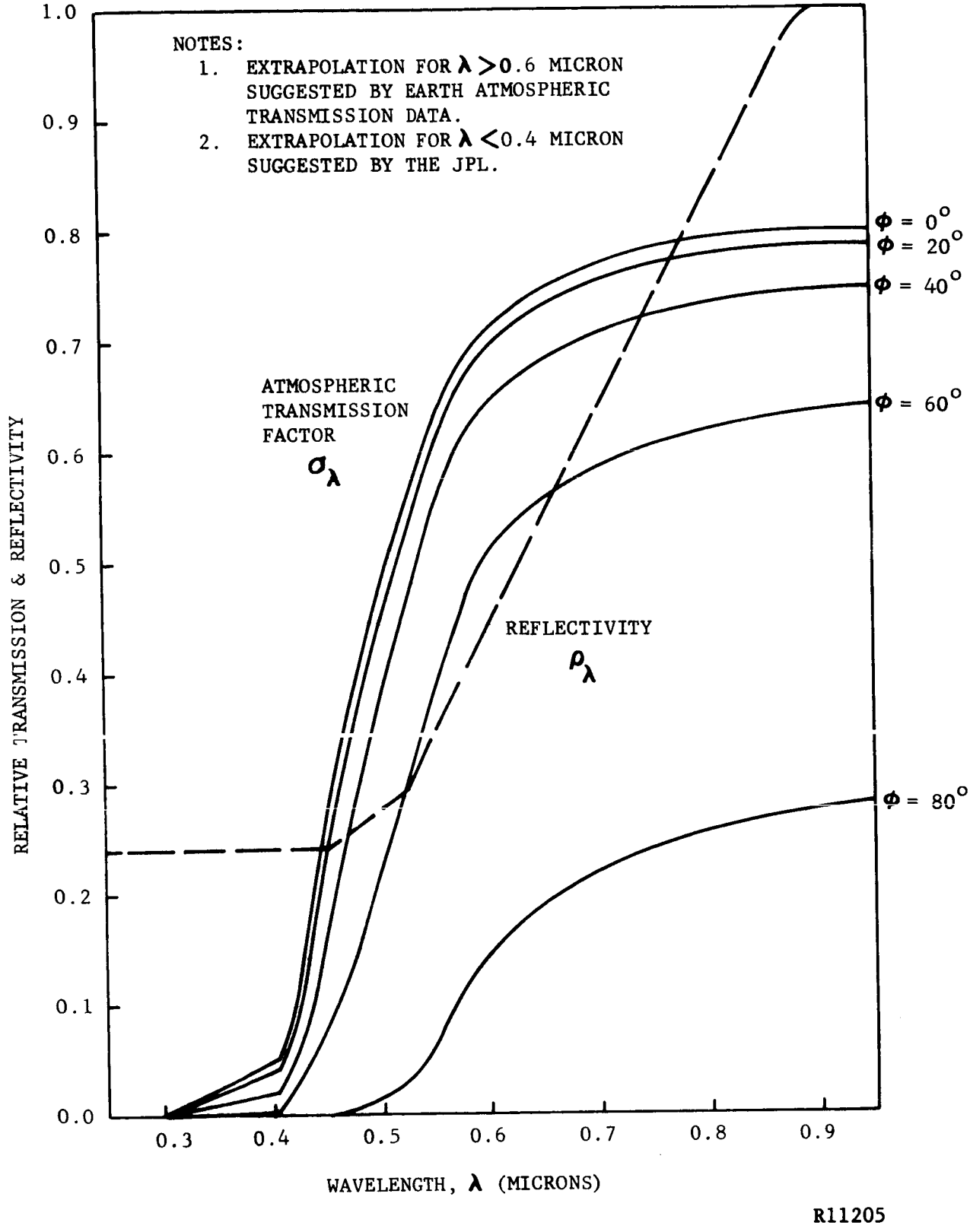

FIGURE 63. SURFACE REFLECTIVITY AND ATMOSPHERIC TRANSMISSION OF MARS

5.3.4 SENSORS

The rms signal current I_s generated in the sensor by the flux of Equation (33) is proportional to the responsivity R_λ (amperes/watt) of the sensor. Integrating over the entire spectrum,

$$I_s = (\pi/4)^2 \, K \, D^2 \, \alpha^2 \, \rho \, \xi \int S_\lambda \, R_\lambda \, d\lambda \text{ amperes} \qquad (42)$$

The minimum detectable signal is that which barely exceeds the noise generated within the sensor and associated electronics. A fundamental source of noise is the statistical fluctuation of the signal itself. The rate of arrival of photons from a source is statistically fluctuating, and the magnitude of this fluctuation sets a limit on the threshold signal-to-noise ratio of a detector. Although quanta obey Bose-Einstein statistics rather than classical statistics, in the wavelength region of interest here the difference between the two models of random variables is negligible. If t is the dwell time over which the camera observes an average of n protons, then the average rate of arrival of photons is n/t, and according to the model the rms fluctuation is $\sqrt{n/t}$. The corresponding rms fluctuation in the number of photoelectrons generated in the detector is $\sqrt{N_e}$. For an ideal quantum detector, therefore, the average signal-to-rms noise ratio is

$$\frac{N_e}{\sqrt{N_e}} = \sqrt{N_e} = \sqrt{\frac{t}{e} \, I_s} \qquad (43)$$

where e is the electron charge in coulombs.

In real detectors, additional noise mechanisms are always present so that the signal-to-noise ratio is less than ideal. Internal noise mechanisms within a solid-state detector and its electronic circuits usually appear as low frequency variations, their amplitude diminishing with frequency ("1/f noise"). For this reason, mechanical interruption by chopping the incident radiant flux is normally required in order to place the electrical signal at a higher "noiseless" frequency region where it may be properly amplified. Subsequently, the signal is demodulated to its normal low frequency.

Because the noise mechanism associated with solid-state detectors is easily identifiable and predictable, a host of descriptive performance parameters have been suggested, foremost of which are detectivity D^* and

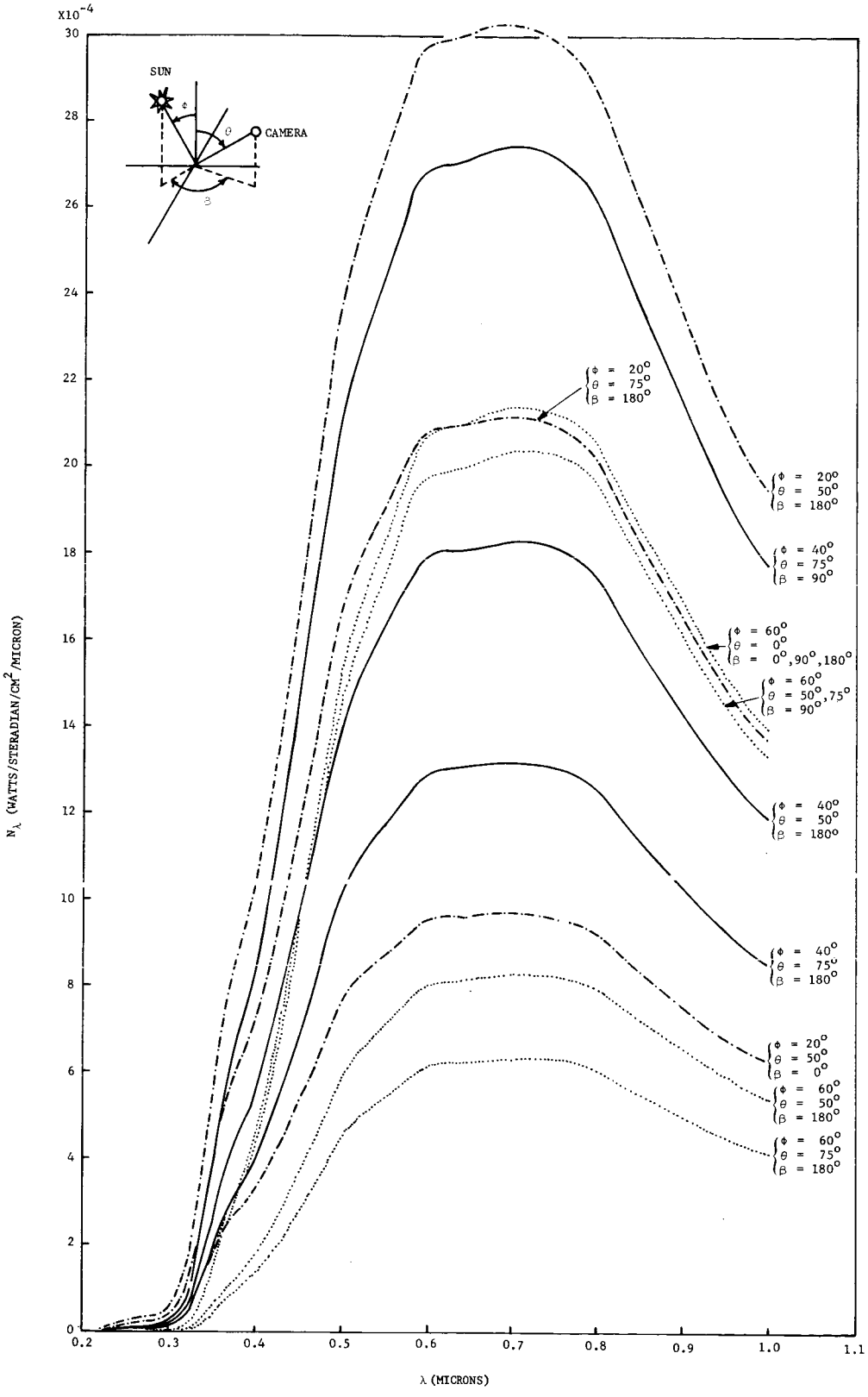

FIGURE 64. BALANCE OF MARS SURFACE

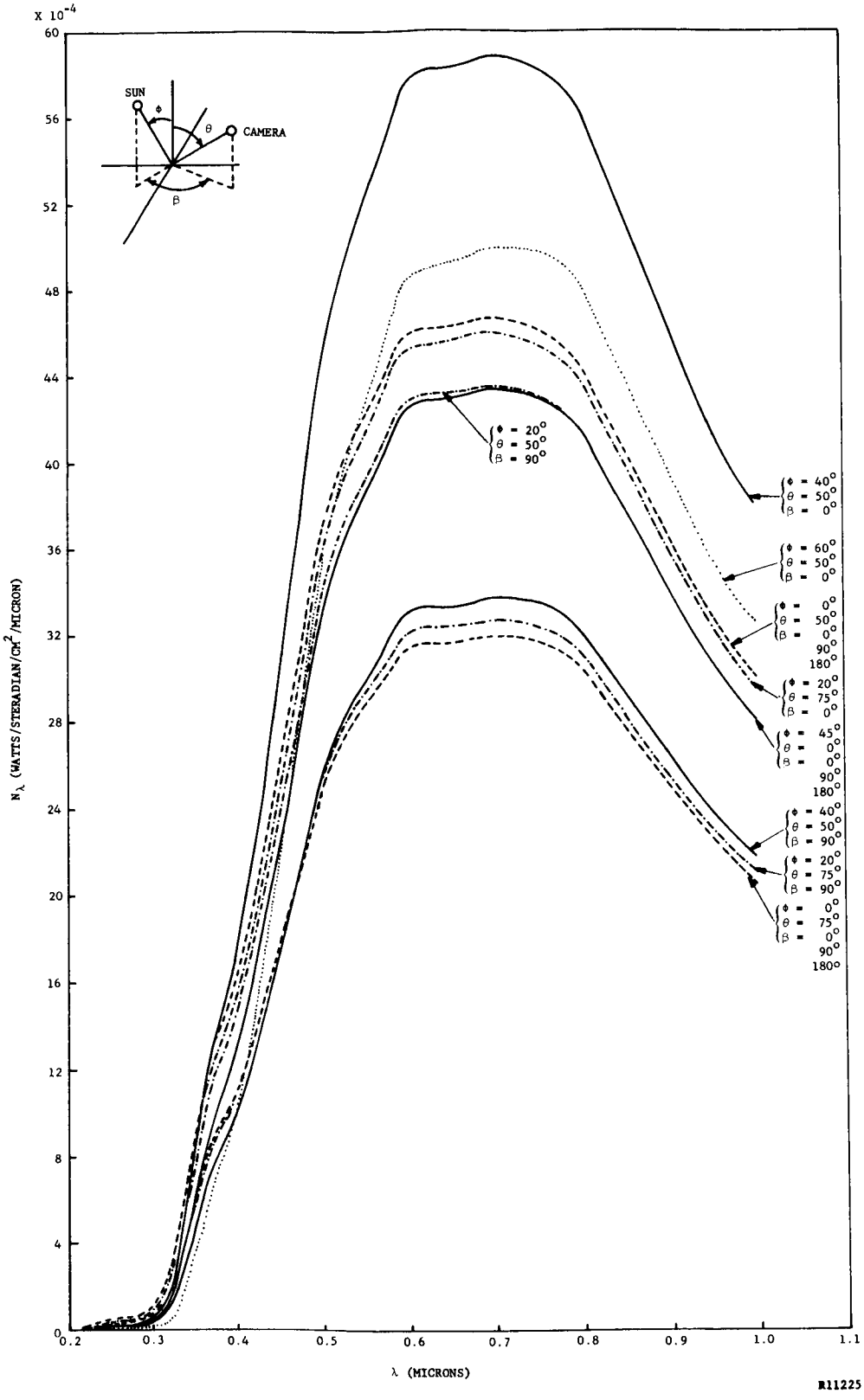

FIGURE 65. BALANCE OF MARS SURFACE

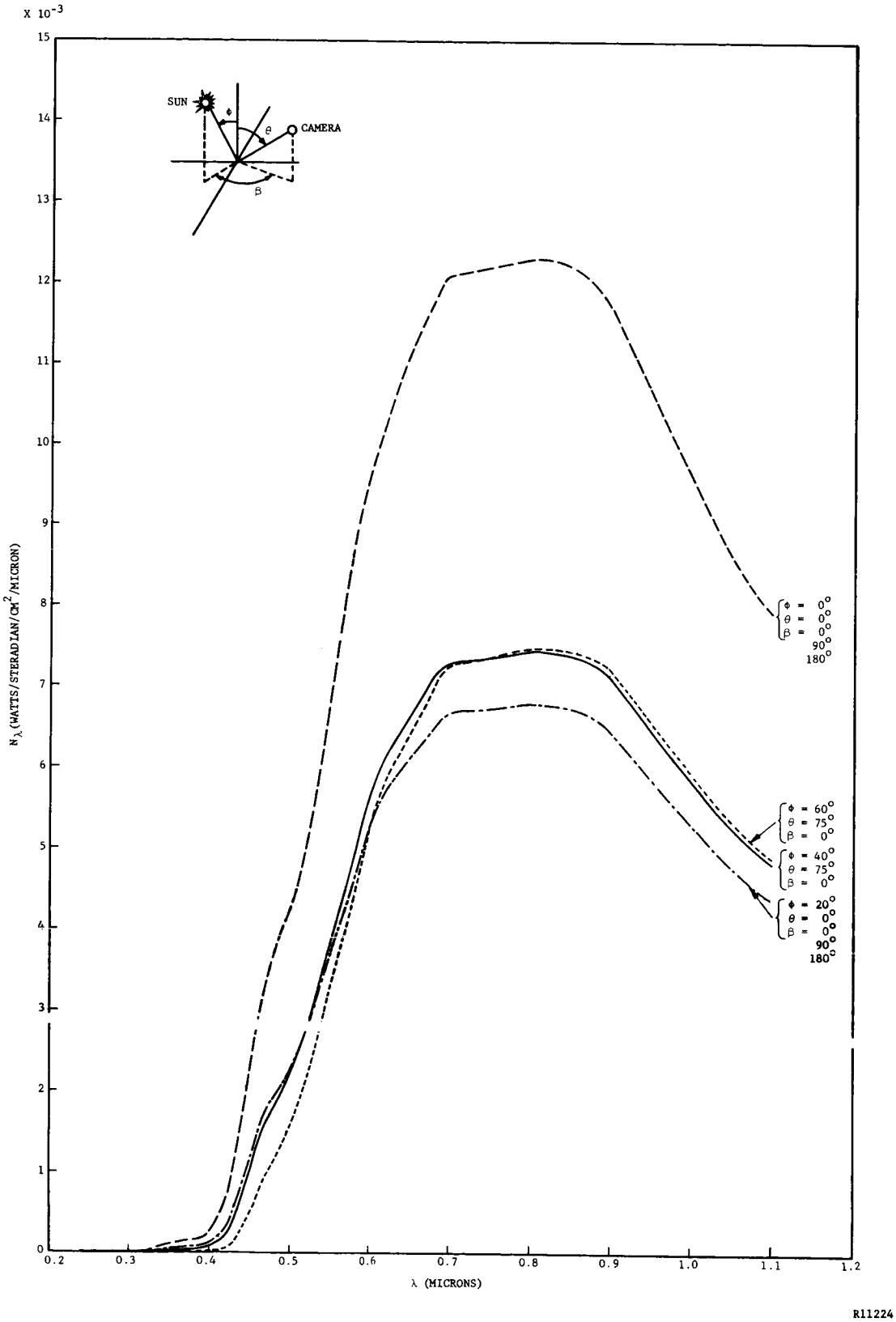

FIGURE 66. BALANCE OF MARS SURFACE

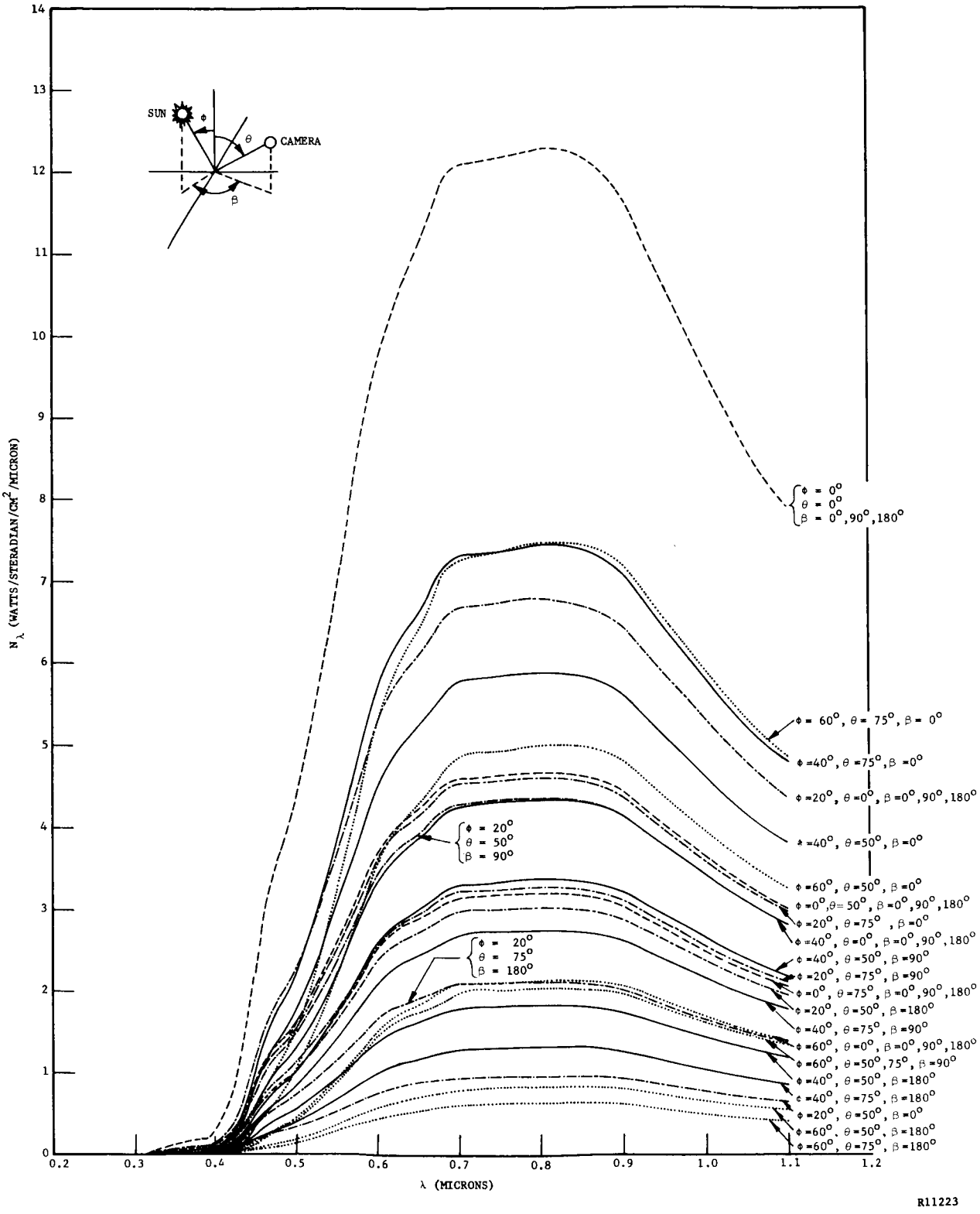

FIGURE 67. BALANCE OF MARS SURFACE

noise equivalent power NEP. Complete system performance may be specified in these terms. Monochromatic detectivity D* (pronounced D-star) has been defined for a 1 cps bandwidth:

$$D^*_\lambda = (A\Delta f)^{\frac{1}{2}} \frac{dV_s/V_n}{P_\lambda \, d\lambda} \quad \text{cm-cps}^{\frac{1}{2}}\text{/watt} \tag{44}$$

where

A = sensor area illuminated during laboratory measurement of D^*, cm^2

Δf = noise bandwidth of circuit in which sensor is to operate, cps

dV_s = differential signal resulting from the radiation $P_\lambda \, d\lambda$, rms volts

V_n = noise, rms volts

P_λ = radiation on the sensor per unit wavelength, watts/micron

$d\lambda$ = differential wavelength, microns

After rearranging, integrating, and substituting Equation (33), this becomes

$$V_s/V_n = \frac{(\pi/4)^2 \, K \, D^2 \, \alpha^2 \, \rho \, \xi \, D^*_{max}}{\sqrt{\Delta f}} \int S_\lambda \, D^*_{\lambda,n} \, d\lambda \tag{45}$$

The normalized detectivity $D^*_{\lambda,n}$ is related to the peak or maximum detectivity by

$$D^*_\lambda = D^*_{max} \, D^*_{\lambda,n} \tag{46}$$

The "effective power" P_e watts on the sensor includes only that illumination from the source which produces an output from the detector. Denoting the sensor transfer characteristic or responsivity by R_λ then

$$P_e = \int P_\lambda \, R_{\lambda,n} \, d\lambda \tag{47}$$

where

$$R_\lambda = R_{max} \, R_{\lambda,n}$$

But $D^*_{\lambda,n} = R_{\lambda,n}$

$$P_e = \left(\frac{\pi}{4}\right)^2 K D^2 \alpha^2 \rho \xi R_{max} \int S_\lambda D^*_{\lambda,n} d\lambda \quad (48)$$

Another parameter that is used to describe sensor performance is Noise Equivalent Power NEP. It is the input required to produce a unity signal-to-noise ratio:

$$(NEP)_\lambda = \frac{P_\lambda d\lambda}{dV_s/V_n} \quad (49)$$

Again, the value of NEP is not a constant but must be associated with a particular spectral source. If the detector is intended to be used with tungsten lighting, the NEP will usually be specified as being measured with black bodies ranging from 2870 degrees K to 2950 degrees K.

If the equivalent noise input is expressed in luminous flux, lumens, instead of radiant flux, watts, then it may be called Noise Equivalent Lumens NEL and

$$D^*_{max} = \left(\frac{\sqrt{A\Delta f}}{NEL}\right) r \quad (50)$$

where r is a conversion factor from lumens to watts which is tabulated for some detectors.

Because of the limited quantity of data and since there is no requirement to generate that data at super speeds, there does not appear to be a minimal bandwidth constraint on data acquisition. Also, if a memory system is used as a time buffer prior to transmission, then the only possible restriction could be to record motion such as dust storms. However, for this presentation that condition has not been assumed to be within a definition of the MFC mission. Consequently, since image point dwell time may be long there does not appear to be any great need to quantitatively evaluate the high impact capability of an "exotic" detector such as a multiplier phototube which is considerably more sensitive and "faster" than a solid state detector. Also, photoemissive surfaces may be degraded or even damage by direct high intensity radiation; they also require high voltage dc-dc convertors.

Cooled solid-state detectors are not seriously considered here because of the added complexity of storing low temperature liquids for cryogenics

into which they must be immersed for sensitive operation. Lead telluride, tellurium and germanium are therefore not considered.

Another criterion for selection is that based upon reasonable mission objectives it would not appear wise for the first lander on the Mars surface to conduct imaging in any wavelength spectrum other than either the visible or near infrared region. The detector should exhibit a major portion of its useful spectral response between 0.3 and 1.5 microns so that it can be efficiently matched to the radiation spectrum. This eliminates indium autimonide, indium arsenide, lead sulfide, and lead selenide.

Thermocouples, thermistors and Golay cells although operable in the uncooled state are much to insensitive and slow to warrant serious consideration. The detectors that are left are shown in Table 5.3-II Known characteristics considered to be of major importance are peak detectivity D^*_{max} (λ max, f_c, 1); wavelength at which D^*_{max} occurs, λ max; chopping frequency, f_c; sensitive area, A; a figure of merit as a measure of sensitivity defined by

$$\text{Sensitivity} = \frac{\int D^*_{max} N_{\lambda,n} \, d\lambda}{A^{\frac{1}{2}}} \quad \text{cps}^{\frac{1}{2}}/\text{watt} \qquad (51)$$

where $N_{\lambda,n}$ is the relative radiance spectrum on the Martian surface; time constant; wavelength region; and typical load resistance. Although information on temperature ranges for both stable (linear) operation and unit survival and shock resistance is of vital importance, data on it is so sparse that it is virtually non-existent for most types.

Other parameters which are either redundant or have second order effects are

(1) output impedance,

(2) voltage or current requirements,

(3) dynamic range,

(4) size and shape of housing,

(5) bandwidth, and

(6) relative spectral response.

TABLE 5.3-II

PARAMETRIC COMPARISON OF SOLID-STATE DETECTORS FOR HRF CAMERA

TYPE	SPECTRAL REGION, μ	D^*_{max}, cm-cps$^{\frac{1}{2}}$/watt	λ_{max}, μ	CHOPPING FREQUENCY, cps	SENSITIVE AREA X 10^4, cm^2	SENSITIVITY+, cps$^{\frac{1}{2}}$/WATT	TIME CONSTANT, MILLISECS	LOAD RESISTANCE, MEGOHMS	MANUFACTURER
Si	0.4-1.2	5.3×10^{11}	0.90	600	2	1.3×10^{13}	5	51	TI (LSX-511)
GaAs	0.4-0.9	2.9×10^{11}	0.80	90	77	1.2×10^{11}	1,000	5	Philco
GaAs	0.4-0.9	4.0×10^{11}	0.80	400	100	1.5×10^{11}	1,000	10	Philco
Cu-Cu_2O	?	1.1×10^{11}	0.52	90	380	?	670	1	Philco
Tl_2S	0.5-1.3	2.2×10^{12}	0.90	90	?	?	530	?	---
Se-SeO	0.3-0.9	1.2×10^{11}	0.55	90	?	?	910	?	---
Si	0.4-1.2	4.0×10^{12}	0.85	90	2500	2.9×10^{12}	5,800	5	RCA Canada
Si	0.4-1.2	5.0×10^{12}	0.55	270	2500	3.6×10^{12}	5	?	ENL(ED5500)
Si	0.4-1.2	5.0×10^{12}	0.70	270	2500	3.6×10^{12}	5	?	ENL(ED5-9000)
CdSe	0.3-0.9	2.4×10^{11}	0.75	90	100	2.0×10^{10}	26,000	1	RCA
CdS	0.3-0.6	1.2×10^{11}	0.55	90	28	1.4×10^{13}	290,000	1	PEMC

+See text.

Because of the elimination process just discussed, of the parameters listed in Table5.3-IIthose qualities that should receive prime attention are (1) a medium to low time constant, (2) very small sensitive area, (3) low resistance, (4) high sensitivity, and (5) medium to high chopping frequency.

Even though the sensitive areas for both the cadium sulfide and cadmium selenide detectors in Table 5.3-II tend to assure a confident estimate in extrapolated performance to the required 10^{-4} cm^2, their time constants are much too large to be useful. On the other hand time constants of the ENL silicon detector are excellent but linear extrapolation from large to small detector operation is not justified. Their sensitivity values may not be a realistic measure of performance for small chips. For both of the above reasons the RCA silicon detector is also a risky choice. Of those remaining not enough is known about thallous sulfide, selenium-selenium oxide and copper-cuprous oxide to allow any of them to be selected. Finally between gallium arsenide, and TI silicon the choice is clearly the latter even though it has been reported that Philco's GaAs is stable to 230°F as compared to 145°F for TI's silicon.

In summary, the LSX-511 silicon photo transistor is selected as the detector model for this study. It has good sensitivity while uncooled and being used at moderate scanning rates. The data quoted is very reliable for the small area and high chopping frequency since it recently was put through exhaustive test and evaluation for use with the Lunar Facsimile Capsule. It is relatively inexpensive, and considerable experience has been logged with large quantities of this detector for a multiplicity of uses. This detector's spectral transfer characteristic is a good match to the solar spectrum and its dynamic response is much wider than the electronic circuitry. Because of its small physical size (housing) and mass it has been impulsively shocked at many thousands of g's without incurring damage or change in operation. Silicon transistors were also used in the Lunar Seismometer Capsule for Ranger Flights 3, 4, and 5 because they could survive the extreme temperatures of sterilization while germanium could not.

5.3.5 PERFORMANCE

This section summarizes by way of a set of illustrative graphs the photometry, optics and picture coverage as trade-off performance of the HRF camera.

Figure 68 shows the spectral distribution of radiation from the sun outside of both the Earth's and Mars' atmospheres. The relative shapes of the curves are identical. The absolute curves differ merely by the loss in radiation with the square of the distance from its source, the sun.

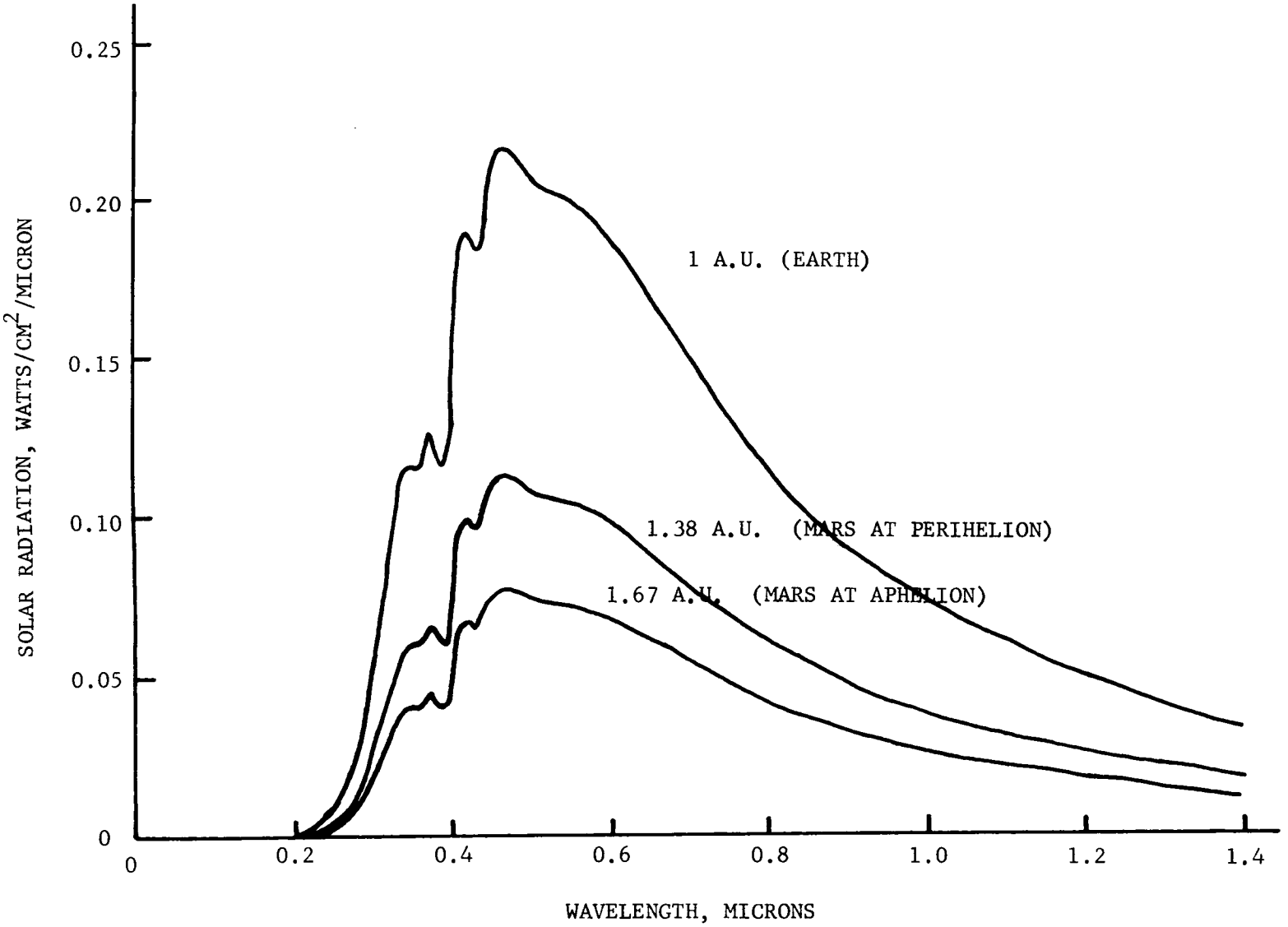

SUNS RADIATION OUTSIDE OF ATMOSPHERE

FIG. 68

Based upon published data, both the atmospheric attenuation and reflectance of Mars are given in Figure 69 . It is interesting to note that the atmosphere within this wavelength region has similar absorbing properties to that on earth. Figure 69b shows that the average reflectance is much higher and more variable for Mars than for the moon where it varies from 0.04 in the maria to 0.2 at the craters. Given these values, it is also assumed that the reflectance of the moon is not wavelength dependent. It should be mentioned that the data above 0.7 microns on both curves of Figure 69 are reasonable extrapolations of that obtained from JPL. Also the reflectance is an average value for the entire surface as viewed from a great distance.

Another effect that changes the magnitude of radiation reaching the camera is the scattering characteristic of the surface. At JPL's recommendation, the photometric function is used. With the geometry as defined in Figure 70, the maximum and minimum spectral radiances one can expect on the surface are shown for the mission in which Mars is at perihelion. To obtain these curves, the atmospheric attenuation of Figure 69 has been modified to account for the sun located at other than the zenith. Notice that the Notice that the reflectance characteristic shifts the sun's radiation spectrum toward the near infrared making it a better match to silicon than even at the earth's surface. Note also that at 0.8 microns the range between the threshold peak radiance and the maximum peak radiance is from about 1 to 12 mw/cm^2/ster/micron. Although an extreme geometric condition is used to establish the threshold, conservation suggests that a level one order of magnitude below that shown should be assumed to account for unforseen variations in reflectance and more severe scan angles.

In Figure 71 is shown a peak threshold radiance of 0.1 mw/cm^2/ster/micron in accordance with the above discussion. These curves show theoretical performance using an LSX-511 silicon detector which yields a peak-to-peak signal to rms noise ratio of 15 db at threshold. At a bandwidth of 1500 cps (assume the use of a memory system) and at 0.1 degree resolution note that the lens aperture required is only about 2.5 mm whereas for the moon 9.5 mm was necessary. Even though the LRC bandwidth was 60 cps and the moon is closer to the sun and there is no lunar atmospheric attenuation, the difference in assumed reflectance models allows the lens to be smaller. Of course the lens may be made larger for the MFC and increased resolution can be gained. A practical upper value for the size of the lens of present camera designs would be about 10 mm which would yield a resolution of about 0.03 degree. A lower limit would be about 1 mm.

Not illustrated in Figure 71 is the large gain in resolution that can be achieved by scanning and transmitting the data in real time, say at 3 cps (12 bits per second at 4 bits per data point). However, a more useful system would be one which scanned at a 1500 cps rate and used a time buffer for slow playback. With 0.1 degree resolution the near field would be at a distance of about 2-1/2 feet.

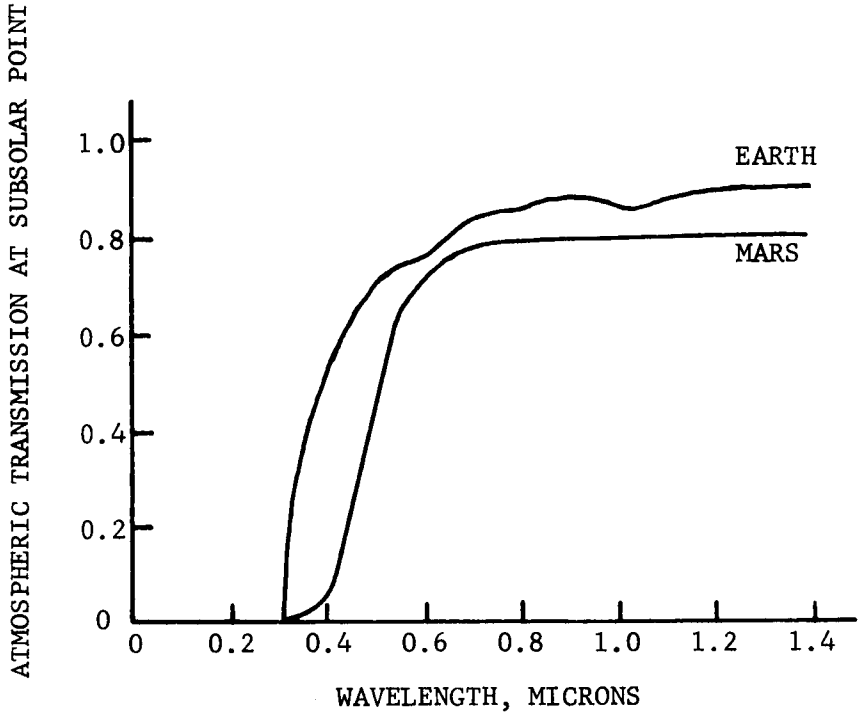

(a)

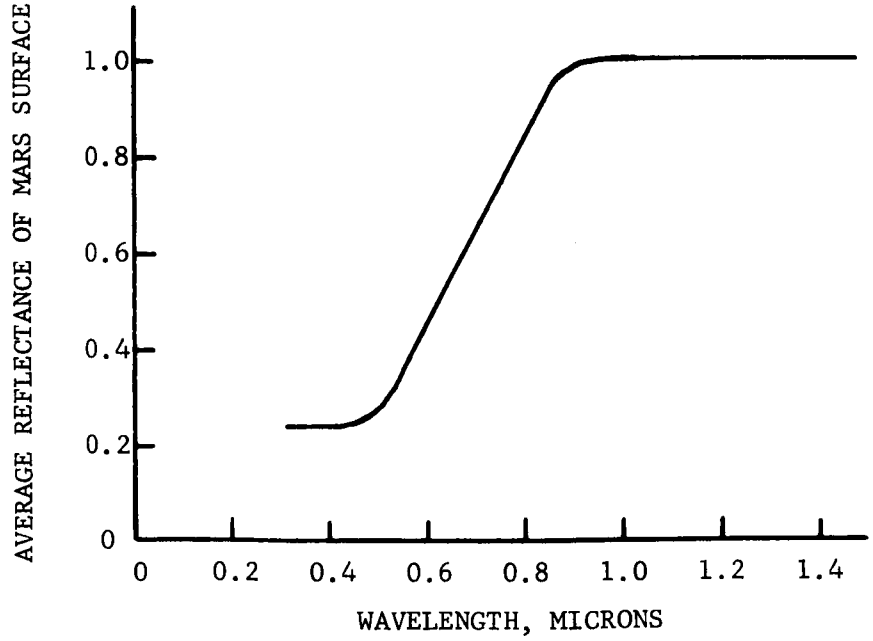

(b)

FIGURE 69. ATMOSPHERIC ATTENUATION AND REFLECTANCE OF MARS

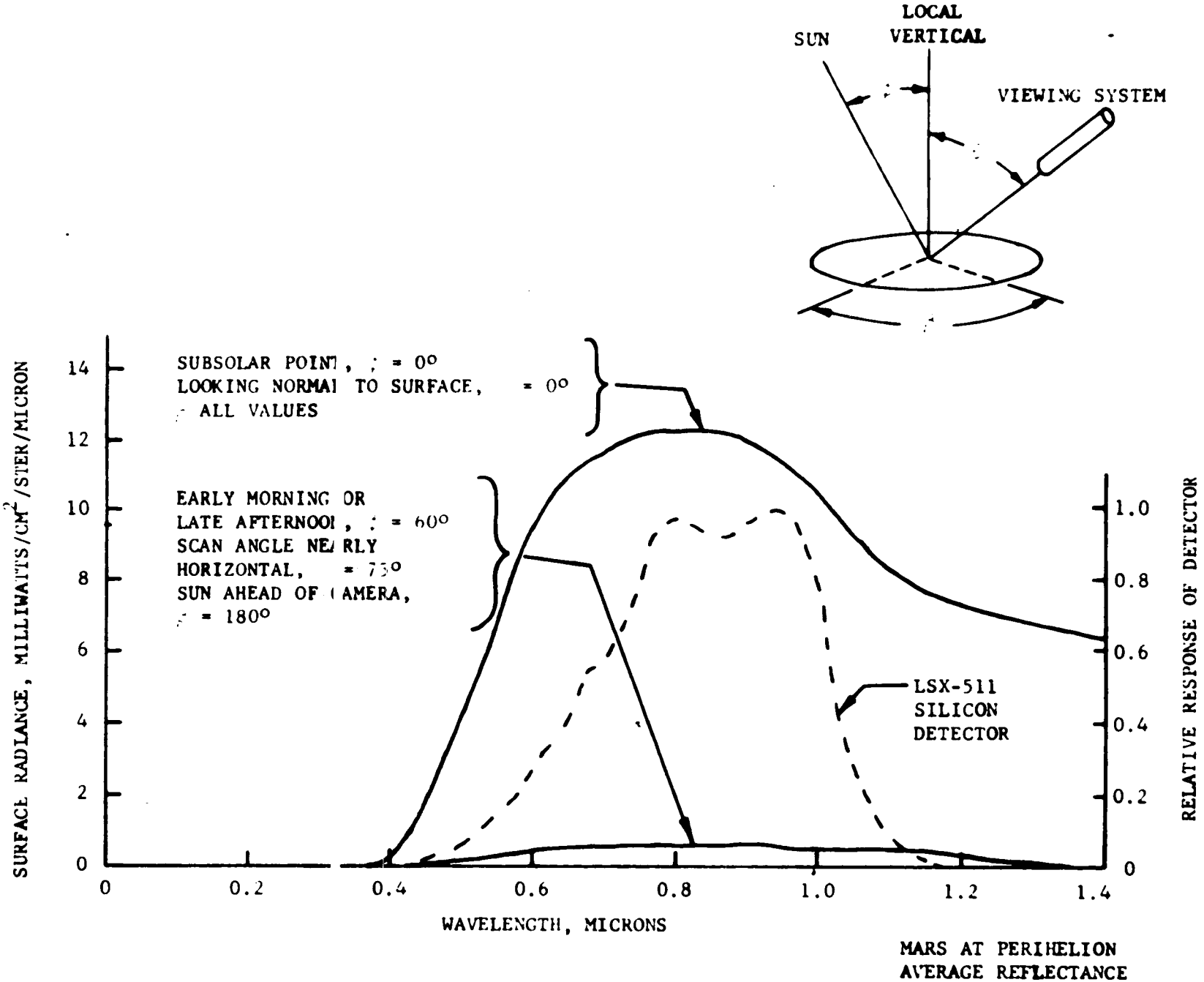

MARS AT PERIHELION
AVERAGE REFLECTANCE

FIGURE 70. VARIATIONS IN SPECTRAL RADIANCE ON MARS SURFACE

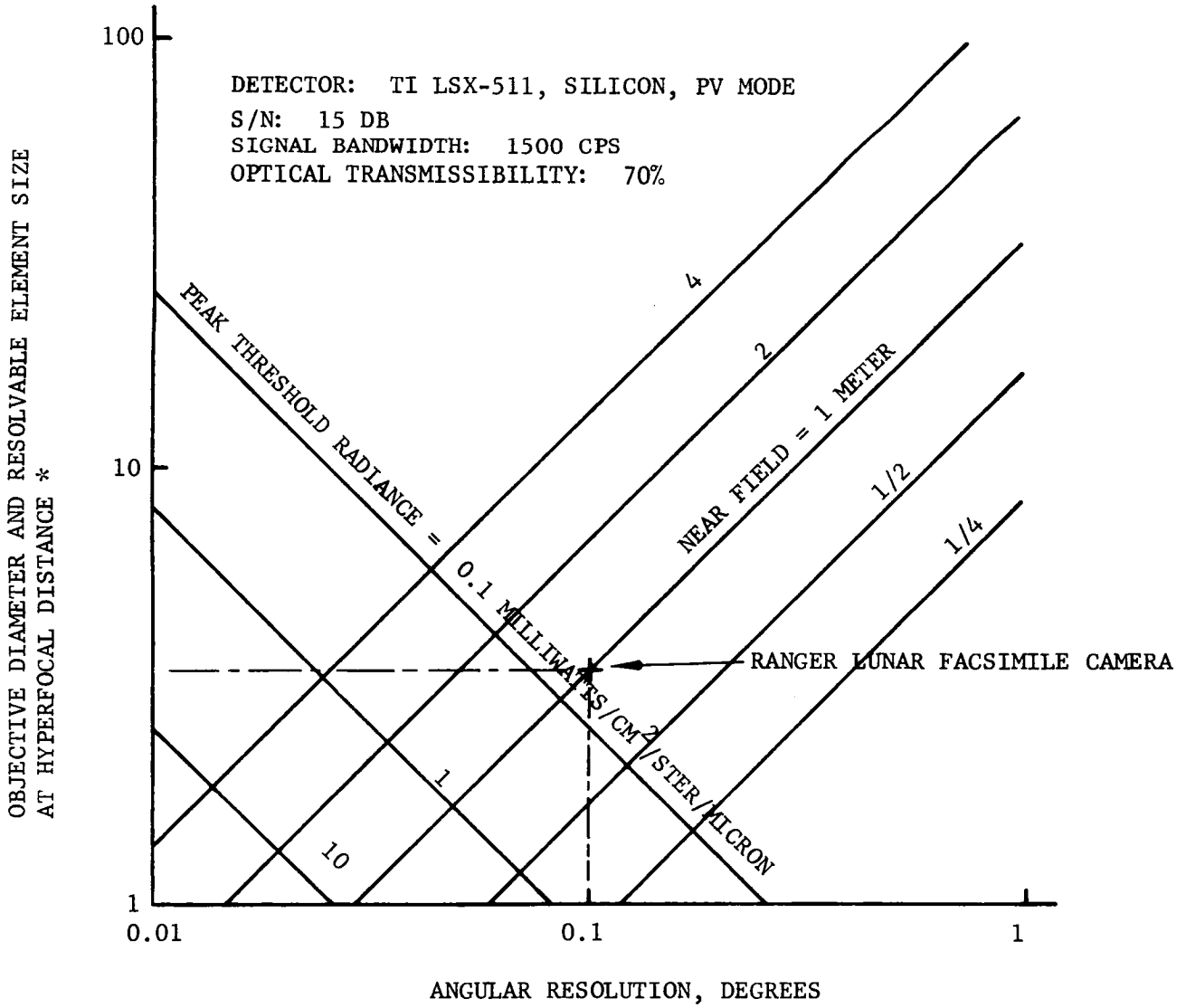

* Hyperfocal Distance is Twice the Near Field for Fixed Focus Optics

FIGURE 71. LIGHT GATHERING POWER OF HRF CAMERA ON MARS SURFACE

Given the total number of picture bits that can be accommodated by the power supply and telemetry system, from Figure 72 the resulting view field may be found. For example, if one million bits can be transmitted and 4 bits per picture element are generated during analog-to-digital conversion then 1/4 million 0.1-degree picture elements covering a view field of 2500 degrees^2 would comprise the picture. This could be a square 50^o x 50^o or a rectangle 10^o x 250^o or 7^o x 360^o or even many smaller pictures the total coverage of which would be 2500 degrees^2. The number of equivalent $\sqrt{2}$ shades of grey would be $2^4 = 16$ which is analogous to a dynamic range of $2^{16/2} = 256{:}1$ or 48 db. The gain in picture coverage by going to 3 bits per picture element is only 8 degrees on a square format and does not appear to be worth the factor of 2 sacrifice in grey levels.

Even though Ranger telemetry was analog not digital, the number of equivalent picture bits have been determined to be about 8 million (3.74 bits per picture element). The operating points are shown on Figure 72.

Finally, having chosen the resolution and near field, choice in selection of the remaining optical parameters is shown in Figure 73. With the same size pinhole as that used for the LFC, the lens would be little more than cut glass with a focal ratio of about f/30.

5.3.6 MECHANIZATION

The MFC consists of the subsystems as depicted in the functional diagram of Figure 49. A mirror surface scans uniformly through a vertical angular field of view and directs radiation from the scene into the clear aperture of the objective. An internal pulsed light source shares the scanning mirror to provide electronic synchronization during mirror dead (scene vignetting) time. The vertical scanning assembly is also rotated in azimuth to provide a 360 degree horizontal angular capability. Power is supplied to the vertical and horizontal scanning drive motors from an amplifier which is frequency stabilized. A stability reference signal may also be transmitted to the playback system to assist in reproduction of the facsimile picture.

The camera contains a fixed focus optical viewing assembly. The objective lens collects radiation from the scanning mirror and then transforms the radiation onto a detector. A small diameter pinhole is placed close to the detector, near the image plane of the objective, to define an instantaneous field of view and the near field distance. The interior of the telescope contains several graduated light baffles and many smaller baffles or threads on the inside of the tube to limit unwanted reflections. The tube also is coated with a low reflectance optical black paint to reduce light scattering. A mechanical chopper is located between the pinhole and detector near the image plane to modulate the incident

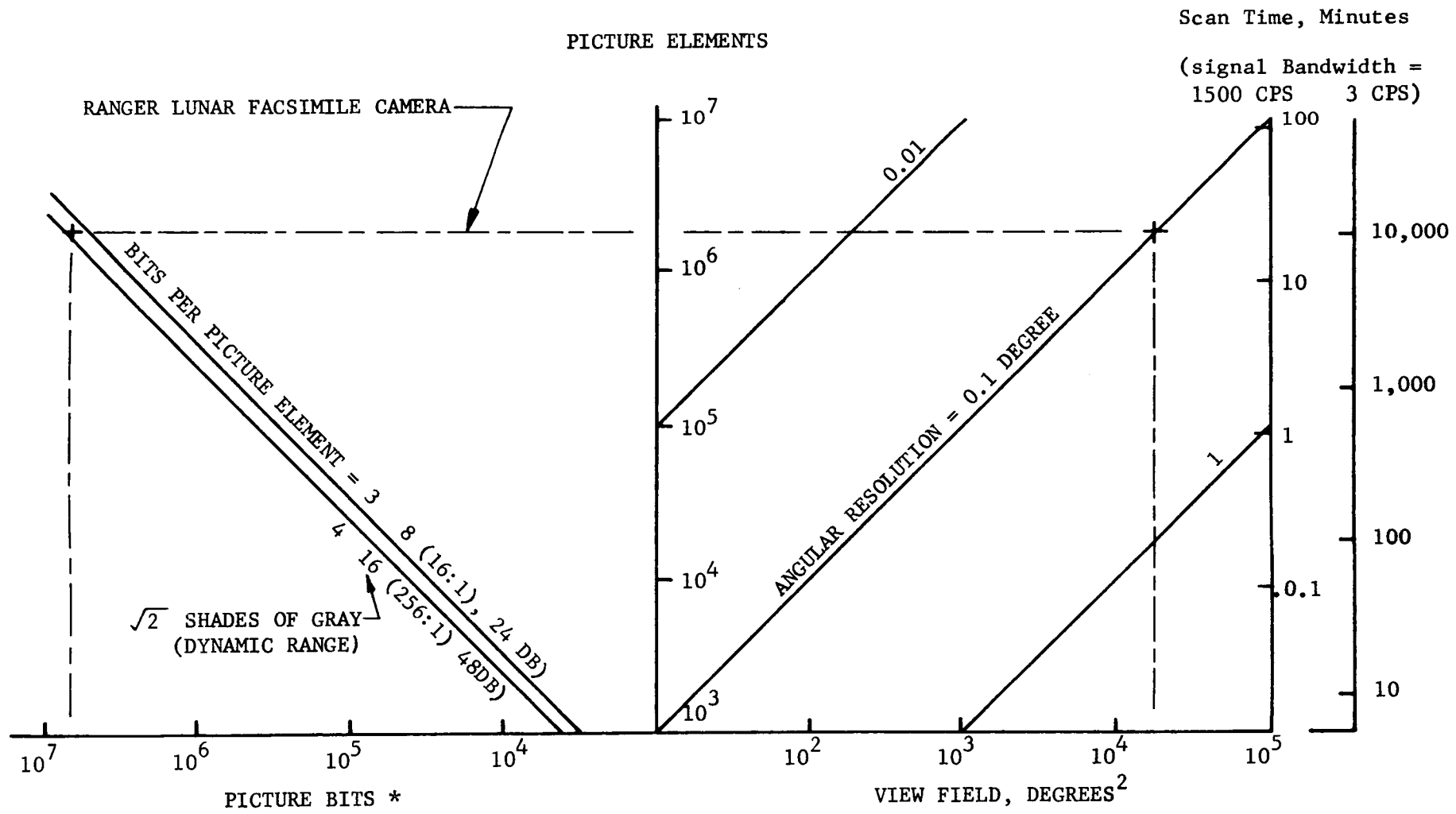

* TOTAL BITS TRANSMITTED IS GREATER BY ABOUT 10 PERCENT
BECAUSE OF SYNCHRONIZATION BITS

SCAN EFFICIENCY = 50%

FIGURE 72. HRF PICTURE COVERAGE TRADE-OFF CHARACTERISTICS

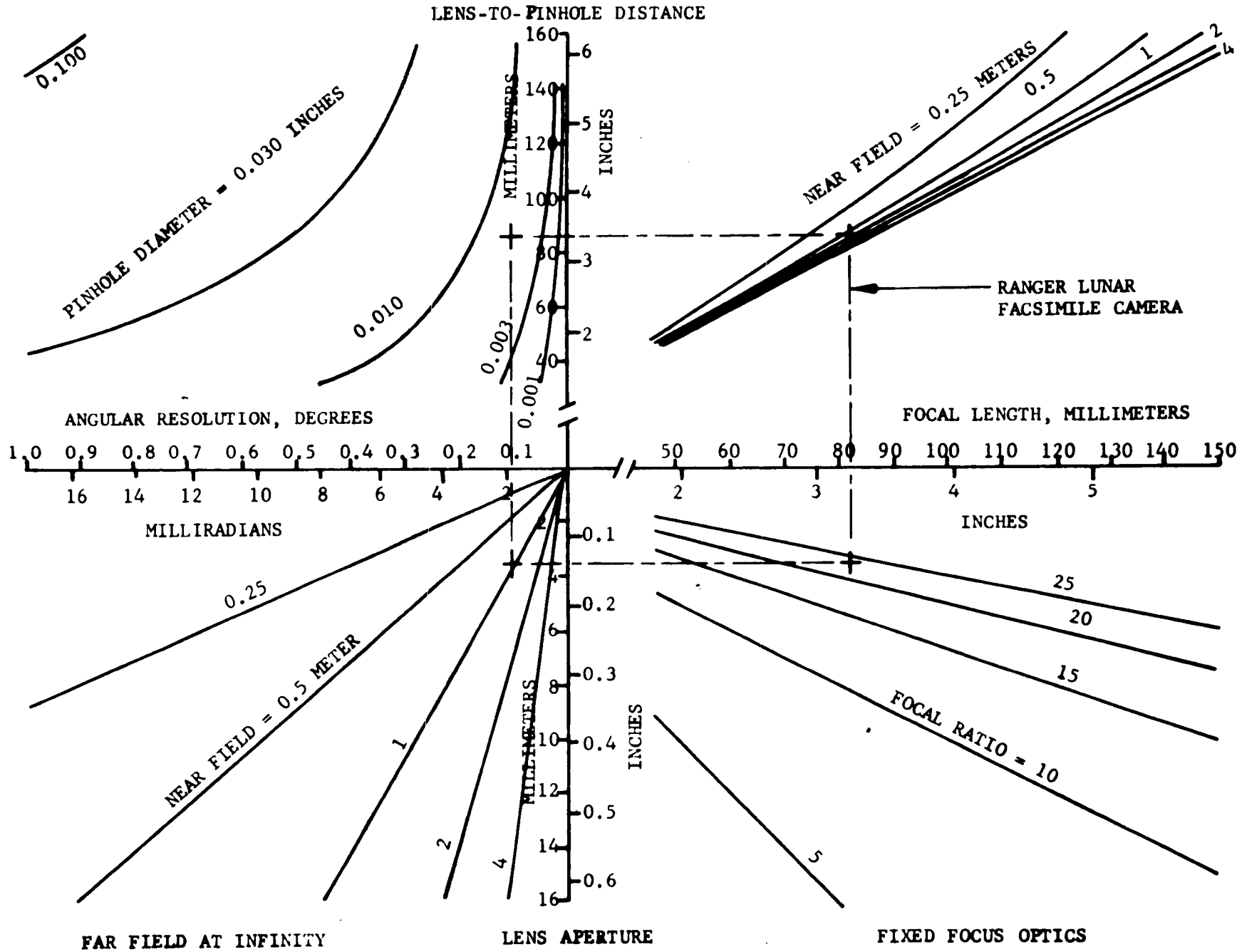

FIGURE 73. RELATIONSHIP AMONG HRF CAMERA OPTICS

radiation to permit a.c. electronic signal amplification. If desirable, the chopper disk can be fabricated of optical transmitting material and sectors coated to provide a spectral filter chopper. A suitable detector is positioned to collect all of the modulated radiation passing through the pinhole. The detector signal from the scene and the optical synchronization pulse are amplified by the preamplifier and further electronically processed and transmitted to a playback system.

a. Components. Referring again to Figure 49 , the system components are as discussed below. A typical concept of the high resolution (HRF) camera may be seen in the schematic layout of a typical camera in Figure 74 showing both rotating and a nodding mirror scanning concept. The optical window transmits radiation from the scene to the scanning mirror. The primary function of the window is to provide a seal. The length of the window limits the total vertical scan angle and the width should be sufficiently wide not to vignett the instantaneous field of view. The thickness should be such that the flatness and parallelism should not limit the optical abberations.

The mirror assembly provides a high reflective flat surface which uniformly scans through a vertical scan angle. The implementation of the scanning mirror can be accomplished by several techniques, two of which are illustrated in Figure 74. Figure 74b depicts a camera utilizing a nodding mirror quite similar in design to the Lunar Facsimile prototype camera previously developed by Aeronutronic. Figure 74a illustrates a spinning mirror design normally associated with, but not limited to, fast scan modes. The optical properties of a mirror are such that the scene angle of incidence equals the reflectance angle so that as a mirror facet rotates the instantaneous field of view continuously scans the total vertical angular scene field and directs the radiation within the instantaneous field of view onto the objectives. Vignetting occurs at both the leading and the following edges of a mirror facet resulting in a strip of lower brightness at the top and the bottom of the facsimile picture. Therefore, only the non-vignetting portion of the mirror is used to produce a picture and the resulting vignetting time is utilized for transmitting synchronizing and stability reference signals.

The vertical drive gear train provides mechanical drive to the scanning mirror. It is important that the scanning mirror scan speed be constant so that the resulting facsimile picture will not retrace the scene and give redundant information or skip portions of the scene. The data bandwidth would also be effected which would cause the contrast (film density) to be reproduced incorrectly. The data bandwidth is directly independent on the drive worm and gear ratios since they determine the rotational rate of the scanning mirror.

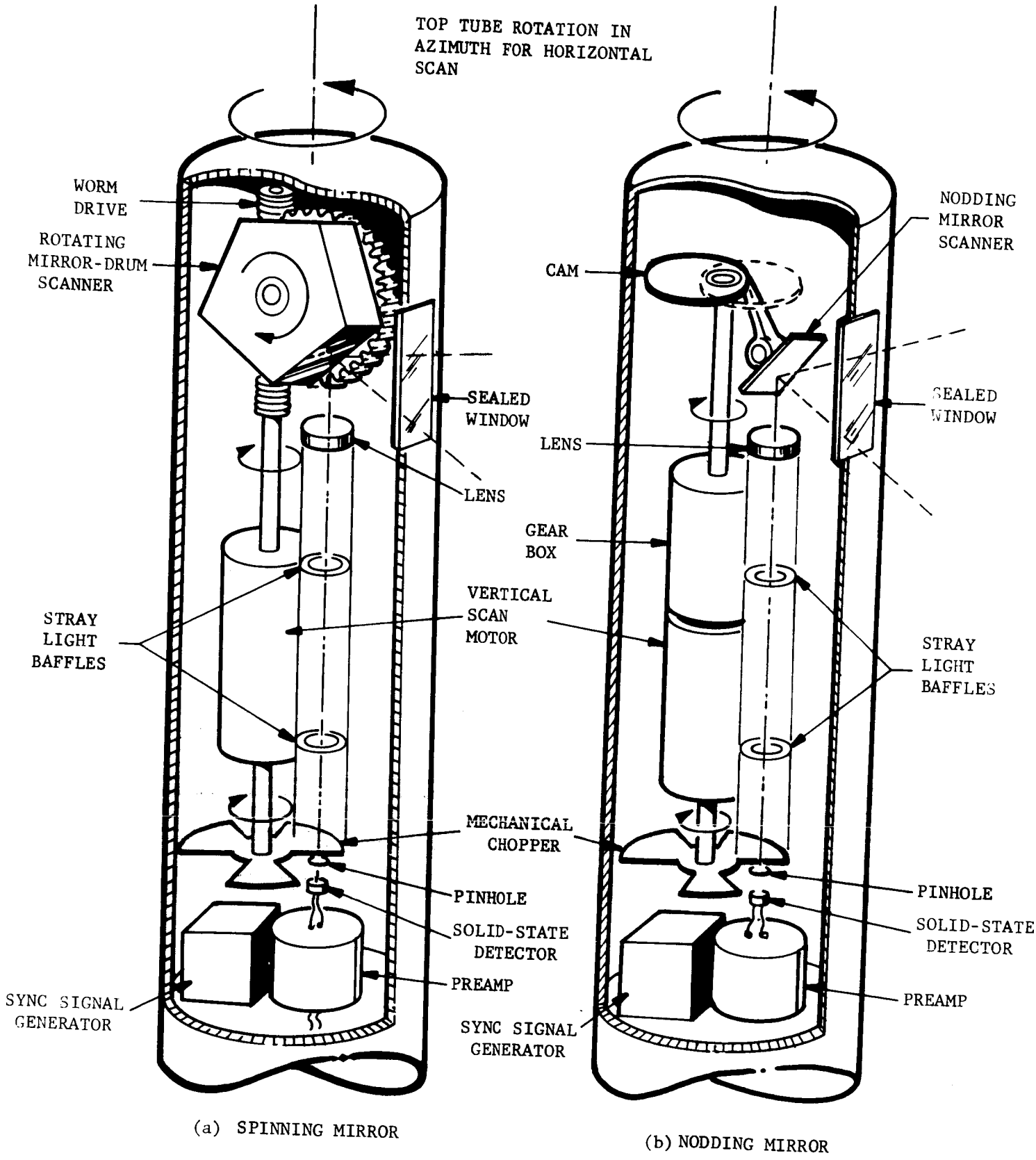

FIGURE 74. EXAMPLES OF HRF MECHANIZATION

Vertical and azimuth drive hysteresis synchronous motors are used to ensure reliable video and scanning synchronization. Motor drive signals may be derived from a frequency standard. The frequency standard output is amplified to control power transistor switches. These switches connect either motor at the frequency standard rate typically between +14 volts and - 14 volts resulting in a 28-volt peak-to-peak square wave.

The azimuth drive worm is mounted to the base structure which does not revolve. The worm gear is hubbed into the azimuth tube and contains sufficient teeth to revolve the azimuth tube at the desired rpm compatible with the vertical scan. It is important to keep the azimuth revolving structure to a minimum size and weight to reduce the power requirements of the drive motor.

The gear box may be used to gear down the normally high rpm motor to provide a smooth azimuth scan motion compatible with the vertical scanning mirror.

A frequency standard (such as a tuning fork) is utilized to provide motor drive signals to ensure scanning synchronization. The amplified frequency standard output is used to drive both the vertical and horizontal scanning motors. A stability reference signal may also be transmitted for similar use with the playback system.

A synchronous optical pulser may be positioned so that the angle between the synchronization pulse and the scan line beginning can be measured directly and become a constant of the camera system. The synchronous optical pulser is implemented by using a smaller collimated light source mounted within the field of view of the mirror but outside of the non-vignetting scan field. The light source would be located so that a leading edge of a facet on the vertical scanning mirror could observe the light source and the detector returned to a zero input condition to facilitate blanking of the video signal prior to scanning the normal field of view. The collimated bundle diameter should be kept small so that positioning during installation will not be critical. The light source is a tungsten filament lamp powered by rectifying and smoothing the mirror drive motor power supply.

The objective is used to collect scene radiation reflected from the scanning mirror. The objective is located vertically below the mirror assembly and is an achromat lens coated and corrected for the scene spectral region of interest. The lens is optimized for both diameter and focal length. The diameter is optimized to minimum scene irradiance (low-lights) to ensure that the detector will produce a signal-to-noise ratio of at least 2:1. The focal length is optimized within the constraints of the pinhole diameter to produce the desired instantaneous field of view and 100 percent square wave response at the hyperfocal

distance. The pinhole is electroformed on a small disk of nickel foil and aligned in its mount to lie on the optical axis and in or near the focal plane of the lens.

The Mar's surface spectral radiometry dictates that a silicon detector be used as the camera transducer to achieve maximum spectral response. The detector and preamplifier for the Mars Facsimile Camera are considered as an integral unit due to the fact that the preamp must be located as close as possible to the detector to minimize detector lead capacitance. The size of the detector must also be kept small so that the inherent capacitance will not limit the detector response time or increase the noise signal. The detector should be positioned to receive all of the radiation transmitted through the pinhole aperture. The detector signal is amplified and then transmitted to the remote playback system to produce a facsimile picture of the scene scanned by the camera.

b. Previous Designs. Aeronutronic has designed and developed prototype subassemblies and supporting ground equipment for the Lunar Facsimile Capsule (LFC) shown in Figure 75. Two prototype capsule assemblies were subjected to severe environmental tests, including impacts up to 198 feet per second and 4300 peak-g loads followed by long-term functional testing at 10^{-6} Hg vacuum. No degradation of any kind due to impact was experienced, and the six 360-degree pictures taken with Prototype No. 2 Assembly exceeded all design objectives for picture quality. The capsule has a calculated reliability of 96.5 percent. From 8-1/2 to 9 hours are required to produce a 360-degree horizontal view by 50-degree vertical view picture. Table 5.3-III lists the weight, volume and power requirements for the Lunar Facsimile Camera.

Figure 76 depicts a design for the development of a fast scan, high resolution facsimile camera which offers all of the desirable performance features of the LFC and provides a complete 360-degree panoramic coverage 500 times faster. The detector illustrated is a multiplier phototube, because of the time constants associated with the fast scanning mode of operation. The fast scan HRF camera design contains demonstrated principles of operation, simplicity of design, well-known fabrication techniques, reliable operation, and expected performance meeting or exceeding that required. The estimated weight budget for the fast scan HRF camera is given in Table 5.3-IV.

5.3.7 STEREO AND MULTISPECTRAL CONSIDERATIONS

The advantages of stereo recording the Mars surface would include photogrammetric determination of quantitative surface information and an improvement in the realism of the presentation of the finished product after playback. Both benefits are realized through stereo viewing in the absence of fiducial markings on the Mars surface by which comparative

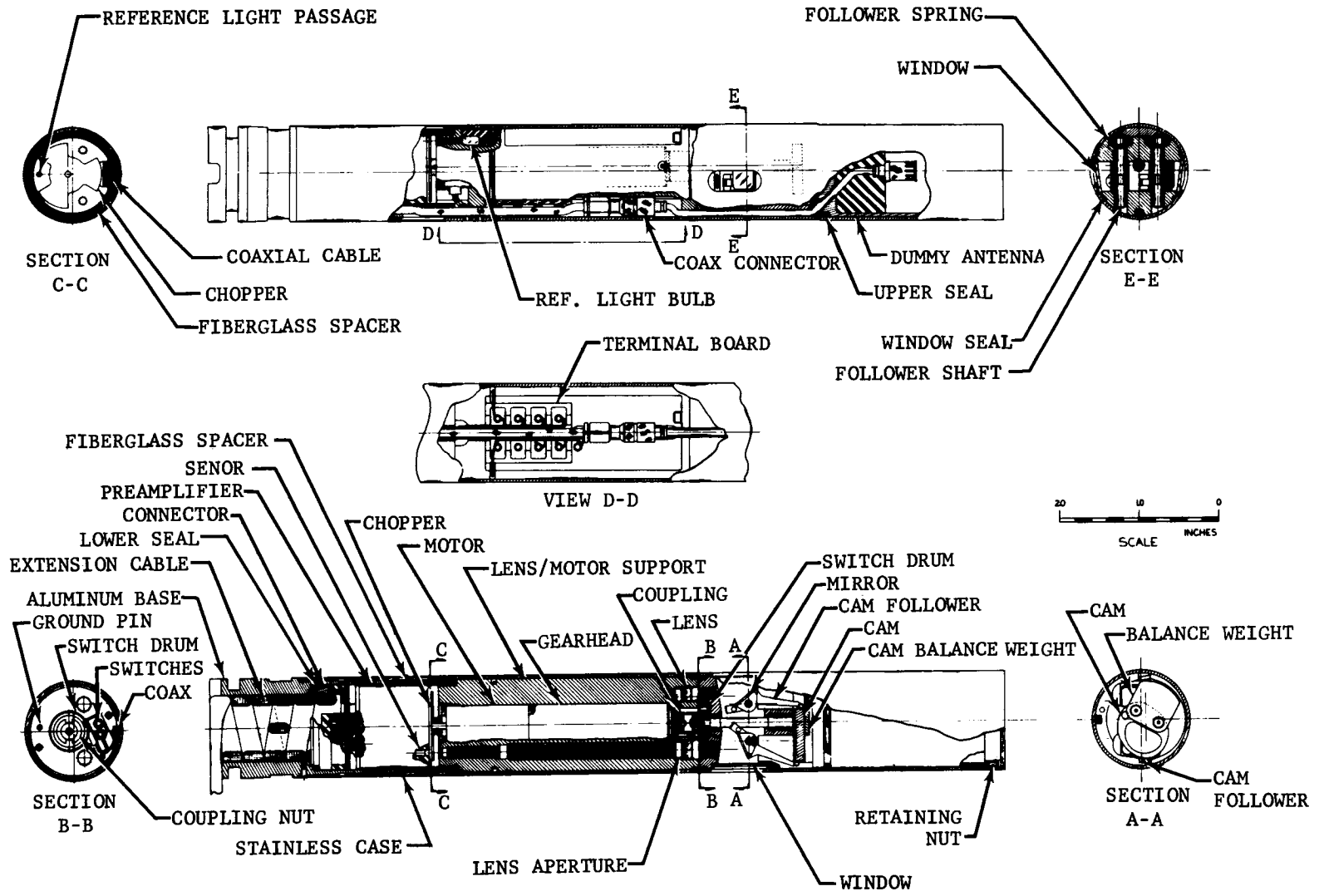

FIGURE 75. PROTOTYPE LFC TOP TUBE

TABLE 5.3-III

WEIGHT, VOLUME AND POWER REQUIREMENTS FOR LFC

SUBASSEMBLY	WEIGHT ALLOCATION, POUNDS	VOLUME ALLOCATION, CUBIC INCHES	CONTINUOUS POWER, WATTS
Top Tube Assembly	1.2	12.0	
Preamplifiers (2)			0.15
Motor			5.0
Ref. Lamp			0.50
Azimuth Drive Assembly	0.60	6.0	
Motor			5.0
Motor Drive Elec.	0.7	14.8	5.0
Signal and Sync E[illegible]	0.85	20.0	0.10
Total	3.35	62.8	15.75

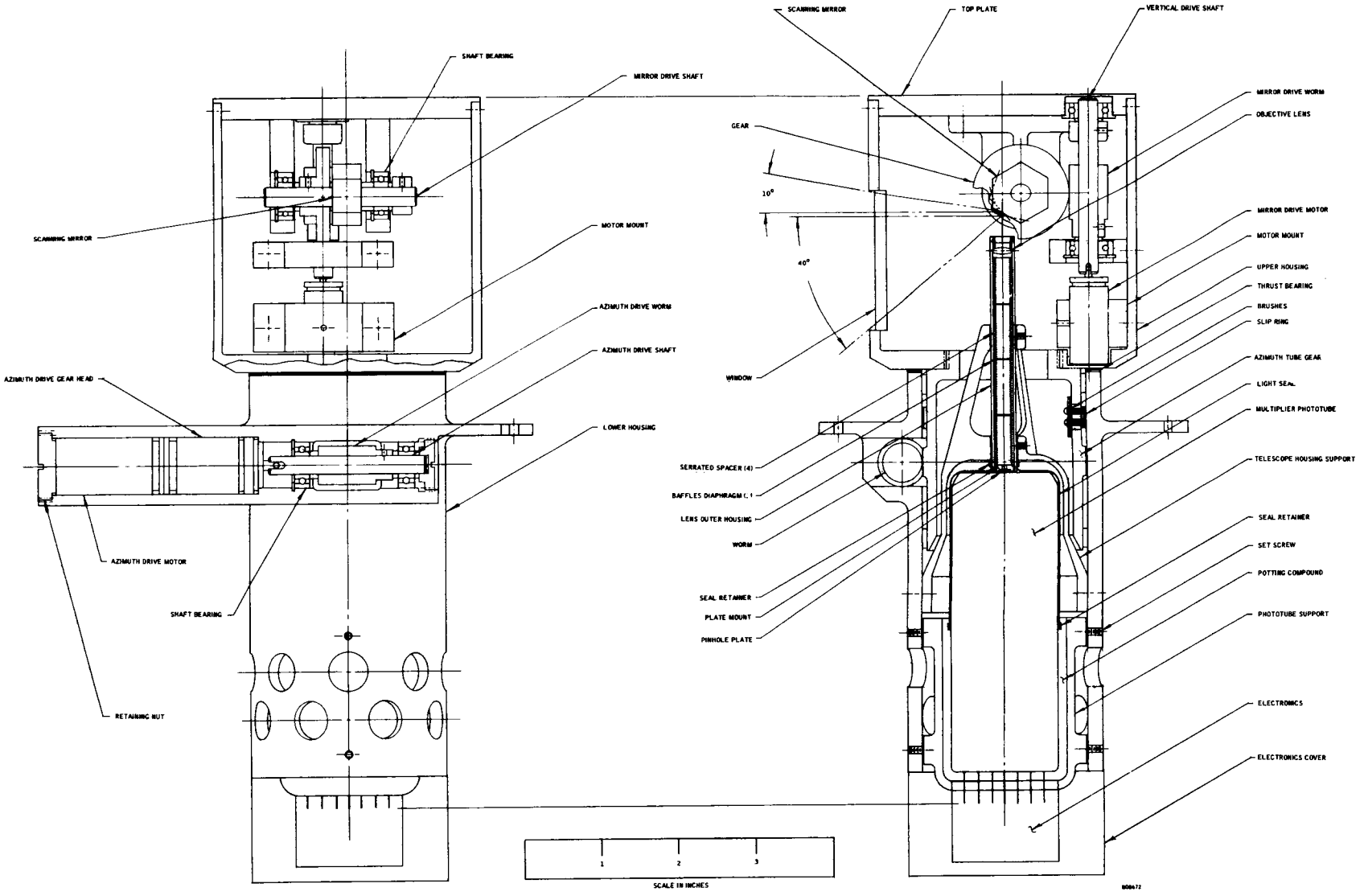

FIGURE 76. DESIGN OF A FAST SCAN HRF CAMERA

TABLE 5.3-IV

BREADBOARD FAST SCAN HRF WEIGHT BUDGET (ESTIMATED)

SUBASSEMBLY	WEIGHT (POUNDS)
Top Tube Assembly	2.04
Azimuth Drive Assembly	1.33
Telescope	.36
Sensor Assembly	.72
Interface Hardware	1.10
Electronics	3.00
TOTAL	8.55

size or distance measurements can be made. The use of objects deployed from the capsule into the field of view or the utility of delayed duplicate pictures using changing shadow angle effects would certainly enhance monocular viewing. It should be noted that either a stereo or duplicate picture scheme requires additional transmission of picture bits and might be precluded by the power limitations imposed by the number of batteries encased in the capsule.

Implementation of stereo scanning can be accomplished either by two sensors (individual objectives) separated either horizontally or vertically along a known baseline or by monocular duplicate viewing accomplished by a known linear displacement of the basic head after completion of the first horizontal sweep. The basic limitation to obtaining scientific enhancement of the picture data is the difficulty of obtaining a long baseline between the two correlated viewing positions. The error in establishing the distance to an object from the basic parallex angle is proportional to the distance squared and the angular resolution of the system, and inversely proportional to the baseline dimension. The sensitivity of the distance error to angular convergence error limits the usefulness of stereo measurements to relatively close distances. For a stereo base of 150 mm and an angular resolution of 0.1^{o}, the accuracy of distance measurement is as follows

DISTANCE (METERS)	DISTANCE ERROR (METERS)
0.25	0.00074
1.0	0.012
10.0	1.2
30.0	10.0
50.0	30.0

Thus, for 0.1^{o} resolution and a stereo base of 150 mm, the useable distance measurement range is limited to less than 50 meters. At distances much less than 50 meters objects could be assessed with fair accuracy. At the near point of the field of view (about 1 meter), the granularity of surface material may be measured to millimeter size.

The subjective enhancement of the lunar surface pictures afforded by vertical stereo coverage is very difficult to assess. For instance, normal stereo projections use a horizontal baseline and since one does not usually view a scene with the head turned sidewise the stereo pictures taken with a vertical baseline may lose subjective quality simply because it is taken from a less familiar posture. Also, the second

picture taken by monocular duplication may show different shadow lengths in the two pictures. This may not significantly effect the quantitative scaling of the picture, however, the overall subjective appearance may be considerably degraded by this effect. Since the vertical stereo method is an unusual method of taking stereo pictures, it may be advisable to perform simple experiments using the previously developed Aeronutronic Facsimile Camera to take delayed pictures on Earth to simulate the effect of Sun motion and to evaluate the effects, if any, of the vertical baseline.

Several possibilities exist to acquire a stereo capability for either vertical or horizontal baseline operation. The vertical drive mechanism depicted in Figure 4a was purposely mounted so that it could be easily relocated to simultaneously drive two vertically displaced spinning mirror systems. The duty cycle scan efficiency of the mirror as shown is less than 50 percent so that if two mirror assemblies are required they can time-share their data by alternately recording a scan from one then the other; a mode similar to the original Aeronutronic prototype slow scan Lunar Facsimile Camera. After time sharing the data and allowing for insertion of sync and blanking pulses, utilization of rf transmission time and, hence, power will be greater than 90 percent efficient.

For horizontal baseline stereo, there are two types to consider. Two cameras can be used, each spatially fixed relative to the other. In this case, the baseline is continually changing throughout the azimuth sweep. The line data is time-shared between cameras as described above. The efficiency of scanning being less than 50 percent requires no modification to either camera. One of the cameras would not need a reference frequency source since it would be synchronously controlled by the other camera.

The constant horizontal baseline concept requires only one camera assembly but two sets of optics. The scanning mirrors in this case would be similar to those utilized in the slow scan camera. During less than 50 percent of the sweep, one camera would receive radiant flux from one mirror as it scans down. When this scan is completed, a mirror at the other side reflects flux into the second telescope while sweeping up. Both sweeps use the same detector and signal separation is accomplished at the remote playback station through utilization of the synchronization pulses.

The nodding mirrors perform the vertical scanning and the azimuth scan drive could be located at the end of a bell crank to turn the entire assembly around a radial arm. This technique requires 180 degrees of azimuth sweep before the fields of view begin to overlap to provide

stereo pictures. Therefore, a 360-degree monoscopic picture is recorded during the first 180 degrees azimuth sweep and then stereoscopic pictures during the remainder of the total 360° sweep.

The spectral reflectance of the Martian surface peaks at about 0.8 microns. The bulk of the effective radiation is at longer wavelengths than the cut-off response of the human eye. The facsimile pictures will depict scenes similar to those commonly recorded by infrared film. The interpretation of such photographs will require specialized training since objects acquire a different enhancement than is normally observed in a solar balanced spectrum photograph.

There exists the prospect of taking monoscopic color pictures with a facsimile system which is only slightly modified from the basic system used to take monoscopic black and white pictures. The same basic hardware and the same basic communication equipment can be used to transmit channels of color information. A system consideration in transmitting channels of color information is the fact that the radiation level at the sensor in each color band is reduced from that existing in the monoscopic black and white system. The amount of reduction would be dependent on the spectral bandpass and transmission of the filters used to isolate the spectrum bands.

One convenient method of implementing the color separation would be to coat a quartz chopper disk in segments with different filter materials and to coat the desired opaque sections to produce a reflection surface. If more than one filter material is used on alternate segments, the fundamental frequency component would assume a lower value and the rms amplitude would be lower since each filter would time share a scene. For instance, if three filters were used the effective radiation level would be reduced by the ratio of the total effective energy (H_T) available to the effective energy transmitted by one of the filters (H_{F1}).

$$\text{Energy Reduction} = \frac{H_T}{H_{F_1}}$$

Using three filters implies that any one filter assumes a fundamental frequency of 1/3 of the nominal frequency of the chopper and a rms amplitude degradation of 1/3 as shown below.

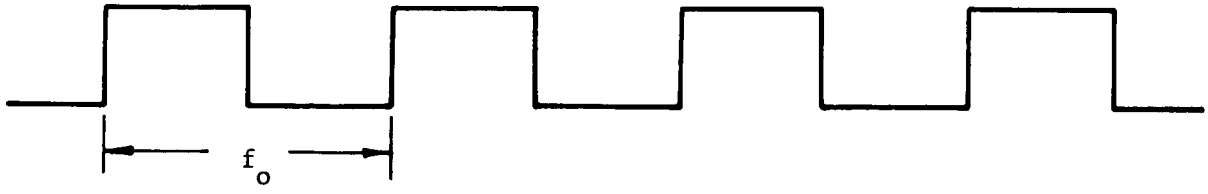

Black and White Picture (f_o cps frequency component at $\sqrt{2}/\pi$ amplitude)

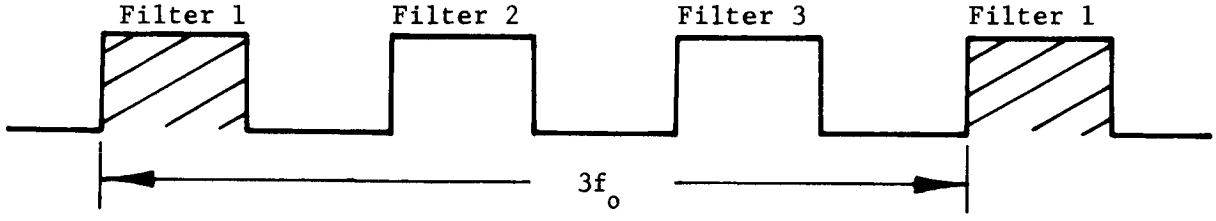

Three-Filter Picture ($f_o/3$ cps frequency component at $\sqrt{2}/3\pi$ amplitude)

The total filter number one degradation for this case would be

$$\text{Total Degradation} = 3 \times \frac{H_T}{H_{f_1}}$$

The loss of energy arising from the use of filters can be regained by degrading the angular resolution of the system. This may be an acceptable procedure since the occurrence of color may be more significant than the attainment of increased resolution in a black and white picture.

REFERENCES

1. Opik, E. J., "Teh Atmosphere and Haze of Mars," Journal of Geophysical Research, October 1960, Vol. 65, No. 10, pp 3057-3063.

5.4 TELECOMMUNICATIONS

5.4.1 REQUIREMENTS

Communication will be required between the Mars Facsimile Capsule (MFC) and the Earth for data transmittal to Earth, and possibly for Earth Command to the MFC. Two basic methods are considered: 1) direct MFC-Earth, and 2) relay via the spacecraft (S/C). Orbital relays are also a possibility but were not within the scope of this study. It is assumed that the MFC contains data storage capability as required, so the data acquisition and transmission rates may be selected independently.

The general communications problems may be deduced from the mechanics of the situation. The MFC will be communicating between fixed points on two spinning planets, a vast distance apart with a very limited payload capability on Mars. The NASA Deep Space Network (DSN) is scheduled to have stations at Goldstone, Canberra, and Madrid with the command and reception capabilities assumed in this report by the end of 1967. (Reference 1). These stations are approximately 120^{o} apart and within $\pm 40^{o}$ of the Equator. Their placement permits continuous surveillance and command of objects more than 10,000 miles from Earth. There need be no communication blind periods due to Earth rotation. However, there will be blind periods (ignoring a system of orbiters or satellites) due to the rotation of Mars which has a sidereal period of 24 hours, 37 minutes.

The required communication distance as a function of calendar date is shown in Figures 77 and 78. The extremes of Earth-Mars distance are 0.4 and 2.6 AU. The relative velocity between Earth and Mars or the S/C will typically be the order of 18 km/sec. This results in a doppler carrier frequency shift of 140 kcps at 2,300 mc. For velocities much smaller than the speed of light, the doppler shift is given by $f = \frac{V_r}{c} \cdot f_{static}$, where V_r is the radial velocity, C is the velocity of light and f_{static} is the frequency with no relative motion. (Reference 2). There are also much smaller doppler frequency changes due to the rotation of Earth and Mars. The doppler effects occupy a much larger frequency region than the data modulation spectrum. However, the carrier signal is tracked at the receiving station so that excess reception bandwidth together with an attendant power penalty are avoided.

The MFC telecommunications considerations are not unique and are very similar to those of the present Mariner C. Of importance are the long transit time, the large communications distance, and special impositions due to the hard landing capsule environment. The latter suggests a simple rugged system of limited size and weight.

5.4.2 FORMAT AND ERROR CONSIDERATIONS

The MFC is a wideband experiment and the amount of data transmitted is likely to be limited by the primary power available in the MFC. It is

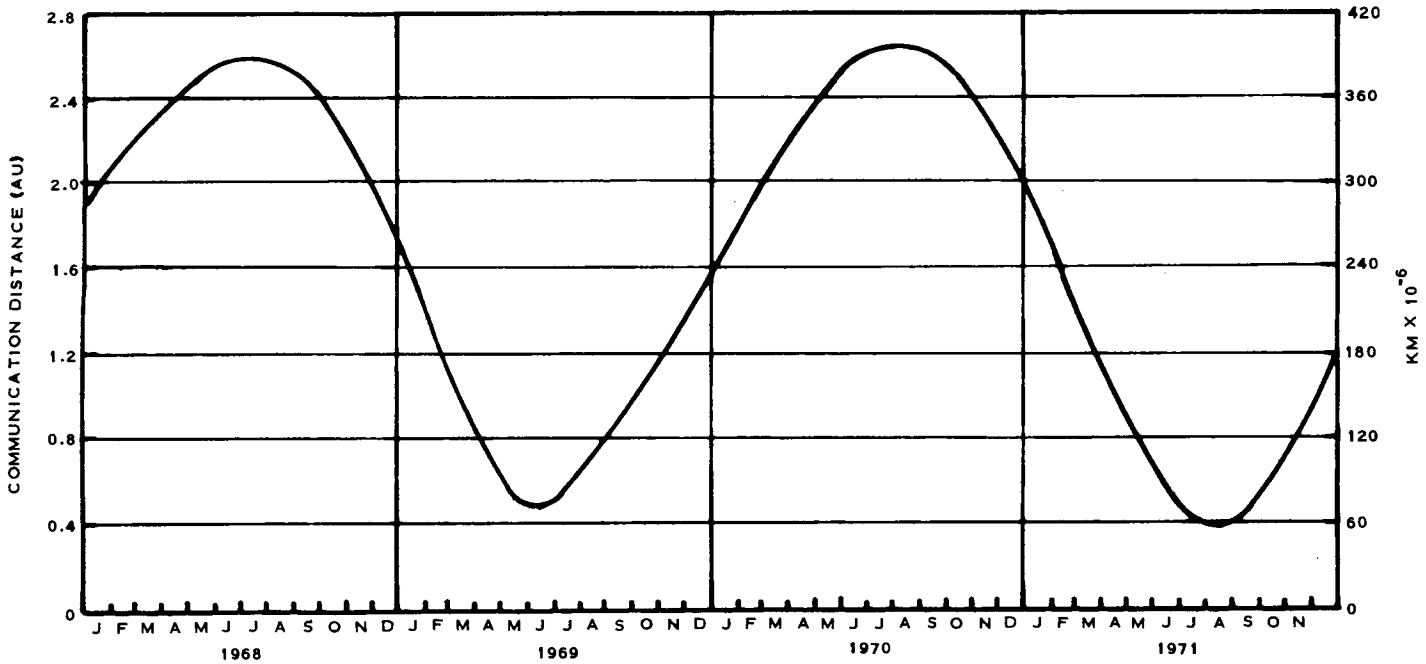

R11219

FIGURE 77. - MARS TO EARTH COMMUNICATION DISTANCE 1968 - 1971

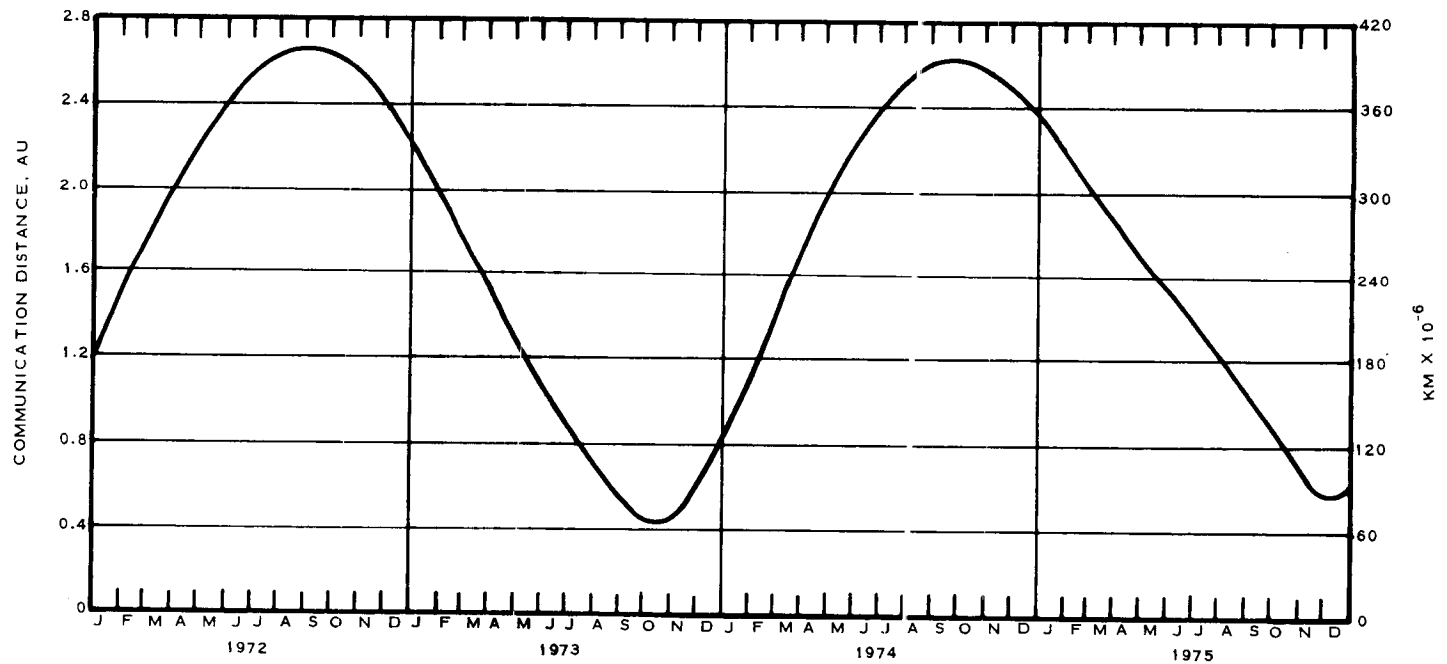

FIGURE 78.- MARS TO EARTH COMMUNICATION DISTANCE 1972 - 1975

important, therefore, to select a system which is efficient in terms of the amount of data transmitted per watt-hour of energy expended. It is seen in Section 5.5 that the RF power achievable is in the range 10 to 20 watts. Therefore, the data transmission rate is relatively low and direct analog modulation of the carrier is not practical as a very large modulation index would be required resulting in a poor threshold. Recent analyses have shown that Analog/FM/PM is approximately 3 to 6 db poorer than PCM/PSK/PM. It is therefore assumed that the picture data (elements) will be digitized for transmission. This will be most convenient for storage in the MFC if also required. A different quantized system (Reference 3) recently disclosed by JPL, designated MFS, is very promising and is discussed in Section 5.4.3.

A possible MFC data format, very similar to that of Mariner C, is shown in Section 4.4.2. This particular format is convenient to use for 4 bits per picture element. Approximately 20% of the data bandwidth is required for synchronization.

There are subjective effects of picture quantization which should be examined. These effects result from the fact that the eye is very sensitive to step changes in intensity. The eye senses these even when relatively small, especially when there are large areas to compare, and as the quantization increments are increased the effect becomes quite objectionable. The rms error criterion for quantization error would appear to be a useful one since it weighs large errors more heavily than the small ones which may arise in various other parts of the system. However, some experimental evidence is needed to assess the pictorial effect for various quantization increments. Fortunately, two recent papers, References 4 and 5, are available which display still scenes of differing resolution. Note that in Figures 31 and 32 of Ref. 4, reproduced here as Figure 79 (with considerable loss in detail), only 3/4th of the encoding range is assigned to the scene. Therefore, the pictures for 2, 3, 4, 5, 6, and 7 digits represent, in order, 3, 6, 12, 24, 48, and 96 shades. These pictures demonstrate that four bits (12 shades) give a pleasing picture with little apparent loss of detail. While it is generally agreed that 6 bits are needed to approach the appearance of a good analog system, this represents a 33% reduction in the number of scene elements which can be transmitted with a fixed number of bits. Since the MFC is bit limited a trade-off must be made between total scene data and scene resolution. Such a trade-off was out of the scope of this contract as it involves subjective as well as quantitative analysis.

Reference 5 is primarily concerned with methods for improving the appearance of pictures of quantized shading. The author, Roberts, proposes a scheme in which pseudo-random noise is added to the picture signal before quantization and the same noise is subtracted from the received signal before display. This scheme breaks up the edges in the picture due to quantization and distributes the errors throughout an area, making it less noticeable. Roberts also recommends the use of "companding", compressing the dynamic range of

FIGURE 79. TV PICTURE SHOWING THE EFFECT OF ADDING ONE DIGIT AT A TIME, STARTING WITH TWO DIGITS AND ENDING AT SEVEN DIGITS

the signal before transmission and expanding it to its original range after reception. Since the eye perceives brightness as the square root of intensity, higher errors can be tolerated in bright areas. For a uniform channel, the signal should be compressed by the factor square-root-two before transmission.

The use of Roberts' scheme for the reduction of resolution with the addition of pseudo-random noise is not suggested for the MFC application. There is some added complexity and the pseudo-random sequence must apparently be at least one raster in length. The apparent improvement would appear to be objectionable from a scientific viewpoint, as it is entirely subjective. The information content of the transmitted pictures is slightly reduced by the added noise.

It is considered valid to assume that the various errors from different sources are not correlated so that these may be added on a mean-square basis.

$$E_T^2 = E_F^2 + E_Q^2 + E_{res}^2$$

where

E_T = total rms error in the reconstructed video signal

E_F = rms error due to fluctuation noise in the communication channel

E_Q = rms quantization error

E_{res} = rms "residual" error

Of the many possible error sources only E_F and E_Q are controlled by the communications link design. Therefore, all other errors have been considered together as E_{res}. E_{res} (residual) is the error remaining when E_F and E_Q are removed. E_{res} includes all the error sources in the optics and electronics of both the camera and the reproducer.

An exact expression for E_F, normalized to full scale value of 1, is (Reference 6):

$$E_F = \sqrt{\frac{\epsilon}{3} \cdot \frac{2^N + 1}{2^N - 1}}$$

where

N = number of bits per word, and

ϵ = bit error probability

It is assumed intuitively that if fluctuation noise causes no more than one word (picture element) in 100 to be in error the picture will be faithfully reproduced with very little loss of information. Therefore, if $N = 4$, $\epsilon \cong 1/400 = 2.5 \times 10^{-3}$, and

$$E_F = \sqrt{\frac{2.5 \times 10^{-3}}{3} \cdot \frac{17}{15}}$$

$$= 3.075 \times 10^{-2}$$

The normalized rms quantization error is $1/2\sqrt{3}$ times the quantization increment (Reference 7). So, for $N = 4$

$$E_Q = \frac{1}{2\sqrt{3}} \cdot \frac{1}{2^N}$$

$$= \frac{1}{2\sqrt{3}} \cdot \frac{1}{16}$$

$$= 1.804 \times 10^{-2}$$

If it is assumed that $E_{res} = 3 \times 10^{-2}$ is a practical figure, then

$$E_T = \sqrt{(3.075)^2 + (1.804)^2 + (3.0)^2 \times 10^{-2}}$$

$$= 4.66 \times 10^{-2} = 4.66\% \text{ of full scale.}$$

A total error under 5% rms is in keeping with the requirement for 13 levels of resolution. This is also a worst case error as the communications systems will be designed for $\epsilon = 2.5 \times 10^{-3}$ to be worst case. Just a 2 db margin will reduce the bit error probability by a factor of 10 and E_F by $\sqrt{10}$ to 1%. Then

$$E_T = \sqrt{1^2 + (1.8)^2 + 3^2} \times 10^{-2} = 3.64\%.$$

Above 3 db margin the fluctuation error becomes negligible and

$$E_T = \sqrt{(1.8)^2 + 3^2} \times 10^{-2} = 3.5\%.$$

5.4.3 DIRECT LINK

Calculations have been carried out which relate transmission bit rate, transmitter power, and distance as shown in Figure 80 . Details of the calculations and assumptions made are given in Table 5.4-I. Except for transmitting antenna gain, other parameters either are not controllable or are set at the best attainable values. The effect of transmitter antenna gain change is readily investigated by adjusting the power output scale to keep the product of antenna gain and power a constant (e.g., a 3 db change in gain modifies the power scale by a factor of 2).

The calculations are based upon use of the Mariner C, or similar, data format. This is a very efficient system which the DSN is already equipped to handle and for which performance data are known. Recent theoretical work (Reference 8) indicates that approximately 1 db improvement may be obtainable by utilizing a single sinusoidal subcarrier. The straight line portion of the curves (Figure 80) are for constant modulation indexes for the Mariner C data and sync subcarrier of $\theta_d = 0.908$, and $\theta_s = 0.451$. These are the maximum values allowed (with tolerances) to prevent loss of carrier lock which occurs if the phase shift (including phase noise) exceeds 90^o. At the x's on the curves, the carrier tracking system is at threshold (worst case value). To maintain carrier lock at lower power the modulation index must be reduced to leave a greater fraction of power in the carrier and the curve dips down becoming asymptotic to the power required for tracking. Operation in the curved region is less efficient in terms of bits/watt-hour and should be avoided if the MFC experiment is energy limited, as is currently indicated. It would be useful to improve the threshold of the carrier tracking system, if possible, to increase the efficiency of operation at low bit rates. The most obvious way would appear to be through reduction of the carrier tracking bandwidth which is taken as 12 cps, the present minimum value at the DSIF. Reduction of this value would require development of an extremely phase-stable transmitter. This would be difficult in the MFC application where a pressure mount RF crystal is probably necessary because of its impact resistance. It was demonstrated on the Ranger program that transmitters utilizing pressure mount crystals can be made sufficiently stable to operate within the 12 cps bandwidth.

There is one other modulation method of interest which was reported recently by JPL (Reference 3). It is a multiple level FSK designated MFS for "multiple frequency shift". It is a non-coherent system and avoids the carrier tracking threshold of coherent PM. Comparison of the two systems displays an advantage for MFS approximately equal to the modulation loss factor of the PSK data subcarrier. This is to be expected if both systems

TABLE 5.4-I

DIRECT CAPSULE-EARTH PCM/PSK/PM MARINER C FORMAT

NO.	PARAMETER	VALUE	TOLERANCE	SOURCE
1	Total Transmitter Power 10 watts	+40.00 dbm	+2.0 - 0db	Hanson ADP
2	Transmitting Circuit Loss	- 2.00 db	+1.0 -0.5db	Hanson ADP
3	Transmitting Antenna Gain	+12.00 db	+0 -2.0 db	Harrington ADP
4	Transmitting Antenna Pointing Loss	-3.00 db	+3.0 - 0 db	Harrington ADP
5	Space Loss	-263.17 db	--	Link ADP
6	@ 2295 MC, R = 1 AU KM Polarization Loss 92.9 x 10^6 S. Mi.	-0.25 db	±0.25 db	Harrington ADP
7	Receiving Antenna Gain	+61.0 db	±1.0 db	Wall JPL
8	Receiving Antenna Pointing Loss	-1.0 db	±0.1 db	Wall JPL
9	Receiving Circuit Loss	-0.1 db	±0.1 db	Wall JPL
10	Net Circuit Loss ∑ 2 through 9	-196.52 db	+5.45 -3.95db	
11	Total Received Power 1 + 10	-156.52 db	+7.45 -3.95db	
12	Receiver Noise Spectral Density (N/B)	+183.83 dbm/cps	+.76 -.67 db	Wall JPL
13	T system = $30^{\circ}K \pm 5^{\circ}K$ Carrier Modulation Loss	-4.1 db	+.9 - .0 db	Link ADP
14	Received Carrier Power ∑11 + 13	-160.66 dbm	+8.35 -4.95db	
15	Carrier APC Noise BW ($2B_{LO}$ = 12 cps)	+10.79 db	+0 - 0.41 db	JPL Memo #33-83
16	CARRIER PERFORMANCE - TRACKING (one-way) Threshold SNR in $2B_{LO}$			
17	Threshold Carrier Power			
18	Performance Margin			
19	CARRIER PERFORMANCE - TRACKING (Two-way) Threshold SNR in $2B_{LO}$			
20	Threshold Carrier Power			
21	Performance Margin			

TABLE 5.4-I (Continued)

NO.	PARAMETER	VALUE	TOLERANCE	SOURCE
22	CARRIER PERFORMANCE Threshold SNR in $2B_{LO}$	+6.0 db	---	R. Wall JPL
23	Threshold Carrier Power $\sum$ 12 + 15 + 22	-167.04 dbm	+0.76 -1.08 db	
24	Performance Margin 14 - 23	+6.38 db	+9.11 -6.03 db	
25	DATA CHANNEL Modulation Loss θ_o = 0.809	-4.6 db	+0.6 -0.7 db	Link ADP
26	Received Data Subcarrier Power 11 + 25	-161.12 dbm	+8.05 -4.65 db	
27	Bit Rate (1/T) 8.33 b/s	+9.21 db·cps		
28	Required ST/N/B $P_e = 2.5 \times 10^{-3}$	+7.5 db	±0.5 db	Link ADP
29	Threshold Subcarrier Power 12 + 27 + 28	-167.12 dbm	+1.26 -1.17db	
30	Performance Margin 26 - 29	+6.00 db	+9.31 -5.82db	
31	SYNC CHANNEL Modulation Loss θ_s = 0.451	-10.5 db	+0.2 -0.3 db	Link ADP
32	Received Sync Subcarrier Power 11 + 31	-167.02 dbm	+7.65 -4.23 db	
33	Sync APC Noise BW ($2B_{LO}$ =)			
34	Threshold SNR in $2B_{LO}$ 1 cps	+11.0 db	±0.5 db	Link ADP
35	Threshold Subcarrier Power 12 + 34	-172.83 dbm	+1.26 -1.17 db	
36	Performance Margin 32 - 35	+5.81 db	+8.91 -5.42 db	

COMMENTS:

Item 1 Power is a variable in the parametric plots. 10 watts is a practical value for a small, 12" to 16", capsule payload.

2 Cables and connectors 1.5 ±0.5 db, Isolator 0.5 ±0.1 db.

3,4,6 These data are representative of a small helix of about 40° half-power beamwidth.

6 Distance is also taken as an independent parameter for the parametric plots. 1 AU is approximately the mean distance (or greater) for likely launches during 1969.

TABLE 5.4-I (Continued)

12 $\left(\frac{N}{B}\right)_{dbm/cps} = 10 \log \frac{KT}{10^{-3}} = 30 + 10 \log 1.38 \times 10^{-23}$

$+ 10 \log 30 = 30 - 228.60 + 14.77 = 183.83$ dbm/cps.

13, 25, 31 Reference 8 presents the relationship between modulation index and modulation loss. The indexes $\theta_D = 0.809$ and $\theta_s = 0.451$ are taken from Ref. 9 and are taken to be maximum values.

	0.809 rad.	46^o 21'
	0.451 rad.	25^o 50'
θ_{peak}	1.260 rad.	72^o 11'

15 A phase-stable crystal-controlled transmitter will be utilized in the capsule to permit use of the 12 cps tracking loop bandwidth.

28 Noise is allowed to corrupt not more than 1 picture element per 100. If 4 bits are utilized per element a bit error probability of $1/400 = 2.5 \times 10^{-3}$ can be allowed (i.e. essentially all corrupted words have only 1 bit in error). From Figure 25 Ref. 11 ST/N/B is found to be about +6 db. Adding 1.5 db for practical factors as suggested in the reference gives 7.5 db.

It is seen ~~from the table~~ that all three thresholds have a nominal margin of about +6 db and a small positive minimum (negative tolerance) margin. To maintain these margins, a reduction in transmitter power must be accompanied by a reduction in modulation index and data rate. The fraction of total power left in the carrier is approximately doubled by halving the modulation index. If both θ_s and θ_D are halved the following results:

	P $\theta_D = 0.809$ $\theta_s = 0.451$	P' $\theta_D = 0.404$ $\theta_s = 0.225$	Power Ratio P'/P
M_C	0.386	0.804	2.080
M_D	0.346	0.120	0.347
M_S	0.089	0.041	0.460

The margin in the table will be maintained if the transmitter power is reduced to 10/2.08 = 4.8 watts and the bit rate reduced to 8.33 x 0.347 = 2.9 bit/sec. Since the power in the sync channel dropped less than that of the data channel, a slight improvement in the bit rate would be obtained by increasing the ratio θ_D / θ_s. However, it is likely that sync detection will become less efficient as the detection bandwidth drops below 1 cps (and a very stable crystal or fork reference is required). A plot of bit rate versus power becomes asymptotic to 10 x 0.386 = 3.86 watts, the power required for tracking.

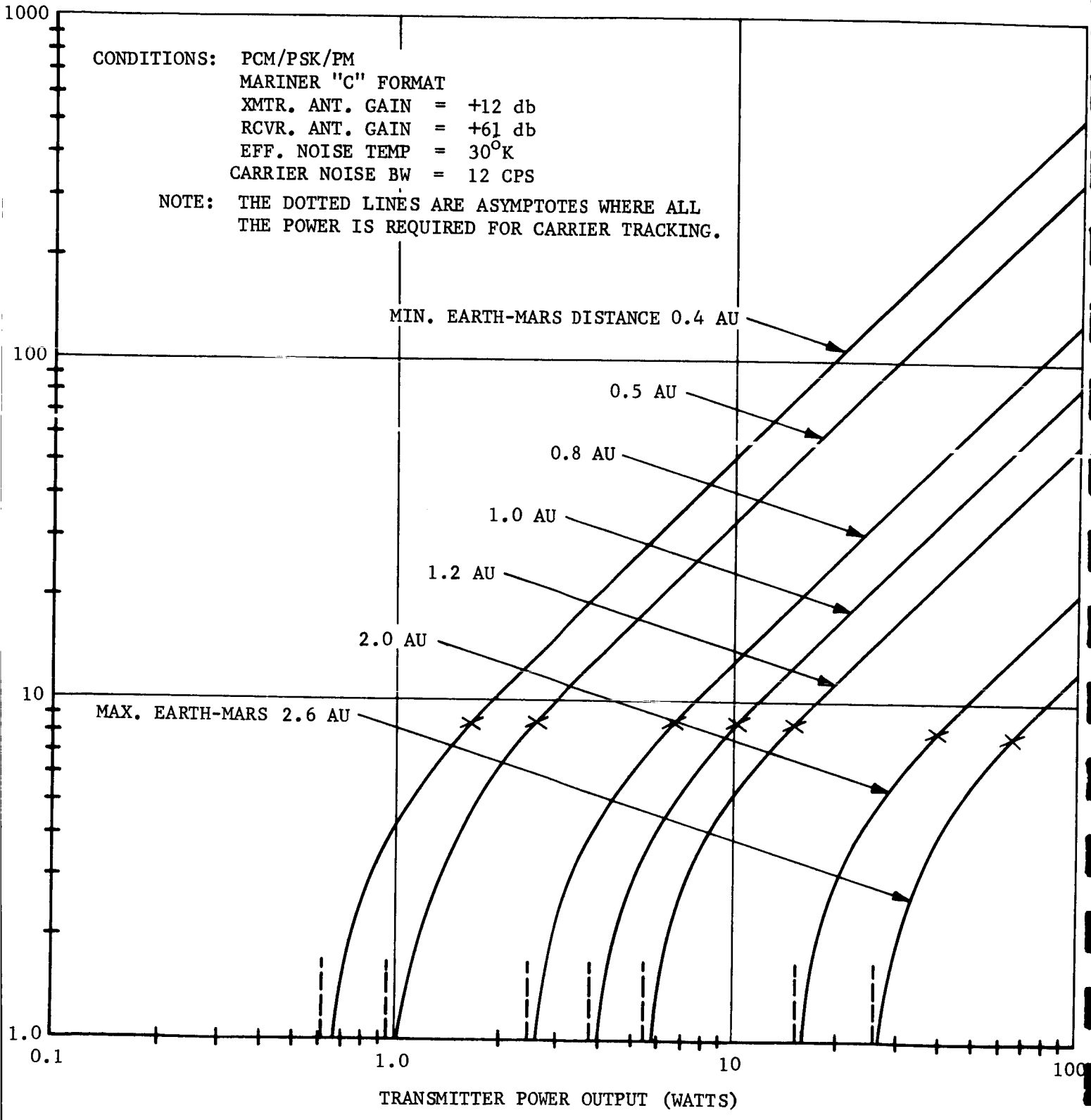

R11198

FIGURE 80 . TRANSMISSION CAPABILITY FROM MARS.

are operated with near optimum detection. The power advantage for MFS is 4.6 db in the linear region of the curves of Figure 80 , and its advantage would increase below 8 bps. To achieve this performance, a complex detection system is required (as was used in the Venus radar bounce experiment). It is not known whether this system will be implemented operationally in the DSN. If it should be, MFS would be a prime candidate for the MFC application because of its considerable power advantage. This would reduce the weight of batteries required for a fixed amount of data and would simplify the transmitter development.

A 16-level (frequency) MFS system would be comparable to the PCM format described in Section 4.4.2 with 4 bit resolution of each element. An MFS system of up to 32 levels is considered practical.

5.4.4 SPACECRAFT RELAY

A study was made of the merits in the use of the flyby spacecraft as a relay for the MFC-to-Earth data transmission. The relay method would appear to have merit if the already existing transmitter/power system (of estimated 20 watts RF output) and the relatively high gain (assume +23 db) Earth pointing antenna on the S/C could be utilized.

Analysis of the MFC communications via the S/C requires separate consideration of two communication links; that of the capsule to S/C, and the S/C to Earth. The S/C to Earth link may readily be analyzed using the calculations for direct transmission given in Section 5.4.3. It is assumed that the RF power is 20 watts and the antenna gain is +23 db.* Table 5.4-I is applicable except for an 11 db improvement (12.6 x in power) in transmitting antenna gain and a 3 db increase in power. Figure 80 may be used with the power scale reduced by the factor 1/12.6. Therefore, at 1 AU distance it would be possible to utilize a transmission rate of 210 bits/sec. from the spacecraft to Earth based upon parameter values considered to be conservative for 1969 launches.

The MFC to S/C link requires entirely different considerations. Figures 81 , 82 , and 83 show the communication geometry for a typical flyby/lander Mars mission. The trajectory was chosen to yield a near equatorial landing site. The lander was separated at 200,000 km, and its speed increased 100 meters/sec. to assure line of sight contact with the vehicle for a period after landing. The periapsis altitude employed was 1500 mi. Through the use of a somewhat larger periapsis altitude, it would be possible to eliminate the dip below the horizon which occurs about 1.5 hours after landing. It is assumed that the MFC antenna would have

---

* This assumes a modest growth in power of +3 db over that of Mariner C and a comparable antenna.

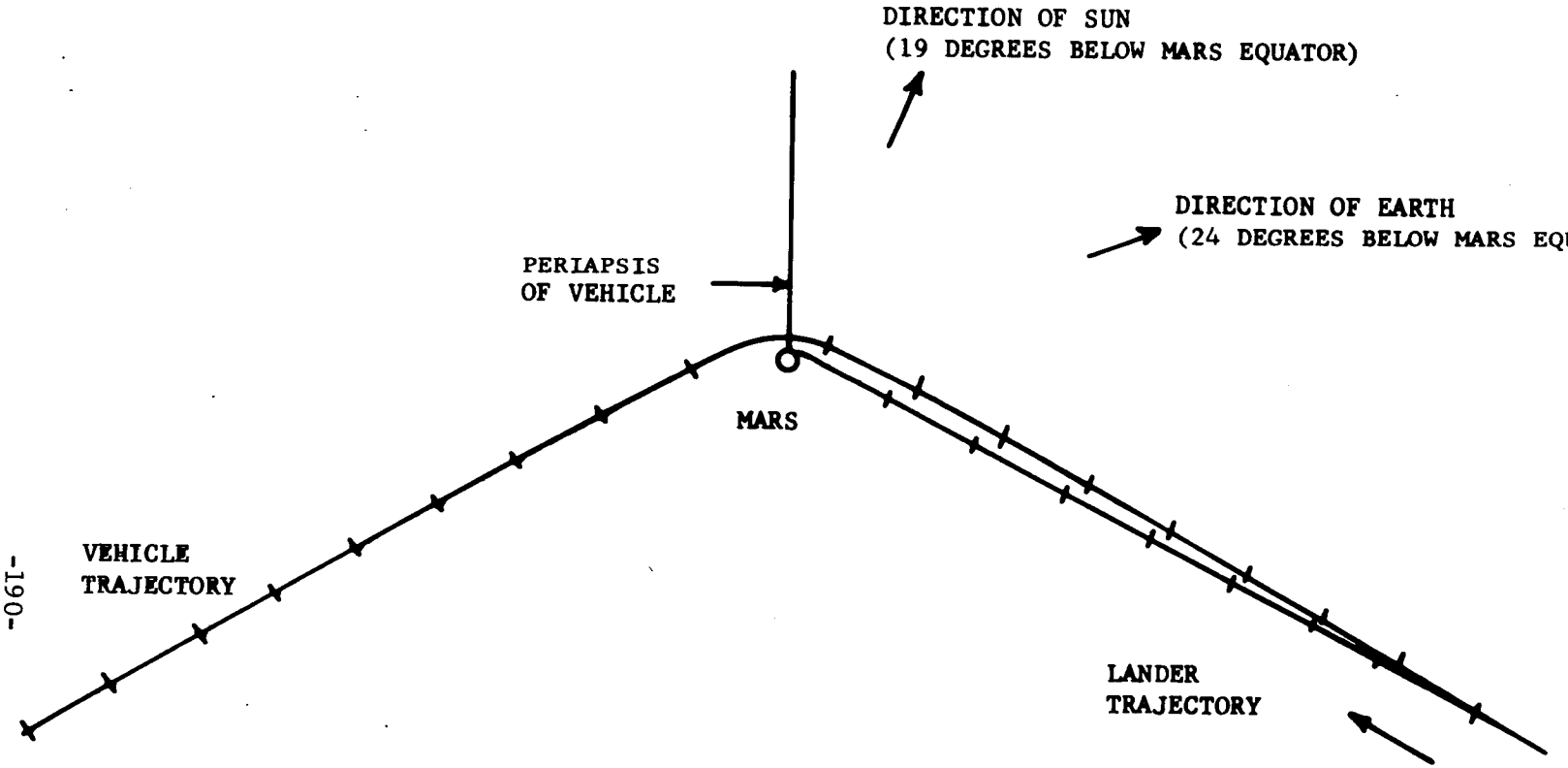

LAUNCH DATE: 22 MAY 1971

ARRIVAL DATE: 15 DECEMBER 1971

INCLINATION OF ORBITS TO MARS EQUATORIAL PLANE: 6.28297 DEG.

EACH TIME POINT REPRESENTS 2 HOURS

FOR THE VEHICLE: PERIAPSIS TIME, 18.25 HOURS
PERIAPSIS DISTANCE, 1.70 MARS RADII

FOR THE LANDER: IMPACT TIME, 17.53 HOURS
IMPACT LATITUDE, -0.278 DEG.

LANDER SEPARATION
TIME = 0
DISTANCE = 58.47 MARS RADII
$V_\infty = 2.81991 \frac{KM}{SEC}$

SCALE:

5 MARS RADII
17,000 KM

FIGURE 81. MARS FLY-BY AND LANDER TRAJECTORIES, 1971 TYPE I MISSION

R11207

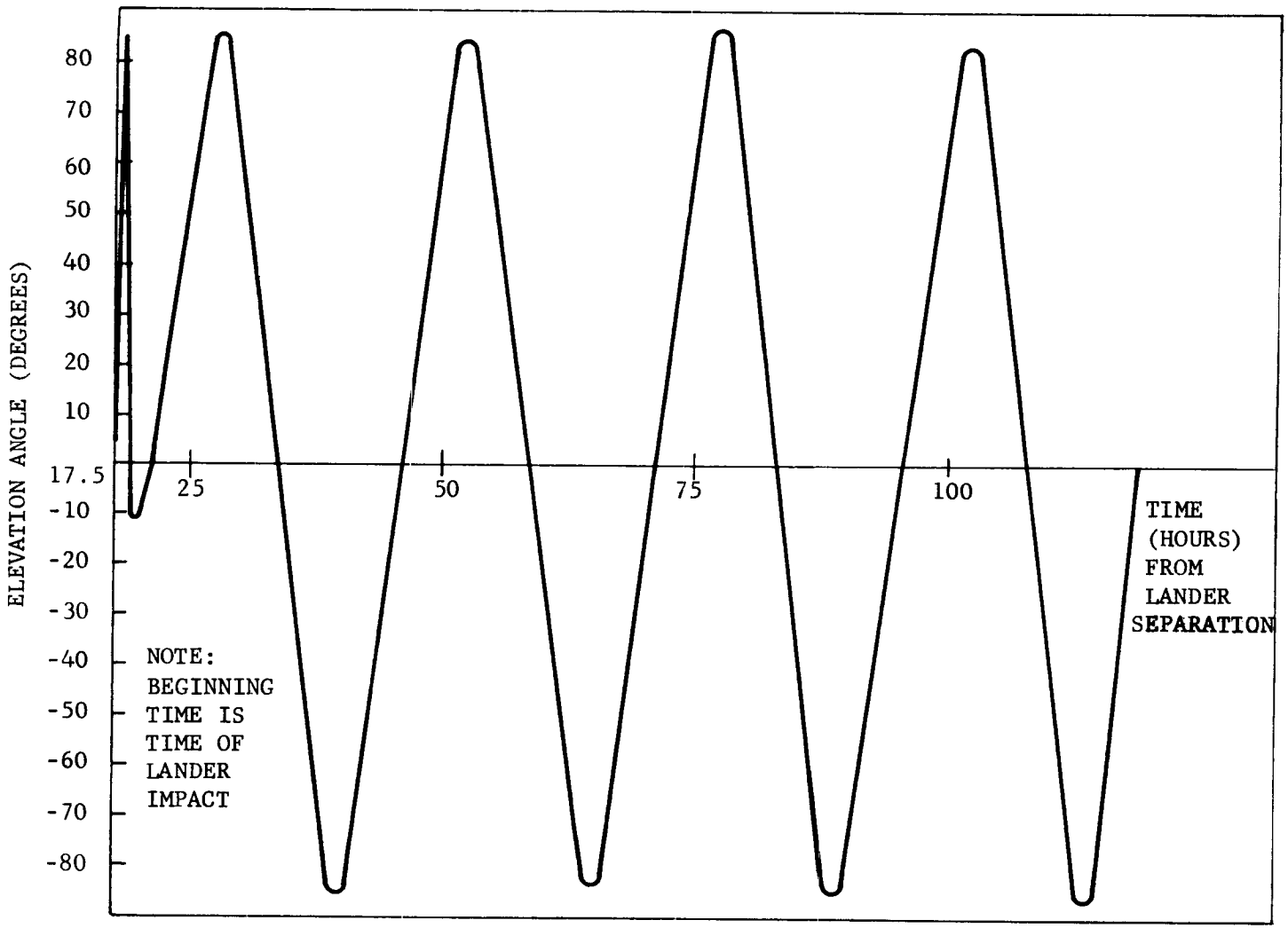

FIGURE 82. ELEVATION ANGLE VS. TIME FOR FLY-BY VEHICLE, 1971 TYPE I MISSION.

R11190

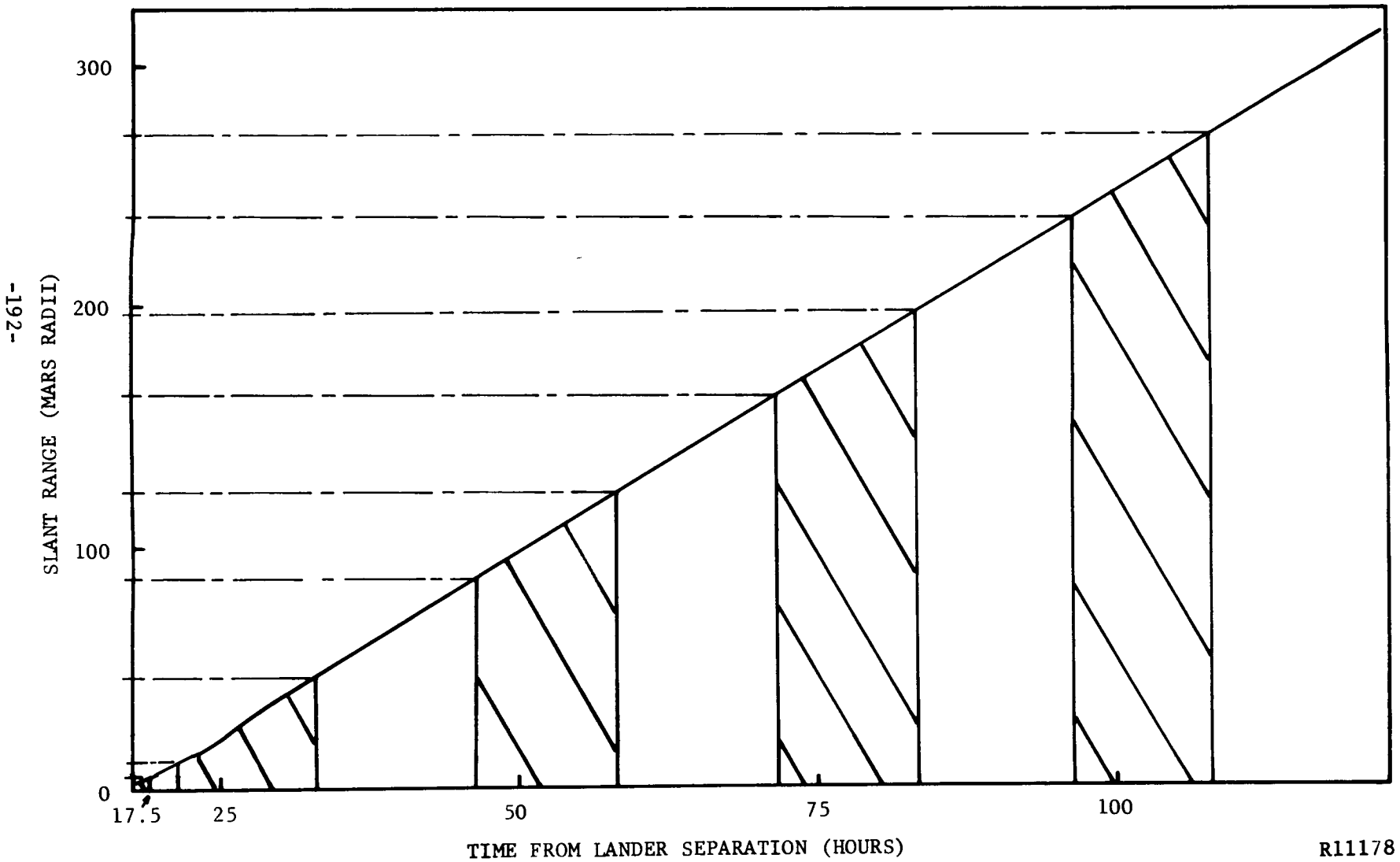

FIGURE 83. SLANT RANGE VS. TIME FOR FLY-BY VEHICLE 1971 TYPE I MISSION

essentially hemispherical coverage so that pointing would not be required, and that transmission is possible from the MFC to the S/C whenever the S/C is at least 5° above the Mars horizon. With these assumptions the periods available for transmission can be seen from Figure 82 , for a typical 1971 flyby/lander mission. The transmission periods and the communication ranges (from Figure 83) are tabulated in Table 5.4-II.

TABLE 5.4-II

TABLE OF COMMUNICATIONS INTERVALS

Period of Transmission Available Capsule to S/C, Hours after Separation	Interval Hours	Range, KM Minimum	Range, KM Maximum
1. 17.5 to 19.0	1.5	10,200	20,400
2. 21.5 to 33.0	11.5	35,700	156,300
3. 46.5 to 58.0	11.5	297,500	417,000
4. 71.5 to 83.0	11.5	554,500	670,000
5. 96.0 to 107.5	11.5	805,000	922,000

The typical transmission period available (11.5 hours) is nearly 1/2 the Mars day; however, for the trajectory shown the first available transmission period is short, 1.5 hours, followed by a dip of 2.5 hours below horizon. Other trajectories could eliminate this dip. However, even for the case tabulated, if power is a limitation it is preferable to attempt all transmission during the first interval. For example, the ratio of available time for the first two periods is 11 to 1, subtracting 0.5 hours for margin. The ratio of maximum distances is 156,300/20,400 = 7.67. Since the maximum data rate varies inversely as the square of the distance and $(7.67)^2 = 58.9$, over 5 times as much information can be transmitted during the first brief interval as compared to the next longer interval with equal transmitter power. Also, for the later intervals the sun lighting conditions are unfavorable during most of the transmission period so that MFC data storage would still be required.

The most useful communications analysis will be for the maximum range of the first interval, 20,400 KM. A fixed antenna on the S/C of 30°

beamwidth can be pointed to cover the MFC during the period of transmission. Such an antenna would yield a gain of about +14 db. A minimum scene of 24^{o} by 24^{o} with 0.1^{o} resolution represents a total transmission of 276 kilobits assuming N = 4 and 15% added bits for synchronization and identification. This represents a transmission rate of 77 bits/sec over a one-hour interval.

An important question to be answered is whether a reliable method for S/C receiver acquisition of the MFC RF signal can be found. This is because the frequency shifts will be very large compared to the modulation bandwidth. One important frequency effect is that due to doppler. The S/C is receding from Mars at approximately 2.8 km/sec, causing a frequency shift of 21.6 kc if a 2300 mc carrier were used, or 2.2 kc if the frequency were reduced to 230 mc. The doppler effect due to Mars rotation is 10% as large (surface velocity = 0.24 km/sec). These (doppler) effects are known a priori and could be accounted for with some uncertainty in receiver tuning. There are also other random effects which are estimated as follows:

a)	$\pm$ 0.005% Recvr. L.O. instability	=	$\pm$ 11.5 kc at 230 mc
b)	$\pm$ 0.005% Trans. instability	=	$\pm$ 11.5 kc
c)	$\pm$ 0.0025% Trans. shift at impact	=	$\pm$ 5.8 kc
	Total (peak)		$\pm$ 28.8 kc

The one-shot nature of the transmission suggests a wideband non-coherent receiver for reliability; however, it is found that the power required at 2300 mc is prohibitive. In reaching this conclusion, operation at 230 mc was assumed which reduces path loss by 20 db as compared to 2300 mc. Operation at still lower frequencies should be considered but antenna implementation becomes a problem. At 230 mc, +14 db gain requires a parabola of 3.5 ft. diameter or an equivalent antenna on the S/C. The MFC antenna, for hemispherical coverage, might be wire turnstile at the top of the extension tube, with each arm at least 15" long. To achieve usable performance, a system was assumed using the PCM/PSK/PM format in which the S/C receiver has a 60 cps tracking bandwidth at 230 mc and has a built-in search function which scans until lock is achieved. This complicates the receiver but is well within the state of the art and lock-on times of a minute are reasonable with a sweep of $\pm$50 kc.

Another advantage of VHF operation is that increased transmitter efficiency is possible. Two S-band solid state transmitters are described in Section 5.5 which depend upon the generation of 36 to 40 watts at 382.5 mc. Therefore, to put the relay system on a competitive basis, a 40-watt transmitter is assumed (of about 40% efficiency). Calculations are shown in Table 5.4-III which indicate the feasibility of transmitting from the capsule to the S/C at 100 b/s for 1 hour (to 20,400 km) for a total of 360 kilobits total.

TABLE 5.4-III

CAPSULE - S/C PCM/PSK/PM

NO.	PARAMETER	VALUE	TOLERANCE	SOURCE
1	Total Transmitter Power 40 watts	+46.00 dbm	+2.0 -0.0db	Hanson ADP
2	Transmitting Circuit Loss	-2.00 db	+1.0 -0.5db	Hanson ADP
3	Transmitting Antenna Gain	+2.00 db	+1 -2.0db	Harrington ADP
4	Transmitting Antenna Pointing Loss	---	---	
5	Space Loss	-165.9 db		
	@ 230 MC, R = 20,400 KM			Harrington ADP
6	Polarization Loss	-1.5 db	±1.5 db	
7	Receiving Antenna Gain	+14.00 db	+1 -3 db	Harrington ADP
8	Receiving Antenna Pointing Loss	---	---	
9	Receiving Circuit Loss	-1.5 db	±0.5 db	Hanson ADP
10	Net Circuit Loss 2 through 9	-154.9 db	+5 db -7.5db	
11	Total Received Power	-108.9 dbm	+7 db -7.5db	
12	Receiver Noise Spectral Density (N/B)	-163.6 dbm	± 1db	
	T system = 3200°K			
13	Carrier Modulation Loss	-4.1 db	+0.9 -1.0 db	
14	Received Carrier Power	-113.0 dbm	+7.9 -8.5 db	
15	Carrier APC Noise BW ($2B_{LO}$ = 60)	17.8 db	±1 db	
	CARRIER PERFORMANCE - TRACKING (one-way)			
16	Threshold SNR in $2B_{LO}$			
17	Threshold Carrier Power			
18	Performance Margin			
	CARRIER PERFORMANCE - TRACKING (Two-way)			
19	Threshold SNR in $2B_{LO}$			
20	Threshold Carrier Power			
21	Performance Margin			

TABLE 5.4-III (Continued)

NO.	PARAMETER	VALUE	TOLERANCE	SOURCE
	CARRIER PERFORMANCE			
22	Threshold SNR in $2B_{LO}$	6.00		
23	Threshold Carrier Power 12 - 15 - 22	-139.8 dbm	±2 db	
24	Performance Margin	+26.8 db	+9.9 -10.5 db	Worst case +16.3 db
	DATA CHANNEL			
25	Modulation Loss θ_o = 0.809	-4.6 db	+0.6 -0.7 db	
26	Received Data Subcarrier Power	-113.5 dbm	+7.6 -8.2 db	
27	Bit Rate (1/T) 100 b/s	20 db·cps		
28	Required ST/N/B_e P_e^W = 10^{-2}	7.5 db	±0.5 db	
29	Threshold Subcarrier Power	-136.1 dbm	± 1.5 db	
30	Performance Margin	+22.6 db	+9.1 - 9.7 db	Worst Case +12.9 db
	SYNC CHANNEL			
31	Modulation Loss θ_s = 0.451	-10.5 db	+0.2 -0.3 db	
32	Received Sync Subcarrier Power	-119.4 dbm	+7.2 -7.8 db	
33	Sync APC Noise BW ($2B_{LO}$ =) 12 cps	+10.8 db		
34	Threshold SNR in $2B_{LO}$ 1 cps	+11.0 db	±0.5 db	
35	Threshold Subcarrier Power	-141.8 dbm	±1.5 db	
36	Performance Margin	+22.4 db	+8.7 -9.3 db	Worst case +13.1 db

COMMENTS:

A worst case margin of 12.9 db remains which could be removed by reducing power to a very readily obtained 2-watts which would also avoid possible corona breakdown. However, part of the margin might better be traded-off in simplifying the required S/C receiver. For the calculations, assume data and synchronization performance comparable to that attained at the DSIF (Reference 10) and assume receiver noise and carrier threshold equal to that of the Mariner C S/C receiver with the addition of a search function. Also increase the carrier APC (automatic phase control) noise bandwidth from 20 cps for the Mariner C receiver to 60 cps to simplify implementation. The calculations are based upon a bit error probability of 2.5×10^{-3} which is the desired overall value. Finally, the S/C to Earth link should be upgraded by a factor of ten which requires a 2 db increase in transmitter power or a comparable reduction in retransmission bit rate.

One other factor which must be considered is the relative reliability of relay transmission versus direct transmission. JPL has carried out a rather detailed reliability comparison, Reference 12, for the Mariner 69 and Voyager projects. In the JPL analysis, capsule transit time, T_i, is taken to be 4,000 to 8,000 hours (166.7 to 333.3 days). The capsule operation time or experiment duration is taken to be between 10 and 2,500 hours (presumably covering a wide variety of experiments). For standby condition of the capsule during transit, a failure rate 20% of normal operating value is assumed mainly to account for out-of-limit parameter deviations rather than catastrophic failure of parts. Representative data comparing the reliability of direct and relay telemetry and command are shown in Figure 5.4-8, taken from Reference 12. The upper pair of curves, for P_t (CR) = 1, assume that the capsule release (CR) and landing function has performed properly. There is a distinct advantage for the direct approach which is not surprising when it is considered that 6 series subsystems are involved compared to 19 for the relay method. For command transmission there is no significant difference in reliability between the two methods for experiment times up to 100 hours. Beyond this point the direct method becomes advantageous.

5.4.5 EARTH COMMAND

It may be desirable to have an Earth-MFC command capability to control the MFC-Earth data transmission interval and possibly also control the HRF camera. The additional equipment initially required in the MFC will weigh approximately 3 lbs.,with subsequent control functions being added at essentially the cost of the necessary activation or control devices.

A telecommunication design control table, Table 5.4-IV, indicates more than adequate performance of the command link at 1 AU distance assuming the receiving (capsule) antenna is to be a helix of +12 db on axis gain and up to 3 db pointing loss. By June 1965, three DSN stations, those at Goldstone, Canberra, and Madrid, are scheduled to have command capability with 10 kw RF power and 85 ft. antennas of +51.0 db gain. These stations are approximately 120° apart and within $\pm 40^{\circ}$ of the Equator. Their

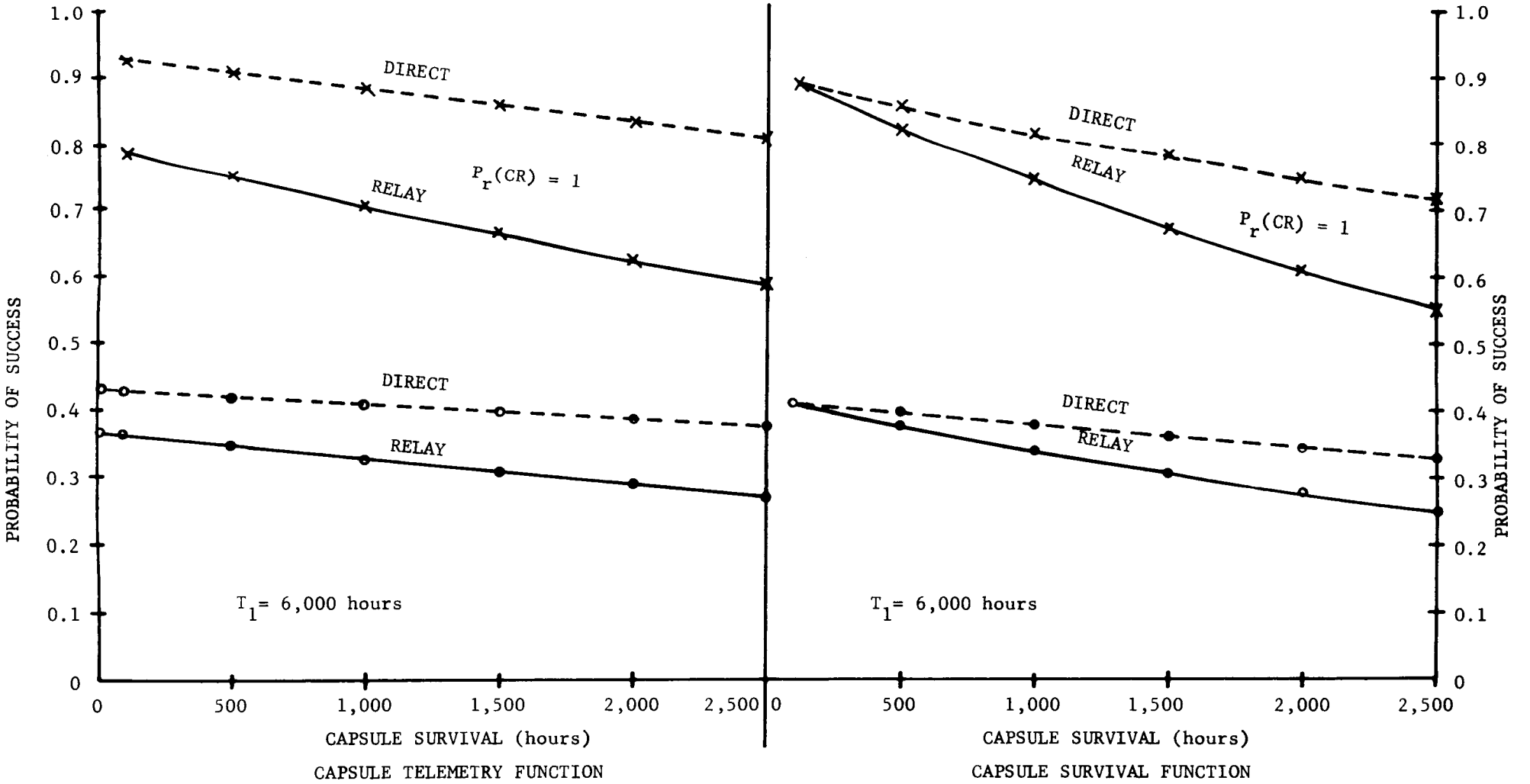

FIGURE 84. RELIABILITY COMPARISON, DIRECT VS. RELAY COMMUNICATION

TABLE 5.4-IV

EARTH TO MFC COMMAND

NO.	PARAMETER	VALUE	TOLERANCE	SOURCE
1	Total Transmitter Power 10 kw	+70.0 dbm		JPL Memo No. 33-83
2	Transmitting Circuit Loss	-0.4 db		" "
3	Transmitting Antenna Gain	+51.0		" "
4	Transmitting Antenna Pointing Loss	---		
5	Space Loss @ 2115 MC, R = 1 AU	-262.5		Link ADP
6	Polarization Loss	-0.3		Harrington ADP
7	Receiving Antenna Gain	+12.0		
8	Receiving Antenna Pointing Loss			
9	Receiving Circuit Loss	-2.0		*
10	Net Circuit Loss $\sum$ 2 through 9	-202.2 db		
11	Total Received Power	-132.2 dbm		
12	Receiver Noise Spectral Density (N/B)	-170.0 dbm/cps	+1 -0 db	
13	T system = NF = 4 db Carrier Modulation Loss x .846	-0.7 db		*
14	Received Carrier Power	-132.9 dbm		
15	Carrier APC Noise BW ($2B_{LO}$ = 20 cps)	+13.0 db-cps		*
16	CARRIER PERFORMANCE - TRACKING (one-way) Threshold SNR in $2B_{LO}$			
17	Threshold Carrier Power			
18	Performance Margin			
19	CARRIER PERFORMANCE - TRACKING (Two-way) Threshold SNR in $2B_{LO}$			
20	Threshold Carrier Power			
21	Performance Margin			

TABLE 5.4-IV (Continued)

NO.	PARAMETER	VALUE	TOLERANCE	SOURCE
	CARRIER PERFORMANCE			
22	Threshold SNR in $2B_{LO}$	+6.0 db		*
23	Threshold Carrier Power $\sum 12 + 15 + 22$	-151.0 dbm		
24	Performance Margin 14 - 23	+18.1 db		
	DATA CHANNEL			
25	Modulation Loss x .154	-8.13 db		*
26	Received Data Subcarrier Power	-141.3 dbm		
27	Bit Rate (1/T) 1 bps	0 db		
28	Required ST/N/B $P_e = 10^{-5}$	+9.6 db		
29	Threshold Subcarrier Power $12 + 27 + 28$	-160.4 dbm		
30	Performance Margin 26 - 29†	+20.1 db †		
	SYNC CHANNEL			
31	Modulation Loss			
32	Received Sync Subcarrier Power			
33	Sync APC Noise BW ($2B_{LO}$ =)			
34	Threshold SNR in $2B_{LO}$			
35	Threshold Subcarrier Power			
36	Performance Margin			

COMMENTS:

* Values taken from J. C. Springett, "Command Techniques For the Remote Control of Interplanetary Spacecraft", Proceedings of the 1962 National Telemetry Conference, Vol. 2.

† Springett includes 4 db "detection loss" which would reduce margin to 16.1 db.

placement permits continuous surveillance and command of objects more than 10,000 miles from Earth.* At a distance of 2 AU, path loss would be increased 6 db which is readily accommodated.

One bit/sec. command rate was assumed as this was standard for Mariner C. However, for the MFC few commands would be required and bit rate would not be an important factor. Also, extreme low probability of error would not be necessary to prevent a catastrophic error so short command words could be used. Therefore, a command bit rate well under 1 bps could be used.

It may be desirable to acknowledge commands. If so, this can be accomplished with the camera data transmission system. A coherent transponder is not necessary as (presumably) ranging is not desired.

A preliminary design has been carried out for a suitable command receiver for low weight, high impact application. It is shown in block diagram form in Figure 85 . The receiver will respond to PCM/FM/PM commands from the DSIF facility. It employs a low noise, high gain, circulator-coupled tunnel diode RF amplifier followed by a hybrid ring balanced mixer. This first mixer utilizes tunnel diodes to obtain a low noise, low loss conversion. The first IF amplifier and the second balanced mixer use three UHF silicon transistors. The combined gain of these two stages will be 40 db minimum. The second IF amplifier, phase demodulator and subcarrier discriminator circuits are of standard design. Oscillator frequency stability will be on the order of 5 PPM.

The phase reference signal and all of the mixer injection frequencies are obtained from a single phase stable crystal controlled oscillator. Step recovery diode frequency multipliers will be employed due to the very high efficiencies and circuit simplicity obtainable with these devices. It is estimated this receiver could be packaged in 30 $in.^3$ and weigh about 2.0 lbs., including the circulator of 0.5 lbs. With the use of another circulator, a single antenna could be shared for transmit and receiver. There would not, however, be simultaneous transmit and receive capability. Earth would command the MFC transmission on for a predetermined length of time, and further command would await cessation of transmission.

5.4.6 DSIF PARAMETERS

The DSIF parameters assumed in various places through Section 5.4 are summarized here for ready reference. It is expected that all of these capabilities will be operational by the end of 1967, according to Reference 1. Even if

---

* In addition, the Goldstone Venus site has a 100 kw transmitter and 85 ft. antenna for R&D but which can be made available for operational use.

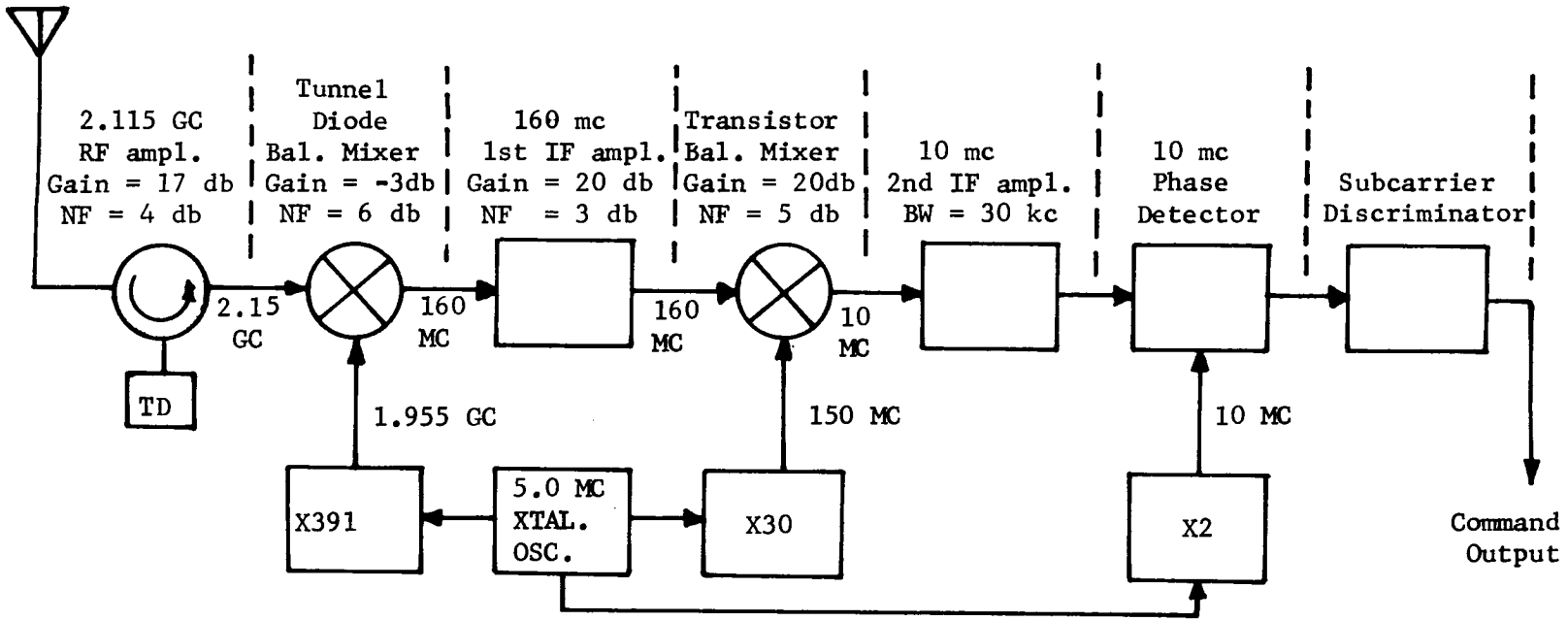

FIGURE 85 S-BAND COMMAND RECEIVER

schedules slip, they should be installed and operating by the expected 1969 MFC launch.

Data Reception

Receiving antenna gain	6.0 ± 1.0 db
Receiving antenna pointing loss	1.0 ± 0.1 db
Receiving circuit loss	0.1 ± 0.1db
Effective system temperature	$30^{o}K \pm 5^{o}K$
Carrier tracking bandwidth	12 cps
Carrier threshold SNR (one way track)	0 db for maintenance of lock 50% of time; + 6 db for telemetry data

It is assumed that carrier lock and synchronization to the Mariner C format are accomplished within 2 minutes at 8-1/3 bps data transmission rate.

Command Transmission

Transmitter power (100 KW at Goldstone only if required)	10 KW
Transmitting antenna gain	+ 51.0 db
Transmitting circuit loss	0.4 db

5.4.7 CONCLUSIONS

It is concluded that there are several feasible modes for transmission of the MFC data to Earth. The most straightforward method in terms of proven techniques would be to utilize a Mariner C or similar format (PCM/PSK/PM) in a direct transmission to Earth. This permits a relatively low data rate, 2 to 20 bps, and requires an impact resistant S-band transmitter of 10 to 20 watts RF output. A new system, MFS (multiple frequency shift), is promising and if the required detection equipment is implemented in the DSN, this system offers a 4.5 db improvement over the PCM/PSK/PM format and also simplifies the transmitter implementation.

Transmission via the S/C (spacecraft) as a relay is also feasible and a transmission bit rate of 100 to 200 bps is attainable with a transmission period of 1 to 1.5 hours utilizing a VHF (230 mc) transmitter of 4 to 10 watts. This transmitter would be much simpler to implement than an S-band

unit. Use of the spacecraft as a relay requires a new S/C receiver development, limits other S/C uses, and operates at somewhat degraded reliability. Using the minimum number of shades of gray, it will be necessary to ensure that the encoding range is covered for a given scene. This implies use of signal compression and/or an adaptive encoder. The square-rooter helps in this regard as it reduces the dynamic range in decibles by a factor of 2.

REFERENCES

1. "System Capabilities and Development Schedule of the Deep Space Instrumentation Facility, 1964-68", (Revision 1), JPL Technical Memorandum No. 33-83.

2. SPACE TECHNOLOGY, Edited by Howard S. Seifert, John Wiley & Sons, Inc. 1959. p.23-14.

3. Goldstein, R. M. & Kendall, W. B., "Low Data Rate Telemetry", Paper No. 65-26, AAS Symposium on Unmanned Exploration of the Solar System, Feb. 8-10, 1965, Denver, Colorado, JPL EDP-261, Section X.

4. R. L. Carbrey, "Video Transmission Over Telephone Cable Pairs by Pulse Code Modulation", Proc. IRE, Sept. 1960, pp. 1546-1561.

5. L. G. Roberts, "Picture Coding Using Pseudo-Random Noise", IRE Trans. on Information Theory, Feb. 1962, pp. 145-154.

6. "Telemetry Systems Study (U), Final Report", Aeronutronic Publication No. U-743, 18 December 1959 (3 vols.), Volume I, Appendix 2, DDC No. AD-234958.

7. W. R. Bennett, "Methods of Solving Noise Problems", Proc. IRE, 1956, p. 611.

8. "On the Allocation Power in a Synchronous Binary PSK Communications System", J. J. Stiffler, Proc. of the 1964 National Telemetry Conference.

9. "Square Wave Data Subcarrier for Mariner Telemetry", G. L. Fultz, Internal JPL Memo SPS No. 37-18, July 23, 1962.

10. Functional Specification No. MC-4-310A, "Mariner C Flight Equipment Telecommunication System".

11. "The Mariner Planetary Communication System Design", B. D. Martin, Proc. of the 1962 National Telemetering Conference.

12. "Relay vs Direct System Reliability Analysis", by Edward N. Gordon and Man K Tam, Sept. 25, 1964, JPL Document No. TS3361-64-1, Reorder No. 64-490.

13. Springett, J. C., "Command Techniques for the Remote Control of Interplanetary Spacecraft", Proc. of the 1962 National Telemetering Conference, Vol. 2.

5.5 TRANSMITTER

5.5.1 SUMMARY

Several implementations of an S-Band transmitter suitable for use in the Mariner Mars HRF Capsule have been considered. Desired power levels range from 10 watts to 100 watts. Survival of 3000 g landing impact is required. Choice of the power output stage requires a thorough evaluation of overall transmitter design at these power and "g" levels because of the relatively large mass and critical internal dimensions of applicable vacuum tube devices. Required operating life is short so that vacuum tubes are practical in this regard.

Four types of output stage devices are examined and evaluated including:

(1) Vacuum triode cavity amplifier

(2) Varactor multiplier

(3) Amplitron

(4) Traveling Wave Tube (TWT)

Various transmitter configurations capable of 10 watts output, or 20 watts utilizing paralleled output stages or multiple antennas are shown. These techniques allow use of small tubes and semiconductors with known impact survival history. They also reduce the power requirement of the individual power output stage to that realizable by solid state multipliers which provide greater reliability than large single stage devices. Emphasis is upon the 10 to 20 watt range both because of the availability of active devices and because usable data rates result.

5.5.2 REQUIREMENTS

The telecommunications calculations indicate that output powers in the range of 10 watts to 100 watts may be required at 2295 mc. Overall transmitter efficiency is to be as high as possible to minimize battery weight. Carrier phase jitter must be held below two to three degrees necessitating a stable crystal-controlled source to allow use of the narrow 12 cycle carrier tracking loop bandwidth in the DSIF. As the 20-watt power level is presently beyond attainment with solid state multipliers (without using power summing techniques), use of vacuum tube devices are to be considered which will survive the 3000 g environment. The period of actual data transmission will be the order of 5 to 30 hours. This plus test and checkout time would result in a total required operating life of perhaps 500 hours at most.

5.5.3 CONFIGURATIONS

A number of transmitter configurations are possible depending primarily upon the type of power output stage utilized. All configurations include a solid state 2295 mc crystal controlled signal source consisting of a transistor crystal oscillator, buffers, power amplifiers, and multipliers. This approach is consistent with previous experience with reliable solid state multipliers at high g levels.

Three possible output stage configurations are shown in Figure 86 . The simplest configuration (Figure 86a) utilizes a single 10 to 20 watt output device such as a TWT, Amplitron or varactor multiplier driving a single antenna. This represents the most efficient configuration in terms of size, weight, and dc-rf conversion efficiency but is, of course, dependent upon obtaining a suitable active device which will survive impact.

The configuration shown in Figure 86b utilizes two output stages such as a small ceramic triode cavity amplifier or varactor multiplier each driving a separate antenna to double the total power. An output power level monitor can be included which would reduce bit rate and deviation to ensure maintenance of carrier lock in the event of a drop in output power. Then increased reliability, or at least partial mission success, could result due to the redundancy. Some degradation in overall carrier phase stability results from the random phase jitter contribution of each output stage, but this is expected to be small compared to that of the crystal oscillator.

The configuration shown in Figure 86c utilizes a single antenna driven by multiple output stages through a hybrid power combiner. The hybrid performs the functions of isolation, impedance matching, and power summation. Isolation between output stages provided by the hybrid network prevents mismatch caused by failure of one output stage from seriously degrading power output from the remaining stage. As with the previous approach, small ceramic triodes or varactor multipliers may be used with increased probability of surviving the 3000 g environment. Because of the multiple output stages, carrier phase stability is degraded slightly and volume and weight are increased. Efficiency is also lowered due to the hybrid insertion loss of from 0.5 db to 1.2 db.

A logical extension of the dual output stage using hybrid power combiners is to use four output stages and three power combiners to provide 40 to 80 watts output. With output level monitoring, and bit rate and deviation adjustment provisions three channels can be lost without completely losing communications.

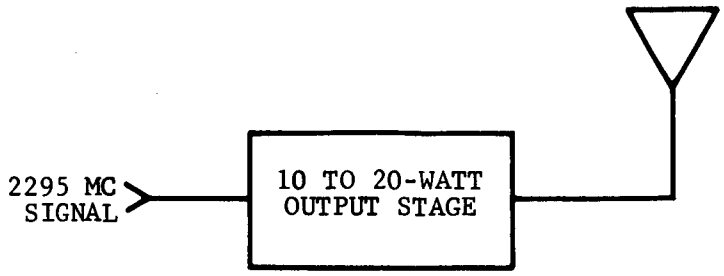

A - SINGLE DEVICE OUTPUT STAGE

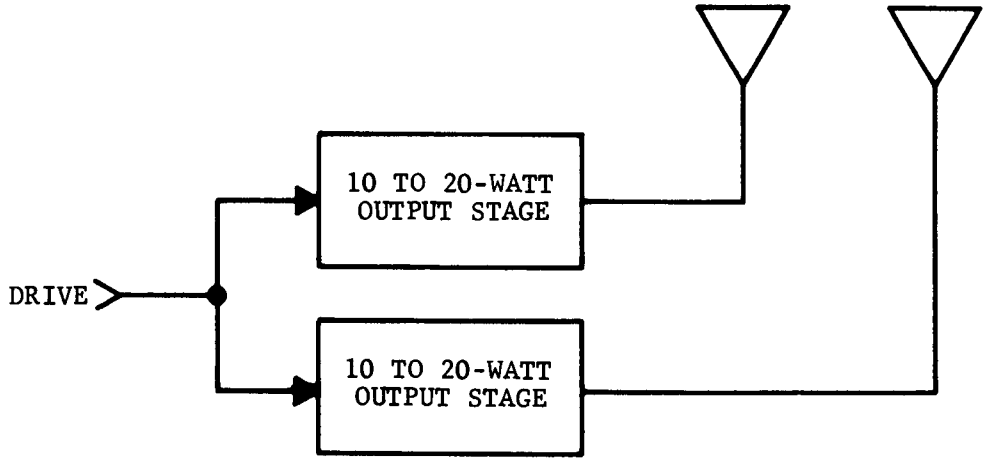

B - MULTIPLE OUTPUT STAGES AND ANTENNAS

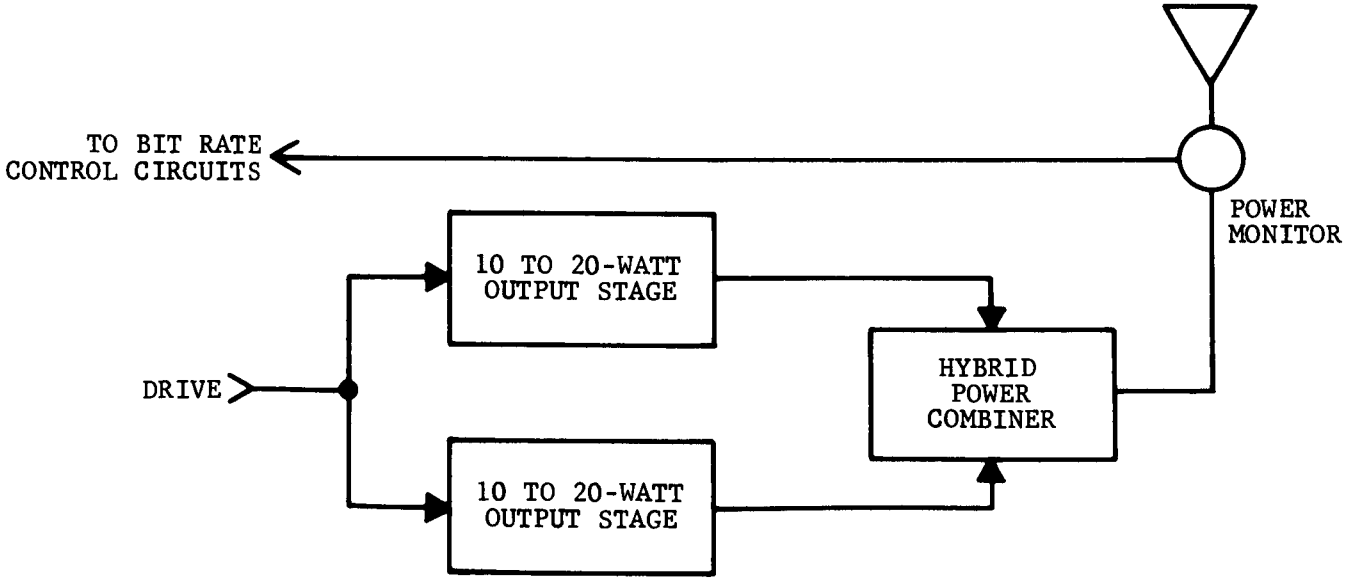

C - MULTIPLE OUTPUT STAGES - SINGLE ANTENNA

R11156

FIGURE 86. VARIOUS S-BAND TRANSMITTER CONFIGURATIONS

5.5.4 OVERALL IMPLEMENTATION

a. TWT Output Stage. Hughes Aircraft Corporation (HAC) has a series of TWT's for operation at 2295 mc, with the following characteristics:

TUBE TYPE	CW POWER OUTPUT @ 2300 MC (WATTS)	SIZE, DIAMETER X LENGTH	SHOCK QUAL. G LEVEL
HAC 314H	2.5	1.375" x 7.982"	450 g by HAC
HAC 349H	10.0	1.588" x 7.982"	No test data
HAC 379H	20.0	1.40 " x 9.06 "	No test data
HAC 394H	5 to 20.0	1.380" x 9.195"	No test data

Figure 87 shows a typical S-Band transmitter configuration utilizing a 20-watt 379H TWT output stage. Because of the high power gain of this tube (30 db) the 2295 mc drive requirement is only 20 milliwatts which allows use of a single stage X20 step diode-type multiplier. This causes an appreciable reduction in both complexity and power levels in the signal source as compared to other designs. In spite of the high overall dc-rf efficiency and relatively small size of this system, it is believed that no existing TWT could be impact qualified without an extensive development program.

b. Amplitron Output Stage. Figure 88 shows an amplitron in the output stage. The drive level requirements exceed that available from a step-diode multiplier so conventional varactor diode multipliers are used at reduced efficiency and some volume and weight penalty. As with the TWT, extensive development would be necessary to ruggedize the amplitron at 3000 g levels. Additional weight results from the requirement for a well regulated power supply.

c. Vacuum Triode Power Amplifiers. A range of ceramic-metal triodes with CW power outputs of 2.5 to 40 watts are available which operate at 2295 mc. These are listed below along with several cavity amplifier packages. As indicated, four of the smallest devices of 2.5 and 5 watts output have been shock qualified at either 3000 or 26,000 g's. These may have been shocked only in one direction at 26,000 g's as they are used in instrumented gun launched projectiles by the Army's Harry Diamond Laboratories. While the largest tubes may be capable of withstanding 3000 g impact with re-design, it is considered that smaller tubes would be more likely candidates. Therefore, the transmitter configuration shown in Figure 89 utilizes 2 triode-cavity amplifiers driven from a solid state 2295 mc signal source to obtain 20 watts output. This represents probably the best configuration in terms of implementation with some degree of impact survival assurance. Use of the triode output amplifiers

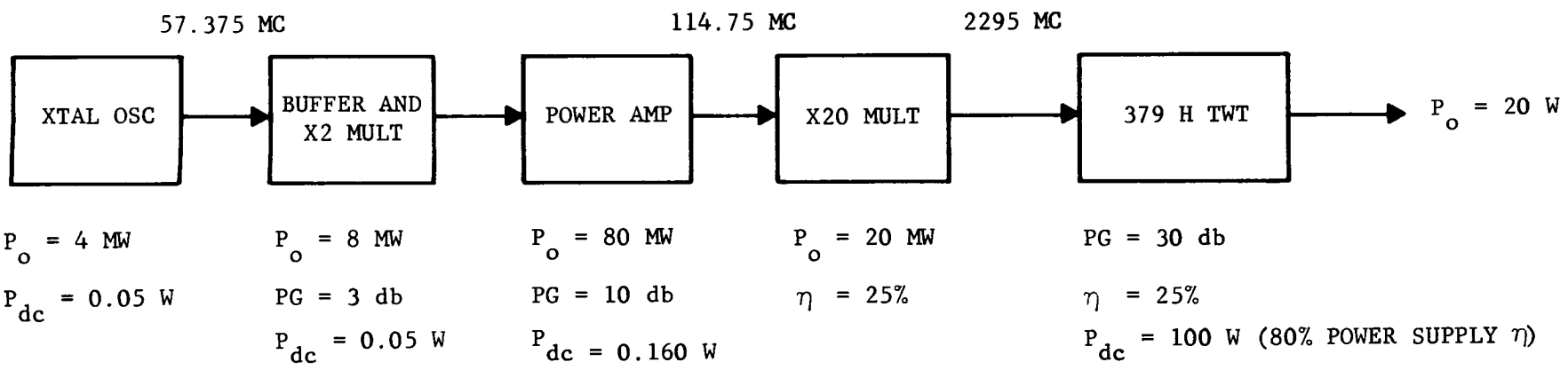

P_{in} = 100.26 W

η = 24.9%

EST VOLUME: 120 IN.^{3}

EST WEIGHT: 6 LBS

FIGURE 87. S-BAND TRANSMITTER TWT OUTPUT STAGE

R11153

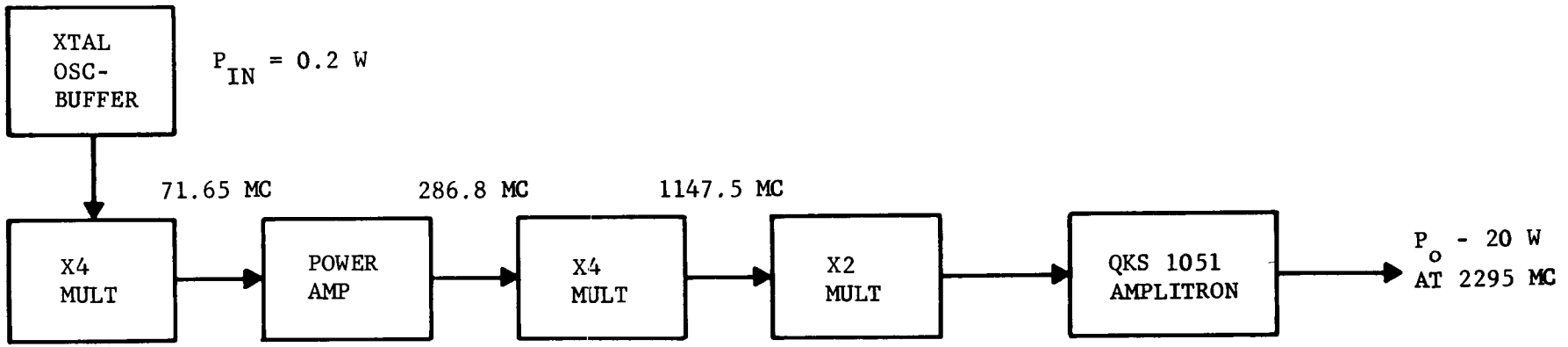

P_{IN} = 52 W

η = 36%

EST VOLUME: 180 IN.^{3}

EST WEIGHT: 9 LBS

* NOTE: 55% PLATE EFFICIENCY
80% POWER SUPPLY AND REGULATOR EFFICIENCY
4 WATT HEATER

FIGURE 88. S-BAND TRANSMITTER AMPLITRON OUTPUT STAGE

R11154

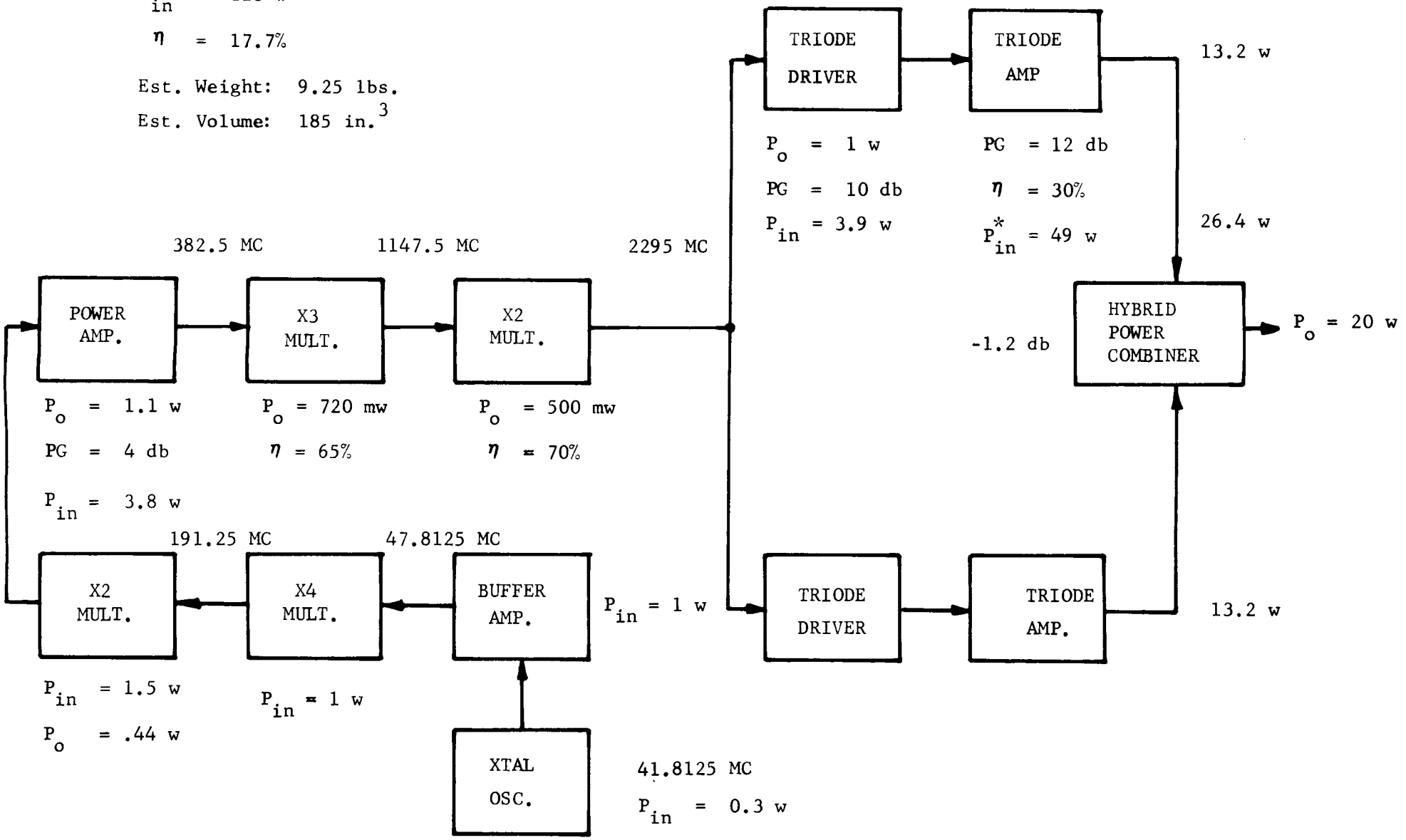

*Includes power supply η = 90%

FIGURE 89: S-BAND TRANSMITTER 10-WATT TRIODE CAVITY AMPLIFIERS

with power gain eliminates the need for a high power transistor amplifier such as used in the all-solid state transmitter. Although the triodes are not as efficient and do not have the power gain of the TWT or amplitron, they appear to be much more rugged and capable of impact qualification.

TUBE TYPE	CW POWER OUTPUT (WATTS) @ 2.3Gc	SHOCK QUAL. G's
GE 2835	5.0	3,000 g's Aeronutronic
RCA A-21509	5.0	3,000 g's Aeronutronic
GE 1372	2.5	26,000 g's Harry Diamond Lab.
GE Y-1124	2.5	26,000 g's Harry Diamond Lab.
Siemens 2C39BA	24.0	No test data
ML-8534	25.0	No test data
Eimac EM 4523*	20.0	No test data
Eimac EM 4524*	80.0	No test data
Resdel P-30H*	10.0	No test data
Trak 2975*	10.0	No test data
GE Z-5267	40.0	No test data
GE Z-5099A	19.0	400 g's General Electric

* Complete cavity amplifier packages 10 db gain.

d. All Solid-State Transmitter. Present limitations on solid state transmitters are inherently those associated with transistor power amplifiers. UHF power transistor capability is summarized in Table 5.5-I. RCA reports 20 watts at 430 mc from a prototype transistor (TA2675) power amplifier (1 device), which in turn results in a 14.5 watt output at 2.2 kmc from a X3 X2 varactor multiplier following a push-pull 40 watt amplifier. The availability of this device makes high power, solid-state S-Band transmitters feasible. A pair of 2N3375's can supply 15 watts output as an amplifier or 10 watts output as a frequency doubler at 383 mc. Harry Diamond Labs is presently using the RCA 2N3375 for gun-launched projectile telemetry at 26,000 g levels with good success. They use it above this level but then they encapsulate the device internally. The TA2675 utilizes the same overlay construction as the 2N3375 and is expected to exhibit the same resistance to impact damage. Similar results can reportedly be obtained from a pair of Clevite's new 3TE240 r-f power transistors rated at 8 watts/device output at 400 mc. There will be no problem in obtaining varactors to handle these output power levels to 15 watts, especially if balanced multiplier circuits with two varactors per stage are used.

TABLE 5.5-I

UHF POWER TRANSISTOR CAPABILITY

TYPE NO.	CIRCUIT (1)	OUTPUT FREQUENCY GC	OUTPUT POWER WATTS	POWER GAIN db	EFFICIENCY % (2)
2N3137	A	0.25	0.50	7.0	NA
	A	0.50	0.25	4.0	NA
2N2884	A	0.25	1.75	5.4	NA
	B	0.25	2.00	---	40
	B	0.50	0.75	---	33
	D	0.50	0.75	---	35
	D	1.0	0.35	---	15
0038	A	1.0	1.0	7.0	50
	B	0.50	2.0	---	70
	B	1.0	1.0	---	50
2N3553	A	0.25	2.5	7.5	NA
	B	0.50	1.5	---	30
2N3375	A	0.25	3.0	6.0	50
	A	0.50	1.8	5.5	40
	B	0.50	2.5	---	40
	C	1.0	3.5	5.4	NA
Selected 2N3375	A	0.4	8.0	6.0	40
TA2658	A	1.0	1.0	4.5	
	A	1.0	1.4	3.0	
	A	1.5	0.5	3.0	
RCA TA2675 (Prototype)	A	0.43	20.0	6.0	40

1. A = amplifier
   B = oscillator
   C = amplifier/multiplier
   D = oscillator/multiplier

2. NA = data not available

The 2N3375 and the TA2675 are the most suitable for the MFC power amplifier application. A 20-watt design utilizing selected versions of the shock proven 2N3375 is shown in Figure 90. Four devices are required in a push-pull-parallel power amplifier configuration in each output channel. Overall efficiency is low because of the hybrid power combiner loss of 1.2 db and losses associated with paralleling transistors in the 383 mc power amplifier.

An alternate 14.5 watt solid-state design shown in Figure 91 is presented which can be implemented by use of the TA2675 transistor. These units are expected to be available in the third quarter of 1965. This configuration is discussed in detail because it is believed that this approach represents the most direct and efficient solution to the MFC transmitter requirement. This design presumes that a push-pull pair will develop 40 watts at 383 mc. In order to handle this power at 383 mc, balanced varactor multipliers are used which allow operation of the varactors within dissipation ratings. Past experience with balanced multipliers has yielded conversion efficiencies of 65 - 70 percent when tripling from 144 mc - 432 mc at 100 watt input levels. Circuit symmetry provides harmonic rejection for spurious suppression. Efficiency is high because no additional lossy filters are required. This design, therefore, utilizes balanced tripler and doubler multipliers both for high power high efficiency frequency conversion, and for spurious rejection. Overall efficiency of the transmitter is expected to be 11.6 percent.

The crystal controlled oscillator and the buffer amplifier stages of Figure 92 are operated in the common base configuration at the crystal frequency of 47.8125 mc. Phase modulation is achieved in the collector circuit of the buffer amplifier. The use of a balanced modulator allows large deviation angles while maintaining excellent linearity. The very high f_T of the 2N2708 allows both high gain and efficiency to be realized.

Three push-push frequency doublers are employed in the transmitter. Past experience with this circuit indicates that its performance far exceeds that attainable with either single transistor or varactor doublers. Due to the symmetrical nature of the circuit and the fact that parametric mode frequency multiplication is not being employed, spurious or unwanted outputs are virtually non-existent. Isolation between the input and output circuits is high and neutralization is not required.

The push-pull power amplifier design of Figure 93 is based upon the RCA TA2675 transistor described earlier. Reported amplifier performance for this device states an output power of 20 watts CW at 430 MC. Standard RCA practice is to specify a transistor at the point where a minimum of 6 db power gain and a minimum 40 percent collector efficiency is available. These values should not be constructed as being the maximum gain, efficiency or output power available from the device.

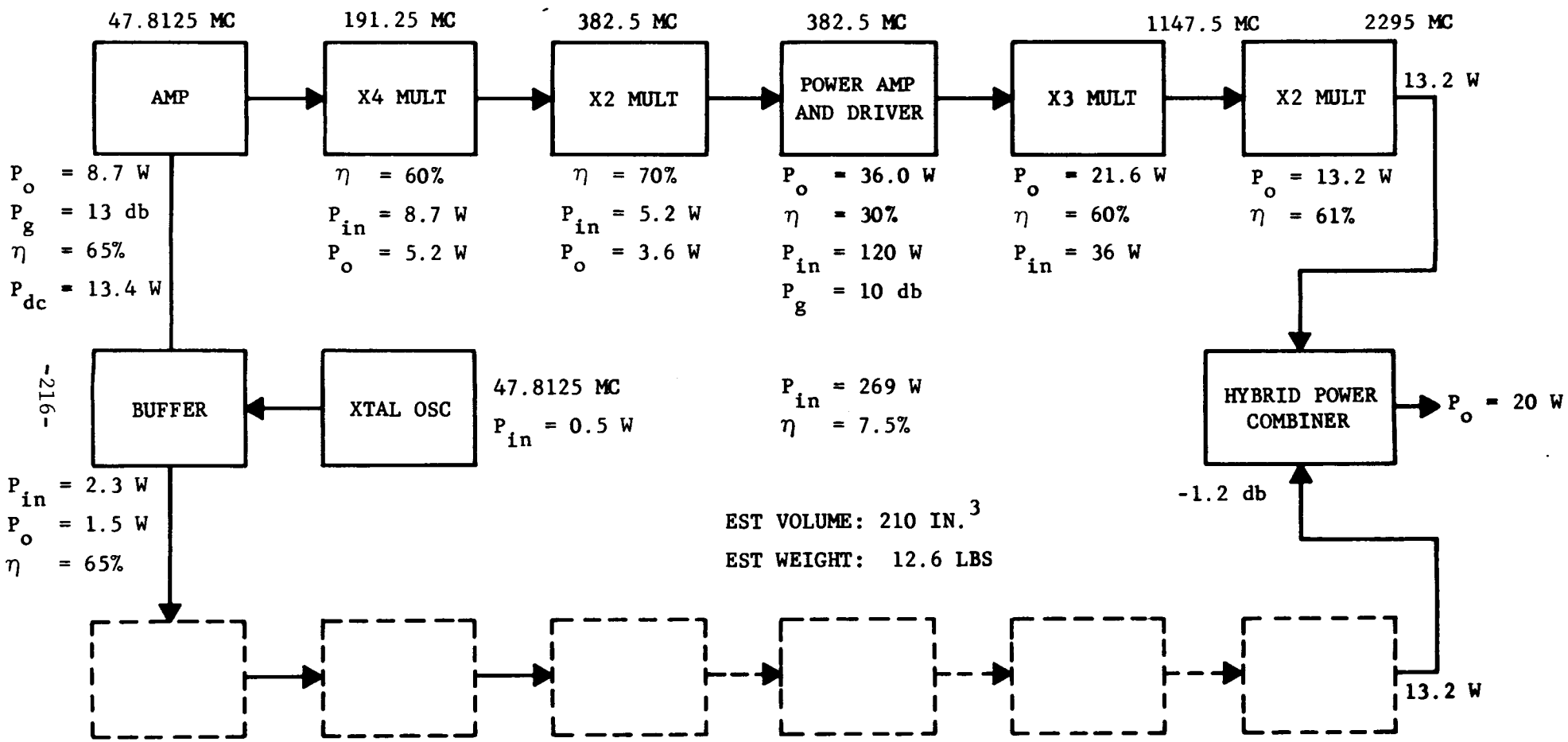

R11157

FIGURE 90. S-BAND TRANSMITTER, SOLID STATE 13 WATT PER OUTPUT CHANNEL.

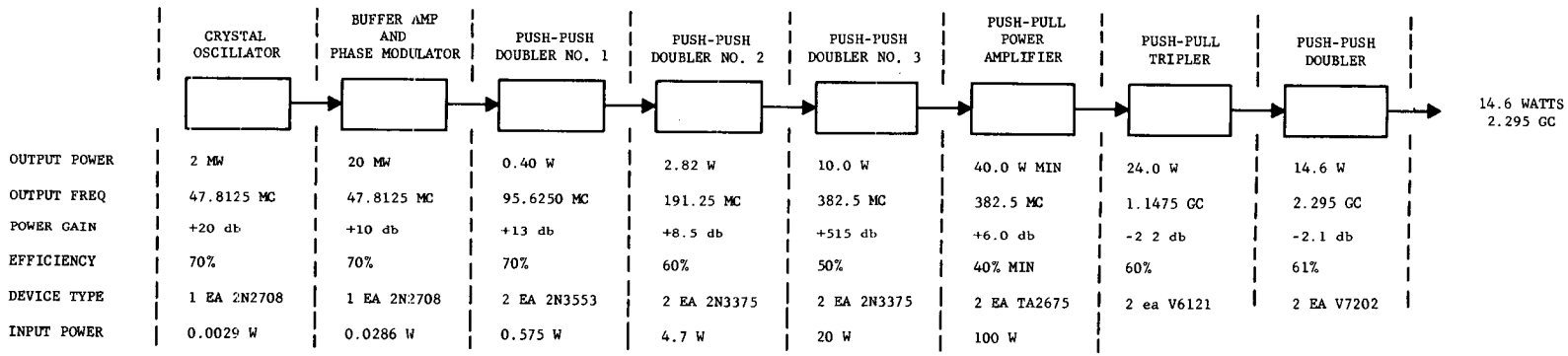

FIGURE 91. BLOCK DIAGRAM, HIGH POWER SOLID STATE S-BAND TRANSMITTER

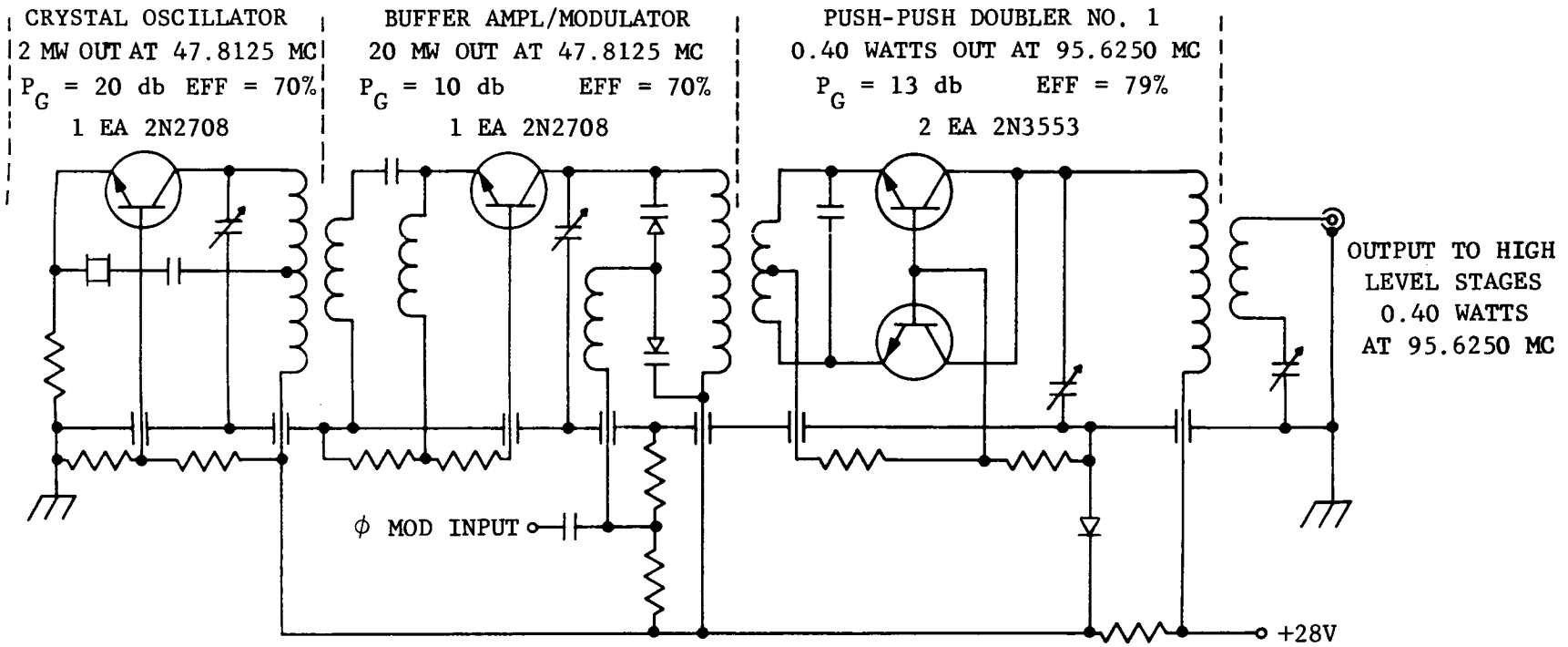

FIGURE 92. OSCILLATOR, BUFFER/MODULATOR, AND PUSH-PULL DOUBLER

R11159

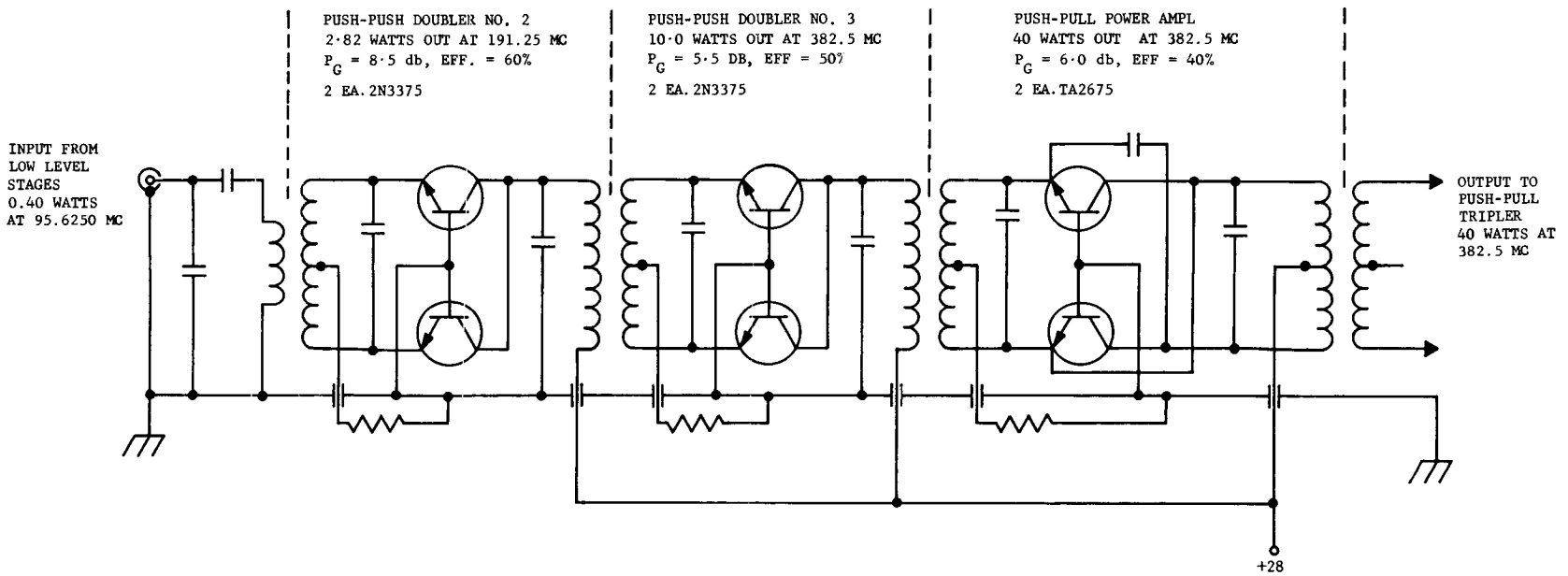

FIGURE 93. TRANSISTOR FREQUENCY MULTIPLIER AND POWER AMPLIFIER

The push-pull amplifier design is straightforward with neutralization being readily accomplished through the use of capacitive cross-coupling. Critical device matching is not required since they are, in effect, isolated from each other during their respective conduction angles. Even order harmonic rejection constitutes the second major advantage inherent with this configuration. Thus the even order signals generated by the previous doubler stages will not be propagated but will instead be cancelled.

Varactor frequency multipliers must be employed in the final two stages of the transmitter due to the power and frequency limitations of available transistors. The same advantages inherent in balanced diode mixers and transistor multipliers are recognized in balanced varactor frequency multipliers. Figure 94 depicts the evolution of the balanced doubler.

A basic single ended doubler is shown in Figure 94a. L_ω and C_ω tune the diode to the input frequency while the desired second harmonic output is tuned by $L_{2\omega}$ and $C_{2\omega}$. L_ω is calculated as a function of frequency and the varactor characteristics. The value of $L_{2\omega}$ is always equal to one-fourth the value of L_ω.

$$L_\omega \propto (2\pi f)\ (C_D)(V_{BR})$$

and

$$L_{2\omega} = \frac{L_\omega}{4}$$

The general case equation for N order is:

$$L_{N\omega} = \frac{L_\omega}{N^2}$$

It should be noted that the value obtained for $L_{2\omega}$ is exactly equal to the inductance measured from the center-tap to either end of L_ω. Figure 94b indicates how the second harmonic component may be obtained through use of this technique. The diode is charged during only half of the input waveshape and "discharged" during the following half cycle. This alternate half cycle may be used to advantage by driving a second varactor. The second diode may in fact replace the tuning capacitor C_ω which results in a balanced diode system. Since the desired output is taken from a point common to both diodes, the center tap, the resulting circuit is termed push-push. The completed push-push doubler is shown in Figure 94c .

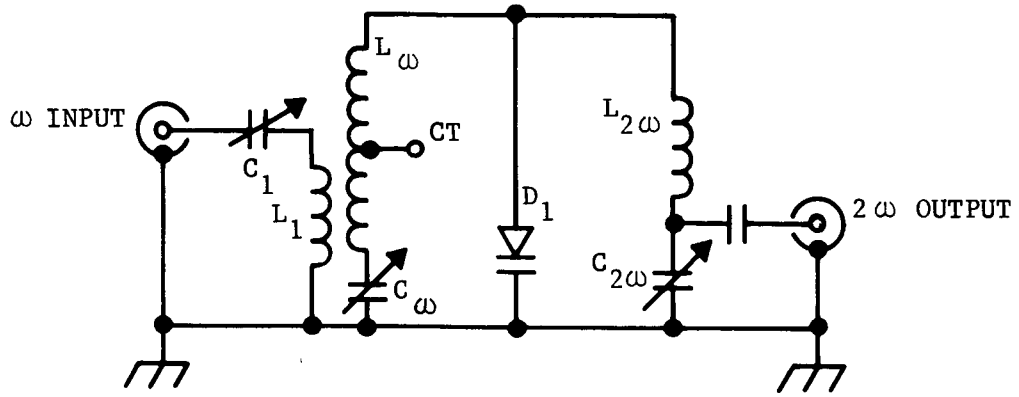

(A) THE BASIC DOUBLER

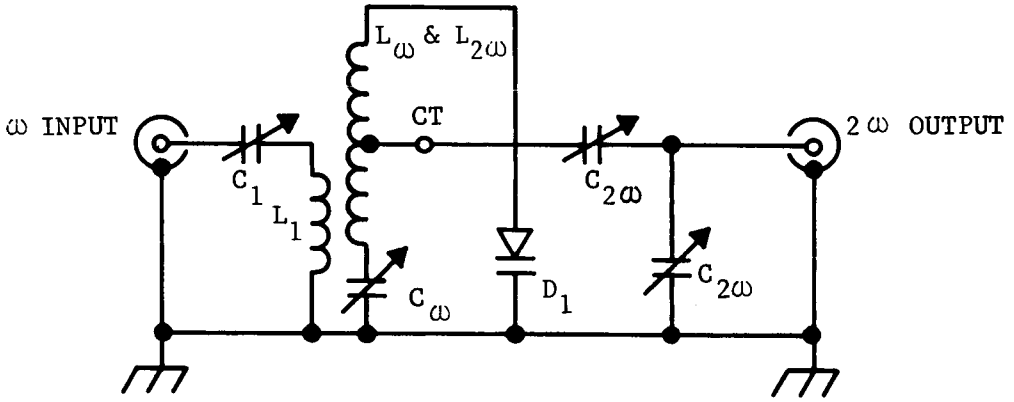

(B) THE CENTER-TAPPED EQUIVALENT

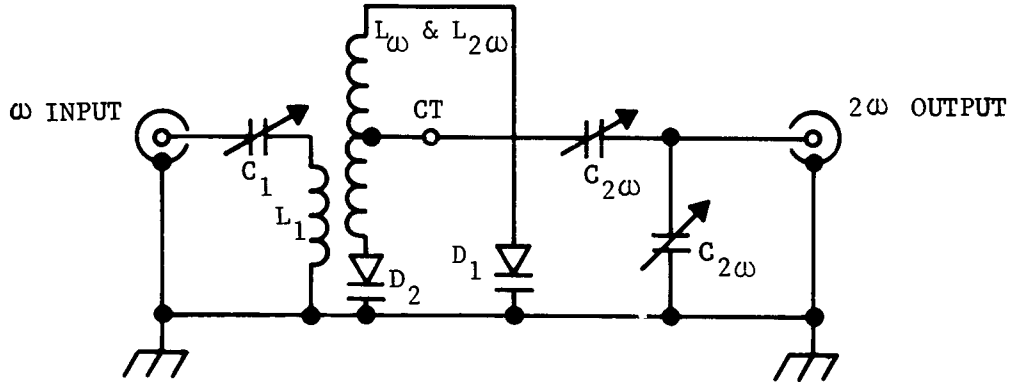

(C) THE BALANCED DOUBLER

R11165

FIGURE 94. BALANCED DOUBLER CONCEPT

A simple extension of this technique yields a push-pull tripler configuration. Two possible circuit types are indicated in Figure 95. The first type would find application where a single ended output was required; while the second type supplies a balanced, push-pull output. This second scheme is used to drive the symmetrical, cavity doubler output stage.

The balanced cavity doubler functions in exactly the same fashion as its lumped-constant equivalent described above. Figure 96 details the complete multiplier chain.

In this case the cavity line, L_4, is a foreshortened half wave length at the input frequency, which serves as L_ω, and a foreshortened full wave length at the desired second harmonic output frequency. The push-pull input is derived directly from the balanced tripler. Output tuning is accomplished by C_4, C_5 and a portion of the cavity line.

The principal sources of information for the design carried out above are listed in a bibliography at the end of this section.

5.5.5 CONCLUSIONS

Table 5.5-II compares the characteristic of the four approaches examined. The triode cavity amplifier with solid state driver configuration may be the most practical of all configurations examined, especially if two antennas could be utilized to eliminate the hybrid. It is intermediate in efficiency and impact resistance. If a suitable 20 watt tube becomes available, this approach becomes even more attractive. Crossed field amplifiers are not presently available at S-Band and do not seem to offer any significant advantages at low power levels over TWT's. Drift tube klystrons require elaborate frequency control circuits and may not lend themselves well to high phase stability or phase modulation. Transistors are about to become available with power capabilities above 40 watts (per pair) at 380 MC. The all solid state approach should be examined further is an output power in the range of 15 to 30 watts or less is required.

The following advantages are inherent in the all solid state design:

(1) Greatest probability of impact survival based upon prior testing of similar multiplier chains.

(2) No pressurization of HV power supplies to minimize arcing.

(3) Minimum impact qualification costs.

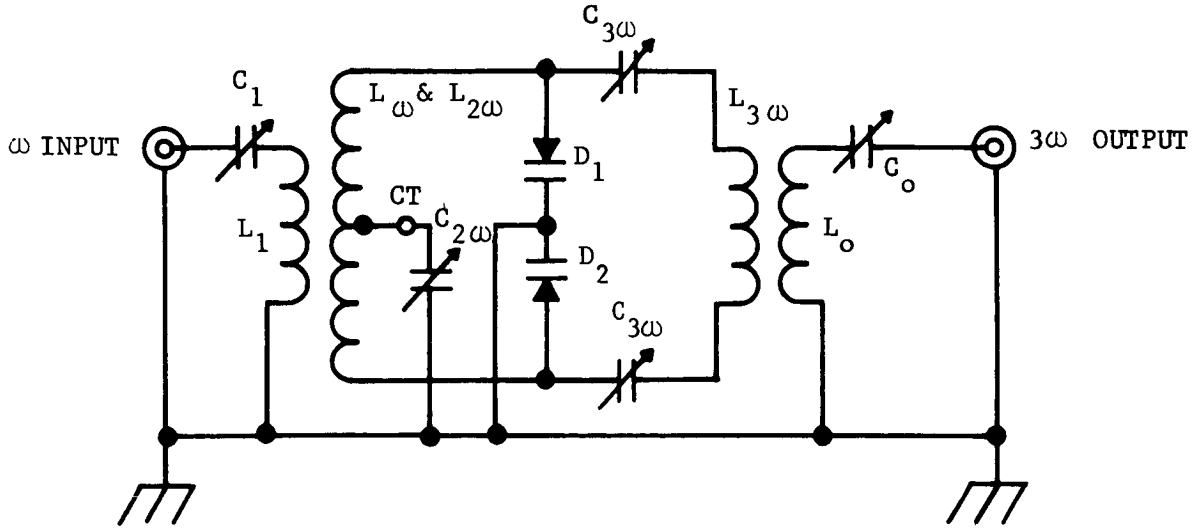

(A) BALANCED TRIPLER WITH SINGLE ENDED OUTPUT

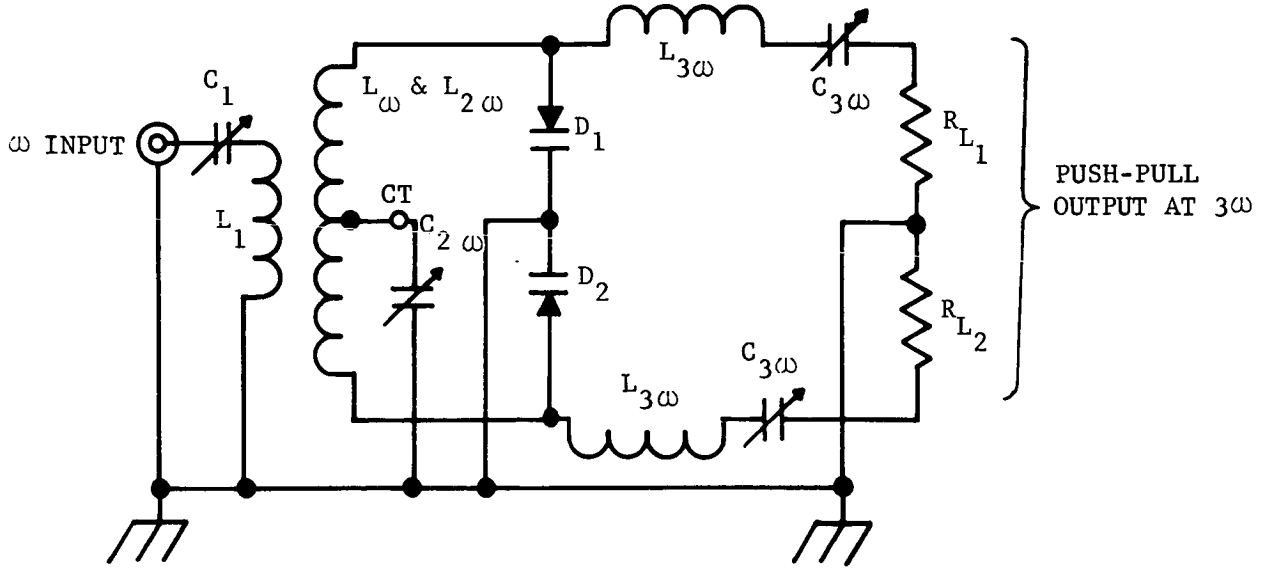

(B) BALANCED TRIPLER WITH PUSH-PULL OUTPUT

R11167

FIGURE 95. BALANCED TRIPLER

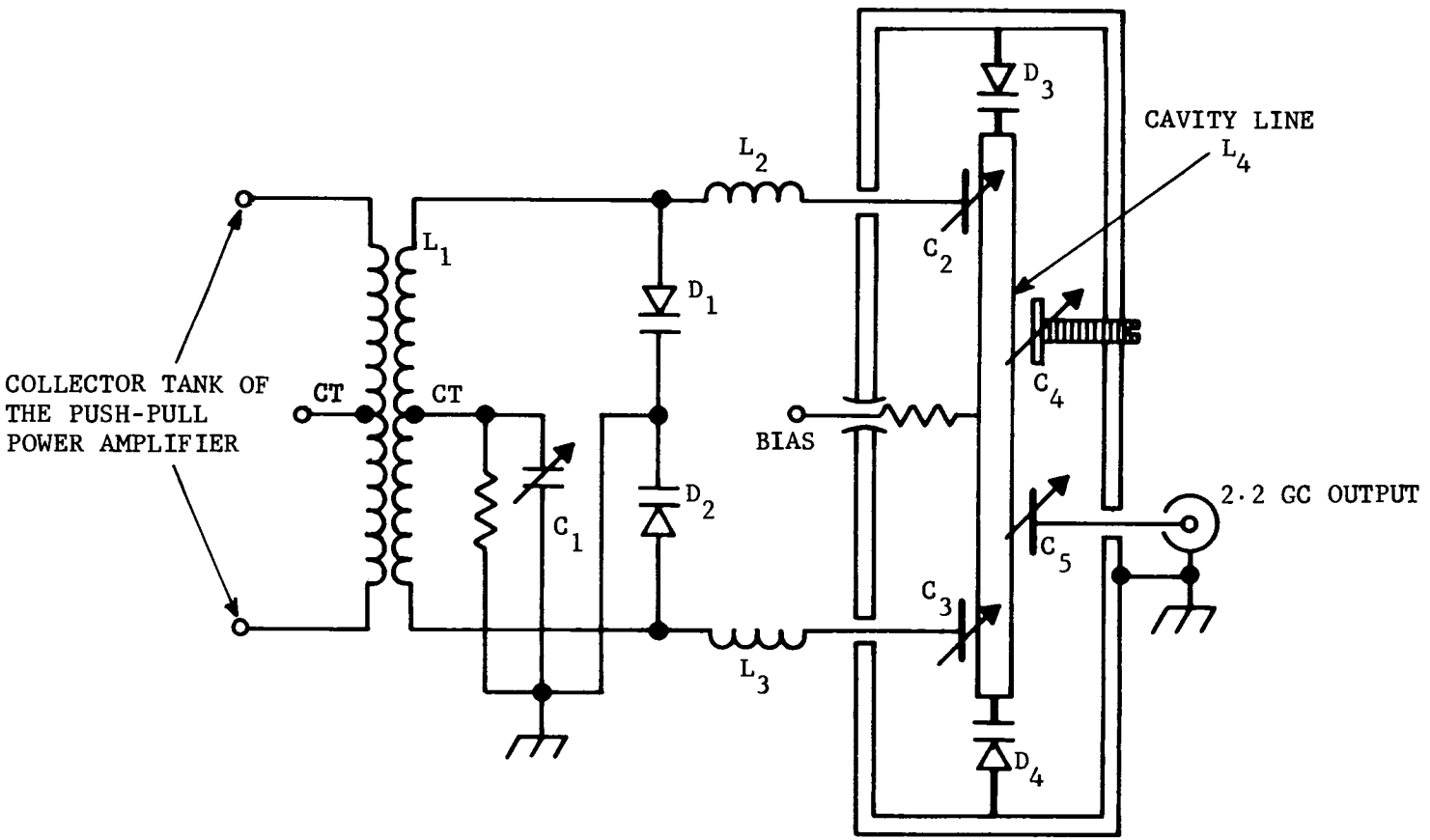

R11166

FIGURE 96. BALANCED TRIPLER AND DOUBLER CIRCUITS

TABLE 5.5-II

SUMMARY OF S-BAND TRANSMITTER CHARACTERISTICS

	TWT	AMPLITRON	TRIODE CAVITY	ALL SOLID STATE USING SELECTED 2N3375	ALL SOLID STATE USING RCA TA2675 DEVICE
Power Output	20 w	20 w	20 w	20 w	14.6 w
Power Input	100.2	52	113	266	126
Efficiency, Percent	24.9	36	17.7	7.5	11.6
Weight, Pounds	6	9	9.25	12.6	9
Volume, in^3	120	180	185	210	139
Degree of Impact Resistance	Poor	Poor	Fair	Good	Good
Density, lb/in^3	0.05	0.05	0.05	0.06	0.065

Disadvantages of the solid state approach include:

(1) Low overall efficiency, estimated 7.5 to 11.6 percent.

(2) Highest carrier phase jitter due to additional multiplier channel (X48).

BIBLIOGRAPHY

FOR SOLID-STATE TRANSMITTER DESIGN

Amplifier/Multiplier

Radio Handbook, 15 Edition, 13-8, pgs 258-260.
Published by Editors & Engineers Ltd.

Push-Pull Amplifiers in General

Radio Handbook, 15th Edition, 13-4 through 13-7, pgs 251-258.

Applied Electronics, 13th Printing, pgs 438-448
Published by Wiley & Sons, Inc.

Transistor Power Amplifiers

Transistor Circuit Design, 1st Edition, Chapter 25
Published by McGraw-Hill

Design of Large-Signal VHF Transistor Power Amplifiers
RCA Application Note No. SMA-36

Varactor Multipliers

Varactor Applications, 1st Edition
Published by The M.I.T. Press

Frequency Multipliers and Harmonic Generators Using Varactor Diodes
Semiconductor Products, November 1962

Frequency Multiplication with Varactors
RCA Application Note SMA-13

VHF Power Sources Using Varactor Multipliers
RCA Application Note SMA-22

Design of Microwave Power Sources Using Varactors
RCA Publication No. ST-2701

5.6 ANTENNA

5.6.1 REQUIREMENTS

The basic requirement of the antenna is that it radiate microwave energy, of the appropriate polarization, towards the Earth and that the angular energy density radiated in the direction of the Earth be sufficient to satisfy the requirements of the telecommunications link. The electrical and physical characteristics that the antenna must have in order to perform the above function are listed below.

a. Physical Characteristics of Antenna. In the current conceptual design, the antenna will be stowed in a folded configuration atop the camera tube until the capsule comes to rest on the Martian surface. After the camera tube is deployed, the antenna is erected so that it and the tube are colinear. Therefore, the physical characteristics of the antenna must ensure that it survives impact and that it remains accurately erected under the environmental conditions listed below and that it has the desired electrical and radiation characteristics. A detailed electrical and mechanical design of the antenna would define the requisite physical characteristics.

b. Antenna Environmental Factors

(1) Temperature. There are two modes of temperature environment to which the antenna is subjected. The first is the sterilization process which occurs while the antenna is stowed in its non-erected configuration within the capsule. For flight qualification, the antenna must erect properly and operate satisfactorily after three cycles of 36 hours each at 145 degrees C.

After deployment on the Martian surface, the antenna must operate in a maximum atmospheric temperature around zero degrees C. The amount of direct heating by sunlight depends upon the physical structure and is probably not important in view of the low atmospheric temperature. The minimum night time atmospheric temperature is near -68 degrees C. The antenna should function properly during exposure to the daytime temperatures and following exposure to the night time minimum temperature.

(2) Impact. The antenna must withstand 3000 g to 5000 g while in its stowed configuration within the capsule. This level of shock should not impair the erection or electrical function of the antenna.

(3) Wind Loading. In view of the location atop the camera tube, the antenna should present a low cross-section to the Martian winds. In addition, the structure must be sufficiently rigid that the antenna

performance during exposure to wind is not degraded. The maximum wind velocity is 60 meters per second (probably in late afternoon) and it is less than 30 meters/second 80 percent of the time. The antenna should also be unaffected by wind-carried sand and dust particles.

c. Radiation Characteristics. It is anticipated that the antenna will be erected to point its main lobe along the local vertical after deployment from the capsule. The polarization of the radiated energy should be circular and of the same sense as the receiving antenna. The antenna gain should be sufficient to satisfy requirements of the telecommunications link, but not so high that a too narrow beamwidth unduly restricts the time per day that the Mars-Earth vector lies within the antenna beamwidth (transmission time). These considerations are discussed further in the following section.

d. Electrical Characteristics

(1) Input Impedance. The input VSWR of the antenna should be minimized in order to maximize transmission efficiency and power handling capability.

(2) Power Handling Capability. The antenna should be capable of transmitting 20 to 30 watts into the Martian atmosphere without voltage breakdown. Careful design of the feed point will obviate voltage breakdown problems. Antenna breakdown in the Martian atmosphere is discussed in Section 5.6.3.

5.6.2 ANTENNA GAIN-BEAMWIDTH OPTIMIZATION

This section evaluates various antenna beamwidths for a Mars capsule which has a fixed vertically-oriented transmitting antenna. A conclusion is reached on an optimum beamwidth range for the MFC. The analysis does not consider the practical antenna factors such as wind-loading, efficiency, polarization and mechanization.

It is assumed that the capsule contains an antenna which is erected to the local vertical by gravity. This is a simple, reliable antenna configuration which utilizes the capsule orientation system also required by the facsimile camera. Data is transmitted over the antenna at a preset time which is measured from some event such as landing impact, sunrise, or noon. The amount of data transmission which occurs (for a fixed transmitter output) depends on the antenna gain in the Earth direction and how long the antenna is pointed towards the earth.

a. Communication Geometry. Figure 97 shows the communication geometry involved from the landing site on Mars. For a given antenna beamwidth "β", there is shown a corresponding latitude angle "β" centered on the landing site. If the Earth normal vector is within this region, communication from Mars to Earth is possible at some time during the day. Figure 98 is a planar map of Mars, with a solar referenced longitude, which illustrates the same geometry in a different fashion. The map represents a landing condition for a 1971-type 1 trajectory. The geometry changes very little for any period of several weeks.

The landing site can be thought of as a point on Figure 98which moves across the map at a fixed latitude. Surrounding the landing site is a circle which subtends a solid angle at the center of Mars equal to the antenna beamwidth. Communication with Earth is possible whenever the Earth vector is within this circle.

b. Antenna Gain Versus Beamwidth. The conceptual design of the Mars Facsimile Capsule includes a 10-turn helix antenna, the selection of which is described in Section 5.6.4. Also shown there is an expression for the directive gain as a function of the half-power beamwidth.

$$\text{Gain}_{db} = 10 \log \frac{K}{(\text{B.W.})^2}$$

where

B.W. = Half-power beamwidth in degrees

K = Factor Dependent on sidelobe and backlobe radiation (dissipation losses are accounted for in transmission circuit)

As a helix is made longer, the beamwidth narrows and gain increases, and this relationship is plotted in Figure 99. Using this result, the communication capability in terms of bits/second for a fixed distance and power output can be determined by using Figure 100. Therefore, curves of data rate capability versus antenna beamwidth are also shown in Figure 99 for two distances and a fixed transmitter power. These data rate capabilities exist between the half power points of the antenna beams which have the beamwidths shown on the abscissa.

c. Maximization of Data Transmission.

(1) Transmission Time Per Day. Transmission time per day is dependent on how long the fixed antenna beam encompasses Earth. The maximum possible transmission time per day is

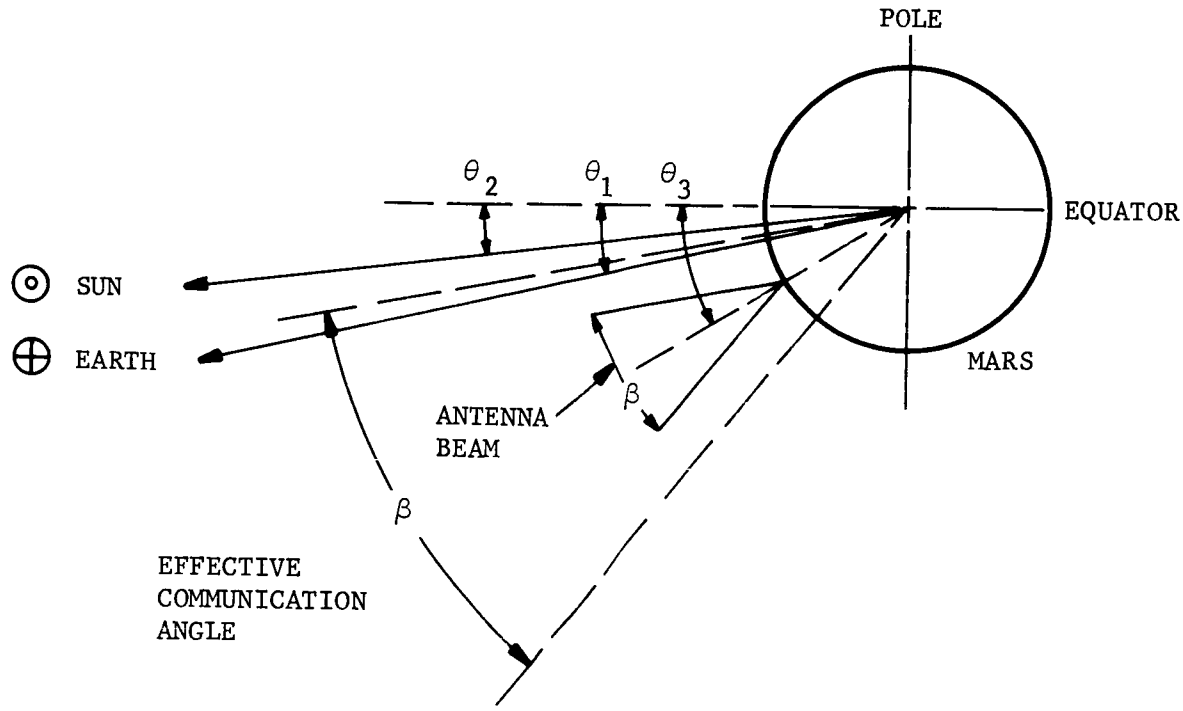

FIGURE 97. EFFECTIVE COMMUNICATION ANGLE

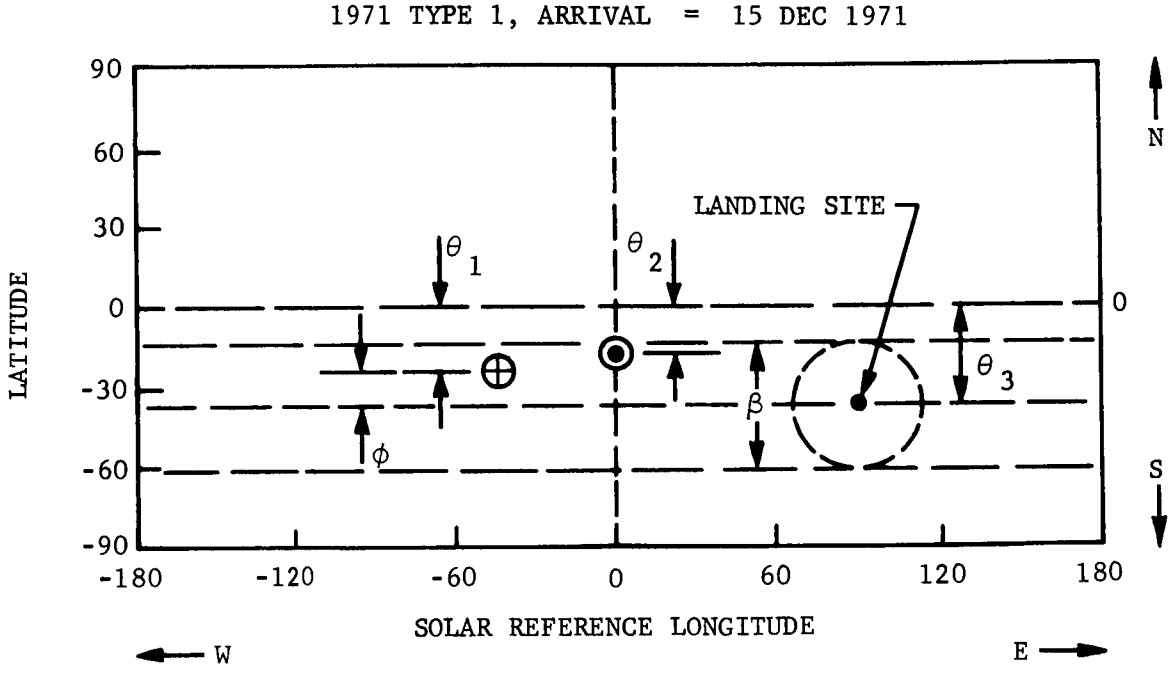

ϕ = ANTENNA POINTING ERROR IN LATITUDE

R11217

FIGURE 98. ANTENNA POINTING ERROR

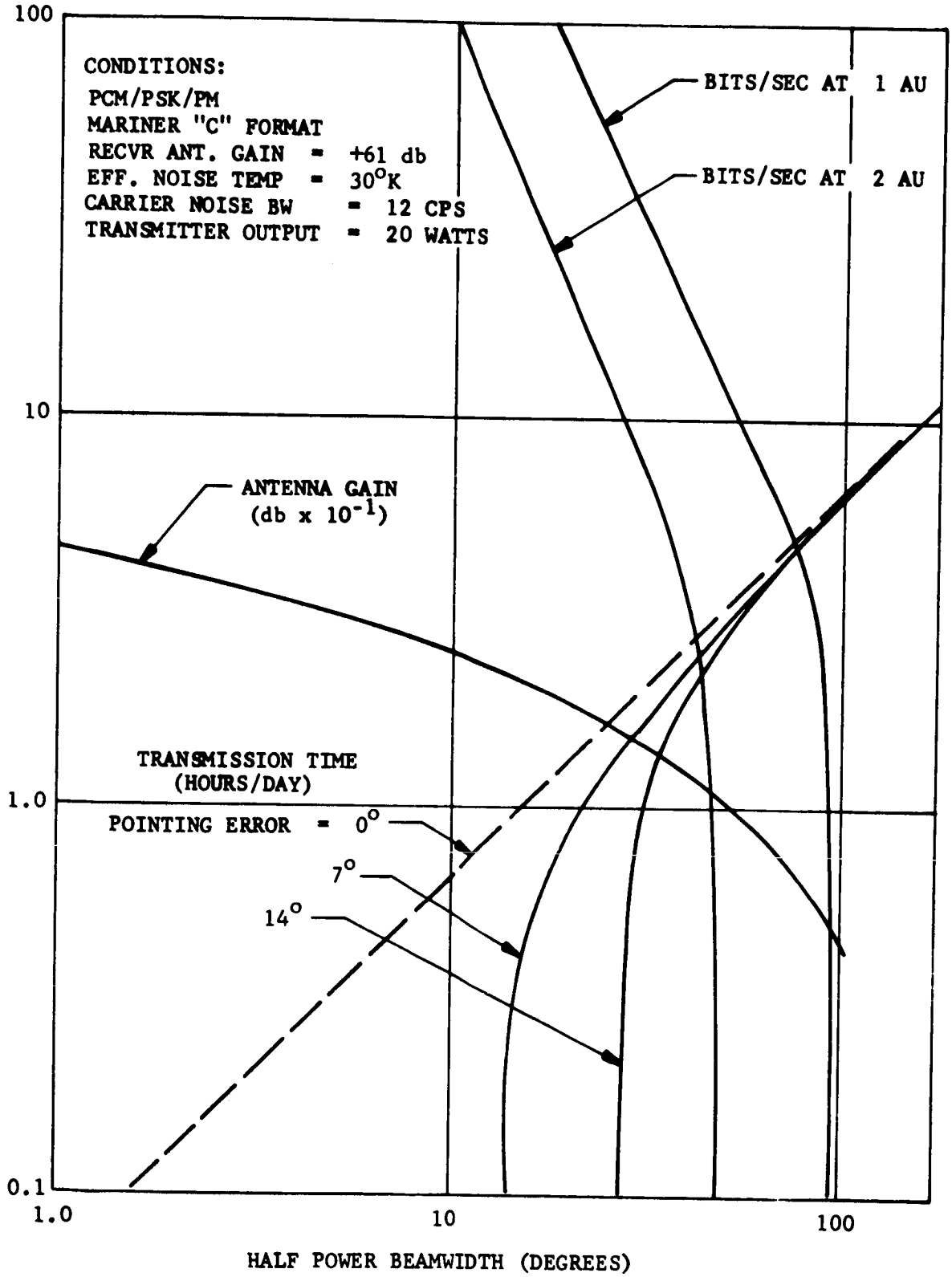

FIGURE 99. TRANSMISSION TIME vs. HALF POWER BEAMWIDTH R11206

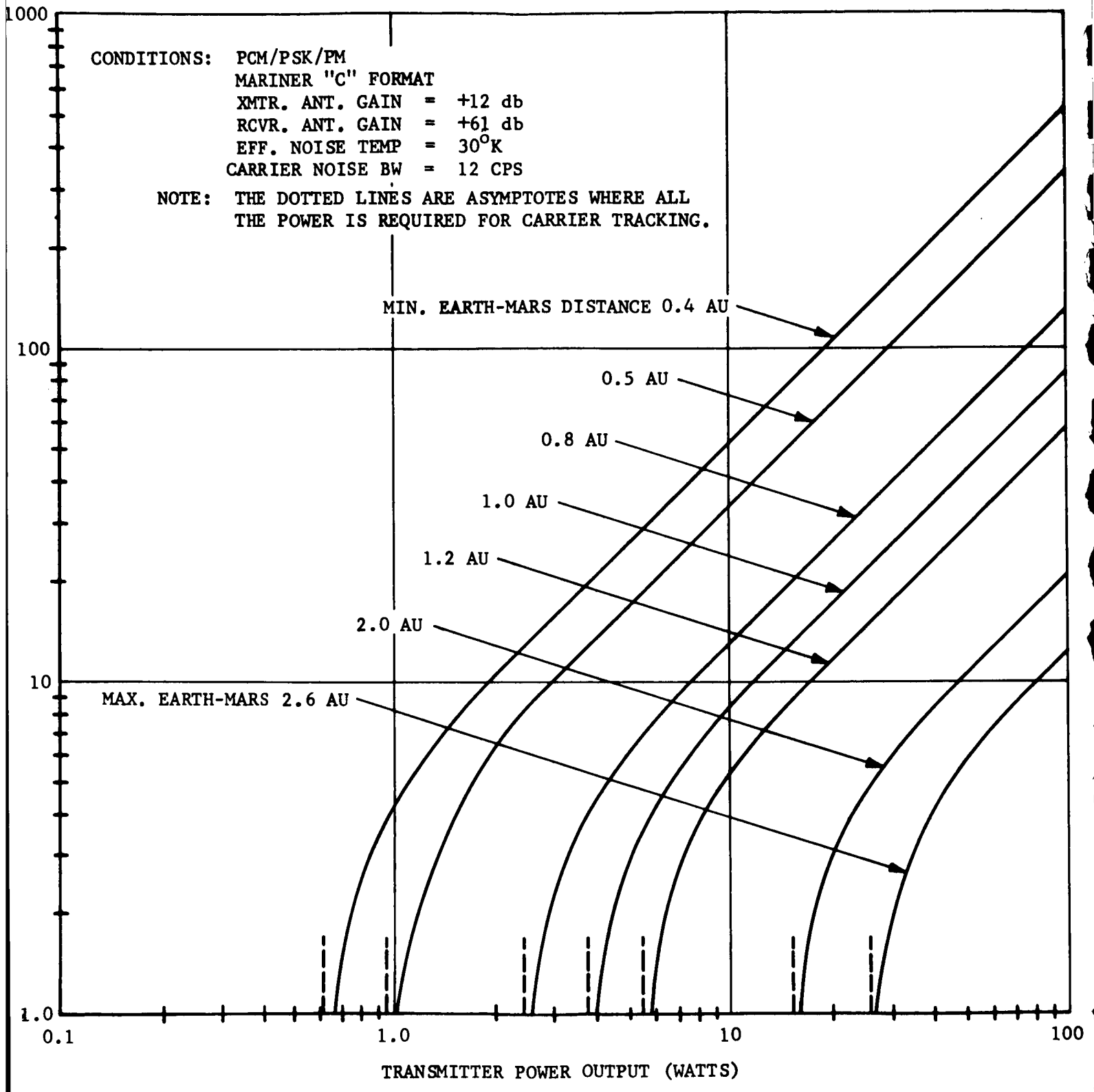

R11198

FIGURE 100. TRANSMISSION CAPABILITY FROM MARS

$$T = 24 \times \frac{\beta}{360^{o}} \text{ hours}$$

where β is that angular portion (beamwidth) of the antenna beam within which the antenna gain is sufficient to maintain communication at a prescribed data rate. In this discussion, β, is the half-power beamwidth.

The transmission time T may be reduced by any of the following pointing loss errors:

(1) Transmission timing error

(2) Landing trajectory error

(3) Vertical erection error

(4) Displacement of the landing site from the latitude where the earth is vertical.

Timing errors are important only when they are a significant part of the daily transmission time. They will be assumed to be negligible for transmission times in the range of one to ten hours. Errors in the longitude direction can be compensated for by transmitting for a longer period of time (at the expense of battery energy). Errors in latitude cannot be compensated for and therefore will be analyzed in more detail.

Latitude pointing error is composed of site displacement plus two independent errors -- vertical erection and landing trajectory. Each of these two errors is made up of many independent components. Therefore, it seems reasonable to sum the antenna pointing error in the following manner:

$$\phi = \phi_s + \sqrt{\phi_L^2 + \phi_E^2}$$

where

ϕ = latitude pointing error

ϕ_s = site displacement in latitude from the Earth vector

ϕ_L = landing error in latitude

ϕ_E = erection error of antenna from vertical

The reduction of the transmission time by the latitude pointing error is best explained by the following sketch:

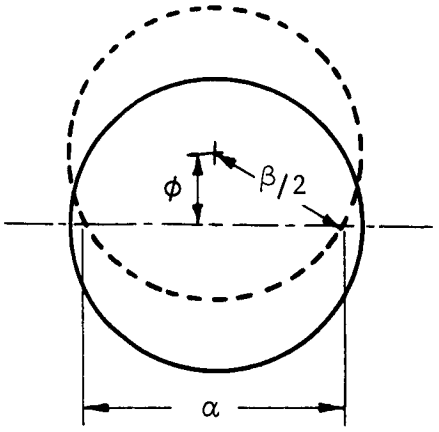

ϕ = latitude pointing error

β = antenna beamwidth

α = effective beamwidth

$$\phi^2 + \left(\frac{\alpha}{2}\right)^2 = \left(\frac{\beta}{2}\right)^2$$

or

$$\alpha = 2\sqrt{\left(\frac{\beta}{2}\right)^2 - \phi^2}$$

The preceding equation naturally shows that when the latitude pointing error is equal to one-half the antenna beamwidth, the effective beamwidth becomes zero. Since, transmission time

$$T = 24 \times \frac{\alpha}{360^\circ} \text{ hours}$$

this means the transmission time is also zero. Figure 99 shows the useful transmission time per day versus antenna beamwidth for the three cases of antenna pointing error equal to 0°, 7°, and 14°. A typical value for the pointing error will be calculated

$$\phi = \phi_s + \sqrt{\phi_L^2 + \phi_E^2}$$

with $\emptyset_s = 0$ (by site choice)

3 $\emptyset_L = 6.8^\circ$ (according to JPL)

3 $\emptyset_E = 5^\circ$ (estimate)

$$\emptyset = 0 + \sqrt{(6.8)^2 + (5)^2} = 8.4^\circ$$

This result shows that a useful antenna should not have a beamwidth less than 16.8 degrees.

A Mars Facsimile Capsule which utilizes a conventional chemical power source will have a limited operational life measured in days rather than months. The cold nature of the Martian night means a considerable amount of energy is required to survive each additional day. Therefore, it is necessary to maximize the total amount of data which can be transmitted to Earth each day. If the transmitter is limited in power output, then it becomes necessary to optimize the antenna gain and beamwidth.

The expression below gives the amount of data which can be transmitted each day under the stated conditions.

Data Amount = (Bit Rate) X (Transmission Time)

Conditions:
PCM/PSK/PM
MARINER "C" FORMAT
RECVR. ANTENNA GAIN = +61 db
EFF. NOISE TEMP = 30°K
CARRIER NOISE B.W. = 12 CPS
TRANSMITTER OUTPUT = 20 WATTS

This function is plotted in Figure 101 with antenna beamwidth as the variable. For a distance of 1 AU and a pointing error of 7°, the maximum transmission capability is 2.6×10^5 bits/day for a beamwidth of 19°. However, the curves show this is not a reliable operating point because a small increase in pointing error could eliminate all transmission. A better operating point would be at a beamwidth of 40° to give a transmission capability of 1.5×10^5 bits/day.

It is concluded from Figure 101 that for 1 AU, the optimum antenna beamwidth falls within the range of 20° to 70°. This corresponds to an antenna gain range of 19 to 7.5 db. Once a specific mission is established and a maximum pointing error is stipulated, refinements may be

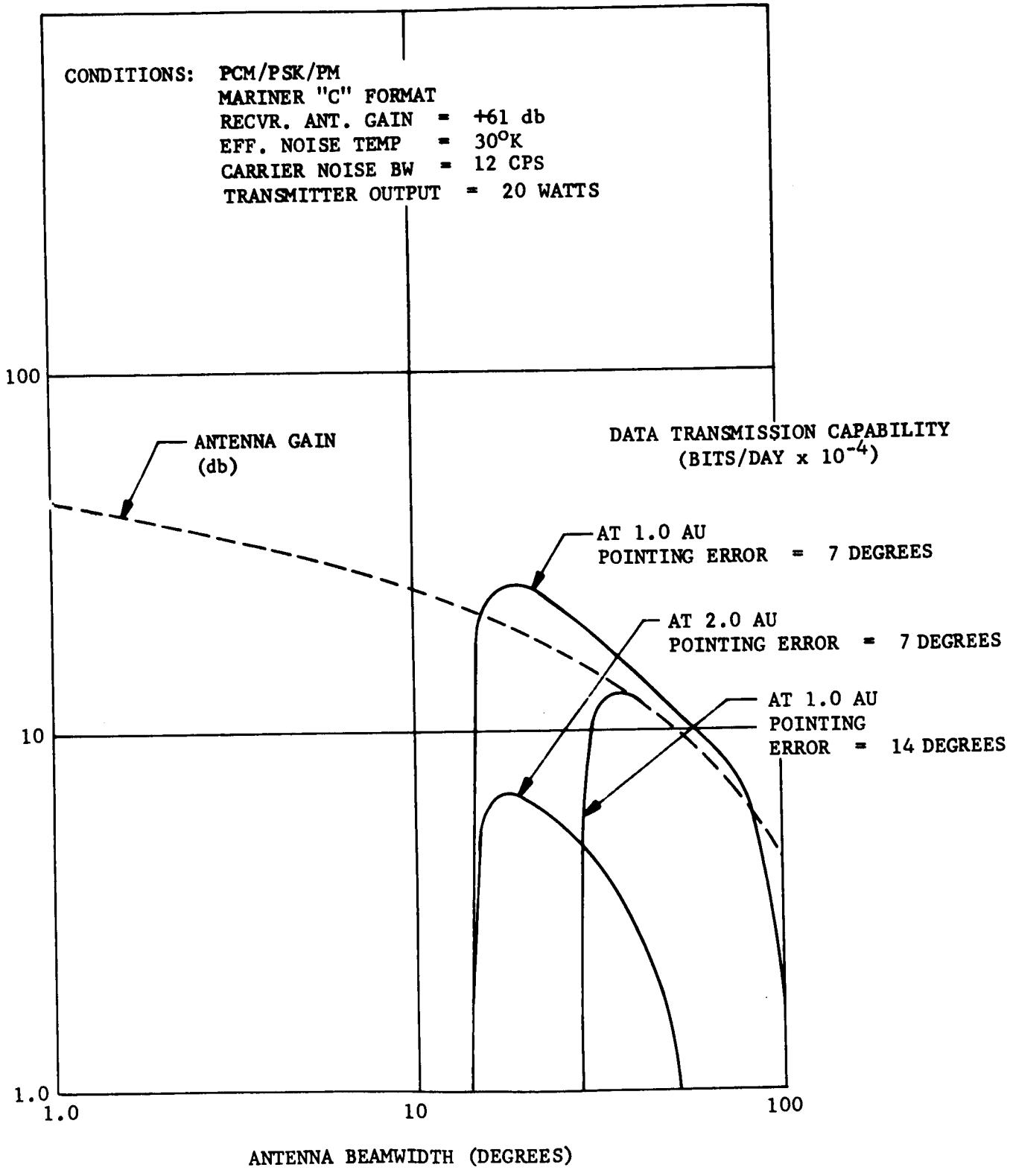

FIGURE 101. TOTAL BITS TRANSMITTED vs. ANTENNA BEAMWIDTH

R11204

made in the above analysis to include optimization of transmitter power and antenna gain. Also, practical considerations of antenna deployment, wind loading, efficiency, polarization and fabrication may impose further restrictions on the antenna design, and these are discussed in Section 5.6.4.

5.6.3 ANTENNA VOLTAGE BREAKDOWN

The high frequency breakdown of antennas and other components in the Earth atmosphere has been investigated in detail, and the mechanism of breakdown is fairly well understood. Generally, the problem is not amenable to analytical solution, and the most useful results to date are empirical data and curves derived from systematic experiments. High altitude simulators have been used extensively, both in research efforts and in routine testing of operational hardware.

Despite the fact that the constituents of the Martian atmosphere are largely conjectural, the same investigative techniques are being used in order to establish the voltage breakdown characteristics (power-handling capability) of antennas operating on and near Mars.

The stipulated Martian atmosphere is as follows:

Nitrogen	35 mb	(87.5%)
Carbon Dioxide	3 mb	(7.5%)
Argon	2 mb	(5.0%)
	40 ± 20 mb	

The total surface pressure of 40 mb corresponds to about 30 mm Hg. Recent publications (Reference 1) indicate that there is no ambient ionization below about 100 kilometers and thus, surface conditions on Mars can be simulated adequately by using a vacuum chamber.

Investigators at Raytheon (Reference 2) and General Electric (Reference 3) have performed breakdown tests in which the Mars atmosphere was partially simulated. In the former, a 1 mc bandwidth antenna with 140 degree beam-width (type unknown) was found to have a maximum power capability of 50 watts. In the GE tests, pure argon was used at pressures between 0.1 and 4.0 millibars and the antenna was a quarter-wave monopole designed for 240 megacycles. The conclusions were that the breakdown power levels in argon are about 50% lower than in air for the same antenna. The minimum breakdown power level was a pressure of approximately 0.4 millibard in both air and argon. The report stated that the use of pure argon

represented a worst case, since the addition of other elements would raise the breakdown level by increasing the electron loss by attachment. This should be especially true if water vapor is present, since published results (Reference 4) indicate that the breakdown power goes up as humidity increases.

An experimental study (Reference 5) was also performed which included antenna breakdown measurements in the presence of a gas mixture which was essentially the same as the stipulated Martian atmosphere listed above. The results showed that the breakdown power levels in the simulated atmospheres were essentially the same as in Earth's atmosphere air. After this conclusion was established, subsequent tests were performed in air for various antennas including monopoles, crossed dipoles and helices. The minimum power to cause breakdown of a 6-turn axial mode helix at 3000 mc/s was found to be about 125 watts at a pressure of 3 mm Hg. At 15 mm Hg (about half the Martian surface pressure) the peak pulse power required for breakdown increased to more than 6000 watts. Since the transmitter power for the Mars Facsimile Capsule telecommunications link is probably in the range of 20 to 30 watts, the helix antenna (described in the following section) proposed for operation at the Martian surface pressure of 40 $\pm$ 20 millibars should not encounter voltage breakdown.

5.6.4 ANTENNA DESIGN

The previous discussion has established the performance specifications for the Mars Facsimile Capsule antenna. The size of the radiating structure is limited by the space available in the capsule prior to deployment and wind load factors during transmission. The optimum beamwidth range for maximum data transmission per day was deduced for a fixed transmitter power and specified distances and pointing errors.

a. Selection of Antenna Type. The optimum beamwidth is shown to be in the range of 20 to 70 degrees, corresponding to antenna gains of 19 to 7.5 db. The telecommunications analysis of Section 5.4 is based on a nominal antenna gain of 12 db, with a 3 db pointing loss at the half-power points.

The "frequency-independent" class of antennas, typified by the conical log-periodic spiral, is not considered here because the beamwidths are generally broader than 70 degrees. The same is true for the turnstile and conical helix antennas. It is further concluded that an antenna type should be chosen which could be easily adapted to future changes in gain requirements by simply varying the size of the radiating structure.

Array type antennas are not considered because of the difficulties associated with erecting and feeding such devices. The helix and the

parabolic reflector are two of the more suitable configurations remaining for discussion. The helix antenna is inherently adaptable to applications requiring erectable devices because it closely resembles a coil spring. Either mechanical erection or inflation may be used to deploy the helix; in fact, inflatable helices have been commercially available for some time. The parabolic reflector and feed combination form a more complex electrical and mechanical structure. The reflector surface and the feed location must be established precisely for efficient antenna operation. A comparison of the helix lengths and parabolic reflector diameters required for various values of gain are shown in Figure 102. The paraboloid has a significant size advantage for gains above 13 db. However, the wind load factor is much more severe for the reflector than the helix. Assuming a helix enclosed in a circular cylindrical sock, the maximum wind force (Reference 6) for a 12 db gain helix is 1.1 pounds including a gust factor of 1.5. The maximum wind force for a 12 db gain paraboloid, exclusive of feed structure, is 4.1 pounds. These calculations were made using a maximum dynamic pressure of 3.96 psf, which was calculated for the maximum Martian surface pressure of 60 millibars and wind velocity of 60 meters/sec. The helical antenna is chosen, therefore, because of its ease and reliability of erection, mechanical and electrical simplicity, and low stowed volume and wind loading.

A plot of the gain versus beamwidth for the helix antenna is shown in Figure 103. The gain in db is defined as

$$G = 10 \log \frac{K}{(B.W.)^2}$$

where

B.W. = half power beamwidth in degrees.

K is a factor dependent largely upon the level of the sidelobe and backlobe radiation intensity relative to the level in the main beam. In much of the early literature, K has been taken as the number of square degrees in a sphere or approximately 41,250, thus assuming that all the energy radiated by the antenna is distributed evenly throughout the prescribed beamwidth. In practice, K is determined by accurately measuring antenna gain and beamwidth.

An excellent discussion (Reference 7) of more accurate values of K indicates that this factor is not a constant but depends upon the details of the antenna design. As an example, a parabolic reflector which is only two wavelengths in diameter has higher sidelobes than predicted and a K = 27,900. By doubling the size of the reflector, the level of the

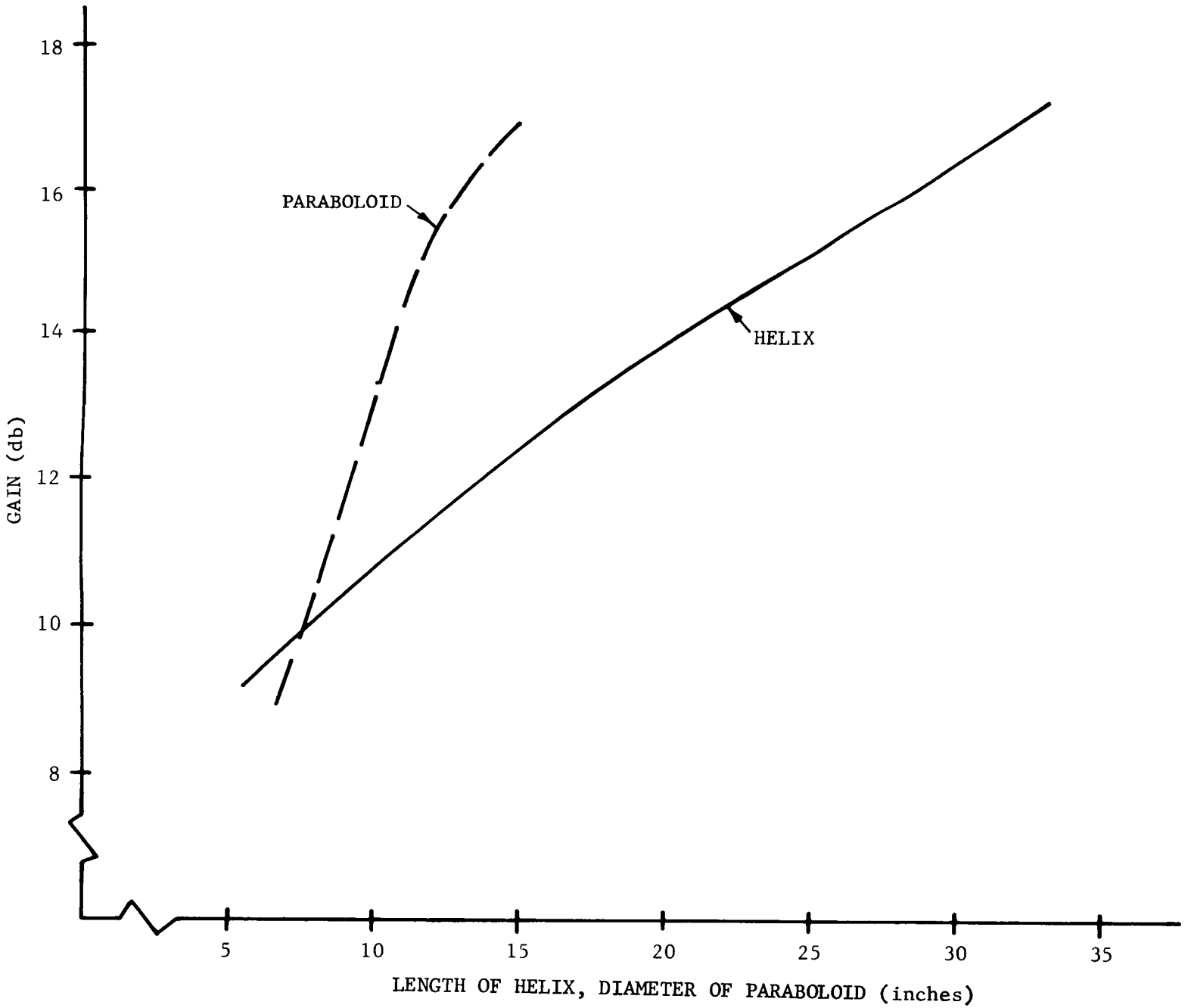

FIGURE 102. GAIN VS. SIZE

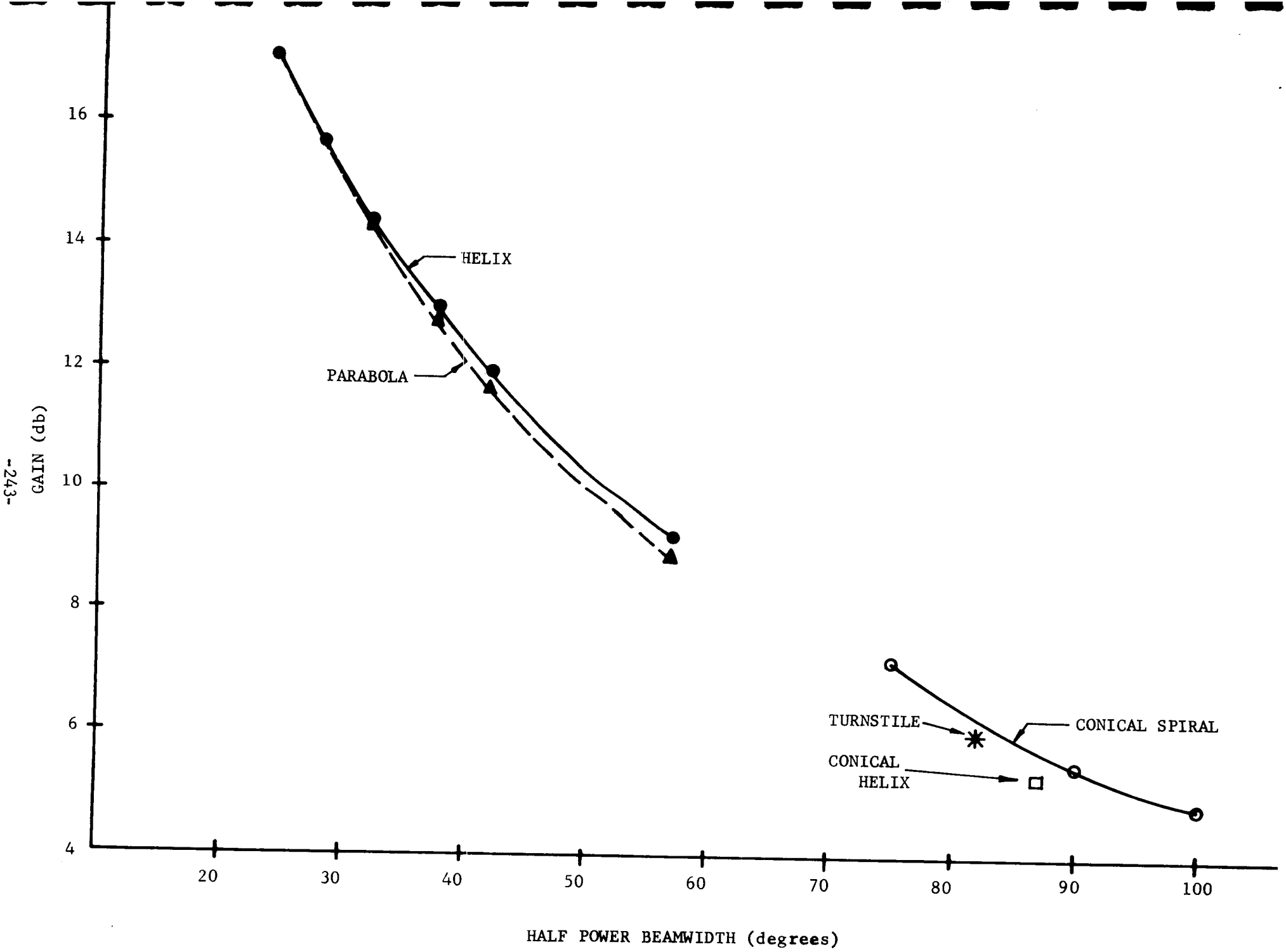

FIGURE 103. ANTENNA GAIN VS. BEAMWIDTH

sidelobes and their angular displacement from the main beam are reduced, and K = 34,000, and increase of 0.86 db. Similarly for the helix antenna (Reference 8), the side and backlobe radiation is reduced as the helix is made longer, and the angular displacement of the sidelobes from the peak of the main beam is reduced. When a radiation pattern is essentially a figure of revolution, as assumed here, sidelobes of the same angular width and relative intensity will degrade antenna gain to a lesser extent as their angular displacement from the main beam peak decreases. As a helix is lengthened, its main beam becomes narrower, the angular width and angular displacement of its sidelobes decreases, and the level of back radiation decreases. These latter three factors all contribute to an increasing K as the main beamwidth decreases. The measured radiation patterns (Figures 6 through 20 of Reference 8) demonstrate the above pattern characteristics. The helic gain-versus-beamwidth curve of Figure was plotted by using Stegen's value of K = 30,000 for the narrowest beamwidth considered and gradually decreasing this to 25,000 for the broadest beamwidth helix.

The relations between gain and size for a paraboloid and a helix are shown in Figure 102. The helix data was plotted by taking the measured by taking the measured beamwidths-versus-number of turns from Figure 21 of Reference 8. The helical lengths are somewhat pessimistic, since the circumference of the experimental helices was 0.92 wavelengths. If the circumference of the helix is increased to 1.1 wavelengths, a significant beam narrowing occurs, although the length of the helix is held constant. For helices no longer than 3 wavelengths, this narrower beamwidth means increased gain. The paraboloid gain-versus-diameter curve is based on a 55 percent aperture efficiency. This is probably the best that can be obtained with an unfurlable device.

b. Preliminary Antenna Design. The eventual choice of an erection technique for the helical antenna would evolve from consideration of sterilization and operational temperatures, impact survival, wind loads, degradation from wind-carried particles, power handling capability, weight, stowed volume, and other factors. Since such a decision is not within the scope of the present study, mechanical erection is arbitrarily chosen for the purposes of presenting a conceptual design.

The sketch in Figure 104 indicates the dimensions of the antenna envelope, which is a circular cylinder. The following table summarizes the electrical and mechanical characteristics of the 12 db gain helix. For higher gains, the only numbers that change are number of turns and length. These, however, increase rapidly with increasing gain, as shown in Figure 102.

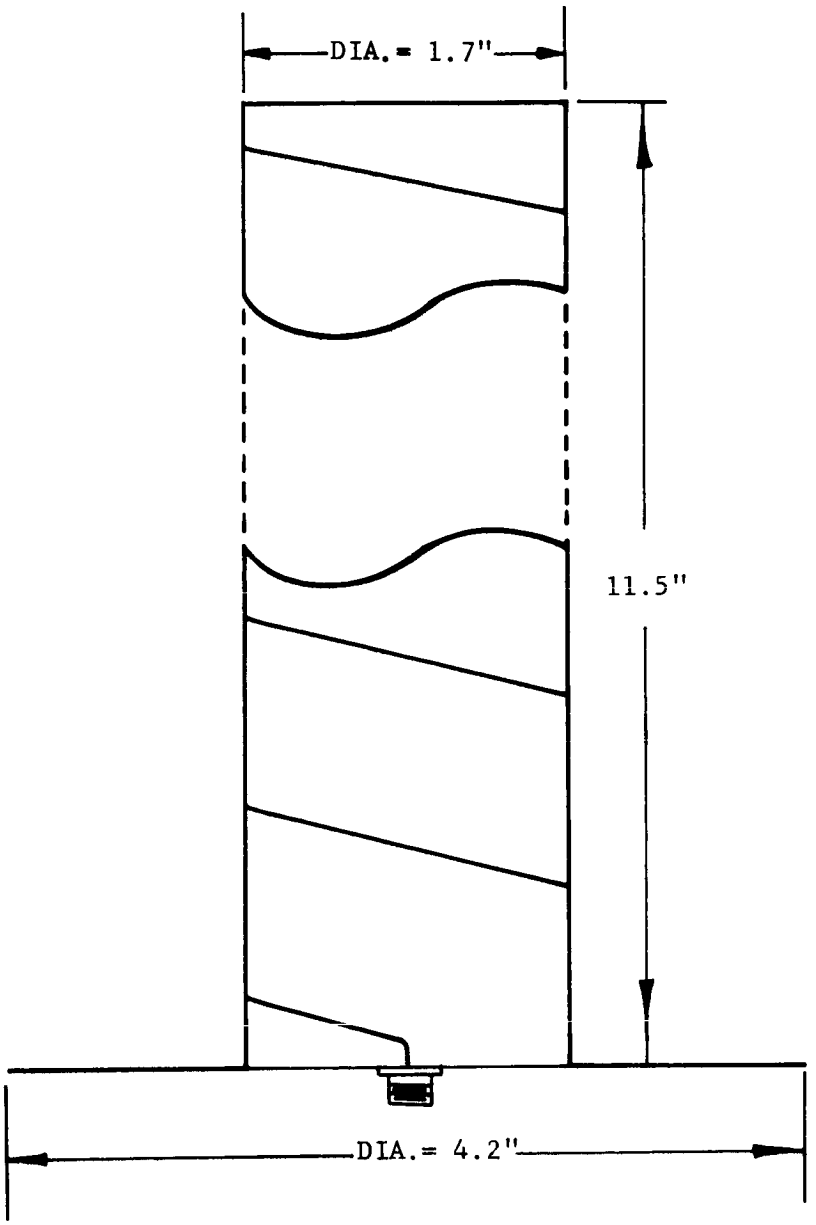

FIGURE 104. TEN TURN HELIX ANTENNA

Gain	12	db
Half Power Beamwidth	42	degrees
Number of turns	10	
Length (excluding ground plane)	11.5	inches
Ground Plane Diameter	4.2	inches
Helix Pitch Angle	13	degrees
Helix Diameter	1.7	inches

Any of several types of mechanical telescopes, metal or dielectric, may be used in the center of the helix. The telescope projects a flat, circular dielectric disk the proper distance along the axis of the antenna, thus deploying the helical winding which is terminated at the disk. The winding itself should have high electrical conductivity and should deploy so that the pitch angle is constant along the helix. The ground plane of the antenna is also erected, and may take the form of radial and concentric wires or closely spaced spiraling wires.

5.6.5 ALTERNATE ANTENNA IDEAS

Besides the vertically-oriented helix, there were other antenna ideas briefly considered during the study but discarded because they are too complicated for a reliable hard-landing capsule. However, they are worth describing because they may have application on more advanced landing capsules. The Mars Facsimile Capsule has rather severe antenna restraints with respect to wind stability, egress from the payload, and power available for tracking or aiming. Also, the high impact shock makes it undesirable to depend on complicated mechanisms.

Three alternate antenna orientation methods, judged not applicable to the MFC, are described below:

a. Fan Beam Antenna - Sun-Oriented. There are several ways to construct a fan-beam antenna which has a radiation pattern much wider in one vertical plane than in the orthogonal vertical plane (reference 9). Two such antennas are illustrated in Figure 105. The objective in using such an antenna on the surface of Mars would be to orient it in such a fixed position that the Earth stays within the beam during much of the time that line-of-sight visibility exists between the landing site and Earth. In other words, the major antenna plane would be made nearly coincident with the ecliptic plane. This method would allow increased communication time with a fixed antenna and would be useful at landing sites away from the equator.

It is assumed that such an antenna would be pointed from a vertically oriented payload. The first pointing step would be to aim the center of the antenna towards the Sun at noon. The final step would be to wait for

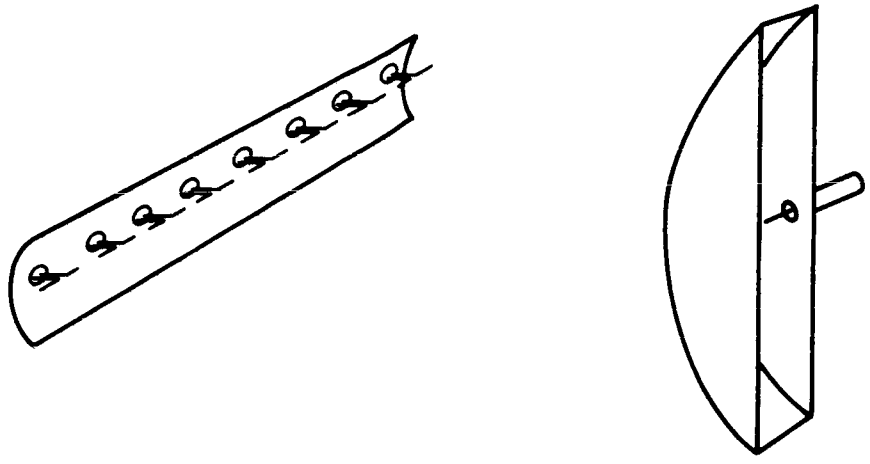

(A) DIPOLE ARRAY WITH CYLINDRICAL PARABOLIC REFLECTOR

(B) PILLBOX

R11161

FIGURE 105. ANTENNAS WITH FAN BEAM PATTERNS

about four hours and then rotate the antenna about its center axis until the Sun appeared in its major plane. The antenna plane would then match the apparent plane of the Sun's motion across the Mars sky. Assuming the angle between the Earth and Sun were small, communication with Earth would then be possible for a considerable period each day.

b. Fan Beam Antenna - Earth-Oriented. The same method described above could be extended to actually make the antenna plane coincide with the apparent plane of the Earth's motion across the sky. This could be achieved by first aiming the antenna as previously described. Then, the antenna could be displaced, at a right angle to its major plane and along the polar axis, the number of degrees by which the Sun and Earth differ in latitude from Mars. This amount changes slowly with time as shown in Section 5.1.2.

c. Helix Antenna - Sun Tracking. The type of helical antenna which is mainly considered in this report could be made more useful if it were provided with a simple tracking mechanism. Tracking of Earth during the Martian day will probably not be possible by optical means because of the sky brightness effect on Mars. Inertial and radio-frequency tracking appear quite complicated. However, it should be fairly easy to track the Sun by optical means unless clouds interfere. Even a coarse tracking mechanism could double the communication time of a 50 degree beamwidth helix antenna. Of course, this method is most useful when the angle from Mars between the Sun and Earth is small. This Sun tracking method would remove the restrictions on landing site locations imposed by the use of the simple vertically-oriented antenna.

REFERENCES

1. Space Physics, Edited by LeGalley & Rosen, Publisher Wiley & Sons, 1964, p. 145.

2. Lee, J.F. "Mars Lander Telemetry Relay System," National Telemetering Conference, June 1964.

3. Voyager Spacecraft System Study Phase I, Final Report, Volume IIb, Pages 4-16 (JPL Contract #950847).

4. Stang, P. F., "Corona and Breakdown as a Function of Humidity at Low Air Pressure," USAF Antenna R&D Symposium, October 1963.

5. Chown, J., and Martin, J. F., "Study of the Breakdown Characteristics of Antennas in the Atmosphers of Mars and Venus," under JPL Contract 950380, February 1963.

6. Brown, J., and McKee, K., "Wind Loading on Antenna Systems," Microwave Journal, September 1964, Page 41.

7. Stegen, R. J., "The Gain-Beamwidth Product of an Antenna," IEEE Trans. on Antennas and Propagation, July 1964, pp 505-506.

8. MacLean, T., et al, "The Bandwidth of Helical Antennas," Trans. IRE A.P., December 1959 (Supplement) pp. S 379-S 386.

9. Kraus, J.D., Antennas, McGraw-Hill, 1950, p. 346.

5.7 CAPSULE ELECTRONICS

5.7.1 DATA HANDLING

Data handling for the Mars Facsimile Capsule consists of converting the photo detector output to a digital signal and storing it for playback until conditions for Mars to Earth transmission are optimum. In summary, it is anticipated that the data handling system for the capsule will consist of very compact micro-circuitry for the analog to digital converter and logic circuits. The space and weight for a suitable A/D converter need not exceed 5 cubic inches and 5 ounces. The particular data storage method remains to be selected, however, its selection will be based upon a trade-off between minimum weight and maximum reliability. Tape recorders can be developed which store 10^6 bits, weigh approximately 8 pounds and occupy 60 cubic inches. Because of their electromechanical complexities extensive testing may be required before sufficient reliability can be achieved to survive the stringent environment of the capsule. Conversely, magnetic core storage for 10^6 bits would occupy 200 cubic inches and weigh 25 pounds. Such units have already been built and perform with good reliability. The large units have not been tested at high impacts but small units display outstanding resistance to shock.

a. Analog to Digital Converters. The analog to digital converter for the Mars Facsimile Capsule has very modest requirements relative to the current state of the art. The required sample rate is not expected to be more than a few thousand samples per second with a resolution of four bits. A suitable A/D converter with a conversion speed of 10 to 20 μs per bit utilizing integrated circuits could be packaged within the constraints of 5 in.^{3} and 5 oz. This estimate is based upon two reported units:

(1) "Integrated Electronic Analog-to-Digical Converter" Proc. IEEE, Dec. 1964, p. 1712.

11 bit (with W.W. precision resistors) resolution.
2 μsec/bit conversion rate
8 in.^{3} volume
0.75 watt power during conversion

(2) Fairchild Technical Data Sheet for Model F-615 (combination integrated circuits and printed circuit boards)

10 bits 75.9 in.^{3} 5 μsec/bit 4 watts
Verbal from Fairchild representative:
Reliapacket (high density) version
12 in.^{3} for 10 bits.

b. Tape Recorders. Tape recorders are functionally well suited to the data storage and playback requirements of the MFC. Continuous sequential recording and playback, which are the requirements of the facsimile signal, can be obtained from a tape recorder by employing its simplest mode of operation.

Continuous loop recorders which would permit recording and playback without rewinding represent a most attractive means of tape handling. An additional advantage is that only one drive assembly is required in this mode of operation although two different speeds will be required. This method, however, poses problems of supporting and moving a sufficient quantity of tape without making the recorder too large and heavy. The more conventional two-reel recorder may also prove to be applicable. The tape storage for two reels is more compact and rugged even though two reels are used. An additional drive must be implemented to rewind but this can be provided by a clutch and gear assembly. Both systems must be equipped with fast record and slow playback drive because of capsule operational requirements to record a picture as rapidly as possible and transmit at a data rate compatible with the transmitter.

A main consideration to implementation of a tape recorder is the requirement to survive the 3,000 g landing impact. The most common application for high impact recorders requires only tape survival, and not post-impact operation as does the MFC application. However, tests of actual recorders have demonstrated operating survival of 3000 g for 3 milliseconds. Considerable experience has been accumulated by several recorder manufacturers in providing recorders for ordnance and impact survival tests. Very compact recorders have been built which survive the shocks as severe as the proposed facsimile capsule, however, much of the data exists in classified reports. The consensus of manufacturers is that recorders to meet the MFC impact requirements are within the state of the art. A tabulation of these recorders is given in Table 5.7-I.

A current difficulty which plagues the application of recorders to extra-terrestial space missions is the absence of a magnetic tape which can survive heat sterilization. The problem stems from the difficulty in finding a heat resistant adhesive to bind the oxide material to the tape. The tape itself is sufficiently heat resistant but the binder softens and sticks to adjacent tape in the reel or to the supports during high temperatures of sterilization. With the recent advent of mandatory heat sterilization, it is anticipated that heat resistant adhesives will be developed in the not too distant future. Of course, this problem can be eliminated by paying the weight penalty which is associated with a metal recording tape.

TABLE 5.7-I

SEVERE ENVIRONMENT TAPE RECORDER PARAMETERS

TYPE OF MEMORY	MEMORY CAPACITY	VOLUME	VOLUME	POWER
Borg Warner R101 Tape Recorder Record only, survives 1000 g for 3 ms shock, two-reel type, in production	1.3×10^7 bits	37 $in.^3$ Transport Only	2 lbs. Transport Only	16 W
Leach MTR 362 Tape Recorder Record only, survives 2000 g for 3 ms, two-reel type	1.4×10^7 bits	33 $in.^3$ Transport Only	1.63 lbs. Transport Only	19.2 W Transport Only
Leach Tape Recorder Estimate, Continuous Loop, 5000 g for 3 ms.	10^5 bits	51 $in.^3$		
Leach Tape Recorder Estimate, Continuous Loop, 5000 g for 3 ms.	10^6 bits	100 $in.^3$		
Borg Warner R30R Tape Recorder Continuous loop type, operates during 175 g of sustained acceleration, in production	1.4×10^7 bits	220 $in.^3$	10.5 lbs.	22 W

c. Magnetic Core Storage. Large magnetic core memories and small ruggedized core memories have both been extensively developed. However, large impact ruggedized memories have not been developed largely because of expense and limited need. Memories in excess of one thousand bits for sequential writing and reading have successfully undergone impact testing at Aeronutronic (Reference 1). This memory, however, did not utilize micro-circuits and consequently is not as small as presently available memory systems. A typical larger memory employing micro-circuits has been developed by Autonetics, Division of North American Aviation. It is capable of enduring launch environments and is 200 cubic inches in volume, weighs 25 lbs., and stores approximately 10^6 bits. The memory is the coincident current type assembled from memory elements .025 inches in diameter. The power required for operation is approximately 40 watts. It utilizes semiconductor micro-circuits and multilayer printed cirduit boards and is compact and readily adaptable to a more ruggedized design. A substantial effort is currently being made to determine and improve the reliability of this memory. The products of this and other similar efforts can be instrumental in producing a reliable ruggedized memory suitable for the Mars Facsimile Capsule. Table 5.7-II lists parameters of the North American memory system, a representative memory plane, and estimates for MFC memories prepared by Electronic Memories, Inc.

Multi-aperature memories developed by Aeronutronic and other manufacturers are potentially suitable to this application but since their main attributes are high speed and non-destructive readout, neither of which is important to the facsimile capsule, it isnot likely that their choice would provide any outstanding advantages. Magnetic film memories which may ultimately provide a high density memory system currently are limited to small high speed data storage.

5.7.2 TIMING AND SEQUENCING

Following impact of the HRF Capsule with the Martian surface, a number of sequentially times events will occur. Depending upon ultimate system design and requirements, these events may include:

(1) Removal of the balsa impact limiter

(2) Venting of the flotation fluid

(3) Porting of the flotation shell

(4) Extension of the camera top tube

(5) Deployment of the antenna

TABLE 5.7-II

CORE STORE MEMORIES

TYPE OF MEMORY		MEMORY CAPACITY	VOLUME	WEIGHT	POWER
Autonetics D26J Computer	Coincident Current (.03 OD core) with read/ write electronics	10^6 approx. 32K words 30 bit words	370 $in.^3$	14 lb.	40 W
Fabri-Tek Hipac	Coincident Current .03 OD Core only	32,000	10 $in.^3$	--	--
Electronic Memories, Inc. (estimate)	Coincident Current Core 6000 g, 20 s	10^4	100 $in.^3$	6 lb.	1.5 W
Electronic Memories, Inc. (estimate)	Coincident Current Core 6000 g, 20 μs	10^5	175 $in.^3$	20 lb.	10 W
Electronic Memories, Inc. (estimate)	Coincident Current Core 6000 g, 20 μs	10^6	900	30 lb.	15 W

(6) Initiation of the camera and data storage

(7) Initiation of the data transmitter

Previous hard-landing capsules have utilized a G switch activated during retro-acceleration to initiate required timing sequences. This switch could be supplemented by a separate timer initiated by a bus separation signal and with a time interval exceeding the 3 sigma landing and erection times. The initial events such as porting and deployment are relatively uncritical in regards to timing accuracy. The time periods associated with these events may extend from 10 minutes to 30 minutes. Time intervals in this range can be easily controlled by the simple RC charging type timer circuits successfully used on past Ranger capsule projects.

In lieu of an Earth-Mars command system, a sequencer may be required to control camera operation and data transmission for 2 to 4 hour periods over a 2 to 4 day span. The camera operating period will be chosen to optimize lighting conditions and the data transmission period will be chosen to match the period when the vertically-oriented antenna is aimed towards Earth. These operating periods can be timed from either the initial landing events or from a time corresponding to a measured location of the Sun (such as sunrise or noon).

5.7.3 IMPACT RESISTANT DESIGN

For the Mars Facsimile Capsule mission, it is required that the electronics withstand impacts to 3,000 g's 500 fps and subsequently operate reliably. While this would have seemed a formidable task a few years ago, sufficient experience and information exists from several sources to put the electronics design within the present state-of-the-art.

Aeronutronic has qualified many individual components and subsystems, bonding methods, etc., for several Ranger payloads. (Reference 2). Extensive shock testing of components, subsystems, and capsules was performed resulting in developed equipment with high reliability at the design level of 3,000 g, 3 msec. Many of the system tests were limited to the design level as this represented a limit for the testing equipment; however, many electrical components and small subassemblies were tested to 12,000 g, 0.4 msec. duration, using instrumented, manually-operated hammers. In a more recent program at Aeronutronic with the development of an instrumented rocket launched device, several additional components were tested. These were subminiature VCO's and summing amplifiers. These devices utilize thin film interconnections and resistors, and pico transistors and diodes. There were no failures after repeated shocking of epoxy encapsulated units. Earlier non-encapsulated units suffered several failures due to lead breakage, primarily due to movement of the larger components (capacitors).

A shock resistant two-watt L-band solid state transmitter was developed and tested at JPL.(Reverence 3). These units have survived repeated shocks at 3,000 g, 200 fps. Impacts of 10,000 g, 200 fps, have been carried out with damage only to a ceramic trimmer capacitor and the RF quartz crystal. The capacitor has already been redesigned and a more rugged RF crystal is under development. JPL has tested the transmitter components and other varied components at shock levels of 10,000 to 20,000 g's, 200 fps.

Various military agencies such as the Army's Harry Diamond Laboratories (HDL) have successfully developed telemetry systems which survive launch from closed-breech guns. The acceleration experienced is of long duration and reaches 250,000 g in the case of projectires instrumented by HDL and fired from a 16-inch gun for upper atmosphere research. In general, they use internal device encapsulation at levels above 25,000 g's. Both G.E. and Fairchild manufacture an "entertainment" line of completely encapsulated transistors with good performance characteristics. The gain-bandwidth product of some of the Fairchild units is in excess of 800 mc and the G.E. devices have been used at 250,000 g's by HDL with good results.

To summarize, it may be said that most types of components and subsystems required for the MFC have been qualified for 3,000 g, 3 msec. duration, shocks or higher. These include a great variety of semiconductors, UHF triodes, passive components, incandescent lamps, trimmer capacitors, potentiometers, connectors, a core storage memory, a sealed silver-zinc battery, hysteresis-synchronous motor, fork frequency standard, RF quartz crystal, etc. Having the required catalog of shock proof components, it is possible to build reliable electronic systems by mounting the components rigidly within a stiff structure to prevent force amplification.

There should be no serious problem in obtaining reliable electrical and electronic subsystems for the MFC. A careful development program will be required including component qualification, careful structural design and packaging, followed by subsystem qualification to establish the desired confidence level of shock survival.

REFERENCES

1. "Impact Investigation of a Solid-State Data Storage Unit" Final Report, Aeronutronic Division, Philco Corporation, October 1962, Publication No. U-1894.

2. "Capsule Impact Technology, Aeronutronic Report No. U-3031.

3. J. O. Lonborg, "High Impact Survival", JPL Technical Report No. 32-647, September 30, 1964.

5.8 POWER SOURCES

Space vehicle electrical power subsystems currently use three energy sources; nuclear energy, solar energy and chemical energy. Associated with these energy sources are converters which transform the available energy into electrical power at rates which are compatible with their respective loads. Photovoltaic solar cells, fuel cells, electrochemical batteries, thermionic and thermoelectric converters are typical devices that are utilized. In the following paragraphs these energy sources and their conversion devices will be examined for their suitability as a power subsystem for the MFC.

5.8.1 MFC REQUIREMENTS

The nominal MFC power requirements are stated below in order to confine the range of evaluation parameters for potential power sources. Since MFC capsule weight and space are at a premium, these are the determining factors for selecting a given power source providing all other requirements can be met. The capsule energy source must endure and function in accordance with the conditions and requirements which are outlined as follows:

a. Sterility. The energy source must be fabricated and furnished to MFC capsule assembly operation in sterile condition as established by standards for interplanetary missions.

b. Assembly Heat Sterilization. Must be capable of surviving type acceptance heat sterilization consisting of three cycles of 145°C dry heat for 36 hours and flight acceptance sterilization of three cycles of 135°C dry heat for 24 hours.

c. Preflight Readiness. Must be in an active state before launch.

d. Launch Environment. Must survive typical launch transients of shock, vibration and decompression.

e. Space Transit. Must survive 6 to 9 months of space environment during transit to Mars.

f. Shock. Must survive a landing shock on Mars of approximately 3000 earth g's of deceleration for 3 milliseconds in an unspecified direction.

g. Operate in the Martian Environment. Mean temperature -40°C, sparse atmosphere 20 to 60 millibars, reduced gravity, etc.

h. Power. Provide approximately 250 watts of electrical power for a minimum of two hours plus several watts of power during standby and camera operation after the Martian landing.

i. Confinement. After capsule assembly the energy source must operate unattended and by remote control because it will be sealed into the capsule envelope. This envelope will also severely limit the amount of heat that can be dissipated from the capsule.

5.8.2 CHEMICAL BATTERIES

Chemical batteries play a substantial role in the supplying of electrical energy to space vehicles.

Even where chemical cells are not the source of power, they are still used extensively for accommodating transient load peaks which exceed the capability of the primary energy source.

Features which make batteries attractive to space applications are ruggedness, compactness, efficiency, availability and reliability. Table 5.8-I lists presently available battery types and their salient features. This is a general list of batteries currently in production and is not limited to batteries used in the missile and space field.

The two general classes of batteries are primary and secondary. The primary battery is supplied in the charged state, is discharged in use and is disposed of because it cannot be recharged. The secondary is normally supplied uncharged, is charged before use and is recharged as required during its useful life.

Space vehicles preflight evaluation procedures normally impose requirements which can only be met by rechargeable batteries; therefore, primary batteries have had very limited application.

Tables 5.8-II and 5.8-III list the most common cell reaction currently in use. The three electrode material combinations generally used for space batteries are nickel-cadmium, silver-cadmium and silver-zinc. They are inherently rugged, lightweight, sealable, rechargeable and can supply high peak loads.

A battery is normally made up of several electrochemical cells each of which is composed of a cathode, an anode and an electrolyte in a separator which isolates the electrodes from each other. This arrangement supports an electrochemical reaction which can be made to take place so that the electrical part of the reaction proceeds by way of a circuit external to the cell, while the chemical part of the reaction occurs by way of ionic conduction through the cell electrolyte.

The type of chemical reaction that can be used in an electrochemical cell is known as an oxidation-reduction reaction, a reaction in which one chemical species gives electrons to another. By separating the two species, one of which is the anode and the other the cathode, and controlling the flow of ions between them, battery engineers make devices in which essentially all

TYPE			ANODE	ELECTROLYTE	CATHODE	NOMINAL VOLTAGE OF BASIC CELL	WATT-HOURS / LB	WATT-HOURS / CU-IN	VOLTAGE REGULATION	SERVICE DUTY	DISCHARGE RATE	SERVICE TEMPERATURE (DRY CELLS)	CYCLE LIFE (SECONDARY CELLS)	APPLICATIONS
PRIMARY	Ready (dry)	Leclanche'	Zn	$ClNH_4$ MnO_2 Cl_2Zn	C	1.5	10	1	Fair	Interm't	Low	30 to 90F		Photo equipment Consumer products Communications
		Mercury	Zn	KOH	HgO C	1.34	30	5.0	Good	Interm't	Low	50 to 160F		Photo equipment Consumer products–Communications
		Alkaline dry cell	Zn	KOH	MnO_2	1.5	47	2.2	Good	Light	Low	40 to 90F		Photo equipment Consumer products–Communications
		Magnesium cell	Mg	MgBr	MnO_2	2.0	50	3.3	Fair	Light	Low			Photo equipment Consumer products–Communications
	Reserve (wet)	Lalande	Zn	NaOH CuO	CuO	0.8	20	0.94	Good	Light	Low			Mine–Marine–Railway Telephone–Telegraph
		Air cell	Zn	NaOH O_2-C	CuO	1.4	20	2.0	Good	Light	Low			Mine–Marine–Railway Telephone–Telegraph
		Water-activated cuprous-chloride	Mg	Water CuCl	CuCl	1.2	21	2.1	Good	Light	Low			Torpedoes Communications
		Water-activated silver-chloride	Mg	Water AgCl	AgCl	1.4	47	5.0	Good	Heavy	High			Torpedoes Communications
		Silver-zinc	Zn	KOH	AgO	1.5	70	5.6	Good	Heavy	High			Missiles–Torpedoes
SECONDARY		Lead-acid	Pb	H_2SO_4 H_2O	PbO_2	2.0	12	1.1	Fair	Light	Med		200-2000	Automotive–Aircraft Submarines
		Nickel-iron (Edison)	Fe	KOH	NiO_2	1.2	13	0.7	Good	Medium	Med		Over 2000	Electric traction Power plant auxiliary service
		Nickel-cadmium (Jungner)	Cd	KOH	NiO_2	1.2	12	1.1	Good	Heavy	High		Over 2000	Aircraft–Photo equipment Communications–Consumer products Satellites
		Silver-zinc	Zn	KOH	AgO	1.5	59	4.4	Good	Heavy	High		10-400	Aircraft–Photo equipment Communications–Consumer products Satellites–Submarines–Torpedoes
		Silver-cadmium	Cd	KOH	AgO	1.1	32	2.6	Good	Heavy	High		300-1000	Aircraft–Missiles–Photo equipment Communications–Consumer products Submarines–Torpedoes

TABLE 5.8-I

CURRENTLY AVAILABLE BATTERIES

TABLE 5.8-II

HALF-CELL REACTIONS, POTENTIALS, AND CAPACITY DATA FOR VARIOUS ANODE MATERIALS

Anode Material	Half-Cell Reaction	Half-Cell Potential (volts)		Theoretical Ampere-Minute Capacity	
		$E°_{Acid}$	$E°_{Base}$	per gram	per cm³
Sodium	$Na = Na^+ + e^-$	2.71		69.9	67.8
Magnesium	$Mg + 2OH^- = Mg(OH)_2 + 2e^-$		2.67	132.2	230
Magnesium	$Mg = Mg^{++} + 2e^-$	2.37		132.2	230
Aluminum	$Al = Al^{+++} + 3e^-$	1.67		178.9	483
Zinc	$Zn + 2OH^- = Zn(OH)_2 + 2e^-$		1.245	49.2	351
Zinc	$Zn = Zn^{++} + 2e^-$	0.76		49.2	351
Indium	$In + 3OH^- = In(OH)_3 + 3e^-$		1.0	42.0	307
Cadmium	$Cd + 2OH^- = Cd(OH)_2 + 2e^-$		0.81	28.8	248
Iron	$Fe + 2OH^- = Fe(OH)_2 + 2e^-$		0.88	57.6	455
Lead	$Pb = Pb^{++} + 2e^-$	0.13		15.6	176
Lead	$Pb + SO_4^= = PbSO_4 + 2e^-$	0.37		15.6	176
Hydrogen	$H_2 = 2H^+ + 2e^-$	0.00		1596	112
Hydrogen	$H_2 + 2OH^- = 2H_2O + 2e^-$		0.828	1596	112

TABLE 5.8-III

HALF-CELL REACTIONS, POTENTIALS, AND CAPACITY DATA FOR VARIOUS CATHODE MATERIALS

Anode Materials	Half-Cell Reaction	Half-Cell Potential (volts)		Theoretical Ampere-Minute Capacity	
		$E°_{Acid}$	$E°_{Base}$	Per Gram	Per cm³
Manganese Dioxide	$MnO_2 + 4H^+ + 2e^- = Mn^{++} + 2H_2O$	+1.23		37.4	188.1
Manganese Dioxide	$MnO_2 + H_2O + e^- = \frac{1}{2} Mn_2O_3 \cdot H_2O + OH^-$		+0.17	18.5	93.1
Mercuric Oxide	$HgO + H_2O + 2e^- = Hg + 2OH^-$		+0.098	14.8	165
Lead Dioxide	$PbO_2 + SO_4^= + 4H^+ + 2e^- = PbSO_4 + 2H_2O$	+1.685		13.4	125
Lead Dioxide	$PbO_2 + H_2O + 2e^- = PbO + 2OH^-$		+0.247	13.4	125
Nickel Dioxide	$NiO_2 + 2H_2O + 2e^- = Ni(OH)_2 + 2OH^-$		+0.49	32	~110
Silver (II) Oxide	$2AgO + H_2O + 2e^- = Ag_2O + 2OH^-$		+0.570	26.0*	193*
Silver (I) Oxide	$Ag_2O + H_2O + 2e^- = 2Ag + 2OH^-$		+0.345	13.9	99.2
Silver Chloride	$AgCl + e^- = Ag + Cl^-$	+0.222		11.2	62.5
Cupric Oxide	$2CuO + H_2O + 2e^- = Cu_2O + 2OH^-$		−0.159	40.4*	261*
Cuprous Oxide	$Cu_2O + H_2O + 2e^- = 2Cu + 2OH^-$		−0.357	20.2	121
Cuprous Chloride	$CuCl + e^- = Cu + Cl^-$	+0.137		16.7	58.9
Bismuth Oxide	$Bi_2O_3 + 3H_2O + 6e^- = 2Bi + 6OH^-$		−0.457	20.7	184
Oxygen	$O_2 + 2H_2O + 4e^- = 4OH^-$		+0.40	201	229
Chlorine	$Cl_2 + 2e^- = 2Cl^-$	+1.360		45.3	68.0

* Calculated on the basis of 2-electron change per mole of oxide.
† Potentials reported are operating potentials, *i.e.*, under load conditions.

of these electrons can be made to flow through an external circuit, thereby converting most of the chemical energy to electrical energy during the discharge of the cell.

The cathode electrode consists of a mass of electron receptive chemicals held in intimate contact with a metallic plate through which electrons arrive from the external circuit during the discharge reaction. This terminal receives electrons and by the conventional definition of current flow is a source of current and is identified as the positive pole (+) of the battery.

A typical reaction which in this case takes place at the cathode of a silver-zinc cell is shown in Figure 106. The chemical reaction is as follows:

$$2\ Ag\ O + H_2O + 2\ e^- \rightarrow 2\ Ag + 2O\ H^- \qquad (1)$$

The stable state of this reaction is indicated by the right hand expression which is also the discharged state. The external circuit supplies the two electrons ($2e^-$) which are required to support the reaction. The theoretical half cell voltage from Table 5.8-II for this reaction is + 0.570 volts.

The anode consists of another chemical which readily gives up electrons and is similarly held into close contact with a metallic member through which the electrons can be conducted into the external circuit. Chemically anode materials are characterized by the ease with which they give up electrons and go into solution, thus forming positive ions. This anode is the terminal of the cell marked negative (-) to be consistent with conventional current flow.

The equation of the companion reaction of the silver-zinc cell that occurs at the anode is:

$$Zn + 2O\ H^- \rightarrow Zn\ (OH)_2 + 2\ e^- \qquad (2)$$

Again the right hand expression is the stable or discharged state and is characterized by an excess of electrons (+ $2\ e^-$) in the right hand expression. The theoretical half cell voltage shown in Table 5.8-III for this reaction is 1.245 volts. The sum of the half cell voltages at the electrodes yields a combined open circuit cell voltage of 1.82 volts.

The third component of the battery is the electrolyte. The electrolyte does not change as a result of the basic reaction but merely provides the medium through which the transfer of ions can take place. Combining equations (1) and (2) yields the over-all discharge (in the direction of arrow) reaction which occur in a complete cell:

$$Ag_2\ O + Zn + H_2O \rightarrow 2\ Ag + Zn\ (OH)_2 \qquad (3)$$

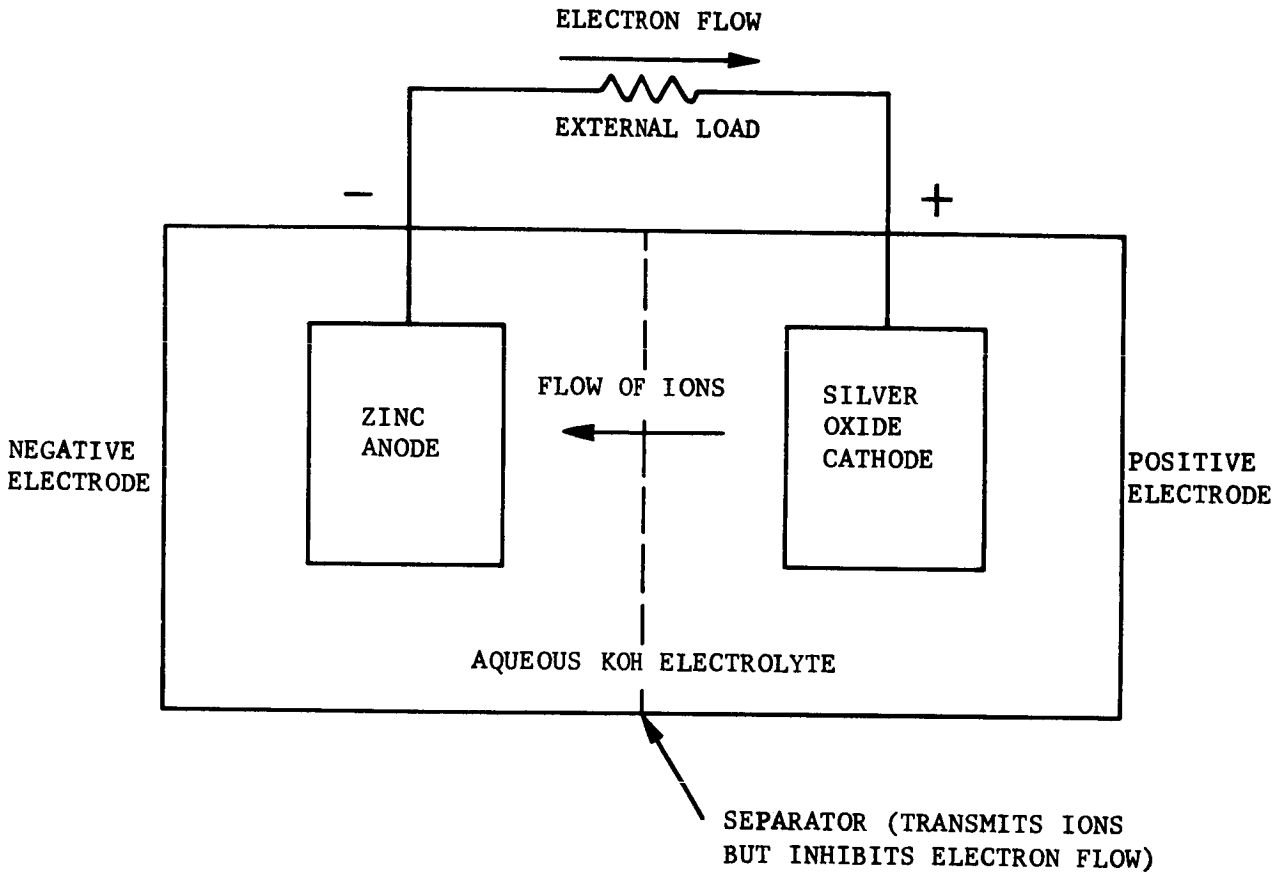

FIGURE 106. RELATIVE FLOW OF ELECTRONS AND IONS IN A SILVER-ZINC CELL CIRCUIT R11199

Equation (3) shows that there is no over-all effect on the electrolyte taking place during discharge. The hydroxyl ions and the electrons balance out between the two equations thus producing no net effect in the electrolyte.

Actually, two reactions occur at the cathode of the silver-zinc cell. The foregoing is the divalent reduction of silver and is the more energetic. It is commonly referred to as the peroxide reaction. The second reaction, which is the monovalent reduction of silver, also occurs. Its equation is also shown in Table 5.8-III. During the charge cycle the transistion between the monovalent and the divalent potential is quite distinct. Its occurrence depends upon the charge rate and the construction of the cathode plate itself. A typical charging curve is shown in Figure 107 .

The previous discussion although highly simplified is representative of the reactions occurring in most alkaline batteries.

a. Battery Construction and Sealing. Batteries can be made capable of surviving shocks due to impacts. Batteries are normally constructed on a cellular basis, that is, a single anode, cathode and separator set are assembled in an insulated container. These separate cells are then assembled into a battery to provide some specific voltage multiple of the individual cell. The individual cell must be designed large enough to produce the required current since it is not practical to connect cells in parallel. Minute differences in cell potential cause excessive circulating currents and differences in internal resistance cause current to divide unequally. Cells operate very well in series as long as they are reasonably similar. The most common type of cell construction is the pocket type where the active materials in porous state are cemented or bonded to metal plates formed with pockets or holes. This method is used more for commercial batteries because it is relatively inexpensive compared to other methods.

A more recent technique of manufacturing battery plates uses the sintering technique. A typical sintered plate uses powdered carbonyl nickel formed around a nickel screen or perforated plate. This formed plate is heated in the presence of cracked ammonia thus producing a porous rigid nickel plaque with a large surface area. The sintering process can be applied to other metallic electrode materials. The sintering process is followed by further processes which deposit or form hydroxides on the surfaces of the plates to give the proper quantity of active material. Rectangular or circular electrode plates are then assembled by pressing them together with the separator materials into thin rectangular of circular blocks. These assemblies are relatively dense and because of the presence of reinforcing metal plates or screens can stand very high impacts when properly supported.

A more specialized type of construction which has been employed less frequently in the fabrication of wet cells, but is commonly used in dry cells, is the "duplex" structure or pile construction (Reference 3). Here a porous zinc disc is attached to one face of a silver foil disc which has a silver-silver

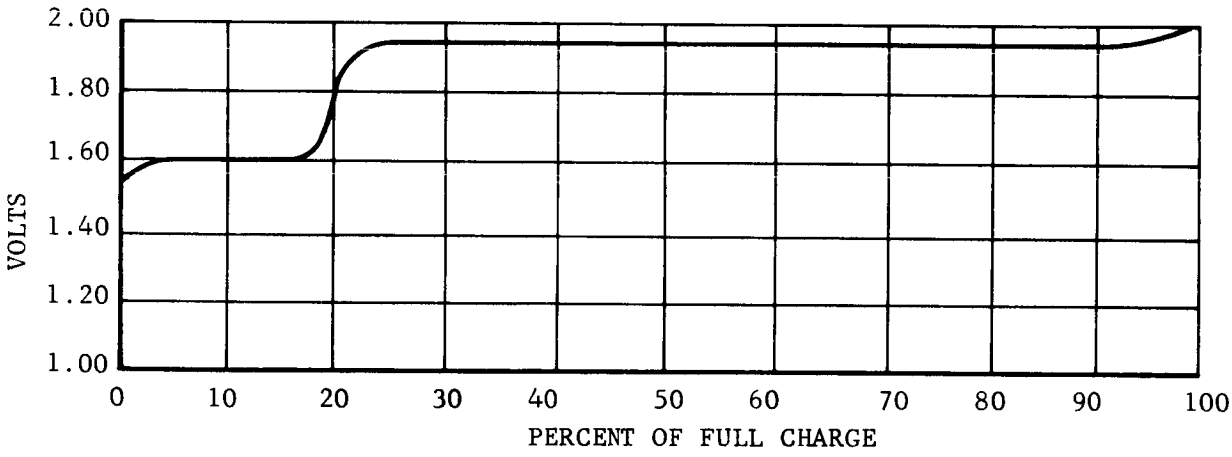

R11164

FIGURE 107. TYPICAL CHARGE CURVE OF THE SILVER-ZINC SYSTEM

oxide disc attached to its opposite face. These assemblies are alternately stacked as shown in Figure 108 with a separator disc to form a series-connected battery pile. By making the electrode and separator discs larger in diameter than the active materials and subsequently embedding the entire battery assembly in a plastic jacket a very rugged assembly is produced. This provides a very compact arrangement of electrodes and results in high energy density. Not much data appears in the literature regarding the shock resistance probably because it has not presented a problem. Typically, 250 mah circular nickel-cadmium button cells have been accelerated at 50,000 g's and higher and continued to operate. This form of construction has been successfully used in the fabrication of a battery for the lunar hard landing capsule. This particular capsule was tested and survived impacts at 3000 g's for durations of 3 ms (Reference 3).

A frequent requirement for space batteries is that they be sealed against gas or liquid leakage. The purpose of sealing the cells is twofold. First, it prevents evaporation of the electrolyte in space vacuum and second, it permits cells to be operated under continuous overcharge condition, where oxygen is evolved at a steady state pressure. It is not difficult to prevent evaporation of the electrolyte, since seals for this purpose need resist only modest pressures. To prevent leakage of oxygen during overcharge, however, is extremely important and considerably more difficult.

Evolution of gas from the electrode occurs because the normal battery reaction is replaced by the water disassociation reaction as the electrodes approach full charge. Recombination of the evolved hydrogen and oxidation is difficult to accomplish and maintain (Reference 11), and has not been accomplished on a practical basis. However, an alternate technique is utilized that takes advantage of the fact that oxygen will enter into a reversible reaction with the metallic cadmium or zinc anode material. To make use of this phenomenon, the cathode, where the oxygen is formed during overcharge, is deliberately formed with less active material than the anode so that oxygen evolution occurs long before hydrogen evolution. This oxygen then diffuses through the electrolyte and separator and reacts with the anode. Because this recombination of oxygen depends upon diffusion of the oxygen through the separator the cell pressure contributes to the reaction and an equilibrium between overcharge rate and cell pressure is reached.

The recombination rates achieved in nickel-cadmium cells are considerably higher than those attainable in standard silver-cadmium and silver-zinc cells (Reference 9). An obvious factor favoring the nickel-cadmium cell is the easier access of oxygen to the impregnated cadmium electrodes through the porous felt separators. A second factor is the effect of soluble organic separator products in the electrolyte of silver cadmium cells. This material produced by chemical attack on the separator is absent from nickel-cadmium cells.

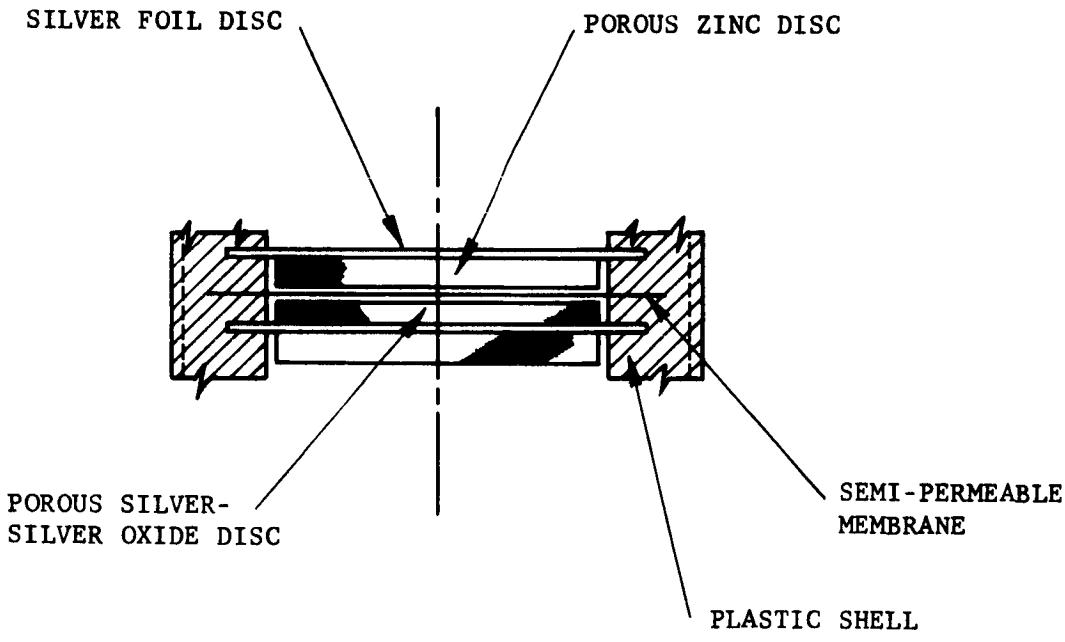

R11201

FIGURE 108. CROSS SECTION OF CELL OF AG-ZN PILE

There is essentially no evolution of oxygen from the silver anode during charge as compared to nickel or lead (Reference 10). Consequently sealed silver-cadmium and silver-zinc cells produce no appreciable pressure rise until the cell is fully charged. As full charge is reached the pressure rises abruptly until an equilibrium pressure is reached which depends upon the oxygen recombination rate and the charge current. The pressure gradually returns to the initial pressure after termination of the charge current.

As has been pointed out, the anode is purposely made with a larger capacity than the cathode. Thus, overcharging produces oxygen at the cathode before the anode is completely charged. The oxygen then diffuses to the anode and is electrochemically reduced. In normal operation, therefore, the anode is never completely charged; accordingly, hydrogen is never evolved. If oxygen leakage occurs, however, the differential between the capacity of the cathode and anode is reduced. When this differential reaches a certain value, hydrogen begins to be reduced at the anode, and excessive pressures develop because there is no mechanism for recombining hydrogen.

Thus, the most important reason for hermetic sealing of space batteries is so that they do not lose their overcharge tolerance through gradual loss of their excess negative capacity (Reference 2). The three methods of sealing cells are with plastic cases, metal cases and combination plastic lined metal cases. Plastic cases are either pre-cast with the battery assembled into them later or the case is formed by encapsulating the assembled battery (pile construction is this type). The metal case, usually stainless steel or nickel plated steel, requires insulated terminals and places the case at the cell potential. The cell must be insulated from surrounding conductors but is inherently rugged.

An insulated metal case combines the good features of both types at the expense of increased weight and cost. For high impact batteries, the most convenient procedure is to utilize a plastic battery shaped to fit the space vehicle structure. This battery is then potted into the structure giving the ultimate in support to the battery (Reference 3).

b. Sterilization. By international agreement, which is advocated in the United States by the National Academy of Sciences, all spacecraft which are designed for extra-terrestrial planetary landings must be sterilized and sealed prior to launch. This sterilization is accomplished by assembling spacecraft from sterile components in a sterile environment. The final sterilization is accomplished by subjecting the spacecraft assembly to a dry heat bake for 24 hours at 135°C. The subassembly components of the spacecraft must also be sterilized before final assembly and therefore they will require another heat sterilization cycle of 24 hours at 135°C. As a minimum, the spacecraft must be capable of sustaining a third cycle of heat sterilization to allow the disassembly of the spacecraft for repairs and subsequent resterilization.

As a means of assuring that the components of the spacecraft are capable of sustaining the preflight heat sterilization procedures, all component prototypes will be qualified by requiring them to survive three cycles of 36 hour heat sterilization at 145°C.

Until recently space batteries which have been evaluated for current requirements have proved to be inadequate to survive the qualifying sterilization procedure at 145°C temperature (Reference 12). However, on 25 January 1965, it was publicly announced by the Astropower Laboratories of the Douglas Aircraft Company that they have perfected an inorganic separator for a silver-zinc cell which permits survival and even operation during sterilization temperatures. Their success has evolved from a three-year independent development program which produced batteries capable of operating for 2000 hours at 100°C while simultaneously surviving 2000 charge-discharge cycles. Fifty hours of operating life is reported at 150°C. Heat sterilization at 150°C for 108 hours of a non-operating battery produces no measurable effect on battery performance. Energy density of this battery is reported to be comparable to conventional silver-zinc batteries.

The main obstacle to obtaining sterilizable batteries has been the unavailability of sterilizable separators. Presently used cellulose type separators are not capable of resisting the chemical attack of the electrolyte and soluble electrode materials upon them at elevated temperature. The solution to this problem is being sought by Radiation Applications, Inc., under contract to JPL. This work is in the initial stage of collecting and screening materials, consequently no results have been reported. Independent research on separators is also being pursued by Carl F. Norberg Research Center of Electric Storage Battery Company.

Success in heat sterilization of electrode materials has been accomplished by specially preparing the electrode and performing the sterilization in the uncharged state. The advantage of this procedure is derived from the fact that the electrode materials are in their most chemically stable state when in the discharged state. Plastic battery case materials are also generally unable to withstand sterilization temperature. Nylon Zytel 38 shows promise as a sterilizable case material but the sealing material is attacked by the KOH cell electrolyte; thus making this case material marginally successful.

Other work on battery sterilization in the industry has generally concluded that nickel-cadmium batteries have the best chance of surviving sterilization. The reason is that the electrode materials are not very soluble in the nickel-cadmium battery; therefore, the caustic effects of their presence in the electrolyte is greatly reduced. In addition, because the electrodes are relatively insoluble, the battery can use more heat resistant separator materials and still operate reliably.

Nickel-cadmium batteries, however, are affected by secondary chemical reactions which tend to irreversibly reduce the battery performance with age.

This process is accelerated by the temperature and pressure of sterilization. Although investigations of this phenomenon are in progress no conclusive data is available on the actual extent of this effect.

Nickel-cadmium button-cell batteries have been produced by Sonotone for which they claim the ability to survive sterilization. Gulton Industries also indicated that they could produce sterilizable nickel-cadmium batteries. Chrietzberg of Electric Storage Battery recommends metal cased nickel-cadmium cells for current sterilizable applications (Reference 13), although they are not presently producing nickel-cadmium batteries. Unfortunately, the highest energy density that could be expected from nickel-cadmium is approximately 12 watt-hour per pound which is below a useful value for the MFC program.

c. Temperature Characteristics. Storage temperatures for silver-zinc and similar batteries normally range from -55 to 100°F with the greatest loss of charge and life occurring at the higher temperatures. Satisfactory operating temperatures are from 0 to 160°F, with the best operation occurring at the higher temperature at the expense of service life and reliability. Optimum storage temperature is near 0°F and optimum operating temperature is near 70°F. These operating temperatures are based on batteries currently in use and therefore not capable of being heat sterilized. Comparing this range of temperatures to the 300°F sterilization temperature illustrates to some extent what happens to batteries when they are heat sterilized.

An insight into some of the low temperature characteristics of an alkaline battery are revealed in the phase diagram of a potassium hydroxide solution shown in Figure 109 . This diagram shows that for highest resistance to freezing the electrolyte should have a KOH concentration of 30 percent. Fortunately, this is fairly close to 20 percent, the best concentration for electrical purposes, therefore, batteries for low temperature survival are quite feasible. Since the electrolyte concentration remains constant during the discharge cycle there is no change in its resistance to freezing with state of charge. There is a tendency for the electrolyte to become slightly diluted as the battery experiences many charge-discharge cycles. However, in a silver-zinc battery where the number of charge cycles are not great this effect is negligible.

Direct effects of temperature on the energy density of typical batteries at the optimum discharge rates are shown in Figure 110 . Referring to the expected mean tempterature on Mars of -40°C, it would appear that even a silver-zinc battery would be approaching marginal performance. However, since the transit temperature would approximately be 0°C as it approaches Mars, good initial battery performance could be expected. Thermal control would be necessary to limit the temperature drop in the initial period on Mars until the first transmission to Earth was begun. At this point the temperature in the capsule would rise substantially because the transmitter would be dissipating approximately 100 to 200 watts inside the capsule. Thermal control again would be necessary to limit the capsule temperature

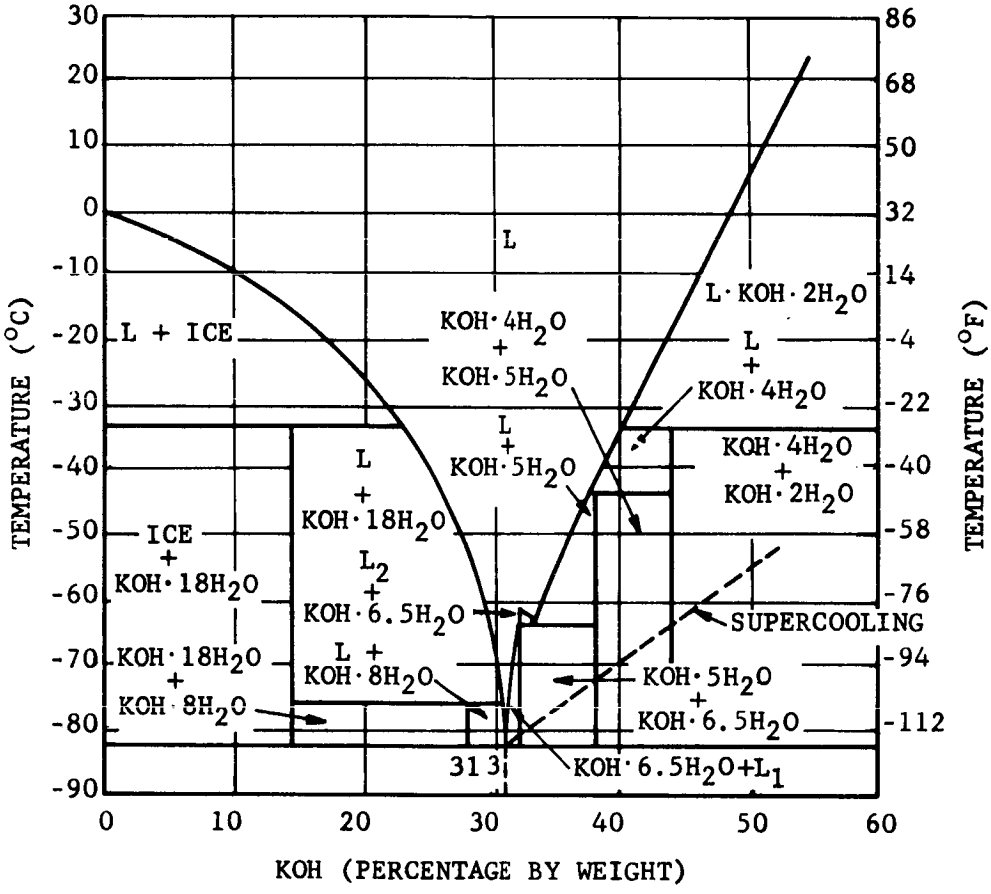

R11202

FIGURE 109. POTASSIUM HYPROXIDE (KOH) ELECTROLYTE CONCENTRATION AS AFFECTED BY TEMPERATURE

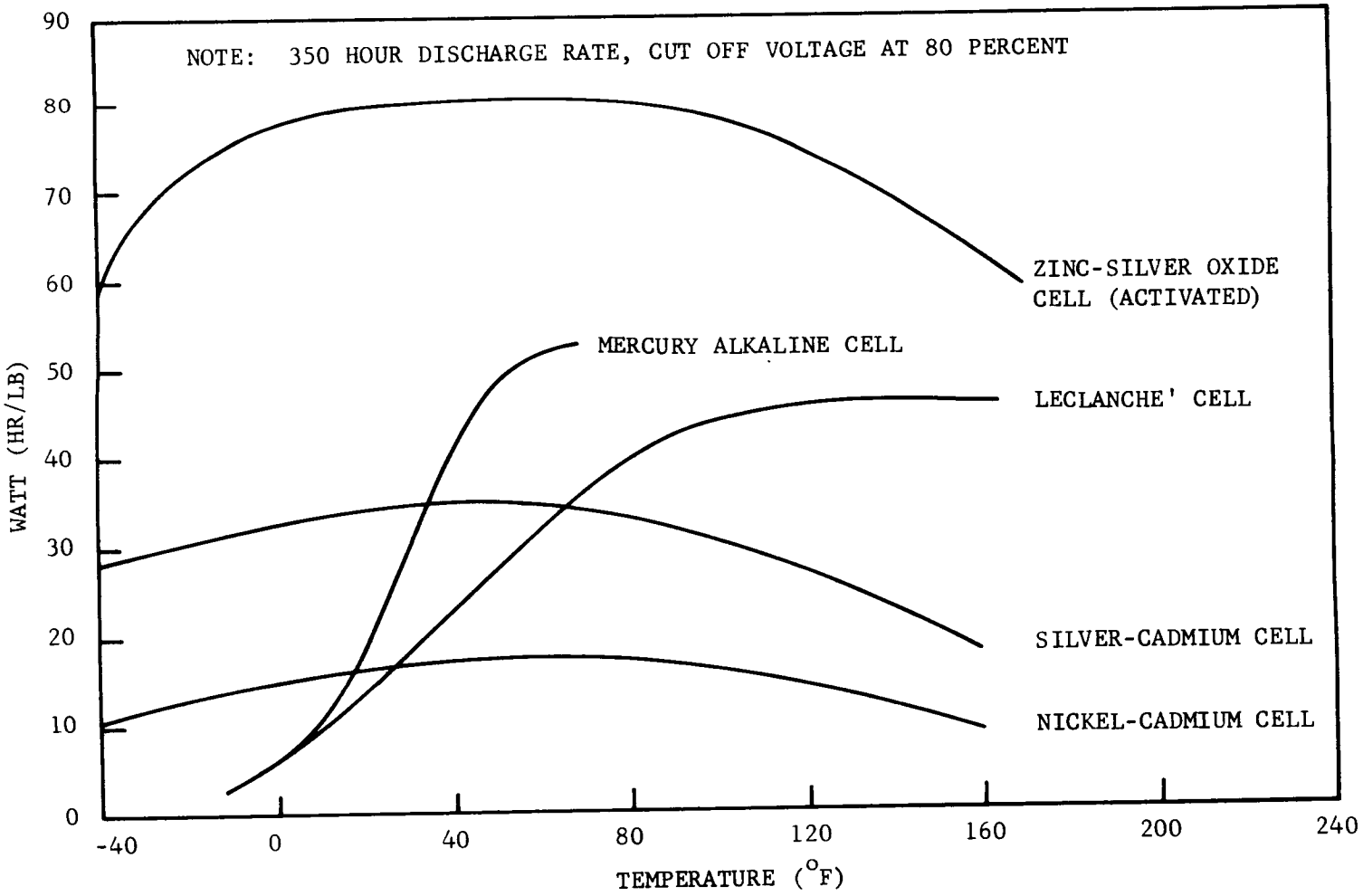

FIGURE 110. MAXIMUM BATTERY CAPACITY VS. TEMPERATURE

rise to an acceptable level. When held to acceptable limits, the temperature rise would affect the battery performance advantageously by raising it to a more efficient operating point. Conversely, if the thermal control were effective in limiting the low temperature while the transmitter is not operated, the silver-zinc battery should operate quite efficiently throughout its Martian life.

Summarizing the temperature effects which must be expected for the MFC mission from a battery point of view, the following facts are revealed.

(1) Capsule sterilization temperature of 145°C for 108 hours must be endured.

(2) Transit temperature of 0° to 20°C for 7 to 9 months must be sustained without appreciably effecting the ultimate battery performance.

(3) Capsule battery temperature on Mars will have to be maintained by thermal control.

(4) Transmitter dissipation will raise the capsule temperature sufficiently to allow good discharge efficiency.

d. Charge Retention. The MFC program requires a battery that could be supplied by the manufacturer in the charged state, survive sterilization, hold its charge for 6 to 9 months, and then perform as required. To meet these requirements simultaneously is beyond the current state of the art. Some ways, however, to achieve satisfactory battery power do exist.

The first possibility is to utilize a battery which is assembled in the uncharged state and filled with electrolyte by the manufacturer. This technique was used in the Lunar hard-landing capsule program. The advantages of this lie in the fact that a more compact and rugged battery can be produced if the battery assembly is done entirely by the manufacturer. This eliminates the usual filling ports. The battery must be kept at a low temperature to prevent deterioration during pre-use storage. The uncharged state is best for storage because the battery chemicals are less active in this state. Also, as was previously stated, sterilization should be done in the uncharged state, after which it would be desirable to charge and test the battery's ability to perform in the course of preflight checkout.

Assuming that the battery has demonstrated satisfactory performance and has been launched, we now are faced with the problem of supplying a fully charged battery at the end of a 6 to 9 month transit time. The prospects of the charge lasting this long are very poor as indicated by the shelf life plots in Figure 111 . These plots indicate that at best we could

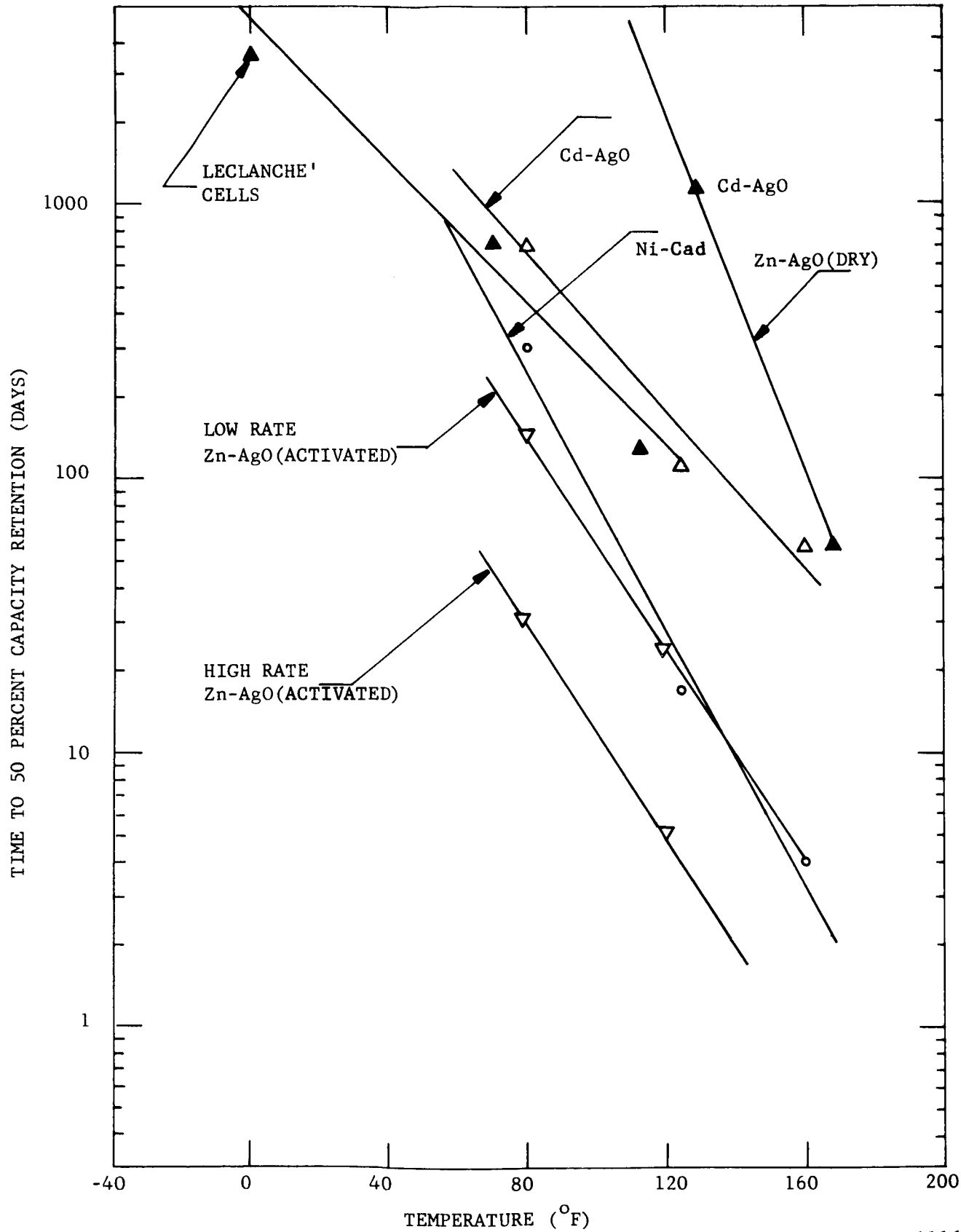

R11163

FIGURE 111. BATTERY SHELF LIFE (APPROXIMATE)

only expect a marginal survival of the battery charge. The main factor in wet battery shelf life is the loss of capacity due to self-discharge.

In addition to the loss of charge through self-discharge, secondary effects such as electrode polarization take place which temporarily reduce the battery's ability to perform. Characteristically polarization of charged batteries stored for several months results in the loss of as much as fifty percent of the battery capacity. It is often possible to restore this loss by passing the battery through several charge-discharge cycles. This loss of charge results from the decomposition of the silver peroxide into silver monoxide. Following the peroxide state, which reduces to monoxide in one or two months depending on temperature, the oxide state reduces to metallic silver which has a tendency to set up an ion barrier on the surface of the active material. In addition to the lost electrical energy that this reduction represents, it also severely limits the accessibility of the remaining charge and recharge capacity due to the ion barrier on the cathode. Remedy of this situation is by means of high rate discharge and charge cycles to restore the metallic silver to its original distribution and performance. In silver-zinc batteries with limited cycle life this is a radical measure not recommended for a highly reliable system. To prevent this deterioration of cell capacity it is necessary to discharge the cell and recharge it at two to three month intervals.

Therefore, long charged stands are undesirable because the charge dissipates through self-discharge and also the battery loses capacity because of its tendency to become permanently polarized. A charged silver-zinc secondary or similar battery will require some cycling to maintain battery performance at an acceptable level at the end of a 6 to 9 month transit.

A second approach to solving the transit and sterilization survival would be to use a reserve type battery which is fabricated in the dry charged state and activated remotely by adding the electrolyte immediately before use. The storage life of the reserve battery is excellent. However, sterilization causes oxygen to evolve from AgO electrodes and oxidize the zinc electrode, (Reference 13), thus losing about 50% of its capacity. This loss combined with the weight penalty of the electrolyte storage and activation mechanism tends to reduce the battery energy density to relatively low value. This potential low energy density coupled with undesirable mechanical complications with respect to shock tend to make this battery in its present state of development a poor candidate for MFC. However, the Missile Battery Division of ESB is investigating the possibility of using Ag_2O as cathode material in a reserve battery. This would eliminate cathode reduction because Ag_2O is stable below 300°C.

e. Nickel-Cadmium Batteries. Nickel-cadmium batteries have been used extensively in space applications especially as secondary batteries for satellites. Nickel-cadmium is outstanding for its recharge capabilities, typically greater than 1000 cycles. In its current state of development it

has good reliability, inherent resistance to impact shock and reasonable energy density.

In the MFC program where the capsule weight is a very critical factor, the nickel-cadmium battery is not an outstanding choice because of its modest energy density. The capsule operational procedures do not require extensive recharge capability; consequently, nickel-cadmium's recharge capability it not of a major significance. Battery manufacturers do claim that it is possible to make nickel-cadmium batteries that are sterilizable. Unfortunately, this has not been thoroughly established and even if it were true the energy density would probably be too low to be very useful.

f. Silver-Zinc Battery. Probably the most important in space applications is the silver-zinc battery. It has the highest energy density of all practical batteries; in fact, under favorable conditions it has demonstrated usable energy densities of 100 watt-hours per pound. It can be designed to have substantial recharge capability while still retaining good energy density thus making it possible to check its performance prior to launch. Because of the silver oxide cathode which reduces to silver during discharge, it has excellent high rate discharge characteristics. Its construction, like most alkaline space batteries is inherently impact shock resistant. Hermetic sealing of silver-zinc batteries is relatively easy to accomplish because evolution of oxygen does not occur until the battery is fully charged. (Reference 10). Also, because oxygen does not disassociate during charge, no loss of charging energy occurs during the battery charge period and it is relatively easy to fully charge.

The main disadvantage of a silver zinc cell is that the charged reaction products are soluble in the electrolyte and the cell requires an ionic membrane separator to prevent interaction of the electrode materials. This membrane which is generally a cellulose material is attacked chemically by the electrolyte and eventually is penetrated by the electrode materials at which time the battery deteriorates rapidly. This effect is quite well understood and batteries can be designed within limits with separator lives as required by specific application.

Figure 112 is the operating characteristic curve of a silver-zinc cell which was built and tested by Astropower. While not conclusive, this curve is evidence that silver-zinc batteries can not only survive the sterilization temperature but can operate at 130^{o}C as well. Additional performance curves in Reference 16 also confirm the repetitive high-temperature capabilities of silver-zinc cells with inorganic separators. Undoubtedly, there are problems of sealing, case materials, electrode fabrication, etc., but clearly a high-temperature silver-zinc battery is feasible.

g. Silver-Cadmium Battery. A battery that is very similar to the nickel-cadmium battery is the silver-cadmium battery, but has a lower charge cycle capability and a higher energy density. It is not as widely

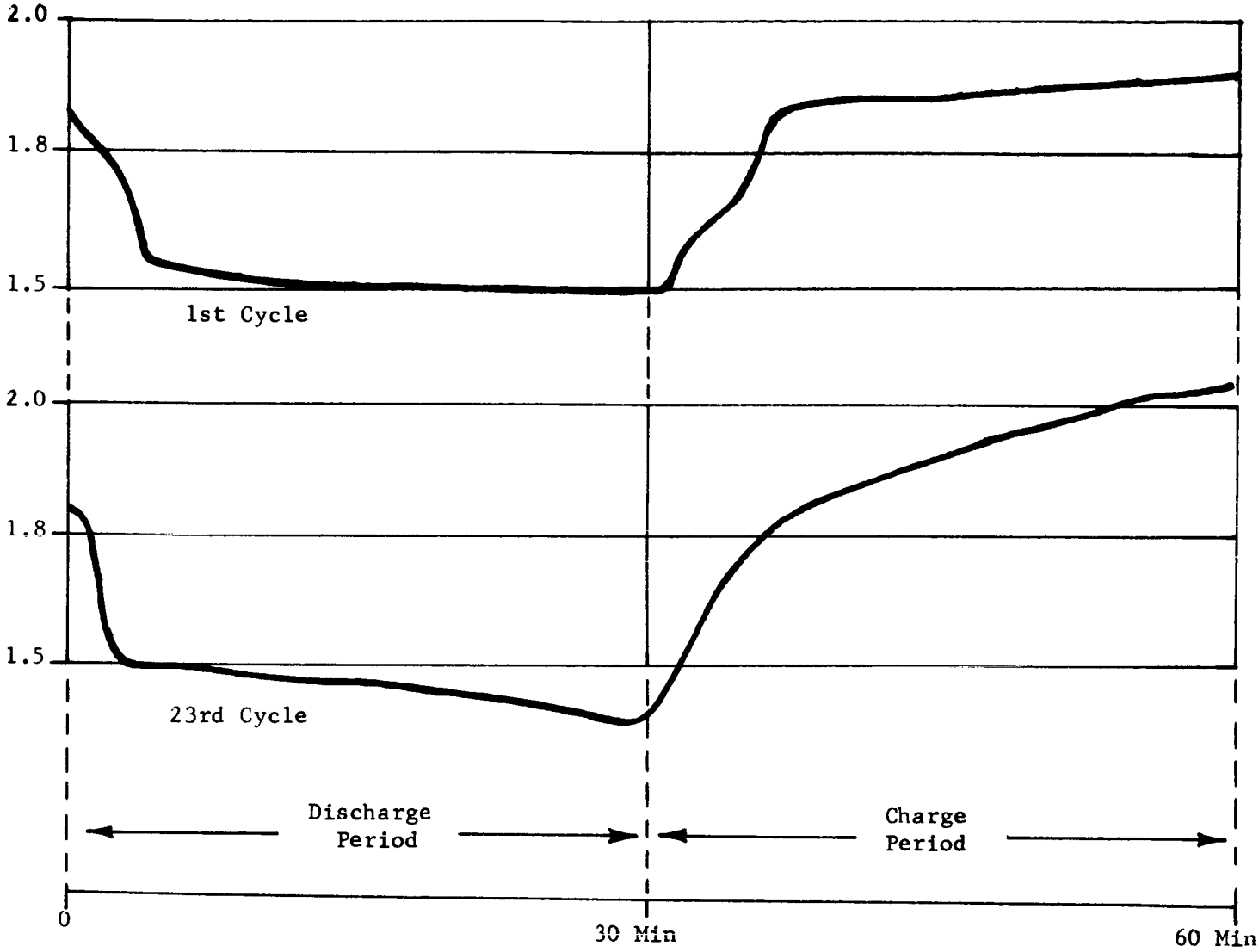

Astro-Power Silver Zinc Battery No. 127-052
30% depth of discharge
30 Minute discharge @ 10 ma/cm^2
30 Minute charge @ 15 ma/cm^2
Temperature = 135^{o}C

FIGURE 112. CYCLE TEST OF SILVER-ZINC BATTERY AT 135^{o}C

utilized because normally a silver-zinc battery is selected if a high energy density is desired and nickel-cadmium is selected if extensive charge cycles are required. However, for the special case where both requirements exist simultaneously, it is a logical choice.

For the MFC program the silver-cadmium battery has little to offer it since its energy density is only one half of the more energetic silver-zinc.

h. Mercury Battery. Because energy density is a prime consideration, the mercury battery must be considered. In addition to its 50 watt-hour per pound energy density, it also possesses a charge shelf life of two years, making it attractive for surviving the capsule cruise period of 6 to 9 months. Its compact cell construction also makes it inherently shock resistant and it had successfully been used in high shock application. Major disadvantages of themercury cell are that it loses its capacity at low temperatures and like most dry cells it has a relatively low discharge rate. It also has no resistance to sterilization temperatures and is not likely to be improved in this respect. A mercury battery is a primary battery which can be manufactured only in the charged state; therefore, its active life begins immediately upon manufacture.

i. Thermal Batteries. Thermal batteries are a class of chemical batteries which are composed of primary cells made with alkali salt electrolyte. At normal temperature these batteries are completely inert because the electrolyte is a solid. However, at temperatures above 350°C the electrolyte becomes molten and the cell ingredients enter into an energetic electromechanical reaction. Thermal batteries for short activation periods have been used extensively with high reliability in missile and fuzing applications. Current state-of-the-art techniques are capable of producing batteries with energy densities of approximately 25 watt-hours per pound for discharge lives of 3 to 5 minutes.

Until recently the use of thermal batteries was limited to the application requiring an active life of only a few minutes; however, during the past six months substantial advances have been made in the state of the art, and during a recent test at Aeronutronic a thermal battery cell operated continuously for 20 hours. It is anticipated that within the near future a cell of similar design will be capable of continuously operating for several days.

Thermal batteries have great potential for the MFC because of the following reasons:

(1) Ability to survive heat sterilization

(2) High energy density

(3) Long Shelf life

(4) High shock resistance

Since the thermal battery operates at temperatures in excess of 350°C, the requirement for terminal heat sterilization in no way affects its operation. In fact, one method of testing a thermal battery for internal shorting is to heat it to its operation temperature and measure its open circuit voltage. Thus, by its inherent nature the thermal battery lends itself to heat sterilization.

Thermal batteries are capable of energy densities in excess of 100 watt-hours per pound. The short life (3-5 minutes) batteries presently available do not exhibit these densities primarily because of the inefficiencies associated with rapid discharge rates; however, when the life is extended to several days energy densities of 60-70 watt-hours per pound can be anticipated. This estimate is based upon a Na - CuCl cell which has an ideal (active element) energy density in excess of 600 watt-hours per pound. With additional development a 50 percent increase in energy densities could be possible through use of a $Na-CuCl_2$ cell.

At temperatures below 150°C the thermal battery is in an inert state and consequently below this temperature it is capable of maintaining its energy potential for indefinite periods of time. This natural capability lends itself nicely to the transient requirements of a Mars mission of 6 to 8 months storage life.

At temperatures below its operating temperature the thermal battery is solid, compact and shock resistant. By utilizing careful packaging techniques the battery should be capable of being designed to withstand the 2500-3000 g impact decelerations expected during the MFC landing.

The thermal battery is a primary battery and, hence, energy used during pre-flight checkout could not be replaced. This would place an extreme reliability requirement on the manufacturing process. A second disadvantage is the thermal problems involved in controlling the capsule temperature due to the heat transfer from the battery.

Section 6.4 of the Appendix gives a design summary of the thermal battery for the Mars Facsimile Capsule. This battery would be capable of furnishing electrical power for a three-day period after landing. It is concluded that such a battery is feasible and will yield a performance of 60 to 70 watt-hours per pound.

5.8.3 FUEL CELLS

The fuel cell, a special application of the principle of electromechanical reactions to the production of electrical energy, has much potential for space use. A fuel cell is an electromechanical device in which the chemical energy of the fuel and oxident is converted directly to electrical energy. It differs from a conventional battery in that the reactants are not stored in the electrodes but rather are supplied from external reservoirs.

This permits the fuel cell to operate as long as the fuel can be supplied to it, thus extending its usefulness greatly beyond that of a conventional battery.

A well developed example of such a device is the fuel cell system developed for the Gemini manned satellite. (Reference 14). The active elements in the Gemini fuel cell are hydrogen and oxygen. The hydrogen assumes the role of the zinc in the anode of the silver zinc battery and the oxygen takes the place of the cathode. A schematic cross section of this fuel cell is shown in Figure 113 . Since the combination of hydrogen and oxygen produces water, the electrolyte that normally is used in batteries would be rapidly diluted; therefore, an electrolyte that is water insoluble is used in the Gemini fuel cell. The electrolyte is actually combined with the separator membrane to form an ion-exchange membrane. This membrane is a sulfonated styrene polymer ten mils thick.

The reactants are introduced to the ionic membrane through porous catalytic electrodes which support ionization. The hydrogen ions permeate the membrane and react with the oxygen at the cathode to produce water and an excess of electrons which release energy in the external electrical circuit.

Fuel cells, like batteries, have high theoretical efficiencies with actual operating efficiencies falling in the 50% to 70% range. Such a hydrogen oxygen fuel cell has a specific fuel consumption of approximately one pound per kilowatt-hour. Energy density of satellite fuel cells approach 600 watt-hours per pound for cryogenic fuel storage and 100 watt-hours per pound for high pressure (gaseous) storage.

An estimate by General Electric indicated that a fuel cell could be developed that could withstand the MFC environment. The electrical power density would be approximately 20 watts per pound, or 12.5 pounds for a 250 watt fuel cell. This estimate is for the fuel cell only and would require the necessary fuel gas control system, fuel storage and coolant system. However, even after these components were added to complete the fuel cell assembly, the overall energy density is as good as a silver-zinc battery but without the sterilization problems. General Electric engineers estimate that because the fuel cell electrolyte is a solid and the cell can be filled with an inert gas, it is capable of surviving sterilization temperatures. The only drawback to the application of the fuel cell to the MFC program would be the difficulties which might be experienced in developing a gas storage and control system which could survive the impact shock. However, it is not considered to be beyond the state of the art.

5.8.4 RADIOISOTOPE BATTERIES

Heat given off during the decay of radioisotopes can be used by a thermoelectric or thermionic converter to generate electricity. Several models have been developed for space application through the Atomic Energy

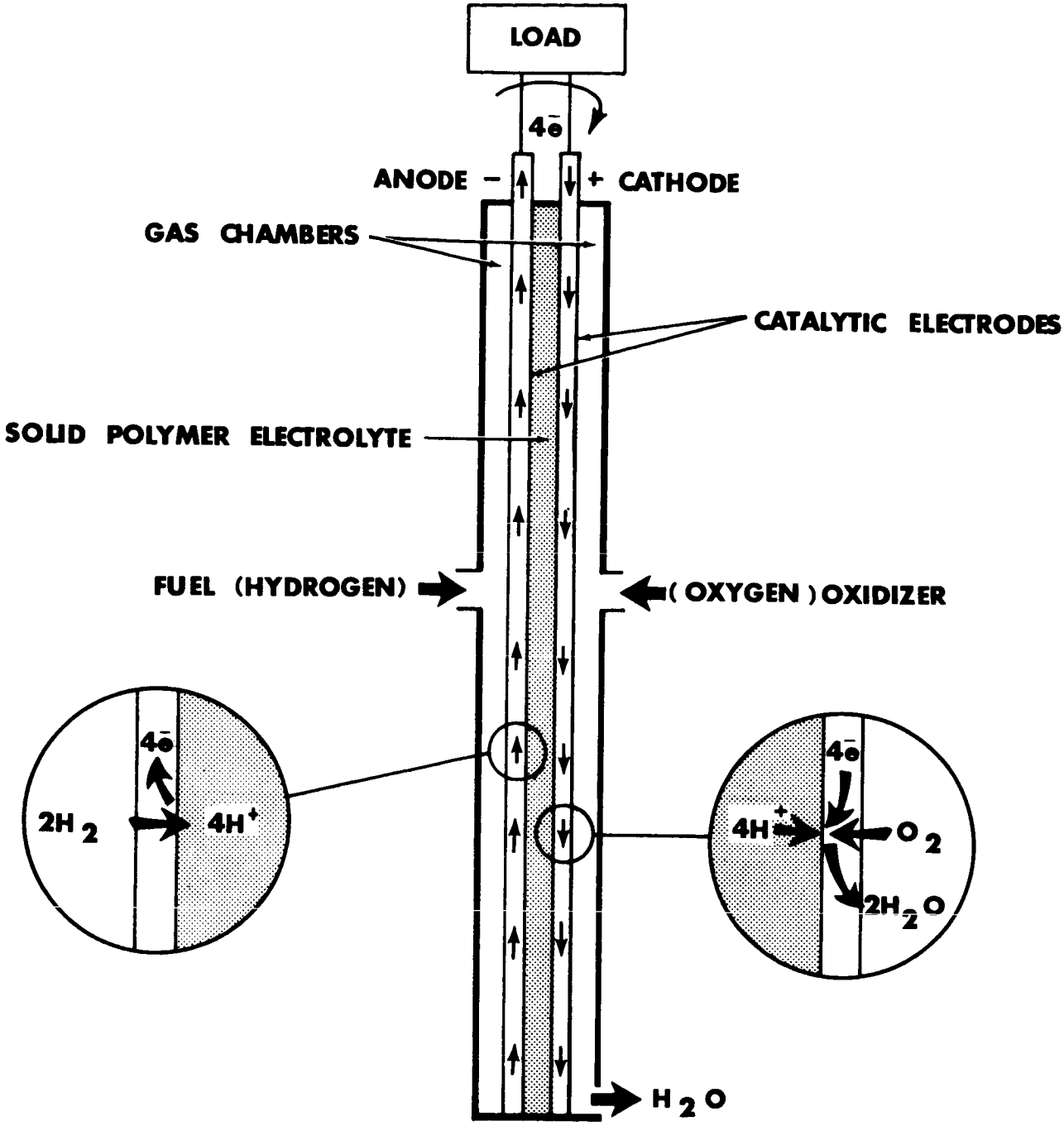

FIGURE 113. SOLID POLYMER ELECTROLYTE FUEL CELL

Commission's program for development of Systems for Nuclear Auxiliary Power (SNAP). Radioisotope models are designated SNAP-1, 3, 5, etc., and reactor models are designated by the even numbers. Typical SNAP batteries are shown in Table 5.8-IV.

Radioisotope batteries are suitable for long life, high energy density sources. Successfully flight tested models have high energy densities of many kilowatt hours per pound, but low power densities of approximately one watt per pound. Batteries utilizing alpha emitters create essentially no radiation hazard because alpha particles normally do not have sufficient energy to penetrate even the capsule walls. Currently, lead-telluride is the only thermocouple material that has been developed to an operational state. Thermionic generators for radioisotope have not reached flight test status to date.

Disadvantages of the radioisotope battery for MFC program result from the high thermal dissipation (95% currently) and the fragility of the lead-telluride thermocouples. Until new or radically improved thermocouples are perfected radioisotope batteries are not a very likely candidate for MFC power source because of the problem of transmitting the heat generated by the radioisotope through the impact limiter during the transit to Mars.

5.8.5 SOLAR CELLS

Solar cells have been widely used as power sources for space experiments. Their ability to convert sunlight to electrical energy is their main recommendation for space applications. Typical solar cell applications performance characteristics are listed in Table 5.8-V.

To be most effective, solar cells must be oriented normal to the ambient solar radiation and even so can only produce 10 watts per square foot in space near Earth. The solar flux at Mars is approximately one-fourth that of Earth with proportional solar cell performance degradation. Some increase in cell efficiency due to the low Martian temperatures would tend to offset the loss of radiation. Additional reduction of performance would also occur as a result of the interference caused by the Martian atmosphere and surface dust.

The main obstacle to applying solar cells to the MFC program arise from the difficulty of deploying and orienting 100 square feet or more of solar cells from the capsule after impact. This difficulty is aggravated by the fact that presently used solar cells are fragile devices, and would require extensive mechanical packaging provisions to insure survival of impact. For these reasons solar cells have not been given further consideration for the MFC program.

TABLE 5.8-IV SPACE VEHICLE NUCLEAR POWER UNITS

DESIGNATION & RESPONSIBLE AGENCY	TYPE	POWER OUTPUT	WEIGHT	AVAILABILITY	REMARKS
SNAP-1A (AEC)	Radioisotope (Ce-144) dynamic	125 to 250 watts	175 lb (at 125 watts)	Current	Radioactive hazards make space use very difficult, if not unlikely
SNAP-2 (AEC)	Reactor-dynamic (Rankine)	3 kw	7001b. (unshielded)	1966	Mercury working fluid
SNAP-3 (AEC)	Radioisotope thermo-electric Pu-238 & PbTe	2.7 watts	5 lb.	Current	Transit 4A 4B
SNAP-7	Strontium (90) titanate fuel $SrTiO_3$	5 to 6 watts		Current	Not space used; used by Navy and Weather Bureau
SNAP-8 (AEC-NASA)	Reactor-dynamic (Rankine)	30 kw	3000 lb. (30 kw) unshielded	1967	Mercury working fluid
SNAP-9A (AEC)	Radioisotope Pu-238 Thermo-electric	25 watts	27 lbs.	1964	
SNAP-11 (AEC)	Isotope-thermo-electric CM-242,PbTe	21 to 25 watts	30 lbs.	1965	
SNAP-10A (AEC)	Reactor-thermo-electric	500 watts	750 lb. (unshielded) 1113 lb. (flight test)	1964	Uses SNAP-2 reactor with germanium-silicide thermo-elements
SNAP-13 (AEC)	Thermionic CM-242	12.5 watts	4 lbs.	1964	Demonstration
SNAP 50/SPUR (AEC-AF)	Reactor-dynamic (Rankine)	100 to 1000 kw	3000-6000 lb. (unshielded)	1973	Potassium working fluid

TABLE 5.8-V

SOLAR CELLS ON SPACE VEHICLES

VEHICLE	STABILITY	CELL MOUNTING	WEIGHT LB.			WATTS AT PERPENDICULAR INCIDENCE	WATTS/LB SYSTEM	ARRAY AREA FT^2	TOTAL WATTS/ FT^2	RATIO ARRAY WT.TO TOTAL WT.
			ARRAY	STORAGE	POWER SYSTEM					
AOA	Non-oriented	Paddles	222	177	399	772	1.94	187	4.14	55
OSO(S-16)	Oriented	Panel	5.2	30.7	59.9	31	0.86	4	7.7	14
EGO	Oriented	Panels	127	201	201	560	2.8	78	7.2	63.4
Relay	Non-oriented	Body	25.8		53.8	35	0.65	17.6	2.0	48
Nimbus B	Oriented	Panels	64		177	410	2.3	43	9.5	36
Tiros (Alpha = 45^o)	Non-oriented	Body	24.5^o		64.5	51	0.79	17.7	2.9	38
Tiros (Alpha = 90^o)	Non-oriented	Body	24.5^o		64.5	25	0.39	17.7	1.4	38
UK-1	Non-oriented	Paddles	8.8		22.8	11.7	0.52	11.0	1.1	38

5.8.6 CONCLUSION

Recently developed sterilizable silver-zinc batteries are ostensibly capable of providing electrical energy required by the MFC mission. As indicated by one manufacturer (Astropower Division, Douglas Aircraft) they are capable of performance comparable to non-sterilizable batteries.

The actual energy density that could be expected for MFC can be arrived at somewhat intuitively. The anticipated discharge time for the battery will be at least ten hours which is long enough to allow good battery efficiency. The energy density for this rate is 80 watt-hours per pound. (Reference 8). Weight penalty will be imposed by the impact requirement which reduces the energy density to approximately 60 watt-hours per pound. (Reference 3). Temperature should not affect the end of life battery performance since an optimum operating temperature exists as the final demands are made upon the battery. Assuming that the Astropower separator is applicable to the capsule environment and that 10% performance penalty will be experienced in its utilization, and another 15% penalty is encountered because of transit life, we can expect an energy density of around 40 watt-hours per pound. The energy density penalties are summarized below:

Penalty	Percent Loss
Impact Resistance	25%
Sterilizable Separator	10%
Transit Life Loss	15%
Delivered Energy Density	E_d is related to optimum energy E_{op} as follows:

$$E_d = (\%\ \text{losses})\ E_{op} = (25 + 10 + 15)\ 80 = 40\ \text{W-H/lb.}$$

Other energy sources such as solar cells, radioisotope batteries and fuel cells have been considered and found to be unsatisfactory for the MFC. Solar cells have low power density and must be carefully oriented toward solar radiation. Deployment and orientation of sufficient cells from the capsule to provide the necessary power would be very difficult. Radioisotope batteries cannot be used because the large amount of waste heat that must be conducted away from the capsule during transit. Fuel cells are an attractive source of energy but because of their complexity and sensitivity to operating temperature they also are not considered satisfactory in their present state of development.

SELECTED REFERENCES

1. Morehouse, D. K., Glicksman, R., and Lozier, G. S., "Batteries", Proc. of IRE, August 1958, Vol. 46, pp. 1462 - 1483.

2. Francis, Howard T., "Space Batteries", NASA Technology Handbook,' NASA-SP-5004, U. S. Government Printing Office, 1964, Washington,D.C.

3. "Lunar Rough Landing Capsule Development Program, Final Technical Report", Pub. No. U-2007, Aeronutronic Division of Philco Corp., Feb. 20, 1963, Newport Beach, California.

4. "Fuel Cells for Spacecraft", January 1964, Direct Energy Conversion Operation of General Electric Co., Lynn, Massachusetts.

5. Rex A. Barner, "Space Vehicle Power Source Handbook", Publication SSD-TDR-64-8, Aerospace Corporation, May 21, 1964, Los Angeles, California, STAR No. N64-22556.

6. Padwo, Saul, "The Battery Field, A State-of-the-Art Survey", Electrical Design News, Janury 1963 Issue.

7. "Energy Data Book", Yardney Electric Corporation, New York, N.Y., 1962.

8. Menetrey, W. R., "Chemical Systems", Energy Conversion Systems Reference Handbook, Vol. VI, WADD, Tech. Report No. 60-699, Wright-Patterson Air Force Base, Ohio. September 1960.

9. Charkey, Allen, Dalin, G. A., "Research and Development Studies of the Silver-Cadmium Couple for Space Applications", Third Quarter Progress Report, 31 March 1964. NASA STAR No. N64-24846, Goddard Space Flight Center, Greenbelt, Maryland.

10. Howard, Paul L. and Solomon, Frank, "Sealed Cadmium Silver Oxide Batteries", 14th Annual Power Sources Conference, 1960, Lib. Ref. No. QC603-U5.

11. Fleischer, A., "Sealed Nickel-Cadmium Batteries", Proceedings, 15th Annual Power Sources Conference 1961.

12. A. A. Uchiyama, "Battery Sterilization Studies", Space Program Summaries, Vol. IV, October 31, 1963, JPL, Pasadena, California.

13. Chrietzberg, A. M., Company Correspondence, Electric Storage Battery Co., December 17, 1964, Raleigh, North Carolina.

14. "Fuel Cells for Spacecraft", General Electric Company, Direct Energy Conversion Operation, January 1965, Lynn, Massachusetts.

15. R. W. Schult, W. T. Stafford, "Electromechanical Energy Sources", Electro-Technology, July 1961.

16. C. Berger, "Representative Cycle Test Data on Astropower Laboratory Silver-Zinc and Silver-Cadmium Test Cells", Supplement to SM-48441, Douglas Aircraft Company, Inc.

17. J. C. Duddy and J. F. Arms, "Sealed Zinc-Silver Oxide Secondary Batteries", 14th Annual Power Sources Conference, 1960.

5.9 THERMAL CONTROL

5.9.1 INTRODUCTION

Thermal control subsystems for the MFC are required to begin operation after a "high g" impact on the surface of Mars has been accomplished. The MFC has a balsa wood sphere impact limiter which is assumed to be removed from the inner payload sphere following impact. Figure 114 shows the MFC payload after equipment erection on Mars. The payload sphere is assumed to be supported on extension legs with Mars atmospheric gases being free to circulate over the entire sphere surface.

Thermal trade-off studies have been performed assuming Mars impact to be time zero; (i.e., Earth pre-launch, launch, 8-month space flight, and Martian re-entry heating analyses are not considered as part of this trade-off study). The MFC temperature is assumed to be controlled within acceptable limits at all times prior to Mars impact. It is assumed, however, that the MFC has been sterilized @ + 275°F temperature for a suitable period (on the order of 24 hours) prior to launch from Earth.

The following MFC dimensions and weights are considered as nominal departure points for trade-off study thermal analyses:

(1) Balsa sphere impact limiter diameter is on the order of 5-6 feet.

(2) Payload sphere diameter is on the order of 1.5 feet.

(3) Total weight of MFC just prior to impact (impact limiter plus payload) is approximately 300 to 600 pounds.

(4) Payload sphere weight is on the order of 100 pounds.

The use of radioisotope thermoelectric generator energy sources for the MFC is considered to be outside the scope of this trade-off study.

Table 5.9-I lists the nomenclature which is used throughout the thermal control section.

5.9.2 MARS ENVIRONMENTS

The Mars environments used for this study have been defined by JPL and are given in Section 6.1. The pertinent environments for thermal analyses are summarized below for convenience.

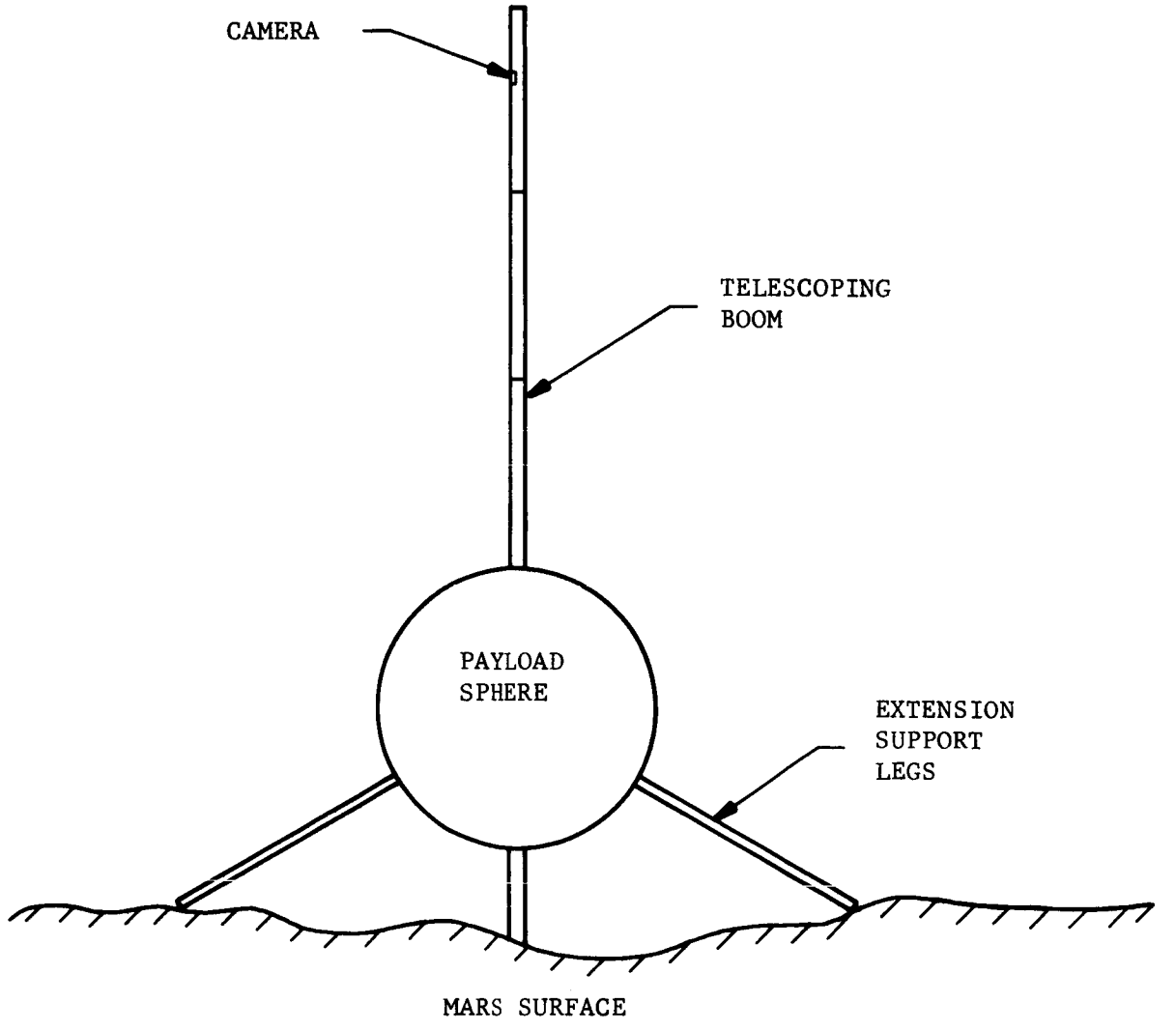

FIGURE 114. MFC PAYLOAD SKETCH

TABLE 5.9-I

NOMENCLATURE

A	Heat Transfer Area (ft^2)
c	Specific Heat (Btu/lb F)
D	Diameter (ft)
F	Radiation Geometry Factor (Dimensionless)
h_c	Convective Heat Transfer Coefficient (Btu/ft^2hr F)
h_r	Radiation Heat Transfer Coefficient (Btu/ft^2hr F)
k	Thermal Conductivity (Btu/ft^2hr F/ft)
ℓ	Thickness (insulation) or length (ft)
n	Number of MFC extension support legs
p	Power Dissipation (Watts)
Q	Heat Loss (Btu/hr)
Q'	Heat Gain (Btu/hr)
S_s	Solar Heat Flux at Mars Surface (Btu/ft^2hr)
t	Time (hr)
T	Temperature (^oR)
T'	Temperature (^oF)
U	Overall Heat Transfer Coefficient (Btu/ft^2H F)
W	Weight (lb)
α	Absorptivity (dimensionless)
α_s	Solar Absorptivity (dimensionless)
ϵ	Emissivity (dimensionless)
σ	Stefan-Boltzmann Constant = $.173 \times 10^{-8}$ $Btu/ft^2hr^oR^4$
τ	Duty Cycle Period (hr)
A	Ambient Mars Atmosphere
c	Cross-Section
eff	Effective
G	Ground Surface
i	Initial
P	Payload
S	Solar, Surface, Sphere

3-1

Atmospheric Temperature

Day:	-10 F (max.)	(6 ft. above ground)
	+100 F (max.)	(at ground surface)
Night:	-90 F	(0 + to 6 ft. above ground)

Ground Surface Temperature

Day:	+100 F (max.)
Night:	-100 F

Atmospheric Pressure

60 millibars	(max.)	(0.88 psia)
40 "	"	(0.59 psia)
20 "	(min.)	(0.30 psia)

Wind Velocity

$v < 197$ fps (always)
$v < 99$ fps (80% of the time)

Atmospheric Composition (By Weight)

Carbon Dioxide (CO_2)	7.5%
Nitrogen (N_2)	87.5%
Argon (A)	5.0%

Mars Period of Rotation

One revolution in 24.6 hours

Mars Solar Constants (Outside Atmosphere)

Min. Distance Between Sun-Mars	$\Longrightarrow$	S = 232 Btu/ft^{2}hr
Max. Distance Between Sun-Mars	$\Longrightarrow$	S = 159 Btu/ft^{2}hr
August 1969 Landing	$\Longrightarrow$	S = 227 Bth/ft^{2}hr
December 1971 Landing	$\Longrightarrow$	S = 212 Btu/ft^{2}hr

Average Atmospheric Solar Transmittance (deduced from JPL data)

Ø *	Transmittance
0^o	0.61
40^o	0.55
60^o	0.45

* Angle between Sun and Mars surface local vertical.

The solar heat flux at the surface of Mars is presented in Figure 115 as a function of Mars/Sun included angle. For 1969-71 missions, the solar heat flux during the day is approximately 100 to 140 Btu/ft^{2}hr for landings within $\pm$ 30% of the Mars equator. (Note, the inclination of the Mars equator to the orbital plane is 25°).

Various heat transfer parameters which are applicable for the Mars environments are presented in Figures 116 and 117. Mean convective heat transfer coefficients for a sphere are shown in Figure 116 as a function of wind velocity and ambient pressure. These convective coefficients were derived from References 1 and 2. Radiation heat transfer coefficients are presented in Figure 117. A mean background temperature of -50 F is assumed for these radiation coefficients, corresponding to a mean day/night temperature (-10 F day and -90 F night).

5.9.3 TRADE-OFF STUDY THERMAL ANALYSES

a. Trade-off Study Parameters. There are many independent variables which are important in a thermal trade-off study for MFC operation in a Martian environment. Some of the more important independent variables are listed below.

(1) Time (after impact)

(2) Ambient Environment

  (a) Atmosphere and Ground Temperature
  (b) Wind Velocity
  (c) Atmospheric Pressure

(3) Mars Distance from Sun

(4) Mars landing spot

  (a) Shade or sun during the day
  (b) General terrain geometry
  (c) Terrain absorptivity/emissivity radiation characteristics

(5) MFC payload allowable temperature range

(6) MFC initial temperature (at impact)

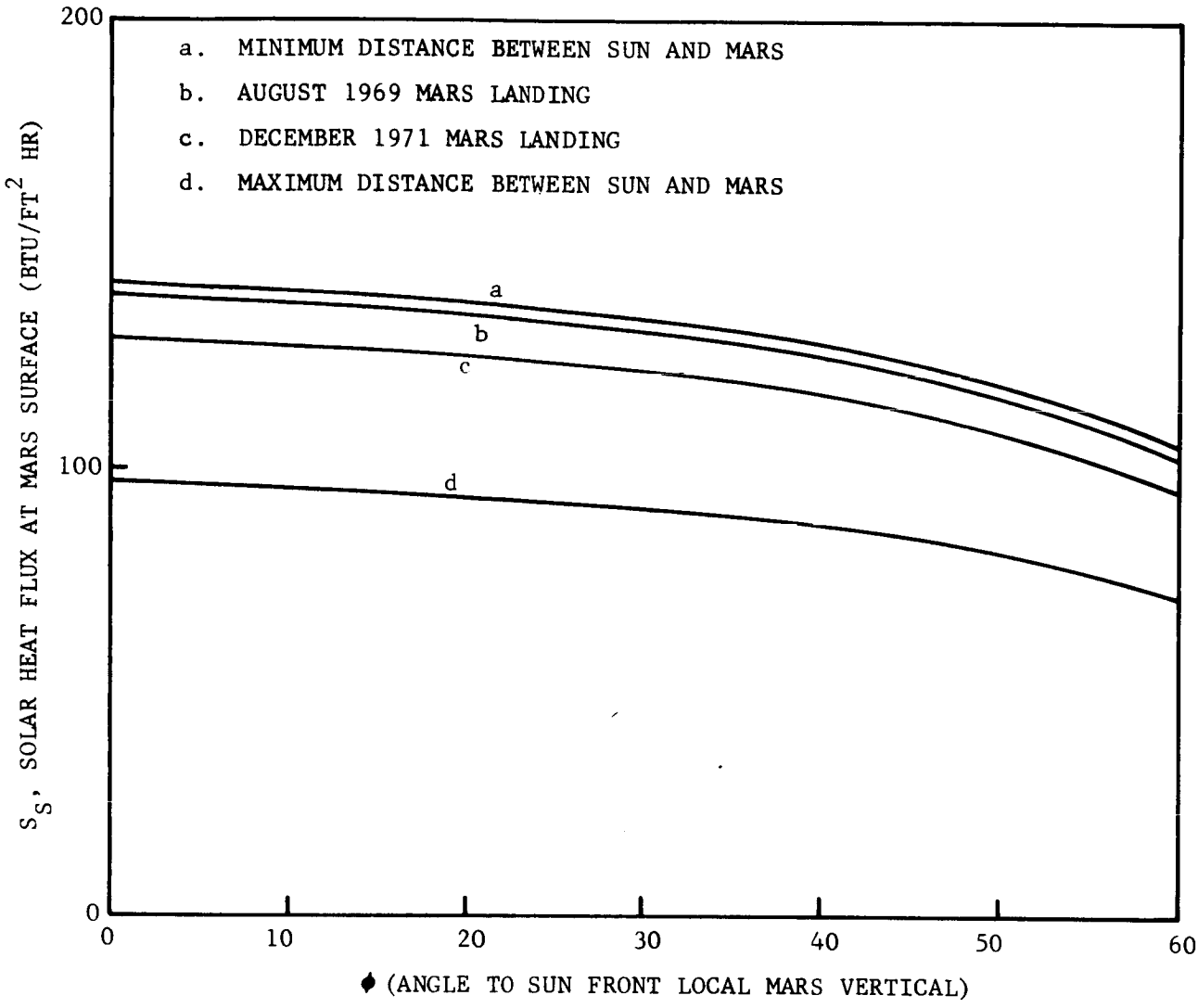

R11176

FIGURE 115. SOLAR HEAT FLUX AT MARS SURFACE

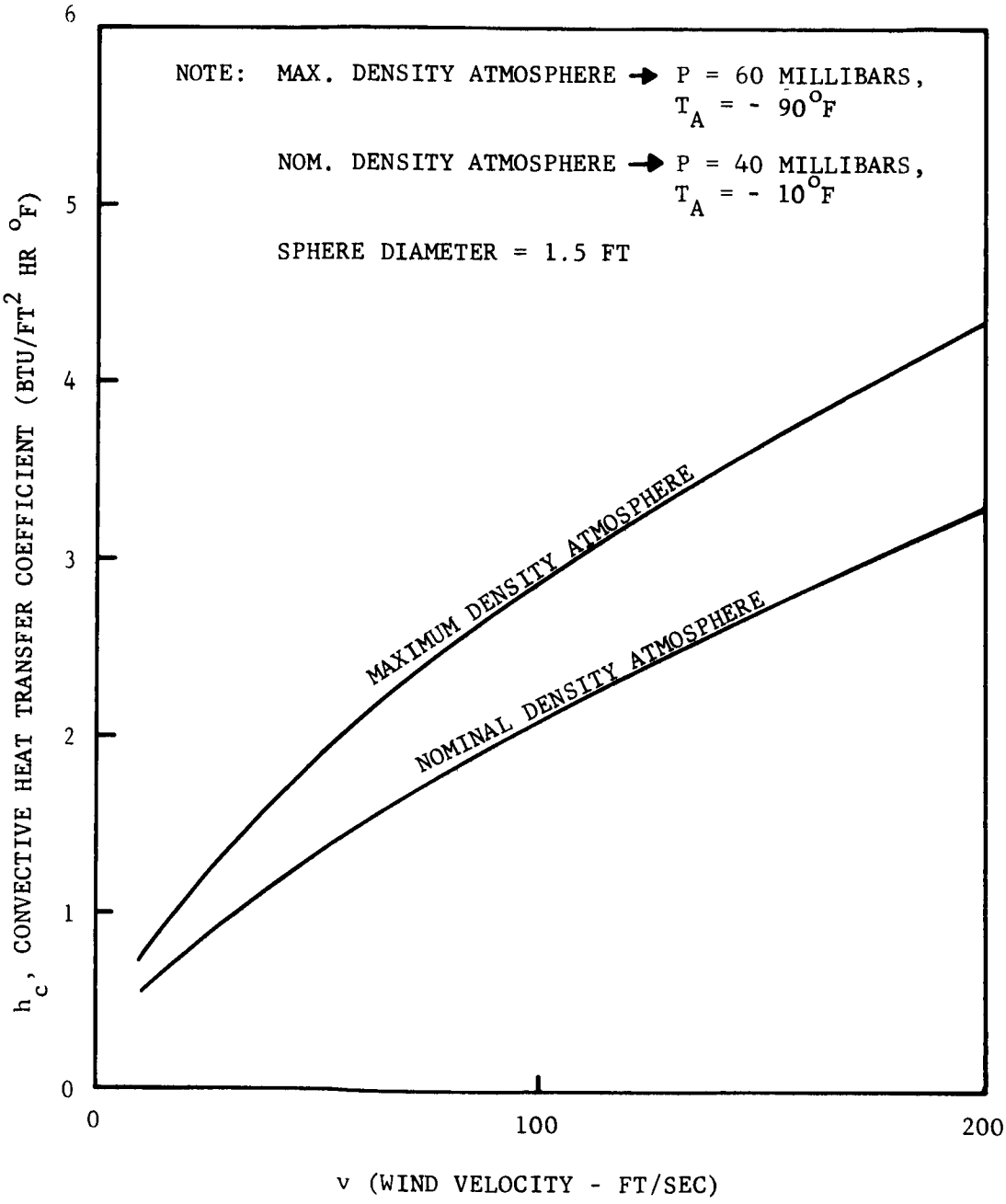

FIGURE 116. MEAN CONVECTIVE HEAT TRANSFER COEFFICIENT FOR A SPHERE VS. WIND VELOCITY R11222

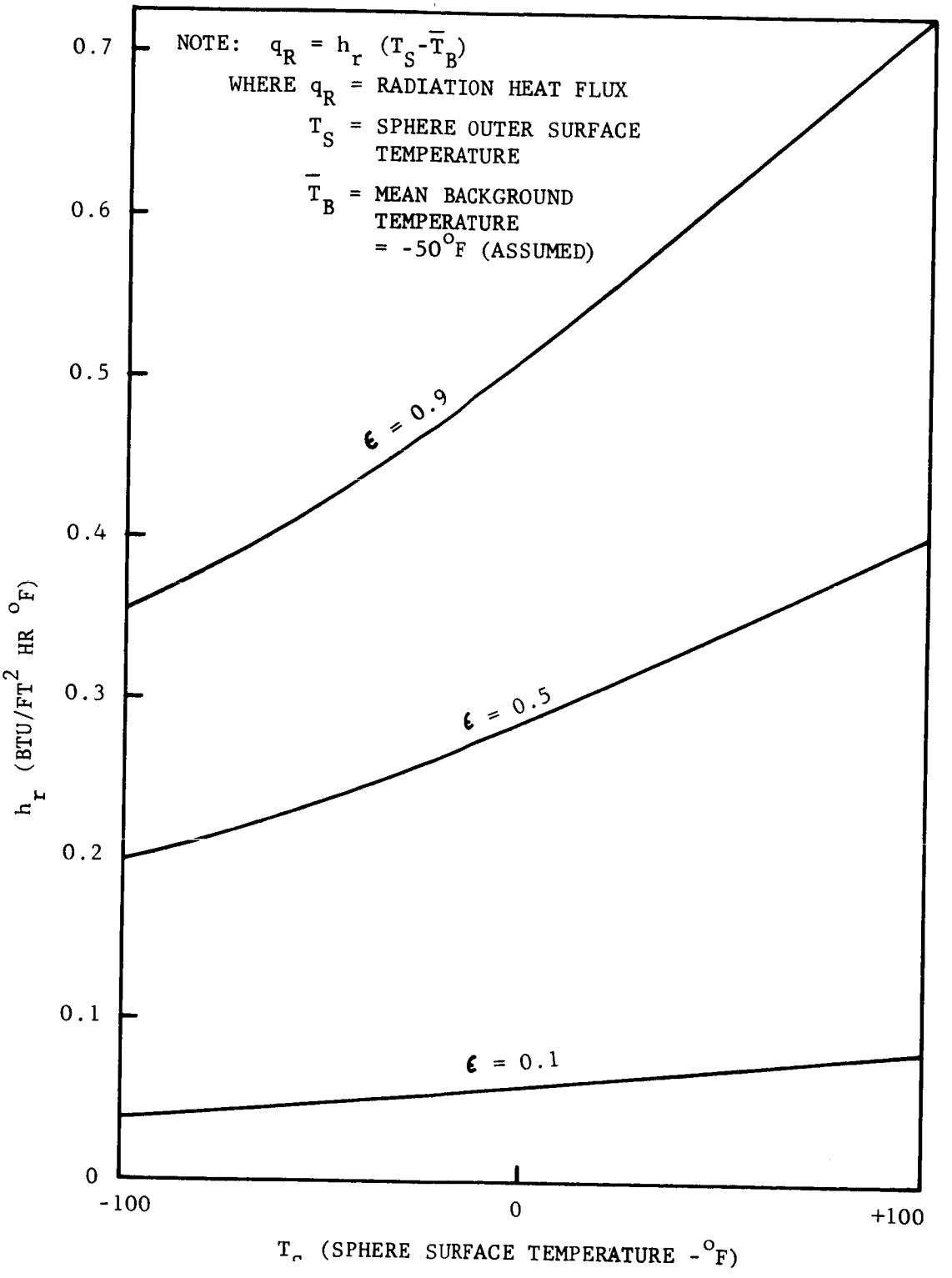

FIGURE 117. RADIATION HEAT TRANSFER COEFFICIENT

R11175

(7) MFC Payload sphere diameter

(8) MFC payload internal power dissipation and duty cycle

(9) MFC payload weight and material thermosphysical properties

(10) MFC payload insulation

The primary dependent variables are, of course, payload temperature and payload thermal control system size, weight, and type.

It is necessary to perform trade-off study thermal analyses for MFC subsystems and components which require temperature control within a more restrictive temperature range than is given by the Mars environmental range (from -100 F to approximately +120 F depending on surface coatings, power dissipation, etc.). Figure 114 shows the MFC major subsystems considered for thermal analysis. These are the payload sphere, camera, telescoping boom, antenna (not shown), and extension support legs. Of these major subsystems, only the payload sphere requires temperature control within a restrictive temperature range. These temperature restrictions are primarily established by power supply (battery) and electronic component operating temperature limits.

In this trade-off study no formal thermal analyses have been performed for the camera, telescoping boom, antenna, and extension support legs. It is relatively easy to thermally isolate these subsystems from the payload sphere by employing conventional thermal insulation. Thus, the payload sphere temperature need not be significantly affected by the level heat transfer from the payload to these subsystems.

The trade-off thermal analysis pertaining to an insulated payload sphere are presented in the following sections.

b. Insulation Thermal Conductivity. It is necessary for the payload sphere to employ thermal insulation just inside its outer wall, in order to protect the payload from the generally cold Martian ambient environment. Several candidate low conductivity insulation materials have been considered for this trade-off study. The thermal conductivity of these candidate materials are shown in Figure 118 as a function of ambient gas pressure. The data shown in Figure 118 is taken from References 3, 4, and 5 with a slight temperature correction being applied, as required, to place the insulation conductivities on a common basis. For the range of Mars atmospheric pressures given in Section 6.1, the conductivity of the candidate insulation materials ranged from 0.005 to 0.015 Btu/ft^{2}hr$^\circ$F/ft. Since these conductivities are of the same order of magnitude, a nominal insulation thermal conductivity of 0.010 Btu/ft^{2}hr$^\circ$F/ft

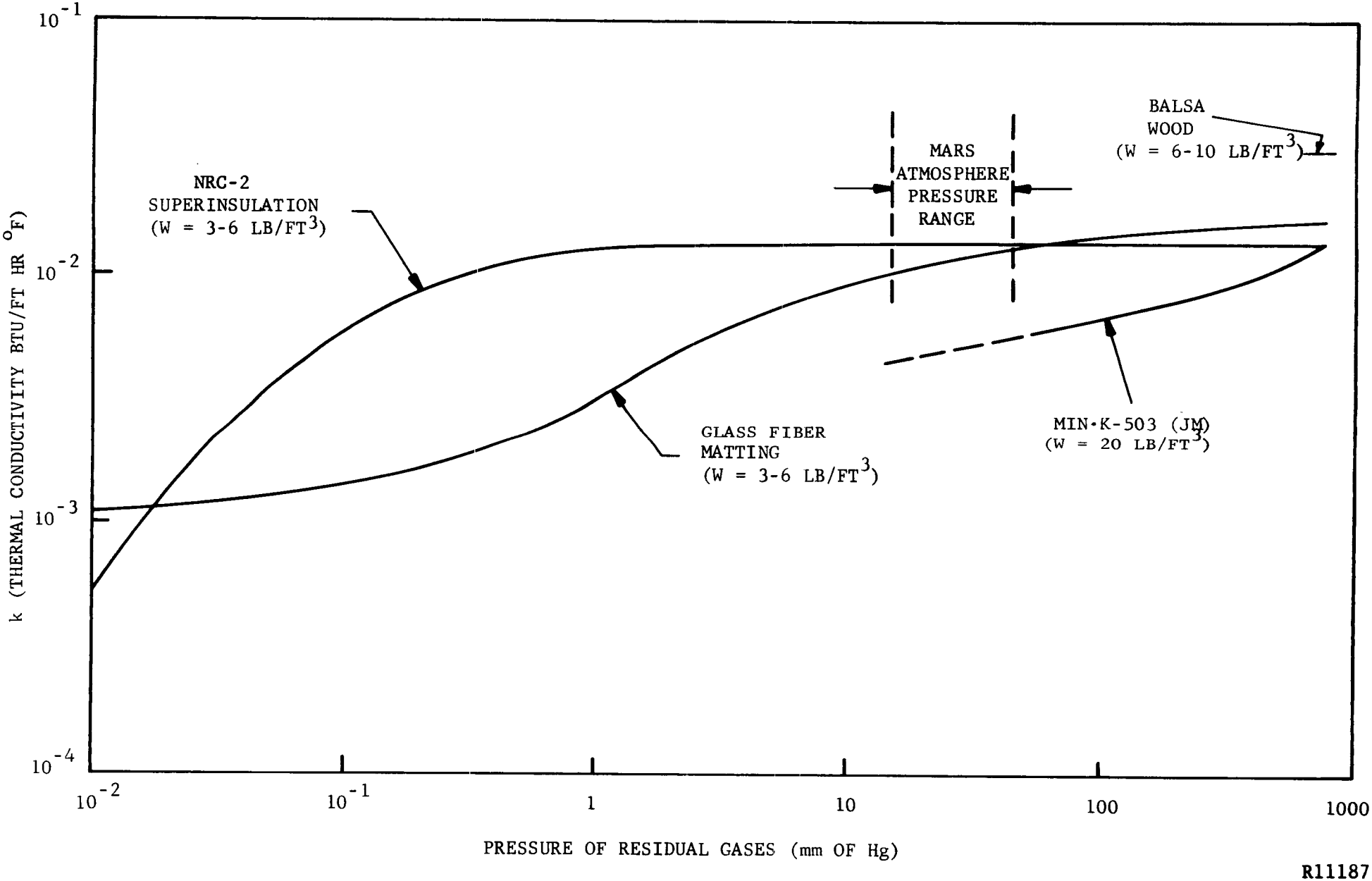

FIGURE 118. INSULATION THERMAL CONDUCTIVITY VS. PRESSURE (EXPERIMENTAL DATA).

has been selected for these trade-off study analyses. As seen from Figure 118 , the specific weight of the candidate insulation materials varies from 3 to 20 lb/ft^3.

c. Payload Sphere Outer Surface Temperature Analysis. In order to determine the net heat transfer from the payload sphere to the Mars surroundings, it is necessary to establish the sphere outer surface temperature for each ambient environment of interest. It is very difficult to perform a proper analysis of the MFC sphere surface temperature for a trade-off study, since the thermal analysis is complicated and requires a computer solution. However, if it is assumed that the sphere has an isothermal outer surface, a relatively simple solution is obtainable for trade-off study purposes. This simple analysis is presented below.

In order for thermal equilibrium to exist at the sphere outer surface, the net heat losses must equal the net heat gains. The heat losses and gains for the sphere are given by the following:

(1) Heat Losses from the Sphere

Radiation Heat Loss to Outer Space:

$$Q = \sigma \epsilon F T_s^4 \left(\pi D_s^2 \right)$$

where F = 1/2 is the geometry factor

Radiation Heat Loss to Mars Surface:

$$Q = \sigma \epsilon F T_s^4 \left(\pi D_s^2 \right)$$

shere F = 1/2 is the geometry factor

Convective Heat Loss to Mars Atmosphere:

$$Q = h_c \left(T_s - T_A \right) \left(\pi D_s^2 \right)$$

Conduction Heat Loss thru Extension Legs:

$$Q = \sum_{i=1}^{n} \frac{k_{eff} A_c}{\ell} \left(T_s - T_G \right)$$

(2) Heat Gains to the Sphere

Solar Heat Gain:

$$Q' = S_s \alpha_s F \left(\pi D_s^2 \right)$$

where F = 1/4 = $\frac{\text{sphere projected area}}{\text{sphere surface area}}$

Radiation Heat Gain from Mars Surface:

$$Q' = \sigma \alpha F T_G^4 \left(\pi D_s^2 \right)$$

where F = 1/2 is the geometry factor

Heat Gain from Internal Power Dissipation:

$$Q' = 3.41 \frac{1}{\tau} \int_0^{\tau} P(t)\, dt$$

where 3.41 = conversion factor from watts to Btu/hr

Equating the heat losses and heat gains, the following relation is obtained:

$$\sigma \epsilon T_s^4 \left(\pi D_s^2 \right) \left(\frac{1}{2} + \frac{1}{2} \right) + h_c \left(T_s - T_A \right) \left(\pi D_s^2 \right)$$

$$+ \sum_{i=1}^{n} \frac{k_{eff} A_c}{\ell} \left(T_s - T_G \right) = \left(\frac{1}{4} \right) S_s \alpha_s \left(\pi D_s^2 \right)$$

$$+ \left(\frac{1}{2} \right) \sigma \alpha T_G^4 \left(\pi D_s^2 \right) + 3.41 \frac{1}{\tau} \int_0^{\tau} P(t)\, dt$$

By combining and simplifying the above equations, the following equation is obtained:

$$\pi D_s^2 \left\{ \sigma \epsilon T_s^4 - \frac{1}{2} \sigma \alpha T_G^4 - \frac{1}{4} \alpha_s S_s + h_c \left(T_s - T_A \right) \right\}$$

$$+ \sum_{i=1}^{n} \frac{k_{eff} A_c}{\ell} \left(T_s - T_G \right) = 3.41 \frac{1}{\tau} \int_0^{\tau} P(t)\, dt$$

When known values of D_s, ϵ, α, T_G, α_s, h_c (from Figure 5.9-3), T_A, k_{eff}, A_c, h, ℓ, and τ are substituted in the above equations, a plot of mean power dissipation versus sphere surface temperature can be obtained.

In order to provide trade-off information, it is assumed that $\alpha_s = \epsilon = \alpha = 0.9$, and that $\sum_{i=1}^{n} \frac{K_{eff} A_c}{\ell} (T_s - T_G) = 0$ (i.e., that conduction effects can be made negligibly small). Approximate values of S_s, T_A, and T_G are taken from the Mars environments given in a previous section of this report and values of h_c are obtained from Figure 116 for various wind velocities.

Figure 119 presents isothermal sphere surface temperatures for various mean heat losses from the sphere surface. Surface temperatures are shown as a function of wind velocity for typical day and night ambient conditions. In Figure 120 , sphere temperatures are presented as a function of sphere heat loss for several wind velocities. Also, it is seen from this figure that the sphere temperature is not grossly affected by changes in solar radiation in the range from 100-140 Btu/ft^{2}hr. Figure 121 shows sphere temperatures on a hot "still" air day as a function of net sphere heat loss.

d. Payload Sphere Transient Temperature Analysis. For the case of no internal power dissipation, the payload sphere transient temperature response can be approximated by a lumped parameter solution given below:

$$\frac{T'_P - T'_A}{T'_{P_i} - T'_A} = e^{-\left(\frac{U A_s t}{W c}\right)}$$

where U, the overall heat transfer coefficient, is further defined by the following equation:

$$U = \frac{1}{\frac{1}{(h_c + h_r)} + \frac{\ell}{k}} = \frac{k}{\ell} \frac{(h_c + h_r)}{(h_c + h_r + k/\ell)}$$

For $k/_1 << (h_c + h_r)$, the above equation reduces to $U = k/\ell$, indicating that the thermal insulation is controlling the rate of heat transfer. If $k/\ell << (h_c + h_r)$, then the transient temperature response equation for a sphere can be approximated by the following equation:

$$\frac{T'_P - T'_A}{T'_{P_i} - T'_A} = e^{-\frac{k \pi (D_s - \ell)^2 t}{\ell W c}}$$

where the mean heat transfer area, A_s, is $\pi (D_s - \ell)^2$. Figure 122 shows a plot of the above approximate equation. It provides a very close approximation to the actual transient temperature response for insulation thicknesses greater than 1/2 inch ($k = .01$ Btu/ft^{2}hr F/ft).

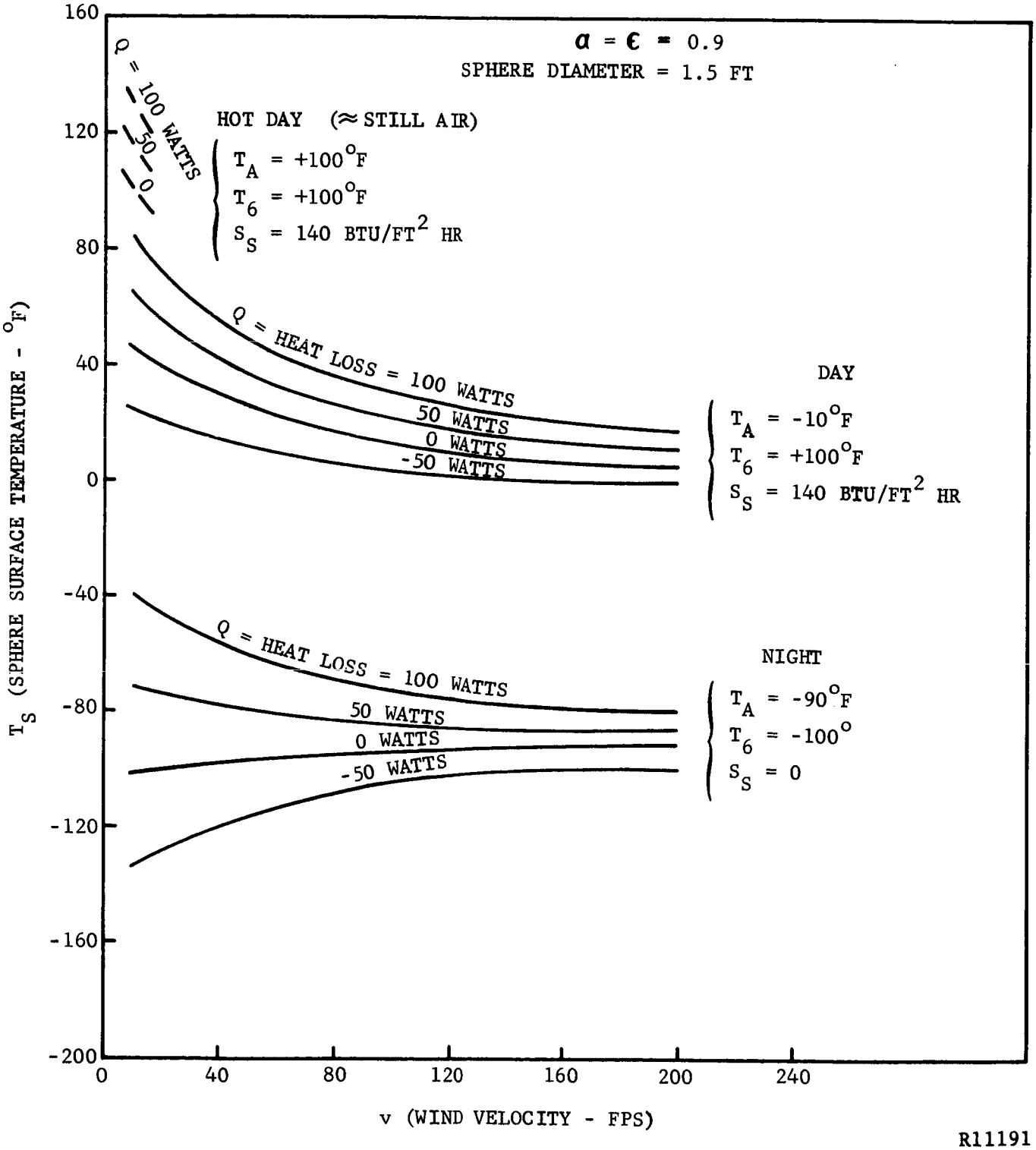

R11191

FIGURE 119. SPHERE ISOTHERMAL SURFACE TEMPERATURE

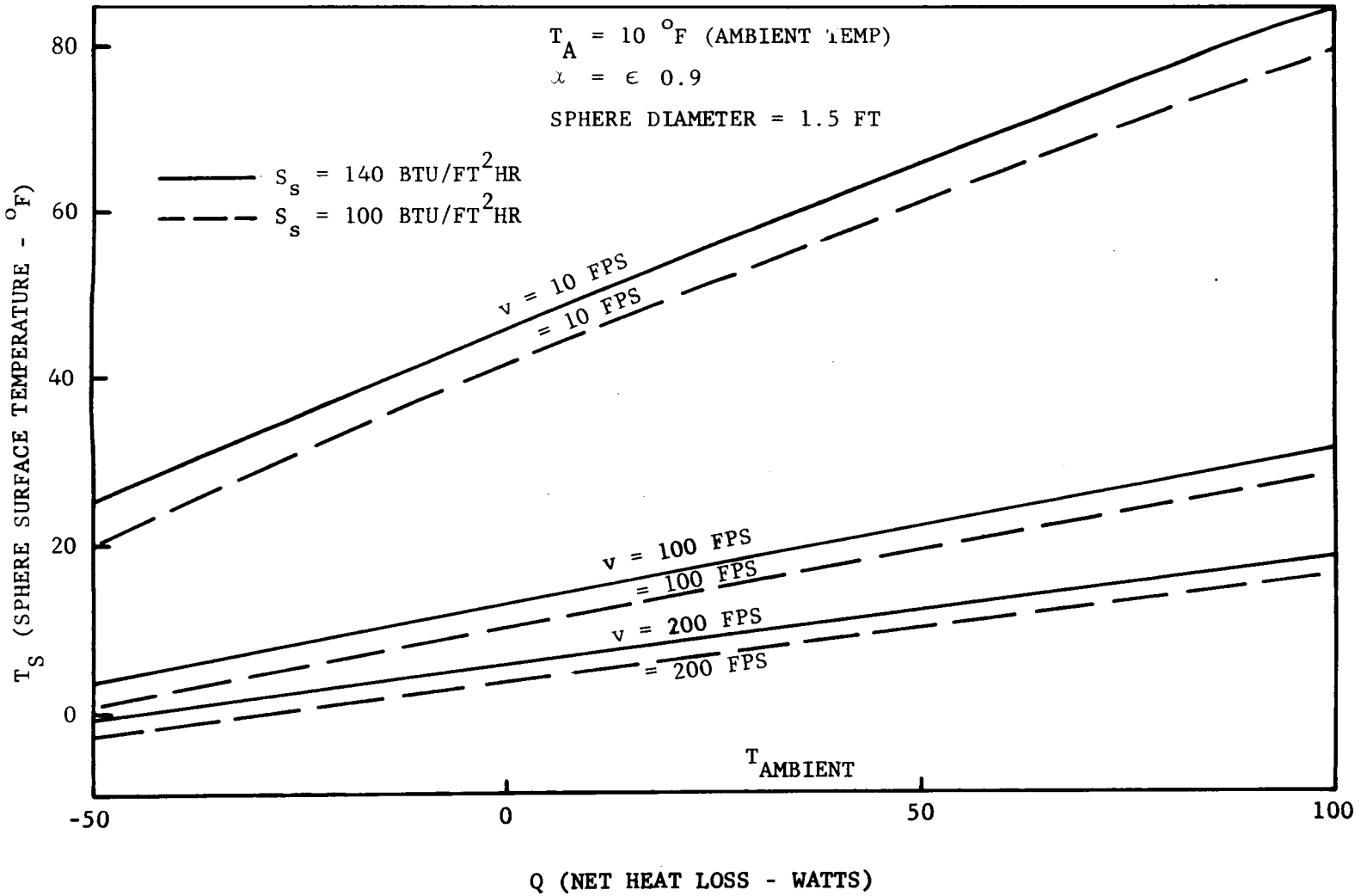

FIGURE 120. SPHERE ISOTHERMAL SURFACE TEMPERATURE

R11215

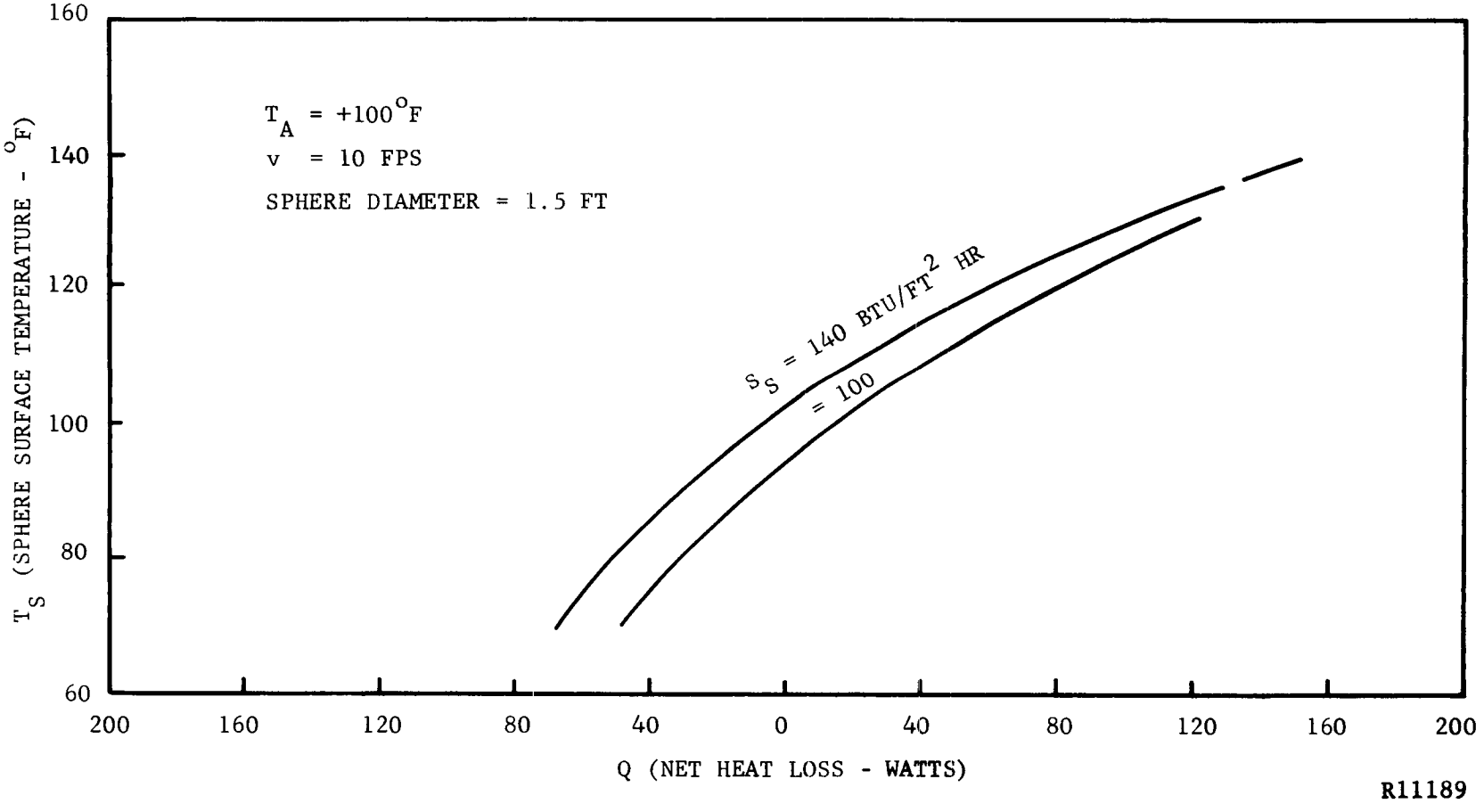

FIGURE 121. SPHERE ISOTHERMAL SURFACE TEMPERATURE

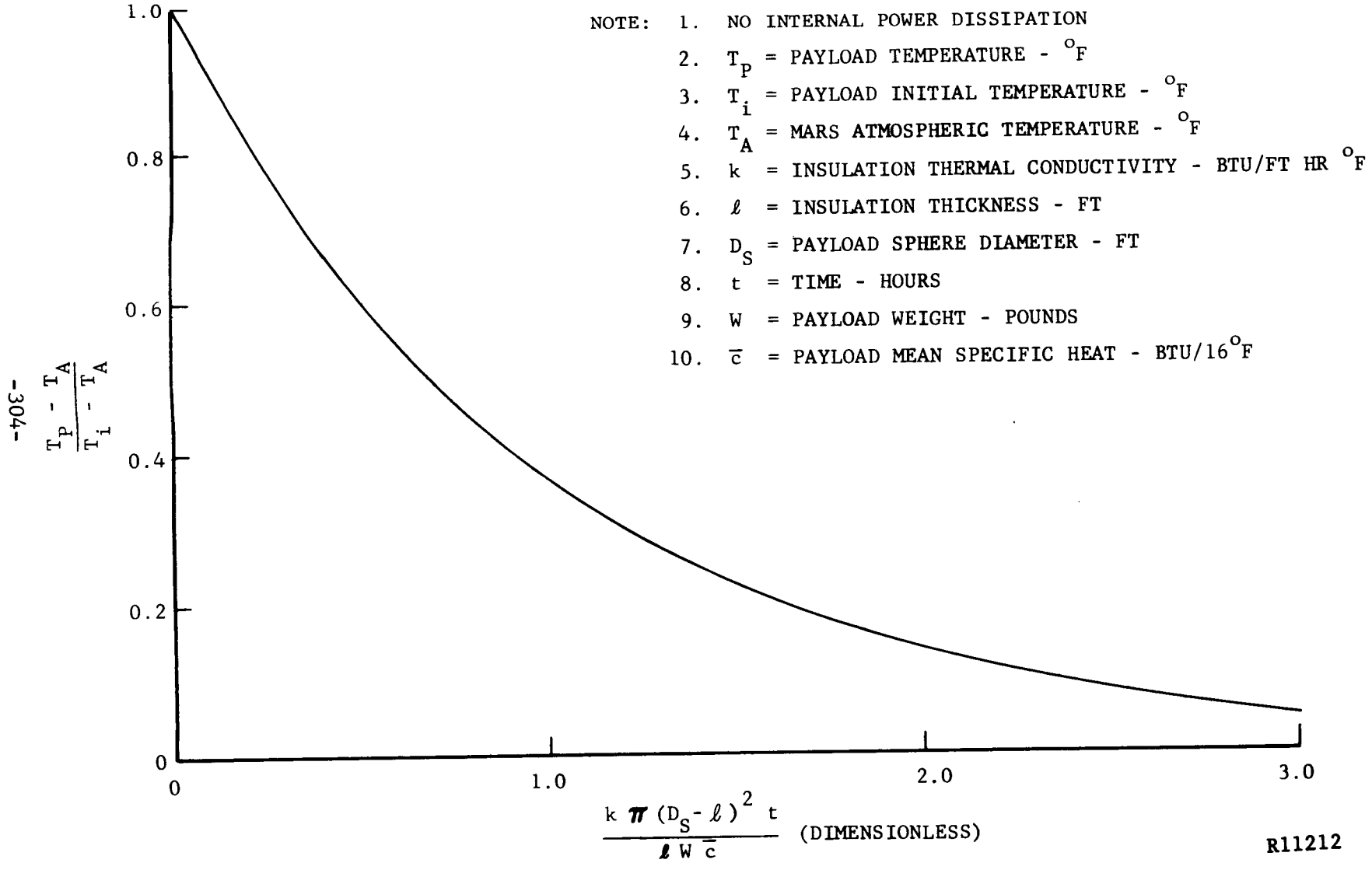

FIGURE 122. PAYLOAD TRANSIENT TEMPERATURE RESPONSE CHARACTERISTICS

It is desirable to provide an estimate of payload cooldown time after MFC impact on Mars. Figure 123 presents minimum cooldown times from an initial +100 F temperature to any desired temperature, for several insulation thicknesses. The cooldown time is termed minimum because the payload is assumed to respond to the minimum Mars ambient temperature of -90 F during the entire cooldown period. It is seen that for an inch of insulation thickness, the payload cooldown time is on the order of 40 hours for a payload temperature decrease to +30 F from a +100 F initial temperature.

When the effects of internal power dissipation are included, the following relation is obtained for payload temperature.

$$T_P' = T_{P_i}' + \frac{3.41 \frac{1}{\tau} \int_0^{\tau} P(t)\,dt - \int_0^{t} \frac{k\pi \left(D_s - \ell\right)^2 \left(T_P' - T_A'\right) dt}{\ell}}{Wc}$$

If the power dissipation term, $3.41 \int_0^t P(t)\,dt$, in the above equation is significantly larger than the heat loss term, $\int_0^t \frac{k}{\ell} \pi (D_s - \ell)^2 (T_P' - T_A')\,dt$, then the average value of T_P' over the time, t, can be used in the heat loss term to simplify the integral; i.e., $\overline{T}_P' = T_{P_i}' + \frac{1}{2}\left[3.41 \left(\frac{1}{Wc}\right) \int_0^t P(t)\,dt\right]$ can be used in the heat loss equation instead of a variable T_P'. Substituting the approximate value $\overline{T}_P'$ into the above equation yields the following approximate relation for payload temperature.

$$T_P' = T_{P_i}' + \frac{3.41 \int_0^t P(t)\,dt - \frac{k\pi (D_s - \ell)^2 t}{\ell} \left(T_{P_i}' - T_A'\right)}{Wc}$$

$$- \left(\frac{1}{2}\right) \frac{3.41}{Wc} \left[\int_0^t P(t)\,dt\right] \left[\frac{k\pi (D_s - \ell)^2}{\ell}\right](t)$$

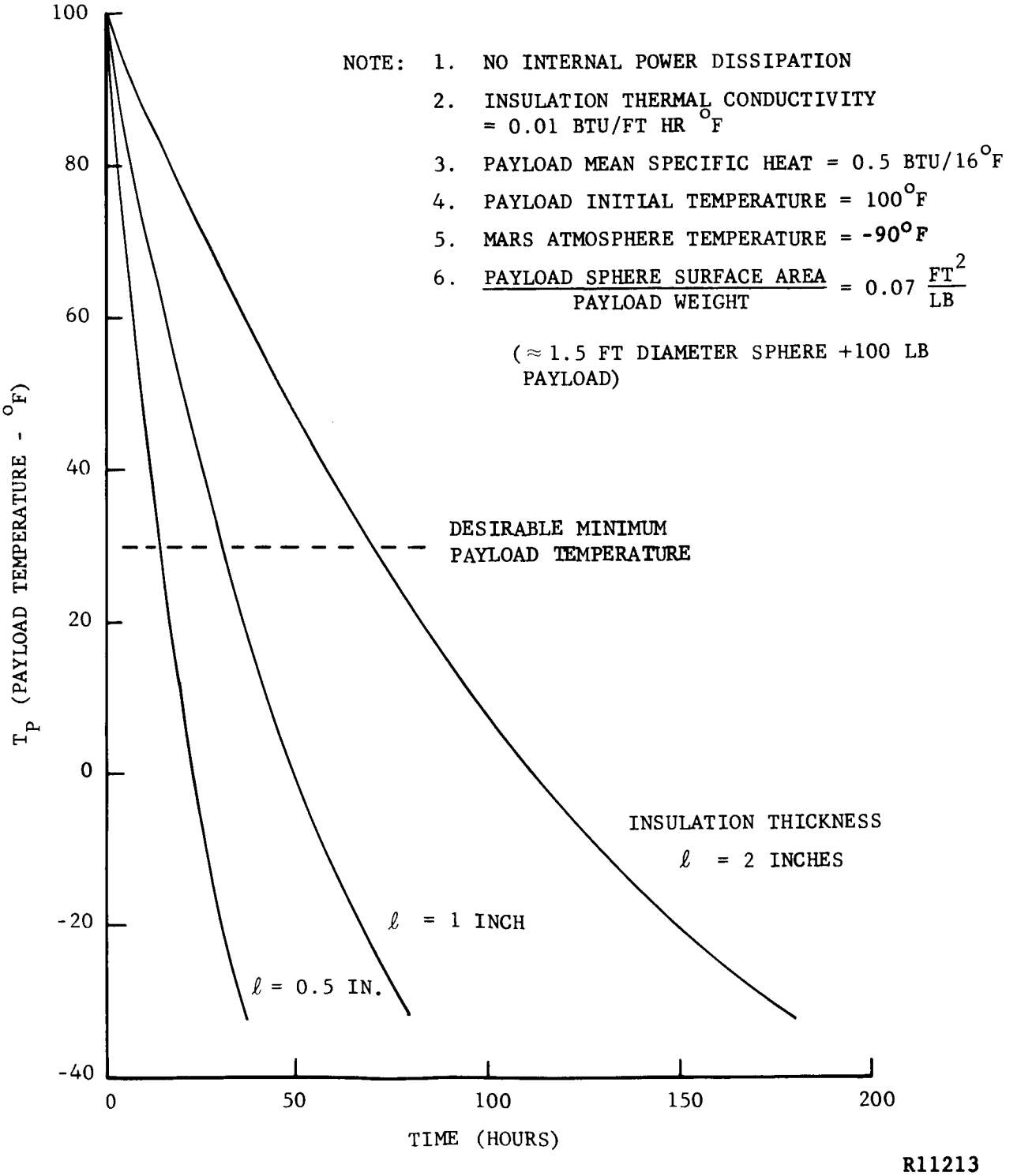

FIGURE 123. MFC PAYLOAD TRANSIENT COOLDOWN TEMPERATURE HISTORIES

The above quotation is not plotted herein, but it was used to determine payload transient temperature responses during transmitter operation for the typical payload temperature histories presented in a later analysis section (f).

e. Payload Sphere Heat Loss Analysis. The heat loss from the payload sphere (through thermal insulation to the outside surroundings) is given by the following conduction equation:

$$Q = \frac{k}{\ell} \pi (D_S - \ell)^2 (T_P' - T_S')$$

Figure 124 shows heat losses from the sphere (in watts) as a function of temperature difference. These heat losses are shown for several insulation thicknesses, with a 1.5 ft. diameter sphere being assumed. Figure 125 presents heat losses as a function of sphere diameter and insulation thickness for an assumed 100°F temperature difference.

For a heat balance to exist, heat losses must equal heat gains. For a typical duty cycle period, the mean heat gain is $Q' = 3.41 \frac{1}{\tau} \int_o^\tau P(t)dt$. Equating heat losses and heat gains, the following relation is obtained.

$$3.41 \frac{1}{\tau} \int_o^\tau P(t)dt = \frac{k}{\ell} \pi (D_S - \ell)^2 (\bar{T}_P' - \bar{T}_S')$$

where $\bar{T}_P'$ and $\bar{T}_S$ are the mean payload and sphere surface temperatures, respectively. This equation can be used to determine the thermal insulation thickness, ℓ, required for a heat balance when values of mean power dissipation, desired mean payload temperature, and mean surface temperature are given. The first two of these values are obtained as inputs from electronic system design and the mean surface temperature is derived from Figure 119 .

An example of the heat balance insulation thickness determination is presented below for an assumed mean power dissipation of 700 w-hr/24.6 hr duty cycle or a mean power dissipation of 28.5 watts. From Figure 119 , a mean outer surface temperature of -40F is obtained for a 200 ft/sec wind velocity ($T_{s_{day}}$ = +8 F and $T_{s_{night}}$ = -88 F). If a mean desired payload temperature of +60 F is assumed, a payload/sphere surface temperature difference of 100F is obtained. For this condition, approximately 0.8 inch of thermal insulation is required for a heat balance to be achieved.

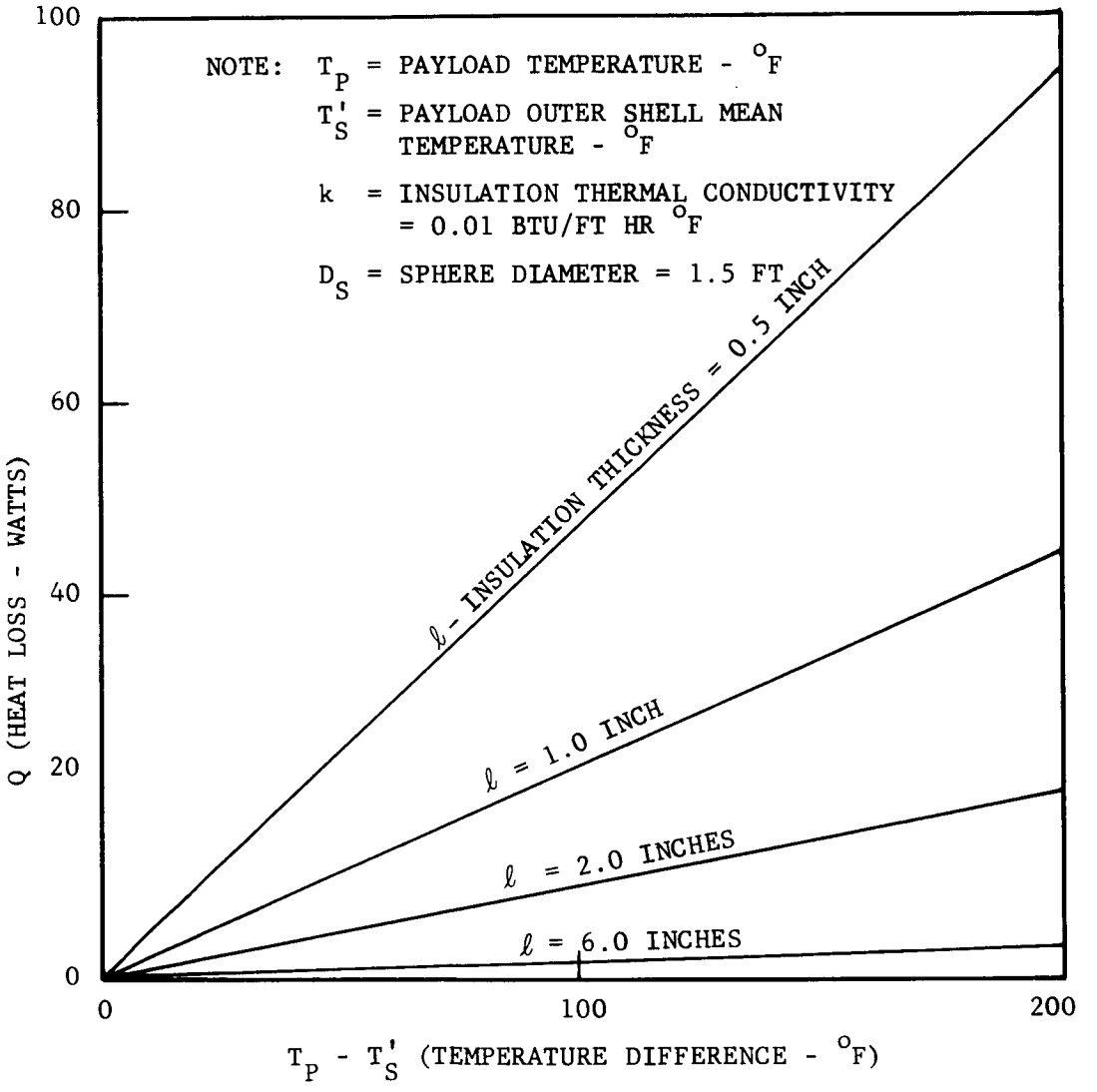

R11214

FIGURE 125. STEADY STATE HEAT LOSS FROM AN INSULATED SPHERICAL PAYLOAD

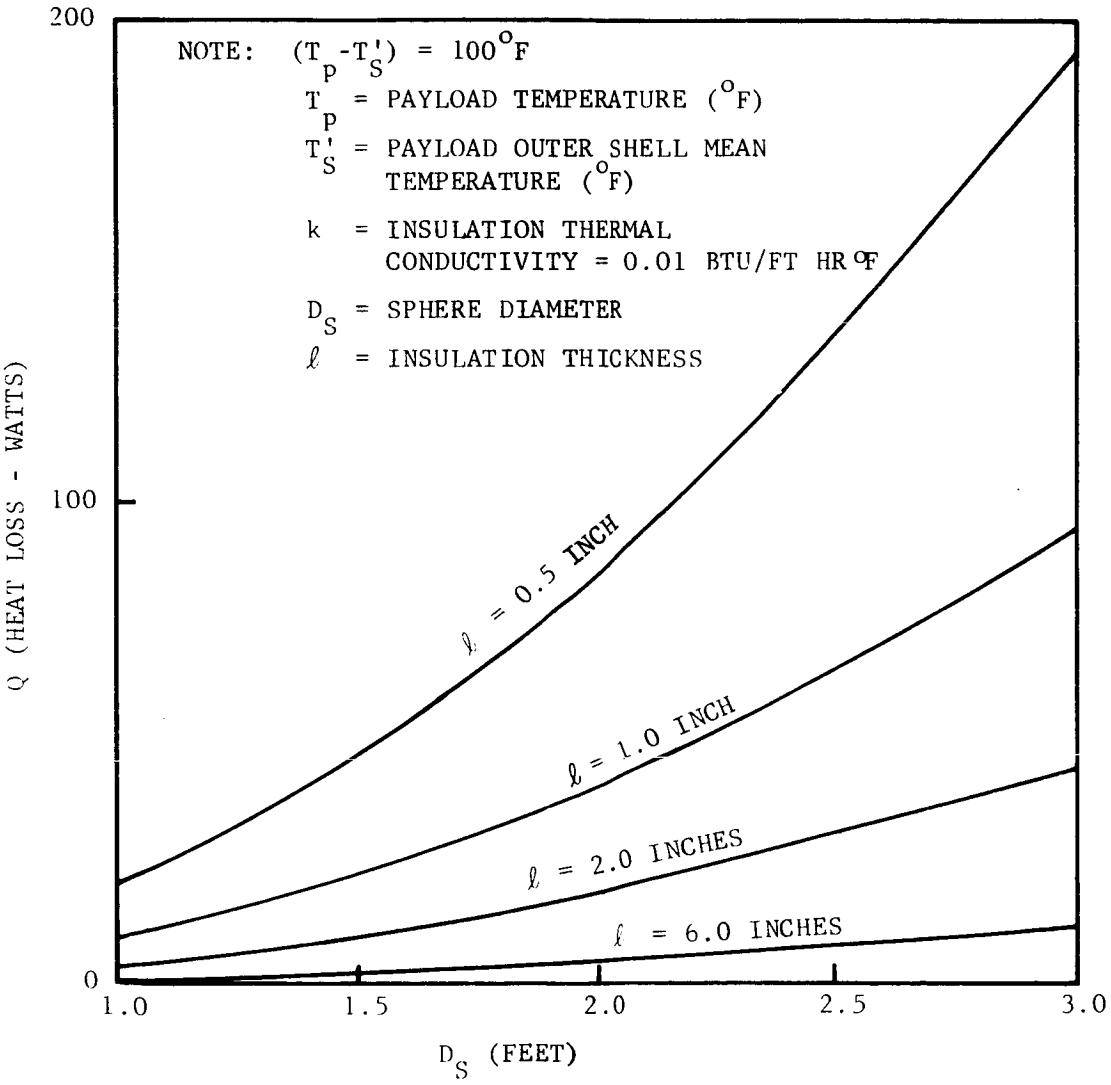

FIGURE 125. STEADY STATE LOSS FROM AN INSULATED SPHERICAL PAYLOAD

R11203

f. Analysis of Temperature Regulation Systems Employing Water. At Martian atmospheric pressures, water boils at temperatures on the order of +70 F to +100 F, as shown in Figure 126 . The boiling temperature can easily be increased, if desired, by artifically raising the pressure in the water boiling chamber (i.e., by employing a pressure relief device in the boiloff system). Water freezes to form ice at a temperature of +32 F almost independent of local pressure. Thus, temperature control between approximately +30 F to +100 F can be provided by a water boiloff/freezing system.

The latent heats of vaporization and freezing are the most important parameters in the thermal analysis of water used for temperature regulations, since most of the heat energy transfer occurs during a phase change. The latent heat of vaporization is 970 Btu/lb (284 watt-hr/lb) and the latent heat of freezing is 144 Btu/lb (42 watt-hr/lb) for water. For water temperatures between freezing and boiling, the water thermal capacity is lumped together with the payload thermal capacity and a simple heat balance is employed to determine payload (and water) temperature.

g. Typical Payload Temperature Histories. Figure 127 presents a typical payload temperature history for a Mars minimum ambient temperature environment. A square wave ambient temperature history is assumed with the day temperature being -10 F and the night temperature -90 F. The assumed sequence of events for the minimum environment MFC mission is the following: Landing at noon; no pictures taken during the remainder of the first day; pictures taken during the second day; data transmission to Earth during the third day. The total assumed elapsed time from impact to data transmission is taken as 47 hours.

The thermal insulation thickness requirement for the payload temperature history is taken as the larger thickness derived for transient cooldown or for the payload heat balance. To obtain a heat balance with a 200 watt power dissipation for 3.5 hours (700 w-hr) assumed daily operation, 0.8 in. of insulation is required. For the transient cooldown period, 1.2 in. of insulation is required. Thus, the 1.2 in. (0.1 ft.) of insulation was used in the temperature history calculation. It is seen from Figure 127 that the payload temperature has gradually increasing characteristics once the daily data transmission cycle has been established. This general temperature increase occurs because the insulation thickness is greater than required for thermal equilibrium, and thus, heat gains are greater than heat losses.

In Figure 127 , it is assumed that water boils at +100 F in order to control the payload maximum temperature. Approximately 0.2 lb. of water per day is required for the 700 w-hr daily power dissipation level and the minimum ambient environment condition. If water is not employed for the minimum temperature environment condition, the payload temperature would eventually stabilize about a mean temperature of +120 F and have a maximum temperature of approximately +145 F.

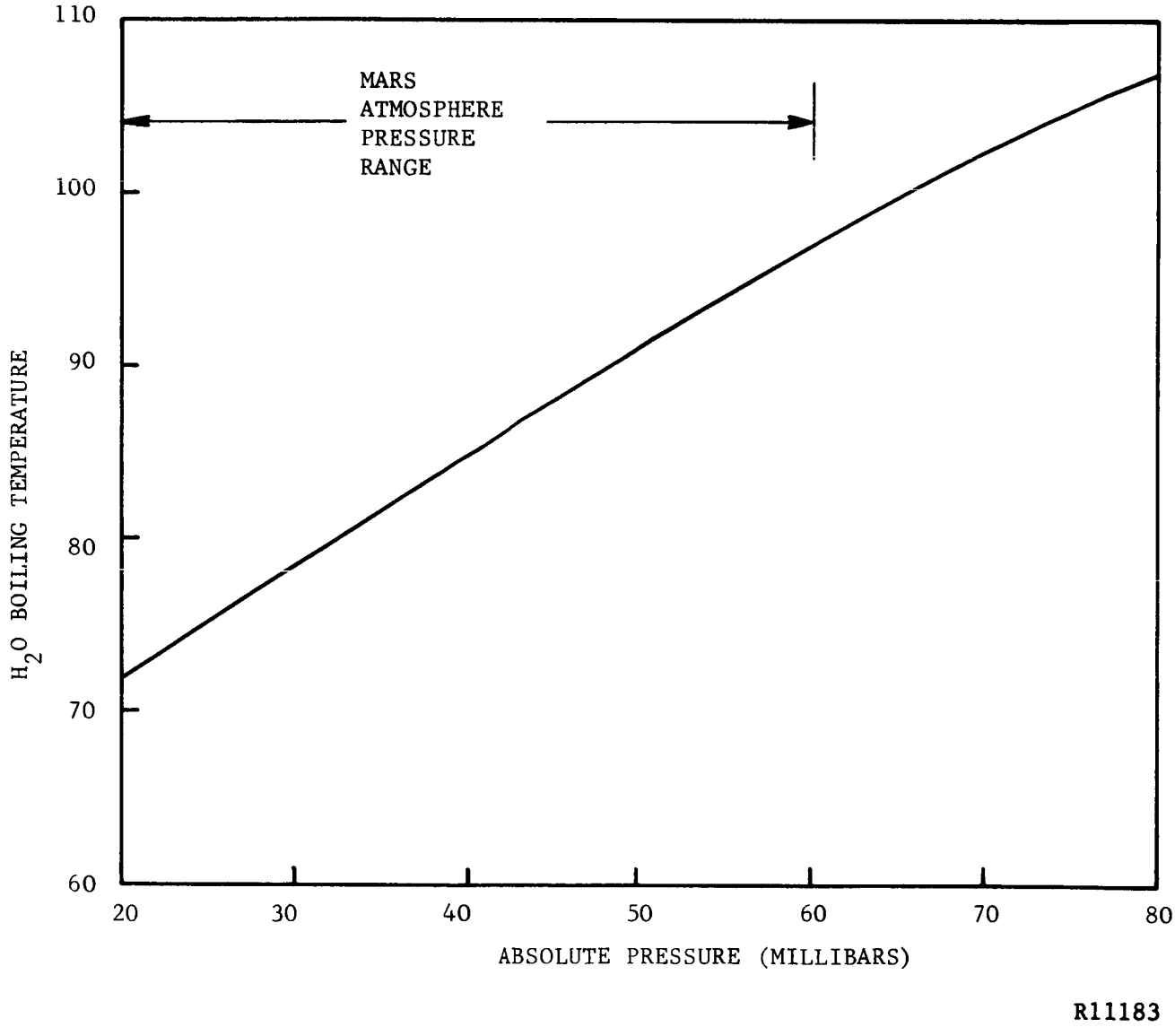

FIGURE 126. WATER BOILING TEMPERATURE AT MARS ATMOSPHERIC PRESSURES

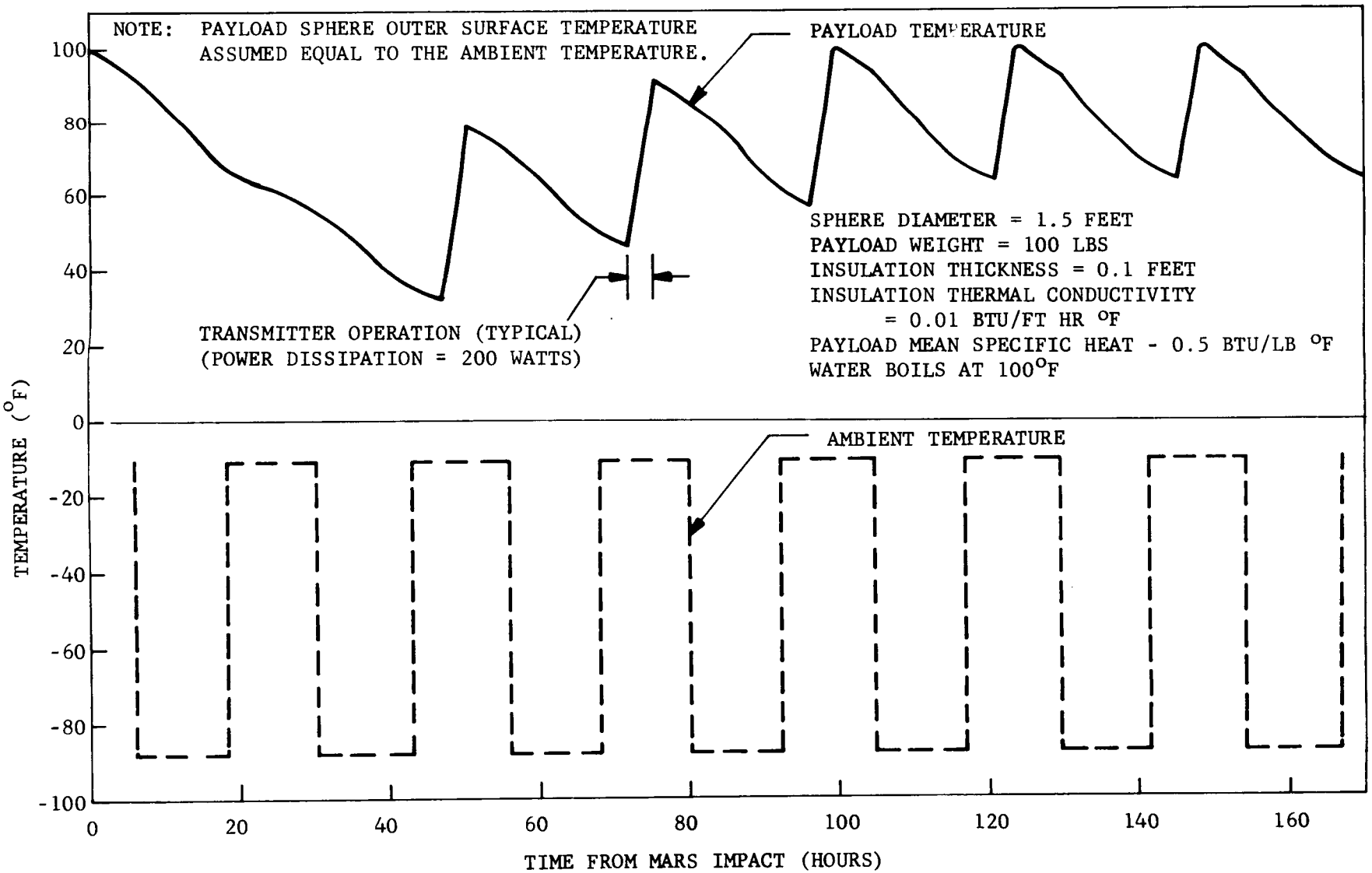

FIGURE 127. TYPICAL PAYLOAD TEMPERATURE HISTORY FOR A MARS MINIMUM TEMPERATURE ENVIRONMENT.

R11179

Figure 127 presents a typical payload temperature history for a Mars maximum ambient temperature environment. The same design parameters (insulation thickness and thermal conductivity, sphere diameter, payload weight, etc.) are used for the results presented in Figure 127 as are given above for Figure 126 . A square wave ambient temperature is assumed with the day temperature being +80 F and the night temperature being -90 F. The assumed sequence of events for the maximum environment mission is given by the following: Landing in early morning; pictures taken during the first day; data transmission during the next day. Total elapsed time from impact to data transmission is 23 hours.

It is seen from Figure 128 that a repetitive temperature cycle is achieved after the second day. It is assumed that water boils at +100 F for the payload temperature calculation in Figure 128 . Approximately 1.0 lb. of water per day is required for the 700 wt-hr daily power dissipation level and the maximum ambient environment condition. If water boiling is not used for temperature control, the payload temperature would eventually stabilize about a mean temperature of +180 F and have a maximum temperature of +205 F. These latter temperatures are bulk payload temperatures (i.e., average payload temperatures). Payload electronic component temperatures can be on the order of 30 to 150 F higher than these.

5.9.4 THERMAL CONTROL SYSTEMS FOR MFC

Thermal insulation is required for the protection of MFC payload sphere equipment from the generally cold Martian ambient environment, regardless of the particular passive or active thermal control system employed. If possible, the thermal insulation thickness should be sized so as to provide a heat balance for the MFC during Mars operation. That is, heat losses from the payload to the ambient surroundings should balance the heat gains due to electronic equipment power dissipation. If heat gains exceed heat losses, a cooling system may be required, and conversely, if losses exceed gains, a heating system may be required.

Only a cursory look at candidate thermal control systems has been undertaken for this trade-off study. The systems considered have been divided into two classes, passive and active. In the following paragraphs the various thermal control systemsare presented together with their advantages and disadvantages.

a. Passive Thermal Control Systems for MFC

Thermal Control System A*

---

* System A recommended for MFC conceptual design.

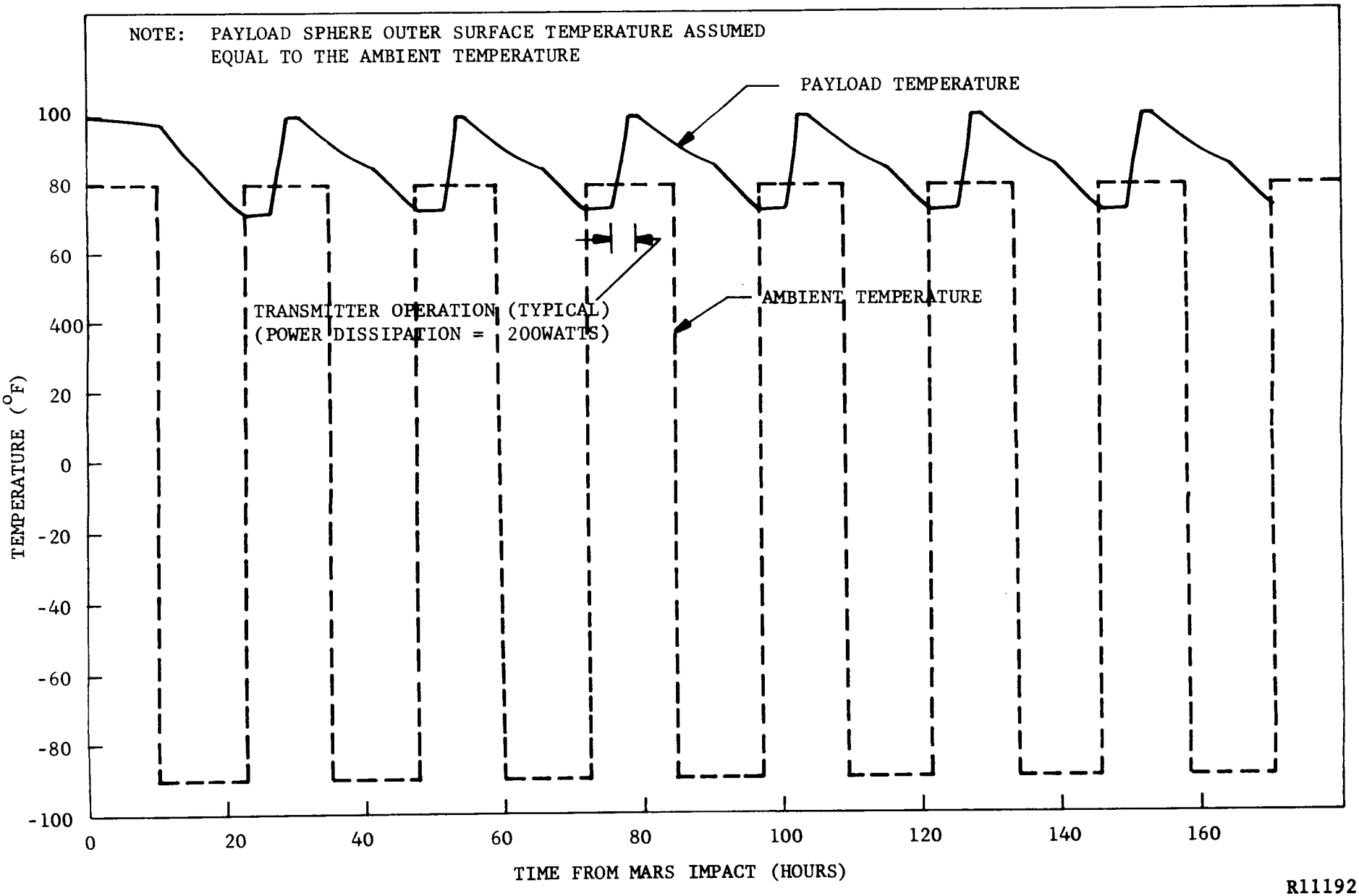

R11192

FIGURE 128.

System Description: Thermal insulation is used to maintain a heat balance and a water boiloff/freezing system is used for temperature control.

Major Components:

1. Thermal insulation

2. Water

3. Water storage container(s)

4. Squib actuated pressure relief valve (actuated after Mars impact)

Operation: Insulation is used to maintain coarse temperature control during transient cooldown following impact and for maintaining a reasonable heat balance during Mars operation. Fine temperature control is achieved by water which boils at approximately +100 F (max. temp.) and which freezes at +32 F. Water boiling thus limits payload maximum temperatures during transmitter operation, and water freezing limits payload minimum temperatures.

Advantages:

1. Lightweight system (especially if a heat balance can be achieved)

2. Simple, reliable system

3. Temperature control between +32 F and +100 F is assured since temperature control is not dependent on a sensor/amplifier/actuator device which could fail during impact, but rather on the boiling and freezing properties of water which are well known.

Disadvantages:

1. Requires a pressurized tank (on order of 50 psia) to meet the sterilization criteria ofheat soak at (+275 F).

2. Requires a valve which allows vapor to escape while retaining the basic water supply. (Such a valve has already been developed for Aeronutronic lunar capsule programs).

Thermal Control System B

System Description: Paint patterns on MFC surface are used in addition to thermal insulation and a water boiloff/freezing system as described for System A.

Major Components: Same components as System A, above, plus external surface paint patterns.

Operation: Same as for System A, above.

Advantages: Same as for System A, above, plus some ability to modify the MFC outer surface temperatures during daytime operation. (Since the high wind environment exists on Mars, the convective heat flux can be significantly greater than the radiative heat flux, and hence, precise temperature control cannot be achieved with paint patterns alone).

Disadvantages: A thermal control system design requiring paint patterns for a major thermal input could easily be aborted by dust on the capsule surface or by the high convective heat fluxes which result at high wind velocity.

b. Active Thermal Control Systems for Heating MFC

Thermal Control Heating System #1

System Description: Pyrotechnic type heating elements are fired when a temperature sensor indicates a minimum payload temperature has been reached.

Major Components:

1. Thermal insulation
2. Pyrotechnic Heaters
3. Temperature sensor/amplifier/actuator system
4. Electronic logic system for firing pyro heaters

Operation: Individual pyrotechnic heater elements are fired to produce an exothermal chemical reaction, as required, to maintain the payload temperature above a desirable minimum.

Advantages: Pyrotechnic heater devices would be development items, but they could supply a relatively large amount of heat energy per unit weight compared to that for electric heaters using conventional power supplies. A pyrotechnic heater employing a mixture of iron filings and potassium chlorate can supply heat energy on the order of 150 watt-hr/lb. (approximately 325 cal/gm) after an ignitor squib initiates the exothermal chemical reaction. This reaction produces iron oxide, potassium chloride, heat energy, and a very small amount of gas. The gas which is produced could easily be contained within the case surrounding the pyrotechnic heater element. Conventional battery power supplies can produce on the order of 25 to 50 watt-hr/lb. of heat energy. Thus, the pyrotechnic heater could supply on the order of 3 to 6 times the heat energy per unit weight than can be obtained from conventional power sources.

Disadvantages:

1. A temperature sensor/amplifier/actuator system is required to energize the heater elements.

2. Electronic system logic is required to set off the pyrotechnic heater elements in sequence.

3. A separate payload cooling system is required.

Thermal Control Heating System #2

System Description: Electric heater plus a power supply provide heat energy as required to maintain minimum payload temperature.

Major Components:

1. Thermal insulation

2. Electric heater

3. Power Supply (batteries)

4. Temperature sensor/amplifier/actuator system

Operation: An electric resistance heater supplies heat to the payload to maintain the temperature above an acceptable minimum. The payload temperature is sensed and the heater power turned on to meet demands.

Advantages:

1. The electric heater/power supply combination may be attractive for a low level power dissipation electronic system; i.e., a constant output from an electric heater together with the electronic power dissipation can provide a heat balance with reasonable insulation thicknesses (less than 2 inches) when the power dissipation is on the order of 200 w-hr/day or less. An additional heater element together with a temperature sensor is required to maintain acceptable minimum payload temperatures.

Disadvantages:

1. This system has relatively high weight principally because of the power supply weight.

2. A temperature sensor/amplifier/actuator system is required.

3. A separate payload cooling system is required.

c. Active Thermal Control Systems for Cooling MFC

Thermal Control Cooling System #1

System Description: Outside Mars atmosphere gases are circulated through the payload for direct cooling. An improved modification of this concept uses a secondary heat transfer loop and isolates the payload from the Mars ambient gases. Gas circulation continues as required to maintain the payload temperature within acceptable limits.

Major Components:

Direct Gas Coolant System

1. Thermal insulation
2. Fan or blower
3. Power supply
4. Temperature sensor/amplifier/actuator system
5. Gas inlet and outlet ports

Secondary Heat Transfer Loop
Additional Components

1. Heat exchanger
2. Additional fan or blower (inside MFC)
3. Elimination of gas inlet and outlet ports, but provision for a heat exchanger installation with access to inside and outside ambient gases is required.

Operation: Mars outside cool atmosphere gases are used for cooling the MFC payload either by direct flow through the payload or by a secondary heat transfer loop. A payload temperature sensor turns off the flow of air when the payload temperature is below acceptable high temperature limits.

Advantages:

1. This may be an attractive cooling system for long time Mars missions. The infinite heat sink provided by the Mars atmosphere is used to remove large quantities of heat over a long period.

Disadvantages:

1. High fixed weight of components

2. Inherent low system reliability when impact load criteria are considered.

3. Requires a separate payload heating system.

Thermal Control Cooling System #2

System Description: Removable or variable thickness insulation is used to provide payload cooling.

Major Components:

1. Thermal insulation

2. Shutters which open and close

3. Temperature sensor/amplifier/actuator system

Operation: Thermal insulation panels are removed (or varied), as required, to maintain the payload temperature below acceptable high temperatures. The payload temperature is sensed and the insulation panels are adjusted as required.

Advantages:

None

Disadvantages:

1. This system does not appear to be practical for mechanical design implementation in MFC.

5.9.5 CONCLUSIONS AND RECOMMENDATIONS

MFC payload temperature control can be provided by a passive system employing thermal insulation and a water boiloff/freezing subsystem during MFC operation in the generally cold Mars ambient environment. This control system is simple and operates as long as battery power is available to operate electronic equipment (or until all of the water boils off). At Martian atmospheric pressures, water boils between +70 F to +100 F and freezes at +32 F. Conventional insulation materials can be used for this system since at Martian atmospheric pressures, the thermal conductivities of "superinsulation" and good conventional insulation are approximately the same. (Superinsulations would be better if it were practical to design a vacuum jacket to surround the insulation. The jacket would of course have to survive the "high g" impact).

It is desirable in this design to provide a balance between heat gains from payload internal power dissipation and heat losses to the Mars ambient surroundings. If the internal power dissipation level is very low so that large insulation thickness requirements result, it may be desirable to supplement the heat generation in the payload with heat from an electric heater or from pyrotechnic heater elements. In this case, a temperature sensor/amplifier/actuator system would be required in addition, and hence, the thermal control system would be an "active" one.

It is recommended that more detailed thermal analyses be performed to extend the scope of this trade-off study. A computer program could be developed to provide a much better estimate of payload sphere surface temperature than that obtained herein for an assumed isothermal sphere surface temperature. More studies should be performed to estimate the probability of having hot (or cold) ambient Mars environments on successive days of MFC operation; (i.e., how often does a zero wind, high temperature day occur? Or, conversely, what is the probability of having 50% or 100% cloud cover during the day?, etc.). A reasonable estimate of the probable ambient environment is required in order to determine the quantity of water which should be carried along for the water boiloff/freezing temperature regulation system.

REFERENCES

1. McAdans, W. H., "Heat Transmission", Third Edition, McGraw-Hill Book Co., Inc., New York, 1954. Pages 265-6.

2. Jakob, M., "Heat Transfer", Volume I, John Wiley & Sons, Inc., New York, 1955. Pages 526-534.

3. Hnilicka, M. P., "Engineering Aspects of Heat Transfer in Multilayer Reflective Insulation and Performance of NRC Insulation", Advances in Cryogenic Engineering - 1959 Conference. Paper D-3, pages 205-6.

4. Strong, H. M., Bundy, F. P., and Bovenkirk, H. P., "Flat Panel Vacuum Thermal Insulation and the Super Dewar Flask". (G.E. Research Laboratory, Schenectady, New York). Advances in Cryogenic Engineering - 1959 Conference. Paper C-2, pages 139-141.

5. Johns-Manville Industrial Insulation Division, "Min-k molded insulation for rockets, missile, spacecraft and aircraft". Bulletin IN-446A 9/62.

5.10 CAPSULE DESIGN

This section is chiefly concerned with establishing the weight and size configurations of complete capsules capable of surviving specified impact velocities. To simplify the task, it is assumed that there is a fixed performance requirement to obtain a $24^{o} \times 24^{o}$ facsimile picture with certain characteristics. It is necessary to use results from Sections 5.1 through 5.9 for estimating the performance capabilities of many of the sub-systems within the capsule. Methods are developed in this section for estimating the weight requirements of the mechanical components which have not been considered in the previous sections. A brief stability analysis is performed to show that the capsule configuration used in the weight estimates will perform adequately on the sloping Mars surface in the presence of wind.

5.10.1 CAPSULE DESIGN CONSIDERATIONS

The primary purpose of the Mars Facsimile Capsule is to obtain a high detail picture of the Martian surface. Thus, the primary design objective is to assure reliable system operation following high "g" impact. Reliable operation is best achieved by simplicity and/or redundancy. It is towards these goals that the capsule design configuration is aimed.

Maximum simplicity is an inherent capsule design feature:

(1) The capsule is capable of surviving omni-directional impacts without reliance on entry deceleration or orientation by an atmosphere of unknown composition.

(2) Payload erection following impact is accomplished passively by means of a flotation fluid in which the inner payload is suspended. This allows payload erection without consideration of unknown terrain features.

(3) Timer initiation is effected by redundant, inertially activated switches.

(4) Erection of the top tube and antenna system is accomplished passively subsequent to porting without further timing events.

(5) Thermal control is accomplished passively by means of insulation and a pressure (temperature) actuated water boiloff system.

There are several schemes whereby redundancy may be introduced into the capsule design; e.g.,

(1) The power supply can be constructed in two modules connected in parallel. If one circuit or cell opens,the other can

supply the necessary power for a reduced life. If an internal short is considered likely blocking diodes could be used to prevent the damaged cell from discharging the one remaining.

(2) The limiter removal device, porting device, and cage-uncage devices could be activated by two or three redundant squibs.

a. Equipment Arrangement. The dictating factors for equipment arrangements are center of gravity location and accessibility. It is necessary that the center of gravity be located in the lower half of the sphere at least a quarter of an inch below the center of buoyancy to allow vertical erection following impact. Thus all of the heavier components should be located in the lower sphere half (i.e., the battery and thermal control fluid). The battery should be located closest to the equator where the two sphere halves separate for accessibility whereas the entire water tankage may be located beneath. Additionally, it is desirable that the fluid be contained in one sphere half to eliminate interconnecting piping which may be subject to leakage following impact. Placement of the battery in the lower sphere half allows direct access to the caging assembly (located diametrically opposite the top tube porting) for a possible battery fill following sterilizatinn via the pre-impact caging foot.

The upper sphere half would contain all electronic sub-assemblies. It is desirable that these sub-assemblies be constructed as separate modules and provided with inter-connecting wiring and connectors. This allows for their ready removal in the event of necessary repairs and/or replacement.

b. Designing for High Impact. The payload impact deceleration loads are dictated by the stroke and density of the limiter as indicated on the impact dynamics curves of Section 5.2. Little control can be exercised in reducing maximum impact deceleration. The payload must be designed to survive the levels imposed. In addition, superimposed on the primary payload deceleration curve is a resonance or "ringing" of the payload structural members and associated components. Thus, to obtain an indication of the total environment within the payload it would be necessary to conduct a laborious analysis of the natural frequencies of the various payload sub-assemblies. Since it is doubtful that such analyses could be made with sufficient accuracy to be of any real benefit, the realistic approach to be taken is to provide as much structural rigidity as possible, thus avoiding all resonance frequencies low enough to be structurally disasterous.

The structural parts should contain no large unsupported areas which could yield and thereby cause permanent deformation following impact. All point loading should be avoided; the forces of impact should be distributed over as large a surface area as possible. The use of flotation fluid as an erecting device automatically accomplishes this goal to the fullest extent

possible for the payload by distributing the impact load over the entire inner sphere

Particular care must be exercised in the design of moving parts within the top tube and azimuth drive assemblies. These parts must be of a minimum mass and should be dynamically balanced or caged if provided with only a single support (e.g., the nodding mirror cam-follower). Also ball bearing supports should be used only on small shafts with low inertial loading and should possess considerable overload capability.

5.10.2 ORIENTATION AND STABILIZATION

It is necessary after impact that the inner spherical payload be erected to local vertical and imparted with sufficient stability to resist the forces of porting, Martian winds up to 60 meters/second, and prevailing slopes up to five degrees.

Alternative erection schemes have been investigated and it is indicated that this event is most reliably accomplished internally by "flotation"; (i.e., a floated inner payload with center of gravity displaced from center of buoyancy thereby allowing passive erection to local vertical). Any consideration of external erecting devices requires a presupposed terrain and hence may be readily defeated when viewed in the diverse conditions which may exist on the surface of Mars (i.e., rocks, craters, or heavy dust).

The stability requirements as dictated by the Martian winds are as follows:

The maximum dynamic pressure exerted on the capsule at rest is

$$q = 1/2\ \rho\ V^2$$

where V_{max} = 60 meters/sec and ρ_{max} is calculated from the partial pressures of the given atmospheric constituents and a minimum assumed atmospheric temperature of 205°K or 6.57×10^{-3} lbs/ft^3 (1/10 of Earth's). Hence,

$$q = 1/2 \left(\frac{6.57 \times 10^{-3} \frac{lbs}{ft^3}}{32.2} \right) \left(60 \times 3.28 \text{ ft/ sec} \right)^2$$

$$= 4.0 \text{ PSF}$$

The footprint required on a presupposed spherical capsule resting on a five degree slope to resist this aerodynamic force is determined as follows:

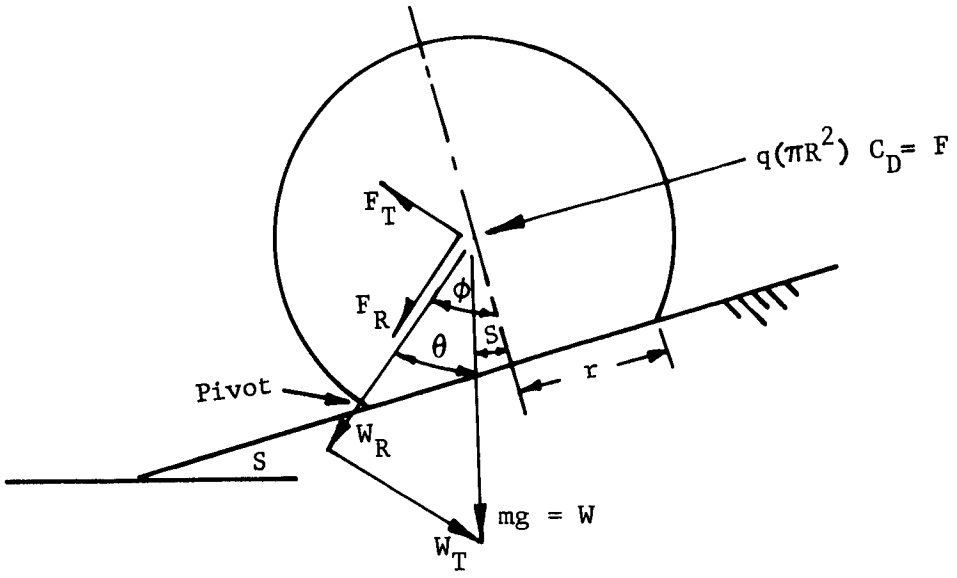

The upsetting moment about the pivot point P is RF cos (90-Ø), whereas the erecting moment due to the weight of the payload is Rmg sin (Ø-S)

where m = mass of payload

g = Martian gravity

= 12.45 Ft/Sec^2

F = Aerodynamic force

= $(\frac{1}{2}\ PV^2)\ (C_D)\ \ (A_p)$

= $q\ \pi\ R^2$ (for a conservative unity drag coefficient)

Equating moments,

$$mg \sin (\phi = S) = R^2 q\ \pi \cos (\phi - S)$$

Letting (Ø-S) = θ, and substituting

$$(m)(12.5)\sin\theta = R^2\ (4.0\ \pi)\ \cos\theta$$

$$\text{or } \tan\theta = \frac{R^2}{m}$$

Thus, the required half angle of the footprint is

$$\phi = S + \tan^{-1}\frac{R^2}{m}$$

Consider the footprint requirements for a typical payload with and without limiter resting on a five degree slope:

Typical parameters:

Impact velocity - 400 Ft/Sec

Limiter diameter - 5 Ft.

Payload diameter - 1.4 ft $\left(\frac{\rho_{Payload}}{\rho_{Limiter}} = 15\right)$

Limiter weight - 450#

Payload weight - 150#

Case I - With Limiter

$S = 5$ degrees

$R^2 = 6.25\ Ft^2$

$m = \frac{600}{32.2} = 18.6$ slugs

$\phi = 5^o + \tan^{-1}\frac{6.25}{18.6} = 23.5^o$

and footprint diameter = 5 sin 23.5 = 2 ft.

Case II - Without Limiter

$S = 5$ degrees

$R^2 = .5\ ft^2$

$m = \frac{150}{32.2} = 4.66$ slugs

$\phi = 5^o + \tan^{-1}\frac{.5}{4.66} = 11^o$ and footprint diameter = $1.4 \sin 11^o = .267$ Ft.

Thus, removal of the limiter diminishes the footprint diameter requirements for wind resistance by a factor of nearly eight.

The stability requirements for porting are minimized by minimizing the magnitude of the porting impulse. Porting would normally consist of "breaking through" the inner fiberglass shells and the outer balsawood cover. However, if these events are performed sequentially the impulse level is reduced. Thus it becomes evident that the stability requirements for both wind resistance and porting are minimized by removing the entire impact limiter prior to the stabilization/porting events. Additionally, this sequence permits the high impulse impact limiter removal event to occur prior to caging the floating payload. This permits any buffeting roll or bounce which might have been imparted to go unnoticed.

A number of methods for stabilizing the inner payload following impact limiter removal have been considered. Each presents essentially the same problems previously encountered in stabilizing the Lunar Facsimile Capsule on the Lunar surface (JPL contract 950462). The only differing factors are the presence of an atmosphere (1/10 Earth's), a heavier payload (by perhaps a factor of two) and a gravity (1/3 of Earth's) or twice that of the moon. The atmosphere does not appear to be of any assistance (but rather a hinderance due to dynamic pressures);however, the greater mass payload and gravitational field essentially increases capsule "weight" by a factor of four (over the lunar surface). This results in a greater inherent stability on a soft surface and also decreases the impulse effects of porting. Additional stability is nevertheless required for the case of resting on a hard surface.

Consideration has been given to removing portions of the impact limiter to leave a doughnut configuration. However, this approach was eliminated when it was determined that the sphere could come to rest with balsa over the flexible linear shaped porting charge thereby hindering porting, and that it does not appear inherently reliable to remove specific portions of the limiter.

A second approach considered was the use of a "foam in place" agent to form a pad beneath the resting payload. This would be an extremely effective means of stabilization since it does not require any specific presumptions about the nature of the surrounding terrain. Such an agent is by nature a two part mixture and although it appears that such an agent could be pre-compounded utilizing a volatile solvent it would be necessary to interpose it between the impact limiter and the flotation shell for release following impact limiter removal. The difficulties associated with mechanization of such a scheme precludes its utilization.

The optimal method for stabilization appears to be the use of six deployable legs mounted on three orthogonal axes. These curved legs would be stowed in a folded position against the flotation shell and passively deployed upon impact limiter removal. The selected orientation could not

allow a leg to interfere with porting unless the capsule were standing on a single leg. In the unlikely event that this occurs it is anticipated that the flexible linear shaped porting charge would completely remove the interfering leg. The governing factors for design of these legs would be that they possess a sufficient erecting moment to lift the entire weight of the payload during all positions of deployment and that their stiffness be sufficient to support the reaction of porting.

5.10.3 WEIGHT ESTIMATES FOR MECHANICAL COMPONENTS

To make weight estimates for the various components of alternative capsule configurations it is necessary that the weight of each component be expressed as a function of the maximum impact deceleration. Although the weight and volume of most operational components are fixed and insensitive to variations in "g" loading in the realm of interest, this is not the case with major structural components (i.e., shells). The weight and thickness of these structural shells and hence the payload diameter and weight are strongly influenced by the imposed impact deceleration loads. The following equations derive these relationships.

a. Flotation Shell. Upon impact, the payload flotation shell experiences two loading functions. The outer surface sees the crushing load of the yielding balsa wood impact limiter. This is reacted on the shell inner surface by a hydrostatic pressure developed by the forward inertia of the floating payload (i.e., insulation shell). The loading condition is as follows:

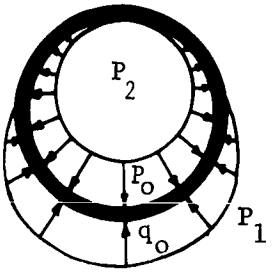

The inward or balsa force can be considered a simple cosine function;i.e.:

$$P_1 = q_o \cos\phi, \quad -\frac{\pi}{2} \leq \phi \leq \frac{\pi}{2} \qquad (1)$$

The outward hydrostatic pressure may be similarly represented as,

$$P_2 = \frac{P_o}{2}(1+\cos\phi), \quad -\pi \leq \phi \leq \pi \tag{2}$$

Hence, the total outward force is

$$\begin{aligned} F_o &= \int_o^{\pi} P_2 \, dA \\ &= \int_o^{\pi} \left[\frac{P_o}{2}(1+\cos\phi)\right]\left[2\pi R \sin\phi \, d\phi\right] \\ &= 2/3\,\pi R^2 P_o \end{aligned} \tag{3}$$

The total inward force is

$$\begin{aligned} F_i &= \int_o^{\pi/2} P_1 \, dA \\ &= 2\pi q_o R^2 \int_o^{\pi/2} \sin\phi \cos\phi \, d\phi \\ &= \pi q_o R^2 \end{aligned} \tag{4}$$

Equating equations (3) and (4) and solving for q_o allows us to express the inward pressure P_1 (Eq.1) as a function of P_o

$$q_o = 2/3\, P_o \tag{5}$$

Substituting

$$P_1 = 2/3\, P_o \cos\phi; -\frac{\pi}{2} \leq \phi \leq \frac{\pi}{2} \tag{6}$$

The net pressure acting on the flotation shell is therefore

$$\begin{aligned} P_{net} &= P_2 - P_1 \\ &= \frac{P_o}{2}\left(1 - \frac{\cos\phi}{3}\right) \end{aligned} \tag{7}$$

The maximum value of this function is $P_o/2$ which occurs at $\pi/2$

$P_o/2$ may be found by equating the previously derived expression for outward force (Eq. 3) to the maximum impact force where

$$F_{max} = n\, g \left(\frac{Wp}{g}\right) = 4/3\, \pi R^3\, n\, \rho_p \qquad (8)$$

Equating, we obtain

$$(P_{net})_{max} = \frac{P_o}{2} = R\, n\, \rho_p \qquad (9)$$

Thus, the maximum load acting on the flotation shell occurs 90 degrees out of phase with the point of impact and has a value of $R\, n\, \rho_p$.

The total stress in the shell consists of a pure compression component plus a component due to local bending. The pure compression is simply the usual membrane stress for a sphere. The bending stress, on the other hand, is more difficult to evaluate due to the complexities inherent in rigorous analytical methods when applied to spherical shells. For purposes of estimating the weight of a flotation shell an approximate approach can be used which provides a closed-form solution.

A mathematical model of the shell is given below consisting of a spherical cap subjected to a uniform pressure load reacted by a distributed mount around the free edge. Setting the edge deflection due to pressure equal to that produced by the bending moment yields

$$\frac{PR^2\,(1-\nu)}{2Et}\,\sin\alpha = \frac{2\lambda^2 \sin\alpha}{Et}\, M \qquad (10)$$

which results in the following expression for the moment:

$$M = \frac{PR^2\,(1-\nu)}{4\lambda^2} \qquad (11)$$

where λ is defined by the equation

$$\lambda^4 = 3(1-\nu^2)\left(\frac{R}{t}\right)^2 \qquad (12)$$

The total stress in the shell is

$$\sigma = \frac{PR}{2t} + \frac{3PR^2 (1-\nu)}{2\lambda^2 t^2} \quad (13)$$

$$= \frac{PR}{2t}\left[1 + \sqrt{\frac{3(1-\nu)}{(1+\nu)}}\right] \quad (14)$$

Substituting Equation (9) for $(P)_{max}$ in Equation (14) and rearranging terms yields the required shell thickness.

$$t = \frac{R^2}{2\sigma}(n\,\rho_p)\left[1 + \sqrt{\frac{3(1-\nu)}{1+\nu)}}\right] \quad (15)$$

The weight of the flotation shell is therefore given by the expression

$$W_{FLOT.} = 2\pi R^4 \left(\frac{\rho}{\sigma}\right)_m (n\rho_p)\left[1 + \sqrt{\frac{3(1-\nu)}{(1+\nu)}}\right] \quad (16)$$

Assuming the flotation shell is made of fiberglass with the following properties:

$$\rho_m = 0.069 \text{ lb/in.}^3$$

$$\sigma_m = 35{,}000 \text{ psi}$$

and

$$\nu = 0.25$$

Equation (9) reduces to

$$W_{\substack{FLOT. \\ SHELL}} = 29 \times 10^{-6} R^4 (n\rho_p) \quad (17)$$

where R is expressed in inches, n (payload deceleration) in g's, and ρ_p (payload density) is in lbs/in^3. This expression for flotation shell weight is presented in Figure 129 as a function of payload radius and the impact deceleration density product.

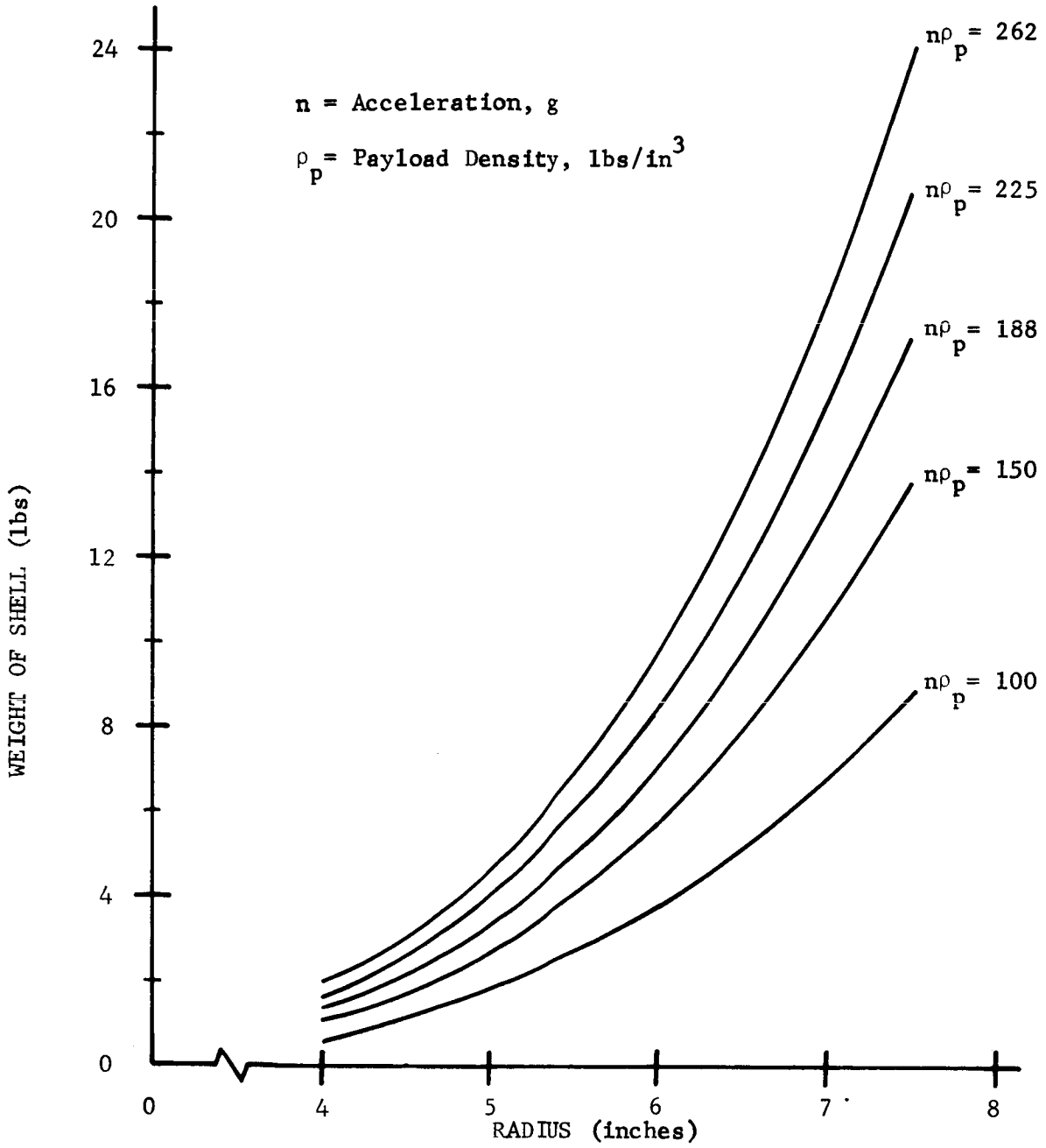
n = Acceleration, g
ρ_p = Payload Density, lbs/in^3
$n\rho_p$ = 262
$n\rho_p$ = 225
$n\rho_p$ = 188
$n\rho_p$ = 150
$n\rho_p$ = 100
WEIGHT OF SHELL (lbs)
0
4
8
12
16
20
24
0
4
5
6
7
8
RADIUS (inches)

b. Insulation Shell. The loads acting on the insulation shell are identical to those acting on the flotation shell except that they are applied in a reverse manner. Thus, the previously derived expression for flotation shell weight applies; i.e.,

$$W_{\substack{\text{INSUL.}\\ \text{SHELL}}} = 29 \times 10^{-6} R^4 (n \rho_p)$$

where R is in inches, ρ_p is in lbs/in.^{3} and n in g's.

c. Payload Structural Shell. The payload sphere is supported by the insulation during impact so that acceleration forces are introduced on one face. A cosine distribution for this induced pressure is assumed; i.e.,

$$\rho_\phi = q_o \cos \phi, \quad -\frac{\pi}{2} \leq \phi \leq \frac{\pi}{2}$$

Since $q_o = 2/3\ P_o$ (Eq. 5) and the maximum hydrostatic impact pressure, P_o, is $2 R n \rho_p$ (Eq. 9), the maximum pressure acting against the aluminum shell of the payload as a function of payload parameters is expressed as follows:

$$(P_o)_{max} = 4/3\ R n \rho_p \qquad (18)$$

The critical pressure load, P_{cr}, under which a spherical shell will buckle, as determined by theoretical considerations, is given by the equation

$$P_{cr} = \frac{2E}{\sqrt{3(1-\mu^2)}} \left(\frac{t}{R}\right)^2 \qquad (19)$$

This is based on a perfect sphere with no variations in thickness, material properties, load distribution etc. A more practical form of this equation is

$$P_{cr} = K E \left(\frac{t}{R}\right)^2 \qquad (20)$$

where the value of K may be selected on the basis of empirical data to account for all the possible imperfections. In this analysis, for purposes of estimating structural weight requirements, a value of K = 0.15 has been

selected. Equating the two pressures P_o and P_{cr} as given by equations (18) and (20) yields the following expression for shell thickness:

$$t = \left(8.90 \frac{R^3}{E} n \rho_p\right)^{\frac{1}{2}} \qquad (21)$$

Thus, the weight of the structure shell may be expressed as

$$W_{\substack{\text{struc.} \\ \text{shell}}} = 4 \pi R^2 t \rho_s \qquad (22)$$

Assuming $\rho_s = 0.1\ \#/in^3$ and $E = 10.5 \times 10^6$ psi (aluminum structure) and substituting equation (21) into equation (22) the payload shell weight expression simplifies to

$$W_{\substack{\text{struc.} \\ \text{shell}}} = R^3 \left[1.16 \times 10^{-3} \sqrt{R\, n \rho_p}\right] \qquad (23)$$

where R is expressed in inches and ρ_p is the payload density in pounds per cubic inch. The weight of the structure shell is plotted in Figure 130 as a function of payload radius for various deceleration density products.

d. Payload Inner Structure. The weight of the structure necessary within the payload shell to distribute the pressure loading among the various components is proportional to the payload volume; i.e.,

$$W_{\substack{\text{Inner} \\ \text{Struc.}}} = C\, V_p\, \rho_s$$

Previous experience with Ranger capsules and other more recent capsule designs indicates a reasonable choice for the constant coefficient is 0.0785. Assuming $\rho_s = 0.1\ \#/in^3$ (aluminum structure) and noting $V_{payload} = V_{comp.} + V_{struc.}$ we obtain an expression for inner structure weight as a function of the housed component volumes.

$$W_{\substack{\text{Inner} \\ \text{Struc.}}} = 7.91 \times 10^{-3}\, V_p$$

where V_p is expressed in $in.^3$.

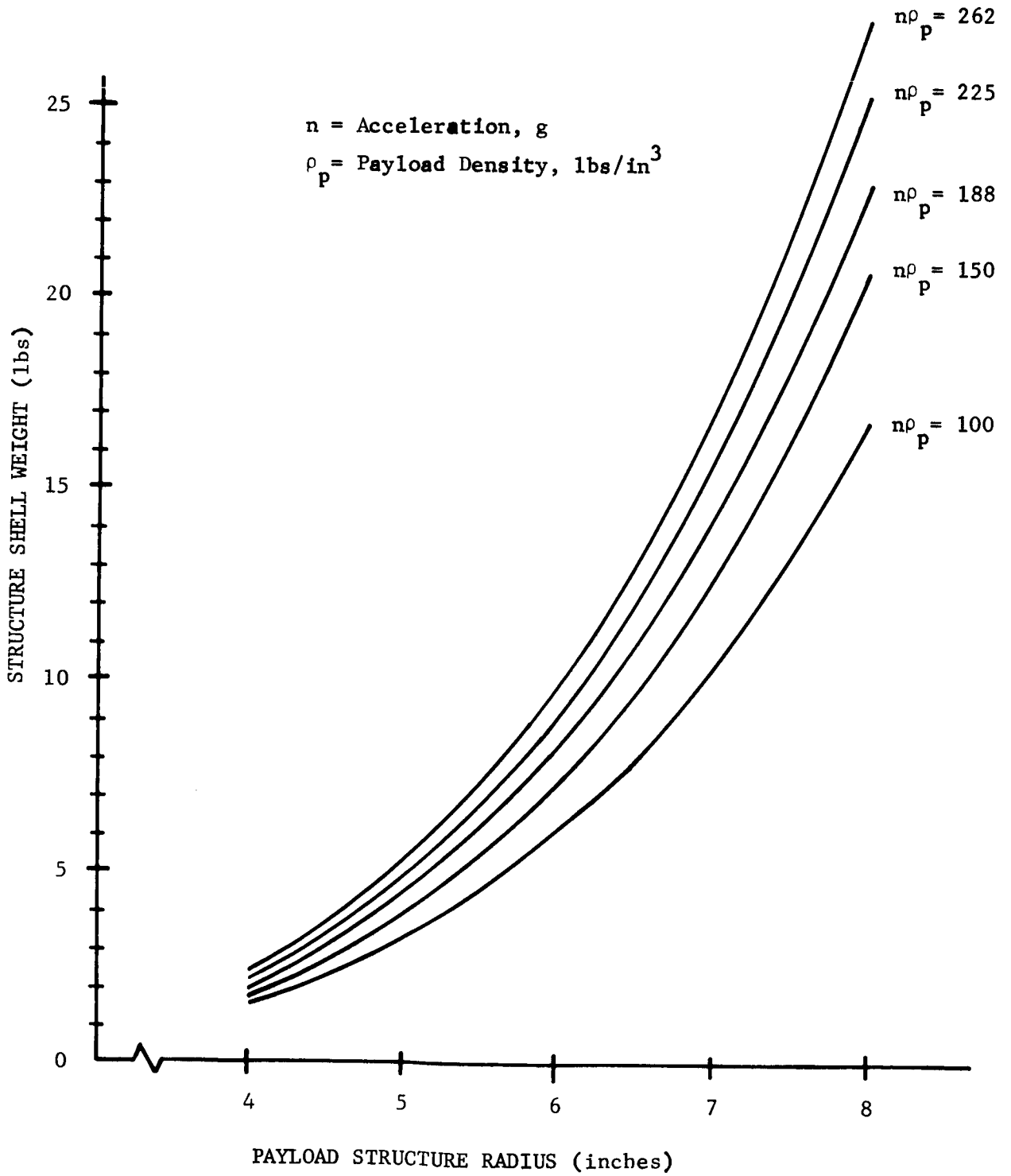

FIGURE 130. WEIGHT OF ALUMINUM STRUCTURAL SHELL

e. Limiter Cover. The limiter cover is composed of two layers of .010 epoxy-fiberglass with an intermediary layer of .030 silicon modified rubber. Its weight is expressed as follows:

$$W = 4\pi R_p^2 \left(\rho_R t_R + \rho_{fg} t_{fg} \right)$$

where

$$\rho_R = 77.7 \text{ lbs/ft}^3$$

$$\rho_{fg} = 121 \text{ lbs/ft}^3$$

$$W_{\substack{lim \\ cover}} = 4.87 R_T^2$$

where

R_p is in ft.

The weight of the flotation fluid and insulation are expressed by similar functions.

5.10.4 CONFIGURATION TRADEOFF CURVES

The size and weight of the total capsule configuration varies with:

(1) The weight and density of the housed components

(2) The impact velocity

(3) The impact load factor

(4) The payload/limiter density ratio.

Since these factors are interrelated, the design of a given payload is of necessity an iterative process.

The volume and, hence, radius of the inner payload (less insulation, structural and flotation shell) is established by:

(1) The fixed operational equipment requirements as depicted in Table 5.10-I

(2) The power supply requirements as dictated by the system configuration tradeoffs summarized in Table 5.10-II

TABLE 5.10-I

MFC FIXED OPERATIONAL COMPONENTS

Operational Components	Weight (lbs)	Volume (IN^3)
Top Tube Assembly	1.20	12.0
Azimuth Drive	.60	6.0
Transmitter	9.25	185.0
Tape Recorder	6.0	40.0
Other Electronic Elements	1.75	50.0
Antenna	1.75	10.0
Extension Mechanism	.40	6.0
Caging Mechanism	1.50	37.0
Porting Mechanism	2.0	5.0
TOTAL	24.45	351.0

TABLE 5.10-II

ESTIMATED MFC BATTERY REQUIREMENTS

1.	Picture size, degrees	24 x 24
2.	Picture elements, 0.1^{o} resolution	5.76×10^{4}
3.	Total bits, 4 bits/element & sync	2.50×10^{5}
4.	Communication distance, AU	1.2
5.	Transmitter output power, watts	20
6.	Transmitter efficiency, %	17.7
7.	Transmitter input power, watts	113
8.	Transmitter antenna gain, db	12
9.	Antenna beamwidth, degrees	42
10.	Antenna pointing error, degrees	8.4
11.	Transmitter bit rate, bps	12
12.	Total required transmission time, hrs.	5.8
13.	Transmission time/day, hrs.	2.0
14.	Minimum days transmission	2.9
15.	Energy required for transmission, watts	655
16.	Total capsule energy, watts	719
17.	Battery energy density, watt-hrs/lb	40
18.	Battery weight density, lbs/ft^{3}	140
19.	Battery weight, lbs.	18
20.	Battery volume, ft^{3}	.13

(3) The thermal control fluid requirements expressed as a function of internal heat dissipation

(4) The internal structure required to house the aforementioned components

Consideration of these factors allows us to calculate the internal radius and weight of the "component payload".

To this, then, must be added the weight and thickness of: 1) the structural aluminum shell, 2) insulation, 3) the fiberglass insulation shell, 4) the flotation fluid, and 5) the figerglass flotation shell. This determines the weight and radius of the "inner payload".

The thickness of the insulation and flotation fluid are relatively fixed by thermal and erection considerations at 1 inch and .1 inch, respectively. The thickness and weight of the flotation and insulation shells are a function of both their radius and impact loading with the former exerting the stronger influence in the realm of interest (i.e., 2000 to 3000 g's). This latter fact allows the shells to be sized from the inside out based on radius and a representative loading of 2500 g's.

The foregoing plus the weight of the limiter removal device, limiter cover, and stabilization legs establishes a "total payload weight" from which an initial determination of impact limiter size and maximum deceleration may be made for use in subsequent iterations. Table 5.10-III presents the weight allocation and load factor determined for the conceptual design configuration. The method of determining these weights is discussed in detail in Section 5.10.5.

To assess the sensitivity of the Mars Facsimile Capsule for various choices of mission constraints and tradeoff parameters invariably ends with the determination of a value for the total battery weight. This battery weight must then be included in the foregoing analysis and a resultant total capsule weight determined. Figure 131 is a plot of total capsule weight vs maximum allowable impact velocity for various battery weights. This figure in conjunction with picking other mission constraints and tradeoff parameters in a manner similar to Table 5.10-II permits the quick assessment of the MFC parameter sensitivity.

5.10.5 MFC SIZING

Case: 400 ft/sec
18 lbs. of battery
719 watt-hours

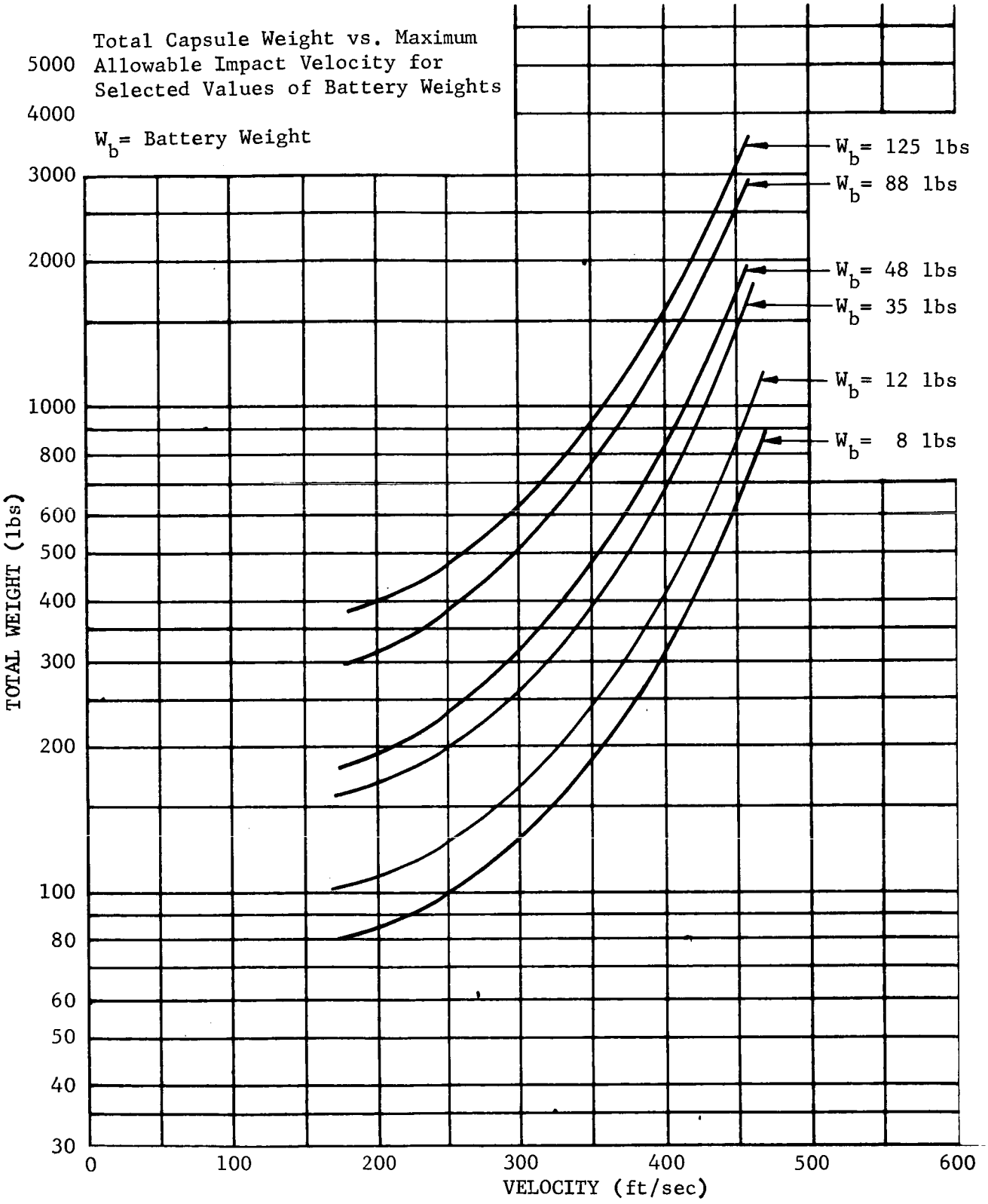
Total Capsule Weight vs. Maximum Allowable Impact Velocity for Selected Values of Battery Weights
W_b= Battery Weight
W_b= 125 lbs
W_b= 88 lbs
W_b= 48 lbs
W_b= 35 lbs
W_b= 12 lbs
W_b= 8 lbs
TOTAL WEIGHT (lbs)
5000
4000
3000
2000
1000
800
600
500
400
300
200
100
80
60
50
40
30
0
100
200
300
400
500
600
VELOCITY (ft/sec)

FIGURE 131.

TABLE 5.10-III

CONCEPTUAL DESIGN WEIGHT ALLOCATION

DESCRIPTION	WEIGHT	
Inner Payload:		
Power Supply	18.0	
Operational Equipment	24.5	
Structure	5.2	
Thermal Control Fluid	1.3	
Total		49.0
Structure Shell	5.5	
Insulation	5.5	
Insulation Shell	8.5	
Flotation Fluid	3.5	
Flotation Shell	10.1	
Stabilizing Legs	3.0	
Limiter Removal	3.0	
Impact Limiter Cover	27.0	
Total		66.1
Total Payload Weight		115.1

Estimated Total Weight	450 lbs.
Outer Radius	2.35 ft.
Inner Radius	0.605 ft.
Load Factor	2500 g's
Limiter Weight	334.9 lbs.

(a) Fixed operational equipment (Table 5.10-I):

$$34.5 \text{ lbs.}$$
$$351 \text{ in}^3$$

(b) Battery:

$$V_b = \frac{(18)(1728)}{140} = 222 \text{ in.}^3$$

(c) Thermal Fluid:

$$W_{tf} = \frac{(.5)(719)}{284} = 1.3 \text{ lbs.}$$

$$V_{tf} = \frac{(1.3)(1728)}{62.4} = 36 \text{ in.}^3$$

(d) Estimated Voids:

$$V_v = (.08)(351 + 222 + 36) = 50 \text{ in.}^3$$

(e) Weight Internal Structure:

$$V_{is} = (7.91 \times 10^{-2})(659) = 52 \text{ in.}^3$$

$$W_{is} = 5.2 \text{ lbs.}$$

(f) Inner Payload Structure:

Volume = 711 in.^{3}

Weight = 49.0 lbs.

Radius = 5.53 in.

(g) Structure Shell:

$$t_{ss} = \left[8.9 \times \frac{R^3}{E} \times (n \rho_p) \right]^{\frac{1}{2}}$$

$$n \rho_p = (2500)(\frac{6.7}{1728} \times 15) = 145 \text{ lbs/in.}^3$$

$$E = 10.4 \times 10^6 \text{ psi}$$

$$R = 5.53 \text{ in.}$$

$$t_{ss} = .145 \text{ in.}$$

Outer radius = 5.67

Volume = 55 $in.^3$

Weight = 5.5 lbs.

(h) Insulation Weight:

Inner Radius = 5.67 in.

Outer Radius = 6.67 in.

$$V_i = 4.19 \left[(6.67)^3 - (5.67)^3 \right] = 473 \text{ in.}^3$$

$$W_i = (.274)(20 \text{ lbs/ft}^3) = 5.5 \text{ lbs.}$$

(i) Insulation Shell:

Inner Radius = 6.67 in.

$$t_{is} = \frac{R^2}{2\sigma} (n\rho_p) \left[1 + \sqrt{\frac{3(1-\nu)}{1+\nu}} \right]$$

σ = 35,000 psi

ν = .25

$$t_{is} = (4.85 \times 10^{-3}) R^2 = .216 \text{ in.}$$

$$V_{is} = (\pi) D^2 t_{is} = 121 \text{ in.}^3$$

Shell density = .07 $lbs/in.^3$

W_{is} = 8.5 lbs.

(j) Flotation Fluid:

Inner Radius = 6.886 in.

Thickness = .1 in.

Density = 100 lbs/ft^3

Weight = $(\pi D^2 t)\ \rho$ = 3.45 lbs.

(k) Flotation Shell:

Inner Radius = 6.986

$t_{fs} = (4.85 \times 10^{-3})R^2 = .236$ in.

$V_{fs} = \pi D^2 t = 144.5$ in.^{3}

Shell density = .07 lbs/in.^{3}

$W_{fs} = 10.1$ lbs.

(l) Limiter Cover:

By successive iteration with the impact limiter design curves the limiter cover weight, total capsule weight, and total capsule radius can be found. For the case at hand:

$W_{\ell c} = 4.87 R^2 = 27$ lbs.

SECTION 6

APPENDICIES

6.1 ENVIRONMENT MODEL

6.1.1 SURFACE MODEL

It is obviously not possible to make any definitive statement as to Martian topography or surface character. The Martian surface has never been seen with a resolution greater than about 75 km. Some inferences and educated guesses can be made, and these must serve until firmer direction is given to speculations, perhaps by a Mars Mariner.

There are no abrupt elevation changes on Mars greater than about 2000 meters unless they lie almost east-west. Such changes would cast shadows observable from Earth. Irregularities in the edge of the disk would also be noticed. A gradual change of almost any amount would remain unnoticed, however. It is even conceivable that the difference between dynamical and optical oblateness is due to a nonequilibrium bulge at the equator, a bulge rising several kilometers above the mean figure. Such gradual changes are not important to a lander in any event. Abrupt elevation changes due to fault scarps could easily exist, although they are not as likely as on Earth. It would be difficult to protect against such a formation anyway, so assume they do not exist. In an actual flight some insurance against fault scarps, volcanoes, etc., can be acquired by avoiding landings in certain suggestive areas.

On a smaller scale one may expect to find a number of meteor craters. Mars is nearer the asteroid belt and has a much thinner atmosphere then Earth. Features such as the Arizona Meteor Crater should exist in significant numbers as well as some larger craters with accompanying

secondary craters and ejecta. Nothing remotely approaching the Moon in either crater size or number is anticipated, however.

There most definitely seems to be dust and sand on Mars. The evidence for this has been set forth in numerous books and articles. The ability of the dark areas to recover from a thorough dusting would indicate that the amount of dust and sand involved, on the average, can be measured in centimeters rather than meters, since the best evidence is that the dark areas are generally, if anything, somewhat lower in elevation than the bright areas.

The existence of ancient ocean basins and sedimentary rocks on Mars can certainly not be ruled out. Neither is there any positive evidence for them. Such positive evidence as exists, polarimetric and spectrometric, is indicative of finely divided oxides of iron in various stages of hydration in the bright areas. This says little about the underlying rocks, although the limonite type dust and sand must obviously come from somewhere. For want of a better guess, basalt can be assumed as the underlying rock.

In summary, assume a basaltic surface, sometimes bare, sometimes with as much as 50 cm of powdered limonite on top of it. It is not easy for wind to move very finely divided material. Assume the sand (Limonite) consists of particles with diameters from 0.5 mm to 3.0 mm. Assume there is a small amount of dust present, diameter 5μ to 50μ, but not nearly enough to fill up the interstices in the sand. Assume there are randomly scattered rocks and boulders with jagged shapes (ejecta, not water worn) in all sizes from 3 mm on up to 2 meters in mean diameter (mass effectively infinite with respect to the payload). Assume the prevailing slopes are gentle (less than five degrees) except for craters. It must be assumed that should the payload land in a crater, however, that it could roll for a considerable distance if its shape were generally spherical.

6.1.2 SURFACE ENVIRONMENT

Winds will never exceed 60 meters/second and will be less than thirty meters/second for 80 percent of the time. The most likely time for high winds will be late afternoon on Mars. The surface pressure is 40 ± 20 mb, consisting of 3 mb of CO_2, 2 mb of A, and 35 mb of N_2. Oxygen has never been detected and is certainly less than 0.1 mb. There are $14 \pm 7\mu$ of precipitable water vapor in the atmosphere.

The absolute maximum daytime ground temperature for a bright area near the equator at perihelion is $310^{o}K$. The atmospheric temperature at a height of 2 meters above that location os $250^{o}K$. The absolute minimum ground temperature for that location is $200^{o}K$ (near sunrise). The minimum

air temperature will be about the same or slightly higher. Use 205°K, if you need a number. Dark areas will generally be five to ten degrees warmer than bright areas during the day. At night? Approaching the poles the minima will remain about the same, while the maxima decrease to a value only slightly greater than the minima.

6.1.3 GEOPHYSICAL PARAMETERS

The Martian gravitational constant GM is 4.297780×10^4 Km^3/sec^2 where M is the mass of Mars and G is the universal constant of gravitation. The mean radius of Mars is 3360 km. The dynamic ellipticity of Mars e is 1/191.8. The equatorial radius is 3374 km, and the polar radius is 3347 km. These numbers are all subject to error, of course, but an analysis of these errors is not critical for the present study.

The period of rotation of Mars is $24^h\ 37^m\ 22\overset{s}{.}6689$. The coordinates of the Martian north pole are $\alpha_o = 316\overset{\circ}{.}55$ and $\delta_o = 52\overset{\circ}{.}85$, epoch 1905.0. The inclination of the Martian equator to the orbital plane may be taken as 25°. Again, possible errors in these values are not critical to the task at hand.

6.1.4 PHOTOMETRIC CHARACTERISTICS

The Sun's electromagnetic output is a reasonably well known quantity. The Martian atmosphere and surface are <u>not</u> well known quantities, making specification of surface light levels and spectral distribution a somewhat problematical undertaking. The best model for the present undertaking would seem to be a simple one, since much elaboration could be as easily in the wrong sense as in the right.

Assume the solar constant is 2.00 $cal/cm^2/min$ at <u>one</u> AU from the Sun, with the spectral distribution as given in Allen's <u>Astrophysical Quantities</u>, 2nd. edition (1963) on page 172. Assume the atmospheric transmission and solid surface reflectivities given by Opik in "The Atmosphere and Maze of Mars," Journal of Geophysical Research, Vol. 65, No. 10 (October 1960), pgs 3057-3063. While not necessarily subscribing to Opik's interpretation, his (Barabashev) data is based on observation and should be satisfactory for this study, although it undoubtedly contains errors due to the small equipment used. The data extends only to 4000 Å. It is generally (though not universally) assumed that there is ozone in the Martian atmosphere. Therefore, assume said atmosphere has essentially zero transmission from 2200 Å to 3000 Å and a linear transition from zero to 3000 Å to the 0.051 at 4050 Å given in Opik's article. Throughout, the visible, discrete absorption should be considered negligible.

Radiation levels and spectral distribution will thus be assumed to be strictly those of the Sun as modified by the assumed atmospheric transmission (given as a function of wavelength) and as reflected from the surrounding terrain (aerrain?) of given reflectivity. Changes in light level due to local topography (landing in the shade of a boulder, etc.) will be more severe than errors in this relatively simple model.

6.2 STUDIES OF BASIC PROBLEMS IN THE DYNAMICS OF CRUSHUP

These studies were performed in order to arrive at a fundamental understanding of some of the essential features of dynamic crushup phenomena. In order to eliminate mathematical complexities which tend to obscure some of the essential physical aspects of the phenomena under consideration, certain simplifications and idealizations were utilized in the analytic studies. The approach adopted was to select mathematical representations which distill out the essence of the problem while avoiding excessive mathematical complexities; that is, to retain the important fundamental characteristics of the physical situation being modeled and thereby highlight and focus attention on the salient features of the phenomena. The studies in this appendix are concerned with the treatment of "one-dimensional problems"which illustrate some important characteristics of the SHOCK WAVE NATURE of the propagation of crushing deformation.

6.2.1 LOAD APPLIED TO CYLINDRICAL MASS

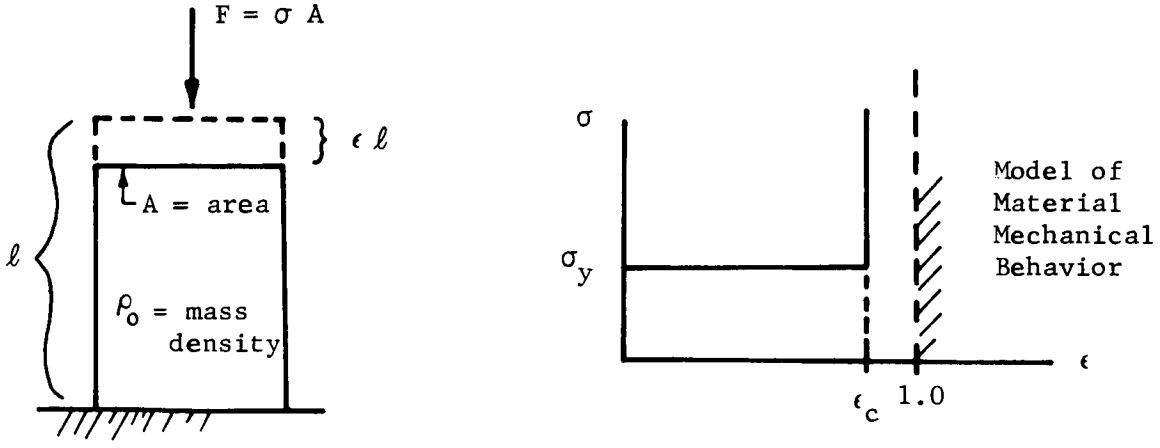

The model adopted to represent the mechanical behavior of the material is a simplified idealization which retains the essential features characterizing the deformation of crushable materials such as balsa wood. Crushing deformation takes place at a constant stress level σ_y until a compressive strain of magnitude ϵ_c is reached. Thereafter compressibility is negligible (relative to the magnitude of ϵ_c) and stress increases at essentially constant strain. At stresses smaller than σ_y, compressibility is negligible compared to the magnitude of ϵ_c. Strain rate effects are not considered. Crushing deformation is dynamically propagated by means of a "shock" process; that is, in a differential time increment a differential element of the material crushes up to the strain ϵ_c. For a finite rate of propagation of crushing deformation the stress in the crushed material (material at strain ϵ_c) must exceed the yield stress σ_y by a finite increment. The stress in the uncrushed material is σ_y. The situation is depicted below.

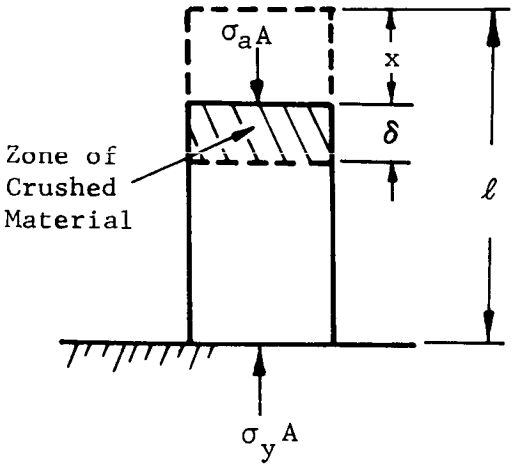

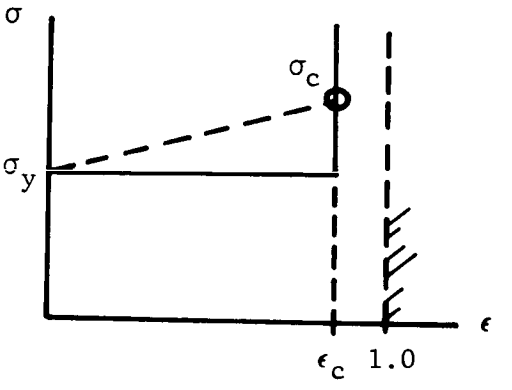

The stress level σ_c in an element of material in the crushed zone exceeds the yield stress σ_y by a finite increment as indicated in the above sketch. For the situation depicted in the above sketch, σ_c will not be uniform (that is, constant) throughout the crushed zone unless the time dependence of the applied stress σ_a is such that the velocity (dx/dt) of the crushed material is constant (that is, $d^2x/dt^2 = 0$). It should be noted that according to the model adopted for the mechanical behavior of the material, as indicated above, the zone of crushed material behaves essentially as a rigid body.

The differential equation governing the dynamic propagation of crushing deformation for the situation under consideration can be obtained from the straightforward application of momentum principles:

$$\sigma_a - \sigma_y = \rho_o \left[(x + \delta) \frac{d\dot{x}}{dt} + \dot{x} \frac{d}{dt} (x + \delta) \right] \tag{1}$$

or

$$\sigma_a - \sigma_y = \rho_o \frac{d}{dt} \left[(x + \delta) \dot{x} \right] \tag{2}$$

where

$$\dot{x} = \frac{dx}{dt}$$

But

$$x = \epsilon_c (x + \delta) \quad \text{or} \quad x + \delta = x/\epsilon_c$$

so that Equation (2) becomes

$$\frac{(\sigma_a - \sigma_y)\epsilon_c}{\rho_o} = \frac{d}{dt} (x\dot{x}) \tag{3}$$

since

$$\frac{d\epsilon_c}{dt} = 0 \tag{4}$$

Integrating Equation (3) between the limits x, $\dot{x}$, t and x_o, $\dot{x}_o$, t_o for a constant applied stress σ_a (that is, $d\sigma_a/dt = 0$):

$$x\dot{x} - x_o\dot{x}_o = \frac{\epsilon_c (\sigma_a - \sigma_y)}{\rho_o} (t - t_o) \tag{5}$$

Integrating again between the same limits:

$$x^2 - x_o^2 = \frac{\epsilon_c (\sigma_a - \sigma_y)}{\rho_o} (t - t_o)^2 + 2 x_o \dot{x}_o (t - t_o) \tag{6}$$

Eliminating $(t - t_o)$ between Eqs. (5) and (6):

$$\dot{x}^2 = \frac{x_o^2}{x^2} \left[\dot{x}_o^2 - \frac{\epsilon_c (\sigma_a - \sigma_y)}{\rho_o} \right] + \frac{\epsilon_c (\sigma_a - \sigma_y)}{\rho_o} \tag{7}$$

For $x_o = 0$, Eq. (7) gives

$$\dot{x}^2 = \frac{\epsilon_c (\sigma_a - \sigma_y)}{\rho_o} \quad \text{or} \quad \dot{x} = \sqrt{\frac{\epsilon_c (\sigma_a - \sigma_y)}{\rho_o}} \tag{8}$$

Eq. (8) is a well known relationship directly obtainable from the classical Rankine-Hugoniot relations governing the general case of one dimensional shock wave propagation.[1] [Note that $d\sigma_a/dt = 0$ in Eqs. (7) and (8).]

If $\sigma_a = \sigma_y$, Eq. (7) becomes

$$\dot{x} = \frac{x_o}{x} \dot{x}_o \tag{9}$$

Eq. (9) is valid only for $x + \delta = \frac{x}{\epsilon_c} \leq \ell$. It is seen that $\dot{x}$ is non-zero only for non-zero x_o and $\dot{x}_o$. Eq. (9) would describe the dynamic propagation of crushing deformation in the following case for $t > t_1$ (replacing x_o, $\dot{x}_o$ in Eq. (9) by x_1, $\dot{x}_1$ below):

$t = t_o$: $x_o = 0$, $\dot{x}_o = 0$

$t_o < t \leq t_1$: $\sigma_a - \sigma_y > 0$

[1] See Goldsmith, W., Impact, Arnold, London, 1960, p. 147.

$$t_o < t \leq t_1 : \quad \dot{x} = \sqrt{\frac{\epsilon_c(\sigma_a - \sigma_y)}{\rho_o}}$$

$$x = \sqrt{\frac{\epsilon_c(\sigma_a - \sigma_y)}{\rho_o}}(t - t_o)$$

$$t = t_1 : \dot{x}_1 = \sqrt{\frac{\epsilon_c(\sigma_a - \sigma_y)}{\rho_o}}$$

$$x_1 = \sqrt{\frac{\epsilon_c(\sigma_a - \sigma_y)}{\rho_o}}(t_1 - t_o)$$

$t \geq t_1 : \sigma_a - \sigma_y = 0$, and replacing x_o, $\dot{x}_o$ in Eq.(9) by x_1, $\dot{x}_1$: $\dot{x} = \dot{x}_1 x_1 / x$

Returning to Eq. (8) and rewriting it as follows:

$$\frac{(\sigma_a - \sigma_y)\epsilon_c}{W_o} = \frac{\dot{x}^2}{g} \qquad (10)$$

where $W_o = \rho_o / g$ = weight density of material

and $g = 32.2$ ft/sec^2, and expressing $\sigma_a - \sigma_y$ in psi and W_o in lb/ft^3 (pcf), with $\dot{x}$ in ft/sec (fps), Eq. (10) becomes

$$\frac{\epsilon_c(\sigma_a - \sigma_y)}{W_o} = (2.15 \times 10^{-4})\, \dot{x}^2 \left[\frac{(\text{psi})/(\text{pcf})}{(\text{fps})^2}\right] \qquad (10a)$$

Eq. (10a) is plotted below

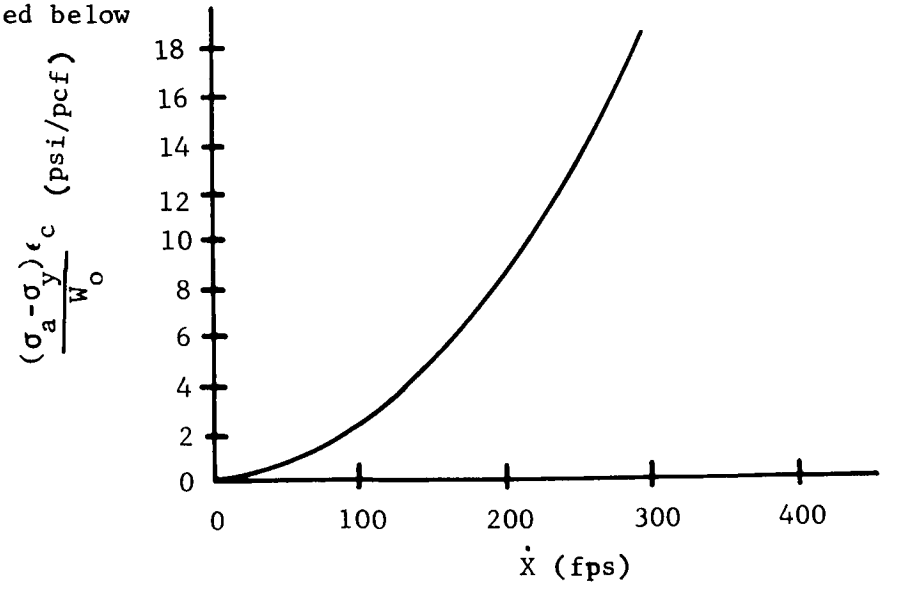

The plot below shows values of $\epsilon_c(\sigma_a-\sigma_y)$ vs $\dot{x}$ for two values of W_o representative of the range for balsa wood:

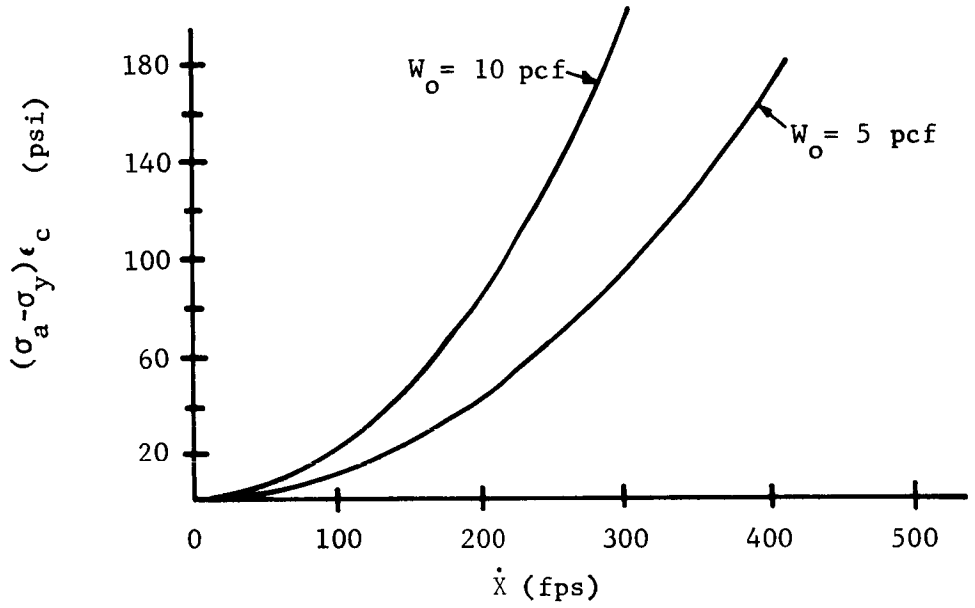

It is seen that for $\sigma_y \sim 10^3$ psi, W_o = 10 pcf, and $\dot{x} \sim 200$ fps or less, then

$\sigma_a - \sigma_y \sim 0.1\,\sigma_y$ or less.

For W_o = 5 pcf, $\sigma_a-\sigma_y \sim 0.1\,\sigma_y$ or less if $\dot{x} \sim 300$ fps or less. For higher velocities $\dot{x}$, $\sigma_a-\sigma_y$ rapidly increases.

6.2.2 IMPACT OF RIGID MASS WITH CYLINDRICAL LIMITER (CRUSHABLE MATERIAL) ON RIGID PLANE

The situation under consideration here is indicated in the following sketch.

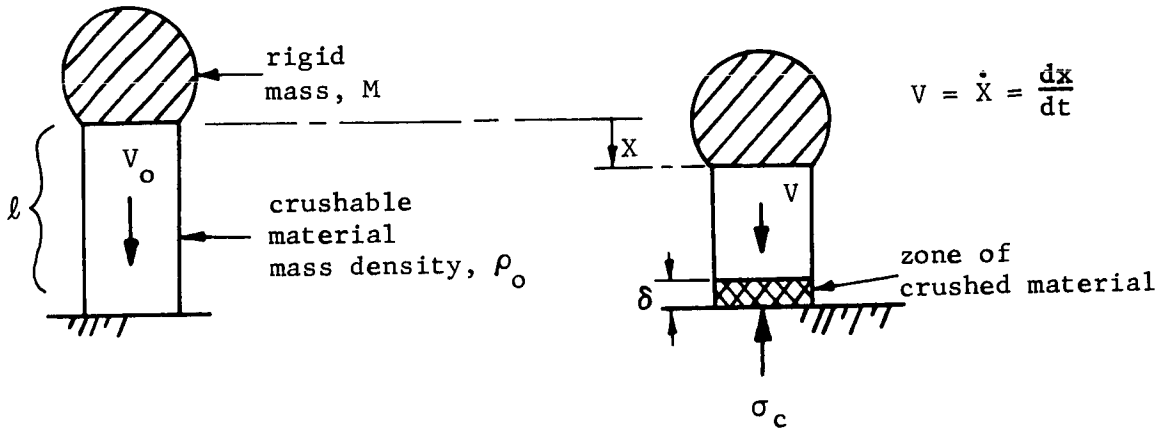

The model for the mechanical behavior of the crushable material is that adopted for use in the previous section. The stress in the zone of crushed material is σ_c. Since the crushed material has been stopped and brought to rest, the material in this zone does not experience any accelerations after the passage of the "crushing front"*, and therefore the stress σ_c is uniform (constant) throughout the zone of crushed material. In the uncrushed material immediately adjacent to (ahead of) the crushing front the stress is σ_y.

Impulse-momentum considerations across the moving crushing front give rise to the following relation between the stress discontinuity $\sigma_c - \sigma_y$ across the front and velocity V of the oncoming material ahead of the crushing front:

---

* At the "crushing front", the finite stress discontinuity $\sigma_c - \sigma_y$ reduces to zero the finite velocity of a "differential element" of mass in a "differential increment" of time.

$$\sigma_c - \sigma_y = P_o(v + \dot{\delta})V \tag{1}$$

Noting that $V = \dot{x} = \frac{dx}{dt}$ (2)

and $x + \delta = x/\epsilon_c$ (3)

so that $V + \dot{\delta} = \dot{x} + \dot{\delta} = \frac{\dot{x}}{\epsilon_c} = \frac{V}{\epsilon_c}$ (4)

Hence, Eq. (1) becomes

$$\sigma_c - \sigma_y = \frac{\rho_o}{\epsilon_c} V^2 \tag{5}$$

or

$$V^2 = \frac{\epsilon_c (\sigma_c - \sigma_y)}{\rho_o} \tag{5a}$$

As in the case of Eq. (8) of the previous section, Eq. (5a) above is a well known relationship directly obtainable from the classical Rankine-Hugoniot relations governing the general case of one dimensional shock wave propagation.

Impulse-momentum considerations applied to the entire mass of the system lead to the following differential equation:

$$\sigma_c = -\left\{\frac{M}{A} + \rho_o \left[\ell - (x + \delta)\right]\right\}\frac{dv}{dt} + \rho_o V \frac{d}{dt}(x + \delta) \tag{6}$$

Using Eqa. (2), (3), and (4), Eq. (6) becomes

$$\dot{\sigma}_c = -\left[\frac{M}{A} + \rho_o \left(\ell - \frac{x}{\epsilon_c}\right)\right]\frac{dv}{dt} \quad \frac{\rho_o}{\epsilon_c} V^2 \tag{6a}$$

Eqs. (5) and (6a) yield the following differential equation:

$$\sigma_y A = -\left[M + A\ \rho_o \left(\ell - \frac{x}{\epsilon_c}\right)\right]\frac{dv}{dt} \tag{7}$$

Equation 7 says that the acceleration of the oncoming mass ahead of the crushing front is governed by the vertical force acting on the area immediately adjacent to and above (ahead of) the crushing front. This force is determined by the yield stress σ_y and the area of the crushing front.

Utilizing the transformation $\frac{dv}{dt} = \frac{dv}{dx} \cdot \frac{dx}{dt}$, in conjunction with Eq. (2), Eq. (7) yields the following differential equation:

$$V\frac{dv}{dx} = \frac{\sigma_y}{\rho_o \ell} \frac{1}{\left[\frac{x}{\epsilon_c \ell} - \left(1+\frac{M}{A\rho_o \ell}\right)\right]} \tag{8}$$

Integrating between the limits V_o, 0 and V,X:

$$\frac{\rho_o}{\epsilon_c \sigma_y}\left(\frac{V^2 - V_o^2}{2}\right) = \log_e\left(\frac{1 + \frac{M}{AP_o\ell}\frac{X}{\epsilon_c \ell}}{1+\frac{M}{A\rho_o \ell}}\right) \tag{9}$$

or

$$\frac{X}{\epsilon_c \ell} = \left[1 - e^{\frac{\rho_o}{\epsilon_c \sigma_y}\left(\frac{V_o^2 - V^2}{2}\right)}\right]\left(1 + \frac{M}{AP_o}\right) \tag{9a}$$

The crushing process ceases when V = 0. The value of x given by Eq. (9a) for V = 0 is then the maximum stroke of the limiter during the dynamic crushing process. (Since $x = \epsilon_c \ell$ is the maximum possible crushing stroke of the limiter, the above equations are valid only for values of $(x/\epsilon_c \ell) \leq 1$. Beyond this point the limiter "bottoms out" and phenomena not modeled in the above mathematical description begin to take place). Denoting the maximum stroke of the limiter (value of x when V = 0) by x_f, Eq. (9a) gives

$$\frac{x_f}{\epsilon_c \ell} = \left(1 - e^{-\frac{\rho_o}{\epsilon_c \sigma_y}\frac{V_o^2}{2}}\right)\left(1 + \frac{M}{A\rho_o \ell}\right) \tag{10}$$

Using Eq. (10), the ratio of the initial kinetic energy of the system to the "quasi-static" energy absorption capability of the limiter (acting through a stroke of length x_f) can be computed to be

$$\frac{\left(M + A\rho_o \ell\right)\frac{V_o^2}{2}}{A\sigma_y X_f} = \frac{\beta}{1-e^{-\beta}} \tag{11}$$

where

$$\beta = \frac{\rho_o V_o^2}{2\epsilon_c \sigma_y} \tag{12}$$

The right hand side of E_q. (11) is always greater than unity for $\beta > 0$. Therefore, for $V_o > 0$ the initial kinetic energy exceeds the "quasi-static" crushing energy absorption capability of the limiter for a stroke of length x_f. The reason for this lies in the finite stress discontinuity $\sigma_c - \sigma_y$ at the crushing front. This finite discontinuity constitutes a shock wave; that is, the crushing deformation is propagated by a finite shock wave at the crushing front. It is well known that mechanical energy is not conserved in the propagation of finite shock waves. Total energy, of course, is conserved, and the energy balance is accounted for by recognizing that a portion of the mechanical energy before the shock appears as heat behind the shock. This is the well known phenomenon of "shock heating". For the analogous situation of finite shock wave propagation in a gas, it is well known that the process is nonisentropic; that is, energy is irreversibly converted into heat across the shock front. The energy thus dissipated as heat increases with increasing Mach number ahead of the shock; that is, with increasing shock strength. In the situation under consideration herein, Eq. (5) shows that the shock strength $\sigma_c - \sigma_y$ at the crushing front increases with increasing velocity of the material ahead of the front. Eqs. (11) and (12) show that not all of the initial kinetic energy of the system is absorbed in mechanical crushing of the limiter, but with increasing initial velocity, an increasing proportion of the kinetic energy is dissipated by shock heating.

Plots of Eq. (11) are shown in Figure 132.

6.2.3 SHOCK HEATING

A stationary plane shock wave (crushing front) is considered. Uncrushed material approaches the front with velocity V and density ρ_o and behind the front the crushed material has density ρ_c and velocity V_c. The stress in the crushed material is

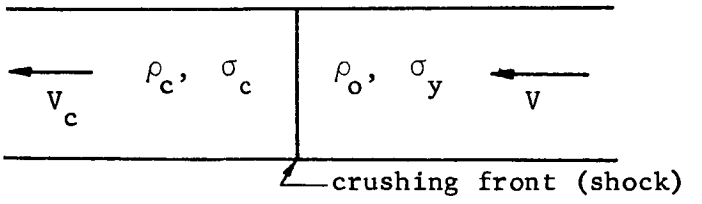

* The "quasi-static" energy absorption capability of the limiter for a stroke of length x is the limiting value as $\dot{x} = dx/dt = V \rightarrow 0$, and is equal to $\sigma_y x$. See previous section; here it is seen that the applied stress approaches σ_y as $\dot{x} \rightarrow 0$.

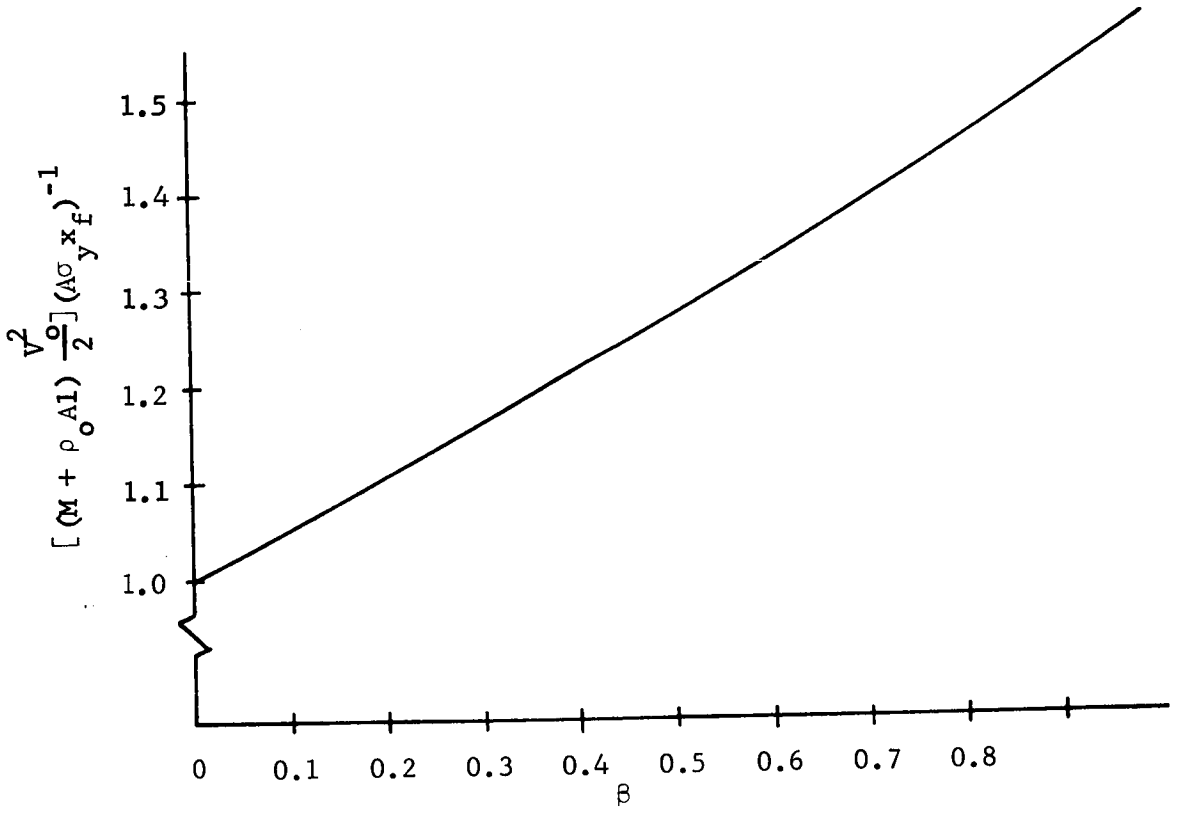

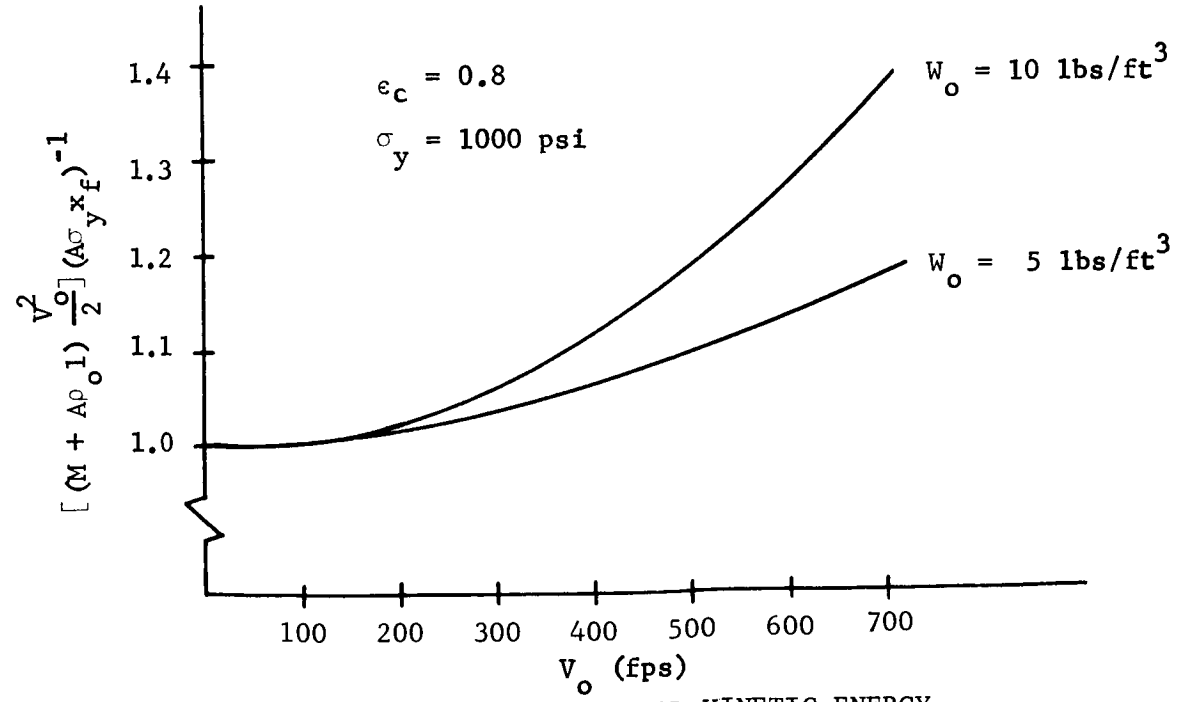

FIGURE 132. RATIO OF INITIAL KINETIC ENERGY TO QUASI-STATIC ENERGY

σ_c and in the oncoming uncrushed material the stress is σ_y . The model adopted to represent the mechanical behavior of the material is the same as that utilized in the previous sections.

A one dimensional crushup shock is considered, so that

$$\rho_o = (1 - \epsilon_c)\rho_c \tag{1}$$

Conservation of mass gives

$$\rho_o V = \rho_c V_c \tag{2}$$

Equations (1) and (2) give

$$V_c = (1 - \epsilon_c) V \tag{3}$$

The equation for conservation of momentum is

$$\rho_o V (V - V_c) = \sigma_c - \sigma_y \tag{4}$$

Eqs. (3) and (4) give

$$\rho_o V^2 \epsilon_c = \sigma_c - \sigma_y \tag{5}$$

The equation for conservation of energy is

$$\sigma_y V - \sigma_c V_c = \rho_o V \left[(\Delta I) + \frac{1}{2} \left(V_c^2 - V^2 \right) \right] \tag{6}$$

where (ΔI) is the increase in specific internal energy (that is, internal energy per unit mass) across the shock, Eqs. (3) and (6) give

$$\sigma_y - \sigma_c (1 - \epsilon_c) = \rho_o \left[(\Delta I) + \frac{V^2}{2} \epsilon_c (\epsilon_c - 2) \right] \tag{7}$$

Eqs. (5) and (7) give

$$\rho_o (\Delta I) = \frac{1}{2} (\sigma_c + \sigma_y) \epsilon_c \tag{8}$$

The energy dissipated by shock heating is the increase in internal energy less the increase in mechanical energy of deformation across the shock, so that the specific (per unit mass) energy $(\Delta E)_d$ dissipated across the shock is

$$\rho_o \ (\Delta E)_d = \rho_o \ (\Delta I) - \sigma_y \ \epsilon_c \tag{9}$$

Eqs. (8) and (9) give

$$\rho_o \ (\Delta E)_d = \frac{1}{2} \ (\sigma_c - \sigma_y) \ \epsilon_c \tag{10}$$

Eqs. (5) and (10) give

$$(\Delta E)_d = \frac{1}{2} \ V^2 \ \epsilon_c^2 \tag{11}$$

where again, $(\Delta E)_d$ is the energy per unit mass dissipated across the shock. Below is a plot showing the energy dissipated in BTU per lb. as a function of the velocity V in feet/sec (fps) for $\epsilon_c = 0.8$.

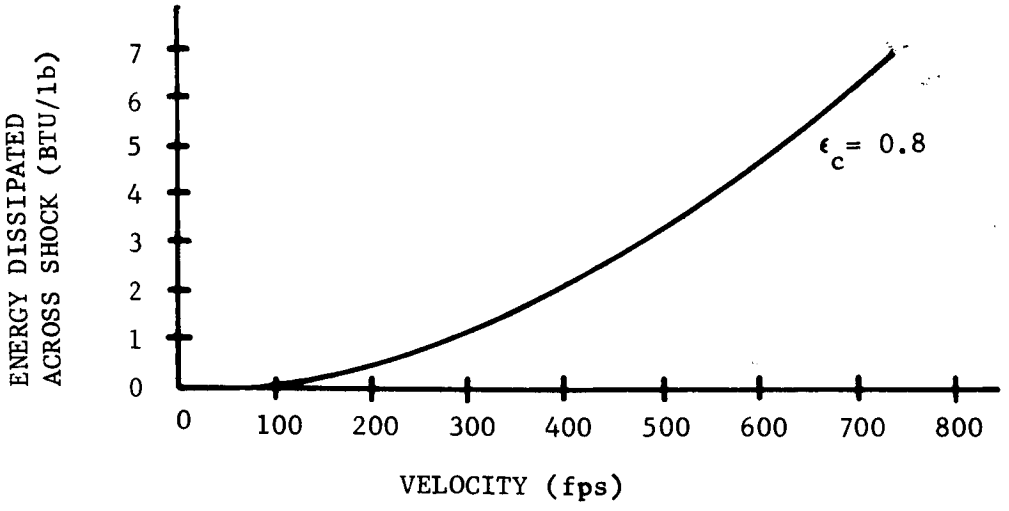

6.2.4 ENERGY BALANCE IN SHOCK WAVE EFFECT

The situation considered is a cylindrical mass impacting a rigid plane, as depicted below:

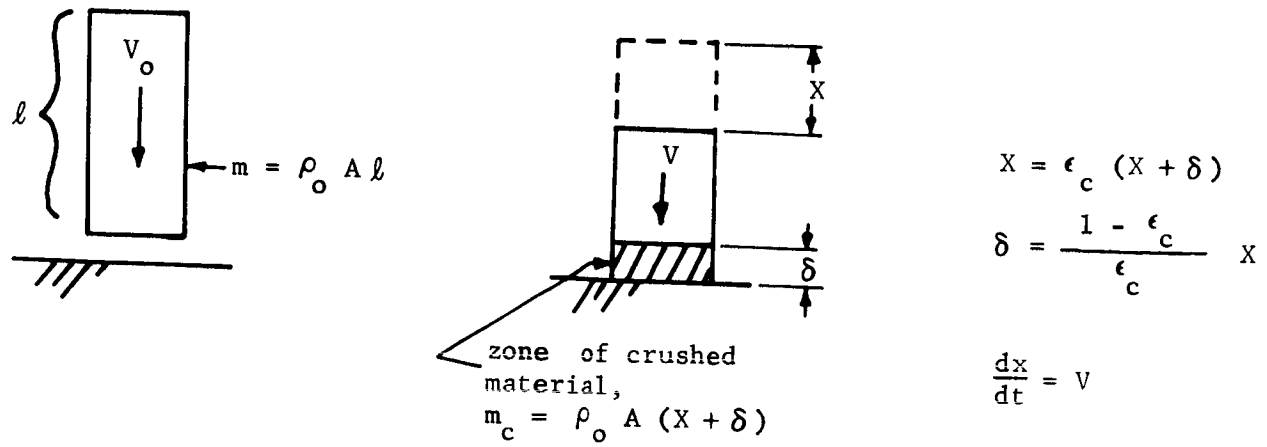

The model adopted to represent the mechanical behavior of the crushable material as it deforms under dynamic crushing conditions is the same as in previous sections.

The stress in the crushed material (which has been brought to rest) is σ_c, and the stress level in the oncoming uncrushed material just ahead of the "crushing front" is σ_y; the finite discontinuity in stress across the "crushing front" is $\sigma_c - \sigma_y$

Conservation of energy across the shock (i.e., the "crushing front") is expressed by the following equation:

$$\sigma_y V = \rho_o \left(V + \frac{d\delta}{dt}\right) \left(\Delta I - \frac{1}{2} V^2\right) \qquad (1)$$

where ΔI is the increase across the shock in specific internal energy (that is, internal energy per unit mass).

Since

$$V + \frac{d\delta}{dt} = \frac{dx}{dt} + \frac{d\delta}{dt} = \frac{1}{\epsilon_c} \frac{dx}{dt} = \frac{V}{\epsilon_c} \tag{2}$$

Eq. (1) becomes

$$\rho_o \Delta I = \frac{1}{2} \rho_o V^2 + \sigma_y \epsilon_c \tag{3}$$

The energy dissipated across the shock is the increase in internal energy less the energy absorbed in the mechanical crushing deformation of the material; that is,

$$\rho_o E_{diss} = \rho_o \Delta I - \sigma_y \epsilon_c = \frac{1}{2} \rho_o V^2 \tag{4}$$

where E_{diss} is energy per unit mass.

Conservation of momentum across the shock is expressed by the following equation:

$$(\sigma_c - \sigma_y)A = V \frac{dm_c}{dt} = \rho_o A \left(\frac{dx}{dt} + \frac{d\delta}{dt} \right) V \tag{5}$$

Using Eq. (2) Eq. (5) yields

$$\rho_o V^2 = (\sigma_c - \sigma_y) \epsilon_c \tag{6}$$

Using Eq. (6) Eq. (4) can be written

$$E_{diss} = \frac{1}{2} (\sigma_c - \sigma_y) \epsilon_c \tag{7}$$

Momentum conservation for the entire system is given by the following equation:

$$- \sigma_c A = \frac{d}{dt} \left[(m - m_c) V \right] = (m - m_c) \frac{dv}{dt} - V \frac{dm_c}{dt} \tag{8}$$

Using Eq. (5) Eq. (8) becomes

$$- \sigma_y A = (m - m_c) \frac{dv}{dt} \tag{9}$$

Writing $\frac{dv}{dt} = \frac{dx}{dt}\frac{dv}{dx} = V\frac{dv}{dx}$ (10)

Eq. (9) becomes

$$-\sigma_y A = (m - m_c) V \frac{dv}{dx} \tag{11}$$

or

$$-\sigma_y A\, dx = (m - m_c) V dV = (m - m_c)\, d\left(\frac{V^2}{2}\right) \tag{12}$$

or

$$-\sigma_y A\, dx = d\left[(m - m_c)\frac{V^2}{2}\right] + \frac{V^2}{2} dm_c \tag{13}$$

Integrating from X = 0, $m_c = 0$; $V = V_o$ to X, m_c V, Eq. (13) yields

$$-\sigma_y Ax = \frac{1}{2}\left[(m - m_c)V^2 - mV_o^2\right] + \int_o^{m_c} \frac{V^2}{2} dm_c \tag{14}$$

The left side of Eq. (14) is the mechanical energy of crushing deformation and the first term on the right hand side is the change in the kinetic energy of the system. According to Eq. (4) the energy per unit mass dissipated across the shock is

$$E_{diss} = \frac{1}{2} V^2 \tag{15}$$

so that the <u>total</u> energy dissipated across the shock during the impact shock compression process from X = 0, $V = V_o$, $m_c = 0$ to X, V, m_c is $\int_o^{m_c} \frac{V^2}{2} dm_c$,
which is the second term onthe right hand side of Eq. (14). Writing Eq. (14) for conditions when the oncoming mass has been brought to rest; that is, V = 0, $x = x_f$, $m_c = m$:

$$\frac{1}{2} mV_o^2 = \sigma_y Ax_f + \int_o^m \frac{V^2}{2} dm_c \tag{16}$$

Eq. (16) shows that the initial kinetic energy of the system is absorbed in mechanical crushing PLUS SHOCK DISSIPATION.

6.3 STUDIES OF SPHERICAL IMPACT LIMITER DYNAMICS

In this appendix, analytical studies are presented for a number of aspects of spherical impact limiter dynamics. A limiter constructed of a crushable material such as balsa wood with radially oriented grain is treated. Only symmetrical impact is considered.

In the first section, impact against a curved surface is considered. Both concave and convex hemispherical surfaces are treated and the results for the limiting case of a flat surface (that is, infinite radius of curvature) are presented. Expressions are developed for the forces acting and the energy absorbed in mechanical crushing deformation. The finite depth of the stopped, crushed material above the impact surface is neglected and the energy dissipated in the shock wave propagation of the crushing deformation is not considered. Calculations based on the one dimensional analysis developed in Appendix 6.2 indicate that for balsa wood the shock wave dissipation energy is only about 5 percent of the energy of mechanical crushing deformation at an impact velocity of 300 feet per second and around 15 percent at 500 fps (corresponding to impact velocity absorbing capability increments of less than 2.5 percent and 7.5 percent, respectively). Physical reasoning based on this analysis indicates an even smaller effect for the case of a spherical limiter. In a subsequent section of this appendix, an analysis is developed which accounts for shock dissipation effects to a first approximation for a spherical limiter impacting a flat surface. Numerical calculations based on this analysis indicate that the impact velocity absorbing increase corresponding to the shock dissipation effect is about 5 percent at around 450 fps impact velocity. Thus, it is felt that the neglect of this effect is justified in an analysis which is aimed at obtaining an initial assessment of the effects of impact surface curvature.

In the second section of this appendix, an analysis is presented of a non-homogeneous limiter which has discrete laminations; that is, the limiter is constructed of a number of layers of crushable material each having radially oriented grain. The properties of each lamination are constant throughout that layer and each layer can have properties (and thickness) different from the others. The aim of the investigation is to provide an analysis which affords an initial insight into the effects of this sort of limiter nonhomogeneity. Impact on a flat surface is treated and shock phenomena are not considered.

The next section of this appendix presents a rather general analysis accounting for shock phenomena in the impact of a mass of crushable material against a rigid surface. Explicit results are presented for a spherical mass and a flat surface.

The problem of payload breakaway, or "the cannon ball effect" is studied in the final section of this appendix.

6.3.1 CURVED IMPACT SURFACE EFFECTS

In this section, the symmetrical impact of a spherical limiter of crushable material against a curved surface is considered. Concave and convex hemispherical surfaces are treated. The aim of the analysis is to afford an initial assessment of the importance of impact surface curvature. As discussed in the introduction to this appendix, shock wave effects are not considered.

Radial sections through the limiter and curved impact surfaces are shown in Figures 133 and 134, for the concave and convex cases, respectively, and the essential features of the geometry of the situation are delineated therein. The outer radius of the limiter is denoted by R, the radius of the impact surface by R_s, and the "impact stroke" by s. The limiter has radial crushing strength σ and cross grain strength, $\alpha\sigma$. The differential vertical force dF_v acting on an elemental ring of the curved impact surface intercepted between the conical surfaces defined by the angles ϕ and $\phi + d\phi$ is

$$\begin{aligned} dF_v &= \left[\sigma (r\, d\phi)(2\pi r \sin\phi)\right]\cos\phi \\ &\quad + \left\{\alpha\sigma\left[(r\, d\phi)\tan(\phi \pm \psi)\right](2\pi r \sin\phi)\right\} \\ &= 2\pi\sigma\left[\cos\phi + \alpha\tan(\phi \pm \psi)\sin\phi\right] r^2 \sin\phi d\phi \end{aligned} \qquad (1)$$

In the above equation and in the analysis to follow the upper sign ($\pm$ or $\mp$) applies to the case of the convex impact surface and the lower sign to the concave surface.

Integrating equation (1) over the surface in contact with the limiter

$$F_v = 2\pi R^2 \int_o^{\phi_f} \sigma\left[\cos\phi + \alpha\tan(\phi \pm \psi)\sin\phi\right]\left(\frac{r}{R}\right)^2 \sin\phi\, d\phi \qquad (2)$$

where from the law of cosines

$$\left(\frac{r}{R}\right)^2 = \left(\frac{R_s}{R}\right)^2 + \left[\frac{R_s}{R} \pm \left(1 - \frac{S}{R}\right)\right]^2 - 2\left(\frac{R_s}{R}\right)\left[\frac{R_s}{R} \pm \left(1 - \frac{S}{R}\right)\right]\cos\psi \qquad (3)$$

Also from the law of sines it can be shown that

$$\begin{aligned} \psi &= \mp\phi \pm \sin^{-1}\left[\left(1 \pm \frac{R - S}{R_s}\right)\sin\phi\right] \\ &= \mp\phi \pm \sin^{-1}\left[\left(1 \pm \frac{1 - (S/R)}{R_s/R}\right)\sin\phi\right] \end{aligned} \qquad (4)$$

The upper limit of integration is found as follows:

Noting that

$$r\sin\phi = R_s\sin\psi \qquad (5)$$

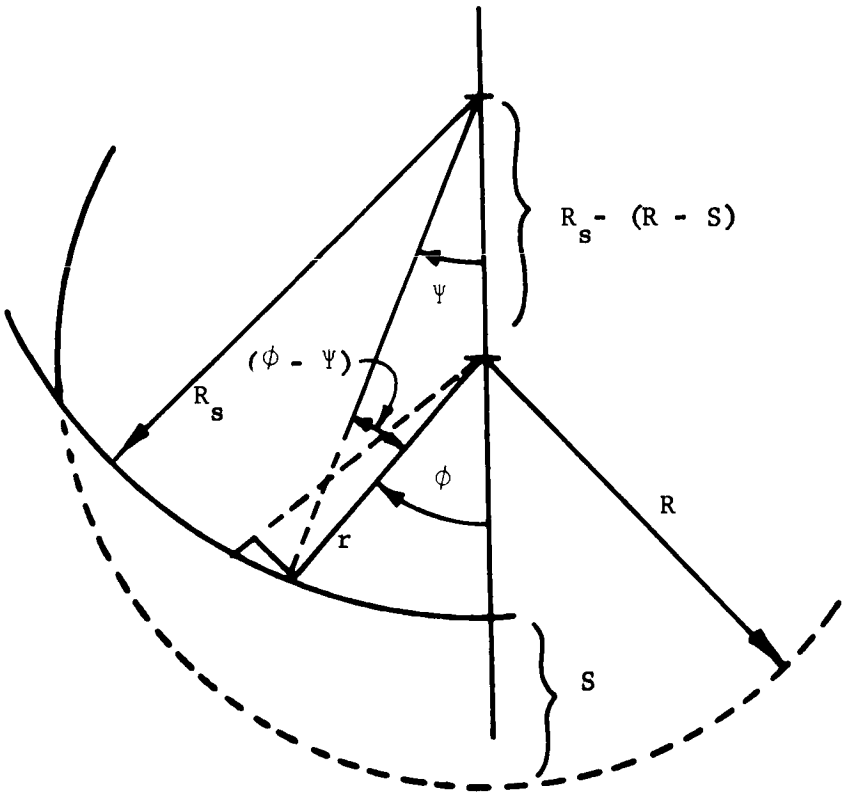

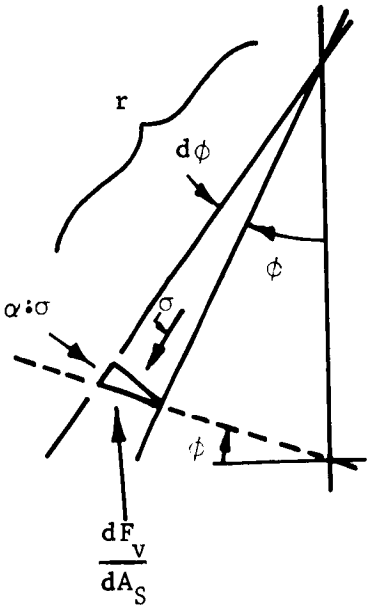

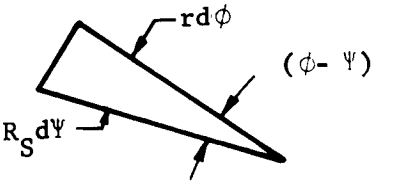

CONCAVE IMPACT SURFACE

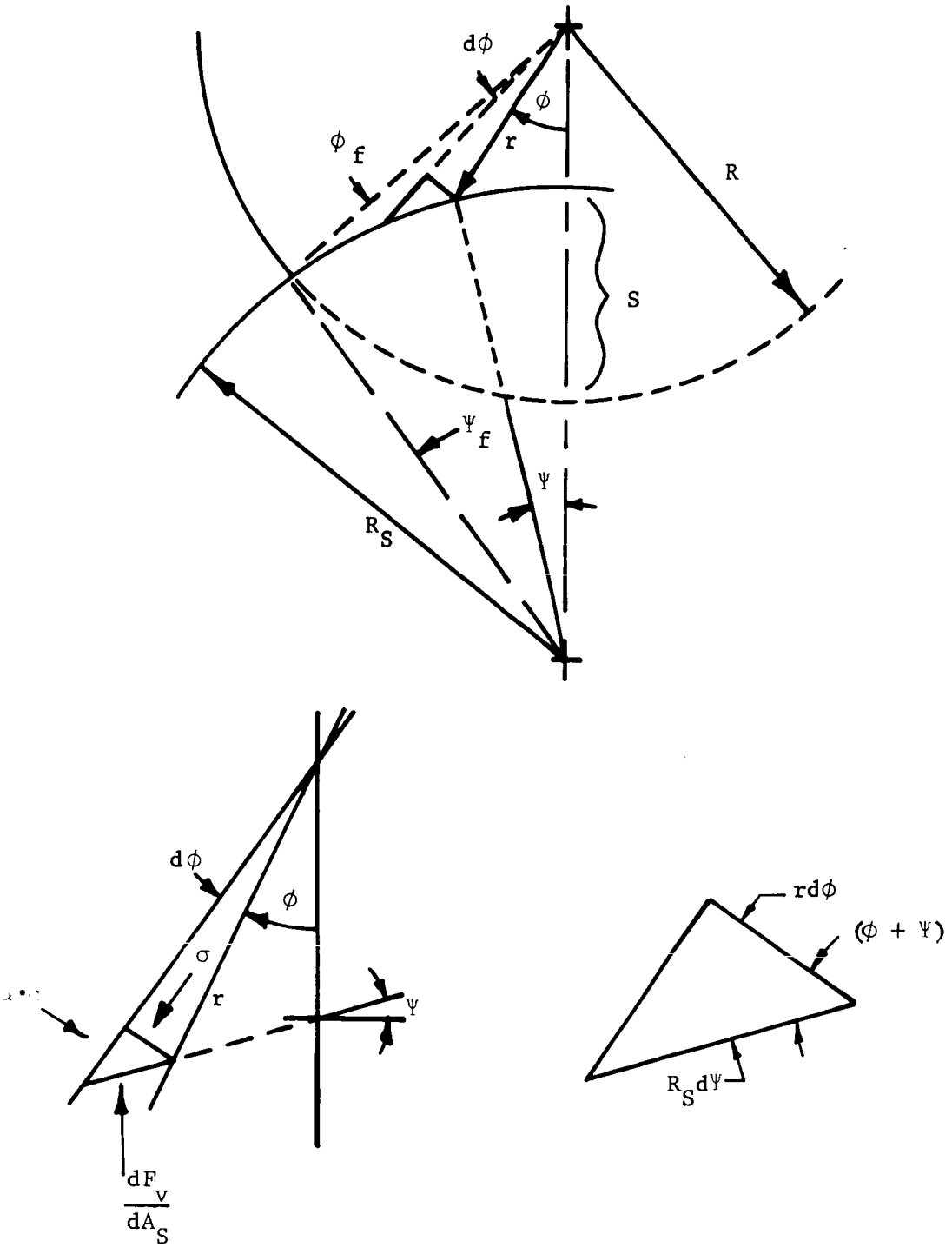

CONVEX IMPACT SURFACE

FIGURE 134

and evaluating Equation (5) at the upper limit of integration ϕ_f, one finds

$$\phi_f = \sin^{-1}\left(\frac{R_s}{R}\sin\psi_f\right) \tag{6}$$

where ψ_f is the value of ψ corresponding to ϕ_f, and can be found from Equation (3) by noting that when $\phi = \phi_f$, $(r/R) = 1$, and $\psi = \psi_f$, so that

$$\cos\psi_f = 1 - \frac{(2R - S)S}{2R_s\left[R_s \pm (R - S)\right]} \tag{7}$$

Evaluating $\sin\psi_f$ from Equation (7) and substituting in Equation (6) gives

$$\phi_f = \sin^{-1}\left(\frac{-\sqrt{\frac{S}{R}\left(2 - \frac{S}{R}\right)\left\{4\frac{R_s}{R}\left[\frac{R_s}{R} \pm \left(1 - \frac{S}{R}\right)\right] - \frac{S}{R}\left(2 - \frac{S}{R}\right)\right\}}}{2\left[\frac{R_s}{R} \pm \left(1 - \frac{S}{R}\right)\right]}\right) \tag{8}$$

As $R_s \longrightarrow 00$, $\psi \longrightarrow 0$ and the curved surface approaches a flat surface. For this case it can be shown that the above set of equations reduces to the following:

$$F_v = 2\pi R^2 \int_o^{\phi_f} \sigma(\cos\phi + \alpha\tan\phi\sin\phi)\left(\frac{r}{R}\right)^2 \sin\phi\, d\phi \tag{9}$$

where

$$\frac{r}{R} = \left(1 - \frac{S}{R}\right)/\cos\phi \tag{10}$$

and

$$\phi_f = \cos^{-1}\left(1 - \frac{S}{R}\right) \tag{11}$$

Equations (2), (3), (4), (8), (9), (10), and (11) have been programmed for high speed automatic digital computation for the general case in which the crushing strength σ is an arbitrary function of radial location in the limiter, expressed by the radius ratio (r/R). Also, the energy of crushing deformation $E_c = \int_o^{S_f} F_v ds$ over an arbitrary impact stroke S_f has been programmed for digital computation. Actually values of $F_v/2\pi R^2$ and $E_c/2\pi R^3$ are computed.

In the case where the crushing strength σ is constant, that is, is independent of (r/R), the integral for the vertical force F_v can be evaluated in closed form. It is convenient to transform the variable of integration, in this case from ϕ to ψ. Noting Equation (5) and also noting from Figures 133 and 134 that

$$r d\phi = (R_s d\psi) \cos(\phi \pm \psi) \tag{12}$$

Equation (2) can be written

$$F_v = 2\pi R_s^2 \int_o^{\phi f} \left[\cos\phi \cos(\phi \pm \psi) + \alpha \sin\phi \sin(\phi \pm \psi)\right] \sin\psi \, d\psi \tag{13}$$

From the geometry of the situation as delineated in Figures 133 and 134, it can be shown that

$$\cos\phi = \left\{\mp R_s \cos\psi \pm \left[R_s \pm (R - S)\right]\right\} r^{-1} \tag{14}$$

and

$$\cos(\phi \pm \psi) = \left\{\mp R_s \pm \left[R_s \pm (R - S)\right] \cos\psi\right\} r^{-1} \tag{15}$$

$$\sin(\phi \pm \psi) = \left\{\left[R_s \pm (R - S)\right] \sin\psi\right\} r^{-1} \tag{16}$$

where r is given by Equation (3). Using Equations (14), (15), (16), and (3), the integrand in Equation (13) can be expressed entirely in terms of the variable ψ, and the resulting expression can be integrated in closed form. Using Equation (7), and after considerable algebra, the following result is obtained:

$$\frac{F_v}{\pi R_s^2 \sigma} = \frac{1 + \alpha}{2}\left(1 - \xi_o^2\right) - \left[q\left(1 - \xi_o\right) - \left(1 - q^2\right) \ln\left(\frac{1 - q}{\xi_o - q}\right)\right](1 - \alpha) \tag{17}$$

where

$$q = \left(1 + p^2\right)/2p \tag{18}$$

$$\xi_o = q - \left(\lambda^2/2p\right) \tag{19}$$

$$p = 1 \pm \left[(R - S)/R_s\right] \tag{20}$$

$$\lambda = R/R_s \tag{21}$$

The corresponding result for a flat impact surface can be obtained either by integrating Equation (9) directly, holding σ constant, or by evaluating the limiting form of Equation (17) using Equations (18) through (21) as $R_s \longrightarrow \infty$. The result is

$$\frac{F}{\pi R^2 \sigma} = 2(1 - \alpha)\, Z^2 \ln Z + \alpha\left(1 - Z^2\right) \tag{22}$$

where $Z = 1 - (S/R)$ (23)

Using Equations (18) and (19) to express the right hand side of Equation (17) entirely in terms of the variable p, and noting from Equation (20) that

$$dp = \mp \frac{1}{R_s}\, ds \tag{24}$$

The energy of crushing deformation $E_c = \int_o^{S_f} F_v ds$, evaluated over an arbitrary impact stroke S_f can be evaluated by direct closed form integration, leading to the following result:

$$\begin{aligned}\frac{\int_o^{S_f} F_v ds}{\pi R_s^3 \sigma} = -\Bigg\{ &\frac{1}{2}\left(\frac{1-\beta^2}{2}\right)\left[(1+\alpha)\left(\frac{1-\beta^2}{2}\right) - (1-\alpha)\right]\left(\frac{1}{p_f} - \frac{1}{p_o}\right) \\ &+ \frac{1}{2}\left[(1+\alpha)\left(\frac{1+\beta^2}{2}\right) - (1-\alpha)\left(\frac{2}{3} + \frac{\beta^2}{2}\right)\right]\left(p_f - p_o\right) \\ &- \frac{2}{3}\left(\frac{1-\alpha}{2}\right)\left(\frac{p_f^2 - p_o^2}{2}\right) + \left(\frac{7 - 13\alpha}{24}\right)\frac{p_f^3 - p_o^3}{3} \\ &+ \left(\frac{1-\alpha}{2}\right)\left[\left(\frac{1}{p_f} - \frac{8}{3} + 2p_f - \frac{1}{3}p_f^3\right)\ln\left|\frac{1 - p_f}{\lambda}\right|\right]\Bigg\}\end{aligned} \tag{25}$$

where

$$p_f = 1 \pm \left(\lambda - \frac{S_f}{R_s}\right) \tag{26}$$

$$p_o = 1 \pm \lambda \tag{27}$$

and λ is given by Equation (21).

The corresponding result for a flat impact surface can be arrived at either by evaluating the appropriate limiting form of the above or by integrating Equation (22) directly. The result is

$$\frac{\int_0^{S_f} F_v ds}{\pi R^3 \sigma} = \frac{2}{9}(1 - \alpha)\left[Z_f^3 (3 \ln Z_f - 1) + 1\right] + \alpha\left[(1 - Z_f) - \frac{1}{3}\left(1 - Z_f^3\right)\right] \quad (28)$$

where

$$Z_f = 1 - (S_f/R) \quad (29)$$

6.3.2 LAMINATED SPHERICAL IMPACT LIMITER

In this section a laminated spherical impact limiter is analyzed. The crushable material of each lamination is considered to have radially oriented grain and the mechanical properties are assumed to be constant throughout each layer. An arbitrary number of layers is considered and the properties and thickness of each layer can be different from those of the others. The aim of the investigation is to provide an initial insight into the effects of limiter nonhomogeneity. Impact on a flat surface is treated and shock phenomena are not considered.

The number of laminations is denoted by n and the outer radius of the i^{th} layer is denoted by R_i. The crushing strength of the i^{th} layer is denoted by σ_i and the cross grain strength ratio by α_i. The outer radius of the limiter is denoted by R and the impact stroke by S, and it is convenient to adopt the following additional notation:

$$\gamma_i = R_i/R \quad (1)$$

$$Z = 1 - \frac{S}{R} \quad (2)$$

When crushup has progressed to a point such that the impact surface has reached the j^{th} lamination, that is $R_j \geq R - s > R_{j-1}$ (3)

or $\gamma_j \geq Z > \gamma_{j-1}$ (4)

Then the vertical impact force is calculated by integrating Equation (9) [with Equation (10)] of the preceding section over each of the crushed layers (that is, laminations j to n) and summing. Denoting the impact force at this stage by F_{v_j},

$$\frac{F_{v_j}}{2\pi R^2} = \sum_{i=j}^{n} \int_{\phi_{i-1}}^{\phi_i} \sigma_i (\cos\phi + \alpha_i \tan\phi \sin\phi) \left(\frac{Z}{\cos\phi}\right)^2 \sin\phi \, d\phi \qquad (5)$$

Noting that σ_i and Z do not vary during the integration, Equation (5) can be written

$$\frac{F_{v_j}}{2\pi R^2} = Z^2 \sum_{i=j}^{n} \int_{\phi_{i-1}}^{\phi_i} (\tan\phi + \alpha_i \tan^3\phi) \, d\phi \qquad (6)$$

The upper and lower bounds of integration are given by

$$\cos\phi_K = (R - S)/R_K = Z/\gamma_K, \quad (K \neq j - 1) \qquad (7)$$

$$\phi_{j-1} = 0 \qquad (8)$$

Also note that $\gamma_n = 1$. Performing the integration indicated in Equation (6) noting Equations (7) and (8),

$$\frac{F_{v_j}}{2\pi R^2} = \sum_{i=j+1}^{n} \sigma_i \left[Z^2(1 - \alpha_i) \ln \frac{\gamma_i}{\gamma_{i-1}} + \frac{\alpha_i}{2}\left(\gamma_i^2 - \gamma_{i-1}^2\right)\right]$$

$$+ \sigma_j \left[Z^2(1 - \alpha_j) \ln \frac{\gamma_j}{Z} + \frac{\alpha_j}{2}\left(\gamma_j^2 - Z^2\right)\right] \qquad (9)$$

The energy absorbed in crushing deformation over an impact stroke S_f, where $R_m \geq S_f > R_{m-1}$, is obtained by integrating the force over each layer from j = n to j = m + 1, and over the crushed portion of the m^{th} layer as follows:

$$\int_o^{S_f} F_v \, ds = \sum_{m+1}^{n} \int_{R_j}^{R_{j-1}} F_{v_j} \, ds + \int_{R_m}^{R-S_f} F_{v_m} \, ds \qquad (10)$$

Using equations (1), (2), and (9), the integration indicated in Equation (10) yields

$$\frac{\int_o^{S_f} F_v\,ds}{2\pi R^3} = \sum_{j=m+1}^{n} \left[\sum_{i=j+1}^{n} \sigma_i \left[\frac{1}{3}\left(\gamma_j^3 - \gamma_{j-1}^3\right)\left(1-\alpha_i\right) \ln \frac{\gamma_i}{\gamma_{j-1}} + \frac{\alpha_i}{2}\left(\gamma_i^2 - \gamma_{i-1}^2\right)\left(\gamma_j - \gamma_{j-1}\right) \right] + \sigma_j \left\{ \left(1-\alpha_j\right)\frac{1}{9} \left[\gamma_{j-1}^3 \left(3 \ln \frac{\gamma_{j-1}}{\gamma_j} - 1\right) + \gamma_j^3 \right] + \frac{\alpha_j}{2}\left[\gamma_j^2\left(\gamma_j - \gamma_{j-1}\right) - \frac{1}{3}\left(\gamma_j^3 - \gamma_{j-1}^3\right) \right] \right\} \right] + \sum_{i=m+1}^{n} \sigma_i \left[\frac{1}{3}\left(\gamma_m^3 - z_f^3\right)\left(1-\alpha_i\right) \ln \frac{\gamma_i}{\gamma_{i-1}} + \frac{\alpha_i}{2}\left(\gamma_i^2 - \gamma_{i-1}^2\right)\left(\gamma_m - z_f\right) \right] + \sigma_m \left\{ \left(1-\alpha_j\right)\frac{1}{9} \left[z_f^3\left(3 \ln \frac{z_f}{\gamma_m} - 1\right) + \gamma_m^3 \right] + \frac{\alpha_j}{2} \left[\gamma_m^2\left(\gamma_m - z_f\right) - \frac{1}{3}\left(\gamma_m^3 - z_f^3\right) \right] \right\} \tag{11}$$

where $z_f = 1 - (S_f/R)$

For a limiter with <u>two</u> laminations, Equations (9) and (11) above reduce to the following: In the outside, or second, layer, the force, F_{v_2}, and the

energy are given by Equations (22) and (28) of the previous section with $\sigma = \sigma_2$ and $\alpha = \alpha_2$. In the inside, or first, lamination

$$\frac{F_{v_1}}{2\pi R^2} = \sigma_1 \left[z^2 \left(1 - \alpha_1\right) \ln \frac{\gamma_1}{z} + \frac{\alpha_1}{2} \left(\gamma_1^2 - z^2\right) \right] + \sigma_2 \left[z^2 \left(1 - \alpha_2\right) \ln \frac{1}{\gamma_1} + \frac{\alpha_2}{2} \left(1 - \gamma_1^2\right) \right] \tag{12}$$

$$\frac{\int_o^{S_f} F_v \, ds}{2\pi R^3} = \sigma_2 \left\{ \left(1 - \alpha_2\right) \frac{1}{9} \left(3 z_f^3 \ln \gamma_1 + 1 - \gamma_1^3\right) + \frac{\alpha_2}{2} \left[1 - z_f - \frac{1}{3} \left(1 - \gamma_1^3\right) - \gamma_1^2 \left(\gamma_1 - z_f\right) \right] \right\} + \sigma_1 \left\{ \left(1 - \alpha_1\right) \frac{1}{9} \left[z_f^3 \left(3 \ln \frac{z_f}{\gamma_1} - 1\right) + \gamma_1^3 \right] + \frac{\alpha_1}{2} \left[\gamma_1^2 \left(\gamma_1 - z_f\right) - \frac{1}{3} \left(\gamma_1^3 - z_f^3\right) \right] \right\} \tag{13}$$

6.3.3 EFFECT OF STOPPED, CRUSHED MASS

Crushing deformation is propagated by a shock wave phenomenon, as indicated in Appendix 6.2. If the mechanical model utilized there is adopted to represent the essential features of crushable material dynamic behavior, the oncoming crushable material is suddenly brought to rest across a "crushing front" and compressed into a relatively small zone between this front and the impact surface as indicated in Figure 135. There has to be a finite discontinuity in stress across this front in order to achieve the sudden finite velocity change, and so the crushing front is actually a shock wave. For the model of material dynamic mechanical behavior utilized in Appendix 6.2, the stress immediately ahead of the crushing front is the crushing strength (that is, the constant stress level at which quasistatic crushing takes place*). The vertical force corresponding to this crushing

*The model does not consider strain rate effects.

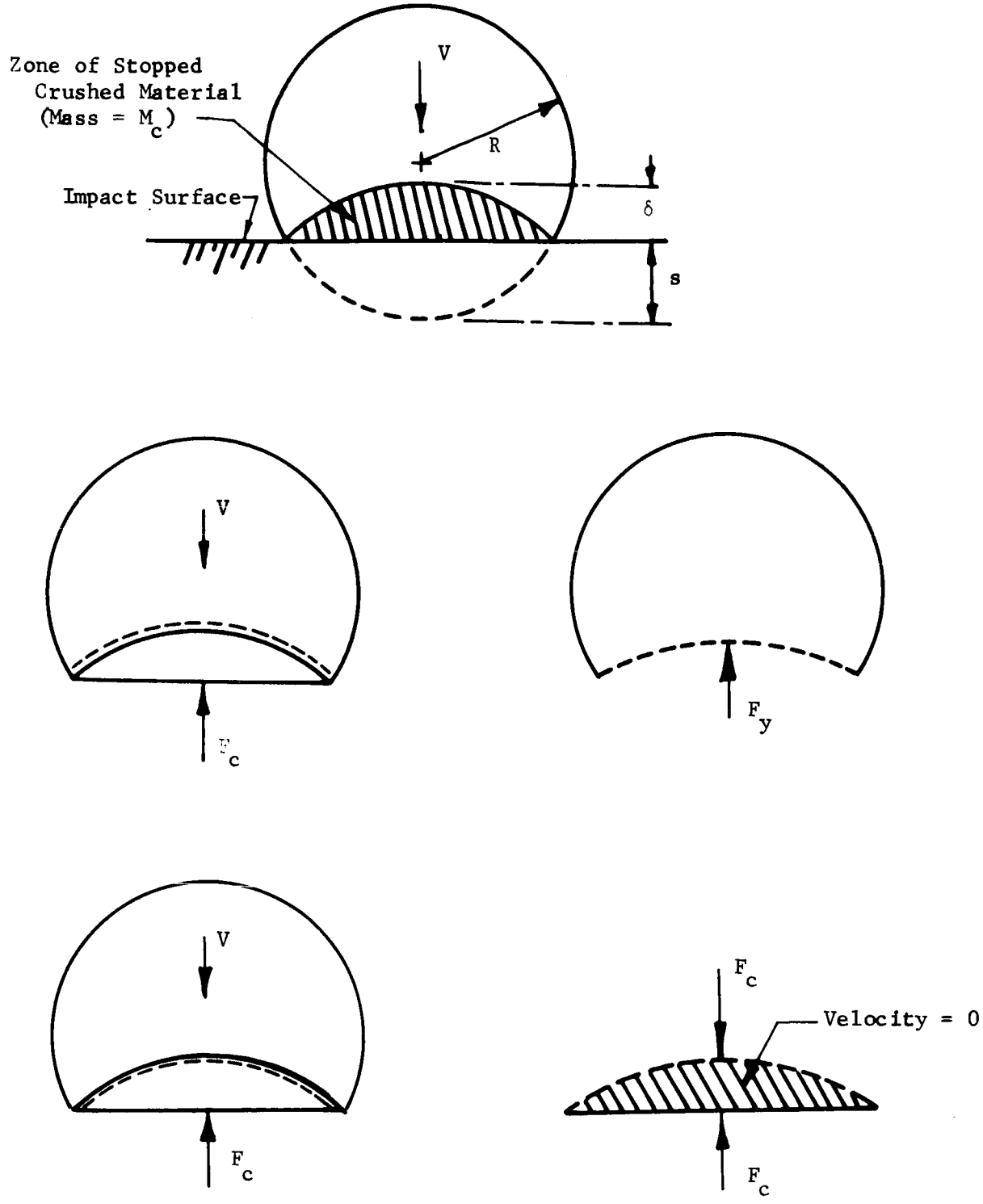

FIGURE 135 CRUSHED ZONE PROPAGATION

stress immediately ahead of the crushing front will be denoted here by F_y and the vertical force immediately behind the front will be denoted by F_c as indicated in Figure 135. The force discontinuity across the front then is $F_c - F_y$. Since the mass of crushed material has been brought to rest and experiences no further accelerations (according to the model adopted, as discussed previously), the vertical force acting at the impact surface is also F_c as indicated in Figure 135. The mass of the entire system will be denoted by m_T and the mass of the stopped crushed material by m_c, so that the moving mass m of the system is

$$m = m_T - m_c$$

Impulse-momentum considerations written for the entire system give

$$- F_c = \frac{d}{dt}(mv) = m\frac{dv}{dt} + v\frac{dm}{dt} \qquad (2a)$$

$$= (m_T - m_c)\frac{dv}{dt} - V\frac{dm_c}{dt} \qquad (2b)$$

Impulse-momentum considerations across the shock wave (crushing front) give

$$(F_c - F_y)\,dt = vdm_c \qquad (3)$$

$$\text{or } F_c - F_y = v\frac{dm_c}{dt} \qquad (4)$$

Equations (2b) and (4) give

$$F_y = - (m_T - m_c)\frac{dv}{dt} \qquad (5)$$

$$\text{or } \frac{dv}{dt} = - \frac{F_y}{m_T - m_c} \qquad (6)$$

$$\text{Noting that } \frac{ds}{dt} = v \qquad (7)$$

where s is the impact stroke as indicated in Figure 3, and using the transformation,

$$\frac{dv}{dt} = \frac{dv}{ds}\frac{ds}{dt} = v\frac{dv}{ds} \qquad (8)$$

Equation (6) can be written

$$vdv = - \frac{F_y\,ds}{m_T - m_c} \qquad (9)$$

Integrating Eq. (9),

$$1/2\ (V_o^2 - V^2) = \int_o^s \frac{F_y\ ds}{m_T - m_c} \qquad (10)$$

where V_o is initial impact velocity.

For a spherical mass impacting a flat rigid surface, if, for a first approximation, the depth (in Figure 135) of the zone of crushed material is neglected, then

$$m_c = \frac{\pi}{3}\ S^2\ (3R - S)\rho_\ell$$

where S is the impact stroke as indicated in Figure 135, R is the radius of the sphere, and ρ_ℓ is the density of the material before crushing. Since the crushing front is essentially a flat surface if δ is regarded as negligible, the force F_y is then essentially F_v given by equations (22) and (23) of section 6.3.2 of this appendix. Then, writing Eq. (10) (for V = 0), the result is

$$V_o^2 = \frac{3}{2}\ \frac{\sigma}{\rho_\ell} \int_o^{x_f} \frac{h(x)}{g(x)}\ dx \qquad (12)$$

where $x = S/R$ (13)

$$h(x) = \alpha x\ (2-x) - 2(1-\alpha)(1-x)^2\ \ln(1-x) \qquad (14)$$

$$g(x) = \beta - \frac{1}{4}\ x^2(3-x) \qquad (15)$$

$$\beta = m_T/(\frac{4}{3}\ \pi R^3\ \rho_\ell) \qquad (16)$$

$$\sigma = \sigma_y = \text{material crushing strength} \qquad (17)$$

$$x_f = s_f/R \qquad (18)$$

where s_f is the final or total impact crushing stroke.

6.3.4 PAYLOAD BREAKAWAY ("CANNON BALL EFFECT")

If the decelerations imposed on the payload during the impact process are sufficiently high it is possible for the stresses in the impact limiter material adjacent to the payload to reach the level at which crushing

commences. If it is assumed that no payload movement relative to the limiter due to crushing of the adjacent limiter material is possible until all the adjacent limiter material in contact with the surface of the LOWER HEMISPHERE of the payload is stressed to the crushing strengh level σ, and if, in addition, it is assumed that there is no interaction between the payload and the limiter on the upper hemispherical interface, as payload movement commences*, then it is easily demonstrated that the force on the payload sphere required to initiate payload movement due to crushing of adjacent limiter material is $\pi R_p^2 \sigma$, where R_p is the payload radius. Hence, the "cannon ball effect" is incipient when the acceleration of the payload reaches $\pi R_p^2 \sigma / m_p$, where m_p is the payload mass. The acceleration produced by the forces acting on the limiter at the impact surface is $F/(m_p + m_\ell - m_c)$, where

$$F = \left\{\alpha\left[1 - \left(\frac{r}{R}\right)^2\right] - (1-\alpha)\left(\frac{r}{R}\right)^2 \ln\left(\frac{r}{R}\right)^2\right\}\pi R^2 \sigma$$

α is the cross grain crushing strength ratio, R is the limiter radius, r = R-s, where s is the "impact stroke", m_ℓ is the limiter mass and m_c is the mass of material crushed during the stroke s. Therefore, the condition for imminent payload movement relative to the limiter (payload breakaway) as a result of crushing of limiter material beneath the lower hemispherical payload-limiter interface is given by

$$\frac{\left\{\alpha\left[1 - \left(\frac{r}{R}\right)^2\right] - (1-\alpha)\left(\frac{r}{R}\right)^2 \ln\left(\frac{r}{R}\right)^2 \quad \pi R^2 \sigma\right\}}{m_p + m_\ell - m_c} = \frac{\pi R_p^2 \sigma}{m_p}$$

That is, payload breakaway will not occur if

$$\frac{\left\{\alpha\left[1 - \left(\frac{r}{R}\right)^2\right] - (1-\alpha)\left(\frac{r}{R}\right)^2 \ln\left(\frac{r}{R}\right)^2\right\}\left(\frac{R}{R_p}\right)^2}{1 + \frac{m_l - m_c}{m_p}} < 1 \qquad (1)$$

Since, obviously $m_l < m_c$, it is seen that payload breakaway can not occur if

---

* Note that if the cross grain strength of the limiter is not sufficient to carry the inertia loads of the mass of the limiter material above the payload (via a loadpath around the sides of the payload, then these inertia loads must be carried thru the payload and breakaway will occur at lower accelerations than predicted by this analysis which neglects this interaction.

$$\left\{\alpha\left[1 - \left(\frac{r}{R}\right)^2\right] - (1-\alpha)\left(\frac{r}{R}\right)^2 \ln\left(\frac{r}{R}\right)^2\right\}_{max} < \left(\frac{R_p}{R}\right)^2 \qquad (2)$$

It can be shown that

$$\left\{\alpha\left[1 - \left(\frac{r}{R}\right)^2\right] - (1-\alpha)\left(\frac{r}{R}\right)^2 \ln\left(\frac{r}{R}\right)^2\right\}_{max} = (1-\alpha)e^{\frac{-1}{1-\alpha}} + \alpha \qquad (3)$$

and occurs at $\frac{r}{R} = \left(\frac{r}{R}\right)_m = e^{-1/2(1-\alpha)}$ (4)

and Equation (4) is plotted in Figure 137.

Equation (3) is plotted in Figure 136 and Eq. (4) is plotted in Figure 137. Numerical calculations showed that limiting values of (R_p/R) given by inequality (2) and Eq. (3) exceeded $(r/R)_m$ given by Eq. (4). This means that the maximum value of the expression on the left side of inequality (2) occurs at the end of the stroke and must be calculated accordingly. Neglecting the finite depth of crushed material around the payload at the end of the stroke yields an upper bound to the limiting value of the radius ratio $(R_p/R)^*$. Inequality (2) can be shown to result in the following equation for this upper bound solution for the limiting radius ratio $(R_p/R)^*$

$$U = e^{\frac{1+\alpha(1-U)}{1-\alpha}} \qquad (5)$$

$$\text{where } U = \left[(R_p/R)^*\right]^{-2} \qquad (6)$$

Equation (5) was solved numerically and the resulting upper bound for the limiting radius ratio is shown in Figure 138. This result corresponds to the physically limiting case in which the material crushes up to (that is, the depth of the crushing stroke is) 100% of the original uncrushed depth; in other words, the terminal crushing strain is 0.1. In addition, the limiting radius ratio for a terminal crushing strain of 0.8 was calculated from inequality (2). Because the maximum value of the expression on the left side of inequality (2) occurs at the end of the stroke and there is a finite depth of crushed material around the payload at the end of the stroke, the relation between (r/R) at the end of the stroke* and (R_p/R) for the calculation of the limiting value of the radius ratio can be shown to be

---

* R-s = r, where s is the crushing stroke as indicated previously.

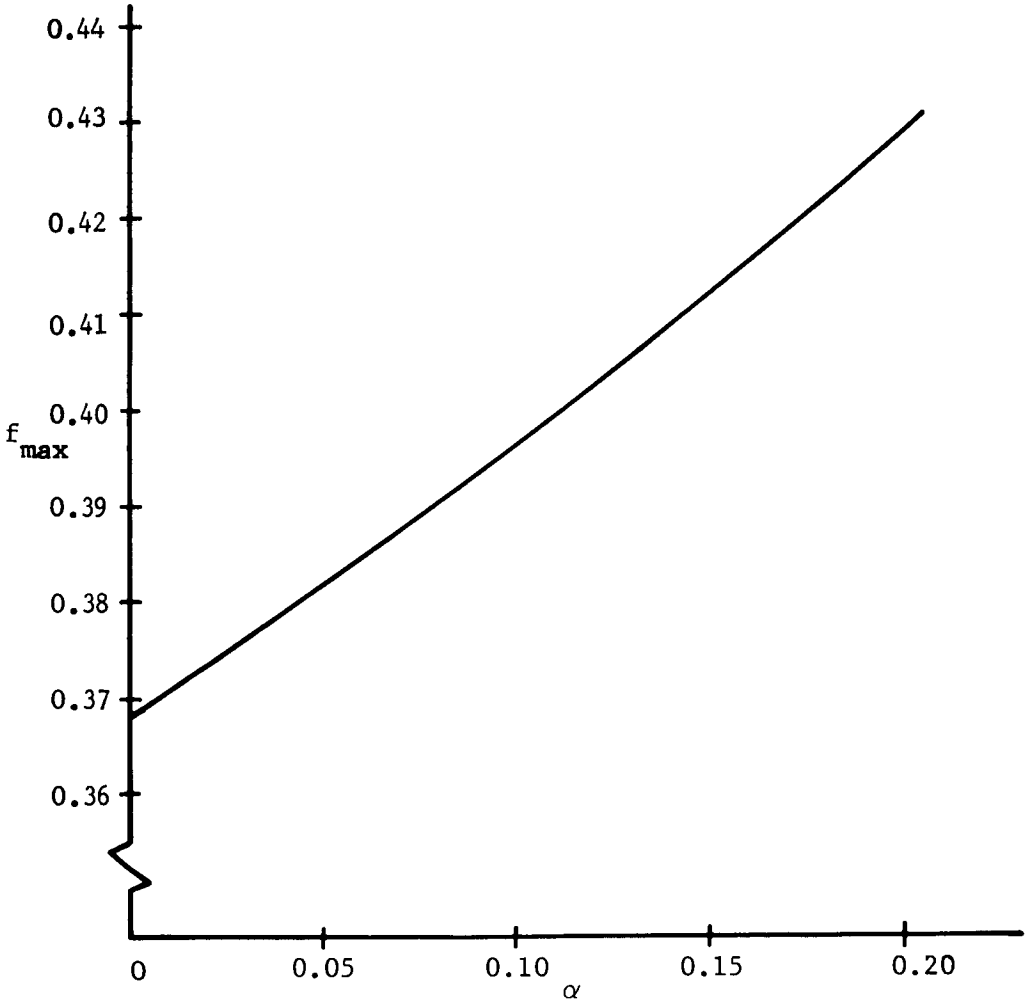

$$f = (1 - \alpha)\left(\frac{r}{R}\right)^2 \ln\left(\frac{R}{r}\right)^2 + \alpha\left[1 - \left(\frac{r}{R}\right)^2\right]$$

$$f_{max} = (1 - \alpha)e^{-1/(1 - \alpha)} + \alpha$$

FIGURE 136. MAXIMUM FORCE VS. CROSS GRAIN STRENGTH RATIO

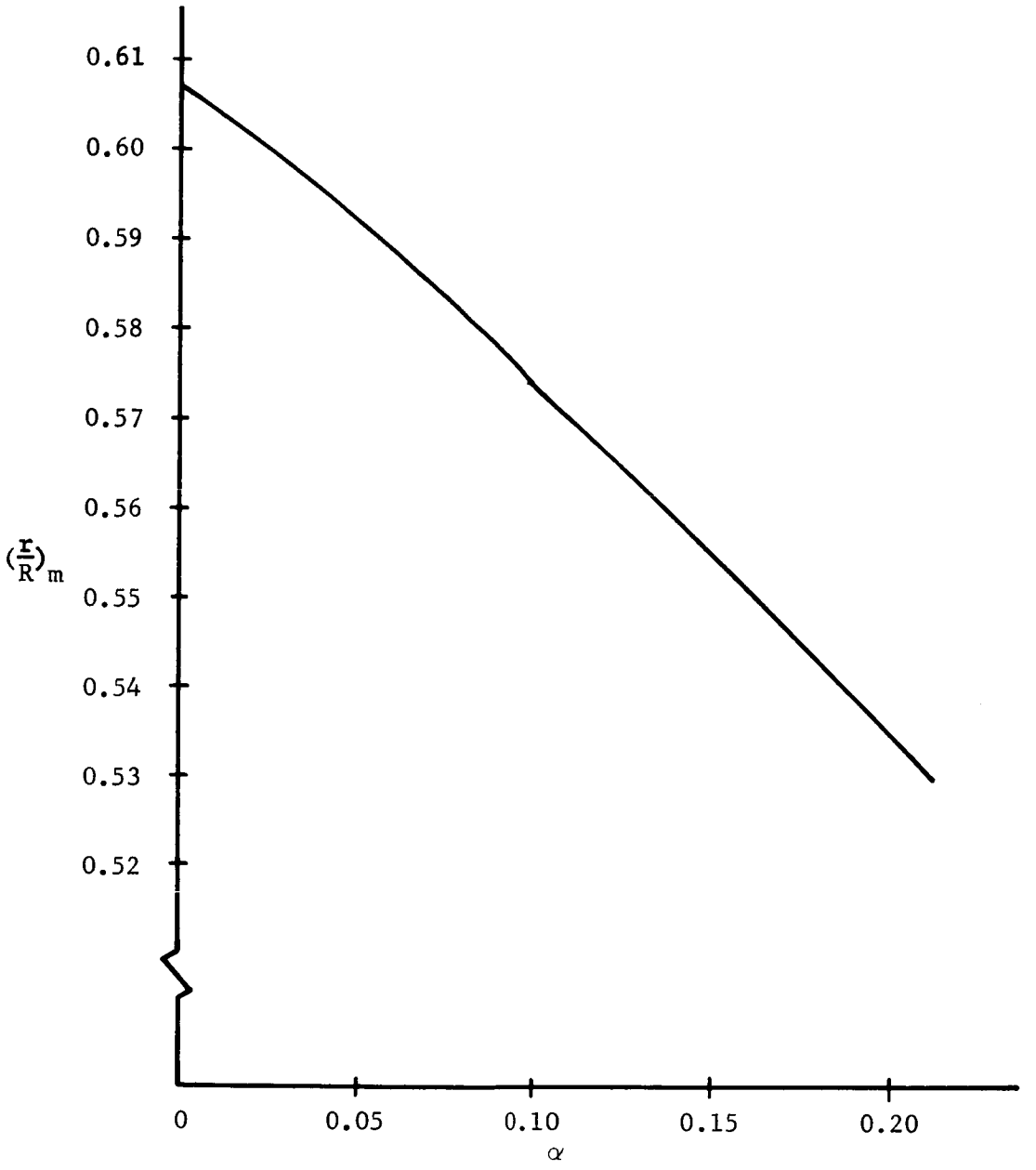

FIGURE 137. RADIUS RATIO FOR PEAK FORCE VS. CROSS GRAIN STRENGTH RATIO

$$\left(\frac{r}{R}\right)_f = 1 - \epsilon_c \left(1 - \frac{R_p}{R}\right) \tag{7}$$

where ϵ_c is the terminal crushing strain and the subscript f denotes the end of the crushing stroke. The limiting radius ratio $(R_p/R)^*$ calculated for $\epsilon_c = 0.8$ is also shown in Figure .

The quantity $(m_1 - m_c)/m_p$ appearing in inequality (1) is given by*:

$$\frac{m_1 - m_c}{m_p} = \left\{ \left(\frac{R}{R_p}\right)^3 \left[1 - \frac{1}{4}\left(1 - \frac{r}{R}\right)^2 \left(2 + \frac{r}{R}\right) \right] - 1 \right\} \frac{\rho_\ell}{\rho_p} \tag{8}$$

where ρ_ℓ and ρ_p are the densities of the limiter material and payload, respectively.

Inequality (1) and Eq. (8) give the following condition on the limiter-to-payload density ratio for no payload breakaway:

$$\frac{\rho_\ell}{\rho_p} > \frac{\left\{\alpha\left[1 - \left(\frac{r}{R}\right)^2\right] + (1-\alpha)\left(\frac{r}{R}\right)^2 \ln\left(\frac{R}{r}\right)^2\right\} - 1}{\left(\frac{R}{R_p}\right)^3 \left[1 - \frac{1}{4}\left(1 - \frac{r}{R}\right)^2 \left(2 + \frac{r}{R}\right)\right] - 1} \tag{9}$$

Limiting density ratios $(\rho_\ell/\rho_p)^*$ computed from inequality (9) above are presented in Figure 139 as a function of (R/R_p) in the region where (R_p/R) is less than $(R_p/R)^*$ given in Figure 138. Curves are presented in Figure 139 for values of the cross grain strength ratio $\alpha = 0.1$ and $\alpha = 0$. The lower dashed curves were computed neglecting the effect of the crushed mass m_c; that is, for $m_c = 0$, or in other words for

$$\frac{m_\ell - m_c}{m_p} = \frac{m_\ell}{m_p} = \left[\left(\frac{R}{R_p}\right)^3 - 1\right] \frac{\rho_\ell}{\rho_p} \tag{10}$$

---

* Neglecting the finite depth of crushed material above the impact surface.

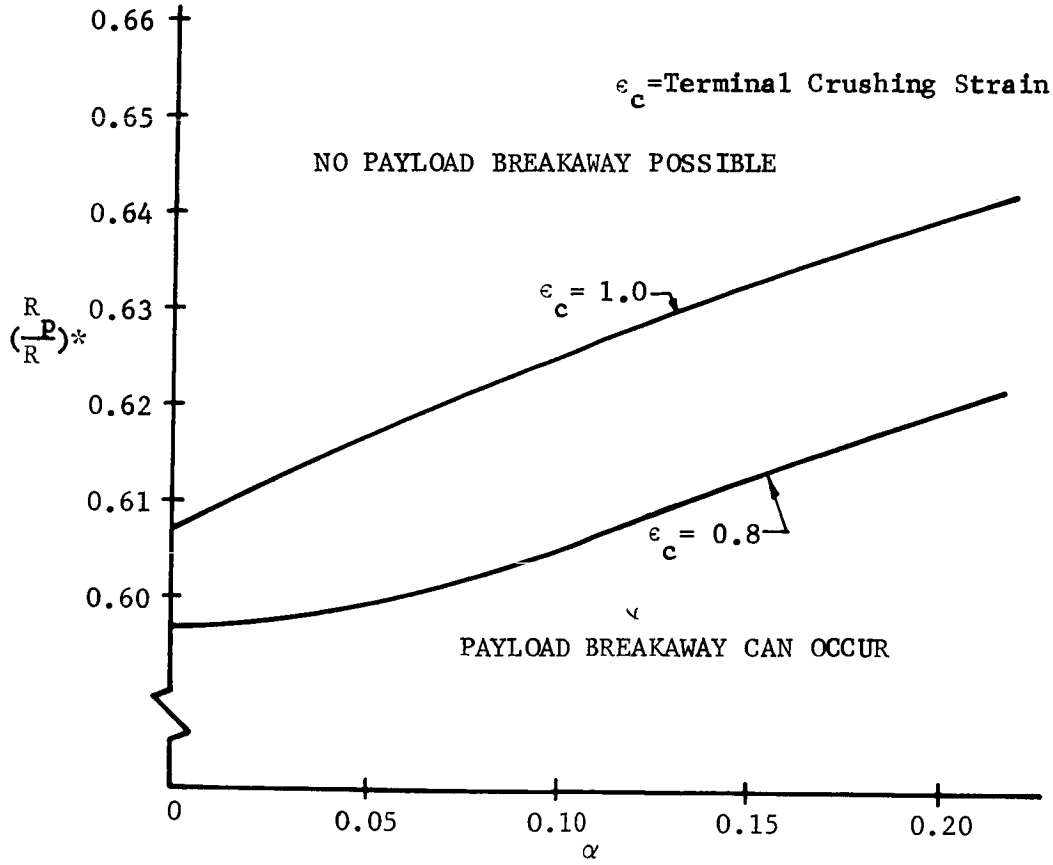

FIGURE 138. MINIMUM PAYLOAD TO LIMITER RADIUS RATIO FOR NO BREAKAWAY VS. CROSS GRAIN STRENGTH RATIO

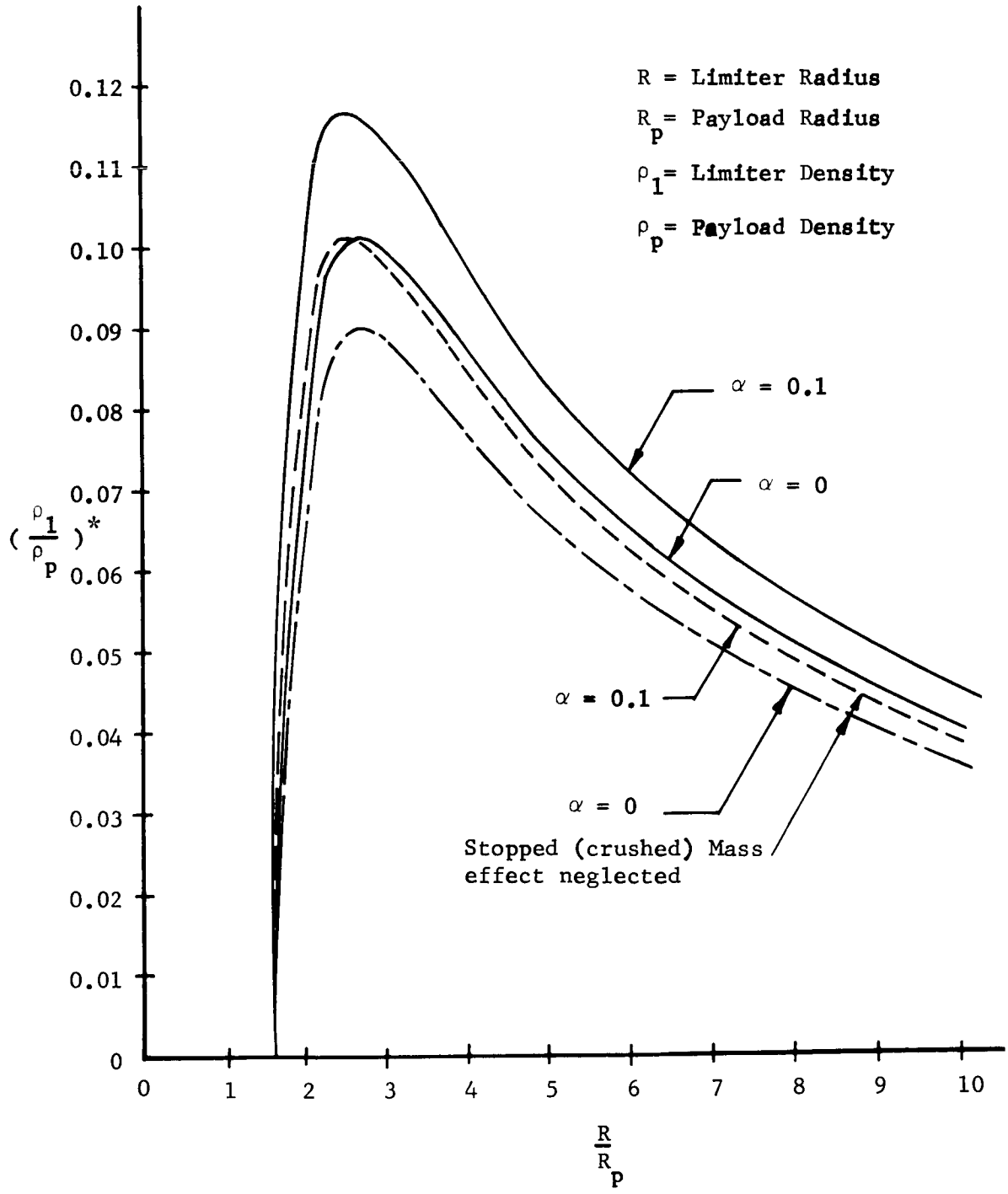

FIGURE 139. MAXIMUM RATIO OF LIMITER TO PAYLOAD DENSITY FOR PAYLOAD BREAKAWAY

It can be shown that the impact velocity which can be absorbed by a spherical limiter is given by

$$V^2 \frac{\rho_\ell}{\sigma} = \frac{3\left\{(1-\alpha)\frac{1}{9}\left[Z^3(\ln Z - 1) + 1\right] + \frac{\alpha}{2}\left[(1-Z) - \frac{1}{3}(1-Z^3)\right]\right\}}{\left[1 + \left(\frac{R_p}{R}\right)^3\left(\frac{\rho}{\rho_\ell} - 1\right)\right]} \qquad (11)$$

where $Z = 1 - \epsilon_c\left(1 - \frac{R_p}{R}\right)$ (12)

The velocity parameter on the left side of Eq. (11) is thus defined in terms of the quantities α, ϵ_c, (R_p/R), and (ρ/ρ_ℓ). Using Eqs. (11) and (12) and Figure 139, the limiting density ratio $(\rho_\ell/\rho_p)^*$ can be plotted in terms of the parameter on the left side of Eq. (11). This is illustrated in Figure 140 for $\alpha = 0$ and $\epsilon_c = 0.8$. (Note from Eq. (11) that as $(R_p/R) \rightarrow 0$ $\left[(R/R_p) \rightarrow \infty\right]$, $V^2\rho_\ell/\sigma_c$ approaches a finite value.

The preceding analysis of the "cannon ball effect" (payload breakaway and crushing of limiter material adjacent to the payload) is based on the assumption that there was no interaction between payload and limiter on the upper hemispherical payload-limiter interface. In order for this to be possible, the inertia loads from the mass of limiter material above the payload must be carried, after payload breakaway, by a load path through the limiter material around the sides of the payload. If the cross grain strength of the limiter is not sufficient to carry these inertia loads, they must then be carried through the payload and will add to the inertia load of the payload being carried through the lower hemispherical payload-limiter interface. The result will be the occurrence of payload breakaway at lower accelerations than if the limiter had sufficient cross grain strength to carry its own inertia loads through the load path around the sides of the payload. (If the limiter has more than enough cross grain strength to carry its own inertia loads through this load path, bonding the payload to the limiter can dump some of the payload inertia forces into the load path through the limiter material around the sides of the payload, thereby tending to raise the acceleration levels at which payload breakaway occurs.)

The cross grain strength required for the limiter to be able to carry its <u>own</u> inertia loads (via the load path through the limiter material around the sides of the payload) can be computed by equating the inertia loads from the top half of the limiter material at payload breakaway (that is, at peak acceleration) to the cross grain force required to crush the limiter material at the sides of the payload. The resulting expression for the cross grain strength <u>ratio</u> α^* <u>required</u> for the limiter to be able just

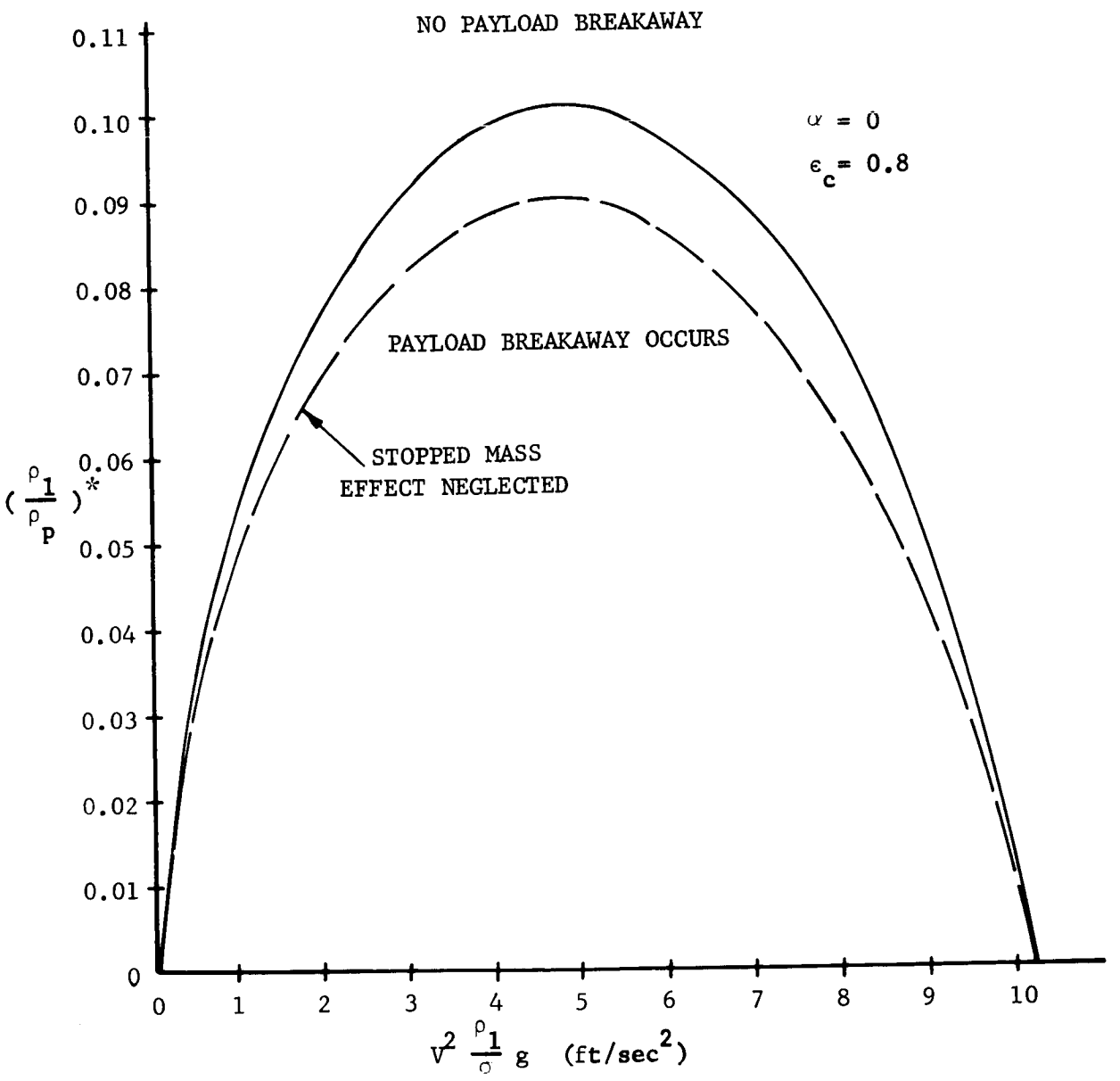

ρ_1 = Limiter Density — σ = Limiter Crushing Strength

ρ_p = Payload Density — g = 32.2 ft/sec^2

V = Impact Velocity — α = Cross Grain strength Ratio

ϵ_c = Terminal Crushing Strain

FIGURE 140. MAXIMUM LIMITER TO PAYLOAD DENSITY RATIO FOR BREAKAWAY VS. VELOCITY PARAMETER FOR = 0

to carry its own inertia loads is

$$\alpha^* = \frac{\left\{(1-\alpha)\left(\frac{r}{R}\right)^2 \ln\left(\frac{R}{r}\right)^2 + \alpha\left[1 - \left(\frac{r}{R}\right)^2\right]\right\}}{\left\{\frac{\rho_p}{\rho_\ell} + \left(\frac{R}{R_p}\right)^3\left[1 - \frac{1}{4}\left(1 - \frac{r}{R}\right)^2\left(2 + \frac{r}{R}\right)\right] - 1\right\}} \left\{\frac{\frac{1}{2}\left[\left(\frac{R}{R_p}\right)^3 - 1\right]}{1 - \left[\left(\frac{R_p}{R}\right)^2\right]}\right\}$$

where R = limiter radius, R_p = payload radius, ρ_p = payload density, ρ_ℓ = limiter density, r = R-s, s = impact stroke at peak acceleration, and is the actual material cross grain strength ratio. Values of α^* computed using the above formula are shown in Figure 141. The computations were for α = 0 on the right side of the expression. Values of α around 0.1 would give somewhat higher values of α^*.

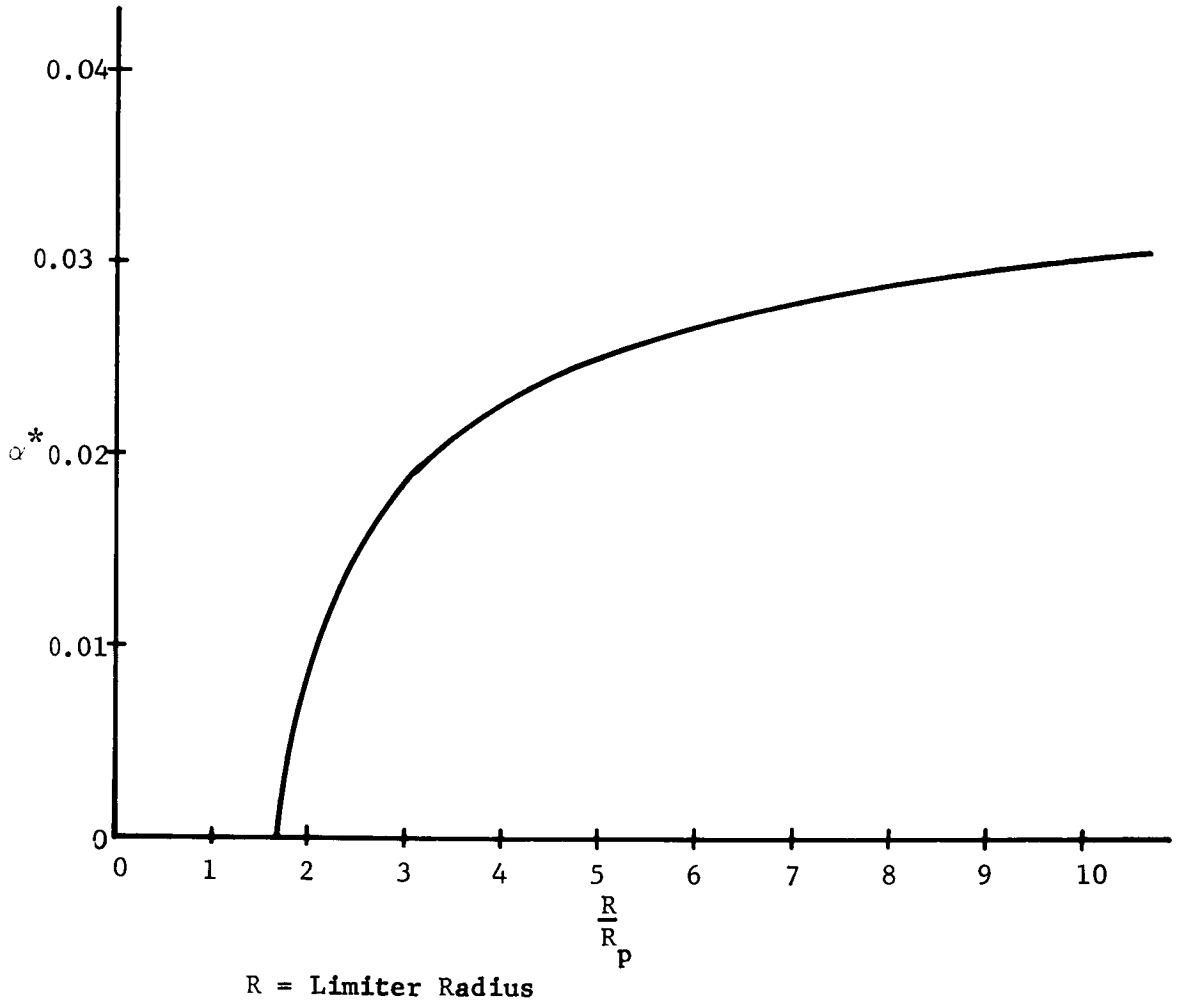

R = Limiter Radius
R_p = Payload Radius
α^* = Cross Grain Strength Ratio Required for Limiter to Carry Its Own Inertia Loads

6.4 THERMAL BATTERY INVESTIGATION

6.4.1 INTRODUCTION

This section is a summary of the concepts involved in the use of a long duration thermal battery for a Mars landing vehicle. For purposes of the study, the following battery requirements are assumed:

Preflight Sterilization -	Capsule assembly is baked at 135°C for 24 hours.
Shock -	3 millisecond duration with 5000g peak (half sine waveform)
Capsule Operation Temp. -	Turn on - 0°C Minimum Temperature rise - 70°
Weight Range -	20 lb. minimum 150 lb. maximum
Power Profile -	Turn-on: 50W for 5 minutes Picture Taking: 5W for 2 hours Transmission: 250W for 3 hours Standby: 2W for 19 hours (This cycle would be repeated for several days)
Voltage Range -	32 volts at start 28 volts end of life
Duration -	3 days
Total Watt Hours -	2400

Preliminary concepts are described for a battery meeting these objectives, based upon present or imminently achievable technology. They lead to an estimated energy density in the range of 60-70 watthours/lb. It is believed that a longer range development effort could provide for an increase in energy density to about 100 watthours/lb.

6.4.2 CELL DESIGN

The most suitable electrochemical system for this application is that utilizing a sodium metal anode and a CuCl cathode, with a solid electrolyte separator. A suitable operating temperature is about 450°C, at which both electrodes are liquid. During operation, the volume of anode material decreases and cathode material increases; consequently, the electrode

compartments must have flexibility to accommodate this change. A bellows type construction is therefore adopted. General configuration for a working cell is as shown in Figure 142 .

The critical aspect of this concept is the separator. It must have adequate ion conductivity while preventing direct contact between the liquid Na and liquid CuCl. Studies are presently underway to develop such a separator. Materials which have shown the greatest promise to date are the synthetic zeolites. Present goals are the development of separator membranes having a voltage drop of no more than 0.6 v at a current density of 50 ma/cm^2. There appears to be little doubt that this is achievable. Continued work on improvement in separator materials should be given high priority in any program to develop a long duration thermal battery.

On the basis of such performance the load requirements specified above for the Mars landing vehicle indicate an electrode area of 440 cm^2. The optimum external shape of the battery, both from the standpoint of practicability of fabrication, and minimization of thermal losses, is a cube. This designates that it be constituted of two parallel connected modules of cells of 1/2 the above area.

On this basis, the basic cell will be 16.7 cm. in diameter and with an area of 220 cm^2. Weight per cell for a battery designed for a three-day period of operation is then found as follows:

Electrode Materials (assuming 75% utilization)	Na	51
	CuCl	223
Separator		33
Anode Case		29
Cathode Case		29
Total Cell		365 gms.

Cell thickness is summed as follows:

Anode Compartment	0.24 cm
Cathode Compartment	0.29
Separator	0.075
Case	0.025
Total Cell	0.625 cm

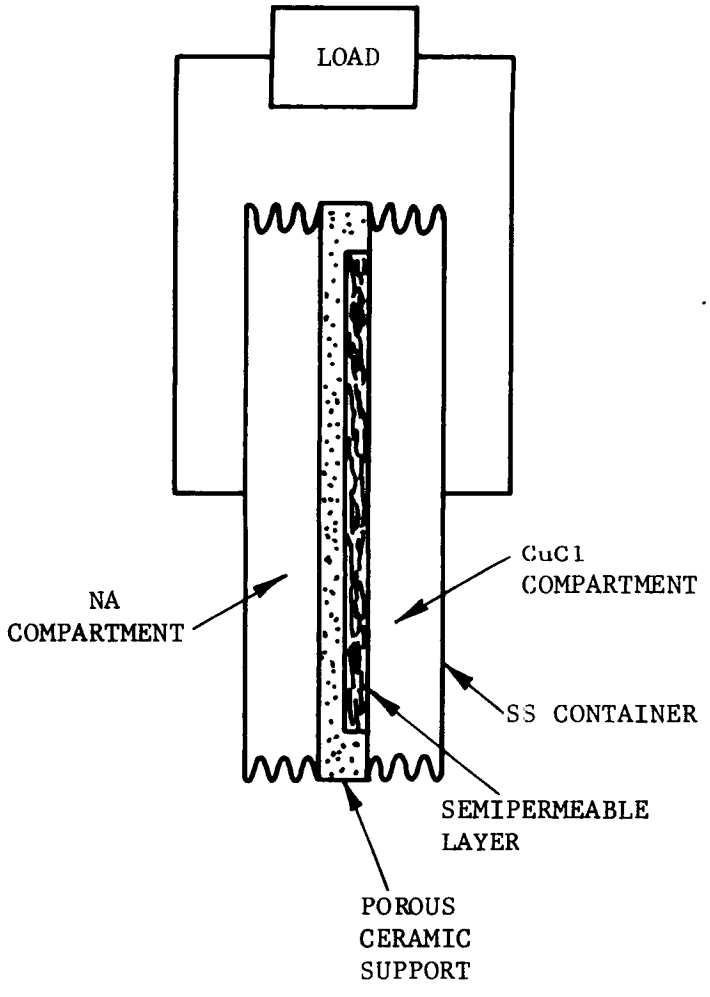

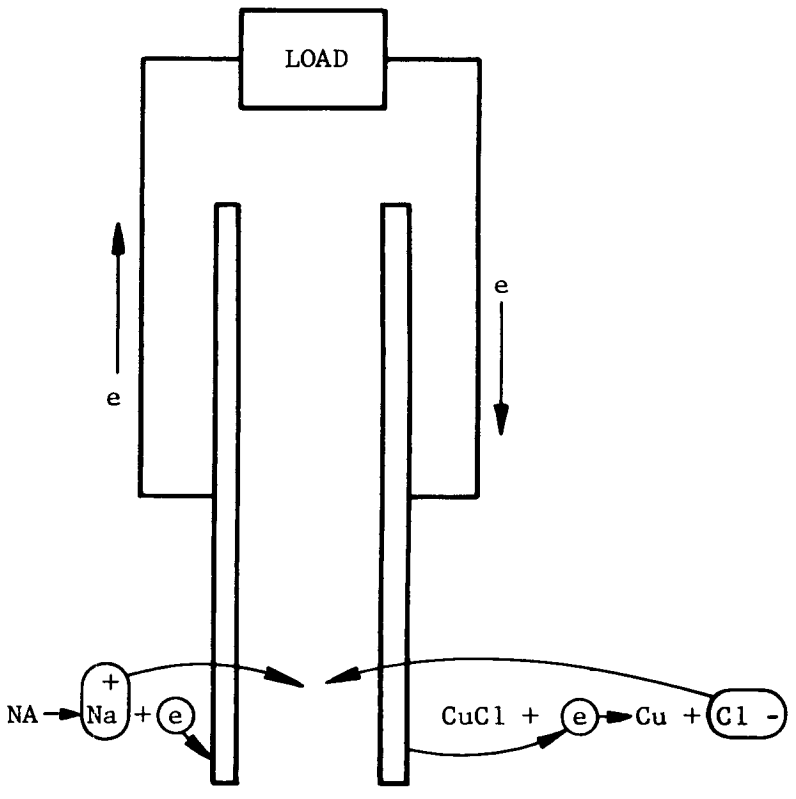

VOLTAGE - 3.2 OC

- 2.5 AT 50 MA/CM^2

OPERATING TEMP - 425^{o}C

DURATION - 72 HRS

ENERGY DENSITY - 130-150 WHR/LB

R11197

FIGURE 42. BASIC CELL CONFIGURATION

6.4.3 BATTERY PACKAGE

The battery will consist of 26 cells of the above configuration in two modules. Activation will occur upon heating to $\approx$ 450°C by the combustion of a pyrotechnic charge. It will be necessary to maintain this temperature throughout the operational life of the battery, so that some means of temperature regulation is required. This amounts to providing a heat source to compensate for the thermal loss. It should be noted such compensation will be provided in part by thermal effects inherent in cell discharge. These vary with load, however, so that some additional source of heat energy is required.

It is proposed to provide the necessary temperature control by means of a resistance coil energized by a bleed load on the battery. This increases battery weight due to an increase in required electrical capacity. Optimizing this weight against the weight of thermal insulation gives a point of minimum total weight for a given capacity in terms of useful load.

The optimization can be approximated by assuming a spherical shape for the battery package and its surrounding insulation. The following results are obtained.

The battery consists of the two modules as indicated above placed in tandem, giving a package 16.7 cm in diameter and 16.9 cm high. This is taken to be approximated by a sphere of radius = 9.5 cm.

The optimization is carried out as follows:

Weight of insulation (W_i)

$$= 4/3\ \pi \left[(9.5 + d)^3 - 9.5^3\right] \rho_i$$

where d = thickness of the insulation

ρ_i = density of the insulation

Heat loss through the spherical insulation shell

$$Q = \frac{-4\pi K \Delta T (9.5 + d)\ 9.5t}{d}$$

where ΔT = temperature differential across insulation

t = duration of discharge

To compensate for the heat loss, an extra weight of cell material must be added, i.e.,

$$W_c = \frac{4\pi K \Delta T(9.5 + d)9.5\ t\ F_g}{D \times F_w\ d}$$

F_g = no. of gms/lb.

F_w = no. of cal/watthour

D = energy density of cell active materials

For the total additional weight, one has

$$W_t = W_i + W_c$$

To obtain the d for minimum weight set,

$$\frac{dW_t}{dd} = 0$$

Setting:

Data for rock wool ($K = 8.95 \times 10^{-5}$ cal/sec. - CM - deg C

($\rho = 0.096$ gms/cc

$\Delta T = 400^{\circ}C$

$t = 2.59 \times 10^5$ sec

$F_g = 452$ gm/lb

$F_w = 860$ cal/watthours

$D = 307$ watthours/lb

One obtains

$$d^2(9.5 + d)^2 + 1.57 \times 10^4 = 0$$

$$d = 7.4$$

Consequently

W_i = 1600 gms

W_c = 2360 gms

W_t = 4000 gms

With these considerations, the preliminary design of a battery package will be as shown in Figure 143 . Basic geometry is a right circular cylinder, 16.7 cm in diameter and 16.9 cm high. It is enclosed by insulation, heating coil, case, and pyrotechnic heating material. This package with outside insulation is shown in Figure 143 . Total package weight is totaled up as follows:

26 cells	9480
Inner thermal Insulation (asbestos)	200
Pyrotechnic	2000
Case (20 mil Ni)	530
Outer insulation	1600
Extra capacity	2360
Total	16170 gms
	35.6 lbs.

For the postulated mission, one thus obtains an energy density of 67.5 watthours/lb.

6.4.4 FURTHER CONSIDERATIONS ON THERMAL INSULATION

It will be noted from the foregoing section that a substantial fraction of the weight of the battery package (i.e., W_t) depends on the outer insulation. The calculation presented herein made use of thermal data for rock wool, which is not a particularly sophisticated material. Other insulation materials may provide reductions in total battery weight and/or volume. In selecting an insulation material for this application, the insulation impact resistance should be considered along with the desirability of achieving minimum battery package volume. A relatively high density insulation material with low thermal conductivity ideally satisfies these requirements (i.e., a material such as Min-k-503).

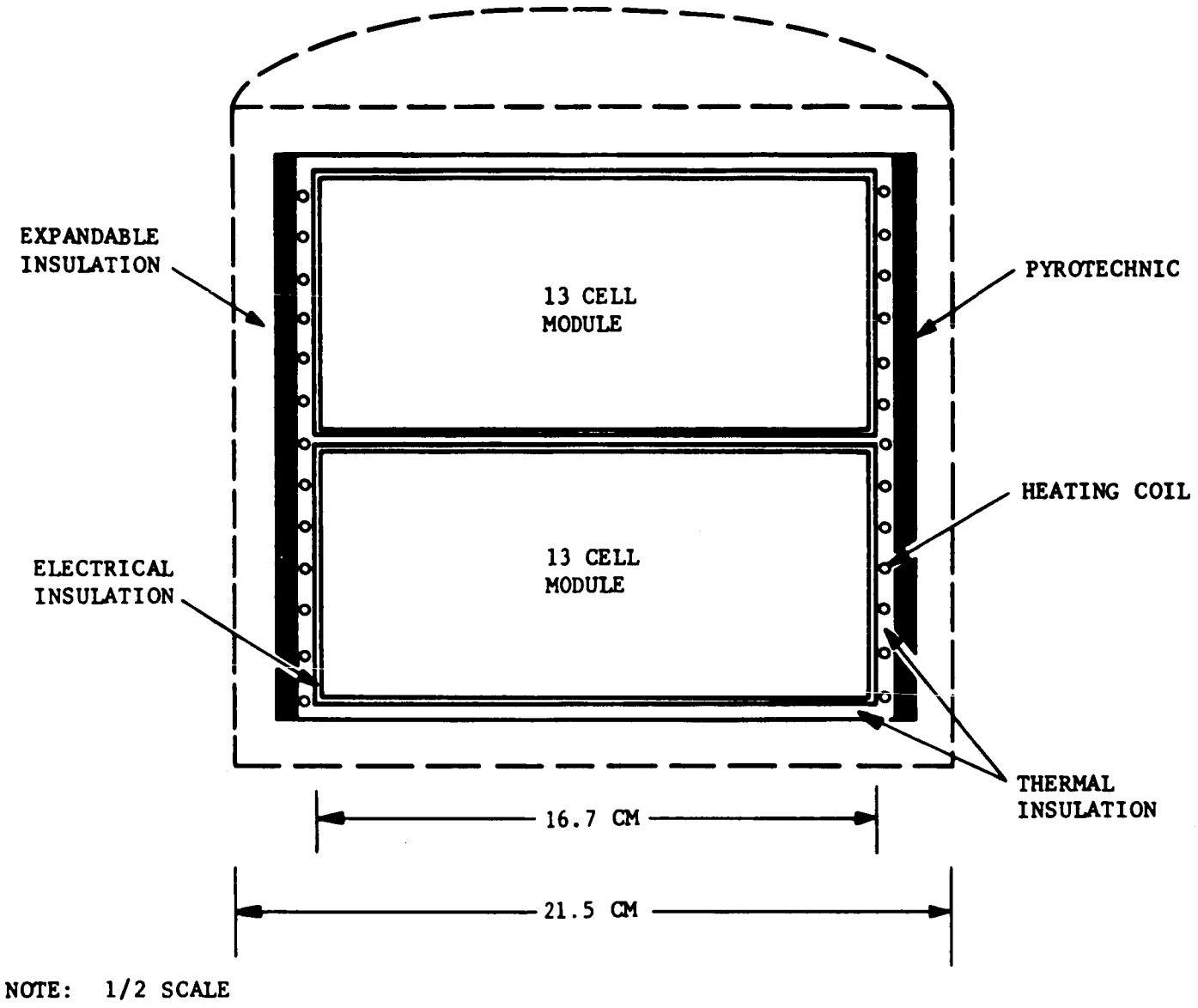

FIGURE 143. LONG DURATION THERMAL BATTERY PACKAGE

Another approach to the battery insulation selection problem is to develop an expandable insulation. This is envisioned to be a high density material present during launch and transit phase of the mission as a compact layer around the battery package. After landing, the material would be expandable, such as by foaming or some other process into a low density material of low thermal conductivity. Suitable materials for such an application are not presently known but their development should not be far beyond present technology. The external dashed line of Figure 143 illustrates the appearance of the package as surrounded by the unexpanded insulation. Figure 144 shows the appearance of the insulation after it has expanded.

Preference between the above two insulation concepts is not clear at this time. Both should be examined in some detail before a final choice for development is made.

6.4.5 FURTHER CONSIDERATIONS ON PYROTECHNIC MATERIALS

Data on pyrotechnic material used in estimation of battery package weight is that for an iron - $KClO_4$ composition conventionally used for such purposes. The heat release can be varied at will by adjustment of composition. The value of 500 cal/gm is used in the calculations.

The maximum heat release achievable with this material is about 1000 cal/gm. However, this is associated with very high combustion temperatures which impose considerable thermal shock on surrounding materials. It is also accompanied by considerable gassing which leads to foaming of the pyrotechnic. If means for accepting these effects can be found, substantial reduction in the pyrotechnic weight becomes possible through use of the full calorific value.

In terms of future developments, attention should be given to pyrotechnic compositions of higher calorific value. For example the reaction of $LiClO_4$ and boron is associated with a theoretical maximum heat release of 3000 cal/gm. In particular it would be desirable to develop compositions having low gas evolution, high calorific value and low ignition temperatures. The latter permits burning at a low temperature by removing the heat quickly as combustion occurs. This minimizes detrimental effects of high burning temperatures on surrounding structures.

6.4.6 TYPICAL CAPSULE INSTALLATION

Figure 145 shows a sketch of a typical thermal battery installation in the MFC payload sphere. Thermal insulation is provided around the battery to maintain the battery cell at an acceptable temperature during battery operation, and also to protect payload equipment from the heat generated by the battery. The weight optimization studies assume that the battery can be treated as an isolated component. The "optimum" thermal insulation

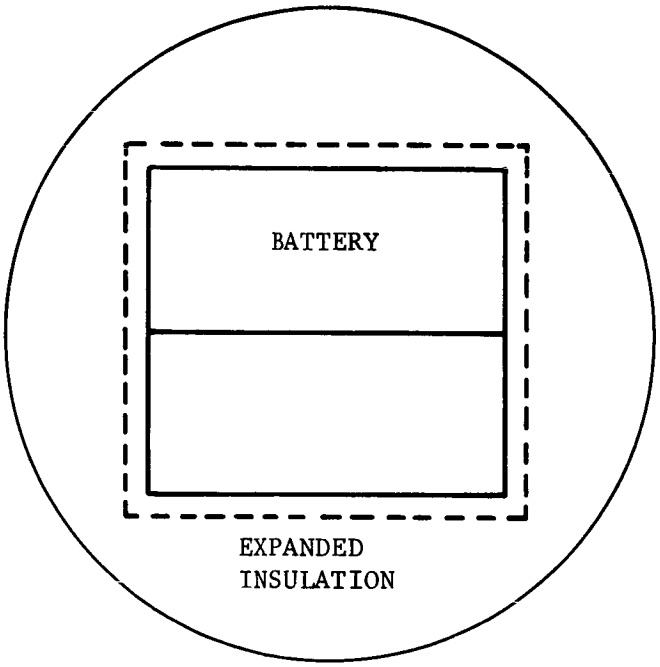

1/4 SCALE

R11188

FIGURE 144. THERMAL BATTERY WITH INSULATION EXPANDED

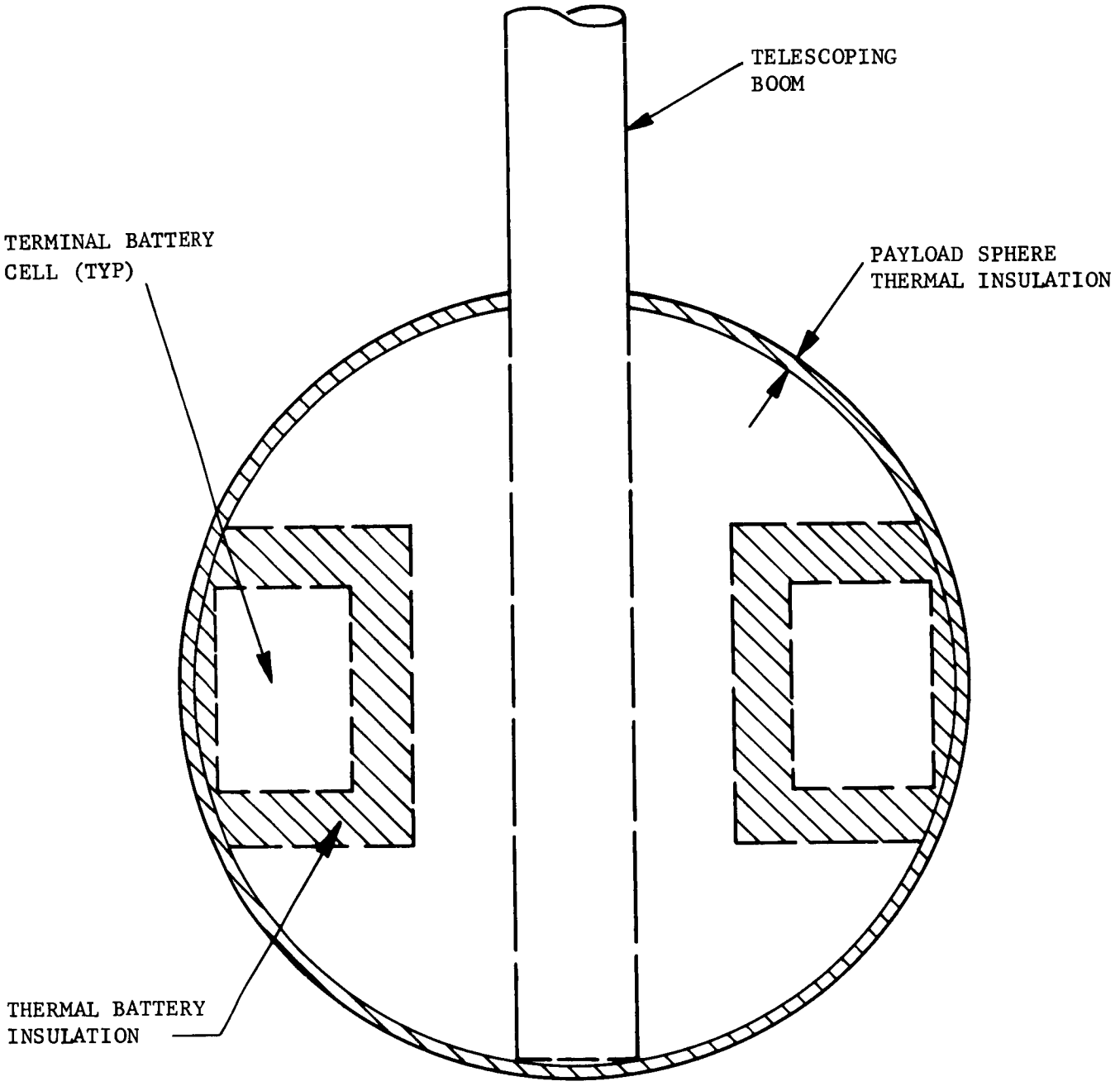

FIGURE 145. TYPICAL THERMAL BATTERY INSTALLATION IN MFC

R11208

thickness presented herein does not necessarily represent the optimum insulation thickness for a thermal battery installed in the MFC payload sphere. However, optimization studies for the installed battery system are beyond the scope of analysis.

Section 5.9 shows the desirability of providing a passive thermal control system employing thermal insulation and water boiloff/freezing subsystem. It is desirable in this design to provide a balance between payload sphere heat gains (from all sources) and heat losses to the Mars ambient surroundings. For the thermal battery installation shown in Figure 145, payload sphere heat gains result from two sources, payload internal power dissipation and thermal battery heat generation. Thus, when a thermal battery is employed, the payload sphere heat gains are increased over those for a conventional battery. In order to achieve a heat balance, the thermal insulation just inside the sphere outer wall must be correspondingly reduced in thickness.

A simplified thermal analysis can be performed if it is assumed that the thermal battery and internal power dissipation heat sources can be lumped together. The payload sphere heat loss analysis shown in Section 5.9.3 can then be utilized to determine the insulation thickness (uniform over the sphere surface) required to achieve a heat balance. For example, the mean heat generation for the "optimum" thermal battery design is 41 watts (continuous). The mean internal power dissipation for payload equipment is on the order of 15 to 30 watts (370 to 740 watt-hr/day). Thus, the total heat gains to the payload sphere are on the order of 56 to 71 watts. These heat gains correspond to insulation thicknesses of 0.42 and 0.33 inches, respectively, for an assumed payload to sphere surface temperature difference of 100 F, an insulation thermal conductivity of 0.01 Btu/ft hr F, and a sphere diameter of 1.5 feet. These thicknesses were deduced from Figures 124 and 108.

A proper thermal analysis of the thermal battery installation is relatively complicated when the effects of internal payload conduction as well as variable sphere outer surface temperature distributions are included in the analysis. The performance of such an analysis is beyond the scope of this tradeoff study.

6.4.7 LONG RANGE DEVELOPMENT PROGRAM

The concepts discussed in the previous sections are compatible with a development program of about 2 years duration. If a longer range program is conceivable, then significant advance in performance become attainable. Such a program should be particularly directed to achieving significant advances beyond present technology in four areas.

a. Higher Energy Electrodes. An increase in cell potential of about one volt is possible, for example by use of the Na - $CuCl_2$ electrochemical

system. Problems associated with containment of highly corrosive fused $CuCl_2$ must be solved.

b. Improvement in Separator Membranes. It is desirable to develop membrane materials showing decrease electrical resistance in terms of the passage of alkali metal ion, but improved selectivity in their permeability. Improvements in bonding and fabrication procedure to produce thinner and more durable membrane is also desired.

c. Improvements in Insulation. Develop materials and techniques for reducing heat losses with corresponding reductions in weight.

d. Pyrotechnic Materials. Development of materials of high calorific value and more attractable burning characteristics.

Additional effort will also be required in areas associated with optimizations in design, materials and methods of fabrication.

6.5 STATISTICAL ANALYSIS OF BALSA TESTS

Table 6.5-I is a summary of the data obtained from the various balsa tests conducted during the Ranger programs. The variables used in the ensuing discussion are defined as follows:

N - number test data

η - specific crush energy ft-lb/lb

ρ - balsa density lb/ft^3

a - η intercept

b - slope

σ_η^2 - variance in η

σ_ρ^2 - variance in ρ

$\sigma_{\eta\rho}^2$ - variance in η unexplained by the regression equation

σ_b^2 - variance in b

r^2 - coefficient of regression (percent total variance explained by regression equation)

$\hat{\sigma}^2$ - variance which as a result of its dependence upon η and/or ρ has N-1 or N-2 degrees of freedom

FORMULAS

General

$$\bar{X} \text{ (mean of X)} = \frac{\sum X}{N} \quad ; \quad \sigma_X^2 \text{ (variance of X)} = \frac{\sum X^2 - \bar{X}\sum X}{N}$$

Specific

$$a = \bar{\eta} - b\,\bar{\rho} \qquad b = \frac{N\sum \rho\eta - \sum\rho\sum\eta}{N\sum \rho^2 - \left(\sum \rho\right)^2}$$

TABLE 6.5-I

CALCULATIONS FOR STATISTICAL ANALYSIS OF BALSA WOOD

	N	$\bar{\rho}$	$\bar{\eta}$	$\Sigma \rho$	$\Sigma \rho^2$	$\Sigma \eta$	$\Sigma \eta^2$	$\Sigma \eta \rho$
May 18, 1960 LCB-004	3	11.5733	22,976	34.72	406.5582	68,930	1,585,010,404	795,342.58
June 3, 1960 LCB-010	5	RESULTS INVALID						
July 29, 1960* LCd-009	7	6.2842	20,645	43.99	277.6667	144,520	3,005,009,000	903,628.30
July 7, 1960	19	9.031	21,976	171.59	1,573.3273	417,538	9,481,704,502	3,759,182.47
July 29, 19 60	10	8.1334	16,259	81.334	662.1482	162,585	2,657,921,467	1,323,463.36
August 9, 1960	6	7.5085	13,055	45.051	338.7205	78,331	1,067,000,629	587,697.81
August 12, 1960	17	8.114	16,916	137.9387	1,151.6508	287,565	5,069,403,147	2,362,658.06
August 23, 1960	51	11.704	17,413	596.90	7,750.0	888,054	15,802,417,996	10,667,217.00
August 31, 1961	16	5.954	15,812	95.262	568.6690	252,985	4,082,587,921	1,510,589.83
September 20, 1961	20	6.325	15,973	126.509	804.3243	319,467	5,176,525,247	2,016,777.58
October 8, 1962 LCb-417	23	6.314	15,018	145.213	921.7252	345,426	5,271,995,528	2,191,547.72
	172	8.5975	17,241	1478.5077	14,454.7902	2,965,401	53,199,575,841	26,118,104.71

*Data taken from helicopter drop test

$$\hat{\sigma}_{\eta}^2 = \sigma_{\eta}^2 \frac{N}{N-1}$$

$$\sigma_{\eta\rho}^2 = \frac{\sum \eta^2 - a\sum \eta - b\sum \rho\eta}{N}$$

$$\hat{\sigma}_{\eta\rho}^2 = \sigma_{\eta\rho}^2 \frac{N}{N-2}$$

$$\sigma_b^2 = \frac{\hat{\sigma}_{\eta\rho}^2}{N\sigma_{\rho}^2}$$

$$r^2 = 1 - \frac{\hat{\sigma}_{\eta\rho}^2}{\hat{\sigma}_{n}^2}$$

Substituting the values from Table 6.5-I yields:

$\bar{\eta}$ = 17,241

$\bar{\rho}$ = 8.60

a = 14,150
b = 359.53
$\Big\}$ η = 14,150 + 360 ρ

$\hat{\sigma}_{\eta\rho}^2$ = 10,875,938, $\hat{\sigma}_{\eta\rho}$ = 3297

$\hat{\sigma}_{\eta}^2$ = 12,123,375, $\hat{\sigma}_{\eta}$ = 3482

r^2 = 5.32 percent

σ_{ρ}^2 = 10.128, σ_{ρ} = 3.18

$\hat{\sigma}_b^2$ = 6243, $\hat{\sigma}_b$ = 79

To obtain a statistical inference from the above information one can test the hypothesis that b = 360 against the alternative hypothesis that b = 0

(i.e., η is independent of ρ) with a level of confidence $\alpha = 0.005$

H: $b = 360$ $\bar{H}$: $b_o = 0$

$$b = b_o + t\hat{\sigma}_b$$

$$t = \frac{b - b_o}{\hat{\sigma}_b} = 4.54$$

The probability associated with a t value of 4.54 is less than 0.0005 and therefore the alternative hypothesis that b = 0 must be rejected.

Another way of stating this conclusion is that it is very unlikely (probability $<$0.0005) that a value of b = 0 could be obtained from a population with a mean of 360 and variance 79.

6.6 TRADE-OFF CURVES FOR IMPACT LIMITER DESIGN

The following eight graphs are auxiliary curves useful in establishing impact capability. Section 5.2.2 of this report describes and utilizes these curves.

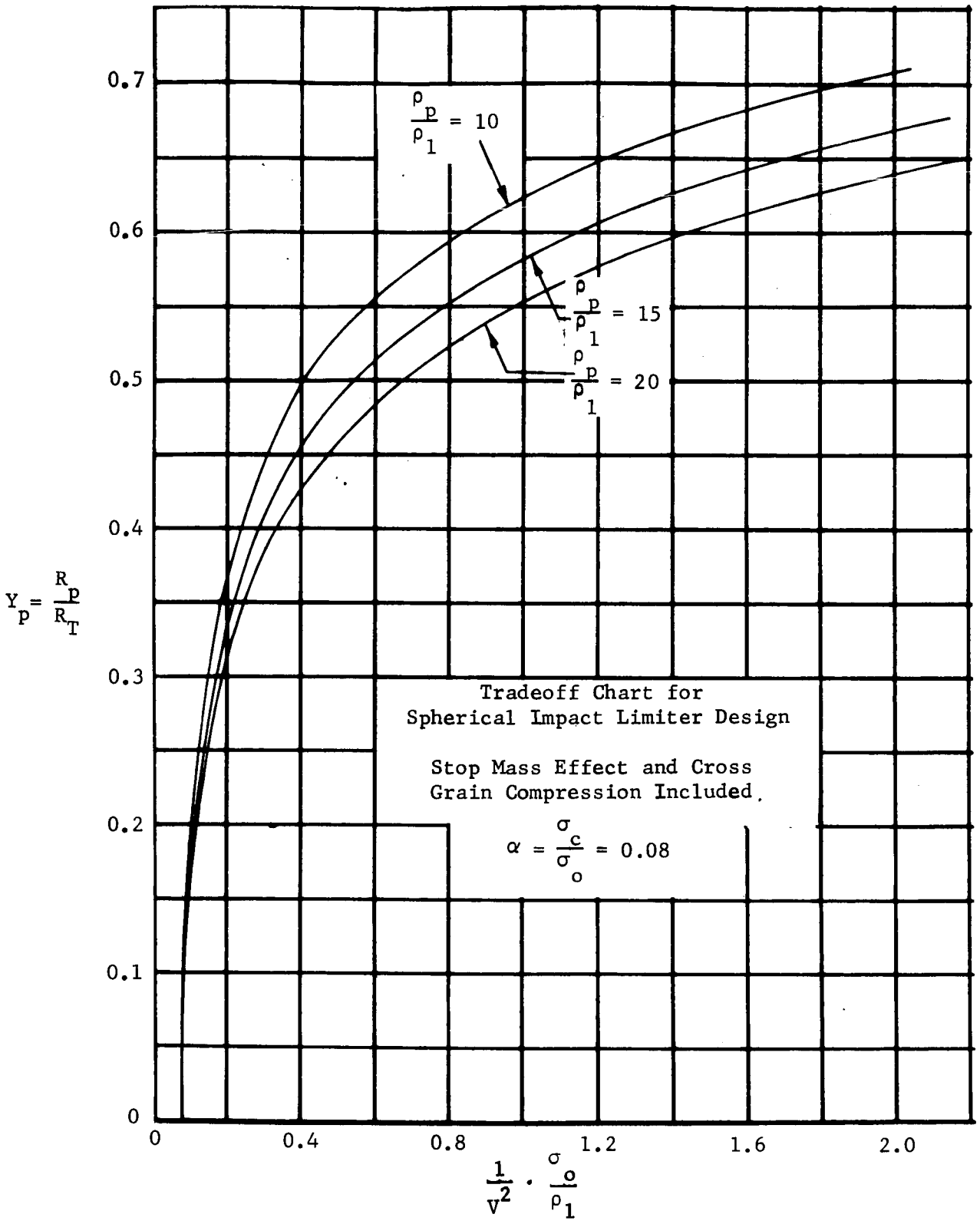
0.7
0.6
0.5
0.4
0.3
0.2
0.1
0
$Y_p = \frac{R_p}{R_T}$
$\frac{\rho_p}{\rho_1} = 10$
$\frac{\rho_p}{\rho_1} = 15$
$\frac{\rho_p}{\rho_1} = 20$
Tradeoff Chart for
Spherical Impact Limiter Design
Stop Mass Effect and Cross
Grain Compression Included.
$\alpha = \frac{\sigma_c}{\sigma_o} = 0.08$
0
0.4
0.8
1.2
1.6
2.0
$\frac{1}{V^2} \cdot \frac{\sigma_o}{\rho_1}$

FIGURE 146.

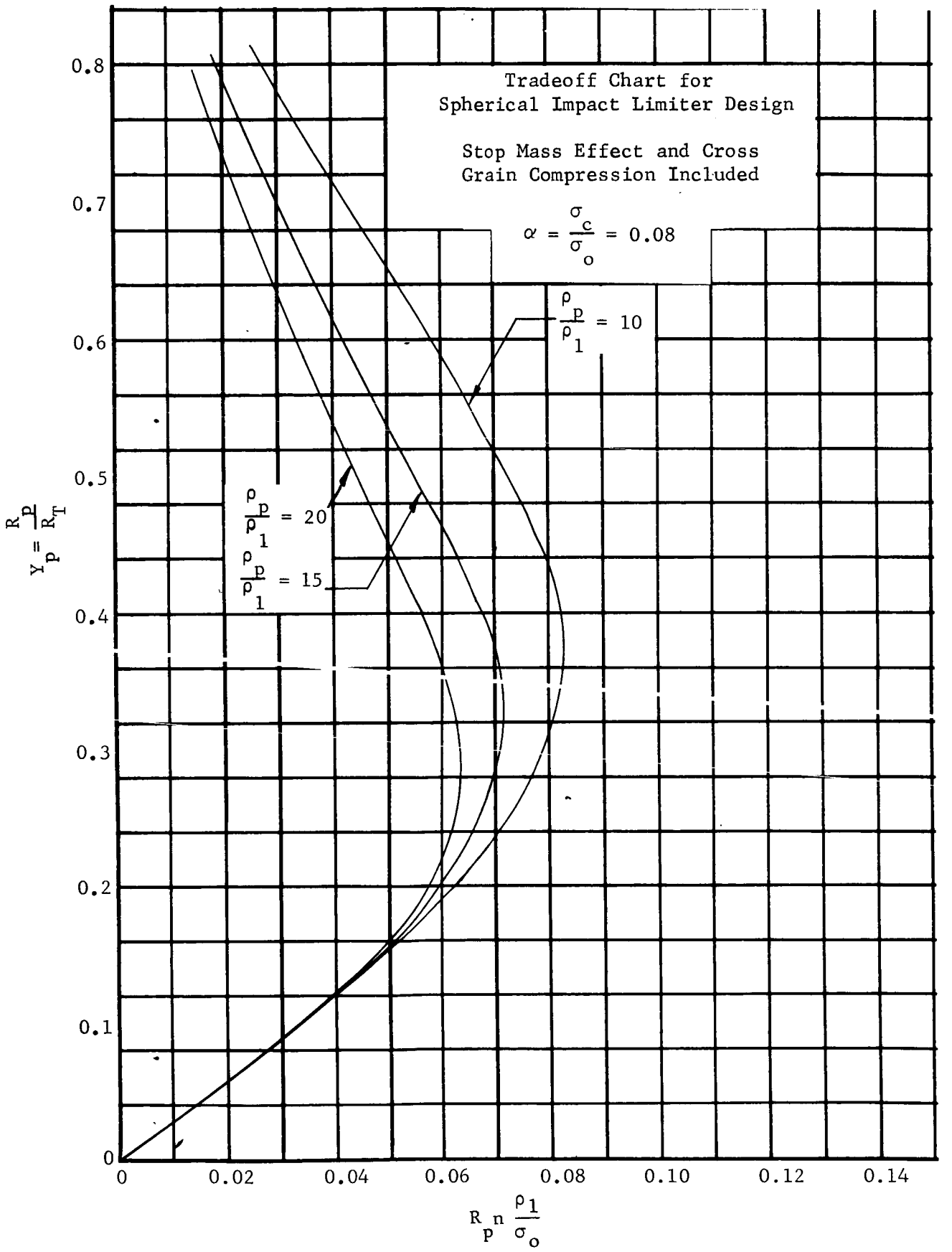
Tradeoff Chart for
Spherical Impact Limiter Design
Stop Mass Effect and Cross
Grain Compression Included
$\alpha = \frac{\sigma_c}{\sigma_o} = 0.08$
$\frac{\rho_p}{\rho_1} = 10$
$\frac{\rho_p}{\rho_1} = 20$
$\frac{\rho_p}{\rho_1} = 15$
$Y_p = \frac{R_p}{R_T}$
0.8
0.7
0.6
0.5
0.4
0.3
0.2
0.1
0
0
0.02
0.04
0.06
0.08
0.10
0.12
0.14
$R_p n \frac{\rho_1}{\sigma_o}$

FIGURE 147.

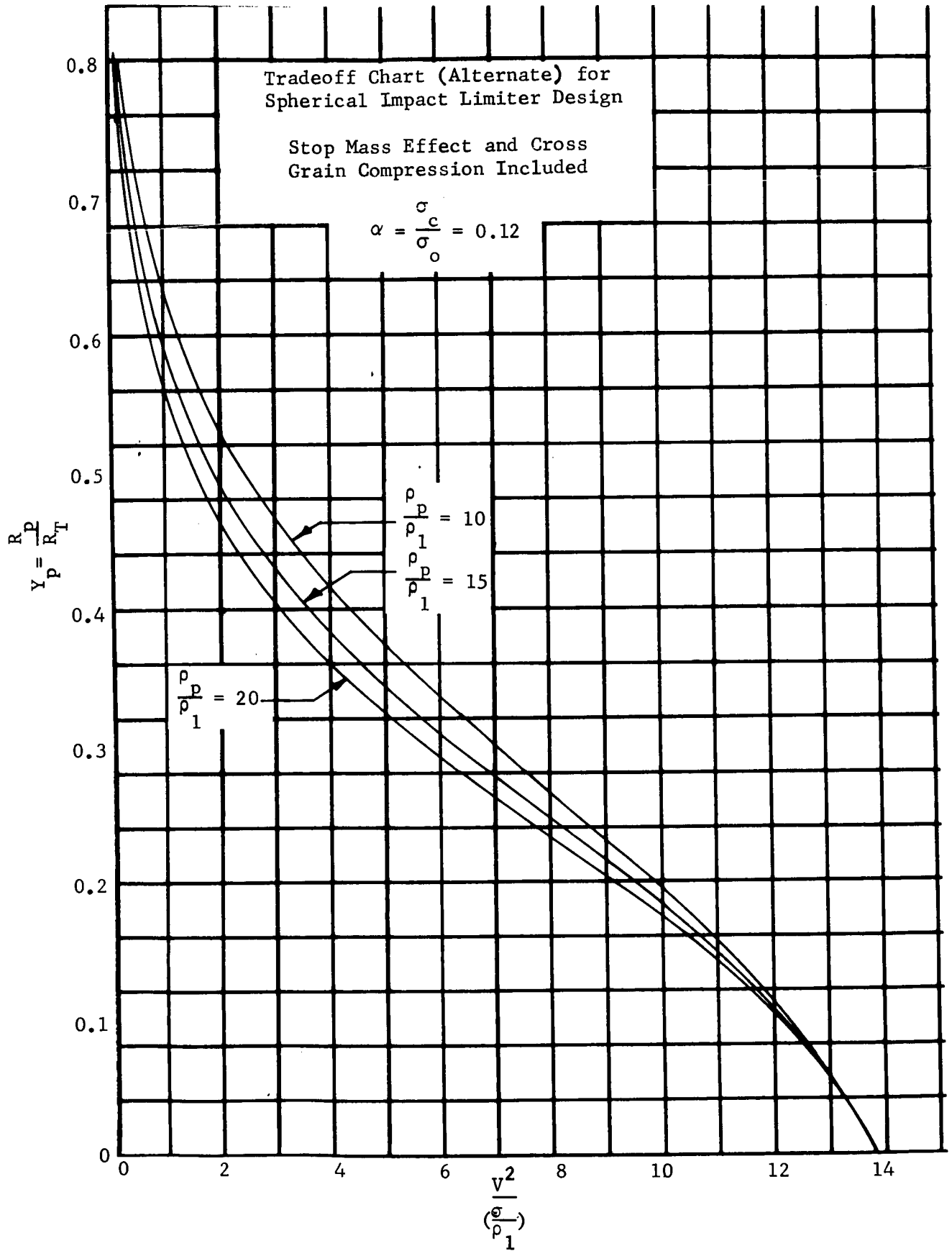
Tradeoff Chart (Alternate) for
Spherical Impact Limiter Design
Stop Mass Effect and Cross
Grain Compression Included
$\alpha = \frac{\sigma_c}{\sigma_o} = 0.12$
$\frac{\rho_p}{\rho_1} = 10$
$\frac{\rho_p}{\rho_1} = 15$
$\frac{\rho_p}{\rho_1} = 20$
$Y_p = \frac{R_p}{R_T}$
$\frac{V^2}{(\frac{\sigma}{\rho_1})}$
0
0.1
0.2
0.3
0.4
0.5
0.6
0.7
0.8
0
2
4
6
8
10
12
14

FIGURE 148.

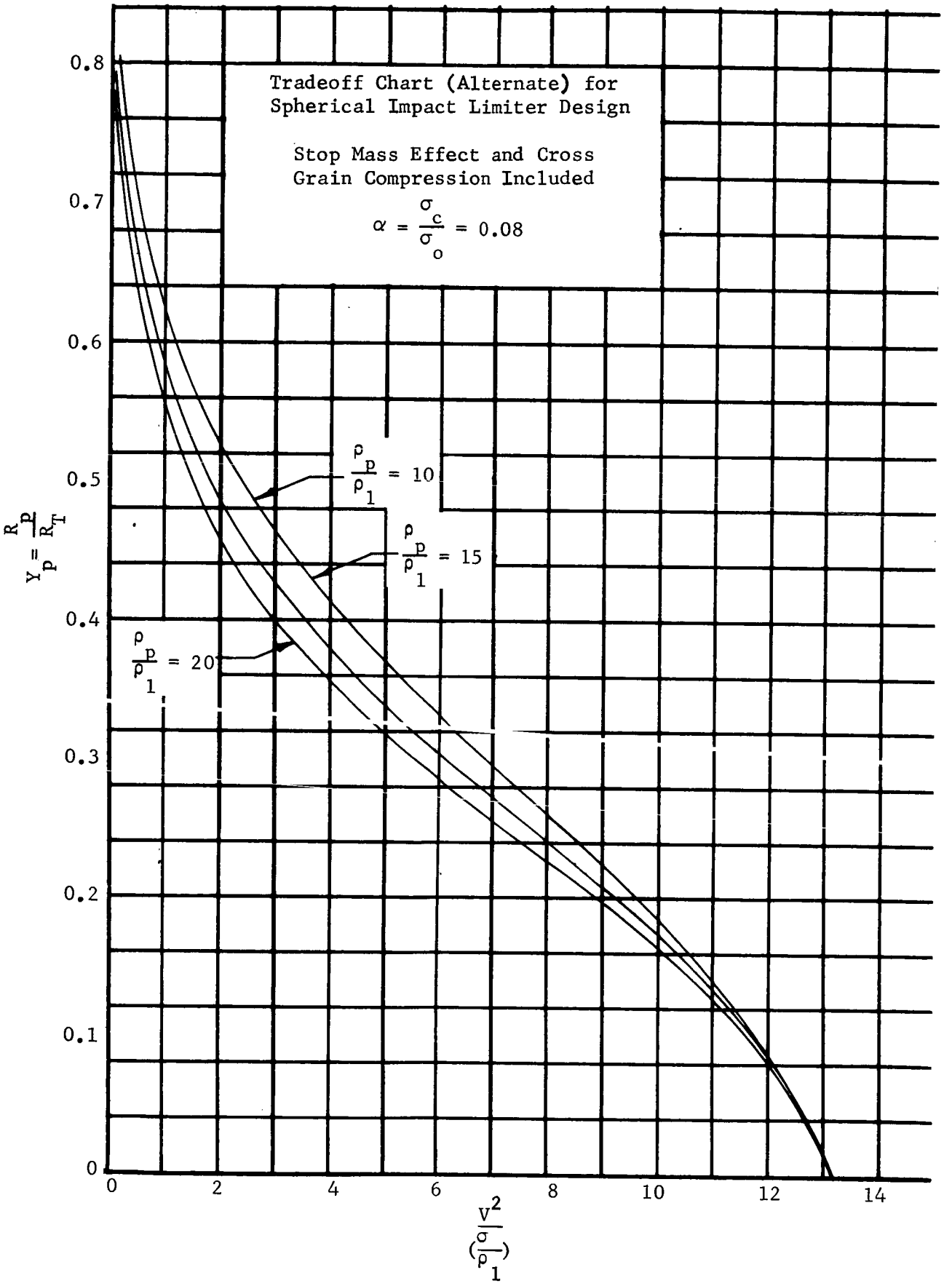
Tradeoff Chart (Alternate) for
Spherical Impact Limiter Design
Stop Mass Effect and Cross
Grain Compression Included
$\alpha = \frac{\sigma_c}{\sigma_o} = 0.08$
$\frac{\rho_p}{\rho_1} = 10$
$\frac{\rho_p}{\rho_1} = 15$
$\frac{\rho_p}{\rho_1} = 20$
$Y = \frac{R_p}{R_T}$
$\frac{V^2}{(\frac{\sigma}{\rho_1})}$
0
0.1
0.2
0.3
0.4
0.5
0.6
0.7
0.8
0
2
4
6
8
10
12
14

FIGURE 149.

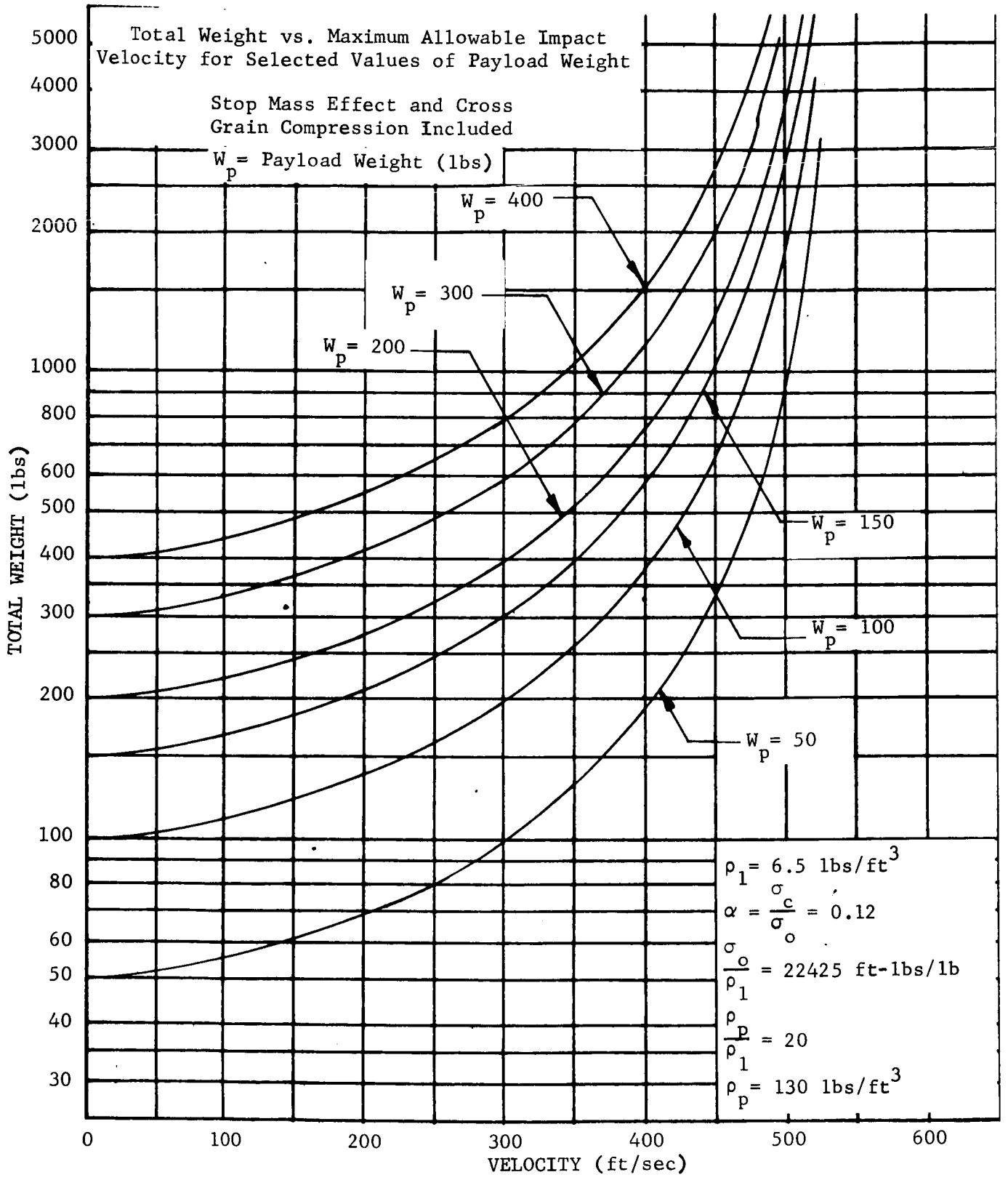
Total Weight vs. Maximum Allowable Impact Velocity for Selected Values of Payload Weight
Stop Mass Effect and Cross Grain Compression Included
W_p = Payload Weight (lbs)
W_p = 400
W_p = 300
W_p = 200
W_p = 150
W_p = 100
W_p = 50
TOTAL WEIGHT (lbs)
5000
4000
3000
2000
1000
800
600
500
400
300
200
100
80
60
50
40
30
0
100
200
300
400
500
600
VELOCITY (ft/sec)
ρ_1 = 6.5 lbs/ft^3
$\alpha = \frac{\sigma_c'}{\sigma_o} = 0.12$
$\frac{\sigma_o}{\rho_1}$ = 22425 ft-lbs/lb
$\frac{\rho_p}{\rho_1}$ = 20
ρ_p = 130 lbs/ft^3

FIGURE 150.

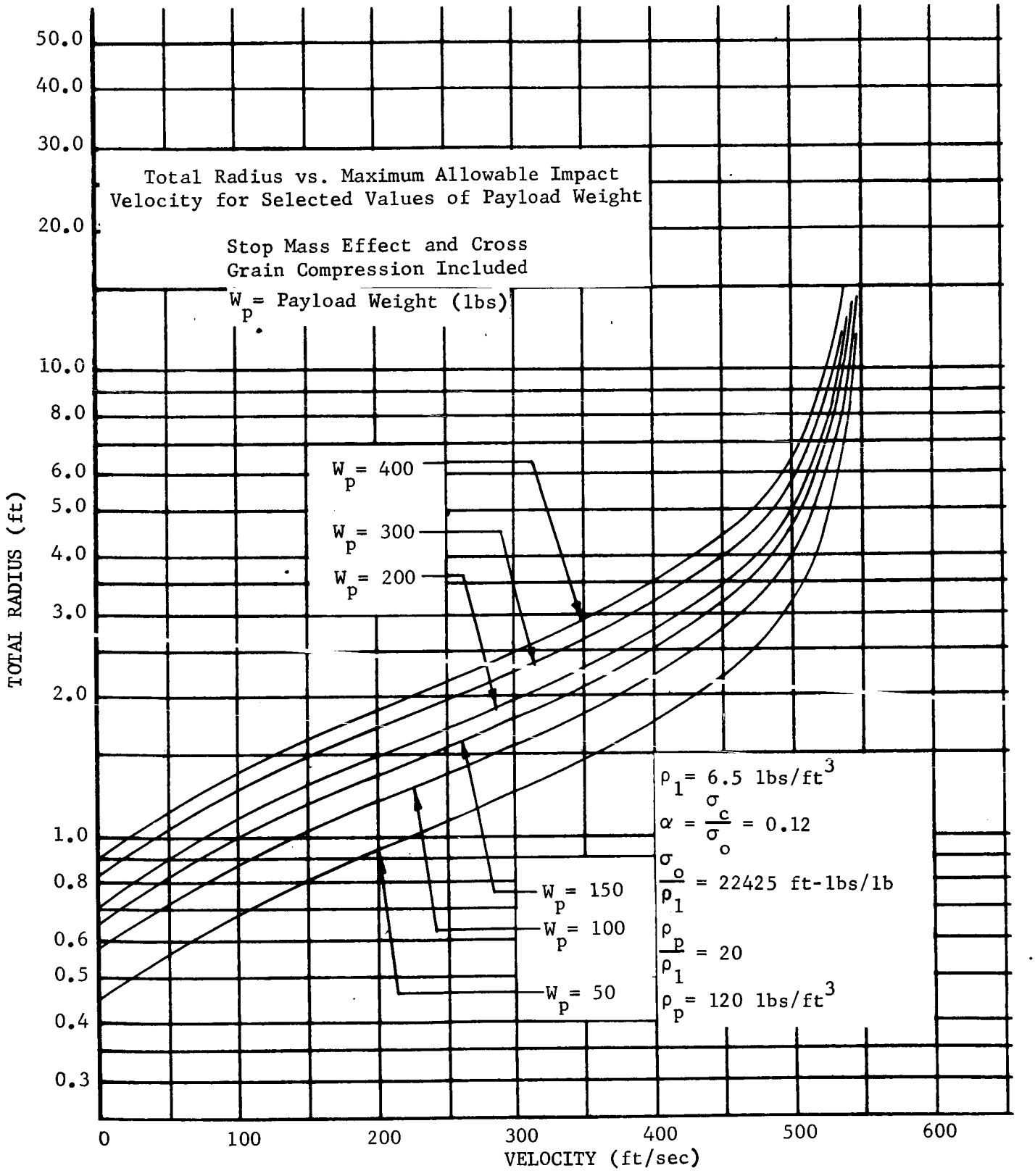
Total Radius vs. Maximum Allowable Impact Velocity for Selected Values of Payload Weight
Stop Mass Effect and Cross Grain Compression Included
W_p = Payload Weight (lbs)
TOTAL RADIUS (ft)
VELOCITY (ft/sec)
50.0
40.0
30.0
20.0
10.0
8.0
6.0
5.0
4.0
3.0
2.0
1.0
0.8
0.6
0.5
0.4
0.3
0
100
200
300
400
500
600
W_p = 400
W_p = 300
W_p = 200
W_p = 150
W_p = 100
W_p = 50
ρ_1 = 6.5 lbs/ft^3
$\alpha = \frac{\sigma_c}{\sigma_o}$ = 0.12
$\frac{\sigma_o}{\rho_1}$ = 22425 ft-lbs/lb
$\frac{\rho_p}{\rho_1}$ = 20
ρ_p = 120 lbs/ft^3

FIGURE 151.

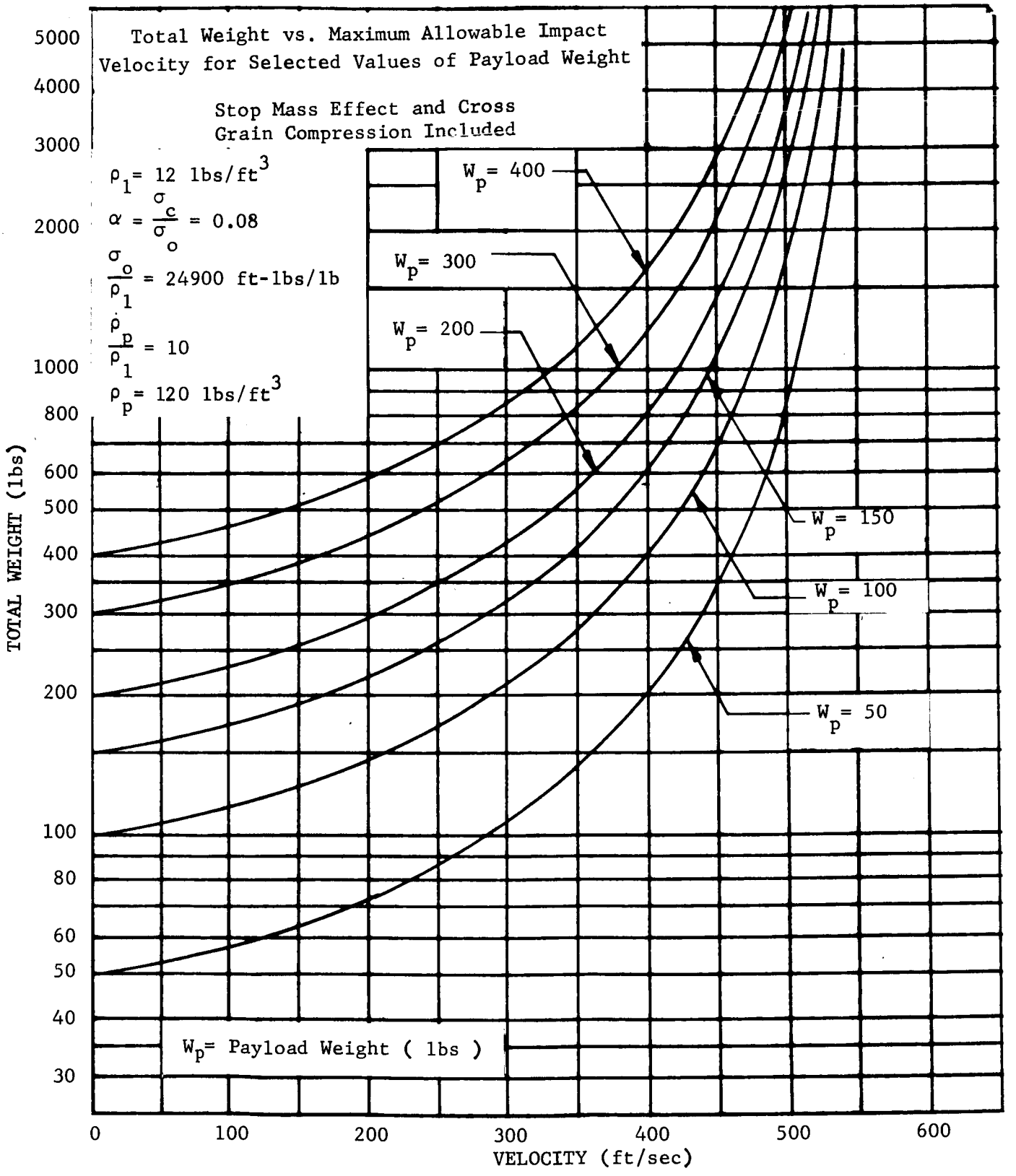
Total Weight vs. Maximum Allowable Impact Velocity for Selected Values of Payload Weight
Stop Mass Effect and Cross Grain Compression Included
ρ_1= 12 lbs/ft^3
$\alpha = \frac{\sigma_c}{\sigma_o}$ = 0.08
$\frac{\sigma_o}{\rho_1}$ = 24900 ft-lbs/lb
$\frac{\rho_p}{\rho_1}$ = 10
ρ_p= 120 lbs/ft^3
W_p= 400
W_p= 300
W_p= 200
W_p= 150
W_p= 100
W_p= 50
W_p= Payload Weight (lbs)
TOTAL WEIGHT (lbs)
VELOCITY (ft/sec)
5000
4000
3000
2000
1000
800
600
500
400
300
200
100
80
60
50
40
30
0
100
200
300
400
500
600

FIGURE 152.

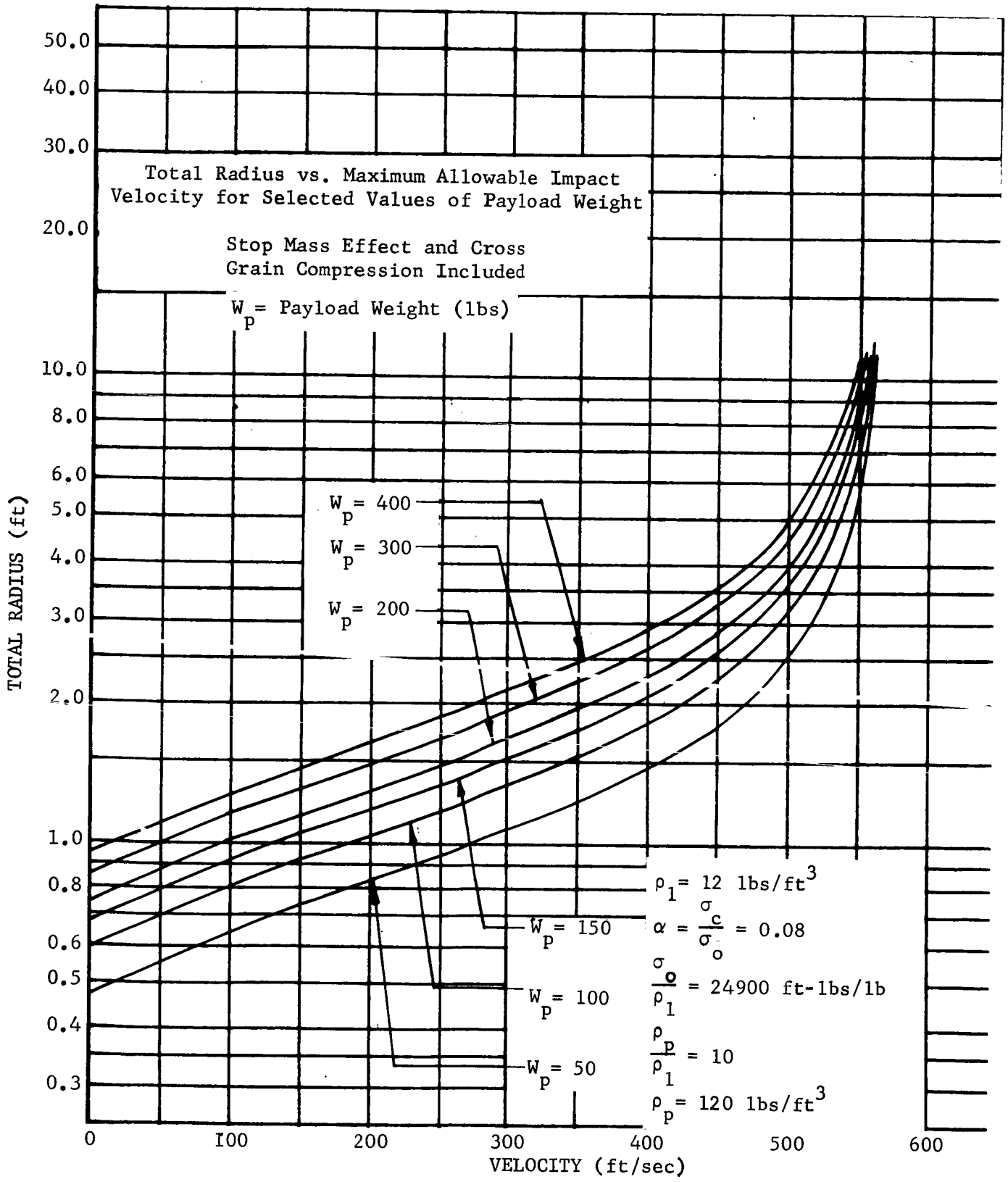
Total Radius vs. Maximum Allowable Impact Velocity for Selected Values of Payload Weight
Stop Mass Effect and Cross Grain Compression Included
W_p = Payload Weight (lbs)
TOTAL RADIUS (ft)
VELOCITY (ft/sec)
50.0
40.0
30.0
20.0
10.0
8.0
6.0
5.0
4.0
3.0
2.0
1.0
0.8
0.6
0.5
0.4
0.3
0
100
200
300
400
500
600
W_p = 400
W_p = 300
W_p = 200
W_p = 150
W_p = 100
W_p = 50
ρ_1 = 12 lbs/ft^3
$\alpha = \frac{\sigma_c}{\sigma_o} = 0.08$
$\frac{\sigma_o}{\rho_1}$ = 24900 ft-lbs/lb
$\frac{\rho_p}{\rho_1} = 10$
ρ_p = 120 lbs/ft^3

FIGURE 153.